



THE UNIVERSITY  
*of* ADELAIDE

# Studies of the MLT/I using Multistatic Meteor Radar

Andrew John Spargo

Thesis submitted for the degree of  
Doctor of Philosophy  
at  
The University of Adelaide  
Faculty of Sciences  
School of Physical Sciences  
Department of Physics

Supervisors:  
Em. Prof. Iain M. Reid  
Assoc. Prof. Andrew D. MacKinnon

May 2021

# Thesis declaration

I certify that this work contains no material which has been accepted for the award of any other degree or diploma in my name, in any university or other tertiary institution and, to the best of my knowledge and belief, contains no material previously published or written by another person, except where due reference has been made in the text. In addition, I certify that no part of this work will, in the future, be used in a submission in my name, for any other degree or diploma in any university or other tertiary institution without the prior approval of the University of Adelaide and where applicable, any partner institution responsible for the joint-award of this degree.

I acknowledge that the copyright of published works contained within this thesis resides with the copyright holder(s) of those works.

I also give permission for the digital version of my thesis to be made available on the web, via the University's digital research repository, the Library Search and also through web search engines, unless permission has been granted by the University to restrict access for a period of time.

I acknowledge the support I have received for my research through the provision of an Australian Government Research Training Program Scholarship.

Signed:

Andrew John Spargo

May 2021



# Abstract

This thesis applies a multistatic meteor radar to an investigation of the dynamics of the mesosphere lower thermosphere/ionosphere (MLT/I;  $\sim 60\text{-}110$  km altitude). The main radar used in the study operates at 55 MHz and is in the vicinity of Adelaide, South Australia, consisting of a monostatic radar at the Buckland Park field site ( $34.6^\circ\text{S}$ ,  $138.5^\circ\text{E}$ ) and a bistatic receiver located about 55 km south-east at a site in the Adelaide Hills ( $35.1^\circ\text{S}$ ,  $138.8^\circ\text{E}$ ). The areas of investigation pertaining to MLT/I dynamics include assessing the ability of a multistatic meteor radar to measure the vertical flux of horizontal momentum and studying the interaction between gravity waves and tidal effects. The thesis also presents a novel phase calibration technique for meteor radars, based on the use of civilian aircraft.

The assessment of this radar's ability to measure MLT/I momentum fluxes demonstrated that a relative uncertainty of about 75% can be expected for a monostatic configuration, assuming a flux magnitude of  $\sim 20 \text{ m}^2\text{s}^{-2}$ , a single day of integration, and a gravity wave field synthesized from a realistic spectral model. The multistatic configuration with a single bistatic receiver is shown to yield a relative uncertainty of about 65% under the same conditions. It is suggested that the increase in precision can be attributed entirely to the increase in the number of meteor detections associated with the combined monostatic and bistatic receivers, rather than due to the existence of a more favourable distribution of Bragg vectors arising from the receiver separation.

A case study of winds around the autumnal equinox of 2018 revealed large modulations in diurnal tidal amplitudes, with peak component diurnal tide amplitudes of  $\sim 50 \text{ ms}^{-1}$  and peak zonal wind velocities of  $\sim 140 \text{ ms}^{-1}$ . In the context of the need to verify the accuracy of momentum flux estimates from the radar, this motivated an investigation into the role momentum transport from gravity wave breaking played in modulating the tidal amplitudes. The investigation showed that while the observed gravity wave forcing exhibited a complex relationship with the tidal winds, the components of the forcing were generally seen to be approximately out of phase with the tidal winds above al-

titudes of  $\sim 88$  km. Additionally, no clear phase relationship between the tides and gravity wave forcing was observed below  $\sim 88$  km.

Following the case study, the altitude and angle-of-arrival (AOA) errors and reduced meteor detection rates associated with suspected receiver phase calibration errors motivated the development of an alternative phase calibration technique. The technique developed was based on the use of echoes from civilian aircraft with known positions. Approximately two weeks worth of aircraft detections with the radar and a 1090 MHz Automatic Dependent Surveillance Broadcast receiver (used to receive aircraft position information) was acquired during November 2019. By taking into account the implied phase correction variability with AOA using a beamforming approach, it was shown that the aircraft-based corrections yielded an equal or smaller meteor height distribution width than the conventionally used empirical phase calibration technique. Assuming that a smaller height distribution width equates to smaller average height estimation errors, this was taken to mean that the aircraft-based approach outperformed the empirical one.

# Acknowledgements

I feel privileged to have worked with so many great people during my PhD candidature. These people deserve all my thanks for the role they've played in shaping me as a person and researcher, and for all the help they've provided along the way.

I'd firstly like to thank my principal supervisor, as well as mentor and manager over the last eight years, Em. Prof. Iain Reid. Iain has patiently provided so much advice and encouragement to me during this time, and the many inspiring technical discussions I've had with him have instilled in me a passion for scientific research and curiosity about nature. Moreover, Iain has shown a lot of empathy while guiding me through some challenging times during my research career. Thank you Iain.

I thank my co-supervisor Assoc. Prof. Andrew MacKinnon, with whom I have been associated since 2009. I am grateful to Andrew for encouraging me to undertake a summer scholarship with the group back in 2011, and for mentoring me through all of the years that followed. From day one I've been amazed by Andrew's humble expertise on radar, electronics, and hardware/software fault-finding abilities, and am grateful to have picked up as much as I have from him over the years. His charismatic, upbeat attitude to life and his endless supply of hilarious stories have also made him incredibly fun to work with.

I'd next like to thank Chris Adami, who has been in every way except on paper a supervisor and mentor to me over the last five years. Chris has not only provided a colossal amount of technical support and oversight to my PhD work, but has been a great friend of mine during this time—always happy to head out for a coffee or dinner at a moment's notice. I will forever appreciate his efforts to challenge my ways of thinking, to come up with innovative solutions to problems that had been pestering me, and to console me when I was having a hard time with something personally. Chris also provided me a great deal of support during preparations for my trip to Kühlungsborn during 2019, and was kind enough to help me settle in when I arrived as well. Having that kind of support when I arrived in a place in which I couldn't speak the language

was everything I could have wished for. Thank you Chris—I look forward to continuing to keep in touch with you in the future.

I'd like to thank Assoc. Prof. David Holdsworth for the role he's played in my development as a researcher over the last five years through the projects he's involved me in and the guidance he's given me. The passion and determination David has for his work and the vast contributions he has made to atmospheric radar signal analysis during his career has been an ongoing source of inspiration for me. Furthermore, I'm grateful for the initial inspiration and encouragement he gave me to explore the aircraft-based phase calibration method.

I owe a great deal of thanks to Prof. Koki Chau for all he has done for me during my PhD candidature. As well as having always been willing to give advice on anything related to radar, I thank Koki for initially suggesting that I visit the IAP in Kühlungsborn, and for providing amazing hospitality when I was over. Best of all, Koki has been the most fun-loving and adventurous of scientists I have ever known, all the while displaying an inspiring level of humbleness about his capabilities as a scientist. It's been a privilege to have worked with him. On this note, I would also like to thank all of those that supported me during my trip to Kühlungsborn and made my stay all the more enjoyable—which include Dr. Ralph Latteck, Dr. Toralf Renkwitz, Dr. Dimitry Pokhotelov, Dr. Marius Zecha, Dr. Gunter Stober, Matthias Clahsen, Hari Charuvil, Juli Jaen, Dr. Maosheng He and Dr. Fede Conte.

I'd like to thank the team at Atrad Pty. Ltd. for the technical support they provided me during my PhD, and also for having me on their team for several months to work on a number of projects. In particular, Richard Mayo, Dr. Jonathan Woithe and Gary Jonas gave up much of their time to guide me, and I really appreciate this.

I'd also like to thank all the students of the "SnAP" group whom over the years I've had great discussions (/arguments) with, ridden bikes with, played board games with, done rogaines with, attempted to surf with, watched our Bae's amazing performance on Survivor 2019 with, failed at completing Escape Rooms with, put up with an unrelenting barrage of puns from (you know who you are!), and inadvertently left pants in the office of (my apologies). These include Tom Chambers, Simon Curtis, Dani Edwards, Dan Field, Baden Gilbert, Andy Heitmann, Jack Moran and Lenard Pederick. I have so many cherished memories of the activities we've done together as a group, and am so grateful for having you all around during some of the rough times of postgrad life. I couldn't have pushed myself through it without you. Thanks guys.

Other members and visitors of the SnAP group and Physics Department I'd like to thank for the great discussions and/or the guidance/help they've provided me over the years include Dr. Stuart Anderson, Dr. Manny Cervera, Dr. Bron Dolman, Assoc. Prof. Murray Hamilton, Dr. Trevor Harris, Dr. Mike Hatch, Dr. David Neudegg, Ramona Rogers, Em. Prof. Bob Vincent, Dr. Bruce Ward, Dr. Wen Yi and Dr. Joel Younger.

I thank Michelle, Michael, Luke, Oliver, Nanna, Nonna and the late Gramps, Nonno and Uncle Dino for the many wonderful and memorable family times over the years.

Finally, I would like to thank my wonderful parents, John and Agnese, for everything. They have been encouraging me to get out there and fulfil my dreams since the year dot, and have provided a level of support and guidance to me that dedicating this thesis to them is the least I could do. I cannot express in words how grateful I am, nor can I possibly hope to repay them for all they have done for me. It is my aim to do all I can to pass on to others the kindness and generosity they have given to me.

# Contents

<b>1</b>	<b>Introduction</b>	<b>1</b>
1.1	The MLT/I and the effects of atmospheric waves . . . . .	1
1.2	Radar measurements of MLT/I-region wind covariances . . . . .	9
1.3	Scope of thesis . . . . .	14
<b>2</b>	<b>Meteors and all-sky interferometric meteor radar</b>	<b>16</b>
2.1	Meteors and their sources . . . . .	16
2.2	Radar echoes from meteor trails . . . . .	18
2.2.1	Different echo types . . . . .	18
2.2.2	Backscatter from underdense meteors . . . . .	19
2.2.3	Forward scatter from underdense meteors . . . . .	22
2.2.4	Altitude distribution . . . . .	24
2.3	Meteor radars used in this study . . . . .	25
2.4	Interferometric meteor radar operation . . . . .	27
2.4.1	Signal transmission . . . . .	28
2.4.2	Signal reception . . . . .	29
2.5	Meteor echo signal processing . . . . .	30
2.5.1	Phase difference estimation . . . . .	31
2.5.2	Radial velocity estimation . . . . .	32
2.6	Angle-of-arrival estimation . . . . .	33
2.6.1	Adapted Jones method . . . . .	33
2.6.2	Alternative approaches . . . . .	35
2.7	Position estimation using the WGS-84 ellipsoid . . . . .	36
2.8	Wind velocity estimation . . . . .	38
2.9	Interferometric meteor radar phase calibration . . . . .	41
2.10	Summary . . . . .	43

---

<b>3</b>	<b>Simulation of meteor radar covariance estimation</b>	<b>45</b>
3.1	Overview of uncertainty estimates in similar studies . . . . .	46
3.2	Simulation description . . . . .	50
3.2.1	Meteor position and detection rate specification . . . . .	51
3.2.2	Wind field specification . . . . .	54
3.2.3	Receiver time series generation . . . . .	58
3.2.4	Parameter estimation . . . . .	60
3.2.5	Removal of background wind and tides . . . . .	60
3.2.6	Covariance estimation . . . . .	61
3.2.7	“Truth value” of the simulated covariances . . . . .	62
3.3	Simulation results . . . . .	63
3.3.1	Spectrum of gravity waves . . . . .	63
3.3.2	Monochromatic gravity wave . . . . .	66
3.3.3	Outlier rejection criteria performance . . . . .	67
3.4	Discussion . . . . .	69
3.5	Suggestions for future work . . . . .	72
3.6	Summary and conclusions . . . . .	73
<b>4</b>	<b>Observations of gravity-wave–tidal interaction</b>	<b>75</b>
4.1	Gravity-wave–tidal interactions in the mesosphere . . . . .	75
4.2	Data set attributes and analysis approach . . . . .	79
4.2.1	High-pass filtering using the wavelet transform . . . . .	81
4.2.2	Density estimation . . . . .	83
4.3	Results . . . . .	85
4.3.1	Covariances across the winter season . . . . .	86
4.3.2	Observed gravity-wave–tidal interaction . . . . .	91
4.4	Discussion . . . . .	93
4.4.1	Observed gravity-wave–tidal interaction . . . . .	93
4.4.2	Issues with applying the uncertainties . . . . .	96
4.4.3	Effects of tides and planetary waves on covariance estimates . . . . .	98
4.5	Summary and conclusions . . . . .	99
<b>5</b>	<b>Meteor radar phase calibration using aircraft echoes</b>	<b>100</b>
5.1	Radar phase calibration methods . . . . .	101
5.2	Overview of aircraft-based phase calibration approach . . . . .	106

---

5.3	Aircraft location retrieval . . . . .	106
5.3.1	Antenna, SDR receiver and signal decoding . . . . .	109
5.3.2	Sample aircraft position distributions . . . . .	110
5.4	Phase correction estimation scheme . . . . .	111
5.4.1	Selection of “candidate” aircraft transits . . . . .	111
5.4.2	Interpolation of aircraft positions . . . . .	112
5.4.3	Extraction of aircraft echoes from the radar data . . . . .	113
5.4.4	Parameter estimation . . . . .	113
5.4.5	Phase correction estimation . . . . .	114
5.4.6	Removal of possible aircraft timing errors . . . . .	115
5.4.7	Processing applied to phase correction estimates . . . . .	117
5.5	Example aircraft phase calibration candidates . . . . .	118
5.6	Phase correction estimates . . . . .	126
5.7	Application of phase corrections . . . . .	128
5.8	Examples of phase-corrected results . . . . .	132
5.8.1	Buckland Park receiver . . . . .	133
5.8.2	Mylor receiver . . . . .	133
5.9	Discussion and recommendations for future work . . . . .	139
5.10	Summary . . . . .	144
<b>6</b>	<b>Aircraft-derived phase corrections for IAP receivers</b>	<b>146</b>
6.1	Experiment configuration . . . . .	146
6.2	Phase corrections . . . . .	150
6.3	Sample phase correction candidates . . . . .	151
6.4	Recommendations for future work . . . . .	154
<b>7</b>	<b>Conclusion</b>	<b>155</b>
7.1	Thesis summary and conclusions . . . . .	155
7.2	Suggestions for future work . . . . .	159
<b>A</b>	<b>Frequency-domain phase calibration of Buckland Park ST radar data</b>	<b>161</b>
A.1	Introduction . . . . .	161
A.2	Experiment configuration . . . . .	163
A.3	Results and conclusions . . . . .	164



---

<b>B</b>	<b>WGS-84 ellipsoid coordinate transformations</b>	<b>166</b>
B.1	WGS-84 ellipsoid parameters . . . . .	166
B.2	Range-AOA $\leftrightarrow$ ENU (East-North-Up) . . . . .	167
B.3	ENU $\leftrightarrow$ ECEF . . . . .	167
B.4	Geodetic $\leftrightarrow$ ECEF (Earth-centred, Earth-fixed) . . . . .	168
B.5	Geodetic $\leftrightarrow$ Transverse Mercator . . . . .	169
<b>C</b>	<b>Publication: Radio Sci., 55, e2019RS006873, 2020</b>	<b>172</b>
<b>D</b>	<b>Publication: Atmos. Meas. Tech., 12, 4791-4812, 2019</b>	<b>192</b>
<b>E</b>	<b>Publication: Earth, Planets and Space, 70:129, 2018</b>	<b>215</b>
<b>F</b>	<b>Publication: Ann. Geophys., 35, 733-750, 2017</b>	<b>231</b>
<b>G</b>	<b>Publication: Ann. Geophys., 35, 567-582, 2017</b>	<b>250</b>
	<b>References</b>	<b>267</b>

# List of Figures

1.1	Atmospheric temperature/density profile . . . . .	2
1.2	WACCM3 temperatures . . . . .	3
1.3	WACCM3 zonal winds . . . . .	5
1.4	Covariance estimation geometry . . . . .	10
2.1	Examples of underdense meteor echoes . . . . .	19
2.2	Meteor detection geometry . . . . .	22
2.3	Davis meteor peak heights for 55 and 33 MHz . . . . .	24
2.4	Locations of Adelaide-based meteor radars . . . . .	25
2.5	Photograph of the Mylor array . . . . .	25
2.6	Photograph of a receiver antenna at Mylor . . . . .	26
2.7	Typical results from the BP and Mylor systems . . . . .	27
2.8	Layout of the 55 MHz BP meteor radar . . . . .	29
2.9	Simulated cross correlation function amplitude/phase . . . . .	32
2.10	Meteor radar interferometer . . . . .	33
2.11	Altitude error arising from assumption of locally spherical Earth . . . . .	37
2.12	Error in direction cosines arising from assumption of a planar Earth . . . . .	39
2.13	Simulation of AOA errors . . . . .	40
2.14	Errors associated with the Holdsworth et al. [2004b] phase calibration technique . . . . .	41
3.1	Position distribution for BP . . . . .	52
3.2	Position distribution for Mylor . . . . .	53
3.3	Amplitude spectrum of the gravity wave spectral model . . . . .	57
3.4	Example of wind output from spectral model . . . . .	57
3.5	SNR/decay time probability distributions . . . . .	58
3.6	Covariance bias distribution (1 day of integration) . . . . .	65
3.7	Covariance bias distribution (10 days of integration) . . . . .	66

---

3.8	Means/standard deviations for a 20-day composite . . . . .	67
3.9	Covariance bias distribution (monochromatic gravity waves) . . . . .	68
3.10	Covariance bias distribution (showing outlier rejection performance) . . . . .	68
4.1	Gravity-wave–tidal interaction model from Fritts and Vincent [1987] . . . . .	76
4.2	Count rates and height distribution for BP-Mylor dataset . . . . .	79
4.3	Phase calibration results for BP-Mylor dataset . . . . .	80
4.4	Example of low-pass filtering using a wavelet transform . . . . .	82
4.5	Tidal amplitude and phase estimation using wavelet transform . . . . .	83
4.6	Comparison of density climatologies . . . . .	85
4.7	Sample of horizontal winds from the BP-Mylor link . . . . .	86
4.8	Winds and covariances (Mar-Sep 2018) . . . . .	87
4.9	Wavelet power spectrum of zonal winds at 88 km . . . . .	88
4.10	Winds and covariances (April 2018) . . . . .	89
4.11	Amplitudes and phases of diurnal and semidiurnal tides . . . . .	90
4.12	Composite day of winds, covariances, and flow accelerations . . . . .	92
4.13	Simulated errors in flow acceleration estimates . . . . .	94
4.14	GSWM-00 simulation of tides at BP . . . . .	96
5.1	Satellite-based phase calibration results for BP . . . . .	104
5.2	Geometry of the aircraft-based phase calibration approach . . . . .	107
5.3	ADS-B receiver equipment . . . . .	107
5.4	Aircraft detections around Adelaide . . . . .	108
5.5	AOA of aircraft detections (with respect to BP and Mylor) . . . . .	109
5.6	Example of interpolated aircraft positions/altitudes . . . . .	111
5.7	Example of interpolated aircraft ranges . . . . .	112
5.8	Example of determining ADS-B receiver time offset . . . . .	115
5.9	Second example of ADS-B receiver time offset determination . . . . .	115
5.10	Distribution of time offsets for BP and Mylor . . . . .	117
5.11	Case 1 . . . . .	119
5.12	Case 2 . . . . .	120
5.13	Case 3 . . . . .	121
5.14	Case 4 . . . . .	122
5.15	Case 5 . . . . .	123
5.16	Case 6 . . . . .	124

---

5.17	Case 7 . . . . .	125
5.18	Results from the phase calibration of the meteor radar receiver at BP. . . . .	126
5.19	As per Fig. 5.18, but for the Mylor receiver. . . . .	127
5.20	Interpolated phase corrections for the BP receiver. . . . .	128
5.21	Interpolated phase corrections for the Mylor receiver. . . . .	129
5.22	Example beamformed power distribution . . . . .	131
5.23	Effect of BP phase calibration on AOAs . . . . .	132
5.24	Effect of Mylor phase calibration on AOAs . . . . .	133
5.25	BP phase calibration results . . . . .	134
5.26	Mylor phase calibration results . . . . .	135
5.27	Effective radar frequency at Mylor . . . . .	137
5.28	Decay time profile at BP . . . . .	137
5.29	Simulated height estimation error at BP and Mylor . . . . .	138
5.30	Comparison of errors in zenith angles . . . . .	143
5.31	Flight density map . . . . .	143
6.1	Locations of IAP meteor radars . . . . .	147
6.2	AOA of aircraft detections (with respect to Kühlungsborn and Moitin) . . . . .	147
6.3	Phase correction results for the KJ link . . . . .	148
6.4	Phase correction results for the KM link . . . . .	149
6.5	Example 1 . . . . .	150
6.6	Example 2 . . . . .	151
6.7	Example 3 . . . . .	152
6.8	Example 4 . . . . .	153
A.1	Example of range-imaged results from the BP ST . . . . .	162
A.2	BP ST array layout and frequency sequence . . . . .	163
A.3	Frequency-domain phase calibration examples . . . . .	164
A.4	Frequency-domain phase calibration results . . . . .	165

# List of Tables

2.1	Experiment parameters used with the BP and Mylor meteor radars, for all data presented in this thesis. . . . .	28
3.1	Meteor detection rates used for the simulations presented here. The rates shown are per day, in 2 km-wide bins centred at the altitude specified. . .	54
6.1	Experiment parameters used with the IAP meteor radars. . . . .	147

# Chapter 1

## Introduction

This thesis is concerned with using radar measurements of the motion of ionized meteor trails to study atmospheric waves between altitudes of about 80 and 100 km. This part of the atmosphere is a subset of the so-called mesosphere-lower thermosphere/ionosphere (MLT/I; 60-110 km). Specific foci of the thesis include estimating the uncertainties of momentum transport measurements, studying observations of the interactions between small-scale waves and tides, and the consideration of an opportunistic way to phase-calibrate radars using echoes from civilian aircraft.

The principal motivation behind studying momentum transport and interactions between small-scale waves and tides in the MLT/I is to improve on shortcomings in the way the effects of these waves are represented in global circulation models of the atmosphere. The purpose of this Chapter is two-fold: (1) to discuss the main effects the waves have on the global circulation in the MLT/I, so as to motivate their inclusion in global circulation models (Sect. 1.1), and (2) to provide an overview of which of these wave effects can be measured using radar techniques, as well as some difficulties in obtaining and interpreting those measurements (Sect. 1.2).

### 1.1 The MLT/I and the effects of atmospheric waves

The vertical structure of the Earth's atmosphere is usually described in terms of layers whose boundaries are defined by turning points in the temperature profile. A representation of these layers for a mid-latitude location during an equinoctial period is shown in Fig. 1.1.

As shown in the simulation output in Figs. 1.2 and 1.3, there are considerable variations in the zonal-mean temperature and wind structure of the MLT/I with latitude and season. At least in the MLT/I, this variability is indirectly controlled by the transfer of

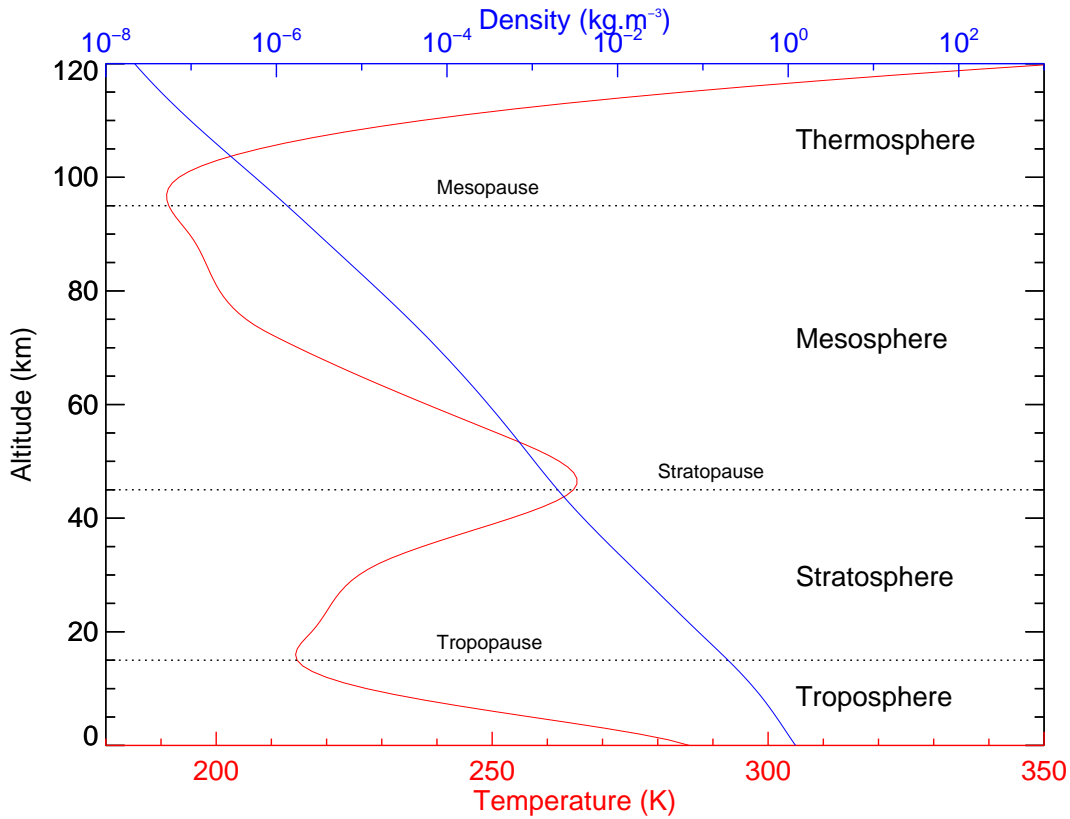


Fig. 1.1: Atmospheric temperature (red) and density (blue) profiles from the NRLMSISE-00 model, for 45°S around the time of the Southern Hemisphere autumnal equinox (late March) (figure from Spargo [2016]).

momentum between different regions of the atmosphere by wave motions. Of principal interest in this thesis is the vertical transfer of momentum associated with the dissipation of these waves as they propagate through the MLT/I.

The waves occupy a spectrum of temporal and spatial scales, and are generally broken down into three classes:

- “Gravity” waves, which are associated with the buoyant restoration of adiabatic displacements of air parcels, with the initial forcing principally provided by topography, wind shear, and/or convection. They occupy periods ranging from approximately 5 minutes up to the inertial period (which is roughly 12 hours at the poles and theoretically infinite at the poles), and spatial wavelengths ranging from several to hundreds of kilometres (see e.g., Fritts [1984]).
- Thermal tides, which in the MLT/I are caused by the diurnal variability in solar heating of ozone in the stratosphere and water vapour in the troposphere. The most dominant tides occur at periods within the first few harmonics of this diurnal

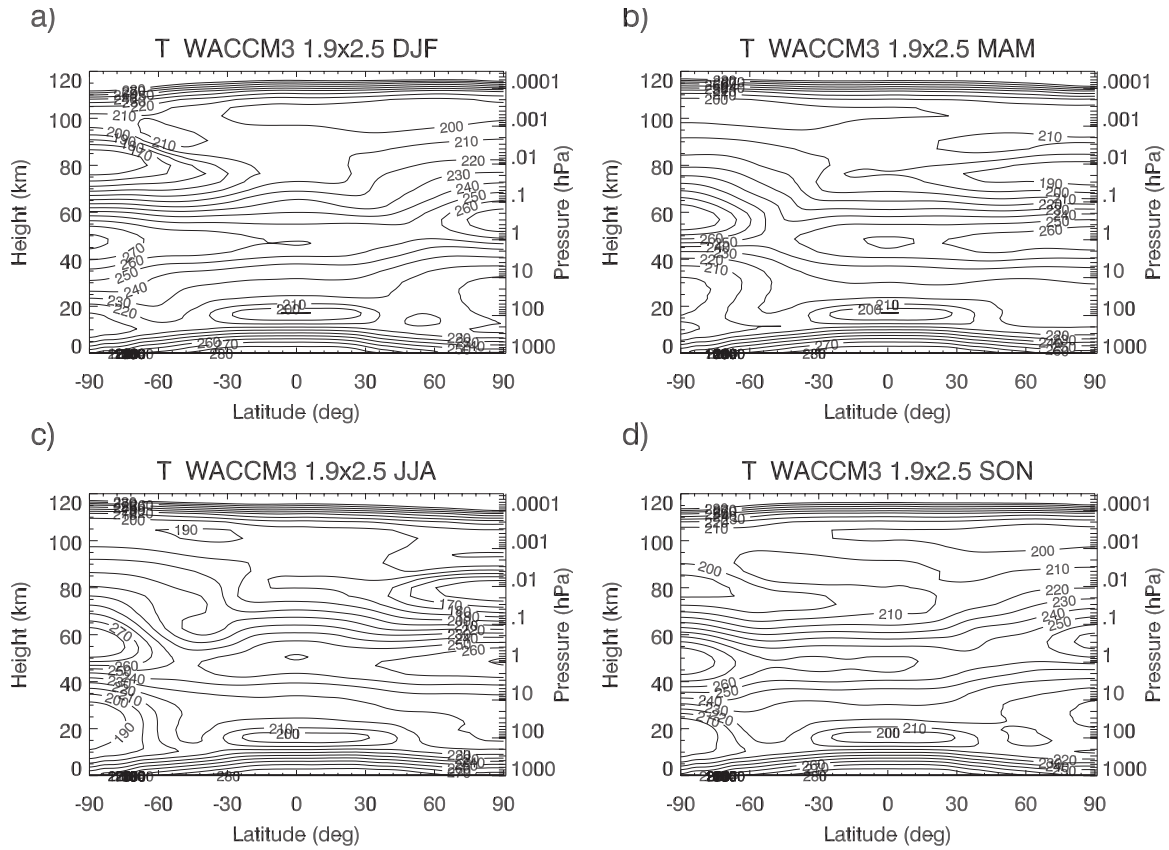


Fig. 1.2: 30-year climatology of WACCM3 temperatures with height and latitude (from Richter et al. [2008], Fig. 4). Each plot represents a different season (which are indicated in the plot titles).

forcing (and are also termed “migrating” tides) and are global in scale (see e.g., Lindzen and Chapman [1969]).

- Planetary waves, which are associated with the variation of the Coriolis force with latitude. They have known modes of variability ranging from a few days up to several months, and are also global in scale (see e.g., Smith [2012]).

Perhaps the most obvious consequence of wave momentum transfer in the MLT/I is the curious feature in Fig. 1.2 that the minimum temperatures of just below 160 K occur at the polar mesopause (altitude  $\sim 85$  km) in the middle of summer. Given the insolation levels during summer at the poles, this represents a significant departure from radiative equilibrium (of the order of approximately 50K, as noted by e.g., Vincent [2015]). Unsurprisingly, the first observations of this phenomenon, which date back to rocket-based soundings of the upper atmosphere in the early 1950s, were baffling to those involved (see e.g., Crary [1950]).

The cause of the so-called “cold summer mesopause” is the adiabatic decompression



(compression) associated with rising (sinking) motions that occur over the poles in summer (winter), which is accompanied by a residual circulation from the summer pole to the winter pole. This conclusion was initially reached as early as the 1950s by Kellogg and Schilling [1951], following their development of a circulation model of the atmosphere up to an altitude of 120 km. However, debate ensued in the following decades as to the mechanism driving this circulation. While the hypothesis that breaking gravity waves were responsible for the circulation appeared in a number of studies published during the 1960s, it was not widely accepted until the landmark work of Lindzen [1981].

The caveat in the model of Kellogg and Schilling [1951] was the existence of the large meridional motions required to satisfy flow continuity. To conserve angular momentum, these would result in zonal motions much larger than those that had been observed up to that time. In fact, the inferred zonal motions accelerated westward during summer and eastward during winter with altitude, unabated. As shown in Fig. 1.3 (from Richter et al. [2008]), the present understanding is that the winds do accelerate in this way up to about 60 km altitude, but then reduce with altitude and change sign between about 70 and 90 km (depending on the latitude and season). This process is often referred to in the literature as the “closing” of the mesospheric wind jets.

To reconcile the unexpectedly small zonal motions, Haurwitz [1961] proposed that frictional forces which decelerate the zonal wind result in the expected meridional motions. As an aside, to give further credence to the existence of a pole-to-pole circulation, he also found that the meridional motions arising from these frictional forces were of the right order and sign to explain the influx of ozone into high latitude regions during late winter and in early spring. A modified version of this frictional force subsequently came to be referred to as “Rayleigh drag” following the work of Leovy [1964]. Although the drag mechanism proposed by Leovy [1964] could explain the meridional motions, it was difficult to reconcile the size of the drag needed to justify the zonal wind deceleration (e.g., Green [1972]). Furthermore, the drag was only sufficient to decelerate the zonal motions to zero, not to reverse them (as discussed by e.g., Dunkerton [1982]).

Somewhat in parallel with these studies, interest in the small-scale oscillations observed in mesospheric wind fields and meteor trails increased. Hines [1960] was the first to propose the idea that many of these oscillations were a manifestation of waves whose restoring force was buoyancy, and termed them “internal atmospheric gravity waves” (“internal” referring to the fact that they oscillate within the fluid rather than on its surface). In particular, Hines made the suggestions that gravity waves:

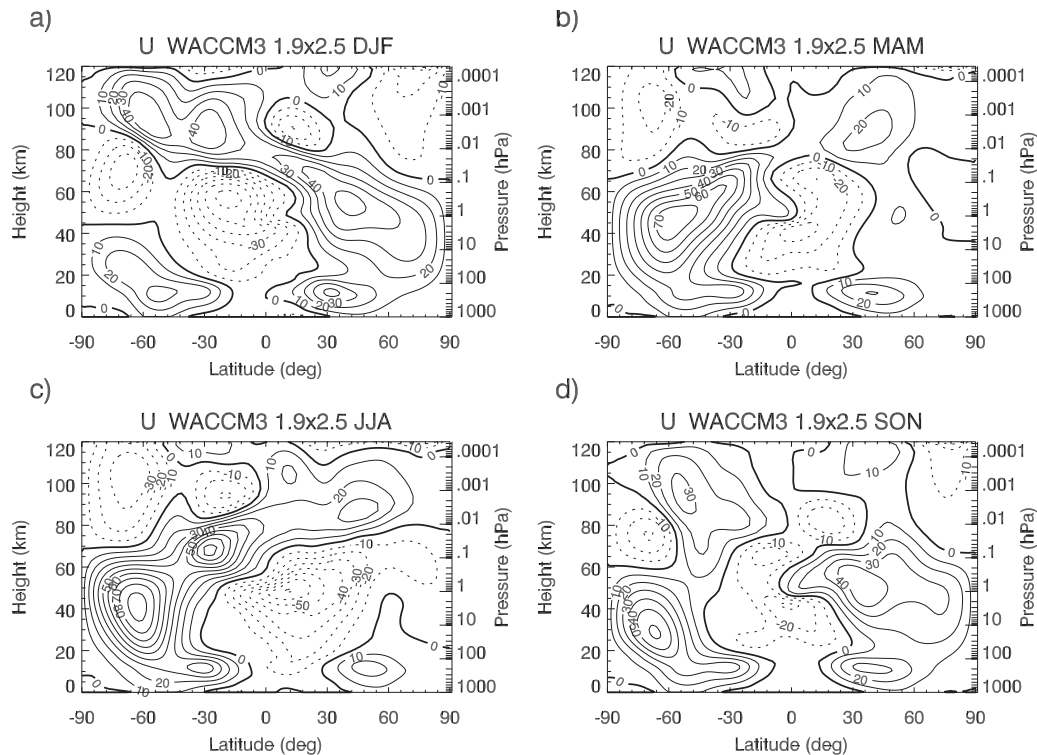


Fig. 1.3: As per Fig. 1.2, but for zonal winds (from Richter et al. [2008], Fig. 3)

1. can transport energy upwards from their source region in the lower atmosphere;
2. will, through conservation of energy, increase in amplitude with height as a result of the decreasing atmospheric density;
3. will “saturate” at some threshold altitude, and simultaneously deposit their energy through the production of turbulence.

In the following years, a number of important advances were made in understanding the effect gravity waves have on the MLT-region (Houghton [1978] provides an overview of the advances up to late 1970s). Key among those are the findings of Bretherton [1966] and Booker and Bretherton [1967], who pointed out that gravity waves are absorbed by the background wind flow at a so-called “critical level” (which occurs when the wave’s phase velocity matches the wind’s) and through momentum transfer accelerate the flow in the direction of the wave’s phase velocity during this process. This process has come to be referred to in more recent literature as “critical level absorption”. Furthermore, Bretherton [1969] and Lilly [1972] showed that gravity waves transfer momentum to the flow in the same way when they saturate. A detailed description of wave saturation processes can be found e.g., in the reviews by Fritts [1984] and Fritts and Alexander [2003].

Lindzen [1981]’s landmark advance was to essentially describe a mechanism linking the critical level absorption, gravity wave forcing, and global meridional circulation processes in the MLT/I. His findings showed that the phase velocities of waves propagating to the mesosphere are sharply limited by critical level absorption in the troposphere and stratosphere. The waves that do reach the mesosphere consequently have a phase velocity spectrum that is “biased away” from the wind profile’s. Following on from previous findings, he confirmed that the momentum divergence associated with the waves’ saturation results in a body force on the wind, tending to accelerate it towards the waves’ phase velocity. This acceleration is synonymous with the drag force earlier envisaged by Haurwitz [1961] and Leovy [1964], except that it also has the capability of reversing the flow. The body force is balanced by a Coriolis torque (an acceleration of the meridional wind in this case) sufficient to satisfy the continuity requirements for vertical motions over the poles. The zonal wind direction and predominant gravity wave phase propagation directions are such that these vertical motions are downward over the winter pole and upward over the summer pole, leading to the observed departures in the temperature distribution from radiative equilibrium.

The momentum transport capability of gravity waves can be inferred from the the size of the covariance between the orthogonal components of the wind field in a region through which the waves are propagating. These covariance terms are typically parameterized as components of the Reynolds stress tensor per unit mass:

$$\frac{\tau_{ij}}{\rho} = \langle u'_i u'_j \rangle, \quad (1.1)$$

which is a  $3 \times 3$  matrix containing the covariances between the fluctuating Cartesian components of the wind velocity. An individual entry of  $\langle u'_i u'_j \rangle$  represents the net momentum flux per unit mass in direction  $\hat{x}_i$  across a plane perpendicular to  $\hat{x}_j$  [AMS Glossary, 2012].

The terms that are important in determining body forces in the atmosphere are the covariances between the horizontal and vertical velocities; these are usually referred to as “vertical fluxes of horizontal (zonal or meridional) momentum”. The zonally-averaged force per unit mass in the zonal direction required to produce a net meridional circulation is given by (e.g., Fritts [1984]):

$$\langle F_x \rangle = -\frac{1}{\rho(z)} \frac{\partial}{\partial z} (\rho(z) \langle u' w' \rangle) = f \langle v \rangle, \quad (1.2)$$

where  $u$ ,  $v$  and  $w$  represent wind velocities in the zonal, meridional and vertical directions respectively, and  $f = 2\Omega \sin \phi$  is the Coriolis parameter, where  $\Omega$  is the (Earth’s)

rotational angular frequency,  $\phi$  is the latitude, and  $\rho(z)$  represents the neutral density as a function of height  $z$ . The angled brackets in this equation denote a zonal average, and in (1.1), an ensemble (e.g., temporal or spatial) average. We also note that (1.2) assumes that the zonally-averaged acceleration of the zonal wind ( $\frac{\partial \langle u \rangle}{\partial t}$ ) is zero (see e.g., Andrews and McIntyre [1976]). Similarly, the force in the meridional direction is given by:

$$\langle F_y \rangle = -\frac{1}{\rho(z)} \frac{\partial}{\partial z} (\rho(z) \langle v'w' \rangle) = f \langle u \rangle. \quad (1.3)$$

As an aside, it should be stressed that atmospheric gravity waves do not intrinsically “possess” momentum, but act to re-distribute the momentum that resides in the mean flow between different altitudes [Fritts, 1984]. A simple thought experiment to understand the momentum transport process is to consider correlated motions in the  $\hat{u}$  and  $\hat{w}$  directions occurring on the boundary between two volumes of laminar flow in a homogeneous fluid; if the size of the oscillation changes over time, it can be inferred that momentum has been transferred between the two volumes. The  $\rho(z)$  normalization is present in (1.2) and (1.3) solely to conserve mass in the case of momentum transfer occurring in the vertical direction. The reader is referred to McIntyre [1981] for a detailed discussion of a number of related thought experiments. In this context, we note his argument that fluxes of momentum associated with internal oscillations in a fluid should be referred to as “pseudo-momentum” fluxes to avoid confusing them with the momentum transfer that occurs in the case of electromagnetic waves applying “radiation pressure” to an object they are incident on. In the interests of being consistent with the literature in this field however, in this thesis we still refer to correlated fluid motions of this kind as “momentum fluxes”.

The fact that gravity waves can control the circulation in the mesosphere means that it is critical to incorporate their effects in global circulation models (GCMs). It is also important that the effects of small-scale, high frequency gravity waves are well-represented in GCMs, as while they do not necessarily dominate the gravity wave energy budget, the relatively large vertical velocity perturbations associated with them result in significant momentum transport between different heights when they dissipate [Fritts and Alexander, 2003]. The considerable computational resources required to accurately model these small-scale waves on a global scale however have long made this task prohibitive (see e.g., Hamilton [1996] for a discussion of the of the grid resolution required for the effects of the waves on the global circulation to be realistically simulated). As

a result, it has been necessary to “parameterize” the wave effects in GCMs (e.g., Kim et al. [2003] and Ern et al. [2011]).

The parameterization process, of which McLandress [1998] and Fritts and Alexander [2003] provide detailed overviews, incorporates at each grid cell a specification of the wave characteristics at the source level, the spectral evolution of the waves as a function of height, and the calculation of a momentum forcing term at the heights of wave dissipation. This information is typically estimated from observational data, and in cases where that data does not exist at the required resolution, the parameterization is performed by making assumptions about these wave properties (e.g., Alexander et al. [2010]). Both McLandress [1998] and Fritts and Alexander [2003] document the diversity of parameterizations that exist for incorporating unresolved gravity wave information in GCMs, and the considerable discrepancies in the derived MLT/I mean circulation characteristics derived from them.

The ongoing improvement in the quality of ground-based observations of gravity wave characteristics and in the accuracy and coverage of global climatologies provided by space-borne instruments has played a critical role in constraining the way gravity wave characteristics have been parameterized into GCMs (e.g., McLandress [1998] and Alexander et al. [2010]). This has progressed to the extent that it is now widely accepted in the modelling community that there is good agreement between global satellite observations of gravity wave effects and their representation in high-resolution GCMs. However, progress remains to be made in correctly incorporating the momentum deposition of small-scale, high frequency gravity waves in GCMs. As Alexander et al. [2010] note in their recent review, the parameterizations’ wave momentum deposition properties and wave breaking heights should be constrained by those observed in both radar and satellite data, but in practice are just tuned to match the zonal mean climatologies provided from satellites.

Fixed ground-based instruments such as radar and lidar have a role to play in providing this small-scale gravity wave momentum deposition information, as in principle they can observe the evolution of a packet of small scale waves above a fixed location. In contrast, satellite observations in general cannot observe the full spectrum of gravity waves at a given location. Ground-based instruments are also well-suited to perform case studies around “hot-spot” source regions of orographically-generated waves, which contribute significant momentum flux divergences to the MLT/I. Alexander et al. [2010] conclude that momentum flux measurements in these regions are needed in particular

to further tighten the wave momentum deposition constraints assumed for small-scale waves in GCMs. As an example of the ongoing effort to address this need, the recent Deep Propagating Gravity Wave Experiment campaign [Fritts et al., 2016; Bossert et al., 2015] has sought to provide information about wave propagation characteristics and momentum deposition effects associated with orographic sources of gravity waves in the Southern Hemisphere.

An area of particular interest in this thesis is the way gravity waves and tidal winds interact through a combination of the critical level absorption and momentum deposition processes. As will be further discussed in Chapter 4, it has proven especially difficult to parameterize these effects into GCMs, with a conclusion to still be reached on how important gravity wave effects are in modulating tidal amplitudes and phases. In addition, as will also be discussed in Chapter 4, few observational studies of gravity-wave–tide interactions have been published, and they have not come to consistent conclusions on the role gravity waves play in these interactions.

As discussed by Liu et al. [2013], ground based radars are uniquely suited to addressing this problem because they can directly observe gravity wave forcing on tides and its variability across many tidal oscillations at one location. Depending on the orbital period, it can take a low-earth-orbit satellite several months to cover a diurnal cycle above a single location. The next section briefly reviews the radar techniques that have been used in the past to make measurements of gravity wave momentum fluxes, and some of the caveats associated with them.

## 1.2 Radar measurements of MLT/I-region wind covariances

Ground-based radars can estimate components of the Reynolds stress tensor per unit mass in (1.1) by acquiring a large sample of line-of-sight Doppler wind velocities and solving an inverse equation to derive the individual wind covariance components (discussed further in Sect. 3.2.6). The basic geometry associated with the wind covariance estimation is shown in the left panel of Fig. 1.4.

In the context of studies of the MLT/I, the radar techniques that have been used for wind covariance component estimation can generally be classed into two categories: (1) those that transmit vertical or near-vertical beams and obtain Doppler velocities from large-scale refractive index irregularities (or “scatterers”) that advect with the wind, and (2) those that transmit all-sky beams and measure the Doppler velocity of specular reflections from ionization trails left in the wake of ablating meteoroids (that also advect

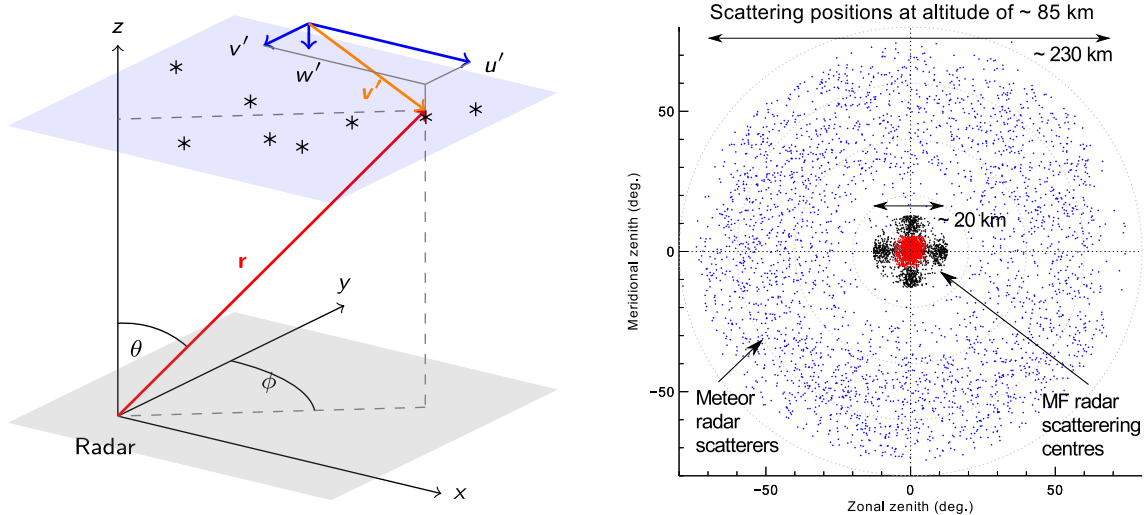


Fig. 1.4: The geometry of estimating wind covariances using line of sight velocities from spatially separated scatterers (left) and the typical scatterer distribution for MF and meteor radars (right).

with the wind). A comparison of the scatterer distributions associated with these two approaches is shown in the right panel of Fig. 1.4. The relative wind covariance estimation performance of these two approaches is discussed below (with the second approach being of principal interest in this thesis and discussed in much further detail in Chapter 2).

Using the medium frequency (MF) radar at the Buckland Park field site, Vincent and Reid [1983] were the first to make direct measurements of the vertical flux of horizontal momentum terms in the MLT/I. Importantly, their study confirmed the approximate agreement between the zonal flow acceleration and theoretical estimates of wave drag required to balance the zonal accelerations due to Coriolis torques imposed by the mean meridional circulation. Their approach determined the  $\langle u'w' \rangle$  and  $\langle v'w' \rangle$  terms from an estimate of the difference between the mean square radial velocities determined from narrow beams at opposite azimuth angles (see Reid [1987] for a detailed discussion of the wave field parameters that may be estimated from such beam configurations). Similar approaches have since been applied to the same system (e.g., Fritts and Vincent [1987], Reid and Vincent [1987], Murphy and Vincent [1993], Murphy and Vincent [1998], and Spargo et al. [2017]) and to other high frequency (HF) and very high frequency (VHF) radars at various sites (e.g., Fukao et al. [1988], Reid et al. [1988], Fritts and Yuan [1989], Fritts et al. [1990], Fritts et al. [1992], Sato [1990, 1993], Sato [1994], Tsuda et al. [1990], Wang and Fritts [1990, 1991], Hitchman et al. [1992], Nakamura et al. [1993], Murayama

et al. [1994], Thorsen et al. [1997], Placke et al. [2014], Placke et al. [2015], Riggin et al. [2016], and Reid et al. [2018]).

A problem that affected most of these studies (in particular those involving radars with relatively broad ( $\gtrsim 3^\circ$ ) transmit and receive beams) was the aspect sensitivity (also referred to as Bragg-anisotropy [Muschinski et al., 2005]) of the partially-reflecting scatterers illuminated by the transmit beam. If the aspect sensitivity was not measured and accounted for, the apparent receive beam zenith angles would overestimate the true values (see Reid and Vincent [1987] and Murphy and Vincent [1993] for examples of approaches developed to perform this compensation), leading to an overestimation (underestimation) of the vertical (horizontal) velocities and their variances.

A more general problem was the fact that the effective beam position could fluctuate in a somewhat random manner about the apparent position due to the propagation of irregularities in the refractive index through the beam volume. To overcome this problem, Thorsen et al. [1997] introduced an extension to the Vincent and Reid [1983] wind covariance estimation approach allowing for radar receive beams with an arbitrary “brightness distribution” (the normalized angular and Doppler-frequency power spectral density; see e.g., Woodman [1997]). This technique is applicable to any radar capable of performing spatial beamforming (i.e., one with multiple spaced receiver antenna channels). Thorsen et al. [1997] applied their approach to an MF radar with a broad, vertically-transmitted beam, and relied on geophysical variability in the brightness distribution to obtain a sufficient number of radial velocity—pointing direction pairs to solve for the mean winds and wind covariances.

The critical assumption required in Thorsen et al. [1997]’s study was that the “true” measured fluctuations in the weighted angle of arrival exceeded those due to statistical estimation errors. Despite the apparent validity of this assumption for the radar utilized, and the retrieval of momentum fluxes that appeared to be physically reasonable, the approach was not widely adopted. It was only revisited recently by Spargo et al. [2017] (see App. F) in an application to data from the Buckland Park MF radar incorporating transmission beamsteering and beamforming on reception. Through the comparison of vertical-beam only and multiple off-vertical beam approaches (from both simulations and the analysis of campaign data), they concluded that the former could be used for reliable estimation of MLT/I momentum fluxes, albeit with significantly less precision.

Another of the issues with using solely near-vertical backscatter is the resulting instability in the inversion used to estimate the covariance terms. This problem was



encountered in the recent study of Reid et al. [2018] (see App. E), where the authors simulated the covariance uncertainties that arise in a configuration of 6-beams centred on the vertical, with a maximum off-vertical angle of approximately  $6^\circ$ . Using the Thorsen et al. [1997] estimator, they found large correlated errors to accumulate in all the covariance components including a horizontal term, and in addition surprisingly found that these errors were larger for smaller errors in the beam position. Through an intercomparison of the two techniques, they also concluded that the Thorsen et al. [1997] and Vincent and Reid [1983] techniques performed similarly, despite the latter not including any compensation for beam position variability.

As pointed out in the review of Reid [2015], MF/HF radars (specifically those that rely on echoes from partially-reflective scatterers in the mesosphere) have become less widely used for studies of the MLT/I in recent years given a number of problems in the interpretation of the wind estimates from them, let alone wind covariance estimates. Contributing to the decline in the usage of MF/HF radars over the last two decades has been the proliferation of relatively inexpensive all-sky meteor radars; these systems have been seen to provide reliable wind estimates at all times of day, are comparatively easy to operate/maintain, and are not susceptible to changing ionospheric conditions. Nevertheless, MF/HF radars are still the benchmark instruments for measuring gravity wave momentum fluxes and so will play an important role in this area in the future, especially as a way of cross-checking meteor radar estimates. Such an intercomparison was performed in the recent work of Placke et al. [2014], using the narrow-beam Saura MF/HF radar in Norway and a VHF meteor radar on the nearby island of Andenes. Their study showed the covariances from the Saura system (which were determined using the Vincent and Reid [1983] estimator) contained significantly less noise than those from the meteor radar.

Hocking [2005] was the first to apply an approach based on the Thorsen et al. [1997] estimator to covariance estimation with meteor echoes from all-sky meteor radars. He concluded that it was possible to measure physically reasonable momentum fluxes using this type of radar with an integration time of around two months. Given the potential it showed for the already widely-installed meteor radars to contribute to global studies of MLT/I momentum fluxes, Hocking's study was followed by a number of others applying a similar approach on different radar systems (e.g., Antonita et al. [2008], Clemesha and Batista [2008], Beldon and Mitchell [2009, 2010], Clemesha et al. [2009], Fritts et al.

[2010a, 2010b, 2012a, 2012b], Vincent et al. [2010], Placke et al. [2011a, 2011b, 2014], Placke et al. [2015], Andrioli et al. [2013a, 2013b, 2015], Liu et al. [2013], de Wit et al. [2014b, 2014a], de Wit et al. [2016], Matsumoto et al. [2016], and Riggins et al. [2016].

Angle-of-arrival uncertainties were not as significant a problem in these studies as they were for those involving vertical beam MF/HF radars, given the specularity of meteor echoes (discussed further in Sect. 2.2.2). However, since an ensemble of meteor echoes encompasses a much larger volume of the atmosphere (see right panel of Fig. 1.4) and covariance terms have typically been estimated across this entire volume, the reduced homogeneity in the wave field statistics across the volume increased the covariance uncertainties. Furthermore, as a result of the inability of meteor radars to detect echoes close to the vertical, uncertainties in covariance components involving a vertical term (i.e.,  $\langle u'w' \rangle$ ,  $\langle v'w' \rangle$  and  $\langle w'w' \rangle$ ) were also typically much larger than in the MF/HF radar cases.

With these concerns in mind, a number of studies have simulated the covariance component uncertainties associated with meteor radars. The results of these are reviewed in detail in Chapter 3. The most important of these at its time of publishing was likely the work of Vincent et al. [2010], which through a Monte Carlo simulation of the meteor radar covariance estimation process showed that it was essentially impossible to measure accurate momentum fluxes with averaging times of less than one month. This study cast doubt over the meteor radar-derived momentum flux estimates that had been published previously—in particular those of Hocking [2005]. The studies that followed this showed momentum fluxes with variable levels of accuracy that essentially increased with the number of meteor detections incorporated in the covariance associated height/time bins, with the results of Fritts et al. [2012b] and Liu et al. [2013] exhibiting the smallest uncertainties and the most realistic climatologies.

The most recent innovation in this area is in the work of Vierinen et al. [2019]. They introduced a technique that uses the spatial and temporal separation between all available pairs of meteor detections to estimate the wind covariance terms at each point in a grid of spatial and temporal scales. This technique in principle can be applied to monostatic (co-located transmitter and receiver) meteor radars, although they generalised the approach to a multistatic (multiple separated transmitters and receivers) configuration of meteor radars (to which the approach is better suited given the possibility of obtaining a higher spatial density of meteor detections). They were able to produce temporal and spatial spectra of horizontal energy terms (i.e.,  $\langle u'u' \rangle$  and  $\langle v'v' \rangle$ ) that were physically

realistic. However, their results were only averaged over a 24 hour period, and there were not enough detections able to produce statistically significant momentum flux estimates (i.e., the  $\langle u'w' \rangle$  and  $\langle v'w' \rangle$  terms). Nevertheless, this approach has great potential to resolve the spatial and temporal spectra of momentum deposition arising from breaking gravity waves.

### 1.3 Scope of thesis

This Chapter has briefly reviewed the important role gravity waves play in controlling the mean and tidal winds in the MLT/I, the shortcomings in the way their effects are represented in climate models, and how ground-based radar measurements complement global-scale satellite studies of gravity wave effects through their ability to resolve the contribution made by waves of different spatial and temporal scales. Particular attention was paid to the importance of measuring the divergence of the vertical flux of horizontal momentum, since this is a proxy for the wave forcing on the background flow. It then went on to discuss some of the difficulties in using radars to make measurements of this particular parameter, which essentially arise from the fact that it is a statistical measurement and many spatially/temporally separated samples are needed to estimate it with sufficient precision.

A major contribution made by this thesis is to provide further insight into the uncertainties inherent to meteor radar-derived estimates of the vertical flux of horizontal momentum. This is done through the use of a simulation of the meteor detection and wind covariance measurement process, and also through validating the measurements via a study of the correlation between measured tidal winds and gravity wave forcing on the tides. The latter study also provides a contribution to the important and as yet unresolved problem of determining whether or not gravity wave momentum deposition plays an important role in modifying the amplitudes and phases of atmospheric tides. The system simulated and that used for the data collection corresponds to a multi-static configuration of meteor radars located in the vicinity of Adelaide, South Australia (34.6°S, 138.6°E).

While carrying out the above work, it was realised that small errors in the phase difference estimates provided by the meteor radars used (which resulted in angle-of-arrival errors and a reduced number of meteor estimates available for the covariance estimation) could not be compensated for using pre-existing phase calibration methods. An opportunistic method that leveraged the proliferation of aircraft echoes in the collected

radar data was developed to carry out the phase calibration. This method was found to out-perform pre-existing methods, and constitutes another major contribution of this thesis.

A detailed overview of meteor radar operation and the signal processing schemes used to determine meteor angles-of-arrival and ultimately atmospheric winds and wind covariances from meteor echoes is provided in Chapter 2. This Chapter also provides an overview of the Adelaide-based meteor radar systems used in this study. In Chapter 3, the model of the meteor radar covariance estimation process is developed and used to evaluate the performance of the estimator for a variety of mesospheric wind fields and data averaging schemes. The same averaging schemes are applied to several months of meteor radar data in Chapter 4 and used to study the interaction between tides and gravity waves. Chapter 5 presents the aircraft-based phase calibration method and its application to two weeks of meteor and aircraft detections from the BP and Mylor radar systems. Chapter 6 shows an application of the same approach to observations from a multistatic network of meteor radars in northern Germany. Finally, conclusions and recommendations for future work are provided in Chapter 7.

## Chapter 2

# Meteors and all-sky interferometric meteor radar

In this thesis, echoes from meteor trails that drift with the background wind are used to infer information about dynamical processes in the mesosphere. Those echoes are detected with spaced antenna meteor detection radars with interferometric (i.e. phase difference measurement and associated position-finding) capability.

This Chapter aims to briefly overview all meteor radar-related concepts that are relevant to this thesis. Meteors and their sources are firstly discussed, followed by the characteristics of radio waves that scatter off ionized meteor trails. The operation mechanism of meteor radars—including the radio wave generation, transmission and reception procedures, and the signal processing applied to the received echoes—is then discussed. Emphasis is placed on describing how the three-dimensional positions and radial drift velocities are estimated, as the accuracy of these is important for correct interpretation of the winds and dynamics.

Correctly compensating for phase calibration errors in meteor detection radars plays a critical role in the accuracy of the obtained three-dimensional position information. It can also be challenging to estimate the values of those calibration offsets. The widely-used empirical method which has been applied to phase-calibrating the results presented in Chapters 3 and 4 is described in this Chapter. A superior direct method is developed in Chapter 5.

### 2.1 Meteors and their sources

A meteor forms when a rocky or metallic object in orbit around the Sun (referred to as a “meteoroid”) penetrates the Earth’s atmosphere, typically at a speed of several

tens of kilometres per second. The collisions that ensue cause molecules to become dislodged from the meteoroid's surface ("sputtering"), and to evaporate if the collisional heating rate is sufficient. When those dislodged/evaporated particles collide again with air molecules, one or both of those involved in a collision may become ionized. The end result of this process is a trail of plasma in the wake of the meteoroid. Such trails are visible to radar, given that the free electrons present will oscillate in response to an incident radio wave, and in turn emit radio waves detectable at a radio receiver.

The vast majority of meteoroids are similar in size to grains of sand, ranging from approximately  $1\ \mu\text{m}$  to  $1\ \text{cm}$  in diameter. These form trails extending about 10-15 km in height between altitudes of about 70 and 140 km. They can be considered to originate from two separate sources concentrated around the Solar System's ecliptic plane: either from a narrow stream of particles associated with a larger parent body such as a comet, or as part of a disperse, more randomly-distributed background. The meteors associated with these are termed "shower" and "sporadic", respectively.

Sporadic meteors make up most of all optical and radar-based detections of meteors from the Earth. They are concentrated in six locations with respect to the Earth's orbit around the Sun: a region towards and away from the Sun (helion and anti-helion, respectively), two regions close to the direction of the Earth's orbit (north and south apexes, respectively), and so-called "toroidal" sources, which are located about  $60^\circ$  above and below the direction of the Earth's orbit. The rotation of the Earth with respect to these sources causes a diurnal variation in sporadic meteor flux rate at a given location on the Earth's surface (with peaks at around 2, 6 and 10 LT [Ceplecha et al., 1998]). Moreover, changes in the angle between the Earth's rotation axis and orbital direction throughout the year also cause these sources to move with respect to the Earth's surface, resulting in seasonal variations in the observed meteor flux at a given location.

Shower meteors manifest as an intense burst of meteor activity over a short period (typically a few hours to a few weeks) at well-defined times of year. Visible meteors associated with a shower event appear to radiate from a small region of the sky at an approximately constant right ascension and declination, known as the shower "radiant". There are roughly a dozen major shower events every year, with each typically named after the constellation in which the radiant occurs.

## 2.2 Radar echoes from meteor trails

The first detections of radar echoes from meteors occurred in the late 1920s [Heising, 1928], largely as a byproduct of the study of propagation characteristics of HF radio waves between ground links and as part of radio studies of the ionosphere. Baggaley [2009] provides a detailed chronology of the development of the field—including the initial difficulties encountered in interpreting the source of the echoes, and the proliferation of studies in the late 1940s that grew out of radar research conducted during the Second World War, most notably at Jodrell Bank in the UK.

The work at Jodrell Bank was a precursor to meteor radar research by the National Research Council in Canada, the University of Adelaide in Australia, and the University of Canterbury in New Zealand. Reid and Younger [2016] provide a historical overview of the meteor work done by the Adelaide group since the early 1950s, which the work presented in this thesis is an outgrowth of. In particular, Reid and Younger [2016] also note the worldwide decline in meteor radar research during the 1970s, and the subsequent resurgence during the 1990s motivated by interest in using meteor radar to measure MLT-region winds.

A more recent development in the field is the widespread deployment of both pulsed and continuous-wave (CW) multistatic meteor radars, again motivated by the suitability of meteor radars to MLT-region wind measurement and the need to better characterise the dynamics of this region. Initiated by a suggestion made in the Reid and Younger [2012] presentation, the first work in the recent development was Stober and Chau [2015], and this subsequently evolved into studies incorporating a network of radars across Germany (see e.g., Vierinen et al. [2019]). At the time of writing, other multistatic meteor radar networks are also under development in Australia, Argentina, Chile, and China.

The next subsections discuss some basic characteristics of the meteor radar echoes used in this study—most of which was discovered during the initial surge in meteor radar research prior to the 1970s.

### 2.2.1 Different echo types

Meteor echoes are generally classified as either “underdense” or “overdense”. Underdense echoes, which make up the vast majority of all meteor returns, are characterised by trail electron densities low enough for the incident radio wave to pass through the

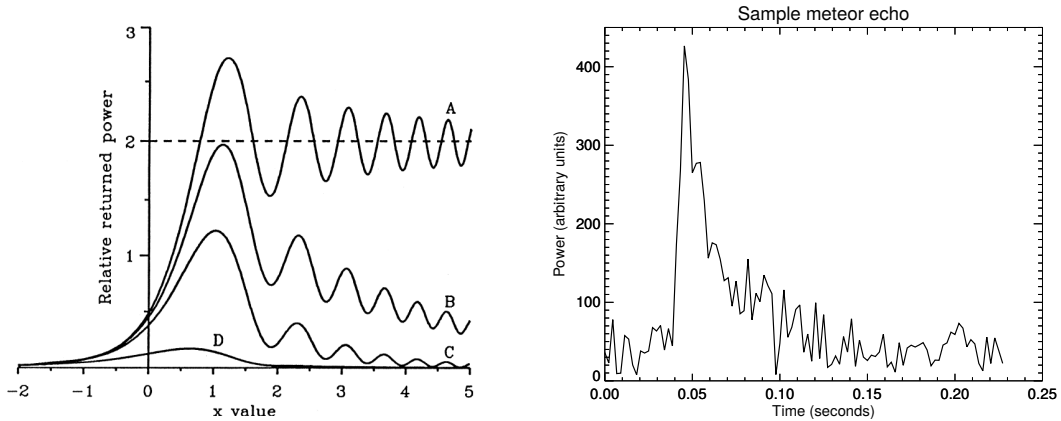


Fig. 2.1: Idealized underdense meteor echo powers (left) for increasing degrees of trail diffusion A-D, and a randomly selected real underdense echo from the BP 55 MHz meteor radar (right). The left figure is from Fig. 7 in Ceplecha et al. [1998], with accompanying description and definition of the  $x$ -axis values in Sect. 4.2.1 of that work.

trail unattenuated, and for the electrons within the trail to be considered as independent scatterers. Underdense echoes are well suited to characterisation of the atmosphere, as they decay in a manner that can be related to local temperature and pressure. The Doppler signatures they yield can also be related to the line-of-sight projection of the wind velocity at the trail location.

In the overdense case, the incident wave is reflected, and secondary electron scattering effects also contribute to the return echo. These echoes decay in far more complex ways than do underdense echoes, and they are not routinely used for temperature/pressure estimation (e.g., Holdsworth et al. [2004a]). Their typically long decay times often result in a distorted trail with multiple reflection points and line-of-sight wind projections [Sugar, 1964], also making them unsuitable for wind estimation. This thesis only makes use of underdense echoes.

A related form of scatter is the so-called meteor “head” echo, in which ionized material surrounding the meteoroid itself is detected. These are considerably weaker than trail echoes, and are generally detectable only by high-power narrow-beam radars (see e.g., Janches et al. [2014]), rather than the all-sky type used in this study [Holdsworth et al., 2004a]. They are not considered further in this thesis.

### 2.2.2 Backscatter from underdense meteors

In the initial stages of underdense trail formation, the free electrons are typically assumed to exist along a cylinder whose diameter is small compared to the radar wave-



length, which in turn is small compared to the trail length. Each electron can also be assumed to backscatter incident radiation coherently. If all the electrons are assumed to be along the trail axis, and the trail axis is perpendicular to the phase fronts from the incident wave, then as shown by McKinley [1961] and more recently Cepplecha et al. [1998] (their Sect. 4.2.1), summing the contributions from each electron yields a radiation pattern at the receiver akin to Fresnel diffraction around a straight edge. Much of that radiation originates from the first Fresnel zone of the trail, the centre of which is at the point corresponding to a minimum path length between the transmitter and receiver.

Meteor radars typically sample at intervals much smaller than typical meteor trail formation times, which enables them to observe multiple Fresnel zones passing over the receiver as the column of free electrons lengthens. Plot A in the left panel of Fig. 2.1 shows the backscattered power expected at a receiver during the formation of an underdense echo; the model is discussed further in Sect. 4.2.1 of Cepplecha et al. [1998]. In passing, it should be noted that the frequency of these oscillations can be used to determine the velocity of the meteoroid.

### **Specularity**

Once fully formed, an underdense meteor trail is generally assumed to scatter incident radio waves under the specular condition; i.e., the scatter is assumed to come from a “specular point” on the trail, notionally located at the centre of the trail’s first Fresnel zone. In this study, the height and wind information derived from backscatter and forward scatter underdense meteor echoes is assumed to be from the trail’s specular point.

As mentioned earlier, Sugar [1964] argues that long-duration echoes may be distorted by wind perturbations, in such a way that there may be several local first Fresnel zones (i.e. specular scattering locations) on the trail. These echoes would likely exhibit a more complex decay than underdense echoes, and would be rejected by the software used in this study as either overdense or non-meteor-like (see Holdsworth et al. [2004a], their Sect. 3.9 and 3.10).

### **Echo decay**

Ambipolar diffusion will immediately cause the diameter of the trail (i.e. the column of ions and free electrons) to increase. Once the trail radius becomes comparable to the

radar wavelength, the destructive interference that results will reduce the echo intensity. Recombination is also known to decrease the number of free electrons available to scatter the incident wave, further reducing the echo intensity (see e.g., Lee et al. [2013]).

In practice, these processes cause underdense meteor echoes to decay to the noise floor within a few tens of milliseconds. Incorporating only diffusion effects, the theoretical time taken for the backscatter echo amplitude to reduce to  $e^{-1}$  of its maximum is given by [McKinley, 1961]:

$$\tau = \frac{\lambda^2}{16\pi^2 D}, \quad (2.1)$$

where  $\lambda$  is the radar wavelength and  $D$  is the ambipolar diffusion coefficient. The temperature ( $T$ ) and pressure ( $P$ ) dependence of  $D$  is embodied in the relation (e.g., Ceplecha et al. [1998]):

$$D \propto \frac{T^2}{P}. \quad (2.2)$$

Plots B-D in the left panel of Fig. 2.1 show the effects of different diffusion rates on a meteor echo, and for reference the right panel shows a randomly selected real meteor echo from the 55 MHz BP meteor radar.

### Wind velocity signature

The background wind velocity and/or turbulence in the vicinity of the meteor trail will cause the trail to drift throughout the duration of the recorded echo. Components of trail position changes that are perpendicular to lines of constant path length (range) between the transmitter and receiver will give rise to changes in the received signal phase—i.e., a Doppler shift of the signal if the rate of change of phase is constant. In such a case the Doppler (“radial”) velocity measured at the receiver is given by:

$$v_r = \mathbf{v} \cdot \hat{\mathbf{r}} \quad (2.3)$$

where  $\mathbf{v}$  is the 3-component wind velocity vector, and  $\hat{\mathbf{r}}$  is the unit vector from the specular point to the transmitter/receiver (see the case for backscatter in Fig. 2.2).

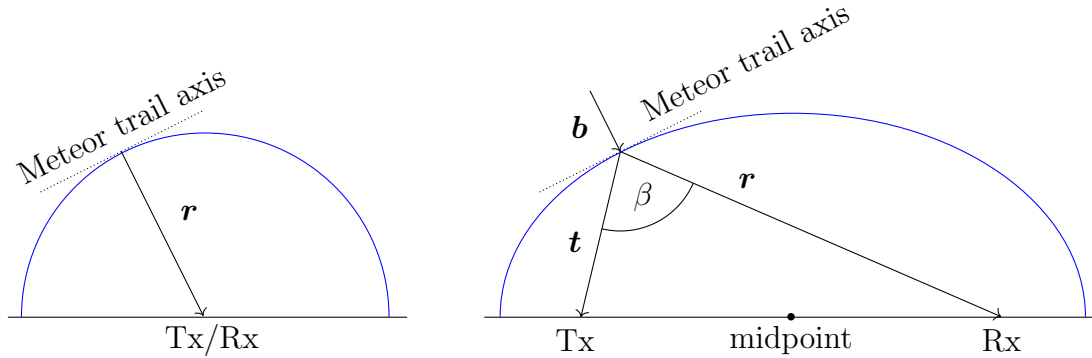


Fig. 2.2: Backscatter (left) and forward scatter (right) meteor detection geometry. In both cases, vector  $\mathbf{r}$  is from the specular point to the receiver (Rx). In the forward scatter case,  $\mathbf{t}$  is from the specular point to the transmitter (Tx), and  $\mathbf{b}$  is the unit vector bisecting  $\mathbf{t}$  and  $\mathbf{r}$  (also perpendicular to the meteor trail).  $\beta$  is the so-called “forward scatter angle”. The blue lines represent a contour of constant path length between the Tx and Rx locations; in the backscatter case this is a circle centred on the Tx/Rx, and in the forward scatter case it is an ellipse with foci at the Tx/Rx locations.

### 2.2.3 Forward scatter from underdense meteors

The previous section pertains to backscatter echoes, in which the transmitter and receiver are co-located, and the radar wave fronts are perpendicular to the meteor trail. Underdense meteors are also known to exhibit specular scatter at oblique incidence (e.g., McKinley [1961] and Sugar [1964]) meaning they can be detected with a bistatic receiver (i.e., one separated from the transmitter). Detections made in this way are often referred to as arising from “forward scatter” meteors (e.g., Ceplecha et al. [1998]).

Changes to the measured Doppler shift and meteor decay time arising from the forward scatter geometry are summarized below.

#### Echo decay

In the forward scatter case, there is a smaller maximum deviation in path length between different points on the trail as the trail radius increases, relative to the normal incidence case. This means the trail has to diffuse more for the same level of signal decay, and in practice means that a forward scatter receiver may be able to detect faster decaying echoes than a backscatter one (i.e., as though it were operating at a larger wavelength). The theoretical echo decay time in the forward scatter case is given by

[McKinley, 1961; Sugar, 1964]:

$$\tau = \frac{\lambda^2 \sec^2(\beta/2)}{16\pi^2 D}, \quad (2.4)$$

where  $\beta$  is the angle made between the meteor-transmitter and meteor-receiver vectors, often termed the “forward scatter angle” (see Fig. 2.2). As an example, a forward scatter angle of  $90^\circ$  will increase the decay time by a factor of 2.

### Wind velocity signature

As shown in Fig. 2.2, lines of constant transmitter-receiver path length in the forward scatter case form an ellipse with the transmitter and receiver as the foci (this contrasts to the backscatter case, where the line of constant path length is a circle). Only components of position changes perpendicular to this ellipse (i.e., along the  $\mathbf{b}$  vector), that are in turn projected onto the  $\mathbf{r}$  vector will yield a measurable change in signal phase at the receiver (e.g., Protat and Zawadzki [1999] and Hocking [2018]). The Doppler velocity measured at the receiver in this case is given by:

$$v_r = (\mathbf{v} \cdot \mathbf{b}) \cdot \hat{\mathbf{r}} = (\mathbf{v} \cdot \mathbf{b}) \cos(\beta/2). \quad (2.5)$$

It should be noted that recent publications using forward scatter meteor detections for wind estimation (e.g., Stober and Chau [2015]) arrive at (2.5) using an alternate approach. Rather than projecting  $\mathbf{v} \cdot \mathbf{b}$  on  $\hat{\mathbf{r}}$  (e.g., Protat and Zawadzki [1999]), they introduce the effective Bragg wavelength for the oblique scattering geometry, given by:

$$\lambda_B = \frac{\lambda}{2 \cos(\beta/2)}, \quad (2.6)$$

and then state that the measured radial velocity is given by:

$$v_r = f_d \lambda_B, \quad (2.7)$$

where  $f_d = 2(\mathbf{b} \cdot \mathbf{v})/\lambda$  is the Doppler frequency projected on  $\mathbf{b}$ . Substituting (2.6) into (2.7) then yields (2.5) as expected. This thesis follows the generalized approach for a bistatic receiver introduced by Protat and Zawadzki [1999].

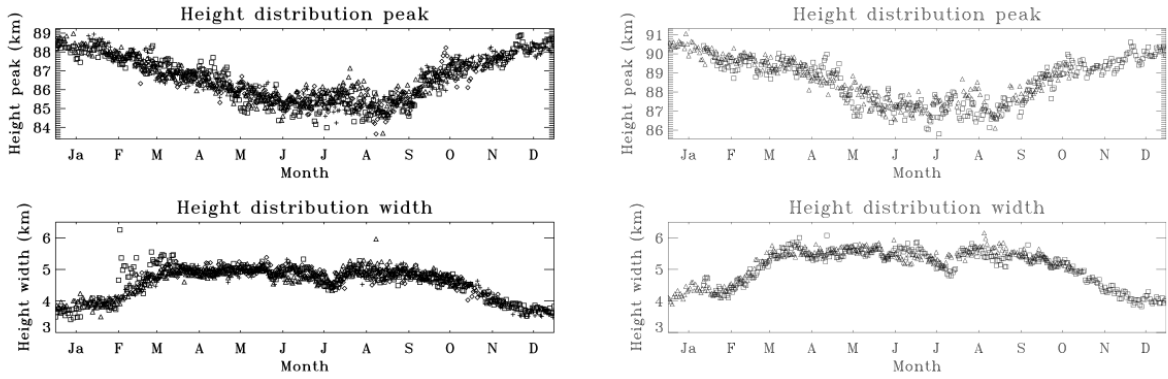


Fig. 2.3: Meteor peak detection altitudes and distribution widths for two meteor radar frequencies at Davis Station, Antarctica: 55 MHz (left column) and 33 MHz (right column) (from Holdsworth et al. [2008], their Fig. 1).

### 2.2.4 Altitude distribution

Meteoroids that enter the atmosphere have a distribution of masses, entry angles and entry speeds. Each of these affects the height at which the meteor trail forms. For instance, higher velocity meteors will form an ionization trail at larger heights than will slower ones, as will meteors that enter at a shallow angle versus those that enter at a steep angle. The end result of these effects is to produce a distribution of trails between altitudes of about 70 and 140 km.

The distribution of trail altitudes actually observed by a meteor radar is dependent on the operating frequency (e.g., Greenhow and Hall [1960], Thomas et al. [1986], and Steel and Elford [1991]). As per (2.2), trails diffuse more rapidly at higher altitudes because of the lower pressure. Since destructive interference occurs as trail radii approach the radar wavelength, echoes decay more rapidly at higher altitudes, and even more so at shorter wavelengths. At a certain altitude for a given operating frequency, most echoes decay before the trail has even fully formed (often referred to as the “radio meteor ceiling” effect). This causes the peak meteor detection altitude of higher frequency radars to be lower than for lower frequencies (see Fig. 2.3, which shows the peak detection altitude and distribution widths for a 33 MHz and a 55 MHz system). In this context, it should also be noted that the increased decay time associated with forward scatter echoes also slightly increases the range of meteor heights detectable for a bistatic receiver, depending on the size of the forward scatter angle (see (2.6) for the effective change in wavelength).

For the 55 MHz radar considered in this thesis, meteors are detected between altitudes of about 70 and 110 km, with a peak around 90 km. Altitude distribution width

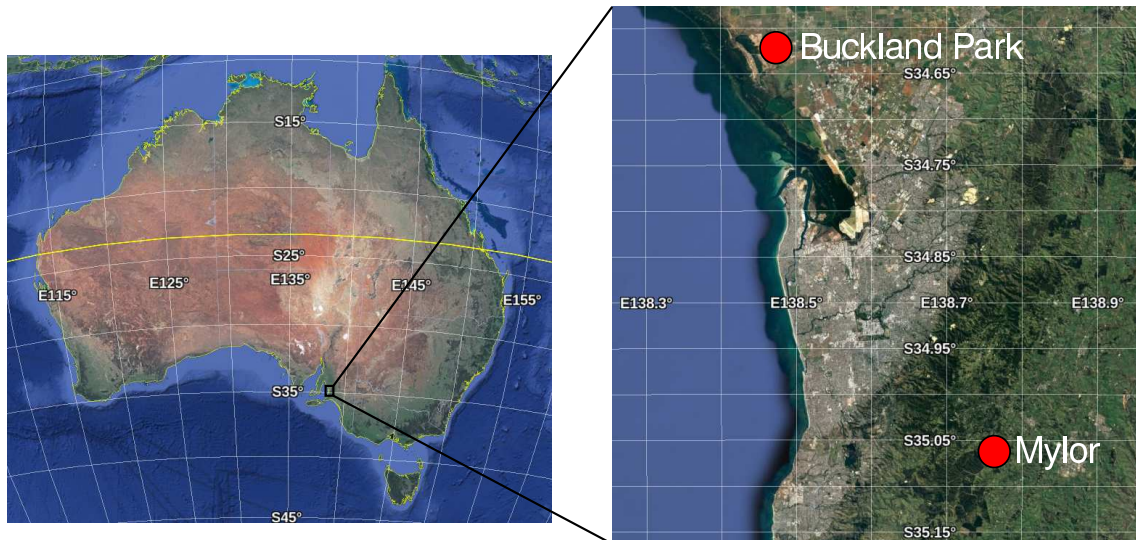


Fig. 2.4: Locations of the meteor radars used in this study.



Fig. 2.5: A photograph of the Mylor array (taken by the author on 29-Aug 2019).

measurements are used extensively in Chapter 5 to assess the performance of meteor radar phase calibration techniques.

### 2.3 Meteor radars used in this study

This thesis predominantly makes use of two 55 MHz meteor radars: a monostatic radar at the Buckland Park (BP) field site ( $34.627^{\circ}\text{S}$ ,  $138.468^{\circ}\text{E}$ ), and a bistatic receiver on a property nearby the township of Mylor, South Australia ( $35.070^{\circ}\text{S}$ ,  $138.752^{\circ}\text{E}$ ) (see map in Fig. 2.4). The two sites are separated by approximately 55 km. Both radars make use of a 5-antenna receiver interferometer (whose antenna configuration is shown in Fig. 2.8), and have used identical experiment parameters for all work presented in this thesis (shown in Table 2.1). To permit accurate range and Doppler velocity estimates at



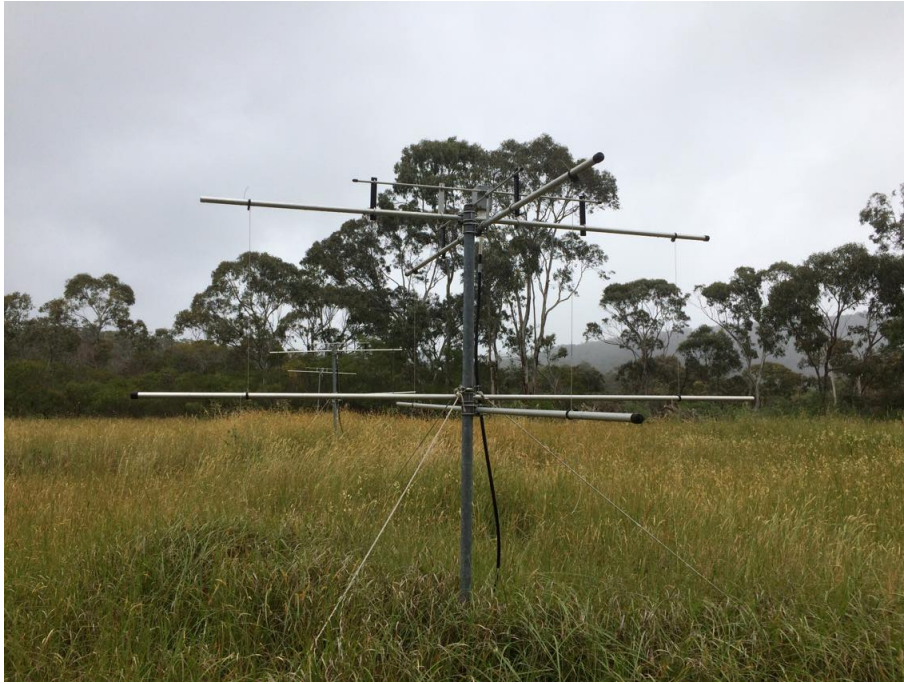


Fig. 2.6: A photograph of one of the receiver antennas at the Mylor site (taken by the author on 01-Dec 2019).

the Mylor site, the system timing, frequency, and clocks at both sites are synchronized with GPS-disciplined oscillators.

The 55 MHz meteor radar at BP was installed in early 2006 as part of a collaboration between Adelaide-based company ATRAD Pty. Ltd. and the University of Adelaide. The system presently shares a transceiver system with a co-located 144-element Stratosphere-Troposphere radar [Dolman et al., 2018]. The receiver at Mylor was installed solely by ATRAD Pty. Ltd. in late 2015.

Typical results from both of these systems are shown in Fig. 2.7. These plots show the meteor temporal/spatial distribution and the estimated mesospheric wind field corresponding to data collected on 07-Apr 2018. As an aside, it should be noted that the peak detection height of the meteors at Mylor is several km higher than that at BP; as discussed in Sect. 2.2.4, while it is expected that a bistatic receiver would on average detect meteors at higher altitudes, much of this difference has been determined to be due to effects of phase calibration errors in the Mylor system. This point is taken up in detail and largely resolved in Chapter 5.

Further details on the operation principles of these radars and the signal processing algorithms applied are described in the following sections.

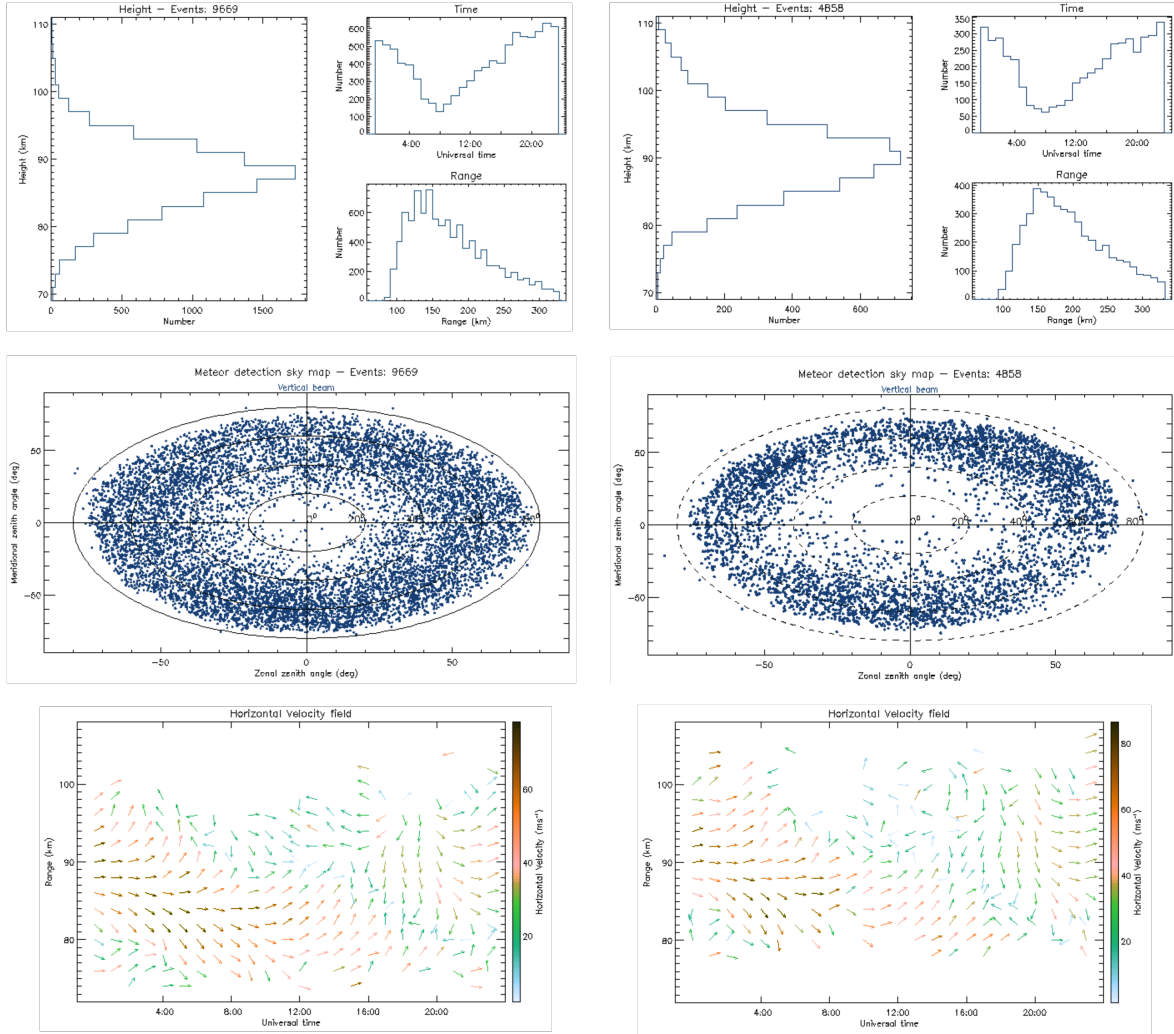


Fig. 2.7: BP and Mylor meteor radar results from 07-Apr 2018). BP data are shown in the left panels, and Mylor in the right panels. The upper panels show the distribution of meteor detections in height, range, and time, the middle panels show the distribution with angle, and the lower panels show the horizontal wind estimates.

## 2.4 Interferometric meteor radar operation

This section provides an overview of the operation principles of an interferometric meteor radar. The 55 MHz system at BP is a typical example of meteor radars used worldwide, and so will be used here as a template for describing meteor radars generally. Broadly, the system consists of the following components:

- a transceiver unit, for the generation and shaping of transmitted pulses/pulse codes, and for the amplification of the received signals;



Parameter	Value
Frequency	55 MHz
Pulse width	7.2 km
Pulse code	4-bit complementary
Pulse shape	Gaussian
PRF	440 Hz
Range sampling	9.0-306.0 km
Range sampling interval	1.8 km
Receiver bandwidth	35.6 kHz
Peak power	40 kW
Polarisation	Circular

Table 2.1: Experiment parameters used with the BP and Mylor meteor radars, for all data presented in this thesis.

- a single folded cross dipole antenna for signal transmission, and an array of 5 cross dipole antennas for signal reception;
- a PC running Linux for scheduling and running the experiments, and recording and analysing the received signals.

### 2.4.1 Signal transmission

The first step in producing a radar pulse is to generate a “carrier” signal at the nominal frequency of the radar. A synthesizer in the transceiver unit produces this in the form of a  $\pm 3$  V continuous wave.

The next step is to generate the desired pulse envelope for amplitude/phase modulating the carrier signal. In all the meteor experiments conducted in this study, the modulating signal is a 4-bit complementary code (see e.g., Fukao and Hamazu [2014], their Sect. 8.3.4 for a motivation behind such use of pulse compression). This envelope is produced digitally by a microcontroller within the transceiver unit. The envelope is subsequently passed through a digital to analogue converter, applied to the carrier signal, and amplified to  $\pm 6$  V.

The modulated pulse is multiplexed into six different lines, which are amplified and subsequently recombined into a single signal with a nominal power of 48 kW. Finally, this signal is split into two separate  $50 \Omega$  transmission lines, each of which is connected

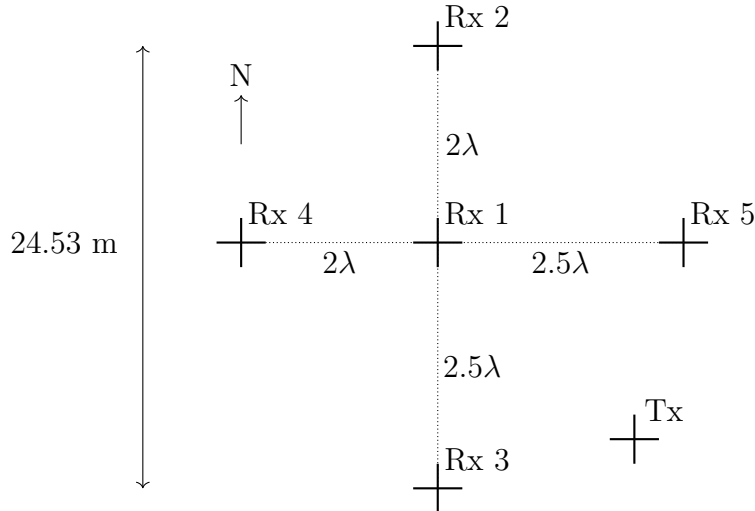


Fig. 2.8: Layout of antennas for the 55 MHz BP meteor radar array. Antenna separations are given in wavelengths ( $\sim 5.45\text{ m}$ ). Note that the transmit antenna location is approximate.

to one of the two  $200\ \Omega$  stainless steel arms of the folded cross dipole transmit antenna. To ensure a minimal amount of signal is reflected back down the transmission line from the antenna, the antenna is impedance-matched to the transmission line through the use of a balun.

One of the transmission lines to the transmit antenna incorporates a  $90^\circ$  delay relative to the other. Given that the antenna arms are orthogonal, the resultant radiated wave is circularly polarized.

### 2.4.2 Signal reception

The receive array consists of 5 antennas arranged into a cross with  $2$  and  $2.5\ \lambda$  antenna separations, following the antenna configuration proposed by Jones et al. [1998] (see Fig. 2.8). Each of these antennas consists of three  $200\ \Omega$  cross dipole elements constructed from aluminium tubing.

The antennas are connected to  $50\ \Omega$  transmission lines by means of a gamma match. Radio waves (notionally with a frequency of 55 MHz) transferred into a given transmission line (which in typical meteor detection cases have an amplitude of a few microvolts) are then passed through a low noise amplifier, which increase the signal power by approximately 20 dB. This amplification stage also incorporates a wideband band-pass filter centred on the carrier frequency, which is intended to remove out-of-band noise/interference from the signal.

The signal is then passed through a downconverter, in which it is mixed with a 135 MHz reference signal. This produces two new signals (referred to as heterodynes), one of which has a frequency equal to the sum of the two input frequencies (190 MHz) and another with the difference (80 MHz). The 190 MHz signal is removed by means of a bandpass filter, and the 80 MHz signal is transferred to a “detector” stage.

In the detector stage, the signal is multiplexed into two channels, each of which is mixed with an 80 MHz reference signal. One of these reference signals has a  $90^\circ$  phase lag relative to the other. The products of this mixing are often referred to as “In-phase” (I) and “Quadrature” (Q) signals, together representable as a complex number (with the I typically assigned the real part, and Q the imaginary). The phase of this complex number embodies the signal phase relative to other receiver channels, and so allows phase differences as a function of position and/or frequency to be estimated. Moreover, a linear phase variation as a function of time implies a difference in the frequencies of the signal incident on the receiver antenna(s) and the detector stage reference signal, which can (in the case of no interference) be interpreted as a Doppler shift of the originally transmitted signal.

The I and Q signals produced in the detector stage are then passed through a filter with an adjustable bandwidth. In the typical case, the bandwidth is chosen to be as close as possible to the effective bandwidth of the transmitted pulse, so as to reduce out-of-band noise power and to avoid range-blurring of the pulse. All work presented in this thesis pertaining to the BP and Mylor meteor radars utilized a bandwidth of 35.6 kHz.

Finally, the filtered I and Q signals are fed to a data acquisition card, in which they are digitized to 16-bit values. In this thesis, these two signals are represented as a complex voltage with time dependence,  $V(t)$ .

## 2.5 Meteor echo signal processing

The signal processing carried out on the recorded I and Q time series can be summarized in the following sequence of steps:

1. Remove sources of coherent interference (manifesting as sharp “bursts” of power across all range gates simultaneously);
2. Apply known receiver channel phase offset corrections;

3. Coherently combine signals from all receivers (using phase differences estimated over 1-second blocks), then flag all points with a combined power above a pre-specified noise threshold;
4. Remove possible “multiple detection” candidates that exist over more than one range gate;
5. Re-estimate phase differences of candidate meteor echo time series truncated to their “start” and “end” points;
6. Re-combine the time series coherently (using the phase differences estimated in the step 5), re-estimate the “start” and “end” times, and repeat step 5;
7. Reject candidates that do not exhibit the rapid rise and exponential decay expected of underdense meteor echoes;
8. Estimate the decay times and radial velocities associated with candidate echoes.

Each of these steps are discussed in detail in Holdsworth et al. [2004a]. In this thesis, the range, phase difference and radial velocity estimates (and their errors) from echo candidates are of great importance, so the methods for obtaining them are now briefly outlined.

### 2.5.1 Phase difference estimation

The mean phase differences associated with a meteor echo measured by a given receiver pair are estimated by computing the cross-correlation function (CCF) at lags  $\pm 1$  and  $\pm 2$ , performing a linear fit to the phase of the CCF across those lags, and extracting the phase at lag 0. For reference, the CCF  $\rho_{ij}$  at lag  $\tau$  for receivers  $i$  and  $j$  is evaluated using the expression:

$$\rho_{ij}(\tau) = \frac{\langle V_i(t) \rangle \langle V_j^*(t + \tau) \rangle}{\sqrt{\langle |V_i(t)|^2 \rangle \langle |V_j(t)|^2 \rangle}}. \quad (2.8)$$

As Holdsworth et al. [2004a] notes (their Sect. 3.6), noise that is correlated between receiver channels will significantly increase the amplitude of the CCF at  $\tau = 0$ , and possibly contaminate its phase. In practice, precluding  $\rho_{ij}(0)$  from the linear fit to the CCF phases compensates for this. A demonstrative example of this (using meteor radar time series produced with the model discussed in Chapter 3), in which identical noise signals have been added to the I and Q signals from both channels, is shown in Fig. 2.9.

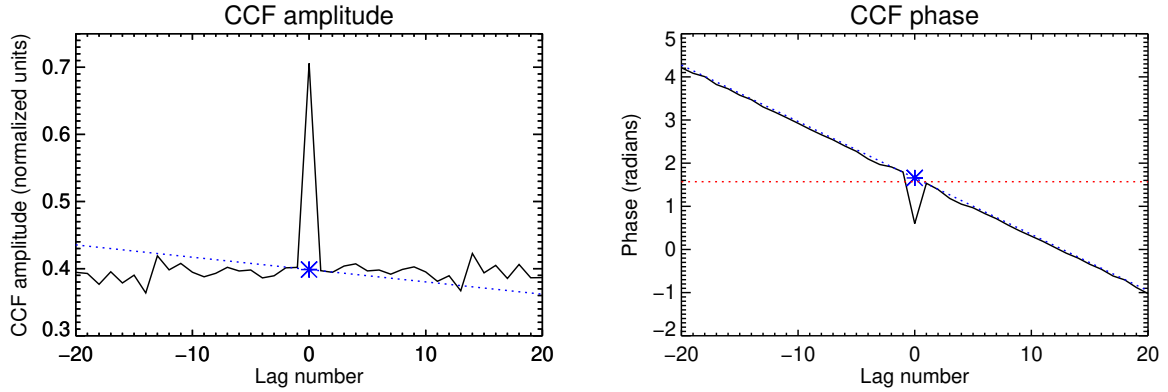


Fig. 2.9: The cross correlation function amplitude (left) and phase (right) of simulated 55 MHz meteor echo time series. The dotted blue line indicates a linear fit of the ordinate value across lags  $\pm 1$  and  $\pm 2$ , and the blue asterisk the interpolated value at a lag of 0. The receiver time series in question both have 1,000 points, an SNR of 5 dB, a decay time of 1 second, a PRF of 440 Hz, and a target radial velocity of  $25 \text{ ms}^{-1}$ . The phase difference between the simulated receiver signals is  $90^\circ$ , which is indicated on the phase plot by a dotted red line.

## 2.5.2 Radial velocity estimation

To estimate radial drift velocities from meteor echo candidates, the CCFs are firstly summed over all possible receiver combinations, and then a least-squares linear fit to the phase of the result across lags  $\pm 1$  and  $\pm 2$  is performed. As with the phase difference estimation, lag 0 is precluded from the fit to avoid the contaminating effects of correlated receiver noise (see the right panel of Fig. 2.9 for an example of the effect this could have on the estimated phase slope). The slope of the fit is then used to compute a time-rate-of-change of phase  $\frac{d\phi}{dt}$ , from which the radial velocity  $v_r$  can be calculated via:

$$v_r = -\frac{\lambda}{4\pi} \frac{d\phi}{dt}. \quad (2.9)$$

As discussed in Holdsworth et al. [2004a] (their Sect. 3.11), the time series used in computing the CCFs is restricted from 0.015 seconds after the “start” time of the echo, to the “end” time. This is done to minimize the effects of the noise floor, Fresnel oscillations in the time series and the velocity of the meteoroid itself on the estimated velocity. Meteor candidates with a projected horizontal velocity of more than  $200 \text{ ms}^{-1}$  are deemed to have been contaminated by one or more of these error sources, and are subsequently excluded from further analysis. In addition, candidates whose least-squares

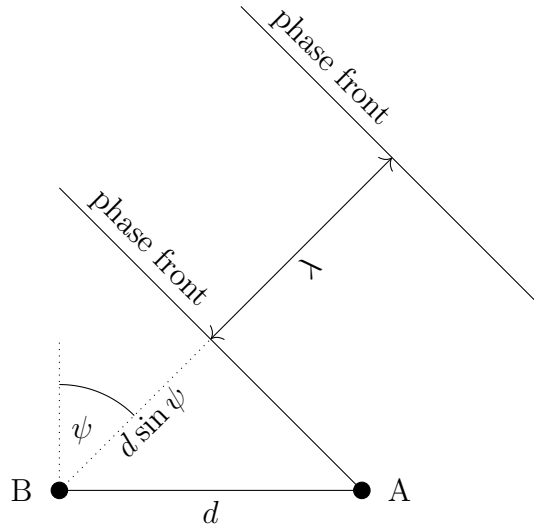


Fig. 2.10: Planar wave fronts inclined at zenith angle  $\psi$  impinging on an interferometer, consisting of antennas at A and B, separated by distance  $d$ . The path difference between B and A is  $d \sin \psi$ , so the phase measured at B is  $\frac{2\pi}{\lambda} d \sin \psi$  greater than at A.

fit slope error exceeds a pre-determined threshold are excluded from further analysis. The estimator of slope error used in the Holdsworth et al. [2004a] work and this thesis is given by the entry pertaining to the slope in the correlation matrix for the above least-squares fit, multiplied by the interpulse interval  $\delta$ . The threshold used is 0.068.

## 2.6 Angle-of-arrival estimation

The angle-of-arrival (AOA) determination approach outlined in Jones et al. [1998] is the one most commonly-applied in meteor radars worldwide to estimate the AOAs of meteor echoes. The approach used in this thesis (aside from an alternative discussed in Chapter 5) uses an adaptation of the Jones method presented by Holdsworth [2005], which is discussed in the next subsection. Some alternative methods that have been proposed are also briefly mentioned in the following subsection.

### 2.6.1 Adapted Jones method

The basic concept behind meteor AOA estimation with a two-antenna interferometer is illustrated in Fig. 2.10. Assuming the radio wave phase fronts (with separation  $\lambda$ , the radar wavelength) associated with a meteor echo are planar, the measured phase difference  $\chi$  along a baseline with known antenna separation  $d$  can be used to determine

the zenith angle  $\psi$  of the echo along that baseline via the expression:

$$\chi = \frac{2\pi}{\lambda} d \sin \psi. \quad (2.10)$$

This expression can be inverted to obtain a unique solution for  $\psi$ , provided  $\chi$  has not been aliased. Aliasing occurs when  $d \geq 0.5\lambda$ , in which case there is a set of (ambiguous) solutions for  $\psi$ .

Unfortunately, for a given error in  $\chi$ , errors in  $\psi$  are larger for smaller values of  $d$ . Additionally, measurements from Jones et al. [1998] showed that mutual coupling between VHF meteor radar antennas induced significant biases in  $\chi$  for  $d \leq 1.5\lambda$ .

The antenna configuration proposed by Jones et al. [1998] (i.e., the use of  $2.0$  and  $2.5\lambda$  baselines shown in Fig. 2.8) may be used to largely overcome these conflicting requirements. Their configuration allows for a phase difference estimate at an antenna separation of  $4.5\lambda$ , which while yielding a set of possible values for the AOA (denoted  $\Psi_{4.5\lambda}$ ), is less susceptible to noise and mutual coupling than a  $0.5\lambda$  estimate. A virtual  $0.5\lambda$  estimate, which may be obtained by summing the  $2.5\lambda$  and  $2.0\lambda$  phase differences, can then be used to unambiguously determine a “noisy” value of the AOA, denoted  $\psi_{0.5\lambda}$ . The  $\Psi_{4.5\lambda}$  candidate closest to  $\psi_{0.5\lambda}$  may then be designated as the “correct” AOA (herein the “0.5-4.5 $\lambda$ ” method).

A problem with the above approach is that error in  $\psi_{0.5\lambda}$  may result in the selection of an incorrect  $\Psi_{4.5\lambda}$  candidate, given the relatively close spacing of those in that set. To reduce the probability of this happening, Holdsworth [2005] proposed first using  $\psi_{0.5\lambda}$  to select a  $\Psi_{2.0\lambda}$  candidate, and using the resulting  $\psi_{2.0\lambda}$  to select the “correct”  $\Psi_{4.5\lambda}$  candidate (herein the “0.5-2.0-4.5 $\lambda$ ” method). In a simulation, they found for typical phase estimation errors that this increased the number of meteors within  $\pm 1^\circ$  of the true AOA by several percent. Negligible difference was observed if the  $2.5\lambda$  spacings were used in place of the  $2.0\lambda$ .

Noting that estimates of  $\chi$  vary linearly with  $\sin \psi$ , Holdsworth [2005] also suggested in the above process to minimize the sine of the difference in AOAs rather than their actual values (i.e., minimizing  $|\sin \psi_{2.0\lambda} - \sin \psi_{0.5\lambda}|$  to find the optimal  $\Psi_{2.0\lambda}$  candidate rather than  $|\psi_{2.0\lambda} - \psi_{0.5\lambda}|$  as Jones et al. [1998] had done). They found that this marginally increased the number of meteors within  $\pm 1^\circ$  of the true AOA.

Once the zenith angles  $\psi_x$  and  $\psi_y$  along the two orthogonal baselines have been found, the zenith angle  $\theta$  may be simply evaluated as  $\sqrt{\psi_x^2 + \psi_y^2}$ , and the azimuth angle  $\phi$  as

$\text{atan2}(\psi_x, \psi_y)$ , assuming that the  $x$  and  $y$  baselines are oriented along the East-West and North-South axes, respectively.

### 2.6.2 Alternative approaches

While the Jones-based algebraic approach for meteor AOA estimation has proven to be reliable, several alternatives have been developed in recent years. They basically seek to overcome some or all of the following limitations of the Jones-like methods:

1. Limited flexibility in antenna configuration. While the orthogonal baselines may be arranged in a “+”, “L” or “T” shape, the antenna spacings must not deviate from  $2.0\lambda$  and  $2.5\lambda$  if the method is to work as intended, and the antennas must also all be at the same height.
2. Only 6 of the possible 10 antenna pairs are used in the estimation of the AOA. In the presence of receiver noise, this could result in a less precise AOA estimate.
3. If extra antennas at arbitrary locations happen to be available, it may not be straightforward to incorporate them usefully in the AOA estimation.
4. Weighting of the different baselines according to phase difference estimation error is not possible.

Younger and Reid [2017] overcame all of these limitations by proposing a method based on computing AOA probability distributions for each antenna pair from the difference between measured and precalculated phase differences. The method computes the sum of AOA probability distributions for each antenna pair, and the AOA with the highest probability is then selected as the “true” AOA. The method also allows the contribution of each antenna baseline to the sum to be weighted, notionally on the length of the baselines but also on the estimated phase difference errors. They found the method to perform as well as the  $0.5\text{-}2.0\text{-}4.5\lambda$  method on the Jones antenna configuration, and to be less susceptible to the aliasing of AOAs to the wrong AOA candidate. In addition, simulations conducted on a 6-antenna pentagonal configuration with a raised centre antenna implied significantly smaller AOA errors at high zenith angles relative to the 5-antenna adapted Jones method.

Both Vaudrin et al. [2018] and Clahsen [2018] also overcame all of the above limitations by implementing a non-linear least squares fitting algorithm that simultaneously solves for parameters in a raw meteor echo signal model, including power, range, decay time,



radial velocity and AOA. The approach offers considerable flexibility in the method used to minimize the objective function of the fit, and also allows for the propagation of errors from the raw signal to each of the estimated parameters. Vaudrin et al. [2018] show that their method yields considerably smaller height estimation errors than the  $0.5\text{-}4.5\lambda$  method when applied to a Jones-like antenna array.

As yet, no work has been published that conclusively demonstrates better AOA-estimation performance than the  $0.5\text{-}2.0\text{-}4.5\lambda$  method at large zenith angles for a Jones-like antenna array. Nevertheless, as found in this thesis in Chapter 5, the typically large phase calibration errors at large zenith angles result in larger AOA errors there, further exacerbating errors arising from the increased sensitivity to phase difference estimation errors. These findings indicate that first resolving those phase calibration errors may be more important than implementing an alternative AOA estimation technique.

## 2.7 Position estimation using the WGS-84 ellipsoid

Meteor altitudes are typically evaluated under a spherical Earth assumption (e.g., Holdsworth et al. [2004a]). To improve the accuracy of the height estimates and to correctly account for the radar systems' height above sea level, the WGS-84 ellipsoid model of the Earth is used in this thesis to compute the meteor's position (largely following the approach of Stober et al. [2018]). From this, the latitude, longitude, and height above sea level may be computed.

The position estimation works in tandem with a range de-aliasing procedure, both of which are outlined below.

### Range de-aliasing

As discussed in Sect. 2.3, this thesis makes use of pulsed radars whose pulse repetition intervals (notionally  $1/440$  seconds) are commensurate with the time taken for the pulse to propagate along the Tx-meteor-Rx path. This means echoes received beyond a range threshold of  $R_{amb} = c\delta/2$  ( $\sim 340$  km in this study), where  $c$  is the speed of light in a vacuum and  $\delta$  is the pulse repetition interval, will be range aliased. Range de-aliasing is performed by firstly producing a range ensemble for each meteor candidate, given by:

$$R_n = R + nR_{amb}, \quad (2.11)$$

where  $n \in \mathbb{Z}$  and  $R$  is the estimated meteor range. In this study, the maximum chosen

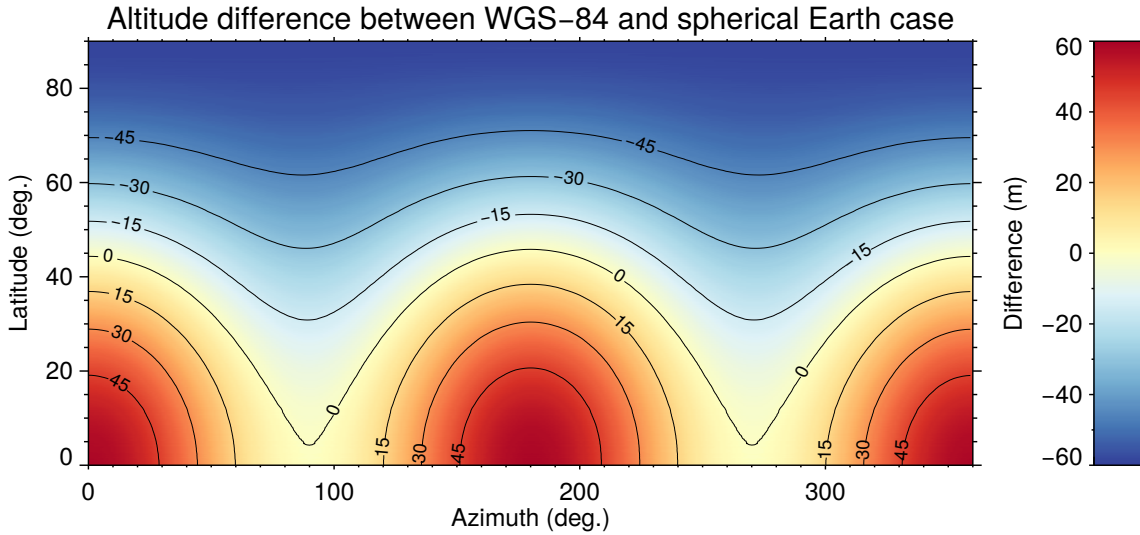


Fig. 2.11: Difference between meteor altitudes estimated assuming a WGS-84 ellipsoidal Earth and a locally spherical Earth with a WGS-84-defined radius. The meteor used had a fixed range of 350 km from the receiver and a zenith angle of  $75^\circ$ .

value of  $n$  is 5, corresponding to a maximum unaliased range of about 1,700 km (well beyond the expected maximum range of meteor detections). An ensemble of heights is then calculated using the procedures outlined below. An echo candidate is rejected if there are no height estimates within the [70,110] km interval (“height unresolvable”), or if there are multiple estimates within this interval (“height ambiguous”).

### Position estimation

The position estimation is done according to the steps below (associated formulae are provided in Appendix B). Inputs to the procedure are the latitude, longitude and geodetic height of the receiver (and transmitter in the bistatic reception case), and the meteor range (possibly part of an ensemble, as discussed above) and the candidate’s AOA.

1. Convert the latitude, longitude and height coordinates of the receiver (and transmitter if appropriate) sites to Earth-centred, Earth fixed (ECEF) coordinates.
2. Use the range and the estimated AOA of the meteor to compute the meteor’s position in the receiver’s local East-North-Up (ENU) coordinates.
3. Calculate the meteor’s position in ECEF coordinates.
4. Convert the ECEF coordinates of the meteor to geodetic coordinates (latitude, longitude, and geodetic height).

As a motivation for this approach, Fig. 2.11 shows the error in the altitude estimate as a function of latitude and azimuth that arises when assuming a locally spherical Earth (with a WGS-84-defined radius as a function of latitude), versus the WGS-84 ellipsoid (for a meteor at a range of 350 km and a zenith angle of  $75^\circ$ , corresponding to a geodetic height of about 100 km). Errors as high as about 60 m arise at the equator depending on the look direction, and the same at the poles regardless of the look direction. While height estimation errors arising from phase/phase calibration errors may be in the range of several km at large zenith angles (see Chapter 5), it is still worth removing these errors given the minimal extra processing required.

## 2.8 Wind velocity estimation

The radial velocity and AOA information associated with a collection of meteor detections can be used to estimate the wind velocity (e.g., Hocking and Thayaparan [1997] and Holdsworth et al. [2004a]), momentum fluxes (e.g., Hocking [2005]), or even turbulence spectra of the wind (e.g., Stober et al. [2018] and Vierinen et al. [2019]). In the case of the mean wind estimate, the goal is to find a single wind velocity vector that best fits the radial velocity-AOA distribution. For  $n$  available meteors, the problem may be formulated as the linear equation:

$$\mathbf{v}_r = \mathbf{A}\mathbf{v}, \quad (2.12)$$

where  $\mathbf{v}_r$  is a  $n \times 1$  vector of radial velocities,  $\mathbf{A}$  is a  $n \times 3$  matrix of direction cosines whose rows read  $[\sin \theta \sin \phi, \sin \theta \cos \phi, \cos \theta]$ , and  $\mathbf{v} = [u, v, w]^T$  is a vector containing the zonal, meridional and vertical wind velocities respectively.

As discussed by Stober et al. [2018] (their Sect. A4), the  $\theta$  and  $\phi$  terms in (2.12) should not be the zenith and azimuth angles to the meteor from the receiver, but the orientation of the  $\mathbf{b}$  vector in Fig. 2.2 in the polar ENU coordinates at the meteor location. This is done to compensate for the rotation of the ENU coordinate system between different locations on the Earth's surface. These rotations of course become pronounced close to the poles, given the large changes in the local north/south direction over small spatial distances. As an example of the effect of the correction, Fig. 2.12 shows the error in the direction cosine terms (zonal:  $\sin \theta \sin \phi$ , meridional:  $\sin \theta \cos \phi$ , vertical:  $\cos \theta$ ) that arise when the correction is not performed, at a latitude of  $45^\circ\text{N}$  and for a meteor altitude of 100 km. The effect generally becomes greater at larger

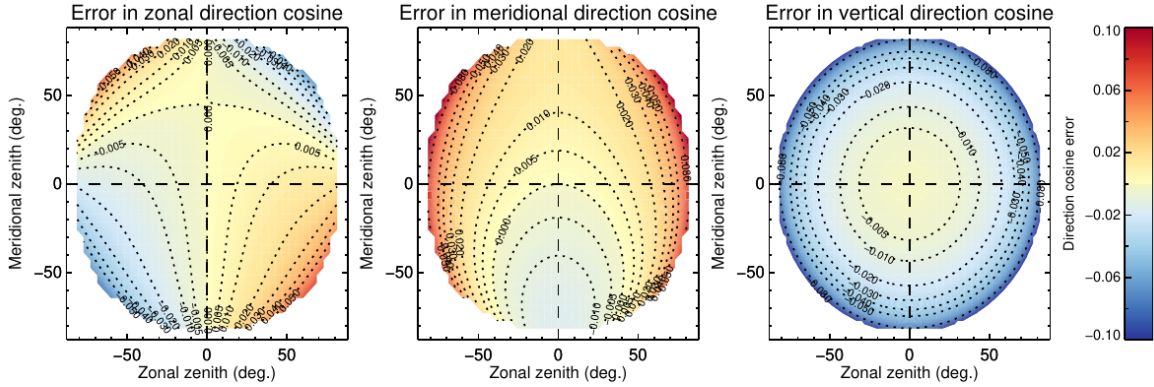


Fig. 2.12: Error in the direction cosine terms arising from assuming a planar Earth, at a latitude of  $45^\circ\text{N}$ . The meteor altitude used in the above plots is 100 km.

zenith angles, with direction cosine errors of up to  $\sim 0.1$  in the meridional and vertical components. As such, this correction is performed for all estimations of wind velocity in this thesis.

In practice, attempts are made to solve (2.12) for a wind velocity when  $n \gg 3$ , making the system of equations overdetermined. This means a “best fit” solution needs to be sought. In this study Singular Value Decomposition (SVD) is used to least-squares solve the system; SVD decomposes a matrix  $\mathbf{A}$  into a product of three matrices:

$$\mathbf{A} = \mathbf{U}\mathbf{\Sigma}\mathbf{V}^T,$$

where in this case  $\mathbf{U}$  is a  $n \times n$  orthogonal matrix,  $\mathbf{\Sigma}$  is a  $n \times 3$  diagonal matrix, and  $\mathbf{V}^T$  is a  $3 \times 3$  orthogonal matrix (e.g., Press et al. [1992]). The least-squares solution to (2.12) may then be written as:

$$\mathbf{v} = \mathbf{V}\mathbf{\Sigma}^{-1}(\mathbf{U}^T\mathbf{v}_r). \quad (2.13)$$

Using the inverse of the SVD output to solve (2.12) rather than the inverse of  $\mathbf{A}$  is done for improved numerical stability. As discussed by Press et al. [1992] (their Sect. 15.4), use of SVD allows for the removal of equations that cause large changes in  $\mathbf{v}$  for only small changes in  $\mathbf{v}_r$  or  $\mathbf{A}$ . Following the recommendation of Press et al. [1992], that is carried out in this thesis by setting to 0 entries in the  $\mathbf{\Sigma}^{-1}$  matrix that have a value greater than  $1 \times 10^5$ .

The wind estimation procedure used in this thesis also incorporates an iterative outlier removal scheme following that proposed by Hocking and Thayaparan [1997] (and

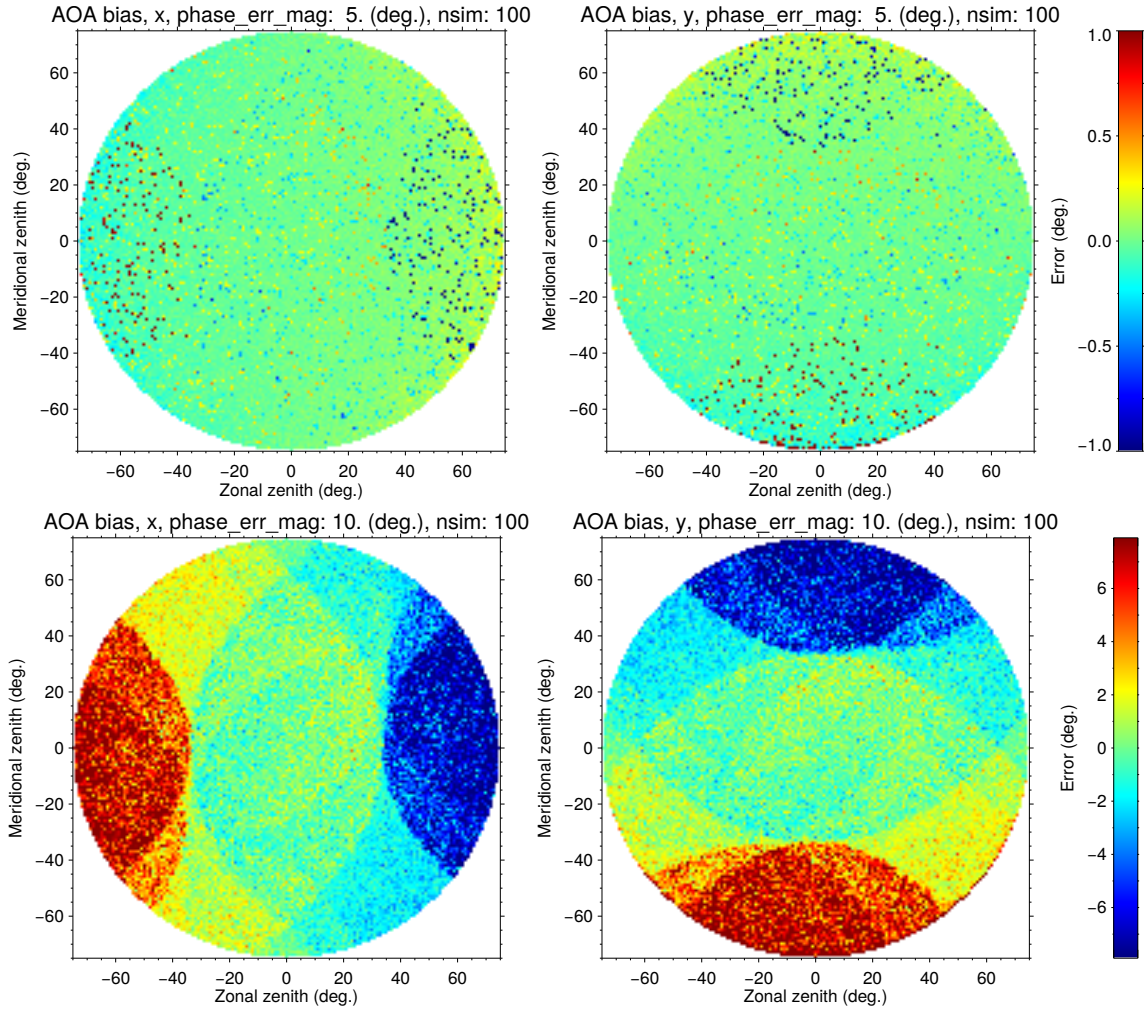


Fig. 2.13: Distributions of bias in AOA that arise when normally distributed phase offsets are applied to the receivers in a Jones antenna configuration. Zonal zenith errors are in the left panel, and meridional zenith in the right. The offsets applied in the upper panel have a standard deviation of  $5^\circ$ , and  $10^\circ$  in the lower panel. Note the difference in colour bar range in the upper and lower panels.

subsequently used by e.g., Holdsworth et al. [2004a]). This involves performing an initial fit for the wind velocities, removing the radial velocities whose value differs from the horizontally-projected radial wind by more than  $25 \text{ ms}^{-1}$ , and repeating the procedure until no outliers are found or until less than 6 meteors remain. The wind covariance procedure used in this thesis also incorporates an approach like this for outlier removal, as discussed in Sect. 3.2.6.

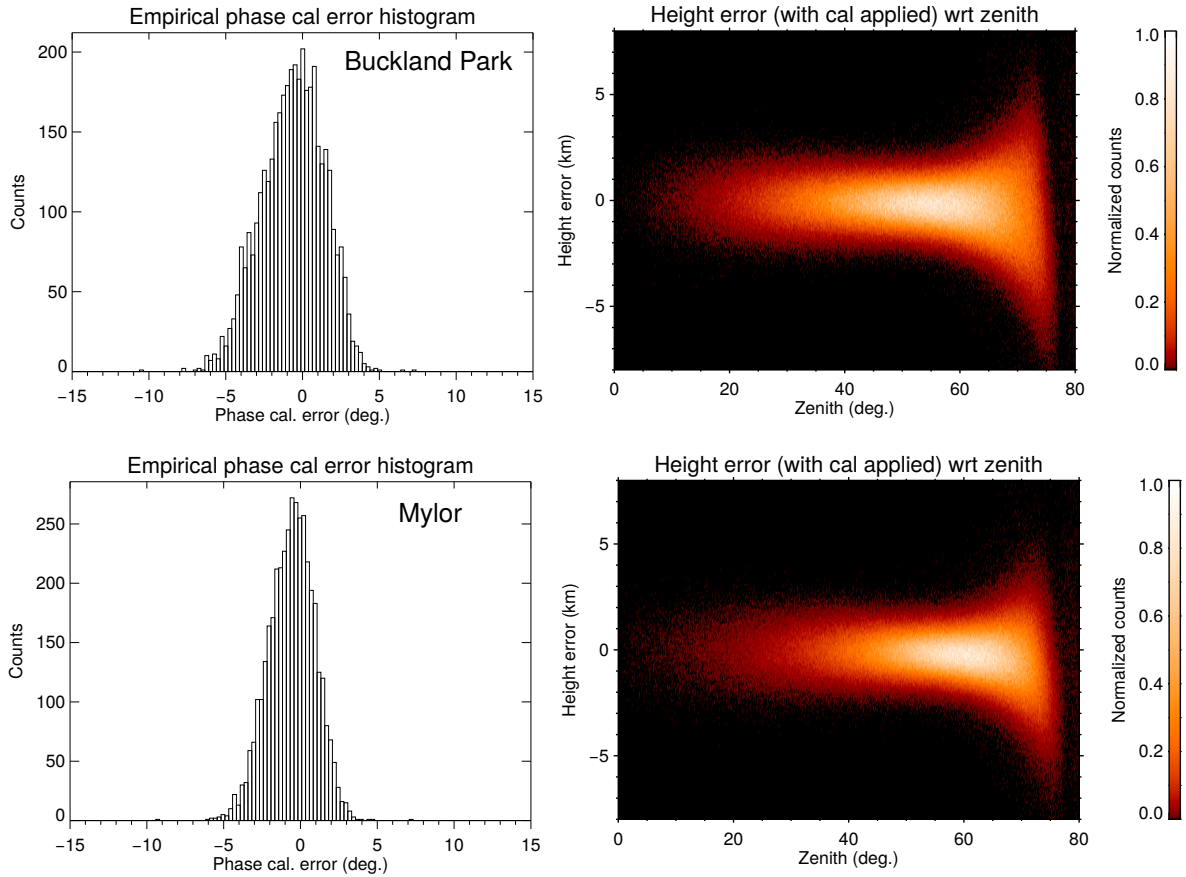


Fig. 2.14: Distribution of phase calibration (left panel) and height (right panel) errors resulting from the application of the Holdsworth et al. [2004b] empirical phase calibration technique. Results for the BP receiver are shown in the top panel, and Mylor in the lower.

## 2.9 Interferometric meteor radar phase calibration

The AOA-determination method introduced in Sect. 2.6 assumes that the measured phase differences are unbiased. Figure 2.13 shows distributions of mean AOA errors as a function of true AOA that result for a Jones antenna configuration when phase calibration errors with a standard deviation of  $5^\circ$  and  $10^\circ$  are applied to each receiver channel. It is clear from this that errors of around  $10^\circ$  often result in the 0.5-2.0-4.5 $\lambda$  method selecting the incorrect AOA candidate, and in turn resolving the AOA evaluated on both baselines to the wrong part of the sky.

Position errors like this could lead to vastly incorrect and/or less precise wind estimates, as well as the assignment of incorrect altitudes to those estimates. It is thus critical to remove these offsets before subsequent processing of the data. While a novel method for phase calibration of meteor radars is introduced in Chapter 5 of this the-

sis, Chapters 3 and 4 make use of an empirical method developed by Holdsworth et al. [2004b], which is now described.

The method, which relies only on archived meteor detections, efficiently searches for phase offsets between antenna pairs on each baseline in a Jones-like antenna configuration that maximise the number of meteor detections within a predetermined acceptable height interval. Referring to the two pairs on a given baseline as  $j$  and  $k$ , each associated with antenna separations  $d_j$  and  $d_k$ , on baseline  $j$  the measured phase differences as may be represented as:

$$\chi'_j = \chi_j + \alpha_j,$$

where  $\alpha_j$  is the phase offset and  $\chi_j$  is the “correct” phase difference. Following Sect. 2.6.1 and assuming  $\chi'_j$  is aliased, there is a set of incorrect candidate AOA's  $\Psi'_j$  corresponding to  $\chi'_j$ . Representing one of those candidates as  $\psi'_j$ , there is also a phase difference on pair  $k$   $\varphi_k$  that will yield that candidate, given by:

$$\varphi_k = \frac{2\pi}{\lambda} d_k \sin \psi'_j. \quad (2.14)$$

Introducing a new phase difference  $\gamma_k = \varphi_k - \chi'_k$  and noting that  $\chi_k = \frac{d_k}{d_j} \chi_j$  leads to the expression:

$$\gamma_k = \frac{d_k}{d_j} \alpha_j - \alpha_k, \quad (2.15)$$

i.e., a term to which the offsets associated with both pairs may be related. A second new phase difference  $\chi''_k = \chi'_k - \gamma_k$  may then be written as:

$$\chi''_k = \chi_k - \frac{d_k}{d_j} \alpha_j. \quad (2.16)$$

This can be re-arranged to find  $\alpha_j$ , which can in turn be used in (2.15) to compute  $\alpha_k$ . Repeating this process on the orthogonal baseline then yields all required phase offset estimates.

As Holdsworth et al. [2004b] discusses, due to phase noise a distribution of  $\gamma_k$  values will result when the technique is applied to an ensemble of meteor detections. Using a simulation, they found that fitting a Gaussian to this distribution and extracting the

peak value led to the most accurate values of  $\gamma_k$ . Additionally, rather than using the  $\alpha_k$  directly evaluated from (2.16), they found that iteratively searching for a value of  $\alpha_k$  (and doing the same for the orthogonal baseline) that maximised the number of meteors within a height interval of 70-110 km led to more accurate phase offsets. The iterative search was performed by first using a grid with  $10^\circ$  spacing encompassing all possible values of  $\alpha_k$ , then defining a smaller grid with  $5^\circ$  spacing centred on the obtained  $\alpha_k$  estimate, and repeating for spacings of  $2^\circ$ ,  $1^\circ$  and  $0.5^\circ$ . This thesis makes use of this approach.

Results from simulating the performance of the Holdsworth et al. [2004b] method on meteor radars used in this study are shown in Fig. 2.14. Briefly, this simulation made use of phase differences produced from real meteor distributions collected from the BP and Mylor meteor radars, added random offsets to each receiver pair, and then attempted to re-estimate those using the phase calibration technique. A total of 1000 realisations of the method applied to 1000 meteor detections have been used. The heights of the input meteors were Gaussian-distributed, with a mean of 92 km and standard deviation of 6 km. Further details on the simulation are provided in Chapter 3.

In agreement with the findings of Holdsworth et al. [2004b], the results indicate 1-sigma phase calibration estimate errors of  $\sim 2^\circ$ . They also indicate 1-sigma post-calibration height errors of  $\sim 1$  km, and  $\sim 2$  km at zenith angles in excess of  $70^\circ$ .

## 2.10 Summary

This first part of this Chapter described some basic characteristics of meteors: their sources in the Solar System, and the reasons behind their variable flux as a function of time of day and their altitude distributions as observed by radars. Both of these aspects have a profound impact on the precision and accuracy on meteor radar estimates of mesospheric momentum fluxes; this is explored extensively in Chapter 3. Moreover, meteor altitude distributions are used in Chapter 5 to validate the performance of phase calibration techniques.

The operation principles of meteor radars and the signal processing algorithms relevant to this thesis were then outlined. Specific attention was given to the Doppler velocity and AOA estimation procedures, as the performance of these is also crucial to the radar's momentum flux estimation capability explored in Chapter 3. Since this thesis makes use of a forward scatter meteor radar system, the differences in interpretation of forward and backscatter meteor echoes was also stressed.



Finally, the empirical phase calibration technique applied to data presented in Chapters 3 and 4 was described. While this technique has long-proved to be essential in compensating for unknown receiver phase offsets in meteor radars, a technique relying on the use of civilian aircraft that slightly outperforms it forms the basis of Chapter 5.

## Chapter 3

# Simulation of meteor radar covariance estimation

One of the main outcomes of this thesis is the use of meteor radar to measure the momentum flux divergence in the mesosphere that arises from the breaking of gravity waves. As mentioned in Chapter 1, this measurement requires an estimation of the covariance between the horizontal and vertical components of the wind field (i.e.,  $\langle u'w' \rangle$  and  $\langle v'w' \rangle$ ). While there may be cases in which large monochromatic waves dominate the gravity wave spectrum (see e.g., Sect. 5 of Fritts et al. [2012a]), it is customary to assume that the horizontal and vertical winds measured at a given position will fluctuate randomly with some level of correlation (see e.g., Kudeki and Franke [1998] and arguments therein). With that assumption, for a given absolute uncertainty in say the  $\langle u'w' \rangle$  covariance term, if the component wind samples are obtained from an ideal “anemometer” they must be sampled for an amount of time that increases as the fraction  $\langle u'w' \rangle / \sqrt{\langle u'^2 \rangle + \langle v'^2 \rangle}$  decreases (e.g., Kudeki and Franke [1998]). In other words, the error in the covariance terms is large when there is a large horizontal flux but little vertical flux.

In the case of sampling with a meteor radar, the error in that covariance estimate is further increased by the need to transform a number of spatially separated line of sight velocity measurements into their Cartesian components (e.g., as first done with meteor radar measurements by Hocking [2005]). Furthermore, receiver noise will lead to uncertainties in those line of sight velocity measurements, and both noise and phase biases will contribute to the position measurements needed to transform the velocities. Knowing how these sources of uncertainty combine in the presence of already large errors due to typically low correlations between horizontal and vertical winds is crucial to correctly interpreting the resulting momentum flux estimates.

In this Chapter, a radar model is developed that simulates the covariance estimation uncertainties specific to the BP and Mylor meteor radar link, in the presence of a wave field derived from a gravity wave spectral model. The next section gives a brief overview of other meteor radar studies that have incorporated methods (other than the approach of simply using the variance of a sample of estimates, as done by e.g., Moss et al. [2016], de Wit et al. [2016], and Egito et al. [2016]) for estimating covariance uncertainties. This is done to contextualize the unique contributions made by the model developed in this work.

### 3.1 Overview of uncertainty estimates in similar studies

Vincent et al. [2010] were the first to consider the uncertainties in meteor radar estimates of the  $\langle u'w' \rangle$  and  $\langle v'w' \rangle$  terms. Their model consisted of monochromatic gravity waves with random phases, propagation directions and amplitudes, with randomly chosen meteor AOAs. To emulate radar measurement errors, they added normally-distributed errors to both the measured AOAs and radial velocities (with standard deviations of  $1.5^\circ$  and  $0.7 \text{ ms}^{-1}$ , respectively). They also simulated a number of different meteor detection rates ( $10\text{-}200 \text{ hr}^{-1}$ ). Their model's default configuration for testing of wind covariance incorporated a spectrum of 9 waves with a small azimuthal spread, an amplitude tapering about that central propagation azimuth, and randomly selected wave periods and phase speeds between 20 and 100 minutes and  $20$  and  $40 \text{ ms}^{-1}$ , respectively. Over 500 realisations, they obtained uncertainties in  $\langle u'w' \rangle$  of 1250% for  $10 \text{ meteors hr}^{-1}$ , and 250% for  $200 \text{ hr}^{-1}$ . In particular, they found that the uncertainty was practically the same for meteor rates  $> 100 \text{ hr}^{-1}$ , and depended only on the complexity of the wave spectrum.

In a study based around two meteor radars in Northern Europe, Placke et al. [2011b] assessed the ability of the radars to measure all components of the Reynolds Stress Tensor, using wind fields from a mechanistic atmospheric model as input. They used an averaging interval of 4 hours, aggregated over a 10-day dataset. They concluded that if the vertical wind fluctuations were less than about  $1/5$  the size of the horizontal fluctuations, the horizontal-vertical covariance terms were unphysical. It is worth noting that Placke et al. [2014] also came to similar conclusions when they compared the meteor radar results against a narrow beam MF radar's.

In two studies pertaining to results from a number of meteors (especially the SAAMER and DrAAMER systems installed in the vicinity of the Drake Passage), Fritts et al.

[2010b, 2012b] assessed the ability of those radars to measure all components of the Reynolds Stress Tensor. Expanding on Vincent et al. [2010]’s approach, their model incorporated real meteor detection distributions, and also tidal features and signal processing to remove them from the radial velocity measurements. Their model did not, however, incorporate AOA uncertainties arising from phase noise/calibration errors, and only superficially assessed the impact of radial velocity uncertainties. Their performance assessment consisted of a large variety of wind field configurations (including individual waves (both stationary and propagating horizontally and vertically), wave spectra, variable tidal amplitudes, and transient wave events). Their results emphasised the difficulty in defining “all-encompassing” uncertainty estimates for the  $\langle u'w' \rangle$  and  $\langle v'w' \rangle$  measurements, given the detection rate dependence on altitude and its sensitivity to the wave field complexity. Overall, they concluded that the monthly integrated estimates of  $\langle u'w' \rangle$  and  $\langle v'w' \rangle$  from the SAAMER and DrAAMER systems would be  $\sim 10\%$  at the centre of the peak detection height, and  $\sim 25\%$  at its edges. These radars obtained on average about 14,000 and 9,000 useable meteor detections per day.

Andrioli et al. [2013a] also performed similar assessments to those in Fritts et al. [2010b, 2012b], on a number of meteor radars in South America. These radars contained considerably lower count rates than the SAAMER and DrAAMER systems (about 3,000 per day on average), and as a result physically reasonable estimates of  $\langle u'w' \rangle$  and  $\langle v'w' \rangle$  for the more complex wave field test cases could not be obtained at any heights, even with month-long averaging. Extending on the work of Fritts et al. [2010b, 2012b], they also simulated the effect of AOA uncertainties on the analysis (by applying randomly distributed errors of  $1^\circ$  to the zenith and azimuth estimates), and determined a contribution to the momentum flux error of less than 2%. However, it should be noted that the only figure they supplied, which was for  $\langle v'^2 \rangle$ , indicated relative errors as high as  $\sim 20\%$  in some time-height bins. Regardless, they argued that this contribution was low and could be neglected.

In a study pertaining to momentum flux estimates from a meteor radar in Hawaii, Liu et al. [2013] also estimated momentum flux uncertainties directly from the data using a bootstrapping method. In their case, they randomly resampled each dataset 100 times, computed the standard deviation over the estimates from those samples, and assigned that to the error of the given quantity. This is an effective method for error estimation, provided the measurements included in each resampling are unique (in their case of having 5 years of data available, this may have generally been the case). Over 5

year, monthly superposed days with two-hourly binning, the absolute uncertainties they obtained for  $\langle u'w' \rangle$  and  $\langle v'w' \rangle$  were typically (depending on the month) around  $\sim 0.5 \text{ m}^2\text{s}^{-2}$  at the peak of the meteor distribution, and up to  $\sim 4 \text{ m}^2\text{s}^{-2}$  at the edges. The actual values obtained for those covariance estimates fluctuated between about -15 and  $15 \text{ m}^2\text{s}^{-2}$ . It should be stressed that while these errors are relatively small, they are associated with integration times much larger than those used in other studies (which have been a month or less for all reported here).

Riggin et al. [2016] also considers the uncertainties in momentum flux estimates derived from the MU radar (operating in meteor mode) in Japan. In contrast to previous studies, they caution the use of long integration times, claiming that they increase the chances of a loss of correlation between the wind components. They supported this claim by showing that in 16 independent cases, their estimates of  $|\langle u'w' \rangle|$  and  $|\langle v'w' \rangle|$  almost exclusively decreased with integration times between 0.5 and 24 hours, asymptoting to a particular value in each case. The authors also claimed that these asymptotic flux estimates were erroneously small, in comparison to those from the radar operated in a narrower, low-zenith-angle beam mode. They argued this arose from a loss of correlation between wind components over the relatively large volume occupied by the meteor returns. While it is clear that further investigation is needed on this particular MU radar dataset, we believe this study illustrates the problem of investigating momentum fluxes over periods long enough for multiple different wave populations or wave packets to pass through an observation volume, but too short (in the presence of measurement errors) to identify a wave signature that is present for the majority of a given season or one that is associated with tidal modulation. It should be noted that the former of these problems is a violation of an assumption for flux estimation with narrow-beam radars originally made by Reid [1987], in that the wind and wave field over the volume spanned by the targets needs to be statistically stationary. We believe a similar case also applies to the loss of correlation spatially: it is probably only feasible to use meteor radar for the measurement of fluxes due to non-transient waves with a large spatial scale.

The work of Matsumoto et al. [2016], which derived momentum fluxes from two equatorial meteor radars, should also be mentioned in this context. They do not describe how they obtained their errors in  $\langle u'w' \rangle$  and  $\langle v'w' \rangle$ , but the fact that their radars are identical and at essentially the same latitude (despite being separated by 4000 km) means the momentum flux may show similar seasonal variability at the two sites. However, in many of the cases in which their datasets overlapped, the discrepancy between their monthly

momentum flux estimates was larger than the sum of the associated 95% confidence intervals. We think this indicates a combination of two things: that their error calculation method generally underestimated the true error, and/or that the wave source characteristics are such that the momentum fluxes at the two sites have significantly different climatologies. Estimates of the momentum flux estimation errors using either a simulation or (because their datasets are sufficiently large) the bootstrapping method used by Liu et al. [2013] would help clarify this.

Collectively, the above studies illustrate the difficulty of estimating momentum fluxes using meteor radar, especially over time periods shorter than a few days. Given the original findings of Kudeki and Franke [1998], which suggest integration times of at least 16 days are required for flux measurements (even in the case of a perfect anemometer) if the flux represents 1% of the mean horizontal and vertical variance, this difficulty is unsurprising.

We believe that the approach introduced by Fritts et al. [2010b], which was to tailor a simulation specifically for their radar system, the signal processing schemes they used and the gravity wave spectra they expected to observe, is the only way to reliably characterise the momentum flux uncertainties. In light of this, the model developed in this Chapter simulates as accurately as possible the momentum flux estimation process used on the BP and Mylor meteor radars. To advance on the Vincent et al. [2010] and Fritts et al. [2010b] work, it incorporates a realistic spectrum of gravity waves as a wind field input, and real spatio-temporal distributions of meteors recorded at the BP and Mylor sites to sample those wind fields. To ensure the effect of AOA and radial velocity errors are accounted for, it also incorporates noise and phase-bias-induced errors in the simulated receiver channels and attempts to re-estimate the true AOA and radial velocity from those.

As well as to build on the previously discussed models, the aim here has been to quantify the uncertainties in the  $\langle u'w' \rangle$  and  $\langle v'w' \rangle$  covariance terms used in a gravity-wave–tidal interaction study in Chapter 4. The model was also initially developed to characterise the dependence of those uncertainties on both the shape and number of receivers in an arbitrary multistatic meteor radar network, and on the spectrum of gravity waves used to generate the input wind field (although results from this are not presented here).

## 3.2 Simulation description

The basic workflow of the simulation (all components of which are elaborated upon in subsequent subsections) may be summarized as follows:

1. Produce a sample of meteors in space and time for each site under consideration, by sampling from realistic spatio-temporal meteor detections corresponding to each site.
2. Specify a wind field based on the superposition of monochromatic gravity waves derived from a realistic gravity wave spectrum, and compute the wind velocities at each of the simulated meteors.
3. Compute the “radial” wind velocity measured at the receiver associated with each meteor detection.
4. For each meteor-site combination, synthesize in-phase and quadrature (IP and Q)-time series for each receiver at the site, based on the “radial” velocity and AOA of the meteor.
5. Add a realistically-sized phase bias and noise floor to each receiver channel.
6. Estimate the “radial” velocity and AOA of the meteor from the simulated time series.
7. Estimate the wave field covariances using the meteors retrieved from different combinations of sites. As will be elaborated upon in Sects. 3.2.5 and 3.2.6, this step also incorporates an estimation of the tidal components in the background wind field, and subsequent removal of those components from the radial velocities. It should also be noted that a number of different integration times are used for the covariance estimate in this work (1 day, 10 days, and a 3-hour-windowed 20 day composite).
8. Return to 1., and repeat for the number of realisations required to produce covariance error distributions (in the next step) of the desired statistical significance and resolution.
9. Compare the estimated covariances with those computed directly from the 3D wind velocities at the meteors and those calculated at 2-minute resolution at the origin of the coordinate system.

### 3.2.1 Meteor position and detection rate specification

To incorporate the dependence of the  $\langle u'w' \rangle$  and  $\langle v'w' \rangle$  uncertainties on the temporal and spatial characteristics of the meteor distribution, we have based the distributions used in the model on real measurements. For both the BP and Mylor sites, the first step was to convert the meteor AOAs to distances from the respective receiver sites in Transverse Mercator coordinates using the method of Bowring [1989] (see App. B). Then, we constructed a composite day of 2D histograms of the meteor position distributions at 5 km spatial and hourly time resolution. Measurements from April-July 2018 inclusive were used to construct these histograms; the data used for BP and Mylor are shown in Figs. 3.1 and 3.2, respectively. These histograms were taken to represent probability distributions for the meteor positions.

The sampling from these probability distributions at the beginning of each realisation is done by firstly prescribing a number of meteor detections for the day of measurements and altitude in question (e.g., 1340 per day at 90 km for the BP radar case; see next subsection for details). The meteors are then distributed in time and space, according to the relative number of samples in each hour and position bin, respectively. This process is repeated for the number of days prescribed in the realisation (for the results presented in this thesis, 1 or 10).

Rejection sampling is used in this work to distribute the meteors according to their underlying probability distributions. Assuming one wishes to obtain a sample from distribution  $X$  with probability density  $f$ , using only samples from distribution  $Y$  with probability density  $g$ , the rejection sampling is performed as follows:

1. Obtain a sample  $y$  from  $Y$  and a sample  $u$  from a uniform probability distribution with bounds  $(0,1)$ .
2. Check if  $u < f(y)/(Mg(y))$ .
  - If this holds, accept  $y$  as being a sample from  $X$ .
  - If this doesn't hold, reject  $y$  and return to step 1.

This process is repeated until the desired number of samples is obtained. The factor  $M$  used in the algorithm must satisfy the relation  $f(x) \leq Mg(x) \forall x$ . In this work,  $g$  is set to be a uniform probability distribution spanning the required range of time of day/positions (0 to 24 hours/-500 to 500 km, respectively).



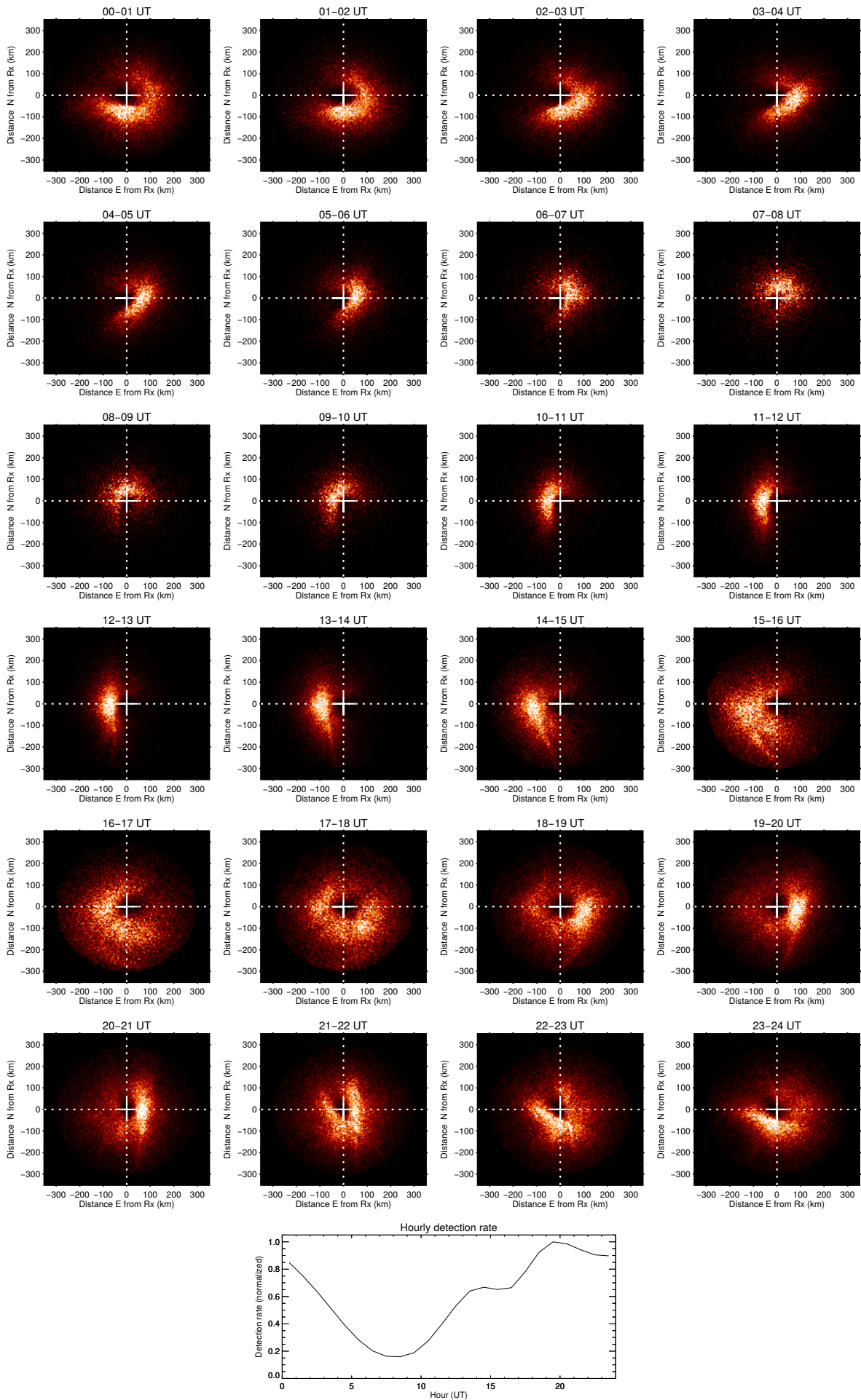


Fig. 3.1: Hour-by-hour position distribution used to simulate meteors at BP.

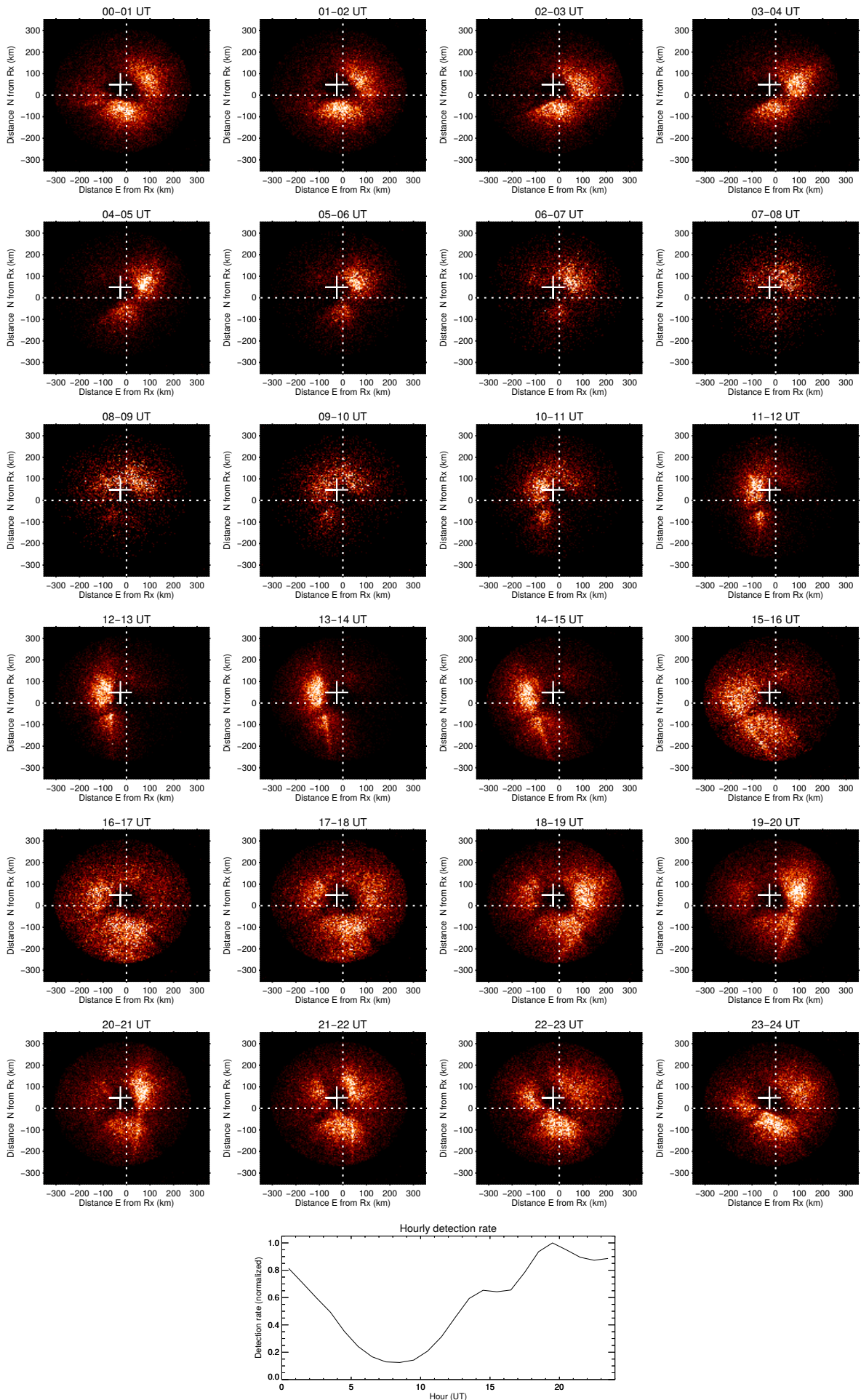


Fig. 3.2: As per Fig. 3.1, but for the Mylor receiver.

Altitude (km)	76	80	82	84	86	88	90	92	96
BP	140	510	780	1080	1360	1480	1340	1010	300
Mylor	20	130	180	380	540	640	690	640	350

Table 3.1: Meteor detection rates used for the simulations presented here. The rates shown are per day, in 2 km-wide bins centred at the altitude specified.

The altitudes assigned to the meteors are derived from a uniform probability distribution, with a centre value of 90 km and a full-width of 2 km (such that the simulation emulates the idea of analysing meteors from a single height bin). To clarify the effect of a variable number of meteor radial velocity/AOA pairs on the covariance error distribution, a variety of meteor detection rates have been simulated. We have endeavoured to make the detection rates used resemble the number of meteors detected across a range of heights by the combined BP-Mylor radar link (even though the simulation itself is performed around a single altitude). The detection rates we have used for different heights, listed in Table 3.1, correspond to those averaged over April 2018 for the two receive sites, in 2 km-wide bins.

### 3.2.2 Wind field specification

The wind field in the simulation is comprised of tidal components and a superposition of monochromatic gravity waves whose amplitudes have a vertical wavenumber and frequency dependence. Diurnal and semidiurnal tidal components are assumed, with amplitudes of 25 and 10  $\text{ms}^{-1}$  respectively. Random phases from a uniform distribution spanning the interval  $[0, 2\pi)$  are added to the phase of the zonal component of the tides at the beginning of each realisation, and the meridional component is set to be in quadrature with the zonal component. The 3D wind velocity associated with the waves at a given time  $t$  and Cartesian position vector  $\mathbf{r}$  can be written as:

$$\mathbf{v} = \sum_{i=1}^{n_m} \sum_{j=1}^{n_\omega} A(m_i, \omega_j) \mathbf{v}'_{ij} \sin(\boldsymbol{\kappa}_i \cdot \mathbf{r} - \omega_j t + \phi_{ij}), \quad (3.1)$$

where  $m$  is the vertical wavenumber,  $\omega$  is the wave's angular frequency,  $n_m$  and  $n_\omega$  are the number of vertical wavenumbers and angular frequencies respectively in the spectral grid,  $A$  is the joint vertical wavenumber-angular frequency spectral amplitude,  $\mathbf{v}' = [u', v', w']$  is the vector of wind component fluctuation sizes,  $\boldsymbol{\kappa} = [k, l, m]$  is the 3D

wave vector, and  $\phi$  represents a (random for each unique  $[m_i, \omega_j]$  pair) phase offset.

As per Sect. 3.2.1, the coordinate system used to specify horizontal position with respect to a reference location (i.e., that embodied by the  $\mathbf{r}$  vector) is based on the Transverse Mercator distances evaluated using the Bowring, 1989 method (which follow the Earth's surface and take into account its ellipsoidal shape). This is used in preference to line-of-sight distances, the use of which would result in “stretching” of the horizontal scales of the waves at large distances from the coordinate system origin. Furthermore, the calculated wind velocities are assumed to be in the local East-North-Up (ENU) coordinates at the associated meteor positions.

To ensure that the correlations between the horizontal and vertical winds take on physically reasonable values, we have allowed the component fluctuation amplitudes to be related by the linear gravity wave polarization relation  $w' = \frac{v_h k_h}{m}$ , where  $v_h = \sqrt{u'^2 + v'^2}$  and  $k_h = \sqrt{k^2 + l^2}$ . The horizontal components are determined by the wave propagation azimuth  $\varphi$ , through the relations  $[k, l] = k_h[\sin \varphi, \cos \varphi]$  and  $[u', v'] = v_h[\sin \varphi, \cos \varphi]$ .

In order to give the wind field a level of “spatially-correlated randomness” akin to what is seen in mesospheric wind fields when no predominant wave scales are present, we have opted to let  $A(m, \omega)$  take on values from a gravity wave spectral model. As discussed in Sect. 3.1, this is in contrast to approaches in the simulations of e.g., Fritts et al. [2010a] and Vincent et al. [2010], who use wave fields generated from the superposition of a small number of monochromatic waves. The vertical wavenumber spectrum we have used (from Gardner et al., 1993, their eqn. (7), and following their nomenclature) is given by:

$$F_u(m) = 2\pi\alpha N^2 \begin{cases} m_*^{-3} \left(\frac{m}{m_*}\right)^s & m \leq m_* \\ m^{-3} & m_* \leq m \leq m_b \\ m_b^{-3} \left(\frac{m_b}{m}\right)^{5/3} & m_b \leq m \end{cases}, \quad (3.2)$$

where  $m$  is the vertical wavenumber of the wave, and following Gardner et al., 1993, their Fig. 1, we let  $\alpha = 0.62$ ,  $N = \frac{2\pi}{3 \times 10^2} \text{ s}^{-1}$  (the Brunt-Väisälä frequency),  $m_* = \frac{2\pi}{1.5 \times 10^4} \text{ m}^{-1}$ ,  $m_b = \frac{2\pi}{5 \times 10^2} \text{ m}^{-1}$ , and  $s = 2$ . The frequency spectrum we have used (Gardner et al., 1993, their eqn. (24)) is given by:

$$B(\omega) = \frac{p-1}{f} \left(\frac{f}{\omega}\right)^p, \quad (3.3)$$

where  $\omega$  is the angular frequency of the wave, and following Gardner et al., 1993, their Fig. 2, we let  $f = \frac{2\pi}{7.2 \times 10^4} \text{ s}^{-1}$  and  $p = 2$ . We then simply assume that the joint vertical wavenumber-angular frequency spectrum is given by the product of these two spectra, i.e.,

$$A(m, \omega) = F_u(m) B(\omega). \quad (3.4)$$

The 2D spectrum we used for results presented here consisted of 80 different vertical wavelengths and wave periods, spanning the ranges 0.5–20 km and 5–240 minutes (uniformly sampled in vertical wavenumber and frequency), respectively. These limits largely encompass the waves responsible for the majority of the momentum deposition in the MLT-region (see e.g., Fritts and Alexander, 2003), whose momentum fluxes are of principal interest in this study. A plot of the spectral model is shown in Fig. 3.3.

The wave propagation azimuths were sampled from a uniform random distribution spanning  $[0, 180]^\circ$  in bearing, with the intention being to emulate a wave field whose westward-propagating waves have been removed from the spectrum through selective filtering. This led to true values for the estimates of  $\langle u'w' \rangle$  that were on average positive, and values of  $\langle v'w' \rangle$  that were on average zero (an example of the typical correlation present in the wind components is shown in the scatterplot in Fig. 3.4). Testing a wider variety of wave field configurations was considered beyond the scope of this thesis.

The horizontal wavenumber  $k_h$  of the wave were defined via the expression (a rearranging of eqn. (15) in Gardner et al. [1993]):

$$k_h = \frac{\omega m}{N}. \quad (3.5)$$

Finally, the values of  $A(m, \omega)$  were used to evaluate the horizontal wave amplitude  $v_h$  via the expression:

$$v_h(m, \omega) = \sqrt{\frac{CA(m, \omega)}{\sum_{m, \omega} A}}, \quad (3.6)$$

where  $C$  is a normalization factor, and  $\sum_{m, \omega} A$  represents the sum of  $A$  over all grid values of  $m$  and  $\omega$ .  $C$  was chosen in a way that resulted in mean values of  $\langle u'w' \rangle$  being in the vicinity of  $20 \text{ m}^2\text{s}^{-2}$ , which is a typical value for this parameter in the MLT-region (see e.g., the discussion in Fritts et al., 2012a). This was approximately achieved in this

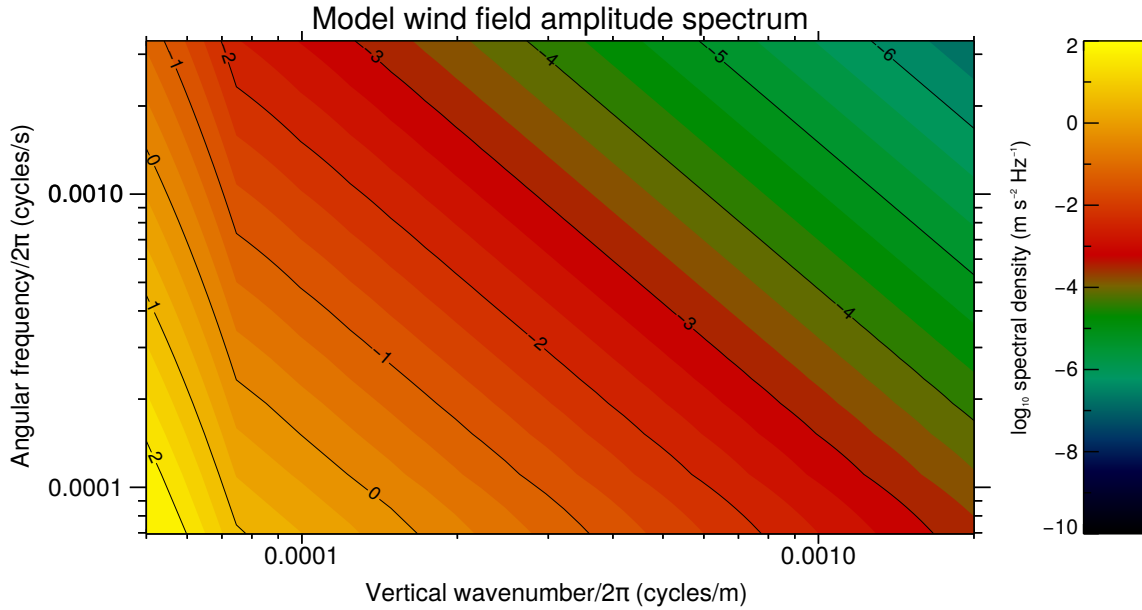


Fig. 3.3: The amplitude spectrum corresponding to the gravity wave spectral model used in this study.

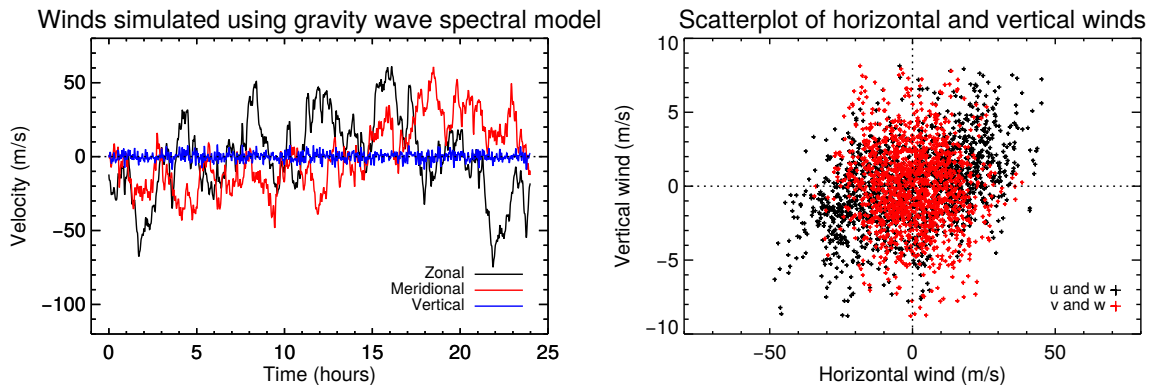


Fig. 3.4: Example of the winds produced for a single 24-hour realisation of the spectral model, sampled at a fixed location. The wind time series are shown in the left panel, along with a scatterplot of them in the right. To make the correlation between  $u$  and  $w$  more evident, tidal effects have not been included in the data used to produce the scatterplot (but are present in the time series plot).

study by setting  $C$  to 1000. Example distributions of the “true” covariances evaluated in the simulation are shown in panels c) and d) of Fig. 3.6.

As discussed by Gardner et al. [1993], the vertical wavenumber spectral model above incorporates waves in the unsaturated, saturated, and turbulent<sup>1</sup> regimes (which are

<sup>1</sup>A saturated gravity wave is one whose amplitude has grown to a size such that wave breaking occurs. Wave amplitudes cannot grow beyond this threshold (or at least, wave breaking will occur until the amplitude drops to this threshold). In this context, “turbulence” refers to the small scale

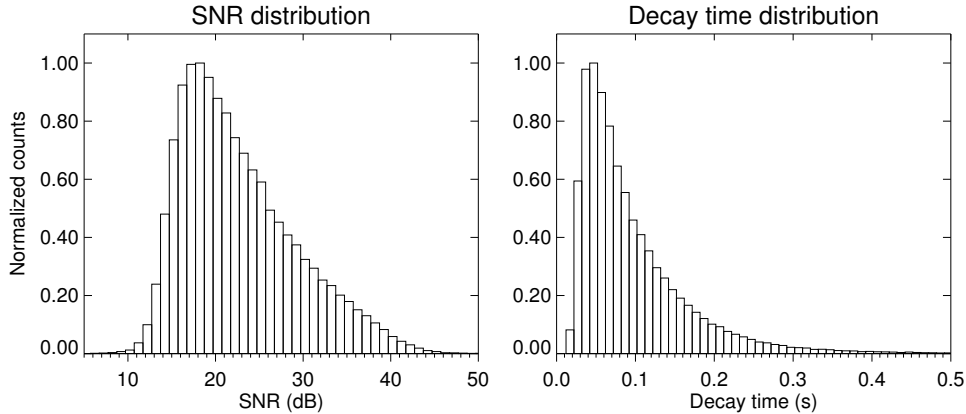


Fig. 3.5: Probability distributions of SNR and decay time used in producing the receiver time series discussed in Sect. 3.2.4.

governed in this order by the conditions in (3.2)), and accurately models the mesopause region at the mid-latitude site (Urbana) considered in their study. Gardner et al. [1993] also notes that few attempts had been made at the time to model the temporal spectra of gravity waves, but that the model in (3.3) adequately accounts for contributions from both saturated and unsaturated waves. Without resorting to implementing a physics-based atmospheric model (which would have a significant computational overhead), we believe that using this model is a simple and effective way to simulate a gravity wave field with realistic spatial and temporal wind field correlations. We also stress in our approach that a independent realisation of the wave spectrum is generated for each realisation of the simulation, allowing for a statistical estimate of the measurement uncertainties.

### 3.2.3 Receiver time series generation

To ensure that realistic radial velocity and position estimation errors are propagated to the covariance estimation, we have opted to generate synthetic receiver time series based on the observables discussed in the previous sections, and to then attempt to re-estimate the observables from the time series. The complex time series for the  $j$ th chaotic perturbations created by the wave breaking process. The basic purpose of the model of Gardner et al. [1993] is to specify how the perturbation amplitudes should vary with the spatial and temporal frequency of the waves for these different regimes, in such a way that the measured spectra of the modelled and observed wave fields match. For a detailed overview of wave saturation processes and turbulence produced through wave breaking, the reader is directed to the review of Fritts [1984].

receiver is written as:

$$V_j(t) = e^{i(2\pi\mathbf{A}\cdot\mathbf{d}-4\pi v_{rm}t/\lambda+\Phi_j)} e^{-t/\tau} + n_j(t), \quad (3.7)$$

where  $\mathbf{A} = [\sin\theta \sin\phi, \sin\theta \cos\phi, \cos\theta]$  (where  $\theta$  and  $\phi$  are the zenith and azimuth angles of the meteor, respectively, as measured from the receiver),  $\mathbf{d}$  is a three-element vector of Cartesian displacements to the receiver antenna in question,  $v_{rm}$  is the radial wind velocity,  $t$  is the time since the beginning of the echo,  $\lambda$  is the radar wavelength,  $\Phi_j$  is a phase calibration offset for the  $j$ th receiver,  $\tau$  is the  $e^{-1}$  decay time of the meteor, and  $n_j(t)$  is a background noise function.

It should be stressed here that the radial velocity  $v_{rm}$  is computed following (2.5)—i.e., by projecting the wind vector derived in (3.1) onto the line perpendicular to the meteor trail (i.e.  $\mathbf{b}$  in Fig. 2.2), and projecting the result onto the vector to the receiver. This is done regardless of whether the receiver being simulated is monostatic or bistatic.

The background noise function consists of values derived from a Gaussian distribution, with a root-mean-square (RMS) value derived from a probability distribution of meteor echo SNRs from the meteor radar at BP. The values used for  $\tau$  are also derived from a probability distribution from this radar's data. In both cases, the data used to generate the probability distributions spanned 1-30 April 2018, and altitudes 70-110 km. Plots of these distributions are shown in Fig. 3.5. In this context, it should be noted that no height dependence in the decay time or background noise level have been utilised in the simulation. The standard deviation of the noise function was computed empirically using the relation:

$$\sigma_{\text{noise}} = 10^{-\left(\frac{\text{SNR}+2.8}{20}\right)}, \quad (3.8)$$

which was derived by computing the SNR for a large ensemble of values of  $\sigma_{\text{noise}}$ , and fitting a linear function to the distribution of  $\sigma_{\text{noise}}$  against  $\log_{10}\text{SNR}$ . SNRs were estimated from the receiver time series autocorrelation function by computing the ratio of the power interpolated across lags  $\pm 1$  and  $\pm 2$ , and the difference between the power at lag 0 and that interpolated.

The phase calibration offsets  $\Phi_j$ , which are set for each receiver at the beginning of each simulation realisation, are intended to embody the consequences of incorrectly estimating the true phase calibration offsets between the receiver channels. Based on the size of the phase calibration errors shown in the simulation results in Fig. 2.14, we



have chosen to apply to each receiver Gaussian-distributed phase offsets with an RMS value of  $2^\circ$ .

### 3.2.4 Parameter estimation

Radial velocities and meteor AOAs are estimated from the synthesized time series following the procedures outlined in Sects. 2.5.2 and 2.6 respectively. It should be noted that with noise and phase biases incorporated in the time series, in rare ( $\sim 1$  detection in every 3000) cases we found the resolved AOA occurred below the horizon. In these cases, the echo in question was simply discarded from the subsequent calculation of mean winds and covariances.

Wind velocities are in turn estimated from the radial velocities and AOAs following the procedure in Sect. 2.8. As discussed in Sect. 3.2.2, the modelled winds are defined with respect to the local ENU coordinates at the meteor location (not the receiver or any other arbitrary location). Accordingly, the assignment of the “AOAs” used in the wind fitting to the orientation of the  $\mathbf{b}$  vector (see Fig. 2.2) in the meteor’s local ENU coordinates compensates for this. Of course, this also means that the “AOAs” used in the wind estimation are slightly different to the meteor AOAs measured from the receiver (see Fig. 2.12 for an example of the change in direction cosines that result from doing this).

It should be noted that wind estimates are produced for both radars individually as well as with the combined detections from both radars. In the latter case, the wind fitting is performed across the combined set of “AOAs” (again, the  $\mathbf{b}$  vector in the meteor’s local ENU coordinates) and radial velocities.

### 3.2.5 Removal of background wind and tides

Prior to estimating the wind covariances arising from the simulated wave activity, the background mean wind and tidal effects are computed, projected onto the radial velocities corresponding to each meteor detection, and removed. This is done to emulate the analysis presented in Chapter 4, in which the momentum fluxes arising from gravity waves (and not tides) are of specific interest.

To remove the previously estimated mean winds and tides from the time series, we have calculated a low-pass filtered version of the hourly-averaged horizontal wind time series using an inverse wavelet transform with a Morlet wavelet basis, linearly interpolated a wind estimate at the time of each meteor, and subtracted the radial projection of

the wind from the radial velocity time series. This is in principle similar to the approach of Fritts et al. [2010a], who applied an S-transform (in preference to a least squares sinusoidal fit) in order to more completely remove transient spectral features around the tidal periods from the time series. Further details of the inverse wavelet transform and examples of applying it to wind time series are in the following Chapter in Sect 4.2.1.

To ensure that the filtered time series pertain to tidal (or longer)-like wind oscillations (and not short-period waves), we select a minimum scale size in the reconstruction of 6 hours. The reconstructed time series is then interpolated to the times of each of the meteors being used in the covariance estimation, and the “radial” component of the wind at each of the meteor positions is subtracted from the measured radial velocity. The “radial” component is calculated using (2.12)—i.e., projecting the wind vector onto the  $\mathbf{b}$  vector (see Fig. 2.2) in the local ENU coordinates at the location of the meteor.

### 3.2.6 Covariance estimation

Following the removal of the mean and tidal components of the horizontal wind from the radial velocities, covariances that pertain predominantly to gravity wave-driven wind perturbations are estimated. The approach we apply is based on those presented by Thorsen et al. [1997] and Hocking [2005]; much like in the wind estimation discussed in Sect. 2.8, it involves using SVD to least-squares solve the following inverse equation:

$$\mathbf{v}_r'^2 = \mathbf{A}'\mathbf{v}', \quad (3.9)$$

where  $\mathbf{v}_r'^2$  is a  $n_{\text{met}} \times 1$  vector containing the squares of the perturbation component of the radial velocities,

$$\mathbf{v}' = [\langle u'^2 \rangle, \langle v'^2 \rangle, \langle w'^2 \rangle, \langle u'v' \rangle, \langle u'w' \rangle, \langle v'w' \rangle]^T$$

is the vector of covariance components, and  $\mathbf{A}'$  is a  $n_{\text{met}} \times 6$  matrix whose rows read:

$$[\sin^2\theta \sin^2\phi, \sin^2\theta \cos^2\phi, \cos^2\theta, \sin^2\theta \sin 2\phi, \sin 2\theta \sin \phi, \sin 2\theta \cos \phi] .$$

It is noted that, as per the wind estimation case, the  $\theta$  and  $\phi$  terms represent the orientation of the  $\mathbf{b}$  vector in ENU coordinates at the location of each meteor, and that the velocities in  $\mathbf{v}_r'^2$  are based on the wind velocities' projection onto  $\mathbf{b}$ . The radial velocities and  $\mathbf{b}$  vectors associated with the meteors detected at both sites may also be combined in the (3.9) formulation.

We found this estimator to be extremely sensitive to errors in  $v_{\text{rm}}^{\prime 2}$  (discussed further in Sect. 3.3.3). A two-step radial velocity outlier rejection procedure was subsequently implemented to remove meteors with dubious square radial velocity/AOA values from the input distribution in an attempt to reduce the bias in the resulting covariance estimates. The first step is to discard all meteors with radial velocity/AOA estimates that have a projected horizontal velocity of  $\geq 200 \text{ ms}^{-1}$  (by virtue of which we argue that measured horizontal velocities above this threshold are “nonphysical”). The second step iteratively discards the meteors that satisfy the criterion:

$$|v_{\text{ri}}^{\prime 2} - v_{\text{rpi}}^{\prime 2}| \geq \left[ \text{median} \left( \sqrt{|\mathbf{v}_{\text{r}}^{\prime 2} - \mathbf{v}_{\text{rp}}^{\prime 2}|} \right) + 5 \times 1.4826 \times \text{MAD} \left( \sqrt{|\mathbf{v}_{\text{r}}^{\prime 2} - \mathbf{v}_{\text{rp}}^{\prime 2}|} \right) \right]^2 \quad (3.10)$$

where  $v_{\text{rpi}}^{\prime 2} = A_{i*}^{\prime} \mathbf{v}'$  is the  $i$ th “projected” square radial velocity,  $\mathbf{v}'$  is the vector of the covariance estimates associated with the meteors in question, “MAD” indicates the median absolute deviation operator, and 1.4826 is the factor to convert a MAD to a standard deviation, assuming the input has a Gaussian distribution. In practice, we have found that the 5 “standard deviations” criterion removes outliers that are large enough to substantially bias the resulting covariance estimates, without iteratively removing an excessive number of samples that are “good”. The intention of using the median and MAD statistics (as opposed to mean and standard deviation) has been to reduce the bias outlying points inflict on the “measured standard deviation” of the distribution of  $|v_{\text{ri}}^{\prime 2} - v_{\text{rpi}}^{\prime 2}|$ .

The performance of the second outlier rejection criterion on simulated data is briefly summarised in Sect. 3.3.3.

### 3.2.7 “Truth value” of the simulated covariances

To evaluate the “truth value” of the simulated covariances—i.e., that used to estimate the accuracy and precision of the covariances derived through inversion of (3.9)—we have opted to compute the covariances using the spectral-model-derived Cartesian wind fields (without tides) at the origin of the coordinate system (at the location of the receiver at BP) at 2 minute resolution (refer to this estimate as  $\mathbf{v}'_{\text{orig}}$ ). We found  $\mathbf{v}'_{\text{orig}}$  to agree extremely closely with that computed at the positions and times of the meteors incorporated in the simulation (refer to this estimate as  $\mathbf{v}'_{\text{met}}$ ). Note of course that  $\mathbf{v}'_{\text{met}}$  is the exact representation of what one would hope to obtain when inverting (3.9).

In the case of using wave fields generated from the gravity wave spectral model discussed in Sect. 3.2.2, we found that the covariances estimated by inverting (3.9) are

more correlated with  $\mathbf{v}'_{\text{orig}}$  and  $\mathbf{v}'_{\text{met}}$  than those computed by summing the covariances associated with each wave in the spectrum<sup>2</sup> (refer to this estimate as  $\mathbf{v}'_{\text{sum}}$ ). Therefore, while  $\mathbf{v}'_{\text{sum}}$  gives the covariances that would be measured over an infinitely large sampling area/time (in a sense the “expectation value” of the covariances), we have refrained from using it as a “truth” value with a view to not overestimating the size of the simulated technique’s measurement errors. It should be noted that this contrasts with the simulations of Fritts et al. [2010b, 2012b] and Andrioli et al. [2013a]; in each of these works,  $\mathbf{v}'_{\text{sum}}$  was used as a truth value.

### 3.3 Simulation results

#### 3.3.1 Spectrum of gravity waves

This section considers the covariance bias distributions associated with a wind field generated using the gravity wave spectral model discussed in Sect. 3.2.2. Three different time integration cases (that are later employed in Chapter 4 on real data) are tested: 1 day (which could be considered a fairly “high time resolution” sampling of day-to-day variations), 10 days (which sacrifices time resolution for measurement precision), and a 20-day composite (which intends to gather enough meteors in each time-of-day bin for a precise covariance estimate, but in doing so ignores day-to-day variations entirely).

#### 1-day integration

The biases for 15,000 realisations of 1-day integrated covariance estimations are shown in Fig. 3.6. It is clear that the  $\langle u'w' \rangle$  term is systematically underestimated, with larger biases present at lower count rates (refer to Table 3.1 for the count rates as a function of height used in the simulation). The width of the bias distribution is also larger at lower count rates. For a simulated mean  $\langle u'w' \rangle$  value of  $\sim 21 \text{ m}^2\text{s}^{-2}$ , the distribution widths imply a 1-sigma measurement uncertainty of  $\sim 14 \text{ m}^2\text{s}^{-2}$  ( $\sim 65\%$ ) at the peak of the meteor height distribution, and  $\sim 30 \text{ m}^2\text{s}^{-2}$  ( $\sim 145\%$ ) at the edges of the distribution, for a multistatic configuration. The same uncertainties are  $\sim 15 \text{ m}^2\text{s}^{-2}$  ( $\sim 72\%$ ) and  $\sim 35 \text{ m}^2\text{s}^{-2}$  ( $\sim 168\%$ ) respectively, for a monostatic configuration.

---

<sup>2</sup>This is likely because the amount of time and space one needs to integrate over to estimate the covariance to reasonable significance for a wave spectrum of the complexity used here is much larger than the integration times considered/volume spanned by the meteors in this work. However, this has not been systematically investigated.

The width of the bias distributions for  $\langle v'w' \rangle$  are also essentially identical to those for  $\langle u'w' \rangle$ . The relative uncertainties in the measurements of this term are meaningless, as the wave propagation directions have been chosen in a way that the mean truth value of  $\langle v'w' \rangle$  is zero. What the results do illustrate, however, is that there is no bias in the case of estimating a covariance with a zero mean, and that there is no change in the measurement uncertainty of the two components arising from the temporal and spatial distribution of the meteors.

It should be noted that  $\langle u'w' \rangle$  is systematically underestimated for both configurations and for all count rate sets investigated, especially at lower count rates (the absolute error ranges from about 20% to 50% of the mean). Subsequent investigation has confirmed that this occurs when an attempt is made to remove the tidal effects incorporated in the simulated wind field (i.e., the tides are largely removed, but so is some of the variance due to the gravity waves). The larger biases at low count rates arise from the inability to define the tidal amplitudes and phases correctly in the presence of wind estimates with larger uncertainties and/or missing wind estimates for particular time bins. Overall, we consider the bias an unavoidable consequence of ensuring that tidal effects are not included in the measured covariances. Further discussion of this point is taken up in the next Chapter in Sect. 4.4.3.

### 10-day integration

Figure 3.7 shows the bias distribution for 1,500 realisations of 10-day integrated covariance estimates. It is clear that the uncertainties in both  $\langle u'w' \rangle$  and  $\langle v'w' \rangle$  are considerably smaller than for 1 day's integration, ranging from  $\sim 11 \text{ m}^2\text{s}^{-2}$  ( $\sim 50\%$ ) at the peak of the meteor distribution, to  $\sim 13 \text{ m}^2\text{s}^{-2}$  ( $\sim 60\%$ ) at the edges. Interestingly, it appears as though the uncertainty is asymptoting to a minimum value with increasing meteor counts, which implies that the use of integration times longer than 10 days (i.e. a larger total number of meteors used to estimate covariances) will lead to diminishing gains in measurement precision (at least for wind fields with waves of periods much less than 10 days). In any case it may not be realistic to assume the wind field is statistically stationary for this amount of time; this point is discussed further in Sect. 3.4.

As per the 1-day integration case,  $\langle u'w' \rangle$  has been systematically underestimated, increasingly so at low meteor detection rates.

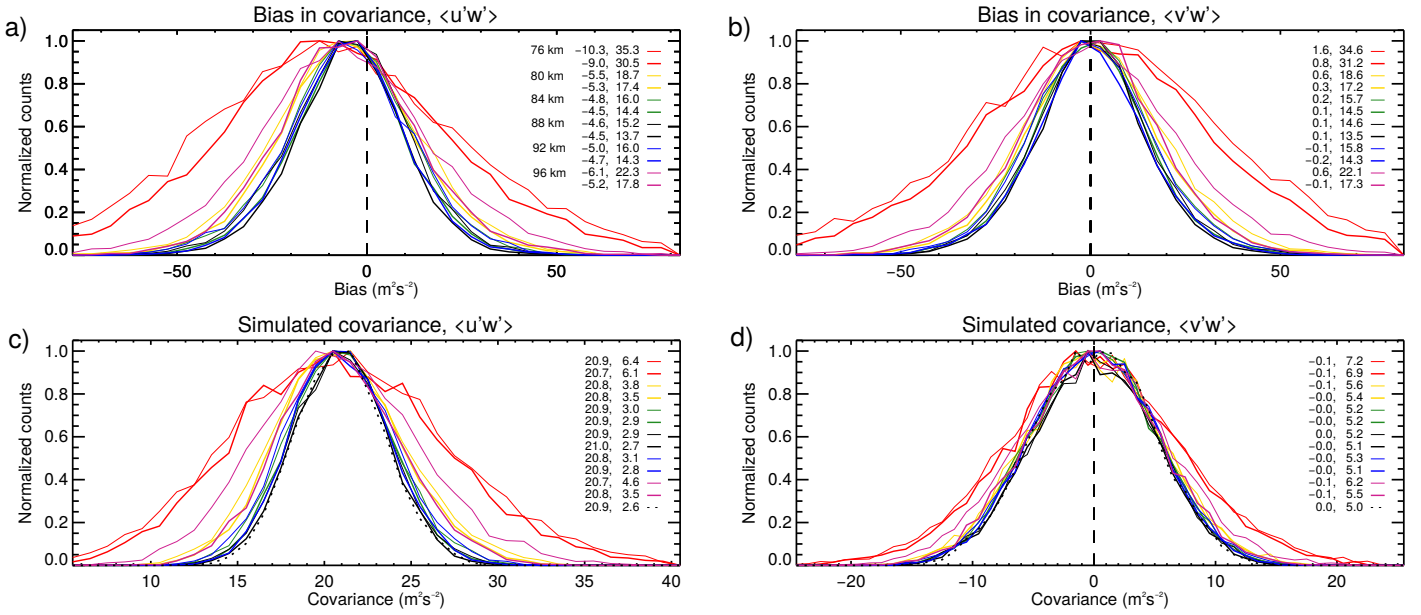


Fig. 3.6: Simulated wind covariance bias distributions for 1 day of integration (panels **a** and **b**) are for  $\langle u'w' \rangle$  and  $\langle v'w' \rangle$  respectively) and the simulated covariance distributions (panels **c**) and **d**) for the same components). As discussed in Sect. 3.2.7, biases are calculated with respect to  $\mathbf{v}'_{\text{orig}}$  (i.e. the covariance derived from the input Cartesian wind velocities sampled at 2 minute resolution at the coordinate system origin). The lower row shows the distribution for  $\mathbf{v}'_{\text{orig}}$  in a dotted black line, and shows  $\mathbf{v}'_{\text{met}}$  (i.e. that computed from the Cartesian wind velocities at the meteor positions and times) in coloured lines. The different line colours in each plot represent different simulated heights, which are a subset of those shown Table 3.1 (as indicated in the legend, red represents 76 km, yellow 80 km, green 84 km, black 88 km, blue 92 km, and violet 96 km). Thick lines show the distribution for the multistatic case (i.e., by combining data from BP and Mylor; see Sects. 3.2.4 and 3.2.6 for details), and thinner lines show the monostatic case (i.e., just BP data). The mean and standard deviation evaluated from the samples' MAD are shown in the left and right columns respectively of the arrays of numbers in each plot figure.

## 20-day composite

Figure 3.8 shows expected values of the covariance bias' mean and standard deviation for 300 realisations of a composite day spanning an interval of 20 days, with three hour time bins, as a function of height from 82-92 km. The highest standard deviations for both  $\langle u'w' \rangle$  and  $\langle v'w' \rangle$  occur in the 6-9 and 9-12 UT bins, and the lowest in the 18-21 UT bin. Given the mean simulated value of  $\langle u'w' \rangle$  is  $\sim 21 \text{ m}^2\text{s}^{-2}$ , the standard deviation

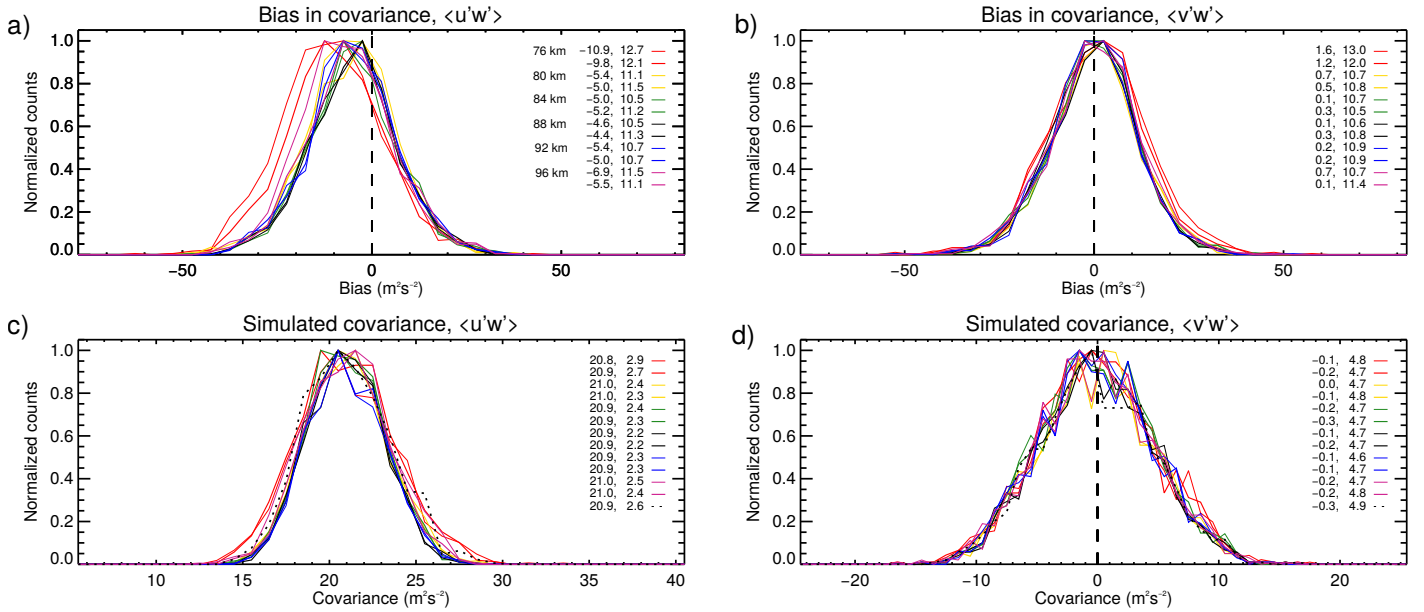


Fig. 3.7: As per Fig. 3.6, but for 10 days of integration.

at the peak of the meteor distribution of  $\sim 15 \text{ m}^2\text{s}^{-2}$  implies a relative uncertainty of  $\sim 70\%$ ) in the 18-21 UT bin. The same figures in the 6-9 UT bin are  $\sim 18 \text{ m}^2\text{s}^{-2}$  and  $\sim 85\%$ , respectively. It should be noted that the standard deviation is as high as  $\sim 21 \text{ m}^2\text{s}^{-2}$  (relative uncertainty of  $\sim 100\%$ ) in the 6-9 UT bin at 82 km.

Once again, a systematic underestimation of  $\langle u'w' \rangle$  is present, which as discussed in Sect. 3.3.1 is an artefact of attempting to remove tidal effects.

### 3.3.2 Monochromatic gravity wave

The previous section considered a wind field containing a multitude of waves whose spatial/temporal scales spanned a large part of the spectrum atmospheric gravity waves are expected to occupy. This section briefly addresses the other limiting case, which is that of a wind field consisting of a single monochromatic wave.

In all simulation realisations for this case, we have set the single monochromatic wave's propagation direction to  $45^\circ\text{T}$ , so as to make the true  $\langle u'w' \rangle$  and  $\langle v'w' \rangle$  covariances equal. A horizontal wavelength and phase speed has been randomly selected for each realisation, from a uniform distribution with bounds  $[10, 60]$  km and  $[10, 40]$   $\text{ms}^{-1}$ , respectively. A 1-day integration is used for the covariance estimate.

The bias distributions for 15,000 realisations are shown in Fig. 3.9. As per the spectral wave field case, the distribution widths are largest at the edges of the height distribution, and narrowest at the peak. However, the widths are far smaller than in the spectral wave field case.

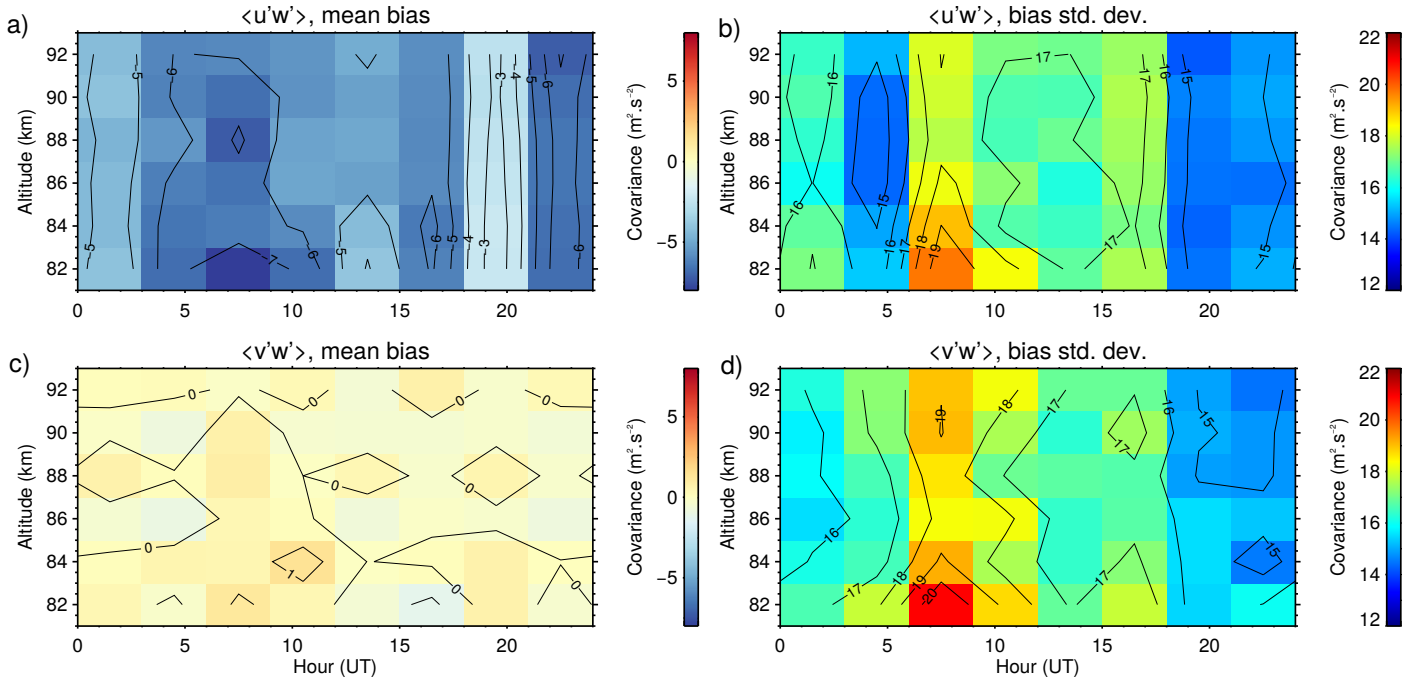


Fig. 3.8: Means and standard deviations of the simulated  $\langle u'w' \rangle$  (panels a) and b), respectively) and  $\langle v'w' \rangle$  (panels c) and d) bias distributions for a 20-day composite, as a function of height, for the BP-Mylor link.

Across all wavelengths and phase speeds, the simulated mean true covariance was  $\sim 38 \text{ m}^2\text{s}^{-2}$ . Therefore, the distribution widths of  $\sim 3 \text{ m}^2\text{s}^{-2}$  and  $\sim 17 \text{ m}^2\text{s}^{-2}$  at the peak and lower edge of the height distribution respectively for the multistatic configuration, translate to relative uncertainties of  $\sim 8\%$  and  $\sim 44\%$ . For the monostatic configuration, the same uncertainties are  $\sim 4 \text{ m}^2\text{s}^{-2}$  ( $\sim 10\%$ ) and  $\sim 19 \text{ m}^2\text{s}^{-2}$  ( $\sim 52\%$ ), respectively.

Similarly to the spectral wave field case, both covariance terms are systematically underestimated (ranging from about 2% to 26% for  $\langle u'w' \rangle$  in the multistatic configuration, at the peak and lower edge of the height distribution, respectively). Interestingly,  $\langle v'w' \rangle$  is underestimated to a slightly lesser degree than  $\langle u'w' \rangle$ .

### 3.3.3 Outlier rejection criteria performance

This section shows the effect of the application of the outlier rejection criterion of (3.10), in the absence of tidal effects and attempted removal of them.

To emulate a radial velocity time series “partially corrupted” with outliers in this section, Gaussian-distributed noise with a standard deviation of  $50 \text{ ms}^{-1}$  has been added to a randomly selected 5% of the radial velocity estimates in a given realisation. We note that radial velocity errors of this size are rare in practice; they have been used to



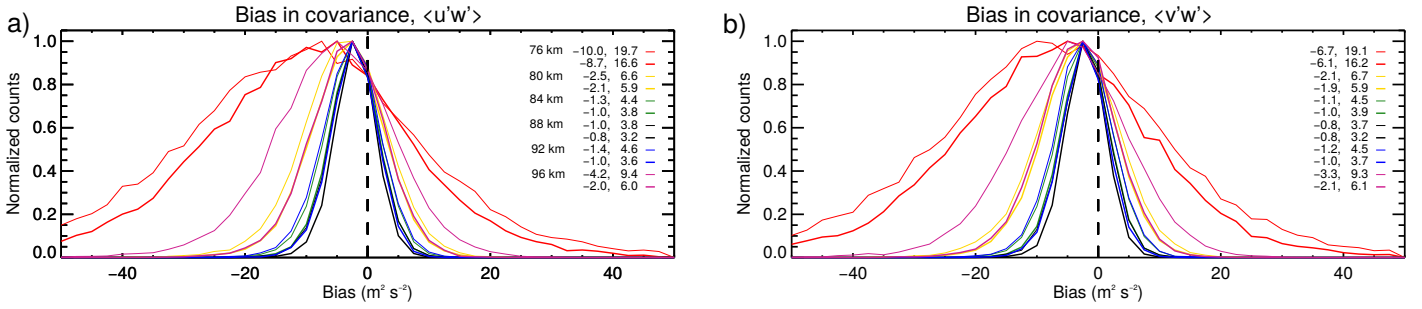


Fig. 3.9: As per Fig. 3.6, but for single monochromatic gravity waves.

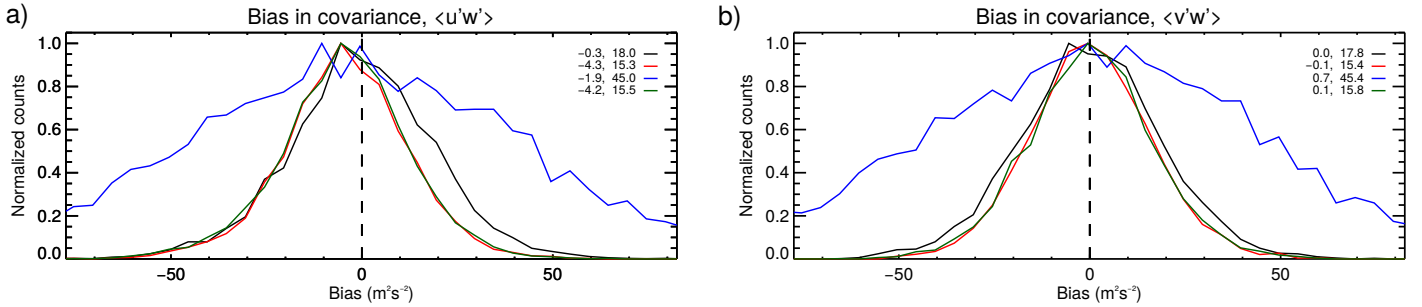


Fig. 3.10: Covariance bias distributions for different combinations of outlier contamination and outlier rejection ( $\langle u'w' \rangle$  and  $\langle v'w' \rangle$  are shown in panels **a)** and **b)**, respectively). Black is no rejection or outliers, red is rejection with no outliers, blue is outliers without rejection, and green is outliers with rejection. The same spectral-model gravity wave field as in Sect. 3.3.1 has been used to produce these results.

test the rejection criterion's robustness, and to allow us to highlight potential downsides of not having the criterion in place.

Figure 3.10 shows the covariance bias distributions for the same spectral-model gravity wave field as applied in Sect. 3.3.1 and for 1 day of integration, for four cases: rejection not applied with no outliers present, rejection applied with no outliers present, rejection not applied with outliers present, and rejection applied with outliers present. The mean true values for  $\langle u'w' \rangle$  and  $\langle v'w' \rangle$  are the same as in Sect. 3.3.1, i.e.,  $\sim 21$  and  $0 \text{ m}^2\text{s}^{-2}$ , respectively.

The application of the criterion is clearly beneficial in the presence of outliers, resulting in a reduction in uncertainty of the  $\langle u'w' \rangle$  estimate from  $\sim 45 \text{ m}^2\text{s}^{-2}$  ( $\sim 214\%$ ) to  $\sim 16 \text{ m}^2\text{s}^{-2}$  (74%). Interestingly, the application of the criterion in the presence of no outliers also results in a slight reduction in relative uncertainty (from about 86% to 73%), although it does result in  $\langle u'w' \rangle$  being underestimated (by about 20%). This point is revisited in Sect. 3.4.

Despite the fact that it appears to introduce a small measurement bias, we still apply

the criterion in the analysis of BP-Mylor data in Chapter 4, so we can be assured that anomalous radial velocities contribute minimally to the covariance measurement errors.

### 3.4 Discussion

In this Chapter, we have attempted to define quantitative estimates for the absolute and relative uncertainties of the  $\langle u'w' \rangle$  and  $\langle v'w' \rangle$  covariance terms as measured by the multistatic BP-Mylor meteor radar, for typical time and height sampling cases. This has mainly been done to quantify the likely uncertainties in the gravity-wave–tide interaction study on BP-Mylor link data presented in Chapter 4, and accordingly, the sampling schemes used in the simulation are exactly replicated on the case study data. The wave field cases used also examined two of the extremes that might be encountered in real observations: a wave field governed by a spectrum of gravity waves (in which the wind field is effectively random with a finite correlation length), and one with individual monochromatic waves.

For the specific wave field we have used, which consists of a spectrum of waves (encompassing periods between 5 minutes and 4 hours and vertical wavelengths between 0.5 and 20 km) associated with a momentum flux of  $\sim 20 \text{ m}^2\text{s}^{-2}$ , 1-day integration times will lead to a relative uncertainty of (at the peak of the meteor distribution)  $\sim 65\%$ , and  $\sim 50\%$  for a 10-day integration. When the results are averaged over many individual monochromatic waves, a 1-day integration will lead to a considerably smaller relative uncertainty of  $\sim 8\%$  (this finding is consistent with the conclusion reached by Vincent et al. [2010]). The 10-day integration of individual waves was not tested (monochromatic wave events lasting this long are extremely unlikely). In reality, the wave field observed is likely to be between these two extremes, and we suggest that the true 1-day integration uncertainties are likely to lie between these predictions.

Aside from the magnitudes of these momentum flux uncertainties, we think there are six other major take-homes from the results:

1. The uncertainties exhibit a strong rate of dependence on altitude (i.e. meteor detection rates) for the 1-day integration case.
2. The use of integration times longer than 10 days appears to minimally reduce the uncertainties.
3. Wave fields with broader frequency/scale spectra will be associated with larger relative uncertainties in momentum flux.

4. In real-world studies, using integration times around 10 days may result in an increased uncertainty due to wave field transience.
5. The change in meteor distribution brought about by using a multistatic meteor radar (versus a monostatic one) appears to lead to no changes in the uncertainties.
6. The performance of the estimator in (3.9) is extremely sensitive to the presence of radial velocity outliers.

The first point is of little surprise, as it has already been predicted by Kudeki and Franke [1998] and from the simulations of Vincent et al. [2010], Fritts et al. [2010b, 2012b], and Andrioli et al. [2013a]. However, the second point implies that the covariance uncertainty will eventually (after a time dependent on the detection rate) asymptote to a value dependent on the complexity of the wave field itself. This is consistent with the findings of Vincent et al. [2010] (who suggested a threshold detection rate of about 250 meteors  $\text{hr}^{-1}$ ), but contrasts with a prediction made by Fritts et al. [2012b]. The latter argued that the covariance measurement error should decrease with the square root of the number of detections, and by extrapolating from the 250% error for a 1-hour integration presented in Vincent et al. [2010], concluded that their relative error for a one-month composite should have been as low as 10%. Our simulations suggest that an increase in precision of this magnitude cannot occur. Moreover, using a similar detection rate and a 3-hour bin in our 20 day composite of a spectral model-derived wave field shown in Fig. 3.8, we obtain a minimum relative error of about 70%. In saying this, we note of course that a relative error of 10% is possible for a considerably less complex wave field.

The second point also implies one will essentially be sacrificing time resolution for minimal gains in measurement precision for integration times longer than 10 days. For this reason, we have not opted to use integration times longer than this in the analysis of the BP-Mylor link data presented in Chapter 4. We note that 10 days of integration is likely an upper limit on the time required for the measurement uncertainty to asymptote to a given value, as we did not test an intermediate integration time between 1 and 10 days.

The third point is evidenced by the distribution widths of the broad spectrum wave field results in Fig. 3.6 being 3-4 times that of the single-wave results in Fig. 3.9 for given detection rates. Physically, this is an indication that wind field covariances associated with a more “complex” wave field cannot be measured as precisely as those

associated with a single gravity wave. This finding is qualitatively consistent with the conclusion reached by Vincent et al. [2010] (for high meteor detection rates) and Fritts et al. [2012b]. It should be noted that this makes it impossible to accurately define the covariance measurement uncertainty for this radar without a-priori knowledge of the wave field and its variation with time.

In the context of this and the fourth point, we make note of Fritts et al. [2012b]’s argument that the relatively low levels of correlation among horizontal and vertical winds assumed in Kudeki and Franke [1998] contrast with the many observational examples of high amplitude monochromatic gravity waves dominating the flow field. An earlier work by Sica and Russell [1999] also investigated the specific question of whether the wave field (in the upper stratosphere) is typically composed of a small number of discrete waves or a continuous spectrum. Upon observing intermittency between two distinct wave periods dominating the spectrum and a “white noise” background, they concluded that realistic parameterization schemes need to account for the intermittency of the discrete and continuous nature of the spectrum. These arguments would suggest that the persistent “broad spectrum” wave field we have assumed in our simulation results presented in Figs. 3.6–3.8 may not commonly be observed in practice. Hence, we tested the monochromatic wave field case. It was considered beyond the scope of this study to implement wave fields with intermittent spectral components.

The fourth point, closely tied to the third, concerns the fact that in real-world studies, the spectral components of the wave field may vary during the integration period. This is particularly problematic for the 10-day window; for example, during a period of intense but short-lived monochromatic wave events followed by more “complex” wave activity, increasing the integration time may actually increase the uncertainty in the covariance estimate of the monochromatic wave activity—not only because of the likely change in the mean covariance, but also because of the “geophysical noise” added to the radial velocity time series by the more “complex” activity. The superposition of such wave events would also likely result in a meaningless mean covariance estimate (unless of course if the period integrated over was long enough to produce a meaningful climatological result).

The fifth point is evidenced by the uncertainties at 84 km for the multistatic configuration (1460 detections) being  $14.4 \text{ m}^2\text{s}^{-2}$  and  $14.5 \text{ m}^2\text{s}^{-2}$  for  $\langle u'w' \rangle$  and  $\langle v'w' \rangle$  respectively, and the corresponding uncertainties at 88 km for the monostatic configuration (1480 detections) being  $15.2 \text{ m}^2\text{s}^{-2}$  and  $14.6 \text{ m}^2\text{s}^{-2}$ . In other words, since these uncertainties are

essentially the same, we surmise that combining the detections from the monostatic and bistatic receivers only offers a lower measurement uncertainty at a given height because of the higher number of meteor detections, not because of any changes to the effective AOA distribution of the meteors. In this context, we stress that it is only the AOAs with respect to the combined receiver site that matters, not the increase in area spanned by the detected meteors (the latter of course aids in wind field mapping (e.g. Stober et al. [2018]), but that is not considered here).

Concerning the sixth point, in Sect. 3.3.3 we showed that the radial velocity outlier rejection scheme of (3.10) substantially increases the covariance measurement precision in the presence of outliers. However, we note that the criterion used (especially the “5 standard deviations” aspect) has not been rigorously tested; we merely selected it on the basis of it removing points in the distribution of  $|v_{ri}^{\prime 2} - v_{rpi}^{\prime 2}|$  (real and simulated) that we had noticed were spuriously affecting the covariance estimates. A more rigorous scheme would adaptively modify the thresholding based on observed characteristics of the wind field, rather than simply the residual of the fit.

A complication arises from the fact that this criterion results in a more precise (albeit less accurate) covariance estimate in the absence of outliers. This also illustrates an important point about the sensitivity of the inversion of (3.9) to the input: it is as though the data that contribute to the accuracy of the measurement actually increase the measurement’s uncertainty, if they are associated with large radial velocity perturbations. This could occur, for example, in the presence of an isolated high-amplitude wave packet moving through the radar volume surrounded by turbulence with a lower wind variance. Dealing with such cases has been beyond the scope of this work.

### 3.5 Suggestions for future work

A subject we have not addressed here is the application of weights to the meteors in the inversion of (2.12) and (3.9) to minimize the errors in the resulting winds/covariance estimates. In particular (as discussed by Hocking [2018]), at the midpoint between the transmitter and receiver sites the  $\mathbf{b}$  vector (see Fig. 2.2) is vertical, meaning that the measured radial velocity corresponds to the true wind velocity projected onto the vertical. Large errors in the inverted horizontal winds/covariances may result in the presence of radial velocity errors here, and at nearby locations where  $\mathbf{b}$  is close to vertical. We decided to ignore the issue on the basis of there being a small number of meteors with sufficiently oblique entrance angles to be detected in this region; at Mylor, we

found about 0.3% of all detected meteors to have effective zenith angles (that is, the zenithal orientation of the  $\mathbf{b}$  vector) of less than  $20^\circ$ . Nevertheless, there is still a need to quantify the usefulness a weighting scheme may have in minimizing errors arising from these meteors.

Another area worth investigating is the accuracy/precision of the covariance estimator introduced in the work of Vierinen et al. [2019], and determining what are suitable integration times for it. Rather than determining a “total” covariance over all spatial and temporal frequencies, this technique estimates a covariance for each cell in a pre-described grid in spatial and temporal separation. The complexity here is that each individual cell may have its own associated wave field complexity, in which case the cells would have different measurement uncertainties. Given that the slope of the momentum flux spectrum across spatial/temporal frequency can in principle be measured with this technique and is an important quantity in climate models, it is important to have a measure of accuracy and precision of those slope estimates.

Finally, this work has not quantified the effect of incorporating tides, the tidal removal filter, or synthesized receiver noise on the covariance estimation bias distribution widths and/or bias value. We omitted this step as our goal was only to predict the nature of the biases as accurately as possible for the BP-Mylor link, not to explain the sources of those biases. Isolating the contribution of these effects to the covariance estimation error may serve to motivate the development of a more robust tidal subtraction algorithm, or suggest the discarding of meteor detections below a certain threshold SNR, for example. Furthermore, it would also enable one to isolate the contribution of wave field complexity to the estimation error.

### 3.6 Summary and conclusions

In this Chapter, a model has been developed to assess the momentum flux (specifically, the  $\langle u'w' \rangle$  and  $\langle v'w' \rangle$  wind covariance terms) measurement capability of the BP-Mylor multistatic meteor radar. This has been done to validate the processing applied in the gravity-wave–tidal interaction study in Chapter 4. To emulate that study as closely as possible, the model has incorporated a realistic wind field derived from a spectral model of gravity waves applicable to the mesosphere, AOA and count rate distributions derived from pre-recorded data, the propagation of realistic levels of receiver noise to the AOA/radial velocity estimation, and the effects of phase calibration errors.

The model showed that for a flux magnitude of  $\sim 20 \text{ m}^2\text{s}^{-2}$  and a single day of in-

tegration, a momentum flux uncertainty of  $\sim 75\%$  can be expected for a monostatic (BP-only) configuration, and  $\sim 65\%$  for a multistatic (BP and Mylor combined) configuration. It was surmised that this increase in precision could be attributed entirely to the higher number of meteor detections associated with the combined configuration.

In agreement with previous studies, we have concluded that the meteor detection rate (and/or total meteor counts arising from integrating time) is the most important factor in determining the measurement uncertainty for a given wave field. In addition, we surmised that the uncertainty asymptotes to a value governed by the complexity of the wave field beyond some threshold number of meteors incorporated in the analysis. We have not rigorously clarified this threshold, but note that for our spectral-model-derived wave field, using more than  $\sim 1,500$  meteors per analysis window led to immaterial increases in precision.

Another factor that greatly affects the measurement uncertainty is the presence of outliers in the input radial velocity distribution. Such outliers may stem from errors arising from low SNR meteors, interference, phase calibration errors, or unusually large wind perturbations in the volume being sampled. We employed a simple outlier rejection scheme to reduce the effects of these, noting that this actually improved the measurement precision even in the absence of noise injected into the radial velocity estimates.

It is clear that the most simple ways to reduce the momentum flux measurement uncertainty are 1) to increase the meteor count rate (especially so for shorter integration times, such as individual days) and 2) to reduce the incidence of radial velocity outliers. To this end, in Chapter 5 a phase calibration technique that outperforms the empirical one used in this simulation and in Chapter 4 is developed. This results in a higher number of meteors within the expected height region and fewer AOA-aliased meteors (which in turn reduces the likelihood of radial velocity outliers).

## Chapter 4

# Observations of gravity-wave–tidal interaction

This Chapter presents an application of the momentum flux estimation procedure simulated in the previous Chapter to a case study of the interactions between gravity waves and the diurnal tide in the mesosphere. The motivations have been 1) to validate the momentum flux measurement capability of this technique coupled to the BP-Mylor meteor radar system, and 2) to contribute to the well-known gap in our understanding of the way gravity waves and tides interact. The latter motivation arose from our observations of curious levels of tidal amplitude variability and a coincident modulation of the gravity wave momentum fluxes, and a subsequent decision to investigate their causes further.

To contextualize the tidal interaction work, the Chapter first gives a brief review of the current state of knowledge of the effects of gravity waves on the diurnal tide in the mesospheric region. Emphasis is given to the lack of observational validation of model predictions of the effects of gravity waves on tides and vice versa.

### 4.1 Gravity-wave–tidal interactions in the mesosphere

As discussed in Sect. 1.1, the gravity wave propagation through the mesosphere is modulated by variations in the background wind (including those associated with tidal activity) through critical level absorption. Dissipating gravity waves also exert forces on the wind in the direction of their phase velocity. Depending on the relative phase of the forcing direction and the tidal wind, this can result in the tide being amplified, dampened, or having its phase shifted. As an aside, the latter process has the capability of altering the observed period of that particular tidal component.



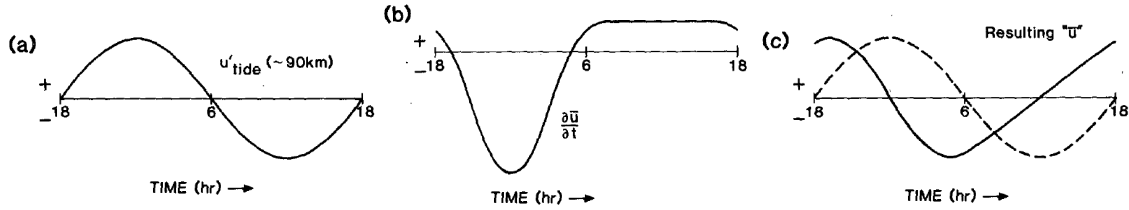


Fig. 4.1: Gravity-wave-tidal interaction model proposed by Fritts and Vincent [1987] (adapted from their Fig. 16). As a function of time of day, (a) shows the diurnal tidal winds without modulation, (b) shows the gravity wave forcing arising from the momentum flux divergence with height, and (c) compares the “apparent” modulated tide (solid line) with the unmodulated (dashed).

The first attempt to explain diurnal variations of gravity wave and tidal activity in terms of this coupling mechanism was made by Fritts and Vincent [1987]. They found a significant diurnal variability in  $\langle u'w' \rangle$  estimates derived from the Buckland Park MF radar, with an altitude variation that was correlated with changes in the amplitude and phase of the diurnal tidal winds. Specifically, with increasing altitude around 90 km they found a sharp divergence in  $\langle u'w' \rangle$  (an increase from negative values), and a reduction in amplitude and an advance in the phase of the diurnal tide (DW1). This led them to propose a gravity-wave-tidal interaction model attributing the divergence in the momentum flux to changes in critical level filtering associated with the tidal motions, and the tidal modulations to the forcing associated with that flux divergence. They also postulated that such a mechanism is likely to act on a global scale, suggesting the importance in accounting for it in global-scale tidal models. A schematic of the model showing the gravity wave forcing as a function of time of day and the resulting diurnal tide modulation is in Fig. 4.1.

Subsequent modelling work by both Miyahara and Forbes [1991] and Forbes et al. [1991] showed that the eddy diffusion arising from breaking gravity waves acts to suppress the amplitude of DW1 at all latitudes in the MLT-region, during both summer and winter. However, while Forbes et al. [1991] acknowledged that the role of gravity wave forcing was not fully understood, both of these works did show that the diurnal modulation in the flow acceleration arising from breaking waves plays an equally important role in the tidal dampening.

Modelling efforts since the above studies have generally agreed that gravity-wave-driven flow accelerations could play a role in causing the observed seasonal variation of DW1 amplitudes, which broadly speaking are maxima at the equinoxes and minima

at the solstices. However, they have not come to consistent conclusions on the overall effect of gravity wave forcing on DW1 (i.e., an amplification or dampening, and the seasonal/altitude dependence of these), nor if this is the sole mechanism responsible for amplitude and phase variability of DW1 in the MLT. Much of this stems from the fact that the effects of gravity wave forcing on tides is dependent on the source spectrum of the waves assumed and/or the parameterization scheme used for them (e.g., McLandress [1998], England et al. [2006], Ortland and Alexander [2006], Ribstein and Achatz [2016], Yigit and Medvedev [2017]). Such a simplification of the gravity wave effects is required because atmospheric tides can only be accurately modelled with a global-scale model (e.g., Liu et al. [2013]). Examples showcasing the disparity in results include:

- Mayr et al. [1998], concluding that gravity wave forcing amplifies the DW1 at all times of year, moreso during the equinoxes than the solstices.
- Meyer [1999], concluding that eddy diffusion influenced the dampening of the diurnal tide during the solsticial period, but that the effect gravity wave forcing had on the tides was unclear.
- McLandress [2002], concluding that gravity-wave–tide interactions are not responsible for causing the observed semiannual variation in tidal amplitudes.
- Liu et al. [2008], concluding that the forcing exclusively amplifies DW1.
- Watanabe and Miyahara [2009], concluding that the forcing amplifies DW1 during the equinoxes, and dampens it during the solstices.
- Lu et al. [2012], concluding that gravity wave forcing can only dampen tidal amplitudes, and that the remaining tidal variability is caused by advection that varies with altitude and latitude.

As pointed out by a number of authors (e.g., McLandress [1998], Liu et al. [2013], Yigit and Medvedev [2017]), additional observational evidence of the forcing small-scale gravity waves impose on tides is critical to addressing this ongoing debate. Owing to the difficulties of making gravity wave forcing measurements however, which include the large measurement uncertainties inherent to radar measurements and the fact that satellites cannot resolve small-scale gravity waves and can take several months to characterise diurnal variations (e.g., Liu et al. [2013]), there have been few studies of this kind published since that of Fritts and Vincent [1987]. Furthermore, they have also

not yielded consistent results on the role gravity wave forcing plays in modifying the amplitude/phase of DW1. Examples include:

- Xu et al. [2009], who used TIMED satellite data to show that the gravity-wave-induced dampening of tidal amplitudes is largest during equinoxes. They concluded from this that dampening cannot cause the observed seasonal variation in tidal amplitudes.
- Lieberman et al. [2010], who showed (also using TIMED satellite data) that while the zonal and meridional gravity wave forcing maximizes at the equinoxes and minimizes at the solstices, the zonal forcing is in quadrature with the zonal tidal wind, and the meridional forcing is out of phase with the meridional tidal wind, leading to a zonal tide with advanced phase and a dampened meridional tide. They also noted that the zonal advection due to variability in the meridional DW1 amplitude also, like the wave forcing, maximized at the equinoxes and minimized at the solstices, but were not able to reconcile if this variability was a cause or an effect of the seasonal DW1 variation.
- Liu et al. [2013], whose measurements from a ground-based meteor radar in Hawaii (20.7°N, 156.3°W) showed that gravity wave forcing tends to slightly dampen the DW1 amplitude below 90 km, but enhance it above 90 km.
- Agner and Liu [2015], whose LIDAR measurements from Starfire Optical Range (35.0°N, 106.5°W) showed that gravity wave forcing can amplify or dampen the DW1 amplitudes, depending on the altitude.

In this study, we add to this existing pool of measurements by estimating the gravity wave momentum flux divergences from combined BP and Mylor meteor radar measurements and investigating their correlation with the temporal and altitude variation in the estimated tidal winds. Rather than being of climatological nature like the aforementioned studies, our analysis is more akin to Fritts and Vincent [1987]’s in that it is focused on a short (20-day-long) period encompassing a sudden enhancement in tidal amplitudes and seeks to provide some insight into whether gravity wave forcing caused this enhancement.

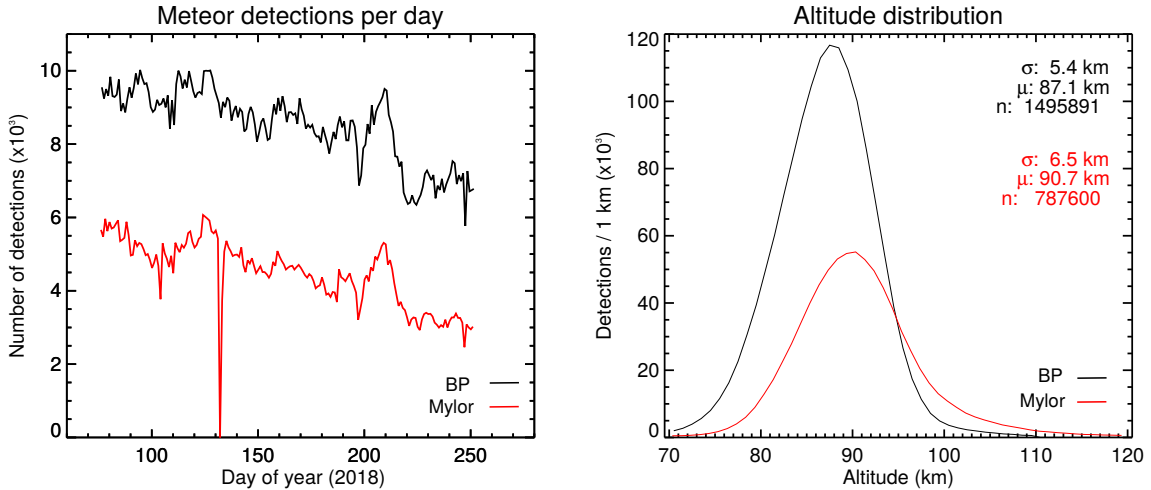


Fig. 4.2: Left panel: Daily meteor detection rates for the BP and Mylor meteor radars (only detections with non-ambiguous heights between 70 and 110 km are included). Right panel: Altitude distribution of the detections for the two radars.

## 4.2 Data set attributes and analysis approach

This Chapter makes use of meteor detection data from the BP and Mylor meteor radars from an experiment run continuously between 17th March 2018 and 9th September 2018. Further information on those radars can be found in Sect. 2.3, and the experiment parameters used for the duration of the study are listed in Table 2.1.

The meteor detection rates and their distribution with altitude are shown in Fig. 4.2. As is evident from the detection rate plots, the dataset is continuous for the entire period under investigation, with the exception of an outage at Mylor for several days around day 130 of 2018. The peak altitude of the detections at BP (87.1 km) is slightly lower than that at Mylor (90.7 km), also with a slightly smaller distribution width (5.4 km and 6.5 km, respectively). Both datasets were phase-calibrated using the empirical approach of Holdsworth et al. [2004b] (described in Sect. 2.9), and as discussed in Chapter 5 (Sect. 5.8), in the Mylor case this approach appears to have led to a peak height several kilometres higher than the true value. The peak height widths in both cases (especially Mylor) are also likely to be overestimates of the true values.

The phase calibration offsets derived for the two systems using the Holdsworth et al. [2004b] approach are shown in Fig. 4.3. While the BP offsets show a small amount of variability, there are substantial discontinuities in those at Mylor (for example, the correction for the Rx 1-2 pair shifts by  $\sim 25^\circ$  over the course of two days around day 160). The causes of these discontinuities have not been investigated. Given the stability

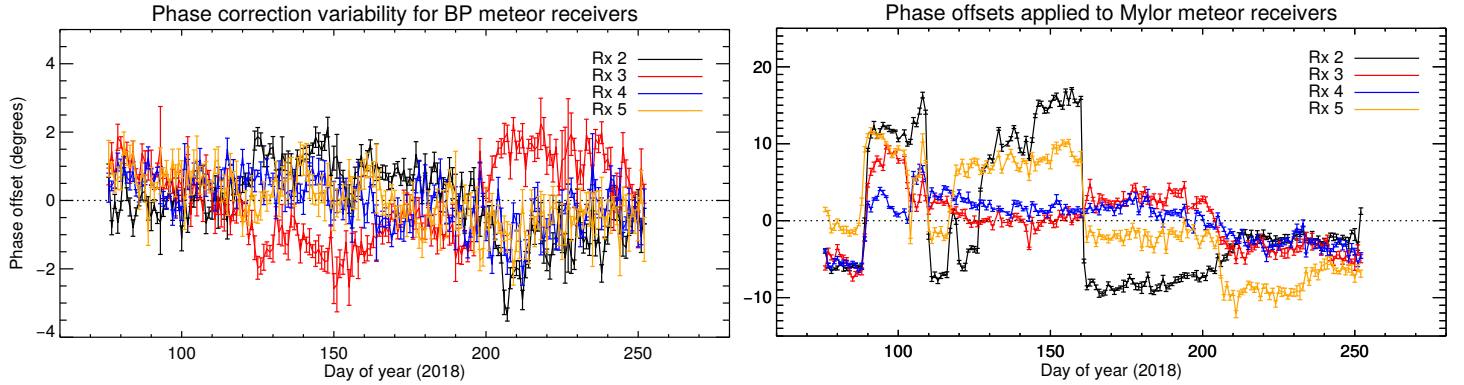


Fig. 4.3: Phase corrections applied to the radars used in this study (derived from the empirical Holdsworth et al. [2004b] technique). BP results are shown on the left, and Mylor on the right. The offsets are with respect to Rx 1 in both cases.

of the BP results, the same set of offsets was used to calibrate the BP data for the duration of this study. In the Mylor case however, the calibration determined for each individual 24 hours of data has been applied. In doing this, we have of course implicitly assumed that the discontinuities in the latter’s offsets are valid.

The covariance estimation procedure performed on the phase-calibrated data exactly follows that tested in the simulations in Chapter 2 (see Sects. 3.2.4–3.2.6). As a brief overview, this procedure incorporates the following (further details are provided where appropriate in the subsequent results section):

1. The estimation of AOAs and radial velocities for each meteor echo candidate.
2. The estimation of mean winds using meteor echoes sampled to 2 km altitude bins and 1 hour time bins (both non-oversampled). Measurements from both radars are used in the wind fitting.
3. The filtering of the tidal and planetary wave components (specifically oscillations with a period  $> 6$  hours) from the radial velocities by means of an inverse wavelet transform. Amplitude and phase information from the tidal components is also retained for further analysis. The next section describes this procedure in further detail.
4. The computation of covariances from the filtered radial velocities from both radars. The iterative outlier removal procedure discussed in Sect. 3.2.6 is also utilized in an attempt to reduce the uncertainties in the covariance estimates.
5. The calculation of flow accelerations from the vertical variation in the momentum

fluxes. This requires knowledge of the atmospheric density, and the method used to obtain this is discussed in Sect. 4.2.2.

### 4.2.1 High-pass filtering using the wavelet transform

Wavelet analysis is a widely-used time-frequency decomposition method that is well-suited to the extraction and characterisation of both periodic and transient features in time series. Transience in the tidal and planetary wave components in the horizontal winds estimated in this study was readily apparent (as evidenced by several figures later in this Chapter), which motivated the use of wavelet analysis here to effect a high-pass filter for the removal of those features from the radial velocity time series prior to covariance estimation. This filtering method has been used in preference to e.g., the least-squares fitting approach employed by Andrioli et al. [2013a], which requires a-priori knowledge of the tidal and planetary wave periods, and also assumes they have a fixed amplitude and phase in any given data window.

Torrence and Compo [1998] provide an overview of all aspects of wavelet transforms relevant to the analysis of geophysical time series, including assigning significance levels to wavelet spectra. Of interest here is the way a time series may be partially reconstructed from its wavelet transform coefficients (in effect an “inverse wavelet transform”) to enact a spectral filter. The time series reconstructed from a wavelet transform can be expressed as (Torrence and Compo [1998], their eqn. (11)):

$$x_n = \frac{\delta j \delta t^{1/2}}{C_\delta \psi_0(0)} \sum_{j=0}^J \frac{\Re(W_n(s_j))}{s_j^{1/2}}, \quad (4.1)$$

where  $\delta j$  describes the wavelet scale separation,  $\delta t$  represents the time separation between adjacent points,  $J$  is the number of wavelet scales,  $C_\delta$  is a reconstruction factor (0.776 for the Morlet wavelet),  $\psi_0(0)$  is an energy scaling factor ( $\pi^{-1/4}$  for the Morlet wavelet),  $s_j$  are the wavelet scales, and  $W_n(s_j)$  contains the complex wavelet transform coefficients at scale  $s_j$ . In reconstructing the hourly-averaged wind time series (regardless of the time series length), we have taken  $\delta j = 0.02$ , in contrast to Torrence and Compo [1998] (Sect. 2f), who choose  $\delta j = 0.125$  in their example with the Morlet wavelet; we have done this to reduce the spacing between adjacent wavelet scales and hence improve the accuracy of the reconstruction. Also in contrast to Torrence and Compo [1998] (their Sect. 2g), we have not applied any zero padding in the application of the wavelet transform. This was done given our finding that the magnitude of artefacts at the ends

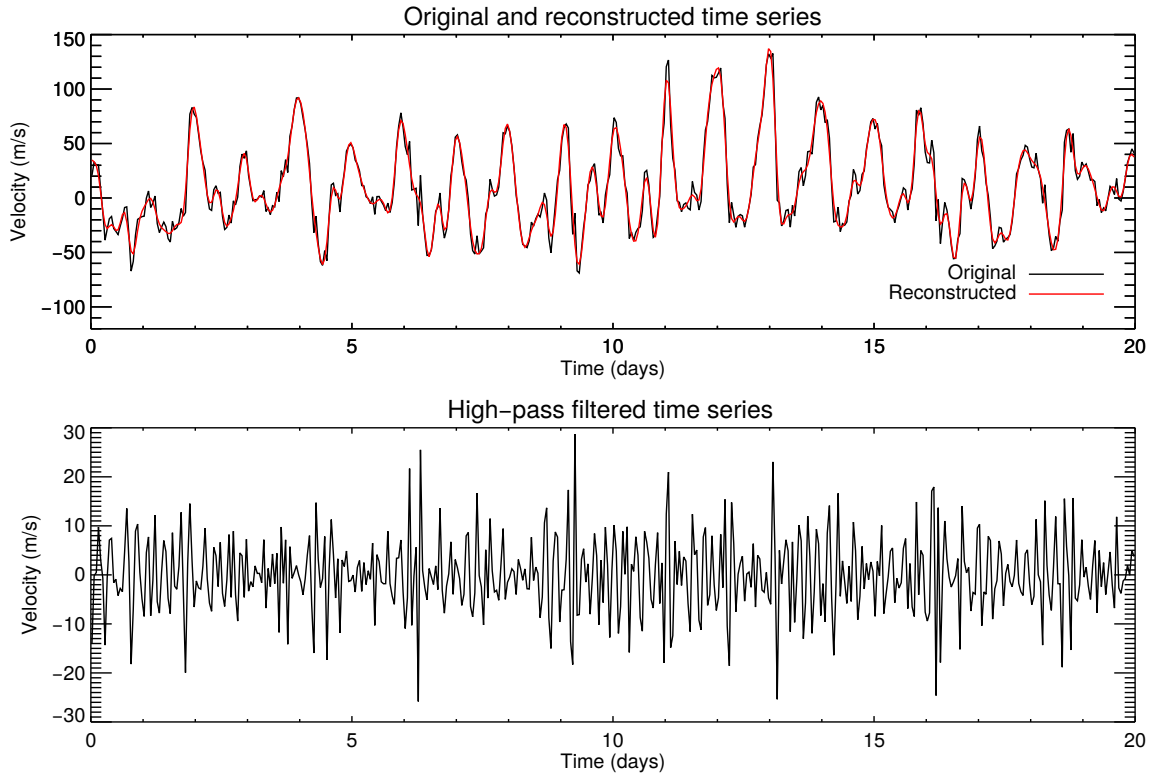


Fig. 4.4: Example of using a wavelet transform to reconstruct a low-pass filtered version of wind time series (upper panel), and subtract it from the original to enact a high-pass filter (lower panel). The dataset used corresponds to 20 days of estimated zonal winds from the combined BP and Mylor meteor radars at 92 km, beginning 5th April 2018.

of the wind time series appeared to be larger with zero padding applied.

As with other spectral analysis techniques, the wavelet transform requires a uniformly sampled time series. Linear interpolation is used in this thesis to fill in any missing hourly-averaged wind data prior to applying a wavelet transform.

An example of a reconstructed wind time series using scales corresponding to periods larger than 6 hours is shown in Fig. 4.4. The number of scales used in the reconstruction is 400 (which corresponds to periods from 6 hours to about 63 days, using  $\delta j = 0.02$  as mentioned as earlier). The tidal components in the winds shown are clearly non-stationary, with an obvious increase in the size of the amplitude of the component close to a period of 1 day between days 10 and 15. The reconstructed time series closely tracks this amplitude modulation, with little of this remaining in the residual time series (the effectively “high-pass filtered” version) in the lower panel.

The amplitude and phase variability at a selected period may also be investigated by performing the summation in (4.1) over a narrow bandwidth of wavelet of scales around the periods in question, while retaining the imaginary components in the wavelet

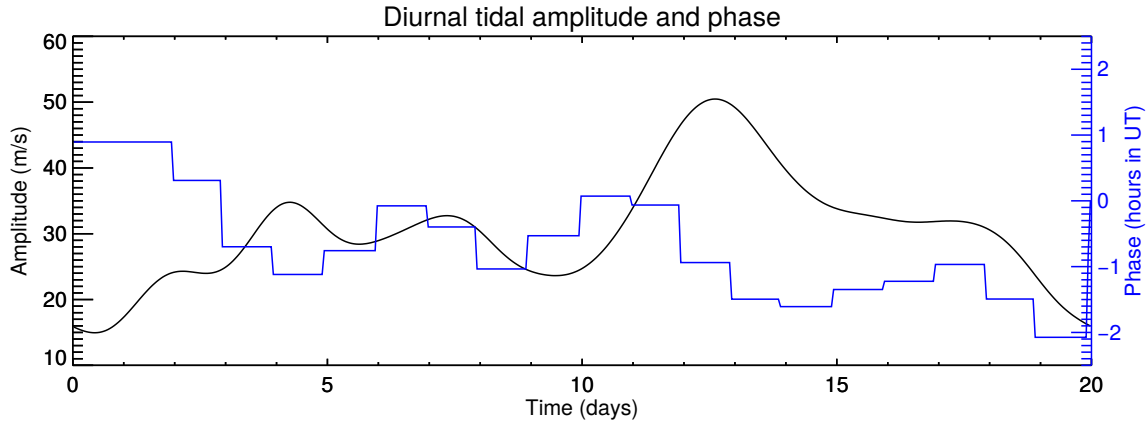


Fig. 4.5: Example of diurnal tidal amplitudes (black) and phases (blue) extracted from the data in Fig. 4.4.

transform coefficients—i.e., calculating

$$z_n = \frac{\delta_j \delta t^{1/2}}{C_\delta \psi_0(0)} \sum_{j=s_1}^{s_2} \frac{W_n(s_j)}{s_j^{1/2}}, \quad (4.2)$$

where  $s_1$  and  $s_2$  are the lower and upper scale limits respectively. As an example of this, Fig. 4.5 shows the amplitude and phase of  $z_n$  for wavelet scales corresponding to periods between 0.8 and 1.2 days. The phases here have been estimated by firstly computing  $\text{atan2}(\Im(z_n), \Re(z_n))$ , converting the result to a value in hours, and then interpolating the hour at which the zero-crossing in the phase occurred. This is because tidal phases are typically interpreted to be the time at which the associated parameter takes its maximum positive value (which is when the complex reconstructed time series is purely real, and hence has a phase of zero). The same approach is used to produce results shown later in this Chapter in Fig. 4.11.

### 4.2.2 Density estimation

The flow acceleration estimates shown later in Fig. 4.12 required the use of an atmospheric density profile. As an aside, it is possible to measure the height of a constant surface using meteor radar (see Younger et al. [2015]), as is used in conjunction with satellite and airglow temperature measurements in Reid et al. [2017] (presented in App. G) to show evidence that airglow emission heights follow heights of constant density. However, since meteor radar density estimations require large meteor count rates and can only reliably obtained at one height, they have not been deemed suitable in this work for the derivation of density profiles. We have instead used data from the Sounding of



the Atmosphere using Broadband Emission Radiometry (SABER) satellite instrument for this purpose.

We have made use of Version 2.0 SABER data acquired online from the [SABER GATS-Inc. website's Custom Data Tool](#). Molecular number density profiles from individual SABER limb scans were used to create atmospheric mass density climatologies. Mass densities were computed from the number densities via the expression:

$$\rho = nM_{air}/N_A \quad (4.3)$$

where  $n$  is the molecular number density ( $\text{cm}^{-3}$ ),  $M_{air}$  is the molar mass of air ( $\sim 0.029 \text{ kg mol}^{-1}$ ), and  $N_A$  is the Avogadro constant ( $\sim 6.02 \times 10^{23} \text{ mol}^{-1}$ ).

To create a climatology of the diurnal variability in density from the data that was representative of conditions around Adelaide during the autumnal equinox, we acquired limb scans with tangent point latitudes spanning  $28^\circ\text{S}$ - $42^\circ\text{S}$ , longitudes  $108^\circ\text{E}$ - $168^\circ\text{E}$ , days 01-March to 31-May inclusive, and years 2008-2018 inclusive. Measurements falling into given time-of-day (hourly) and height (0.5 km) bins were averaged. A spatial sampling region and measurement time-of-year span of this size was necessary to fill all time-of-day bins with measurements. The aggregation of data over 11 years was performed to reduce the level of aliasing arising from gravity-wave-induced perturbations occurring in individual scans.

For comparative purposes, mass densities have also been evaluated using the NRLMSISE-00 model<sup>1</sup>. Mean densities were evaluated across 01-March and 31-May and for the same range of altitudes as in the SABER sampling, calculated for the coordinates ( $34.6^\circ\text{S}$ ,  $138.5^\circ\text{E}$ ) (the location of the BP site).

As shown in Fig. 4.6, the climatology produced using this method exhibited features that were qualitatively consistent with the same time averaging on NRLMSISE-00 model output from Adelaide's location. We did note however that given density surfaces from SABER were, on average, 2 km lower than NRLMSISE-00's predictions between about 80 and 95 km. Nevertheless, the use of the SABER-derived density climatology in the production of Fig. 4.12 yielded essentially identical flow accelerations as those obtained with NRLMSISE-00.

---

<sup>1</sup>The particular version used in this work was the C version maintained by Dominik Brodowski, available at <https://www.brodo.de/space/nrlmsise/>.

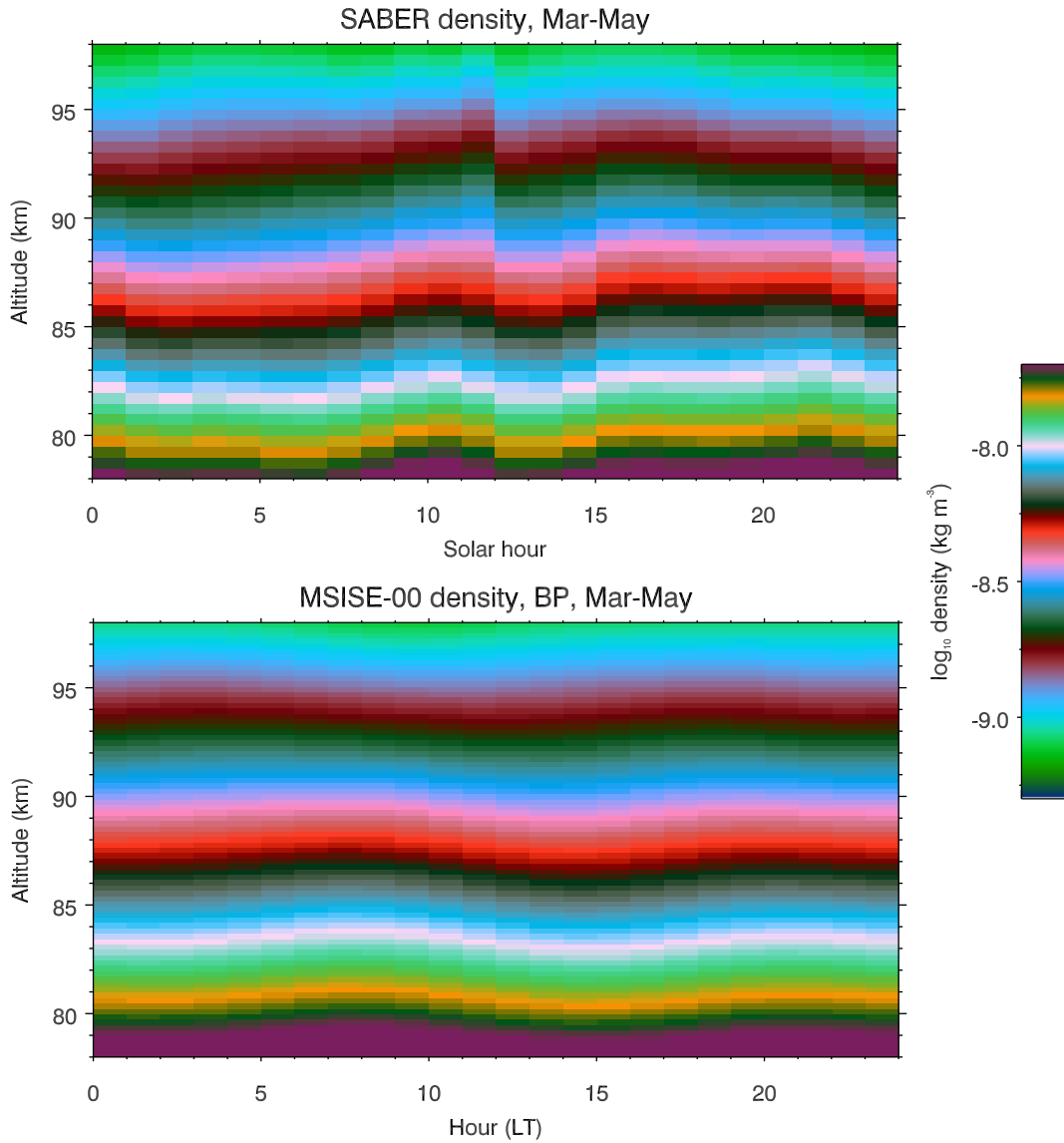


Fig. 4.6: Diurnal variation in atmospheric mass density as derived from SABER data (upper panel) and the NRLMSISE-00 model (lower panel).

### 4.3 Results

An example of the horizontal winds estimated from the BP and Mylor meteor radars using 1-hour time bins and 2 km, non-oversampled altitude binning is shown in Fig. 4.7. This plot is centred on a noteworthy enhancement in the diurnal tide amplitudes (between days 105 and 110 of 2018), in which the maximum hourly averaged wind velocity reaches  $\sim 130 \text{ ms}^{-1}$ . We saw the isolated nature of this as an opportunity to investigate if it was accompanied by any changes in the gravity wave momentum fluxes and whether or not gravity wave forcing may have contributed to the enhancement.

This section firstly analyses the horizontal winds and momentum fluxes over the

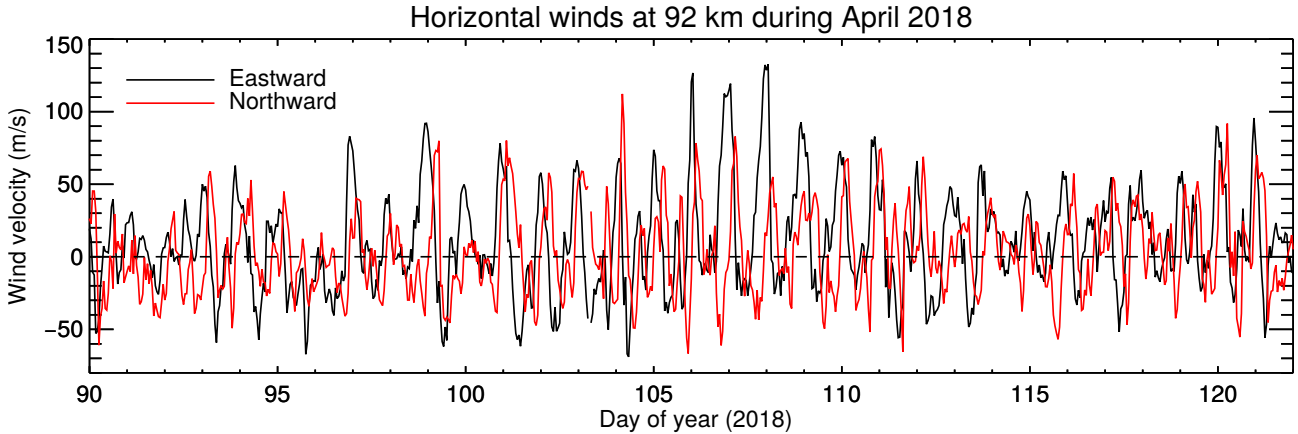


Fig. 4.7: Sample of zonal and meridional winds from the BP and Mylor meteor radars, from an altitude of 92 km.

entirety of the 2018 winter season, and then focuses on the 20 day period centred on this particular enhancement in the tidal amplitudes.

### 4.3.1 Covariances across the winter season

Plots of the mean horizontal winds and the  $\langle u'w' \rangle$  and  $\langle v'w' \rangle$  covariance components from 17th March through to 9th September 2018 are shown in Fig. 4.8. Both quantities have been sampled using 2 km, non-oversampled altitude bins. We chose to evaluate the covariances using 10-day-long windows, with a time shift of 2 days between the centres of adjacent windows, in attempt to resolve the planetary-wave induced modulation of the covariances. A low-pass wavelet filter with a cut-off of 2 days and a 10-day moving average has been applied to the hourly horizontal winds to evaluate the winds shown; the filtering was performed to avoid the aliasing of gravity wave activity and tides into the wind's variability, and the moving average in order to more closely match the temporal sampling of the two parameters. Therefore, the winds shown should provide a good measure of the “background mean winds” responsible for critical level filtering of gravity waves. We stress that these wind fields are only intended to be devoid of tides, not planetary waves (again so that an estimate of the time-varying “background wind” may be obtained). This is distinct from the filter applied prior to evaluating covariances, which was intended to filter out all spectral components with periods above 6 hours.

As is expected for this time of year at a mid-latitude SH site (see e.g., Vincent and Ball [1981]), the eastward winds around 80 km generally increase with time from the autumnal equinox to the winter solstice ( $\sim$  days 80 and 170 respectively) and decrease toward the vernal equinox ( $\sim$  day 265). A wavelet analysis (of the unfiltered hourly-

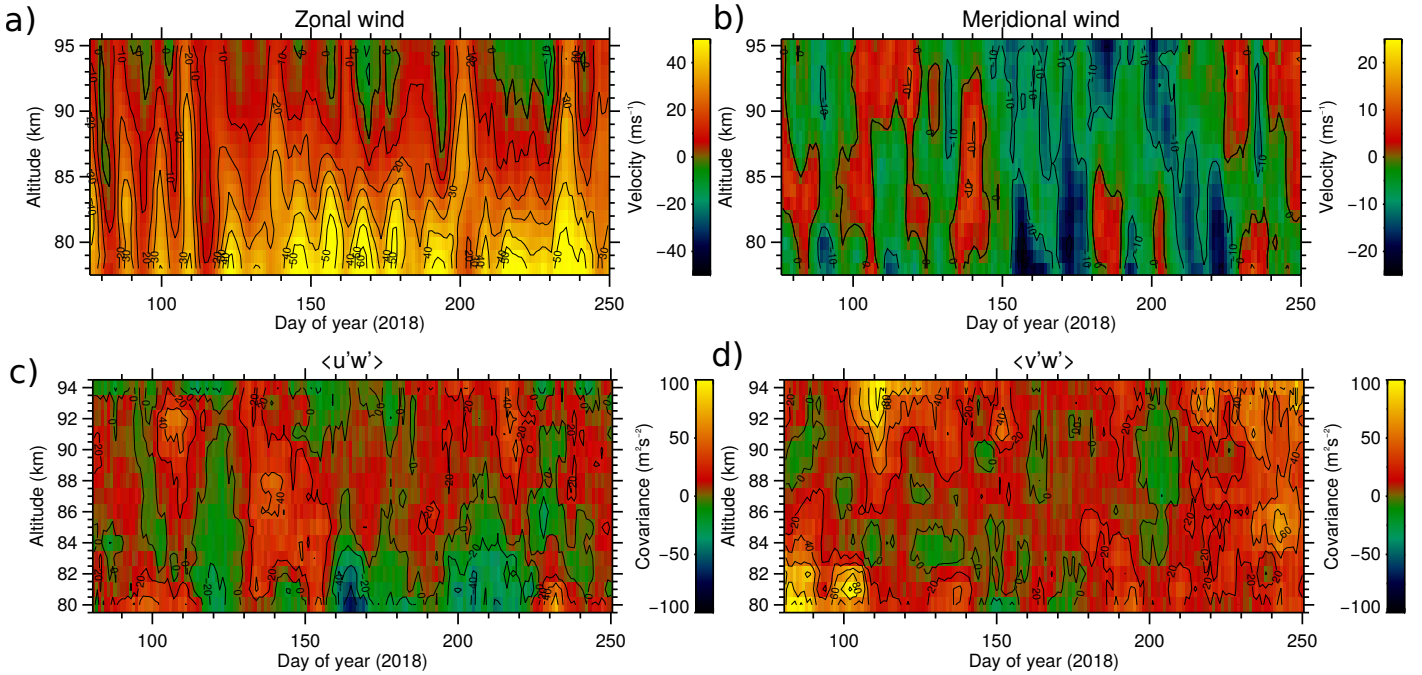


Fig. 4.8: Mean horizontal winds (panels **a**) and **b**) and the  $\langle u'w' \rangle$  and  $\langle v'w' \rangle$  covariance components (panels **c**) and **d**) measured using the BP-Mylor link between 17th March and 9th September 2018. As discussed in Sect. 4.3.1, the winds shown correspond to a 10-day moving average of the hourly-averaged winds with tidal components removed, and the covariances have been evaluated over 10-day windows, with a time shift of 2 days between the centres of adjacent windows.

averaged winds) reveals that much of the shorter term zonal wind variability evident in the figure is transient, and encompasses a spectrum of periods between about 10 and 100 days (a sample of this analysis is shown in the wavelet power spectrum plot in Fig. 4.9). The meridional wind, conversely, has a mean much closer to zero. Much of its variability is confined to periods around 10, 20, 25 and 40-50 days below 90 km, with variability in the 50-100 day period becoming increasingly dominant above 90 km.

The level of (anti)correlation between the covariances and the winds is highly variable. The  $\langle u'w' \rangle$  component appears to be anticorrelated with the zonal wind between 80 and 84 km around the winter solstice, as does  $\langle v'w' \rangle$  with the meridional wind above 88 km across a similar time interval. While pronounced levels of anticorrelation between these quantities in the mesospheric region arising from the critical level filtering mechanism are typical (see e.g., the recent summary provided by Jia et al. [2018])—particularly in the zonal component—departures from these predictions are also not uncommon. As Jia et al. [2018] explains, it is difficult to conceive a mechanism for departures from this theory in the zonal component (given the dominance of eastward winds in the lower mesosphere

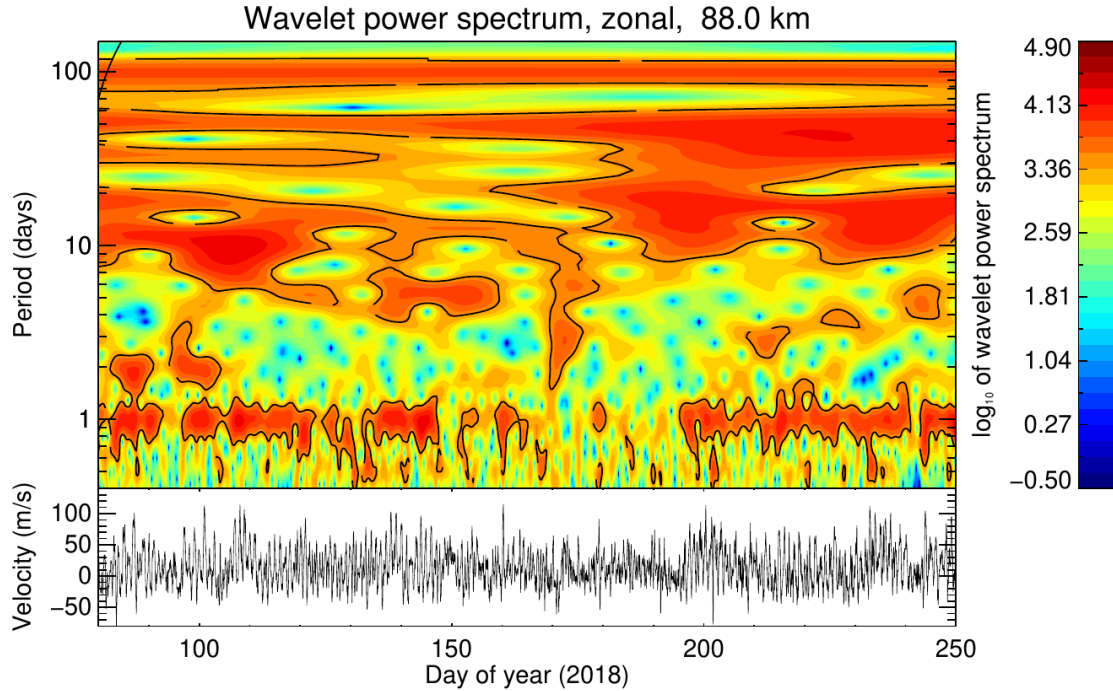


Fig. 4.9: The wavelet power spectrum of the zonal winds at 88 km altitude. 95% significance levels are contoured as a solid line.

during winter), aside from considering that the gravity waves may have propagated from a different location through a region with weak eastward mesospheric winds.

The feature we focus the remainder of this discussion on concerns the coincident enhancement in the  $\langle u'w' \rangle$  and  $\langle v'w' \rangle$  components in the interval spanning days 100 to 120, around 90-94 km. Peak values of  $\sim 50 \text{ m}^2\text{s}^{-2}$  and  $100 \text{ m}^2\text{s}^{-2}$  for  $\langle u'w' \rangle$  and  $\langle v'w' \rangle$  respectively are obtained during this interval. Interestingly, they coincide with a brief enhancement in the zonal winds at the same height, and the peak of the northward phase of an oscillation in the meridional winds with periods spanning 50-100 days.

Figure 4.10 shows an inset of Fig. 4.8, spanning April 2018 (which the aforementioned covariance enhancement is centred on). In an attempt to increase the temporal resolution, the covariances in this figure have been evaluated with 1-day windows, with a time shift of 6 hours between adjacent windows. Tidal components have also been removed from the winds as per Fig. 4.8 through the application of a low-pass wavelet filter with a cutoff period of 2 days. No moving averaging is applied to the winds in this case (since the application of the low-pass filter effectively brings the time sampling of the winds close to that of the covariance's).

This figure shows evidence of a pronounced periodicity around 10 days in the zonal wind, which attains its highest amplitude at approximately day 110 around 85 km. At

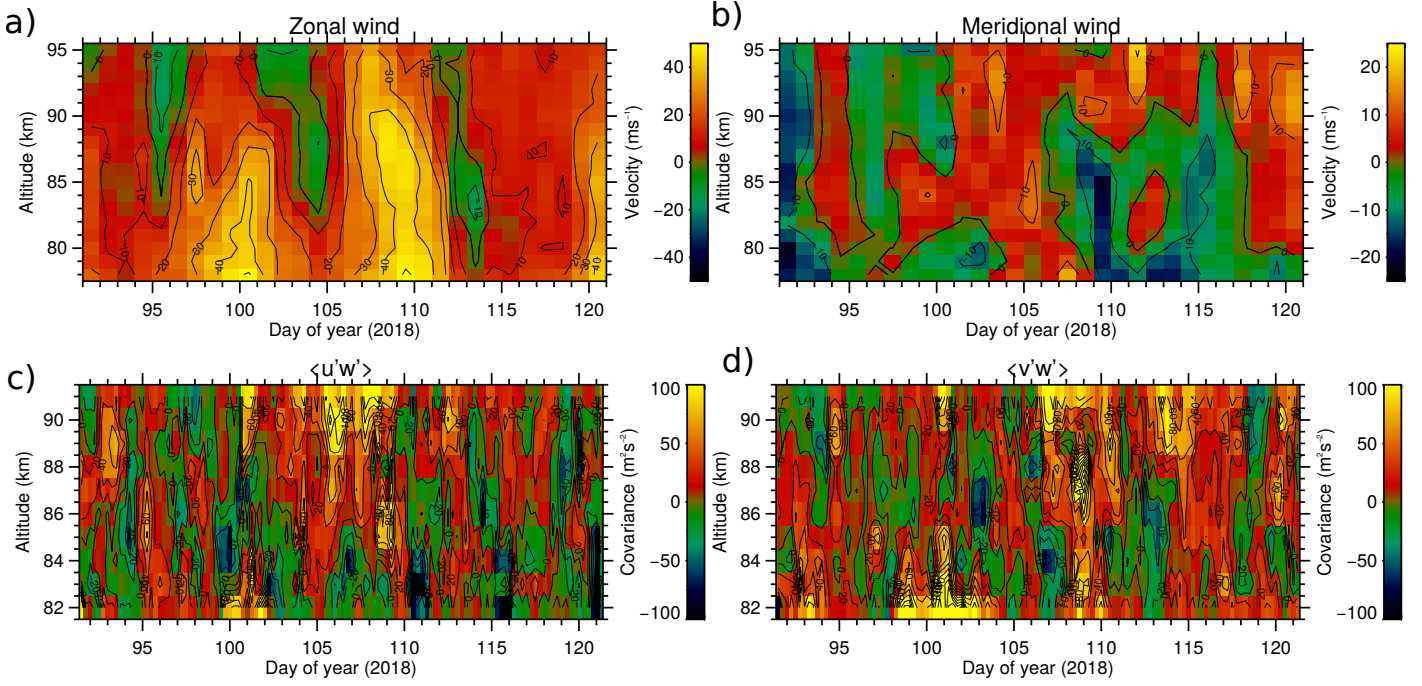


Fig. 4.10: As per Fig. 4.8, but for April 2018. Also, in this case no moving average has been applied on the winds post-tide-removal, and the covariances have been evaluated over windows of length 1 day, with a time shift of 6 hours between the centres of adjacent windows.

this time and in the same altitude region, the mean meridional winds abruptly (over a period of a few days) switch from northward to southward. All of this variability appears to be associated with a superposition of planetary waves. Albeit noisy (owing to the relatively short integration time), the  $\langle u'w' \rangle$  covariance component shows an enhancement between days 105 and 110, and attains especially high positive values (exceeding  $100 \text{ m}^2\text{s}^{-2}$ ) at around 90 km altitude. Interestingly, the  $\langle v'w' \rangle$  enhancement lags that of  $\langle u'w' \rangle$  by several days, with a peak again in excess of  $100 \text{ m}^2\text{s}^{-2}$  around day 110.

We have also noted that this interval is associated with an abrupt enhancement of the amplitudes of the diurnal and semidiurnal tides. Figure 4.11 shows the amplitude of the horizontal wind time series reconstructed from an inverse wavelet transform (see eqn. 4.1), for scales between 0.4 and 0.6 days for the semidiurnal tide, and 0.8 and 1.2 days for the diurnal tide. The diurnal tide in the zonal wind is seen to reach an amplitude of  $\sim 50 \text{ ms}^{-1}$  during day 107 at a height of around 92 km, and  $35\text{--}40 \text{ ms}^{-1}$  in the meridional component around 88 km during day 109. It should be noted that the hourly averaged zonal wind velocity (not shown here) reached a maximum of about  $140 \text{ ms}^{-1}$  at 92 km during this period. The semidiurnal tide, whose amplitude is known to



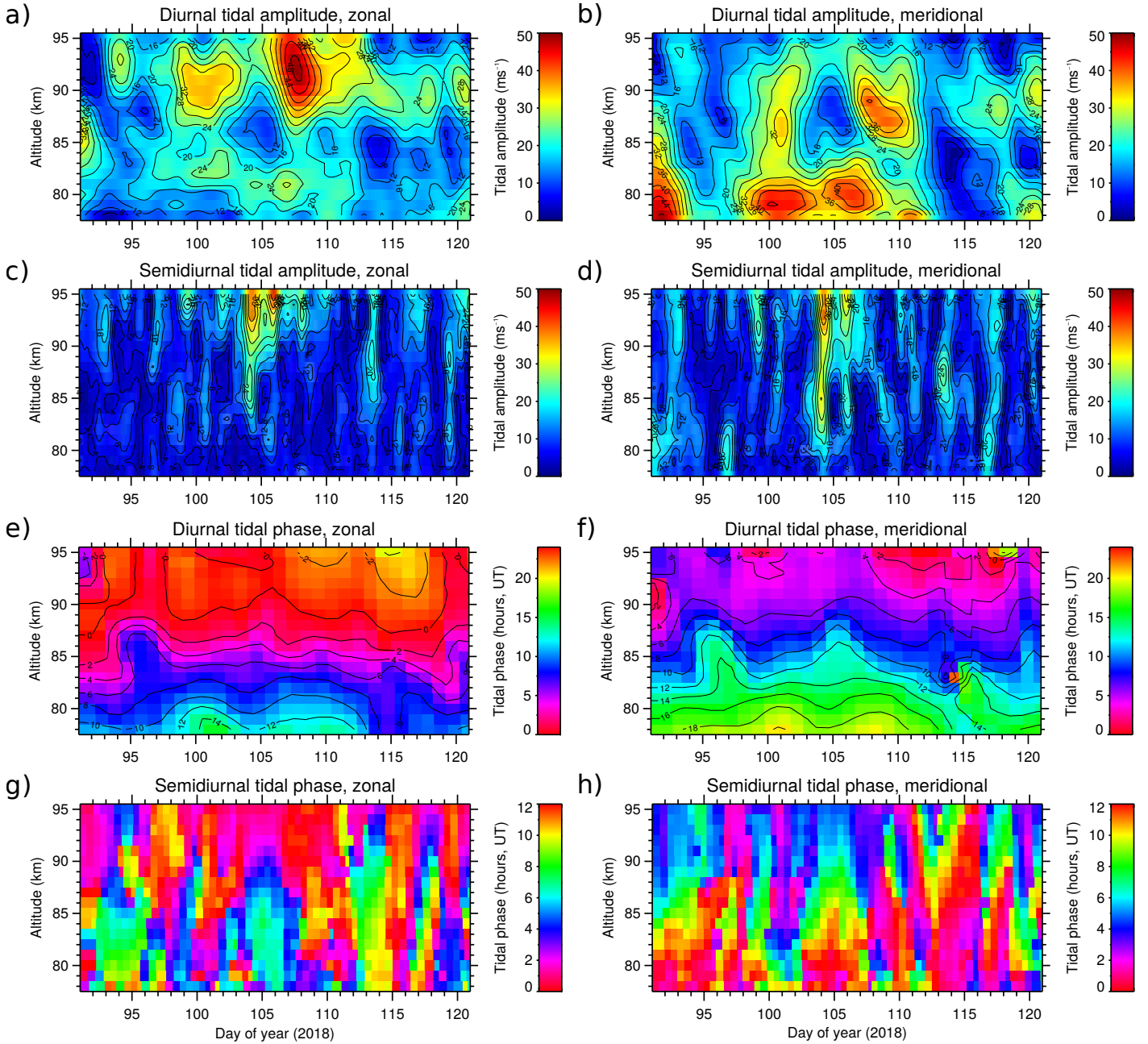


Fig. 4.11: Amplitude of the diurnal (panels **a**) and **b**) and semidiurnal (panels **c**) and **d**) tidal components, and phase of the diurnal (panels **e**) and **f**) and semidiurnal (panels **g**) and **h**) tidal components as measured by the BP-Mylor meteor radar during April 2018.

rarely exceed  $10 \text{ ms}^{-1}$  at Adelaide's location (e.g., Vincent et al. [1998]), also reached an amplitude of  $35\text{-}40 \text{ ms}^{-1}$  during day 104 in both the zonal and meridional components, at a height of around 94 km. The figure additionally shows that the phase of the diurnal tide is modulated, with the time scale of those modulations appearing to follow the phases of the planetary wave activity in Fig. 4.10—although there are no noteworthy

phase changes at the times of the sudden amplitude enhancements. The semidiurnal tidal phase is persistent, and also with a well-defined vertical progression, during the few days in which its amplitude is large, but clearly has little meaningful structure at other times.

The large tidal amplitudes during this period lead us to expect the propagation directions of the gravity waves removed from the wave spectrum by the winds to exhibit a diurnal variation. As discussed in the review in Sect. 4.1, a complicating factor is that these waves may also amplify, dampen or shift the phase of the tide, depending on the waves retained in the spectrum at the wave breaking height; the large variability in the tidal amplitudes during this period indicates that this may have indeed occurred. To provide some clarity on the extent to which the gravity waves have been modulated by the tide and vice versa, in the next section we examine a composite day of the tidal winds, covariances and the implied flow accelerations over a 20-day interval spanning the interval in which the diurnal tide has a reasonably consistent phase and an enhanced amplitude.

### 4.3.2 Observed gravity-wave–tidal interaction

Figure 4.12 shows a composite day of the horizontal winds, covariances, and flow accelerations implied by the covariances, over 5-25 April 2018 (i.e., days 95-115). The composite day consists of time windows of width 3 hours, with a time shift of 30 minutes between the centres of adjacent windows. The height binning again consists of 2 km-width bins with centres separated by 1 km.

The flow accelerations in the zonal and meridional directions have been evaluated using the expressions in (1.2) and (1.3), respectively. These require knowledge of the atmospheric density profile  $\rho(z)$ , and as discussed in Sect. 4.2.2, we used an 11 year climatology of data spanning March-May from the satellite-based SABER instrument to do this. Following the approach of Liu et al. [2013], we also apply a low-pass filter with a cut-off wavelength of 10 km to the vertical profile of the covariance prior to evaluating its density-weighted derivative, in order to remove small-scale fluctuations from it that are clearly not associated with tidal modulation.

As expected from the relatively large diurnal tide amplitudes in Fig. 4.11, both horizontal wind components show a predominantly diurnal variation, with the meridional component lagging the zonal's by approximately 6 hours across the observed height region. The time of the zonal wind maximum occurs around 0 UT at 92 km, and 8-9



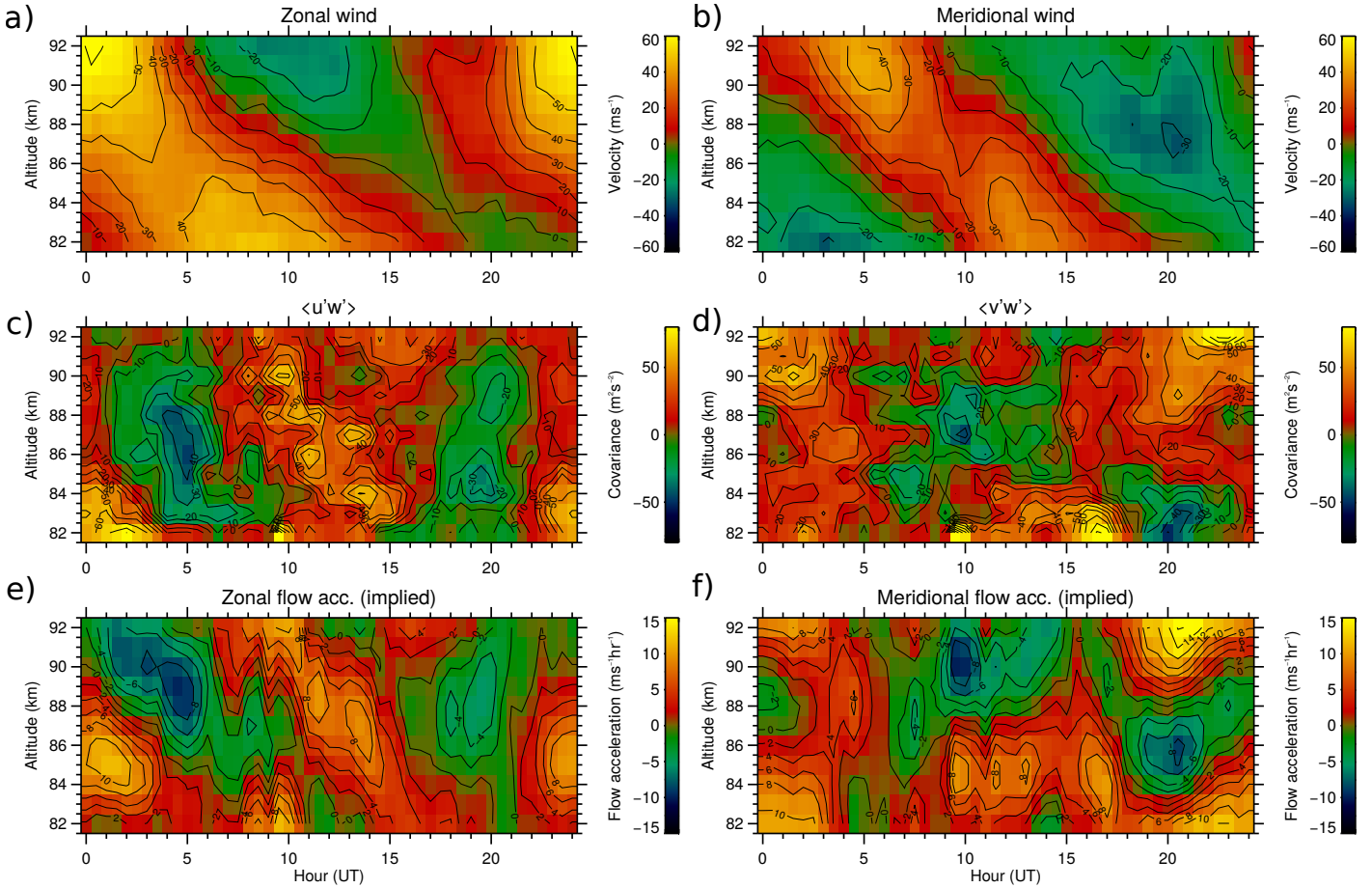


Fig. 4.12: A composite day of the horizontal winds (panels **a**) and **b**), covariances (panels **c**) and **d**) and flow accelerations implied by the covariances (panels **e**) and **f**), spanning 5-25 April 2018.

UT at 82 km.

In contrast, the  $\langle u'w' \rangle$  covariance component shows a predominantly semidiurnal variation with little vertical phase progression, maximising at around 0 and 12 UT, and minimising around 5 and 20 UT. The  $\langle v'w' \rangle$  component is more variable with altitude, exhibiting a semidiurnal variation between 82 and 84 km, and a largely diurnal variation above this. The semidiurnal variation between 82 and 84 km is associated with positive covariances for the entire day except between about 18 and 24 UT, and the diurnal variation above is associated with negative covariances between about 8 and 15 UT and positive otherwise.

Between about 88 and 92 km, the zonal flow acceleration shows a pronounced minimum between 4 and 6 UT, a maximum around 13 UT at about 88 km, and a weaker minimum around 19 UT at the same height. The maximum occurs at a similar time to the corresponding zonal wind minimum, whereas the first minimum lags the zonal wind

maximum by about 5 hours, and the second minimum precedes it by about 5 hours. Conversely, there is little flow acceleration structure below 87 km, other than a broad maximum at about 85 km around 1 UT. These observations are difficult to reconcile for three reasons: (1) the wave forcing is consistent with a rapid deceleration of the zonal wind from 4-6 UT at around 90 km, but there appears to be no positive forcing around 20 UT to accelerate the wind, (2) the strong positive forcing which does occur around 13 UT appears to result in little wind variability, and (3) the positive forcing around 85 km between 23 and 4 UT is associated with an acceleration of the zonal wind, but this acceleration is much smaller than that around 90 km.

From 88-92 km, the meridional flow acceleration shows a small maximum around 4 UT, a minimum at about 10 UT, and a large maximum around 20 UT. As per the zonal case, this leads to a peculiar relationship with the meridional wind; the forcing's positive maximum value occurs at a similar time to the wind minimum, the forcing's negative maximum corresponds roughly with a rapid wind deceleration, and the smaller maximum corresponds with a rapid wind acceleration. As with the zonal component, there is little meridional flow acceleration structure below around 86 km.

## 4.4 Discussion

Our aims in this Chapter have been to contribute observations to the well-known gap in knowledge of gravity wave effects on tides, and in some sense to verify that momentum fluxes estimated from the BP and Mylor meteor radars are physically reasonable and devoid of tide-induced biases. The extent to which we have addressed these aims and our corresponding suggestions for future work are discussed below.

### 4.4.1 Observed gravity-wave–tidal interaction

Our analysis of gravity-wave–tidal interactions, which was centred on a 20-day interval containing an abrupt enhancement in tidal amplitudes, has yielded inconclusive results on whether the gravity wave momentum deposition has on the whole enhanced, dampened or changed the phase of the tidal motions. Nevertheless, the expected uncertainties in the flow accelerations based on the bias mean and standard deviations in the Fig. 3.8 covariances, shown in Fig. 4.13, indicate that the signal components between 84 and 90 km shown in Fig. 4.12 will have well exceeded the noise levels.

The results are complex, illustrating tidal enhancement at some times of day, dampen-

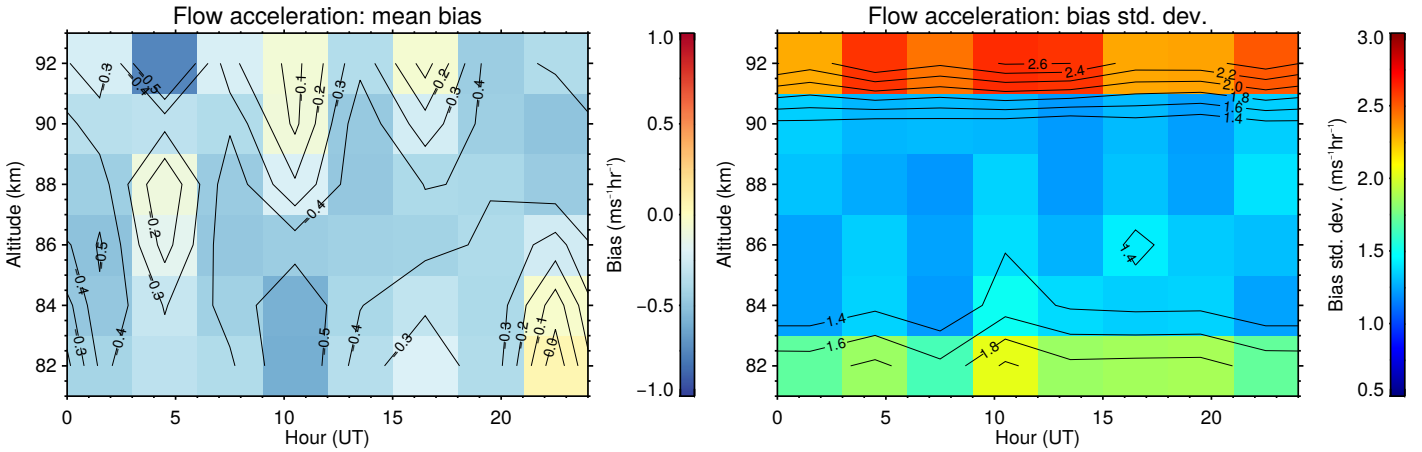


Fig. 4.13: Simulated errors in flow acceleration estimates, using the bias mean and standard deviations in the Fig. 3.8 covariances.

ing at others, and that there are also times in which a forcing is present but no apparent effect on the tide is clear. A broad observation is that the forcing components have a more pronounced diurnal variability between about 86 and 92 km, with the result that the forcing dampens the tide at the tide’s minimum (i.e. westward and southward phase), and shifts its phase at its maximum. Of course, our interpretation is complicated by the fact that we have no knowledge of what the tidal features may have looked like in the absence of gravity wave forcing.

As discussed in Sect. 4.1, it is widely accepted in modelling studies that gravity wave forcing plays a role in the observed seasonal variation of the migrating diurnal tide (DW1) amplitudes (i.e. equinoctial maxima and solstitial minima), and that whether an enhancement or a dampening of the amplitude occurs depends on the gravity wave source spectrum. However, there is still ongoing debate about whether or not the forcing is responsible for all of DW1’s observed amplitude and phase variability. Our study adds to this by showing evidence of a significant level of transience in the zonal wind diurnal tide amplitudes at a mid-latitude site during equinox conditions between about 85 and 92 km altitude, and that gravity wave forcing acted in phase with the tide at certain times of day (around 4-6 UT in our study) during one of the enhancements. This implies that the wave forcing may have contributed to the enhancement at these times. However, we also observed that the forcing should have dampened the tide shortly thereafter (at around 10 UT), and we also did not observe a large in-phase forcing at the opposite phase of the tide (at around 20 UT). Moreover, as a general conclusion, while the phase relationship between the wave forcing and the tide was complex, the both components of the forcing could be considered to be acting more in anti-phase with the respective

components of the tidal winds than in-phase during this enhancement.

Another point to consider is that tides may interact with gravity waves through the diurnal variations in atmospheric stability they induce (i.e., making conditions more favourable for gravity wave breaking and hence wave forcing at particular times of day). As an example, Fritts et al. [1988] showed from observations at Scott Base, Antarctica that the highest levels of turbulence due to convective instability occurred at the times that the vertical component of the tidal wind induced the most negative value of  $dT/dz$  (the vertical temperature gradient). Using temperature perturbations from the GSWM-98 model for the BP site, Holdsworth et al. [2001] also showed that maximum negative values of  $dT/dz$  were in phase with the maximum values of the turbulent velocity measured by the BP MF radar around the autumnal equinox.

On the basis of the finding of Holdsworth et al. [2001], we opted to more closely investigate the temperature structure in the GSWM-00 predictions for BP's location around the autumnal equinox. The model output (incorporating both diurnal and semidiurnal tidal components) is shown in Fig. 4.14. As a rough validation of the output, we see very close agreement between the model predictions and the composite day winds in Fig. 4.12. Turning to the temperature results, we have noted that the maximum negative  $dT/dz$  (of  $\sim -1 \text{ K km}^{-1}$ ) should occur between 1-3 UT across the 85-92 km region at the BP site during the period of our composite day analysis. Curiously, we have observed large positive values of  $\langle F_x \rangle$  at this time just below this region, and an abrupt shift in the sign of  $\langle F_x \rangle$  above it. As Holdsworth et al. [2001] argues, while a  $dT/dz$  of this size is too small to result in static instability, it is still coincident with a large level of gravity wave forcing and the maximum eastward phase of the diurnal tide, which we have observed to be particularly large during this interval. In other words, the times at which we observed extremely large wind zonal velocities associated with the tidal enhancement occurred when the level of gravity wave breaking (and hence wave forcing) should have been at its highest. Whether or not this was a cause or effect of the large zonal winds is unclear.

Overall, our study has highlighted the need for further case studies of transient enhancements in tidal amplitudes, how gravity wave propagation is affected by them, and the role gravity wave forcing plays in causing them. This is in addition to Liu et al. [2013]'s suggestion that longer term observations (spanning several years) are also needed across a wider variety of geographic locations to better characterise the climatological aspects of these interactions.

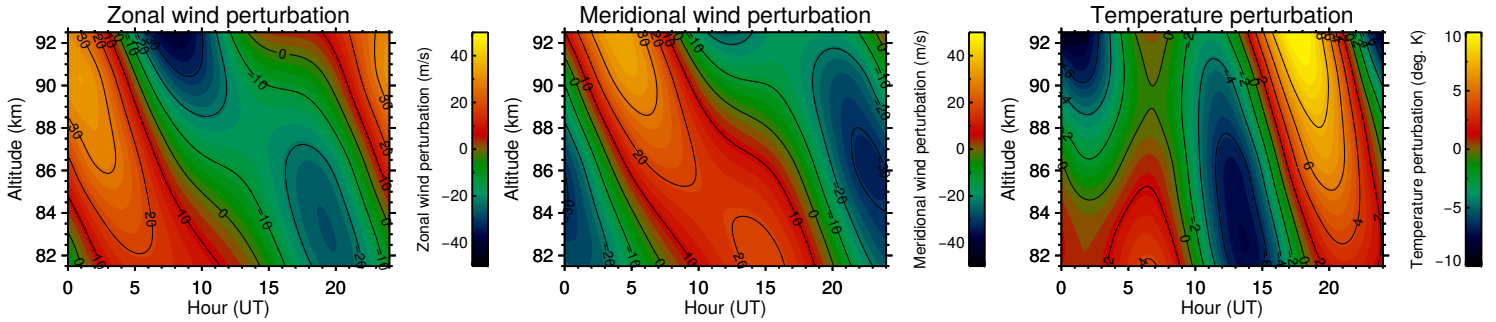


Fig. 4.14: Superposition of the diurnal and semidiurnal tidal component output from the GSWM-00, for the month of April and a latitude and longitude of  $36.0^{\circ}\text{S}$  and of  $138.6^{\circ}\text{E}$  respectively.

As is also pointed out in numerous recent modelling studies (e.g., Ribstein and Achatz [2016] and Yigit and Medvedev [2017]), gravity wave forcing on tides is dependent on the source spectrum of the waves. Therefore, it is important that future observational studies measure the forcing as a function of horizontal and temporal scale of the waves (rather than integrate the forcing over the entire spectrum as done here). The meteor-radar-based approach introduced by Vierinen et al. [2019] may be well-suited to this.

#### 4.4.2 Issues with applying the uncertainties

In Chapter 3, we attempted to quantitatively define estimates for the absolute and relative uncertainties of the  $\langle u'w' \rangle$  and  $\langle v'w' \rangle$  covariance components as measured by the multistatic BP-Mylor meteor radar, for typical time and height sampling cases. We subsequently replicated these sampling schemes on the case study presented here. Even with this replication, we have noted two main caveats in applying the uncertainties directly to the observations:

1. The dependence of the measurement precision on the complexity of the wave field.

As discussed in Chapter 3 (through the differences in the distribution widths of Figs. 3.6 and 3.9 for given detection rates), the relative uncertainties in measurements of non-zero covariance components appear to be dependent on the total frequency/scale span of all the associated waves. Furthermore, as shown by Kudeki and Franke [1998], the uncertainty in  $\langle u'w' \rangle$  and  $\langle v'w' \rangle$  measurements increases with the amount of kinetic energy in the wave field (i.e., that embodied by the  $\langle u'^2 \rangle$ ,  $\langle v'^2 \rangle$  and  $\langle w'^2 \rangle$  components). Taken together, these points mean that the uncertainties in the covariance measurements in for example Fig. 4.10 may vary considerably at a given height as a function of time.

## 2. Transient wave field features.

The spectral components of the wave field may vary during the integration period. This is particularly problematic for the 10-day window; for example, during a period of intense but transient monochromatic wave events followed by more “complex” wave activity, increasing the integration time may actually increase the uncertainty in the covariance estimate of the monochromatic wave activity—not only because of the likely change in the mean covariance, but also because of the “geophysical noise” added to the radial velocity time series by the more “complex” activity.

Despite these caveats, we can broadly conclude that the 10-day integrated covariances (shown in Fig. 4.8), except where the absolute values are smaller than about  $10\text{-}15\text{ m}^2\text{s}^{-2}$ , are likely to be of the correct sign. The correlation length of the features in both the time and height domains also indicates that the noise component in the signal is considerably smaller than the sum of all the modes of geophysical variability. Additionally, at this time integration there is likely to be little difference in the uncertainty at the peak and edges of the height region analysed.

The 1-day integrated covariances (Fig. 4.10), in contrast, are clearly more affected by measurement noise. There is still some degree of temporal-height correlation, especially in the region of consistently high values of  $\langle u'w' \rangle$  between days 105 and 110 above about 86 km, but very little below 84 km. The variability below 84 km is of the same order as the simulations predict for 1 day of integration in a spectral wave field, so it may be that the noise component at these heights is considerably larger than the signal.

The 20-day composite covariances (Fig. 3.8), while clearly affected by measurement noise, do not show fluctuations from bin-to-bin of the same size as the uncertainties predicted in the corresponding simulation. This gives us further confidence in the covariance structures observed there, and also suggests that the wave field being observed over the 20-day period was not as complex as the simulation’s, nor particularly variable.

Unfortunately, it is impossible to know (using the meteor observations alone) if the discrepancies between the 1-day and the 10-day integration (for example, the absolute values of the covariances during the enhancement between days 105 and 110) are a result of statistical noise in the 1-day estimate or a precise estimate of a strong, transient monochromatic wave event using the 1-day integration. The observation of wave features in the MLT airglow (see e.g., Reid and Woithe [2005]) may aid in the interpretation of how “monochromatic” the background wave field is; in future, there is the potential to complement these meteor radar case studies with images of the sodium and hydroxyl

airglow taken nearby the BP site. This, in conjunction with the random resampling method employed by Liu et al. [2013], may lead to more refined uncertainty estimates.

### 4.4.3 Effects of tides and planetary waves on covariance estimates

All of our simulations in Chapter 3 showed that a systematic underestimation of non-zero covariances arises when an attempt is made to remove tidal effects (planetary wave effects were not included in the model), due to the unavoidable removal of some of the wind variability associated with gravity wave activity. This clearly becomes more of a problem in the presence of large amplitude gravity waves with ground-based periods close to those of the tides. A number of questions related to the removal of tidal effects could be raised:

1. What is the importance of incorporating the momentum fluxes of gravity waves with ground-based periods close to the tides in climate models?
2. If those longer-period waves are unimportant, what is an appropriate frequency cut-off for covariance measurements?
3. If those waves are important, what is the optimal way to remove the tides?

With regard to 3., it may be that a wavelet/S-transform has insufficient frequency resolution to define solely tidal features; a long-windowed harmonic fitting (as used by e.g., Andrioli et al. [2013a]) may be more appropriate for filtering purposes if there is a specific interest in gravity wave features close to or between the tidal periods. Of course, this method assumes no variability in the tidal amplitudes, tidal periods, or in the gravity wave spectrum—the first two of which are clearly evident in examples such as Fig. 4.11. The best way forward may be to simply apply both of the methods independently and contrast their effects.

Nevertheless, in light of the concerns about contamination due to tidal and planetary wave effects raised in Andrioli et al. [2013a], we considered it critical to reduce as much as possible the extent to which variations in the amplitudes and phases of these could be interpreted as fluctuations in gravity wave activity. We found the inverse wavelet transform procedure to be a straightforward and reliable way of doing this.

## 4.5 Summary and conclusions

In this Chapter, a case study has been performed into the interactions between gravity waves and tidal activity during the autumnal equinox of 2018 above Adelaide (a mid-latitude Southern Hemisphere site). A key goal of this was to see if gravity wave forcing caused a transient spike in the zonal wind tidal amplitudes. A complex relationship between the phase of the forcing and the tidal winds was revealed, which largely implied a dampening of the tidal motions between about 88 and 92 km altitude. This leads us to believe that the gravity wave forcing was not the only contributor to the tidal variability. However, between the about 4 and 6 UT, the gravity wave forcing was acting in phase with the predominant tidal variation, suggesting that the forcing may have enhanced the tide at this time. This also coincides with the time the highest (eastward) zonal velocity was observed, and according to predictions from the GSWM-00 simulation, the time at which gravity wave breaking was most likely to occur. Coupled with the disparity in the literature of the overall effect of gravity wave forcing on tides and the lack of associated observational work, these findings illustrate the need for further studies into the causes of transient enhancements in tidal amplitudes.

The other aim of the case study was to validate the momentum flux measurement capability of the BP-Mylor radar system. By noting the small amount of noise in the 10-day-integrated momentum fluxes and the fact that the simulated uncertainties were generally smaller than the absolute value of those observed, we are confident that measurement uncertainties have not significantly affected the conclusions mentioned above. As expected, our 1-day-integrated fluxes contained considerably higher noise levels, and we would caution using these to make geophysical inferences.

As mentioned in Chapter 3, the uncertainties in the 1-day-integrated momentum fluxes in particular could be reduced by 1) increasing the meteor detection rate and 2) reducing the incidence of radial velocity outliers—both of which are hampered by a poor-quality receiver phase calibration. The low meteor detection rates from the Mylor receiver relative to that at BP (shown in Fig. 4.2) led us to believe the former receiver may indeed have been compromised by phase calibration errors that were not fully resolved by the empirical Holdsworth et al. [2004b] approach applied in this Chapter. To this end, the next Chapter explores a superior alternative phase calibration technique based on the use of aircraft echoes with known locations.



## Chapter 5

# Meteor radar phase calibration using aircraft echoes

The correct measurement of receiver channel phase differences is critical to the performance of any radar system relying on spaced antennas for AOA estimation or spaced frequencies for range estimation (this thesis is principally concerned with the former, although work performed by the author on the latter is summarized in App. A). While there is an inevitable random error in phase difference estimates due to thermal noise, “systematic” phase offsets are also possible. They are principally known to arise from (see e.g., Chen et al. [2002], Holdsworth et al. [2004b], and Chau et al. [2008]) propagation delays through the transmission lines, variations in ground reflection characteristics (e.g., due to changes in soil moisture content), coupling between the receiver antennas, cables or other parts of the radar hardware, multipath between receiver antennas or nearby objects, or changes in response of the receiver electronics due to environmental changes (e.g., the temperature-induced variability in receiver filter responses). Errors of this nature are herein referred to as “phase calibration errors”.

As discussed in Sect. 2.9, phase calibration errors in meteor radars can severely degrade the accuracy and precision of both the AOAs and altitudes ascribed to individual meteor detections. This in turn can degrade the quality of the subsequently determined wind estimates. Both Chapters 3 and 4 also provided examples of how 1) reducing the incidence of radial velocity outliers and 2) (to an extent) increasing the number of meteor detections in a given altitude bin can lead to improved momentum flux estimation precision. Correctly compensating for any receiver phase offsets aids with this, as 1) it reduces the chances of a meteor AOA being aliased yet still used in subsequent processing (see Fig. 2.13 for consequences of this), and 2) it can reduce the number of meteors discarded for having physically unreasonable altitudes. Of course, ensuring the altitudes

are correct also reduces momentum flux errors arising from using the wrong data to assign an estimate to a particular altitude bin.

As is also discussed in Sect. 2.9, the empirical phase calibration method developed by Holdsworth et al. [2004b] (which was used in Chapters 3 and 4) works extremely well for any applied combination of receiver phase offsets. However, it is generally only able to derive phase corrections to a precision of  $\pm 2^\circ$ . This typically leads to 1-sigma altitude estimation errors of  $\sim 1$  km, although the extremes in the error distribution (which are generally at zenith angles  $\gtrsim 65^\circ$ ) can be in excess of  $\sim 8$  km.

Furthermore, the empirical technique is not able to account for an AOA dependence in the phase calibration errors. In most practical meteor radar installations, obstacles nearby the array (such as buildings and vegetation) are prone to causing multipath and/or delay of received signals with AOAs close to the horizon. The characteristics of the antenna ground plane may also change with AOA of the received signals. Both of these aspects could induce AOA-dependent errors into the phase differences measured between receiver pairs. Removal of such errors is critical if they substantially degrade the accuracy of the AOA estimates.

This Chapter explores the opportunistic approach of performing an AOA-dependent phase calibration of meteor radar receivers using echoes from GPS-tracked aircraft. To contextualize the approach, the next section reviews several alternative phase calibration techniques used with atmosphere-probing MF/HF/VHF radars.

## 5.1 Radar phase calibration methods

A large number of attempts have made in the past to estimate radar receiver channel phase calibration offsets, and it is beyond the scope of this thesis to review them all. The techniques that have been used generally obtain the offsets in one of the following ways:

1. By making assumptions about the nature of the observations of some geophysical phenomenon measured by the radar;
2. By transmitting a signal with known amplitude and phase characteristics into the receivers and/or antennas;
3. By comparing the radar's measured position of a scatterer/source with its known position.

Selected examples from each of these categories that have or could possibly be applied to meteor radar are outlined below.

The Holdsworth et al. [2004b] empirical phase calibration technique is an example of one that relies on geophysical data, as it assumes meteors will occur within a certain altitude range. A related approach, referred to here as “equi- $D$  fitting”, was also introduced in the same work. That technique exploits the typically linear variation of the logarithm of the decay time (or the diffusion coefficient,  $D$ ) with altitude (an example of which is shown later in this Chapter in Fig. 5.28) to search for an optimal horizontal shift to apply to the measured AOA distribution. Phase corrections are then derived from that shift. The equi- $D$  fitting method has been shown to give comparable results to the empirical technique used in this thesis, although the latter is considered more rigorous as  $\log_{10}D$  does not always vary linearly with altitude [Younger, 2011]. In general, the equi- $D$  fitting method can also only be used to give a mean phase calibration estimate for all AOAs, rather than one with AOA dependence.

Another approach relying on geophysical data makes use of the well-known locations of specular echoes from ionospheric irregularities aligned to the Earth’s magnetic field or the equatorial electrojet. In this method, phase corrections are derived from the difference between the expected echo location and the average of an ensemble of measured locations. Such an approach has only been applied on narrow beam VHF radars (e.g., to the 52 MHz Chung-Li radar in Wang and Chu [2001], Kuong et al. [2003] and Lin et al. [2019], and to the 50 MHz Jicamarca array in Chau and Woodman [2001]). It could in theory be applicable to VHF or HF meteor radars, but it would only yield offsets for a small range of AOAs. Furthermore, fluctuations in the echo position (as discussed for example in Lin et al. [2019]) could lead to significant errors in the obtained offsets.

The effectiveness of phase-calibrating with a known signal injection depends on where in the receive chain the injection is performed. Reid et al. [1995] applied this approach on the 1.98 MHz BP array, but for practical reasons the signal was injected directly into the receivers (which each constituted 3 combined antennas and transmission lines) rather than the antennas themselves. While useful for diagnosing faults with the receivers (as well as being robust enough to determine their response to environmental changes), this approach is not able to compensate for phase delays elsewhere in the receiver chain. In a study pertaining to a 28.5 MHz meteor radar, Valentic et al. [1997] went a step further in this context by making use of a re-locatable beacon in the far field of the array. By moving the beacon around the array, they were able to determine not only the

phase offsets for the entire receive chain, but also precise effective receiver locations. A similar approach has also been applied on the Jicamarca array (e.g., Chau et al. [2008]). The use of a drone with a beacon in the far field of the array is undoubtedly the most superior approach for obtaining AOA-dependent phase calibration estimates, but such an approach was not deemed feasible in this work due to licensing considerations.

As an example from the third category, echoes from satellites or rocket payloads have been widely used for phase calibration purposes. Examples that have obtained satellite true positions from optical observations include Sullivan et al. [2006] and Schlatter et al. [2013] for narrow-beam radars in the EISCAT network, and Renkwitz et al. [2015] for the 53.5 MHz MAARSY array. As part of the present work (see the paper by Holdsworth et al. [2020] in App. C), the utility of satellite echoes received on the BP meteor radar antennas (illuminated by the co-located 144-element ST array) for phase calibration has also been briefly tested, with sample results shown in Fig. 5.1. To prepare these results, the reference satellite positions have been determined via propagation of their orbital parameters rather than through optical observations.

The satellite-based approach has proved effective in the aforementioned studies, in which the region being studied was in the same direction as the satellite echoes (close to the zenith). However, satellite echoes associated with all-sky meteor radars have not been reported in the literature, and even if it were possible it would only be feasible to use one of the few larger satellite bodies (such as the International Space Station) at high zenith angles. Another complication is the fluctuations in the apparent AOA that arise from varying levels of refraction of the echo as it propagates through the ionosphere.

Radio stars with well-known locations have also been applied successfully to phase calibration in a number of studies pertaining to narrow-beam VHF radars (e.g., Palmer et al. [1996] for the 46.5 MHz MU radar, Chau et al. [2008] for the 50 MHz Jicamarca array, and Chau et al. [2014] for the 53.5 MHz MAARSY array). These studies have concluded that radio stars offer a simple, robust way of compensating for long-term drifts in the receiver calibration and/or variations due to hardware changes without any need for manual intervention. However, their relatively low signal strength has so far made them infeasible for use on single-antenna meteor radar receivers.

To date, radar phase calibration using aircraft echoes has been reported in three studies. The first two of those, Robertson et al. [1953] and Chen et al. [2002], measured positions of candidate aircraft optically. In particular, Chen et al. [2002]’s study concerned the phase calibration of multiple receive channels of the 52 MHz Chung-Li radar.

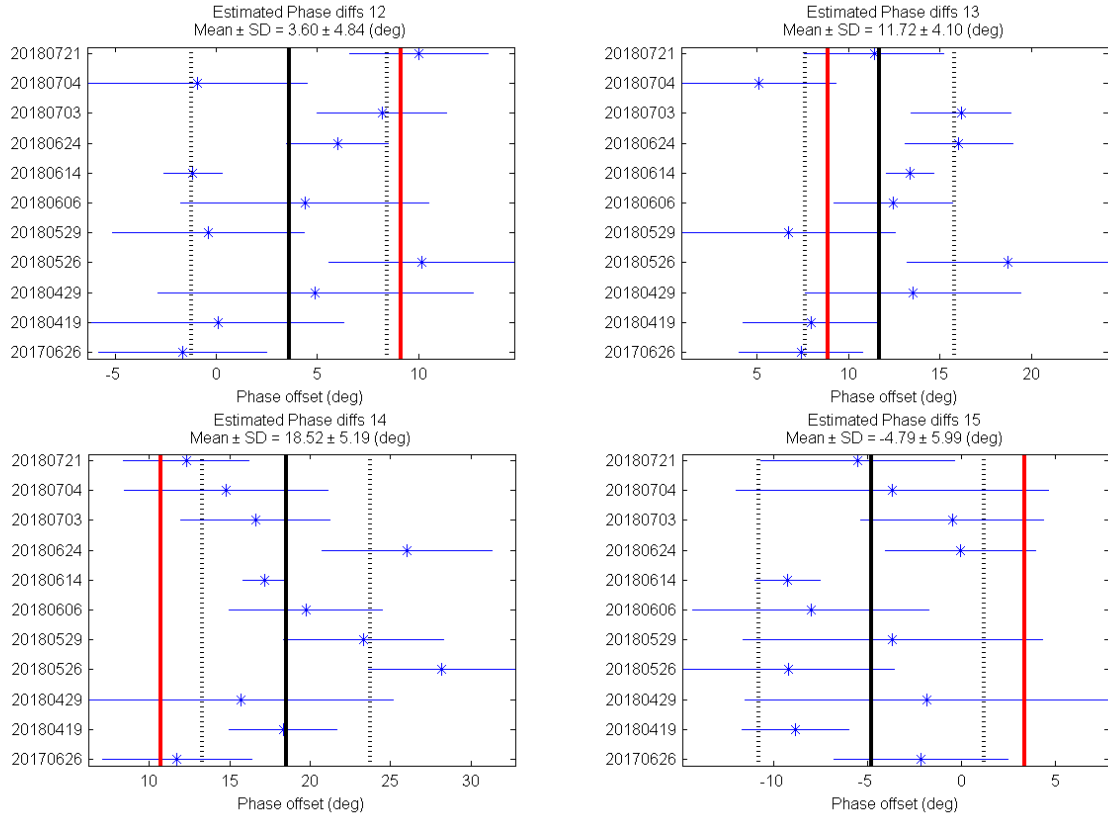


Fig. 5.1: BP meteor radar phase calibration results collected over 11 transits of the International Space Station (based on work performed in Holdsworth et al. [2020]). Individual phase calibration estimates are shown in blue asterisks, with 1-sigma standard deviation of the phase shown as error bars (blue lines). Mean calibration estimates over the 11 transits are shown as vertical black lines, with results from the empirical method of Holdsworth et al. [2004b] shown as vertical red lines. Dates of the transits are shown on the  $y$ -axes. Figure prepared by D. A. Holdsworth, Sep 2018.

They obtained consistent phase offset estimates across several dozen transits (with typical 1-sigma errors in each estimate of  $\sim 5^\circ$ ), and also evidence of a drift in those offsets of several degrees between summer and winter (which they attributed to temperature changes at the site). They conducted their analyses on an aircraft flying on a fixed flight path with respect to the radar, over 2-second intervals in which the aircraft was closest to the radar (which was at an angle close to the radar zenith). Obtaining offsets over a larger range of AOAs may have been possible, but given the beam's small width this was not necessary.

In contrast, the recent study of Lin et al. [2019] made use of GPS-tracked aircraft to phase-calibrate the Chung-Li radar. As in the Chen et al. [2002] study, they made use of several dozen aircraft transits through the beam centre across different seasons,

and obtained consistent estimates across all transits for given receiver pairs (with typical 1-sigma errors in the range of 1-4°, and a variability of several degrees between summer and winter). Their aircraft-based results were also consistent with those derived from echoes from a GPS-equipped drone flown through the beam centre. Curiously, there were notable discrepancies between both of these results and those derived from field-aligned irregularities, which the authors attributed to a non-uniform distribution of scatter within the beam in the latter. Additionally, this further illustrated the need to use long integration times when obtaining calibration estimates from field-aligned irregularities.

We envisioned that an aircraft-based phase calibration approach would offer the following advantages relative to the alternatives in the studies discussed above:

1. Assuming the aircraft position and timing information is correct, phase correction estimates at a given position would be “exact”.
2. The correction estimates should compensate for any source of phase estimation error in the receive chain (whether they be in the receiver units, antenna cables, or the antennas themselves), at any location where there are echoes from aircraft.
3. Setting up an Automatic Dependent Surveillance-Broadcast (ADS-B) receiver station and/or getting access to aircraft position information from a third-party would be straightforward and low-cost.
4. Routine phase calibration estimates would be able to be produced without any need for human intervention.

As well as the general need to improve the meteor detection rates at BP and Mylor for momentum flux studies, giving us further impetus to evaluating the effectiveness of the aircraft-based approach on the BP and Mylor meteor radars were the following factors:

1. The absence of any pre-existing application of an aircraft-based phase calibration to meteor radar systems.
2. The abundance of aircraft echoes in the lower range gates of the BP and Mylor radars.
3. Our suspicion of the quality of (and therefore the need to validate) the previously obtained phase calibration results from the empirical approach of Holdsworth et al. [2004b] on the Mylor system (see Fig. 4.3).

Furthermore, it was clear that there was an opportunity to build on the approach of Chen et al. [2002] by incorporating AOA-dependent phase correction information in the calibration (as well as that of Lin et al. [2019], although this was published after the completion of the present work). The large diversity in aircraft flight paths in the Adelaide area also meant our radar link was ideally positioned to carry this out.

The following sections give a detailed description of the technique that was developed.

## 5.2 Overview of aircraft-based phase calibration approach

The phase calibration approach employed in this Chapter uses aircraft position information derived from a transponder to phase-calibrate a meteor radar that receives echoes from those aircraft. A schematic of the approach and its geometry is shown in Fig. 5.2. The basic procedure used, which is discussed in detail in the sections that follow, is:

1. Run a meteor radar in its standard meteor detection mode, ensuring the raw IP and Q signals at the desired PRF from all channels and range gates are recorded.
2. Archive aircraft locations from an ADS-B receiver located in the vicinity of the radar receiver in question.
3. For each aircraft transit in the vicinity of the radar, search the radar time series for the aircraft echo.
4. If an echo is found, compute the phase differences of the echoes of each receive channel with respect to a given reference channel.
5. Compute the “phase calibration offsets” (the position-dependent differences between the measured phase differences and the ones predicted based on the aircraft’s known location).
6. Apply the phase calibration offsets to meteor echoes recorded by the meteor radar.

## 5.3 Aircraft location retrieval

To facilitate airborne traffic situational awareness, it is becoming increasingly common for civil aircraft to periodically broadcast their positions (derived from GPS) in the form of ADS-B messages using onboard Mode-S transponder systems. The requirements for

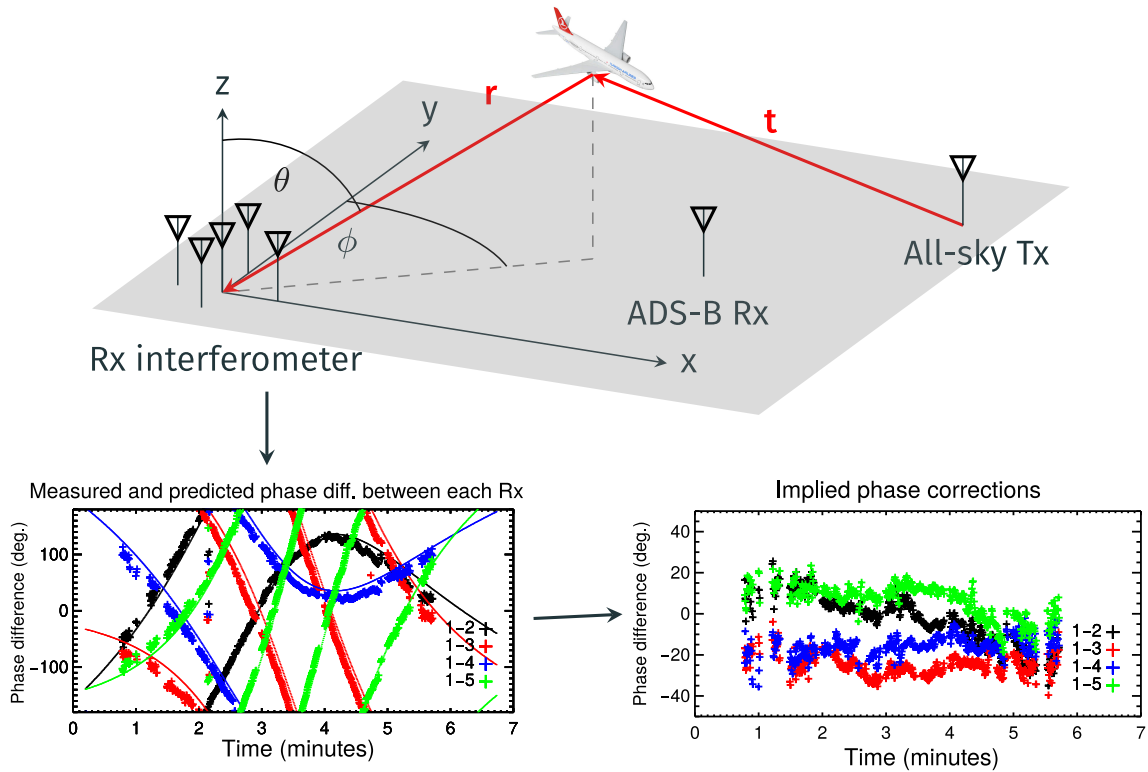


Fig. 5.2: Geometry and basic schematic of the aircraft-based phase calibration approach.



Fig. 5.3: 1090 MHz whip antenna (left) and FlightAware Pro Stick Plus USB SDR Receiver (right) used for reception of ADS-B signals in this study.

ADS-B capability differ depending on the aircraft and airspace under consideration, but for practical purposes it can be assumed that all commercial aircraft flying under Instrument flight rules (IFR) in most parts of the world will have the capability. As a local example, in February 2017 the Australian Government's Civil Aviation Safety Authority (CASA) mandated ADS-B usage in all Australian IFR operations [CASA, 2016].



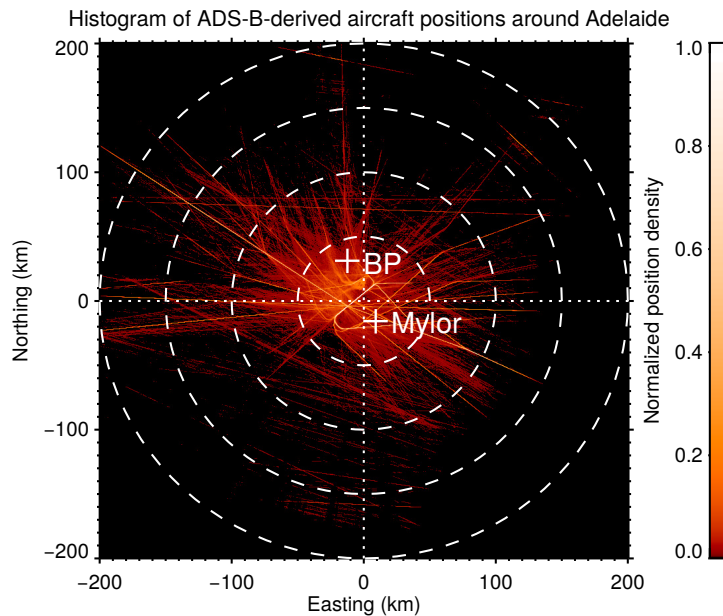


Fig. 5.4: Histogram of aircraft detected around Adelaide between 26-Oct 2019 and 09-Nov 2019 using the ADS-B receiver. Distances are in Transverse Mercator coordinates with respect to the location ( $34.911^{\circ}\text{S}$ ,  $138.663^{\circ}\text{E}$ ). Dashed white circles have been drawn at radius intervals of 50 km. Locations of the meteor radar receivers have been indicated with white crosses.

ADS-B messages are encoded in (typically) 112-bit pulse sequences with a carrier frequency of 1090 MHz. Receiving and interpreting these signals generally requires an antenna capable of receiving at 1090 MHz, and a receiver system to decode the pulse sequence. This is typically done by dedicated ADS-B ground stations, that subsequently relay the position information to air traffic controllers. There are also a large number of hobbyists that set up their own ADS-B ground stations to receive these signals, either for private use or for sharing on flight tracking services such as [FlightRadar24](#) and [FlightAware](#).

Many different products are available to perform the signal reception and decoding. Commercial systems with out-of-the-box functionality typically integrate an antenna and a decoding system into a single unit, and often come bundled with a GPS receiver and a mobile app for real-time display of nearby aircraft (e.g., the [Garmin GDL 52](#)). In the hobbyist/open-source community, there are also many examples of home-made antennas (e.g., on [FlightAware Discussion Forums](#)) and collaborative development of decoding algorithms for use with software-defined radio (SDR) receivers (e.g., the open-source [dump1090 project](#)).

Considering the need for a low-cost solution with the potential of being deployed on

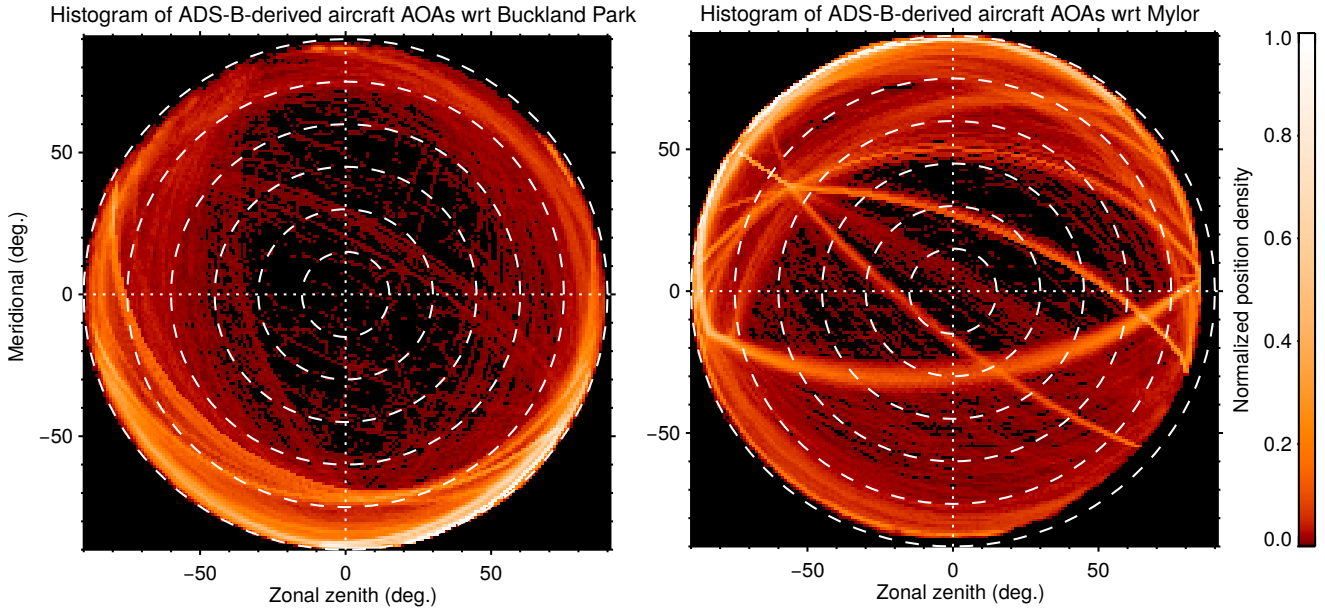


Fig. 5.5: Histogram of the AOAs of aircraft detected around the two meteor radar receiver sites (left: Buckland Park, right: Mylor) between 26-Oct 2019 and 09-Nov 2019 using the ADS-B receiver. Dashed white circles have been drawn at zenith angle intervals of  $15^\circ$ .

multiple radar systems, it was decided to further investigate the use of a cheap 1090 MHz antenna and SDR unit coupled to open-source decoding software. This option was also considered superior to using a pre-existing service such as FlightRadar24, given the potential need for detecting ADS-B messages at the highest time resolution possible (typically 2 Hz), and the possibility that working ADS-B ground stations may not be in the vicinity of the meteor radar in question at all times.

### 5.3.1 Antenna, SDR receiver and signal decoding

In this study, a vertically-mounted [3 dBi 1090 MHz ADS-B whip antenna](#) was used for signal reception, and a [FlightAware Pro Stick Plus USB receiver](#) was used as a SDR receiver (see Fig. 5.3). It was noted during initial trials that this setup was capable of receiving ADS-B signals from aircraft at distances of up to about 200 km. While dedicated ground-based ADS-B stations have been quoted to be able to detect aircraft at distances in excess of 460 km, it was considered that aircraft at distances of greater than about 100 km from the meteor radar receiver would be at too low an elevation angle to be useful for phase calibration purposes. Therefore, this level of performance was deemed adequate.

Signal decoding was performed using the `dump1090-fa` package on a laptop running Debian GNU/Linux 9. By default, this package streamed all decoded ADS-B messages to a network port for real-time display of detected aircraft in a web browser. So as to record the aircraft locations, a script was written to pipe selected parameters (time, latitude, longitude, altitude, speed, and heading) from this port stream to text files with names corresponding to each detected aircraft’s unique 24-bit ICAO<sup>1</sup> hexadecimal identifier.

Since ADS-B messages do not presently contain any timing information, the ADS-B receiver PC needed to use its own clock to time-stamp the messages. To minimise timing errors between the clocks of ADS-B receiver’s PC and the radar’s PC (whose clock was GPS-locked, as mentioned in Sect. 2.3), the ADS-B PC’s clock was synchronized to a Network Time Protocol (NTP) server. To remove residual timing errors arising from a loss of connection to an NTP server or delays in the transmission of ADS-B messages from aircraft, a post-analysis technique based on minimising the discrepancy between radar-derived and ADS-B-predicted radial velocities of each aircraft was developed; see Sect. 5.4.6 for further details.

### 5.3.2 Sample aircraft position distributions

For the main phase calibration work presented in this thesis, the ADS-B antenna was vertically oriented on the roof of a building in the eastern suburbs of Adelaide, at approximately (34.911°S, 138.663°E). Aircraft locations were continuously sampled from this location from about 06:00 UT on 26-Oct 2019 until about 01:00 UT on 09-Nov 2019.

Figure 5.4 shows a histogram of the locations of the aircraft sampled over this period, with respect to the ADS-B ground station location. Some prominent flight paths are visible (for example, those leading toward the Adelaide International Airport about 15 km west of the ground station), as well as a “background” that encompasses most locations within about 50 km of the ground station. The farthest returns are seen to be in excess of about 200 km, with a notably higher maximum range to the west than east; this is due to the presence of the hills east of Adelaide preventing the receipt of ADS-B messages below a few degrees elevation.

The angular position of the aircraft with respect to the meteor radar receiver sites at Buckland Park and Mylor are shown in Fig. 5.5. It is clear that the Buckland Park site has full azimuthal coverage above zenith angles of about 70°, and fairly complete

---

<sup>1</sup>International Civil Aviation Organization.

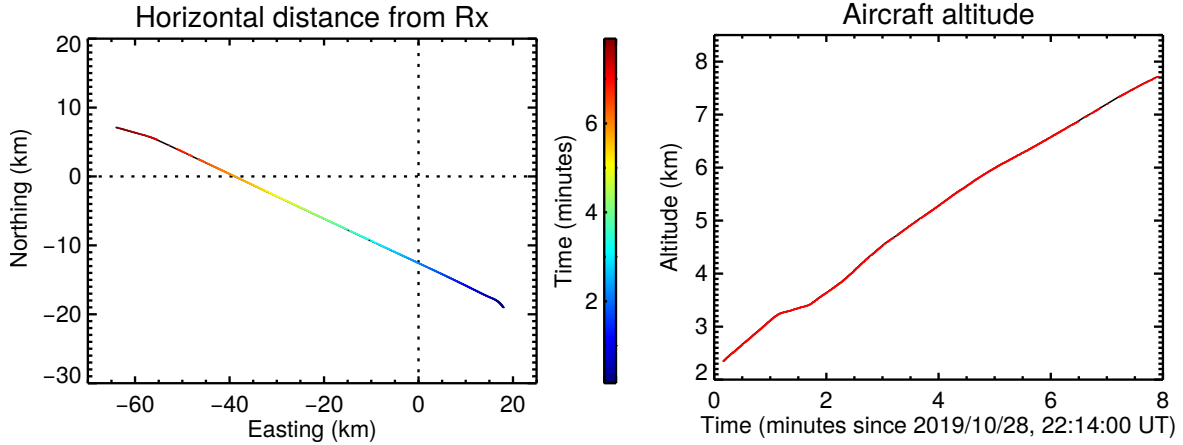


Fig. 5.6: A sequence of ADS-B-measured (coloured dots) and interpolated (solid black line) horizontal positions (left) and altitudes (right) from a sample aircraft. Note the momentary losses of contact with the aircraft, especially after about 6 minutes into the sample.

coverage above  $60^\circ$  except in the north-western quadrant. The Mylor site has a slightly more uniformly distributed coverage, albeit with some maxima around several narrow flight corridors and a pronounced minimum in detections to the north and north-east in the zenith angle ranges  $30\text{-}45^\circ$ . As an overarching comment, considering that meteor detections are expected to mostly occur in zenith angle ranges  $50\text{-}75^\circ$ , the aircraft detections at both sites are expected to provide an adequately filled-in position distribution for the phase calibration.

## 5.4 Phase correction estimation scheme

This section discusses the steps performed in time and range-aligning aircraft detection time series and aircraft echoes from meteor radar data, and the subsequent estimation of phase calibration offsets. The procedure developed attempts to generate phase calibration offsets for each ADS-B-detected aircraft over a prescribed time interval, and the following subsections pertain to the processing associated each with aircraft. Where appropriate, examples are provided of a sample aircraft detection made with the Buckland Park meteor radar.

### 5.4.1 Selection of “candidate” aircraft transits

The procedure firstly searches for “continuous” segments of aircraft detections. “Continuous” segments are denoted by a sequence of more than 10 positions that have a maxi-

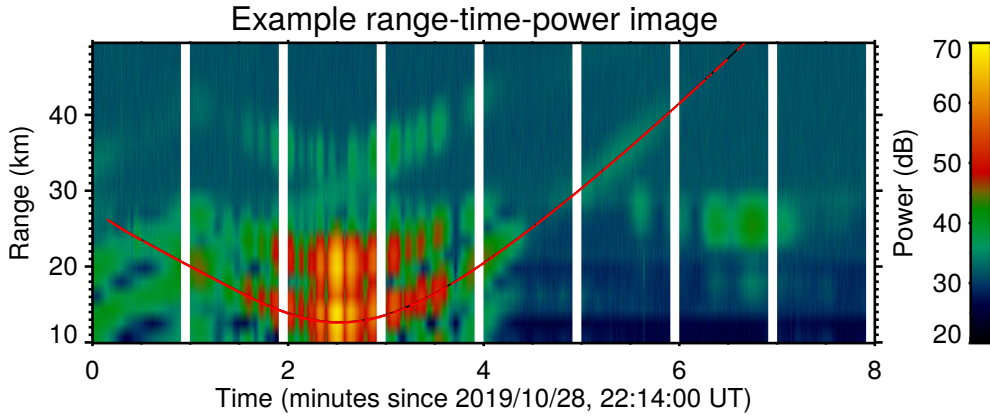


Fig. 5.7: The incoherently averaged (across all meteor radar receivers) power from the aircraft in Fig. 5.6. The predicted range (based on the ADS-B messages) is shown as red dots, with interpolated ranges shown as a solid black line.

imum time gap of no more than two minutes. Any such segment with less than 10 points is not considered for further analysis, and segments with a maximum gap of greater than two minutes are split and processed separately. These criteria were put in place so as to avoid excessive amounts of interpolation in estimating aircraft positions (i.e. zenith and azimuth with respect to the meteor radar) at a specific time (see Sect. 5.4.2).

Positions within a “continuous segment” are considered for further processing if they are at zenith angles with respect to the meteor radar receiver of less than  $85^\circ$ . This criterion was put in place because there was little interest in the nature of the phase calibration offsets this close to the horizon. Aircraft below altitudes of 100 metres above sea level (i.e., taxiing or in the process of taking off or landing) were also excluded.

### 5.4.2 Interpolation of aircraft positions

Computation of phase correction estimates is done over time windows of a fixed length of 2 seconds, with a spacing between adjacent windows of 1 second (i.e., a 50% oversampling) (herein referred to as a “processing interval”). The ADS-B-derived aircraft positions have an inconsistent sampling rate, and so interpolation of them to these time windows is required. Accordingly, the transverse mercator (easting and northing) distances of the aircraft from the receiver and the aircraft altitudes are linearly interpolated to the window times. Figure 5.6 shows the measured and interpolated positions for an example aircraft detection, and the occasional need to interpolate over substantial gaps in the position measurements.

Clearly, the accuracy of the linearly interpolated aircraft positions and altitudes is

compromised if the aircraft accelerates or performs a manoeuvre between any two received ADS-B messages. The criterion for a minimum of 10 points in any given two minute period discussed in Sect. 5.4.1 reduces the severity of the errors arising from this in the data processed further. Once that criterion had been put in place, no cases were noted in which the gap between subsequent ADS-B messages of aircraft close to the zenith of the radar receiver was more than a few seconds. As a result, no scheme has been put in place to flag evidence of aircraft manoeuvres that would significantly affect the accuracy of the measured phase correction terms.

### 5.4.3 Extraction of aircraft echoes from the radar data

Once the aircraft positions are interpolated to the desired times, for each 2-second processing interval the radar time series corresponding to each time at the two range gates on either side of the one nearest to the expected aircraft range are extracted. The signals from all receiver channels at each range gate are incoherently combined, and the mean power at each range gate is computed from the combined time series. The time series at the range with the highest power is then extracted for subsequent processing. Figure 5.7 shows an example of the incoherently combined signal powers as a function of time and range for the same aircraft transit as in Fig. 5.6, with the expected (interpolated) range of the aircraft overlaid.

A rudimentary attempt to remove range-independent sources of interference is also made in this part of the processing. If the incoherently combined power is seen to vary by less than some threshold over the five range gates considered here, that time window is precluded from subsequent processing. Through experimentation, the threshold deemed most appropriate for this purpose was 3 dB.

### 5.4.4 Parameter estimation

Following the extraction of radar data that presumably contains a signature of the target aircraft, the phase differences selected channel pairs, channel-averaged Doppler velocities, and SNR for each channel are estimated. This procedure is performed for each 2-second processing interval.

The approaches for the phase difference and Doppler velocity estimates largely follow those outlined in Sect. 2.5 for meteor echoes. To estimate the phase difference for a given receiver pair, a linear fit is performed to the CCF phase across lags  $\pm 1$  and  $\pm 2$ , with the result at lag 0 extracted. As with meteor echoes, 0-lag interpolation is

performed to remove the effects of noise correlated between receiver channels from the phase difference estimate. Likewise for the Doppler velocity estimate, the CCFs are summed over all possible receiver combinations, and then a least-squares linear fit to the phase of the result across lags  $\pm 1$  and  $\pm 2$  is performed.

The SNR for a given channel is found by computing the signal's autocovariance function at lags  $[-2, -1, 0, 1, 2]$ , and then calculating the ratio of the signal and noise components of the autocovariance at lag 0. Mathematically, this can be represented as:

$$\text{SNR} = \frac{K'_{ii}(0)}{K_{ii}(0) - K'_{ii}(0)},$$

where  $K_{ii}(\tau)$  indicates the autocovariance at lag  $\tau$ , and a prime indicates a value that has been interpolated across lags  $\pm 1$  and  $\pm 2$ .

### 5.4.5 Phase correction estimation

The phase corrections estimated correspond to the difference between the measured phase differences for the  $i$ th receiver pair  $\chi'_i$ , and those predicted based on the aircraft location. The predicted phase differences are calculated using the differences in path length between the aircraft and the receiver elements under consideration. In turn, the path lengths are calculated from the difference in the ECEF coordinates of the aircraft and a given receiver antenna (the coordinates are calculated through a transformation of the corresponding latitude and longitude data using the procedures outlined in App. B). The expression for the predicted phases corresponding to a given antenna pair  $i$  is:

$$\chi_i = \frac{2\pi}{\lambda} (|\mathbf{a} - \mathbf{x}_j| - |\mathbf{a} - \mathbf{x}_k|), \quad (5.1)$$

where  $\mathbf{a}$  is a vector containing the ECEF coordinates of the aircraft, and  $\mathbf{x}_j$  and  $\mathbf{x}_k$  are the vectors in ECEF coordinates of the two antennas constituting pair  $i$ . It should be noted that this assumes the radio wave travels along a direct line of sight between the antenna and the receiver (i.e., that no refraction/scattering of the radio wave occurs).

The correction term for pair  $i$  is then given by:

$$\alpha_i = \chi'_i - \chi_i, \quad (5.2)$$

i.e.,  $\chi'_i \rightarrow \chi'_i - \alpha_i$  through application of the correction.

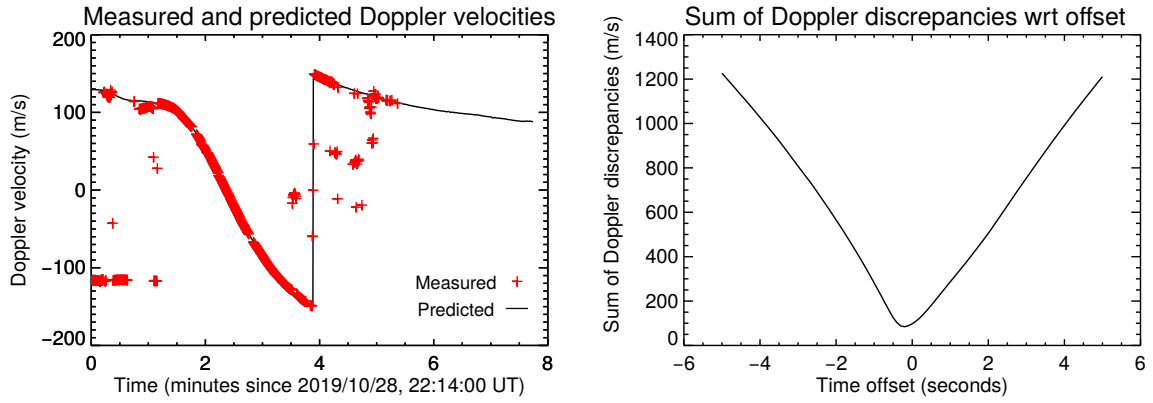


Fig. 5.8: An example of the process of determining the time offset between the ADS-B receiver PC and the aircraft time stamps. A comparison of the measured and predicted Doppler velocities in the left panel, along with the sum of the discrepancies between these quantities as a function of time offset in the right panel (which minimizes at an offset of  $\sim 0.2$  s).

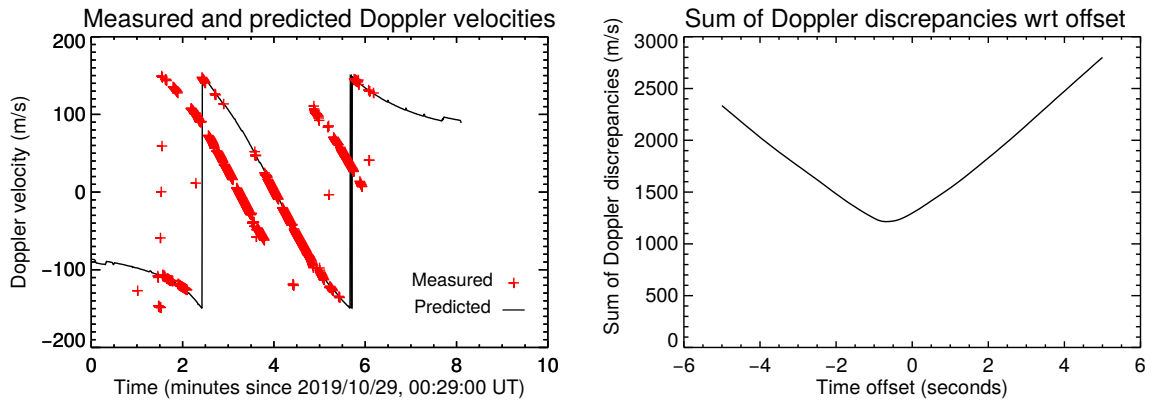


Fig. 5.9: As per Fig. 5.8, but with the presence of multiple range-coincident aircraft echoes. The time offset of minimum discrepancy in this case is  $\sim 0.7$  s.

#### 5.4.6 Removal of possible aircraft timing errors

As discussed in Sect. 5.3.1, offsets between times reported by the ADS-B receiver PC and those that the aircraft ADS-B messages pertain to may result in significant errors in the phase correction estimates, especially when the aircraft is close to the receiver's zenith. A post-analysis technique based on minimizing the discrepancy between the radar-derived and ADS-B-predicted Doppler velocities has been devised to overcome this issue. It should be noted that the approach we have used here is similar to the time synchronization method developed in Lin et al. [2019], which was published after the completion of this work. We additionally note that Chen et al. [2002] made use of aircraft radial velocities to align their radar and aircraft video camera time series,



although did not use an error minimization scheme as used here and by Lin et al. [2019].

To produce the ADS-B-predicted Doppler velocities, absolute velocities are firstly computed by time-differentiating the ECEF (see App. B) coordinates of the aircraft. This is done using a three-point Lagrangian interpolation algorithm, so as to get an estimate of the derivative at each position estimate. In order to reduce the noise in these estimates, the result is also smoothed using a boxcar averaging with a width corresponding to 1/10 of the number of interpolated aircraft positions available.

Following the approach for forward scatter meteors in Sect. 2.2.3, predicted Doppler velocities are then computed using the equation:

$$v_{rp} = (\mathbf{v} \cdot \mathbf{b}) \cdot \hat{\mathbf{r}}, \quad (5.3)$$

where  $\mathbf{v}$  is the 3-dimensional velocity in ECEF coordinates, and as per Fig. 2.2,  $\hat{\mathbf{r}}$  is a unit vector in the direction of the receiver from the aircraft, and  $\mathbf{b}$  is a unit vector bisecting the aircraft-receiver and aircraft-transmitter vectors. An example of the measured and predicted Doppler velocities for the same aircraft as in Figs. 5.6 and 5.7 are shown in the left panel of Fig. 5.8.

The discrepancy minimization works by recomputing the interpolated positions and predicted velocities across a grid of time offsets, and finding the time offset at which the sum of the absolute difference between the predicted and measured Doppler velocities minimizes. Mathematically, this can be expressed as:

$$\arg \min_{\tau} \sum_t (|v_r(t) - v_{rp}(t - \tau)|), \text{ subject to } \tau \in \mathbb{R}, \quad (5.4)$$

where  $v_r$  is the measured Doppler velocity, and  $\tau$  is the applied offset. An example of the discrepancies as a function of  $\tau$  are shown in the right panel of Fig. 5.8; in this example the minimum discrepancy occurs at  $\tau \approx -0.2$  s.

The evaluated discrepancies can be erroneously large if there are range-coincident echoes from other aircraft present during the transit of the tracked aircraft. Such an example is shown in the left panel of Fig. 5.9, in which incorrect velocities at certain times are apparent. To reduce the effect of these on the discrepancy summation, only those points with a discrepancy lower than the median discrepancy at any given offset are ever included in the summation. The drawbacks of this approach are the preclusion of “good” points in the case of no anomalous aircraft echoes, and the inclusion of anomalous Doppler velocities in the case where echoes from other aircraft are predominant. An adaptive approach that compensates for the number of likely velocities from the other aircraft would have been favourable, but was not deemed necessary.

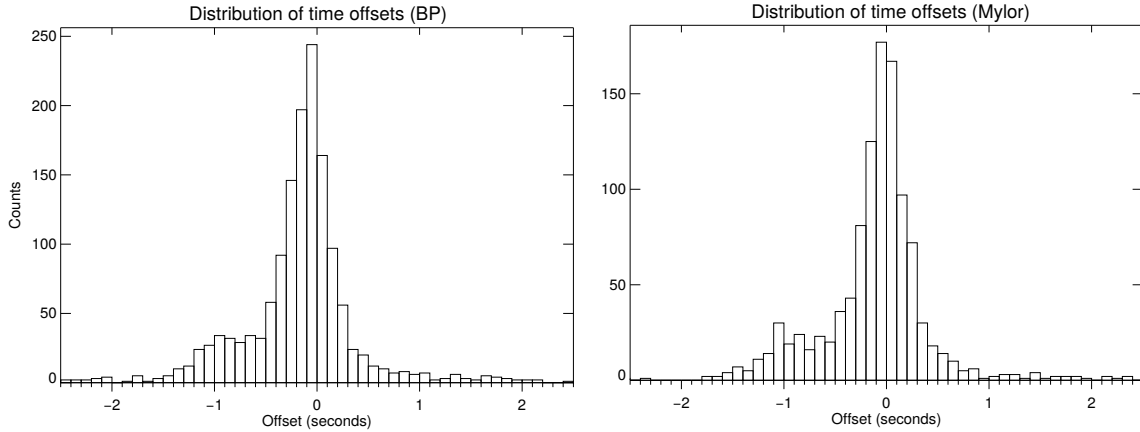


Fig. 5.10: Distribution of offsets applied to the ADS-B receiver PC time stamps, based on minimizing the discrepancies between measured and predicted Doppler velocities. Results for BP are shown in the left panel, and Mylor in the right.

Histograms of the estimated time offsets for all aircraft returns collected from the BP and Mylor receivers are shown in Fig. 5.10. These have been applied in all subsequently presented phase correction estimates. The BP distribution has a mean and standard deviation of  $\sim -0.24$  and  $0.76$  s respectively, with  $\sim -0.17$  and  $0.67$  s respectively for the Mylor distribution. The fact that the estimated time offsets are in the order of a few seconds provides confidence that any residual time offsets could not be expected to be more than a few seconds. Such offsets would have a minimal effect on the phase correction distributions presented in subsequent sections.

### 5.4.7 Processing applied to phase correction estimates

Despite the data processing performed in previous steps (i.e., zenith and altitude cut-offs, attempts to remove range-independent interference, minimization of errors arising from mis-interpolating aircraft positions, and estimating and removing any possible time offsets), a number of obvious outliers/defects were evident in the obtained phase corrections.

The majority of the defects were surmised to be due to multiple range-coincident aircraft echoes at certain times. In this work, an attempt to filter out such echoes was made by comparing the measured and predicted Doppler velocities, and removing points with a threshold discrepancy of  $2 \text{ ms}^{-1}$ . This threshold was deemed large enough to generally remove clearly contaminated echoes, but not so large as to remove points that had velocity errors brought about by noise or minor position mis-interpolations. It should also be noted that this approach also has the ability to remove segments of

transits containing interferers and ground wave effects (see Fig. 5.15).

There are of course cases in which multiple aircraft would have similar Doppler velocities but be at different AOAs (possibly for large segments of a transit). In this case, the algorithm used here would still accept that data for further analysis. In manually inspecting a large number of range-time-power plots of aircraft echoes received at BP and Mylor, the few cases evidencing this were not deemed to have a large impact on the phase correction distributions presented in the subsequent section. However, it should be stressed that this may not be the case for sites with denser air traffic.

In an attempt to remove some of the outliers that remained after this filtering, an iterative outlier removal procedure was implemented. This procedure fits planes to the phase correction distribution of the form:

$$P(\Theta_x, \Theta_y) = A\Theta_x + B\Theta_y + C, \quad (5.5)$$

where  $A$ ,  $B$  and  $C$  are the fit parameters, and  $\Theta_x$  and  $\Theta_y$  are the  $x$  and  $y$  direction cosines, respectively. In this work, any phases which differ from the plane by more than  $5 \times 1.4826 \times \text{MAD}$  are removed from the distribution prior to subsequent processing (note that MAD is the median absolute deviation of the distribution, and 1.4826 is a scaling factor to convert a median absolute deviation to a standard deviation, assuming the input has a Gaussian distribution). This procedure is repeated until no more outliers remain.

## 5.5 Example aircraft phase calibration candidates

This section shows seven example aircraft candidates used in the phase calibration procedure on BP and Mylor meteor radar data. The examples cover a broad range of cases, including ones in which deriving phase correction estimates was straightforward, and others in which challenges were encountered such as range-coincident aircraft echoes, interference between the ground pulse and the aircraft echo, oscillatory phase corrections, and problems in the interpretation of high zenith angle echoes. Shown in each case is a range-time-power plot of the aircraft echo, the aircraft horizontal and vertical position, the aircraft zenith angle, the measured and predicted phase difference and the implied phase corrections, the aircraft SNR, and the measured and predicted Doppler velocities associated with aircraft echo.

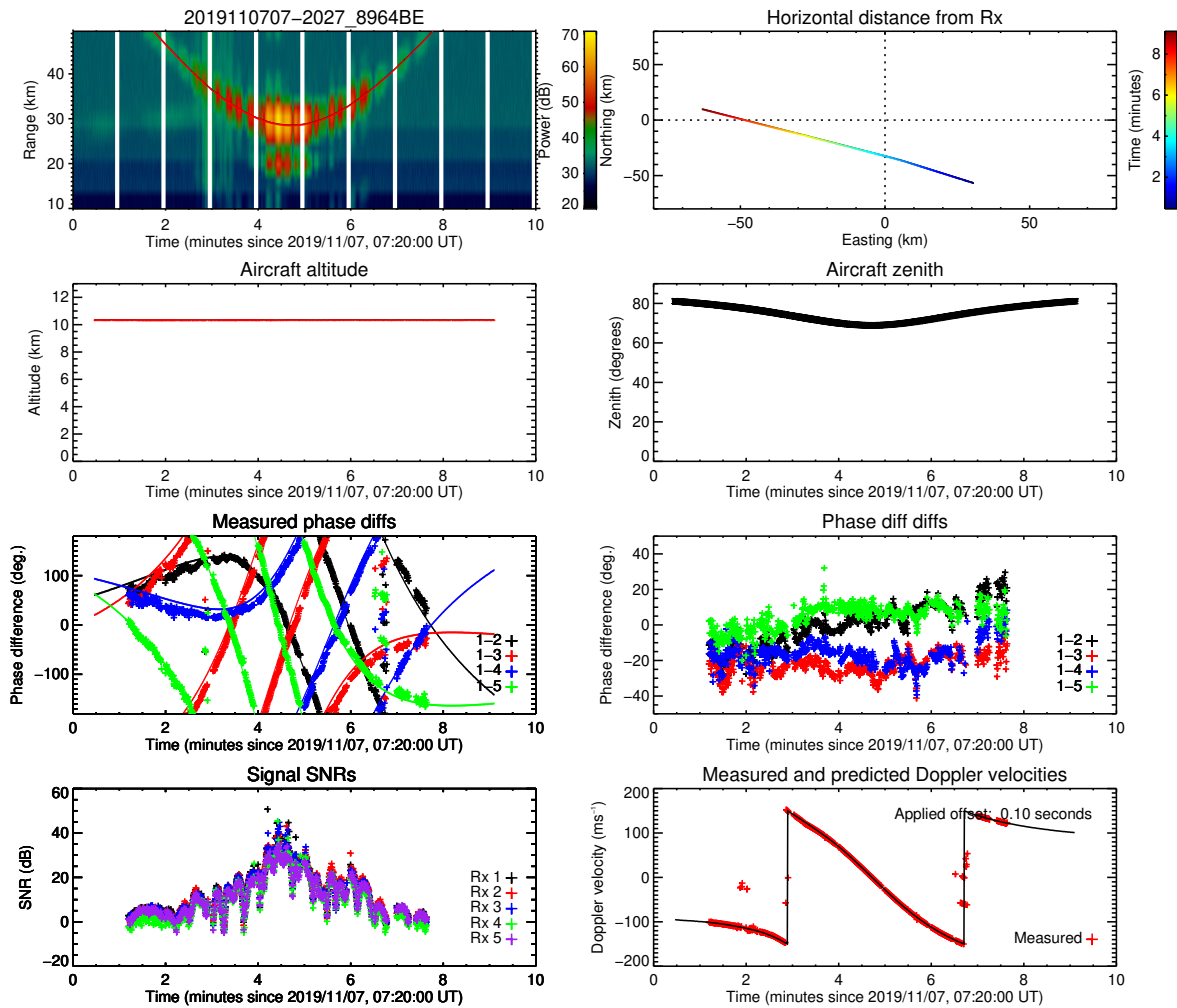


Fig. 5.11: An example of a “good” phase calibration candidate detected with the BP receiver (Case 1).

### Case 1: “Good” candidate at the BP receiver

Figure 5.11 consists of an aircraft at an altitude of just over 10 km, travelling in a south-easterly direction and passing to the south-west of the BP receiver. While there is a characteristic “beating” in the returned power (presumably caused by multiple scattering points off the aircraft body interfering as a result of orientation changes with respect to the receiver), the SNR is consistently high enough to estimate phase offsets that vary smoothly as a function of position.

The estimated Doppler velocities also generally agree well with the predicted in this example, except around the times when the velocity is aliased.

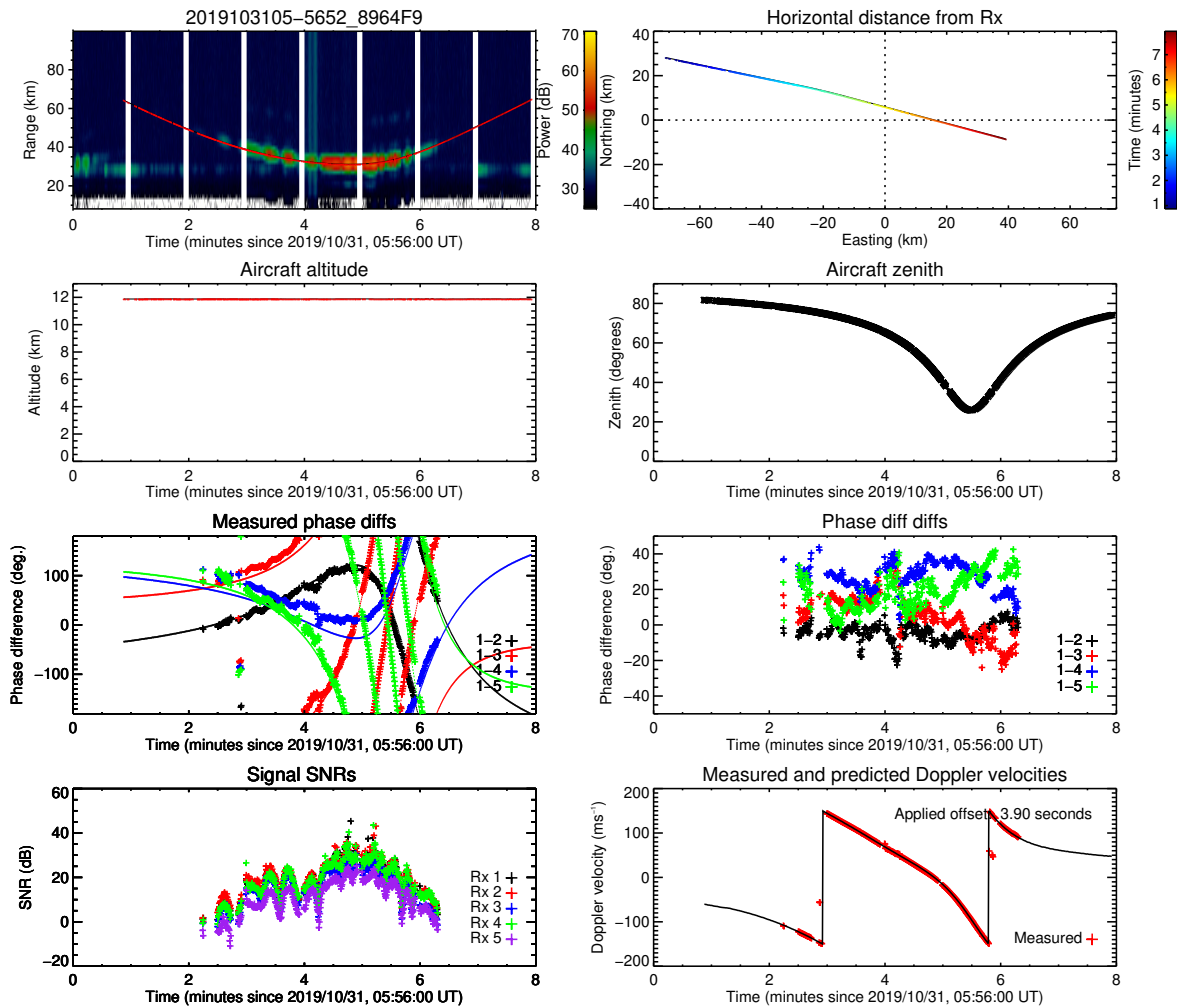


Fig. 5.12: An example of a “good” phase calibration candidate detected with the Mylor receiver (Case 2).

### Case 2: “Good” candidate at the Mylor receiver

In the Fig. 5.12 example, an aircraft is at an altitude of about 12 km, flying in a south-easterly direction to the north of the Mylor receiver. At closest approach it is approximately 8 km from the receiver, and as a result reaches a minimum zenith angle of about  $25^\circ$ . Aside from being affected by some range-independent interference about 4 minutes into the sample, the implied phase corrections again vary smoothly as a function of position, and there is excellent agreement between the measured and predicted Doppler velocities.

It is also worth noting the “drift” in the implied corrections for all receiver pairs after about 5 minutes into the sample. As shown in Fig. 5.19, these features are consistent across a number of aircraft at this position for the Mylor receiver. We expect that the variability is brought about by changes in the phase response of the array, rather than

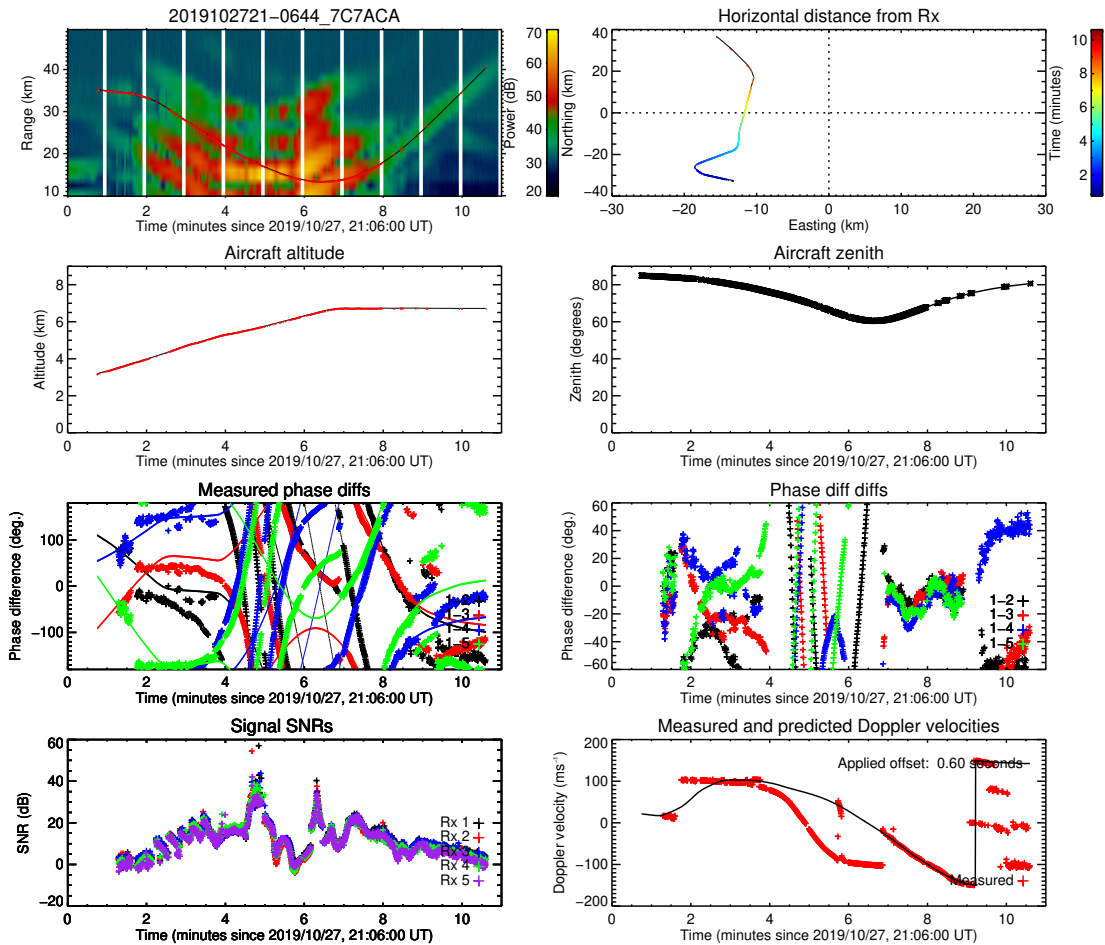


Fig. 5.13: An example of a transit at BP contaminated by multiple range-coincident aircraft (Case 3).

errors in the assumed aircraft position.

### Case 3: Range-coincident echoes at BP

Figure 5.13 shows an example from BP in which multiple range-coincident aircraft are present in the returned echoes. It is clear that between roughly minutes 4 and 7 of the sample, the implied phase corrections vary erratically as a result of the wrong aircraft being tracked. Unsurprisingly, there is also a substantial discrepancy between the measured and predicted Doppler velocities at these times. It is likely that the algorithm “locks on” to the correct aircraft again from minutes 7-9, given the relative stability of the phase corrections and good agreement between the velocities. It is not clear if the correct aircraft is being tracked between minutes 2 and 4.

This example serves to illustrate some of the erroneous phase correction estimates which may have remained after the Doppler velocity filtering. It is expected that the

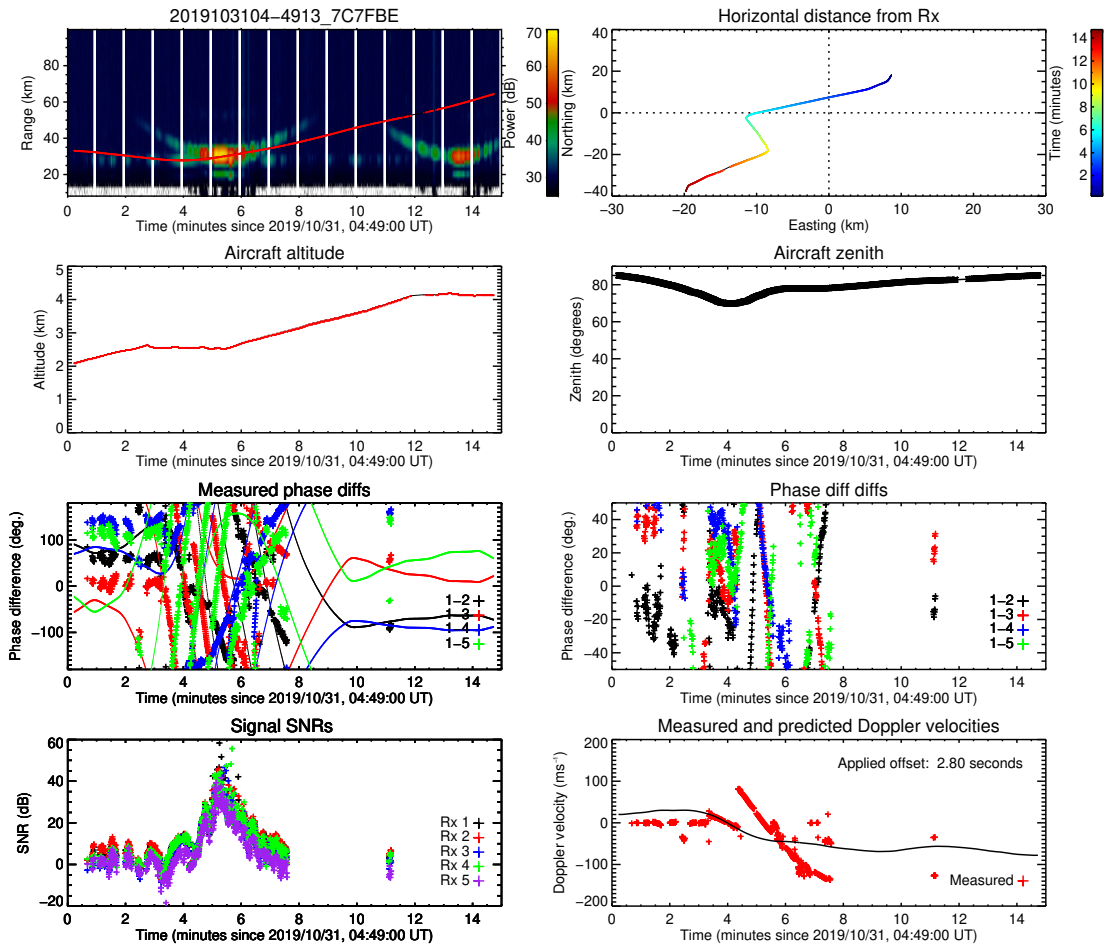


Fig. 5.14: An example of a transit at Mylor contaminated by multiple range-coincident aircraft (Case 4).

iterative outlier removal procedure also discussed in Sect. 5.4.7 would have removed at least some of these.

#### Case 4: Range-coincident echoes at Mylor

In Fig. 5.14, an example from the Mylor receiver is shown in which multiple range-coincident aircraft are present. The contamination is more severe than in Case 3, because the contaminating aircraft has a considerably stronger echo than the one being tracked. There is only a short segment between minutes 3 and 5 for which it appears that the return is predominantly from the tracked aircraft; during this segment, there is reasonable agreement between the measured and predicted Doppler velocities, and the phase corrections are reasonably stable.

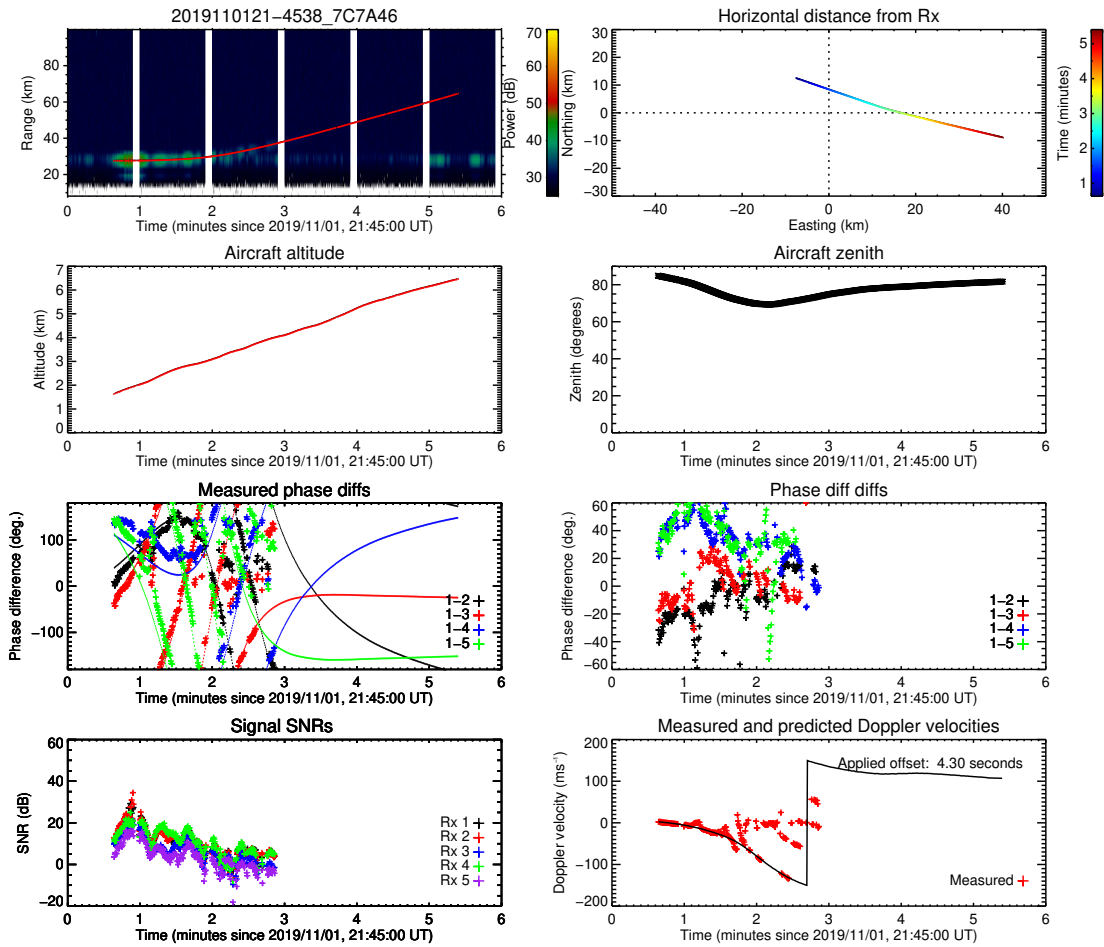


Fig. 5.15: An example of coincident ground wave and aircraft echo, as measured using the Mylor receiver (Case 5).

### Case 5: Coincidence of the ground wave and the aircraft echo

This example consists of an aircraft ascending out of the Adelaide area (from about 1.5 to 6.5 km altitude), travelling in a south-easterly direction to the north of the Mylor receiver. Because of its low altitude and the fact that it flies close to the line of sight between the Mylor receiver and the transmitter at BP, some of the aircraft echo is range-coincident with the ground wave (most notably the part between 1 and 2 minutes after the start time). For reasons that have not been investigated, the ground wave fluctuates in amplitude over a time scale of minutes, and at times becomes comparable to the aircraft echo amplitude. This manifests as erratically-varying phase corrections and measured Doppler velocities as a function of time.

As described in Sect. 5.4.7, phase correction estimates that correspond to erroneous measured Doppler velocities (differing to those predicted by  $> 2 \text{ ms}^{-1}$ ) are not included in any further processing. Aside from the rare cases in which the true Doppler velocities



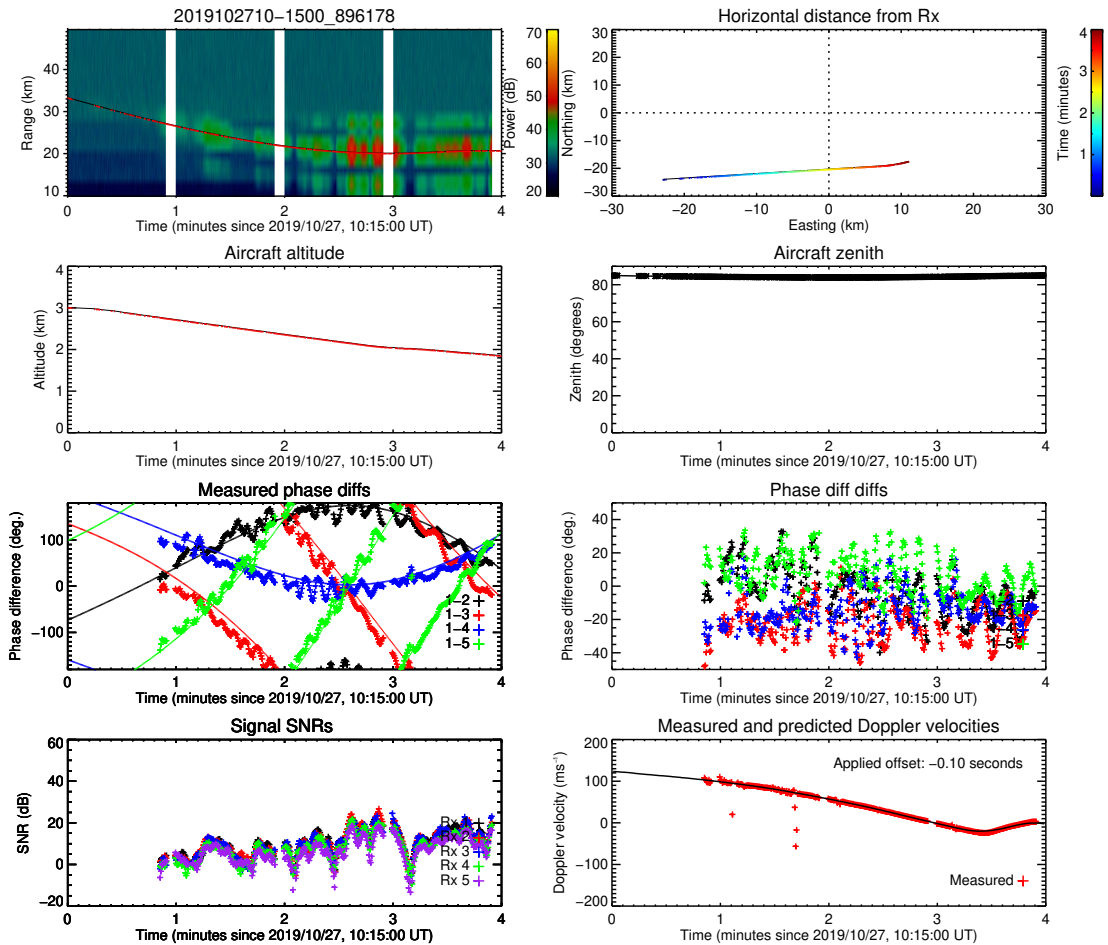


Fig. 5.16: An example of oscillatory receiver phase offsets measured with the BP receiver (Case 6).

are close to zero (as the ground wave generally has zero Doppler), the effect of these contaminated points has largely been mitigated. As mentioned earlier, those remaining points were also subject to an iterative outlier removal procedure, which would have further reduced their impact on the subsequently produced interpolated corrections.

### Case 6: Oscillatory phase offsets

This example considers a low altitude (2-3 km) aircraft travelling west, to the south of the BP receiver (approximately 20 km away at its closest approach). While there is generally good agreement between the measured and predicted Doppler velocities, substantial sinusoidal-like oscillations can be seen in the measured phase differences. The net effect of these is to increase the error in the derived phase corrections.

The source of these has not been determined. As the position distribution for BP in Fig. 5.18 shows, oscillations of this kind are present in many of the returns to the south

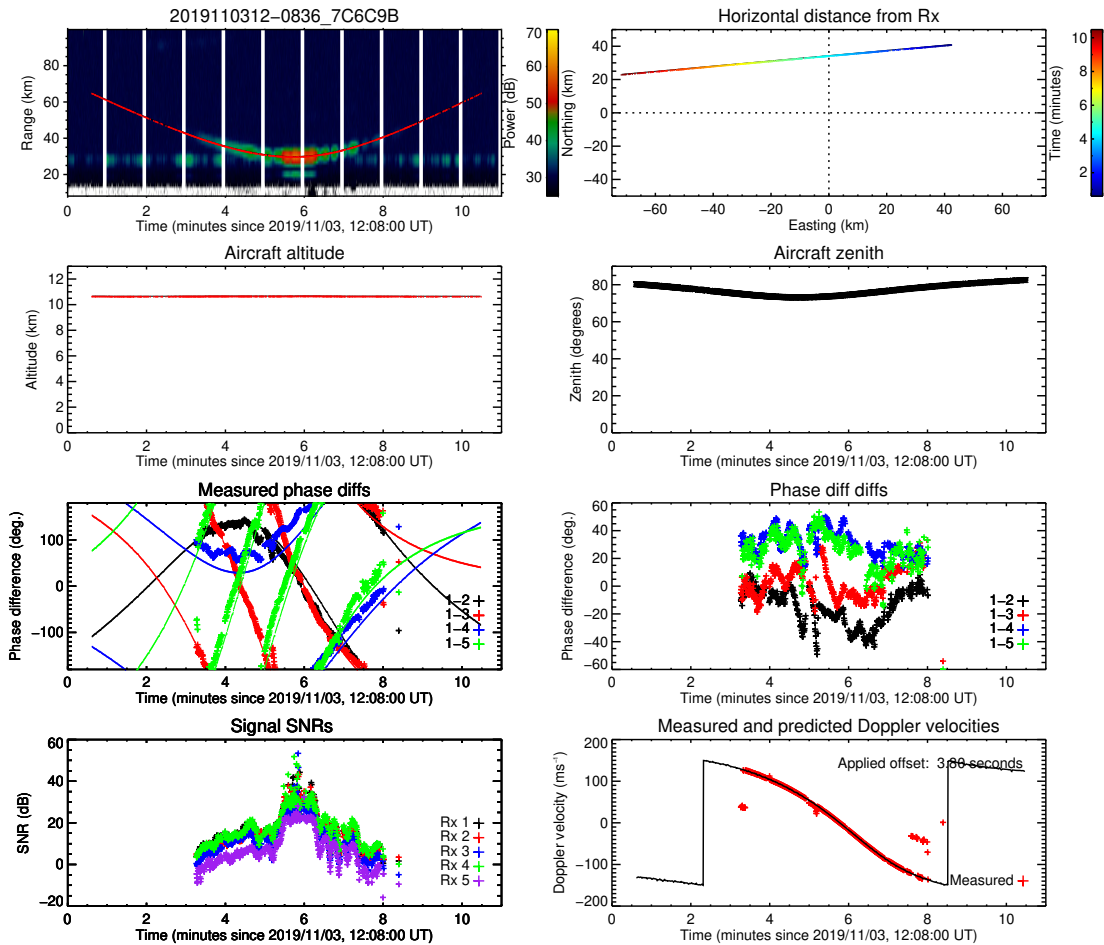


Fig. 5.17: An example of large phase offset deviations measured by the Mylor receiver, corresponding to AOAs in the northern part of the sky (Case 7).

of the receiver, as well as in apparently lower spatial frequency fluctuations to the east. It should be noted that their effect on the phase calibrated results is minimized through the interpolation procedure discussed in Sect. 5.7 largely averaging over them (see Fig. 5.20). This assumes the mean value of the oscillations is correct, which at present is unknown.

### Case 7: High zenith angle phase offsets at Mylor

In this case, an example of the characteristically large phase offsets measured at high-zenith northern AOAs by the Mylor receiver is shown. The aircraft tracked travelled in a south-westerly direction to the north of the Mylor site ( $\sim 30$  km away when it was due north) at an altitude of just under 11 km, and reached a minimum zenith angle of  $\sim 70^\circ$ . Aside from a temporary loss of the aircraft echo just after 5 minutes into the sample, the implied phase corrections vary smoothly with position, but are quite large

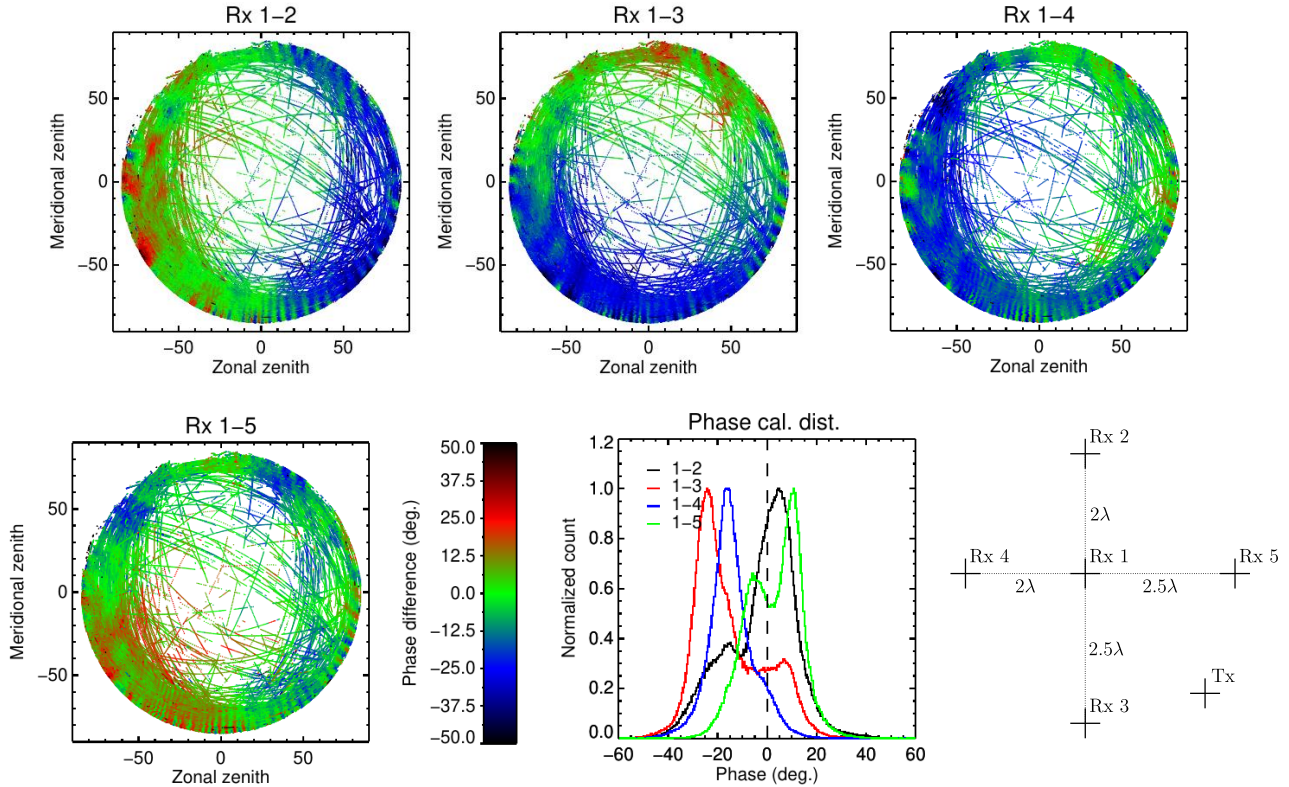


Fig. 5.18: Results from the phase calibration of the meteor radar receiver at BP.

(with absolute values up to  $\sim 50^\circ$  for receiver pairs 1-2, 1-4, and 1-5). The absolute value of the corrections substantially reduces after about 7 minutes into the sample, corresponding to the aircraft moving toward the west-north-west of Mylor. As shown in Fig. 5.18, this result is consistent across many aircraft tracked in this region.

The reason for the large offsets in this region and their rapid variability with position has not been determined.

## 5.6 Phase correction estimates

Between 26-Oct 2019 and 04-Nov 2019, a total of 2,204 aircraft transits and associated radar echoes were processed using the meteor radar at BP, and a total of 1,576 from the Mylor system. The implied phase corrections for each receiver pair with respect to the centre antenna as a function of position for the two sites, along with a histogram of the corrections are shown in Figs. 5.18 and 5.19, respectively. Taken as a whole, these results indicate a need to incorporate phase corrections as a function of AOA, rather than just a single value applicable to all AOAs (which for example might be taken to be the mean of the histograms shown).

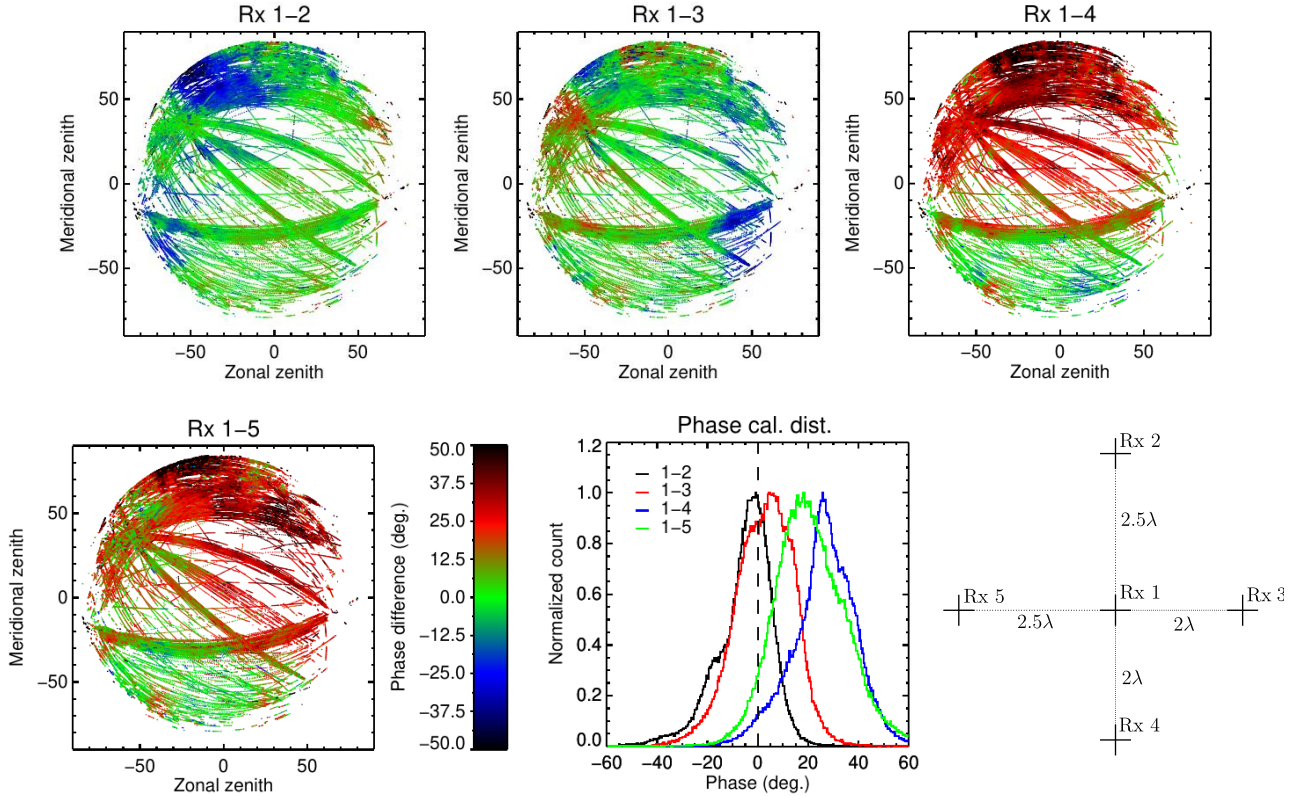


Fig. 5.19: As per Fig. 5.18, but for the Mylor receiver.

The correction variation observed at BP is complex, with large and small scale structures evident in all receiver pairs. In terms of larger scale structure, pair 1-2 (north-south baseline,  $2\lambda$  separation) exhibits a gradient increasing toward the west, manifesting in corrections up to around  $+30^\circ$  in the western sector, and down to around  $-30^\circ$  in the east. In the 1-3 pair (north-south baseline,  $2.5\lambda$  separation) there is a gradient increasing to the north, again with maximum values of about  $+30^\circ$  in the north, and minimum values of around  $-30^\circ$  in the south. In pair 1-4 (east-west baseline,  $2\lambda$  separation), corrections increase to the north-east, with minimum values of around  $-30^\circ$  in the south-west. Pair 1-5 (east-west baseline,  $2.5\lambda$  separation) shows a more complex structure, with maximum values of around  $+30^\circ$  in the south-west, and minimum values of around  $-20^\circ$  in the north-west and north-east.

The implied corrections at Mylor are generally larger than those at BP, with the largest being around  $+50^\circ$  occurring in pairs 1-4 (north-south baseline,  $2\lambda$  separation) and 1-5 (east-west baseline,  $2.5\lambda$ ). Pairs 1-4 and 1-5 also show generally show increasing offsets towards the north. On the other hand, pairs 1-2 (north-south baseline,  $2.5\lambda$ ) and 1-3 (east-west baseline,  $2\lambda$ ) do not show pronounced gradients across the field of view, although there are high spatial gradients toward the north-west for these pairs.

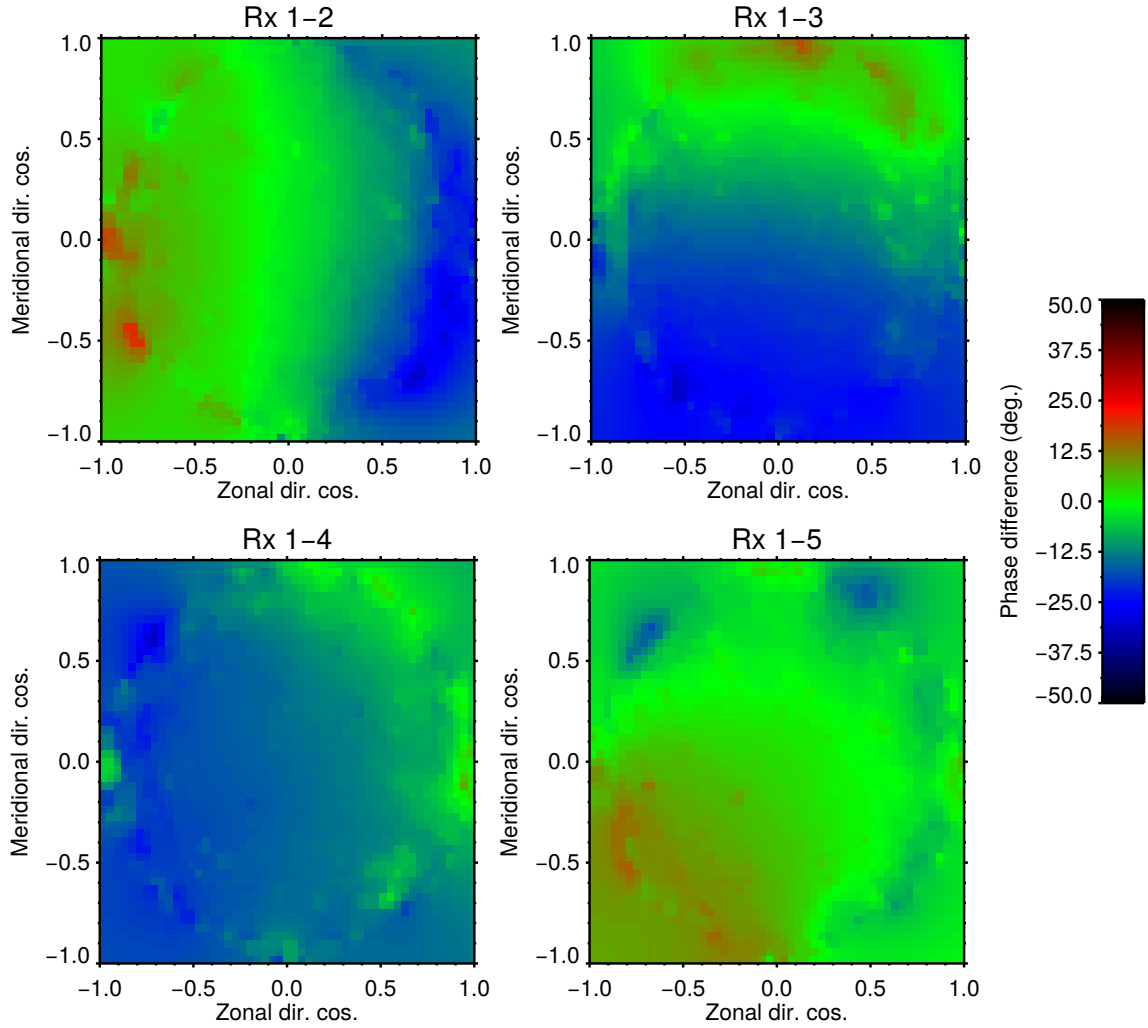


Fig. 5.20: Interpolated phase corrections for the BP receiver.

Determining the cause of the spatial variation in the implied phase corrections has been beyond the scope of this work. Possible causes include the effects of an irregular ground plane, coupling between the antenna elements, transmission lines or receiver system, and multipathing of the received signals between nearby objects and the antennas.

## 5.7 Application of phase corrections

The implied phase corrections presented in Figs. 5.18 and 5.19 are not straightforward to implement in the Jones et al. [1998] AOA estimation method (or its derivatives) outlined in Sect. 2.6.1. Unlike in the Holdsworth et al. [2004b] phase calibration method, where only a single offset needs to be applied to any phase difference measurement, in this case there is a position dependence in the corrections. Therefore, the meteor position needs to be known before the correct offset can be applied.

A beamforming method is used in this work to overcome this problem, with the

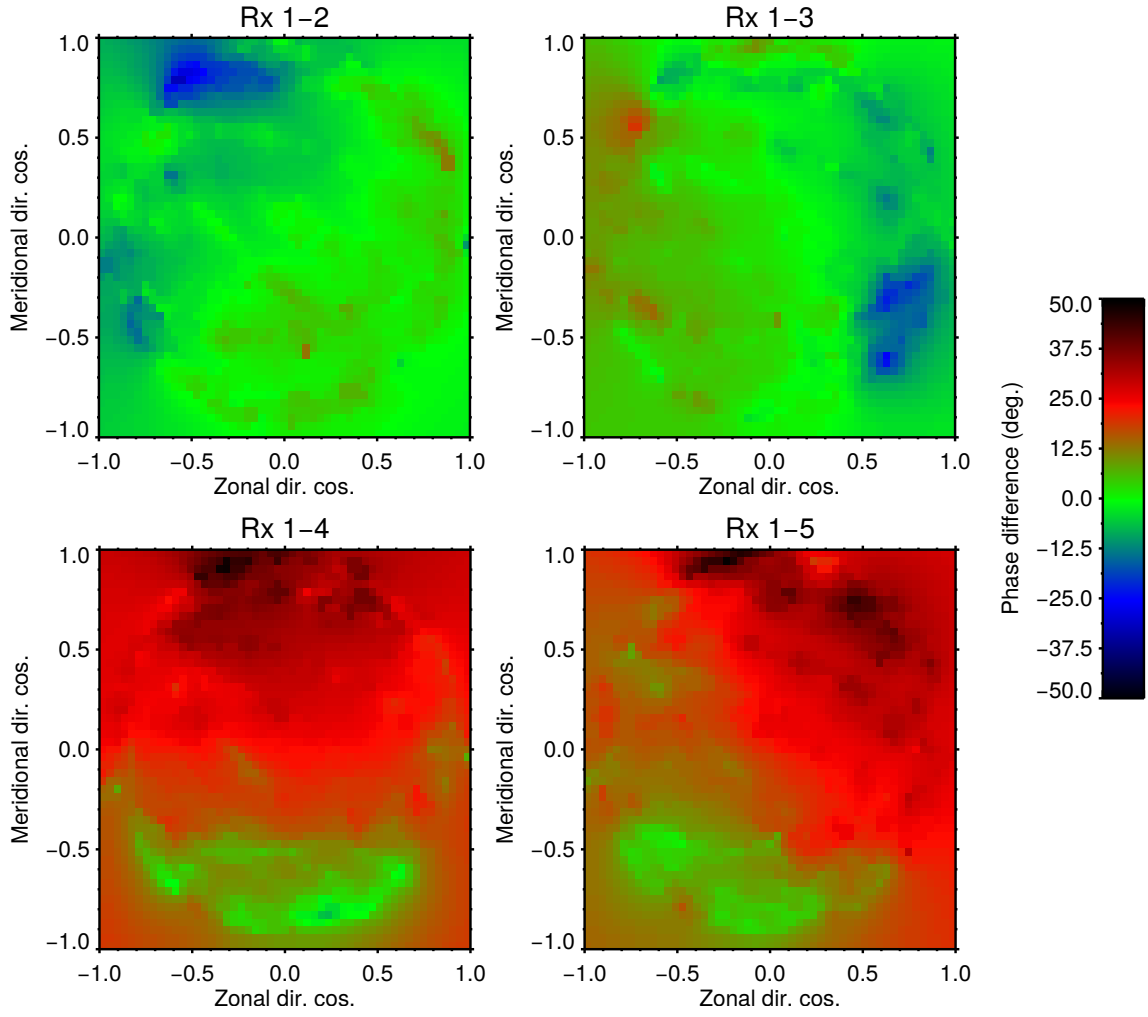


Fig. 5.21: Interpolated phase corrections for the Mylor receiver.

position-dependent phase corrections being used as weights in the beamforming matrix. The synthesized beam power  $B(\Theta)$  (where  $\Theta$  is a vector of direction cosines) may be written in the standard Fourier beamforming case as:

$$B(\Theta) = \mathbf{w}^\dagger \mathbf{R} \mathbf{w}, \quad (5.6)$$

where the  $\dagger$  operator denotes a Hermitian conjugate. The covariance matrix  $\mathbf{R}$  is given by:

$$\mathbf{R} = \begin{bmatrix} s_{11} & s_{12} & \dots & s_{1n} \\ \vdots & & & \vdots \\ s_{n1} & \dots & \dots & s_{nn} \end{bmatrix}, \quad (5.7)$$

where  $n$  is the number of antenna channels (or time series). The individual components

$s_{ij}$  of  $\mathbf{R}$  are given by:

$$s_{ij} = \text{cov}[\mathbf{x}_i, \mathbf{x}_j] = \frac{1}{N} \sum_{k=1}^N (x_{ik} - \mu_i)(x_{jk} - \mu_j)^*, \quad (5.8)$$

where  $x_{ik}$  is the  $k$ th element of the  $i$ th complex receiver time series,  $\mu_i$  is the mean of the  $i$ th time series,  $N$  is the number of elements per time series, and  $\star$  represents a complex conjugate. In the case of only having phase difference data available as in this study, a given element of  $s_{ij}$  simplifies to  $e^{i(\phi_i - \phi_j)}$ . Finally, the weighting vector  $\mathbf{w}$  (in the case of no applied phase corrections) is given by:

$$\mathbf{w}^T = \left[ e^{i\frac{2\pi}{\lambda}\boldsymbol{\Theta}\cdot\mathbf{d}_1}, \dots, e^{i\frac{2\pi}{\lambda}\boldsymbol{\Theta}\cdot\mathbf{d}_N} \right], \quad (5.9)$$

where  $\mathbf{d}_i$  is the distance in Cartesian coordinates to the  $i$ th antenna element from some arbitrarily-defined zero. When these weights are applied in (5.6), the weighted  $s_{ij}$  terms combine in such a way that they constructively interfere at the desired location  $\boldsymbol{\Theta}$ . To apply the phase corrections the weighting vector may be re-written as (and as per (5.2), assuming that the estimated phase corrections are to be subtracted from the measured phases):

$$\mathbf{w}_c^T = \left[ e^{i\left(\frac{2\pi}{\lambda}\boldsymbol{\Theta}\cdot\mathbf{d}_1 + \alpha_1(\boldsymbol{\Theta})\right)}, \dots, e^{i\left(\frac{2\pi}{\lambda}\boldsymbol{\Theta}\cdot\mathbf{d}_n + \alpha_n(\boldsymbol{\Theta})\right)} \right]. \quad (5.10)$$

where  $\alpha_j(\boldsymbol{\Theta})$  represents the correction for receiver  $j$  at location  $\boldsymbol{\Theta}$ .

The AOA estimation is performed by scanning the beamformed power in (5.6) across a regularly sampled grid of positions in  $\boldsymbol{\Theta}$ . Since the phase corrections are irregularly sampled in  $\boldsymbol{\Theta}$ , they need to be rebinned to a regularly sampled grid prior to being incorporated in (5.10). In this work, a 2D inverse distance interpolation is applied to rebin the corrections to a regular direction cosine grid spanning  $[-1, 1]$  in both the zonal and meridional axes, with a resolution of 0.04. To slightly reduce the size of small-scale fluctuations in the interpolation result, the rebinned grid is also smoothed using a 2D boxcar averaging with a width of 3 bins.

The results of the interpolation are shown in Figs. 5.20 and 5.21, for the BP and Mylor sites respectively. It is clear from these that the large scale and many of the small scale features of the raw corrections are reproduced.

Figure 5.22 shows an example of the synthesized beam power for the case of the BP receiver and phase corrections, with a simulated target having  $x$  and  $y$  direction cosine components of  $[0.5, 0.5]$ . As discussed in Sect. 2.6.1, along baselines whose antenna separation  $d \geq 0.5\lambda$ , the phase difference estimate for that baseline will be aliased.



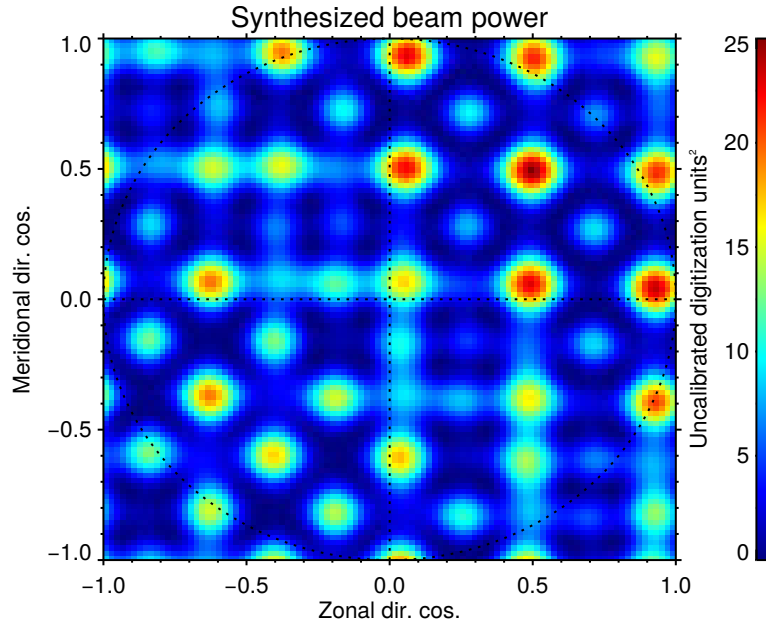


Fig. 5.22: An example of the beamformed brightness distribution for a target with a direction cosine vector of  $[0.5, 0.5]$ .

This manifests in the power distribution as periodic maxima. Given the virtual  $0.5\lambda$  separations inherent to the Jones-like antenna array however, above the horizon the distribution still maximises at a single unambiguous location (assuming that there are no errors in the phase difference and phase correction estimates). This is the only point at which the signals from all 5 receivers will constructively interfere, and can be taken to be the AOA. In Fig. 5.22, this global maximum is at the expected position.

In the interests of reducing computation time, an AOA-finding approach following that used by Clahsen [2018] is used<sup>2</sup> to simultaneously apply the phase correction and find the meteor location. The AOA is estimated from a power distribution such as in Fig. 5.22 by firstly performing a “coarse” scan over all possible target direction cosines (with a resolution of 0.02 in both the  $x$  and  $y$ -axes), followed by a “finer” scan centred on the previously-determined direction cosine (with a range of 0.04 and resolution of 0.0008 on both axes).

Only power maxima occurring above the horizon are used to determine an AOA. In the event that a maximum is found at a zenith angle  $\theta > 80^\circ$ , that maximum is discarded and another search is performed for maxima occurring at  $\theta \leq 80^\circ$ . This check implicitly assumes that AOAs with  $\theta > 80^\circ$  are not physically reasonable and likely a result of receiver noise or a residual phase calibration error. The downside is that

<sup>2</sup>With the exception that Clahsen [2018] find the minimum of an objective function that parameterizes the meteor AOA as well as radial velocity, power and decay time.



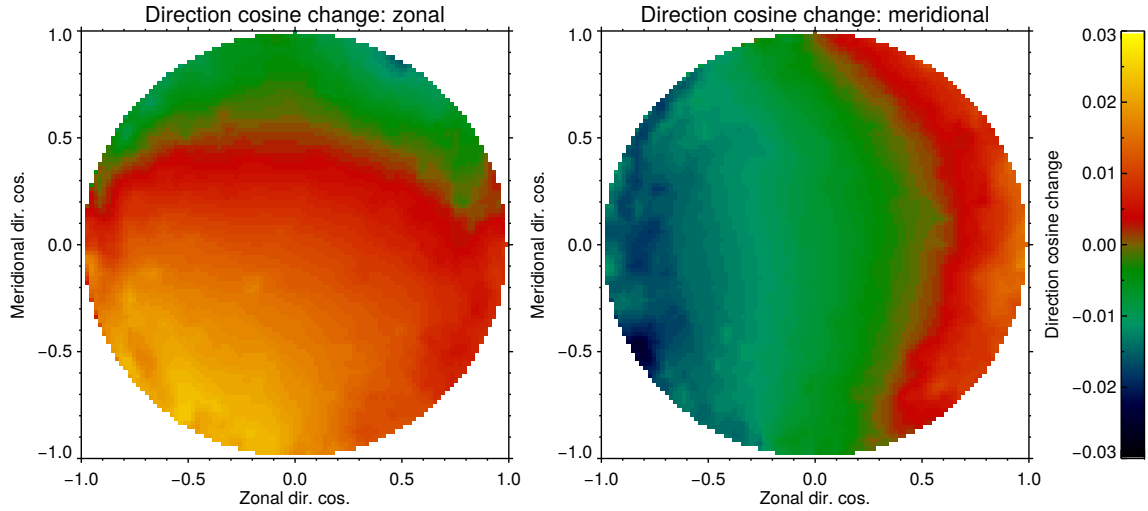


Fig. 5.23: The change in meteor direction cosines that occurs as a result of applying the phase calibration on the BP meteor radar.

the very few meteors whose  $\theta > 80^\circ$  will be erroneously aliased to a different power maximum. It should be stressed that this approach is only applied for statistically testing the performance of the phase calibration, and should not be applied when using meteors for any form of atmospheric characterisation.

Figures 5.23 and 5.24 show the changes in meteor AOAs (in direction cosine form) that will occur as a result of applying the position-dependent phase corrections, for the BP and Mylor sites respectively. These plots were produced by calculating the phase differences that would be measured by a meteor radar for each position on the direction cosine grid, and then attempting to estimate meteor position using the synthesized power distribution approach with the phase corrections applied. The change at BP can to a large extent be interpreted as an anticlockwise rotation about the zenith, whereas at Mylor, the effect at most AOAs is to increase the zenith angle of the meteor.

## 5.8 Examples of phase-corrected results

This section presents the application of the previously discussed aircraft-based phase calibration technique to meteor detections from the BP and Mylor receivers. In both cases, AOA and height distributions of the meteor detections collected between 26-Oct 2019 and 04-Nov 2019 inclusive are used to assess the performance of the technique against no applied calibration and the empirical approach of Holdsworth et al. [2004b].

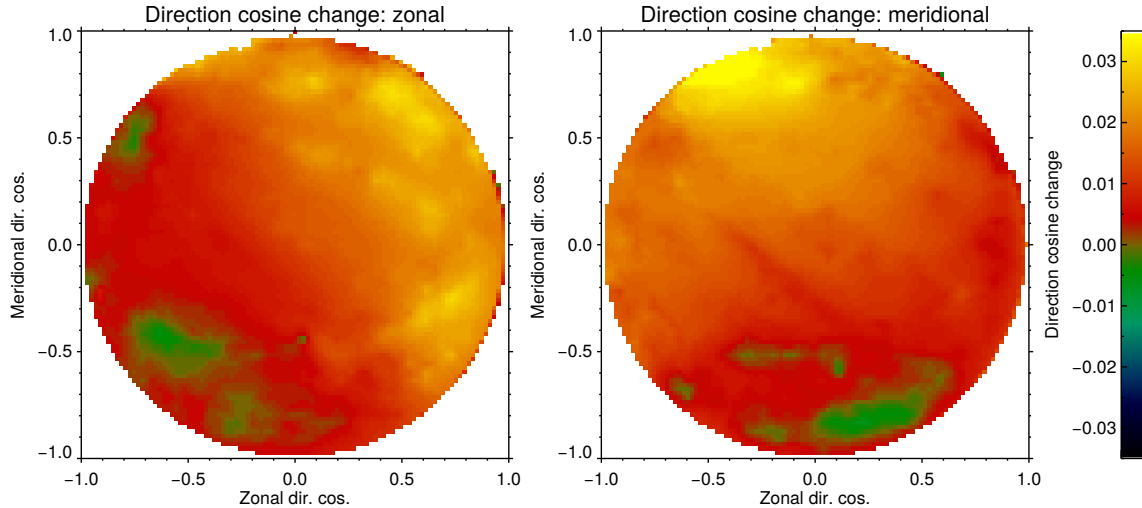


Fig. 5.24: As per Fig. 5.23, but for the Mylor system.

### 5.8.1 Buckland Park receiver

Figure 5.25 shows the different phase calibration scenarios applied to the BP meteor receiver. The empirical calibration increases the number of detections within the 65–120 km height region relative to the no-calibration case (88,111 vs. 83,605), and the aircraft case increases this further (to 90,040). The height distribution width for the aircraft case is also slightly lower than the other two (5.4 km against 6.3 km and 5.7 km for the no-calibration and empirical cases, respectively). At 87.3 km, the peak height of the distribution in the aircraft case is also slightly lower than the other two (87.9 km and 87.6 km, respectively). The position distributions in both the calibrated cases are similar, and do not exhibit the anomalous “nulls” along the line running NW and SE from the transmitter in the no-calibration case.

There is little change in the zenith-altitude distributions amongst the three cases, with the main distinguishing feature being the few anomalous detections between altitudes and zenith angles of  $\sim 100$ –120 km and  $40$ – $60^\circ$  respectively. The mean altitude appears to reduce slightly with zenith angle in all cases (noticeably around a zenith angle of  $\sim 65^\circ$ ). All cases also show a divergence at  $\sim 75^\circ$ , which is clearly a result of phase difference estimation errors—although it should be noted that this divergence is smaller in the aircraft case.

### 5.8.2 Mylor receiver

Results for the different phase calibration scenarios on the Mylor receiver are shown in Fig. 5.26. In contrast to the BP case, the application of the aircraft-derived phase

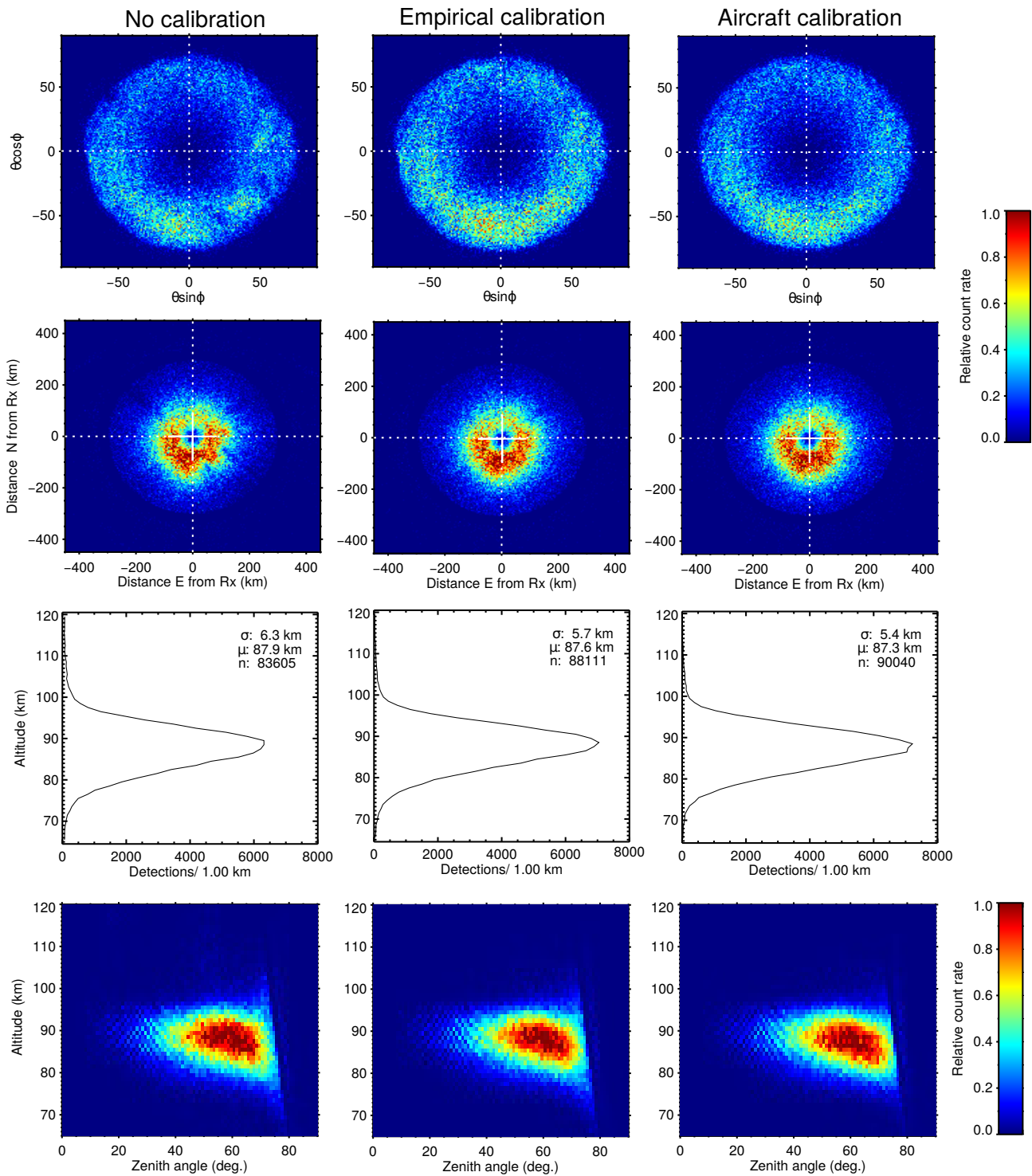


Fig. 5.25: Results of applying no calibration, the empirical Holdsworth et al. [2004b] calibration, and the aircraft-derived phase calibration to the BP meteor radar results from 26-Oct 2019 to 04-Nov 2019 inclusive. AOA distributions are in the first row, horizontal positions in the second row, altitudes in the third row (along with distribution statistics), and altitude-zenith distributions in the fourth row.

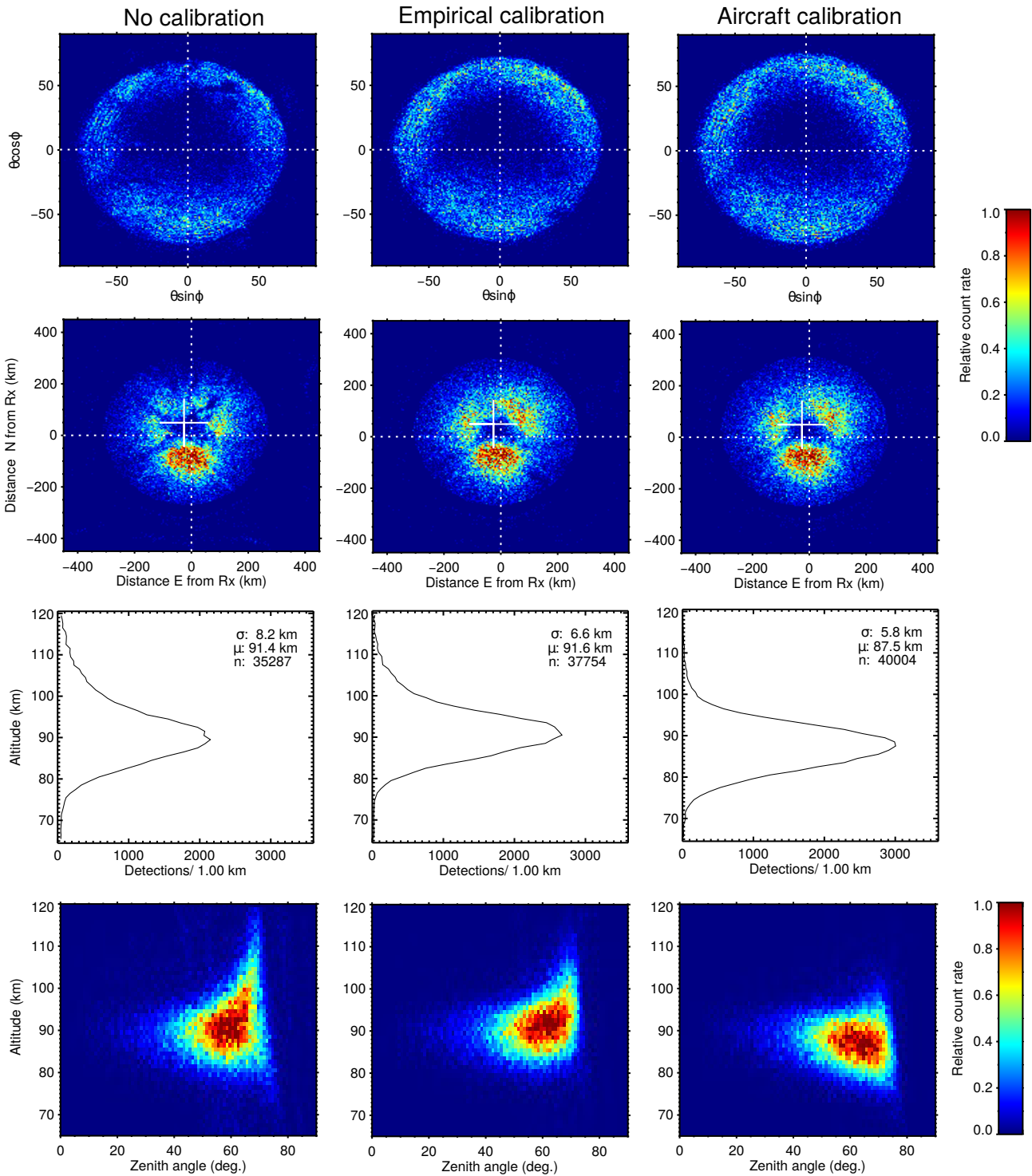


Fig. 5.26: As per Fig. 5.25, but for the Mylor receiver. The location of the transmitter in the horizontal distribution plots is denoted by a white cross.

calibration substantially reduces both the width and peak height of the meteor distribution relative to the empirical calibration; these reduce from about 6.6 to 5.8 km, and 91.6 km to 87.5 km respectively. The reduction in peak height is expected on the basis of the phase corrections increasing the average zenith angle of the returns (shown in Fig.

5.24, while retaining the same ranges. The altitude distribution in the aircraft case also does not diverge at high zenith angles as much as in the empirical and no-calibration cases: the end result of this is far fewer (likely erroneous) detections above  $\sim 110$  km in the aircraft case.

The application of the empirical and aircraft-based calibration also seems to increase the number of detections in regions of the sky to the NE, SW, NW and SE of the transmitter location. These “nulls” in the no-calibration case are almost certainly the result of physically unreasonable altitude estimates resulting from AOAs being aliased to the wrong part of the sky. The aircraft calibration also largely removes a “null” present in the empirical case, close to the SE edge of the meteor distribution.

It is pleasing that the peak altitude in the aircraft calibration case reduces by  $\sim 4$  km to 87.5 km, since this brings it into much closer agreement with the time-coincident BP result (87.6 km for the empirical calibration, 87.3 km for the aircraft-based). The fact that the BP peak heights deviated by only 0.6 km for all phase calibration cases likely implies that those peak heights were close to the true value for those detections. This in turn implies that the calibration at Mylor has largely compensated for what were the true phase calibration offsets.

A caveat to consider in this conclusion is the expected increase in peak detection height associated with the lower effective operating frequency (given by  $f \cos(\beta/2)$ , where  $f$  is the nominal frequency and  $\beta$  is the forward scatter angle). Figure 5.27 shows a histogram of this for the aircraft-calibrated results over the period in which the calibration was applied. The mean of this distribution is 54.46 MHz, with nearly all detections above 53 MHz. In this context, Holdsworth et al. [2008] used essentially identical radar hardware to the BP/Mylor systems at Davis Station in Antarctica, and found the peak heights of the 55 MHz system to occur approximately 2 km below those of a co-located 33 MHz (i.e., a 66% longer wavelength) system (see Fig. 2.3). Based on this result alone, it could fairly be assumed that a frequency difference of about 4% could increase the peak height by a few hundred metres at most.

The fact that the higher peak height associated with the lower effective operating frequency arises mostly from the larger measured decay time for a given trail (see Sect. 2.2.4) can also be used to give an upper bound on the change in peak height expected for such a change in operating frequency at BP. As shown in Fig. 5.28, over the period under investigation the log inverse decay time increases by  $\sim 0.126 \text{ s}^{-1}$  per km. From (2.1), a change in operating frequency from 55 to 53 MHz yields a log inverse decay time

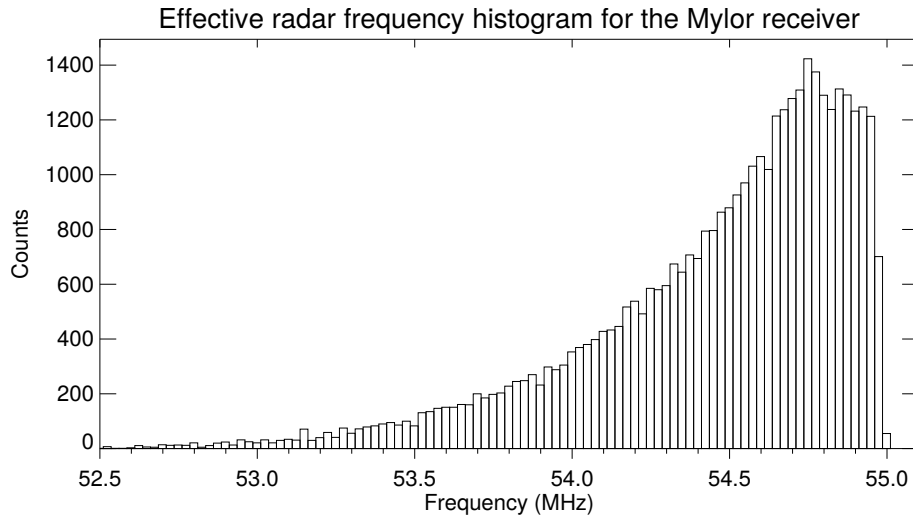


Fig. 5.27: Histogram of effective radar frequency associated with the meteor detections made by the Mylor receiver, in the aircraft phase calibration case. The mean of the frequencies shown is 54.46 MHz.

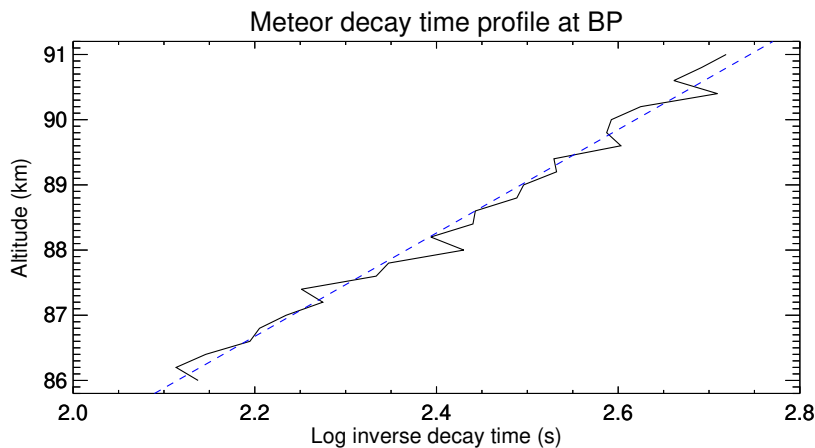


Fig. 5.28: Profile of decay times measured from the aircraft-phase-calibrated results at BP. A line of best fit has been overplotted, which has a slope of  $\sim 0.126 \text{ s}^{-1}$  per km.

change of  $\sim 0.0741$ . Therefore, in this height range a 53 MHz system would on average see a given decay time just under 600 m higher than would a 55 MHz system. Even if the true peak height were to be this much higher at Mylor, it is still greatly exceeded by the 4 km-higher peak height at Mylor measured in the non-calibrated/empirically-calibrated results. This indicates the aircraft phase calibration has brought the peak height closer to what its true value is (relative to the other calibration cases), despite a potential problem with the the peak height at Mylor being lower than at BP.

While the divergence of the aircraft-calibrated results at high zenith angles is smaller than in the other two cases, the divergence that is present (especially the large number

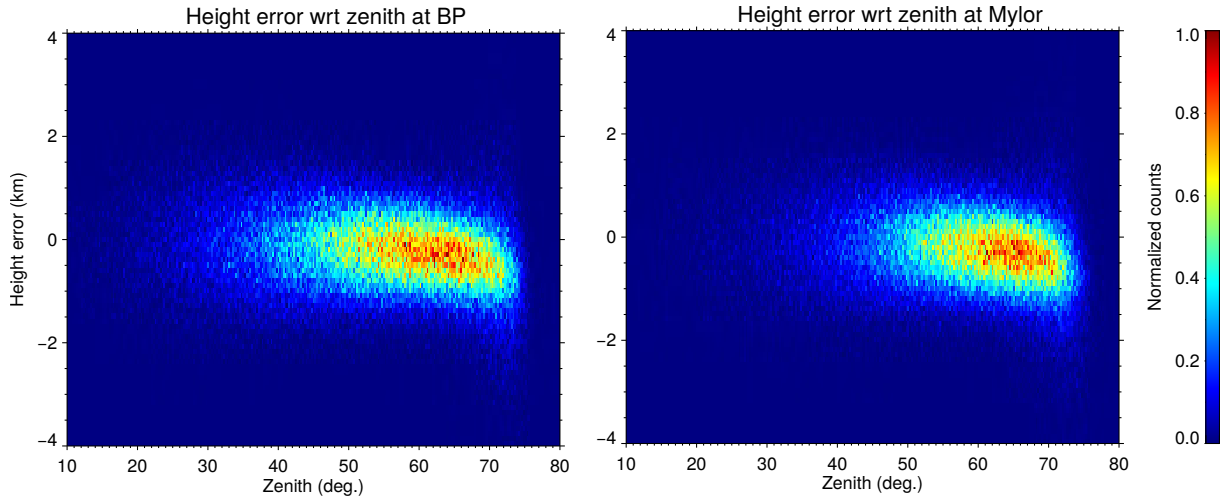


Fig. 5.29: Simulated height estimation error as a function of zenith angle at BP and Mylor, in the absence of phase calibration errors. This incorporates a simulation of the height estimation procedure at the BP and Mylor sites, using the same approach as in the model discussed in Sect. 3.2.4. 100,000 Gaussian-distributed heights, with a mean and standard deviation of 92 km and 6 km respectively, have been used as an input.

of suspect heights  $\lesssim 75$  km at  $\theta \gtrsim 75^\circ$ ) may indicate residual phase difference errors (both systematic and random). Given the size and spatial variability of the corrections at high zenith angles in Fig. 5.19, it would be reasonable to expect some residual phase calibration (i.e., systematic) errors. It should also be noted that in the absence of phase calibration errors but with realistic levels of receiver noise included, using the 0.5-2.0-4.5 $\lambda$  method (see Sect. 2.6.1) to estimate AOAs yields 1-sigma altitude errors of  $\sim 0.75$  km; Fig. 5.29 demonstrates this for the BP and Mylor sites. It is also clear from this figure that the height errors increase for  $\theta \gtrsim 70^\circ$ , and that the method underestimates the true height here (the bias at  $\theta \geq 70^\circ$  is  $\sim 0.6$  km). This is smaller than the apparent height errors in the aircraft-corrected results in Fig. 5.26, so we argue it is likely that a defect in that phase calibration has caused those anomalous heights.

Convoluting this further is the possibility that the measured peak height of specular meteor echoes reduces at high zenith angles. One would expect this to occur for a fixed mass and meteor velocity distribution, since meteor entrance angle increases with zenith angle (to maintain the specular scattering criterion), and meteors travelling more steeply penetrate further into the atmosphere and so ablate at lower altitudes. This has never been tested statistically, most probably due to the difficulty in obtaining statistically significant meteor altitude estimates at zenith angles high enough for this phenomenon to be observable. This hypothesis therefore remains to be investigated.

## 5.9 Discussion and recommendations for future work

The aircraft-based phase calibration procedure developed in this Chapter has revealed a considerable variation in phase offsets as a function of AOA for the BP and Mylor meteor radars. Those offsets were applied to approximately 10 days of meteor detections from the two systems, and reduced the width of the meteor height distribution relative to results corrected with the Holdsworth et al. [2004b] empirical calibration method in both cases (from 5.7 to 5.4 km and 6.6 to 5.8 km for the BP and Mylor radars, respectively). We conclude from this that the technique presented adequately compensated for the phase biases present in both systems. The causes of the offsets were not investigated, but were likely a combination of transmission line delays, mutual coupling between receiver antennas, and signal delays and/or multipath due to vegetation or other objects nearby the antenna arrays. We suspect that the technique could compensate for phase offsets of this kind for any spaced antenna/frequency diverse VHF radar system.

A significant caveat to the technique's good performance is that BP and Mylor are ideally located for its application in terms of air traffic. This is because there are rarely multiple aircraft present in the sky at the same range, yet the aircraft present enable phase correction estimates to be obtained in most parts of the sky. Other meteor radar installations may simply have too much air traffic (i.e., many cases of multiple range coincident aircraft echoes) for the method to be applicable, or too little sky coverage for practically useable phase correction estimates.

Examples in which there are multiple range-coincident echoes present are shown in Chapter 6. These pertain to data taken during a trial of the same methodology at a site in Germany which generally had an air traffic density much higher than that in the Adelaide region. In such examples, the method of discarding data exhibiting significant discrepancies between the measured and predicted Doppler velocities can result in the loss of a lot of "potentially good" data. Furthermore, incorrect phase offsets which happen to be associated with the same Doppler velocity as that predicted will not be discarded. The latter of these issues is further exacerbated in bistatic receivers with a large Tx-Rx separation, in which case aircraft detected close to the line of sight between the Tx and Rx (which is also where the echo strengths will be the highest) will have close to zero Doppler velocity.

To remedy these cases, the aircraft position database would need to be searched for all range-coincident echoes from aircraft other than those being tracked, and then synthesized and removed from the obtained receiver time series. The challenges in doing



this would be 1) that existing phase calibration information would need to be taken into account to correctly synthesize those echoes, and 2) the returned power as a function of range, position and orientation of the contaminating aircraft would need to be known.

Other improvements that should be considered are:

1. For bistatic receivers, synthesis of the transmitter ground wave.

The aircraft transits shown in Case 5 in Sect. 5.5 (Fig. 5.15) and Fig. 6.7 in Chapter 6 show some examples of the bistatically-received aircraft echo being contaminated by the transmitter wave. The contamination is more probable for large transmitter-receiver separations, given the smaller range difference for an aircraft at a given altitude along the line between the transmitter and receiver. The simplest way to remove the ground wave would be to synthesize the associated signal at each receiver channel, and then subtract it. This would require a characterisation of the ground wave's phase and amplitude and their variability with time.

2. Interpolating across erratic variability in the phase corrections.

The Case 5 (Fig. 5.15) and Fig. 6.7 transits also show examples of isolated deviations in the phase corrections that are associated with enhancements in the transmitter ground wave. It may be impossible to compensate for the ground wave in cases like this. This data could be appropriately discarded by removing phase offsets that differ from the expected values by some predetermined threshold (where the expected values are based on previously recorded observations at similar AOAs). This would be more effective than simply removing points with some threshold deviation from a plane fit to all accrued phase corrections, as described in Sect. 5.4.7).

3. Using receiver channel coherences rather than phase differences.

The AOA estimation method outlined in Sect. 5.7 made use of receiver phase differences to compute AOAs (e.g., as done in Holdsworth et al. [2004a]). As discussed in Sect. 2.6.2, Clahsen [2018] introduces a non-linear least squares fitting approach for AOA determination that makes use of receiver channel coherences, which embody both the phase difference as well as a measure of correlation between the channels. The latter of these can be used to weight the relative contributions of each receiver pair to the AOA estimation. This is especially useful if particular receivers have a higher noise level or susceptibility to interference than others.

It may also be beneficial to use coherences in weighting the phase corrections contributing to the interpolated grid of offsets actually used in the calibration. The caveat here is that this will bias the interpolants to estimates with lower noise levels, which may not necessarily be desirable.

4. Using a less computationally expensive and more robust beamforming algorithm to apply the phase corrections.

The reception beamforming algorithm used to apply the phase corrections in this work is computationally expensive, seeing as the beamformer output must be computed at each point in the 2D angular grid. Faster computation times may be achievable by finding the global maximum of the beamformer output using a gradient descent algorithm or least squares fitting approach such as that used by Vaudrin et al. [2018] and Clahsen [2018].

It is also possible for the algorithm used in this work to identify a local maximum (rather than a global one) in the initial coarse scanning, if the difference in the beamformer outputs across a number of maxima is small. Using a higher angular resolution in the scanning grid would reduce the probability of this happening, but would of course increase the computational demand. Again, a gradient descent/least squares fitting approach would enable a more robust determination of the global maximum.

5. Incorporating a more robust method for the removal of interference.

As discussed in Sect. 5.4.3, sources of interference (or contaminating echoes) were removed in this work by precluding data with less than 3 dB of power variation in the 5 range gates surrounding the expected aircraft range. Implementing this scheme has had the side effect of precluding aircraft echoes with an SNR lower than 3 dB, or discontinuities in phase correction time series for echoes straddling this threshold. A more robust approach would be to classify interference as correlated signals in time and range, and remove any such signals from the receiver channels prior to attempting to extract aircraft echoes.

6. Prioritizing lower zenith angles in the time offset removal.

The time offset removal procedure discussed in Sect. 5.4.6 uses the Doppler velocity discrepancies of aircraft at all AOAs to estimate receiver time offsets. While this method has proved effective in removing sources of receiver timing errors, phase difference errors

will be larger for aircraft at lower zenith angles (given the higher rate of change of direction cosines there for a given aircraft velocity). To make the time offsets pertain to lower zenith angles, a scheme that weighted the Doppler velocity discrepancies to lower zenith angles should have been used.

#### 7. Detecting and precluding suspect aircraft location information.

In their study based on ADS-B-derived aircraft position measurements, Lin et al. [2019] used the navigational accuracy parameters in the received message stream to estimate errors in the predicted (i.e., “true”) receiver phase differences. They found that the most imprecise of all the ADS-B returns they used had a 95% confidence interval of 30 m in the horizontal and 45 m in the vertical, which would lead to 1-sigma errors of up to  $\sim 2^\circ$  in the phase corrections. This is considerably less than the standard deviations of the phase corrections they actually obtained (3-4 $^\circ$ ), and so they concluded the position errors could not have significantly contributed to their results.

We did not record the navigational accuracy parameters in our study, and so have not considered the effect of positional uncertainties on the precision of our phase offsets. Given Lin et al. [2019]’s result and the number of position measurements we incorporated in the gridded phase corrections (i.e. in Figs. 5.20 and 5.21), we suspect the contribution of these to our phase calibration procedure is minimal. Nevertheless, the accuracy parameters should be used in future work as an extra level of vetting on the quality of the phase correction estimates, especially if the spatial density of those estimates is low.

In this context, it is important to mention Lin et al. [2019]’s claim that the high air traffic density in the vicinity of the Chung-Li radar led to frequent fails in the decoding of their ADS-B messages, and may have led to some of the position errors described above. They did not define the proportion of measurements for which this occurred. We did not explicitly check for these in either of our ADS-B station set-ups, but from a cursory inspection did not note any indication of clearly corrupted position or altitude recordings. We cannot guarantee they were exempt from our observations, but again note that through incorporating so many points in the gridded phase corrections, we would have eliminated any significant impact arising from them.

Further work should also be done to clarify the source of the phase offsets in the results presented in this work (i.e., the relative contributions of mutual coupling, signal delays, multipathing, and irregularities in the antenna ground). Younger et al. [2013] estimated the contribution of mutual coupling between antennas in the BP meteor radar

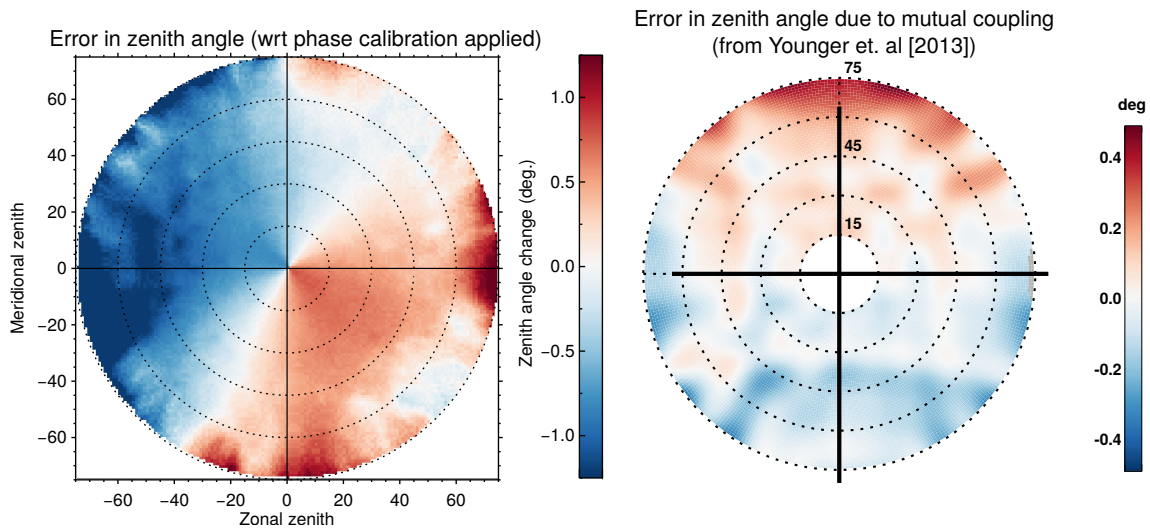


Fig. 5.30: Zenith angle errors as a function of AOA for the BP meteor radar assuming aircraft-based phase calibration results are the true phase offsets (left), and Younger et al. [2013]’s predictions of zenith angle error arising from mutual coupling (right).

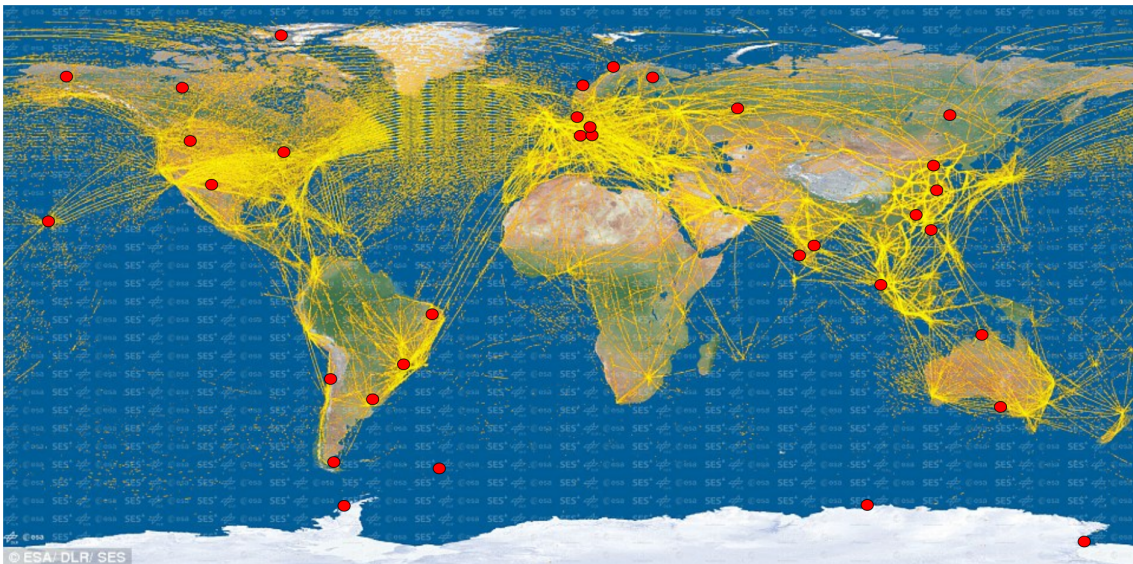


Fig. 5.31: Distribution of aircraft detections around the world from the European Space Agency’s Proba-V satellite (yellow dots), along with selected meteor radar installation locations (red dots). Downloaded from <https://phys.org/news/2015-05-proba-v-world-air-traffic-space.html>, October 2019 (article dated 08-May 2015).

to phase estimation errors, and from these predicted zenith angle errors of up to  $\pm 0.5^\circ$ . The distribution of these zenith angle errors as a function of AOA is shown in the right panel of Fig. 5.30, along with the zenith angle errors expected in this work in the left panel (assuming that the aircraft-based phase calibration results correspond to the “no phase error” case). The latter are considerably larger (with maxima up to about  $\pm 1.5^\circ$ ),

with a distribution that is oriented about  $120^\circ$  clockwise from Younger et al. [2013]’s results. Assuming that the antenna coupling characteristics have not changed since these measurements were performed, these results imply that some other source has caused the phase errors at BP.

Finally, the applicability of the method (in terms of the AOA coverage and the time required to produce useful phase calibration estimates) to meteor radar systems at other locations should be considered. This will of course vary considerably depending on the distribution of air traffic and the positioning of the transmitter(s) and receiver(s) relative to it. As a rough guide, Fig. 5.31 shows the distribution of air traffic around the world, relative to a selection of meteor radar installation locations. It is obvious that most of the radars on this map in locations other than Antarctica (e.g., Germany, China, southern India, North America, and western/eastern South America) at least have the potential to detect aircraft covering a broad AOA distribution, possibly to a greater extent than found in this thesis.

## 5.10 Summary

This Chapter has presented a technique for phase-calibrating the receiver channels of VHF meteor radars that relies on echoes from GPS-tracked commercial aircraft. When used in conjunction with the air traffic distribution in the Adelaide region, the technique appears to outperform traditional meteor radar phase calibration techniques. The method is capable of compensating for any source of receiver phase offsets (such as unknown transmission line delays, mutual coupling between antennas, and signal multi-path) and may also aid in the diagnosis of these problems.

The technique’s strong points are the simplicity of the method, the accuracy of the phase calibration offsets derived for a given aircraft transit, the low cost of the ADS-B receiver it relies on to aggregate aircraft position information, and that it can be run remotely without any need for manual intervention. A number of suggestions have been raised for improving the performance of the presented method, including adequately filtering out range-coincident echoes when the method is used in heavy air traffic environments, removal of ground wave contamination in bistatic radar configurations, and removing erratic variability in the obtained phase offsets.

In practice, compensating for the many possible sources of phase calibration errors in a meteor radar system is a notoriously difficult task. It is also something that often needs to be performed routinely without any interruption to the experiment being conducted,

and preferably without human intervention. Provided a sufficient level of air traffic, the method presented in this Chapter can largely resolve these difficulties.

## Chapter 6

# Aircraft-derived phase corrections for IAP receivers

This Chapter shows a partial application of the phase calibration technique introduced in Chapter 5 to two bistatic 32.55 MHz meteor radars operated by the Leibniz-Institute for Atmospheric Physics (IAP) in Germany. The work was performed by the author with the aid of IAP staff during April and May 2019. The processing performed on the aircraft echoes was identical to that performed on BP and Mylor data discussed in Chapter 5, aside from the absence in this case of the use of the discrepancy between the measured and predicted Doppler velocities to minimize radar-aircraft clock offsets.

Only phase correction distributions for the two radars are presented; application of the obtained offsets to meteor observations is yet to be performed. The motivation in presenting these results is to show the phase calibration’s technique efficacy on meteor radars other than the BP-Mylor link’s, and also to further motivate the suggestions for future work in Chapter 5 (notably working around range-coincident aircraft echoes, removing interference from the ground wave, and smoothing over “jumps” in the phase corrections).

### 6.1 Experiment configuration

As shown in Fig. 6.1, one of the radars (herein “KJ link”) radar consists of a receiver at the IAP site in Kühlungsborn ( $54.119^{\circ}\text{N}$ ,  $11.770^{\circ}\text{E}$ ), and a transmitter about 119 km to the north-east on the island of Juliusruh ( $54.631^{\circ}\text{N}$ ,  $13.374^{\circ}\text{E}$ ). The other (herein “KM link”) consists of a receiver at the IAP site, and a transmitter about 15 km to the south in the township of Moitin ( $53.983^{\circ}\text{N}$ ,  $11.725^{\circ}\text{E}$ ).

The the KJ link is set up much like the meteor radars in the BP-Mylor case: a



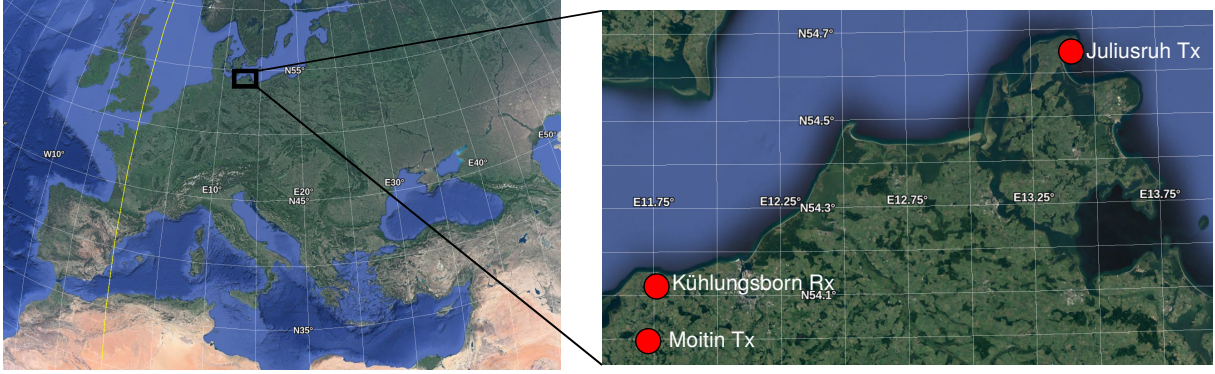


Fig. 6.1: Locations of meteor radars used in this Chapter.

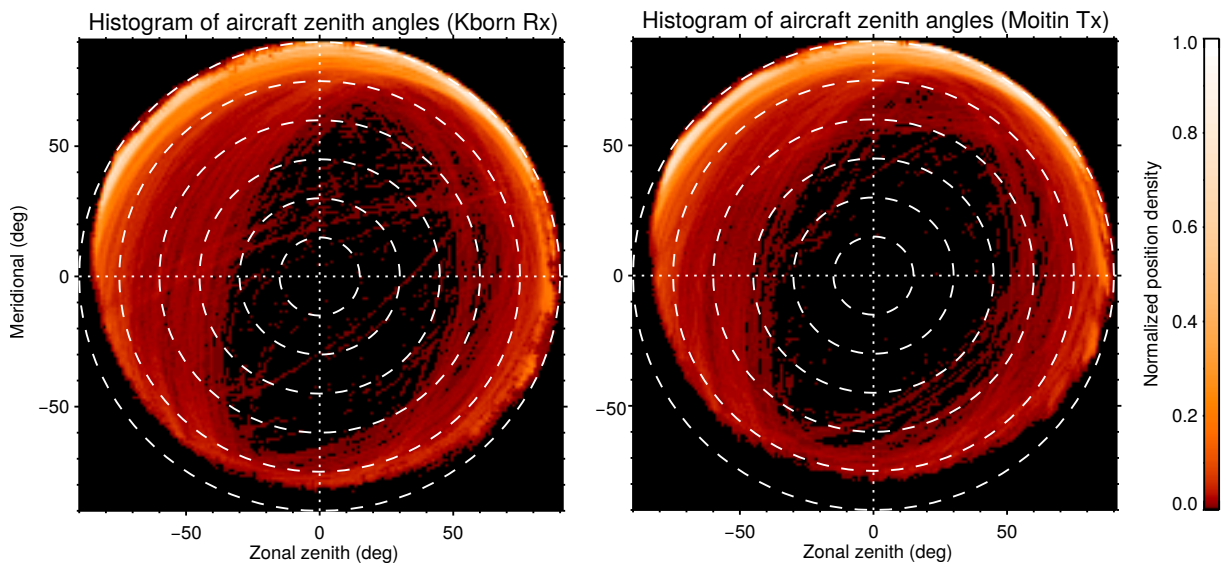


Fig. 6.2: Histogram of the AOAs of aircraft detected at the locations of the Kühlungsborn (left) and Moitin (right) meteor radar arrays.

Parameter	KJ link	KM link
Frequency	32.55 MHz	32.55 MHz
Pulse width	6 km	N/A
Baud width	1.5 km	3 km
Pulse code	4-bit complementary	1000-bit pseudorandom
PRF	625 Hz	N/A
Range sampling	0-229.5 km	0-3000 km
Range sampling interval	1.5 km	3 km
Polarisation	Circular	Circular

Table 6.1: Experiment parameters used with the IAP meteor radars.



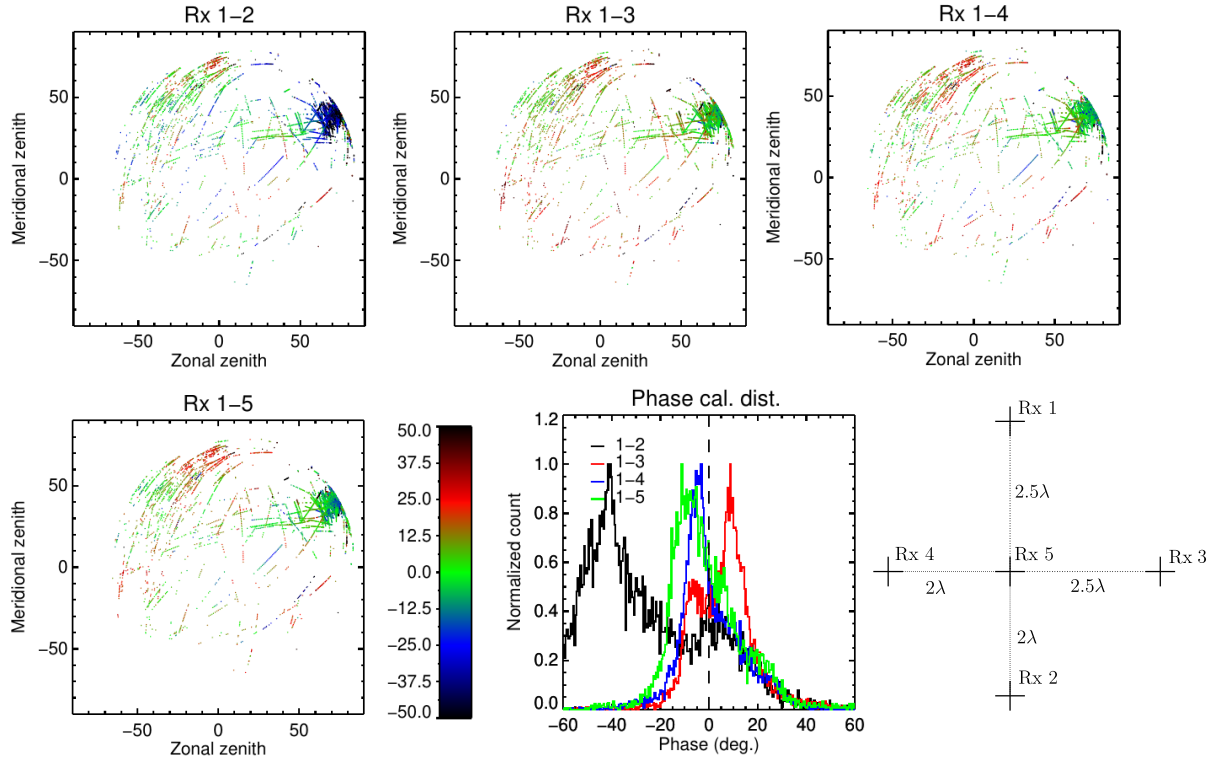


Fig. 6.3: Phase corrections as a function of AOA for the KJ link.

single-element transmitter is used at Juliusruh, and a 5-element receiver in the Jones antenna configuration is used in Kühlungsborn. The experiment parameters used during the phase calibration experiment, which spanned 25-Apr to 29-Apr 2019 inclusive, are shown in Table 6.1. Similarly to the BP-Mylor case, the radar operated in a pulsed mode with 4-bit complementary pulses.

Following the meteor radar design considerations discussed in Chau et al. [2019], the KM link consists of a five-element pentagonal transmitting array at the Moitin site, and a single-element receiver at Kühlungsborn (independent of that used in the KJ link). Such a configuration is commonly referred to as “MISO” (Multiple Input Single Output), distinct from the “SIMO” (Single Input Multiple Output) systems considered in the remainder of this thesis.<sup>1</sup> The transmitting antennas in the KM link made use of orthogonal pseudorandom code sequences, in such a way that the amplitude and phase information pertaining to each transmitter could be separated at the receiver. Each of these corresponds to different antenna channels much in the same way as in a multichannel receiver, and so the interpretation of the phase corrections derived for

<sup>1</sup>As an aside, an interferometric transmitter is preferable from the phase calibration perspective, as regardless of the number of nodes in the receive network, only the phase offsets between the antennas in the transmitter need to be known for accurate AOA estimation.

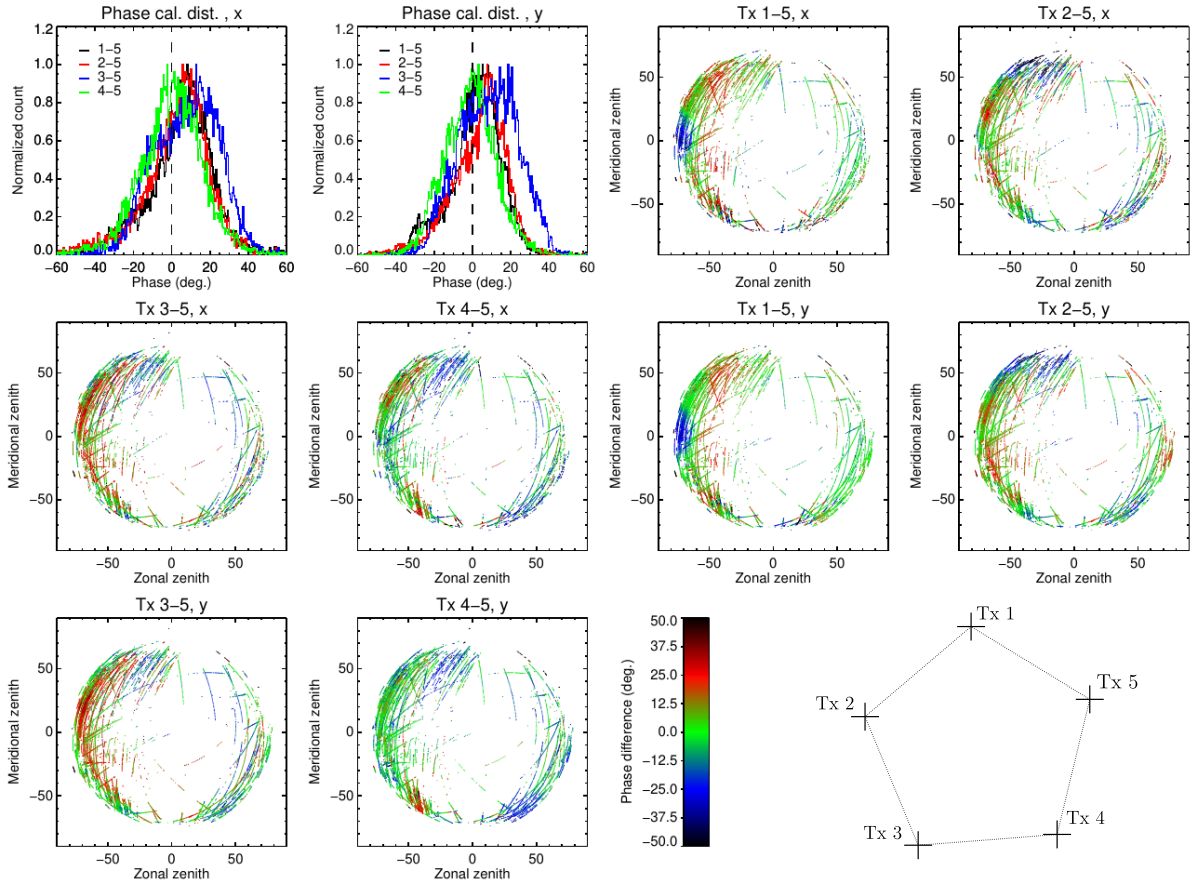


Fig. 6.4: Phase corrections as a function of AOA for the KM link. Results for the two antenna orientations are shown separately (denoted by “x” and “y”, respectively).

them is the same (only that in the MISO case, the corrections pertain to antennas that are transmitted on). The experiment parameters used for the KM link experiment (the phase calibration component of which spanned 04-May 2019 and 06-May 2019) are also shown in Table 6.1.

In the KM link experiment, the orthogonal elements on the receiving antenna were each connected to a separate receiver, so that the circularly polarised signal received from each transmitting element could be broken down into its linear constituents. In this work, phase corrections have been derived for each transmitter and polarisation pair.

The AOAs of the aircraft detected during the trials for both the Kühlungsborn and Moitin sites are shown in Fig. 6.2. There is a full azimuthal coverage at both sites, although the air traffic density is considerably greater to the north of both sites.

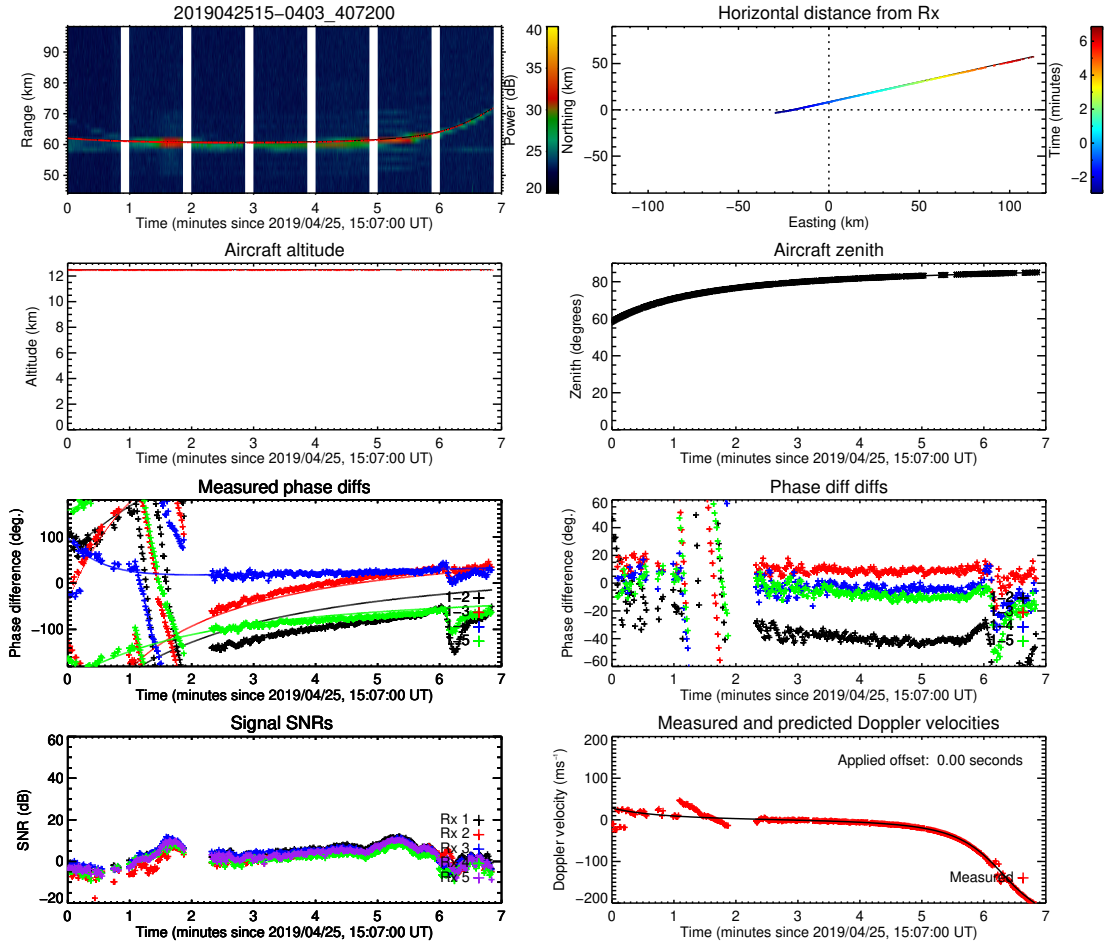


Fig. 6.5: An example of a “good” phase calibration candidate detected on the KJ link.

## 6.2 Phase corrections

The phase corrections obtained for the KJ link between 25-Apr and 29-Apr 2019 are shown in Fig. 6.3. Most of the returns are in a smaller cluster in the direction of the Juliusruh transmitter (north-east), with a few also in the north-western quadrant. There are very few returns south of the receiver site.

Those in the direction of the transmitter show little variation spatially, and the distributions across all AOAs for all receivers show well-defined mean values. The 1-2 pair shows a considerably larger mean bias ( $\sim -40^\circ$ ) than the other pairs, which are all in within the range of  $\pm 20^\circ$ . The reason for the larger offset in pair 1-2 has not been determined.

The phase corrections for the KM link obtained on 04-May and 06-May 2019 are shown in Fig. 6.4 (note that the AOAs are with respect to the transmitting array in Moitin). The corrections across all AOAs (of which there is nearly a complete azimuth of coverage) show distributions with well defined means and similar variances. There is

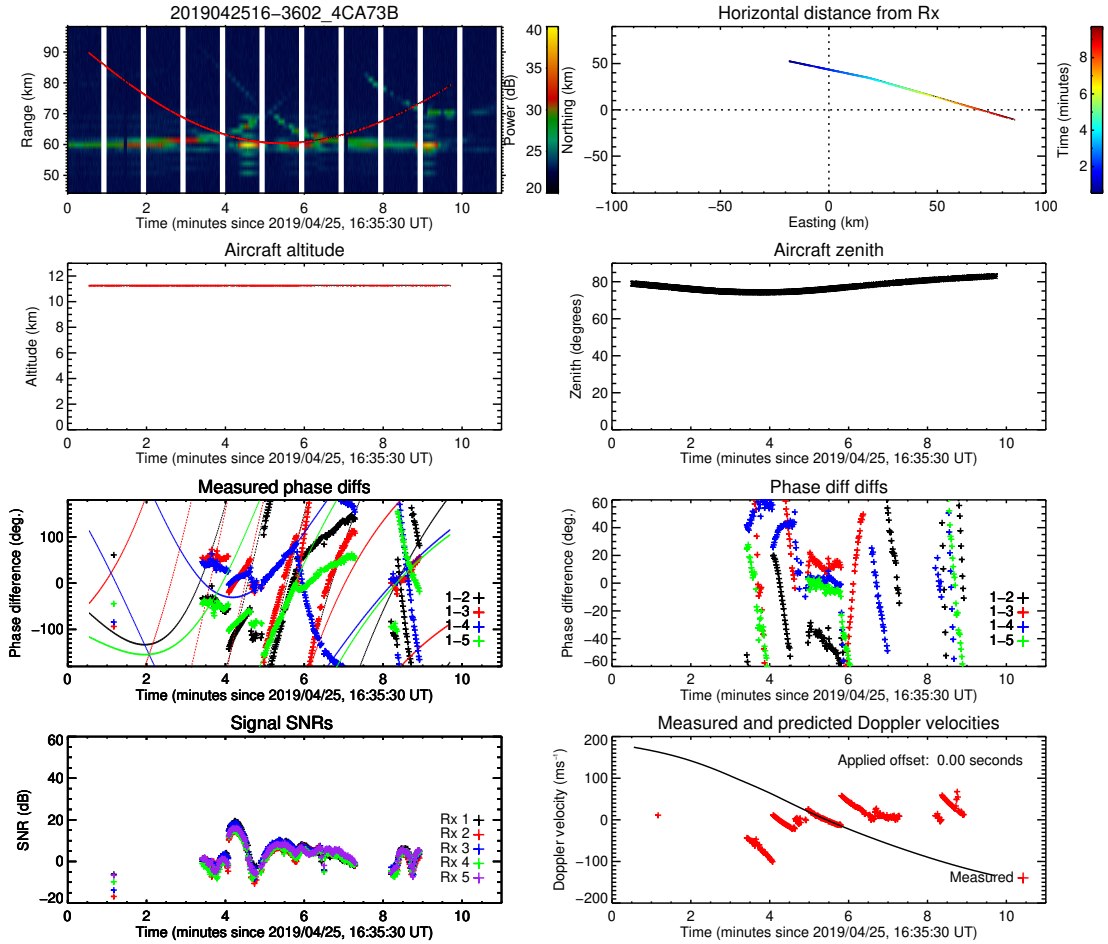


Fig. 6.6: An example of a phase calibration candidate detected on the KJ link, contaminated by multiple range-coincident aircraft.

also little variation among the means for the different transmit channels/orientations. A common AOA-structure among a number of transmitter-polarisation pairs (e.g., 1-5x, 2-5x, 3-5x, 1-5y, 2-5y, and 3-5y) is a smooth variation in the correction with azimuth due west of the array. The cause of this has not been investigated.

Overall, these results validate the technique’s ability to determine localized (in AOA) fluctuations in phase offsets.

### 6.3 Sample phase correction candidates

This section shows four example aircraft candidates used in the KJ link. The first shows a typical “good” example, and the other three illustrate potential difficulties one may encounter in obtaining usable phase correction estimates over a large transmitter-receiver separation ( $\sim 119$  km in this case).

A “good” example is shown in Fig. 6.5. The aircraft in this case was at an altitude of

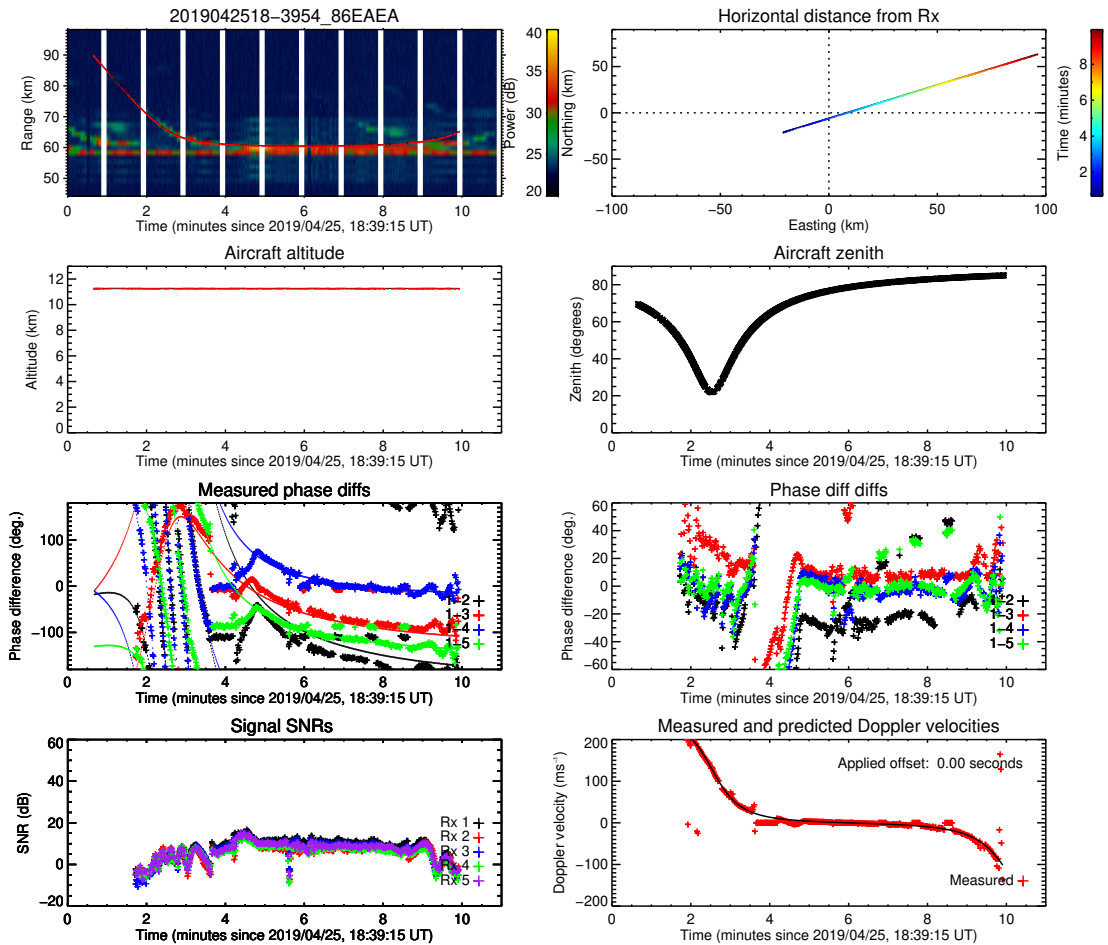


Fig. 6.7: An example of a nearly-coincident ground wave and aircraft echo detected on the KJ link.

just over 12 km, flying in a north-easterly direction toward the transmitter at Juliusruh. Aside from an echo that appears to be from the wrong aircraft before 2 minutes into the sample, the measured phase offsets are consistent between roughly minutes 3 and 6, and there is also good agreement between the measured and predicted Doppler velocities during this segment. This example also shows the large offsets inherent to the 1-2 pair evident in Fig. 6.3.

Figure 6.6 shows an example in which there are multiple range-coincident aircraft with the one being tracked (which was at an altitude of 11 km, flying in a south-easterly direction between the transmitter and receiver). As indicated by both the phase correction and Doppler velocity comparison plots, the correct aircraft is tracked only between minutes 5 and 6 of the transit. The filtering based on Doppler velocity discrepancies would have removed all the contaminated points, so this example again serves to illustrate the utility of that approach. Unfortunately, the high air traffic density at this site means that this problem was often encountered.

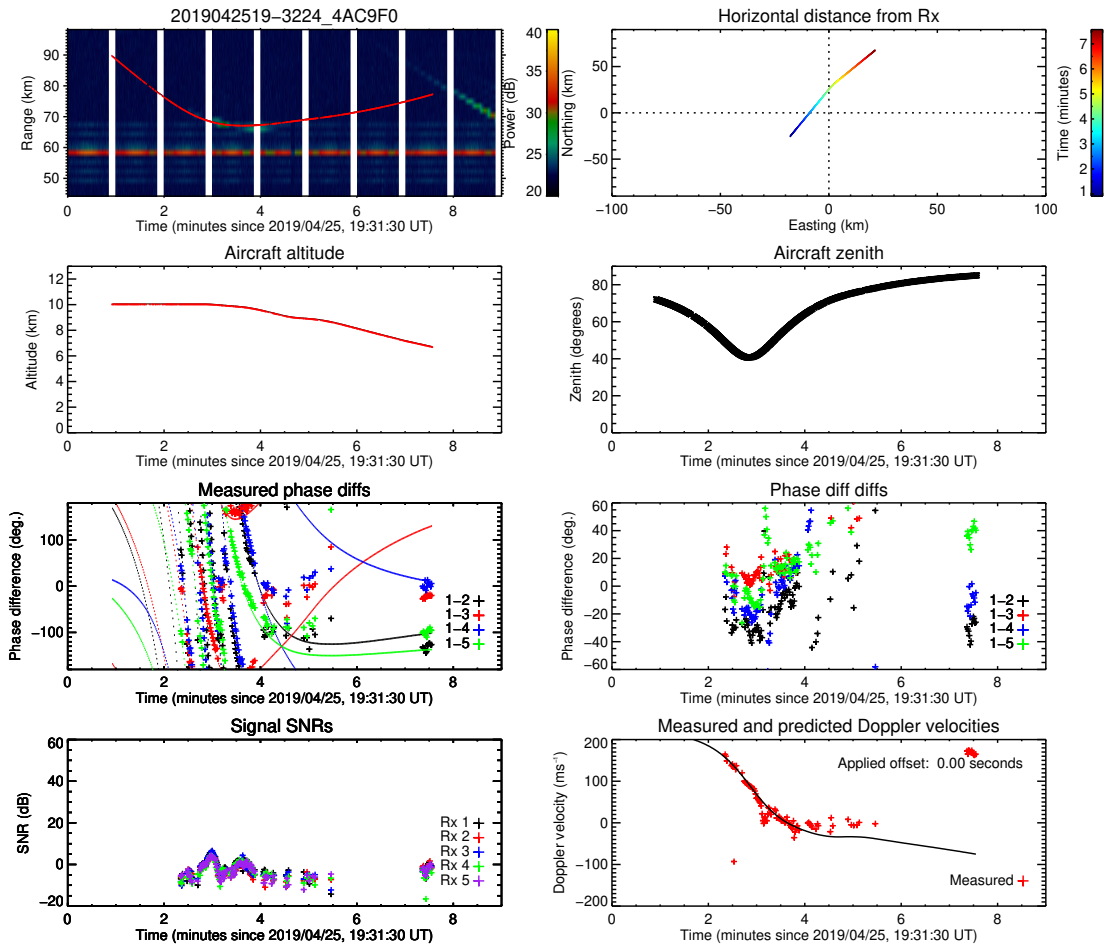


Fig. 6.8: An example of a low-SNR phase calibration candidate detected on the KJ link.

In the Fig. 6.7 example, similarly to the Fig. 6.5 case, an aircraft is flying at an altitude of about 11 km, in a north-easterly direction toward the Juliusruh transmitter. However, the ground wave strength is comparable to the echo strength in this example (and fluctuates considerably), which occasionally influences the measured receiver phase differences. The agreement between the measured and predicted Doppler velocities is generally good, although there is little difference between the predicted Doppler velocity between the transmitter and receiver sites (which is nearly zero) and the ground clutter Doppler (which is also close to zero).

The fourth example in Fig. 6.8 pertains to an aircraft descending from an altitude of around 10 km, flying in a north-easterly direction. The echo SNR from this aircraft is several dB lower weaker than in the other examples considered here, and as a result, there is a higher level of noise in the phase correction values, and poorer agreement between the measured and predicted Doppler velocities. The comparatively large round-trip range for the echo (with a minimum value of  $\sim 130$  km for this echo) is probably the cause of this, and has most likely rendered most the echoes to the north-west of the Kühlungsborn

receiver unusable for phase corrections. This serves to illustrate the limitations of the aircraft-based phase calibration technique for large transmitter-receiver separations.

## 6.4 Recommendations for future work

While the aircraft-based technique shows good potential for use on the KM link ( $\sim 15$  km transmitter-receiver separation), the sparseness of returns on the KJ link ( $\sim 119$  km separation) reduces the technique's utility for phase-correcting meteor observations. Without reasonable coverage of the phase corrections in azimuth and zenith, empirical techniques may provide more favourable results (exactly how much coverage is needed has not been determined, but the superior performance offered from the coverage of the BP and Mylor results is a reasonable guide).

The sparseness of these returns appears to be caused by a combination of low aircraft echo SNRs, contamination from range-coincident aircraft, and interference from the ground wave. It is highly likely that any bistatic system with a similar or larger transmitter-receiver separation would encounter the same issues. The low SNRs for high-range aircraft may be an inherent limitation of the technique that cannot be resolved without receivers with more favourable noise characteristics. However, as discussed in Sect. 5.9, the effects of range-coincident aircraft and/or ground wave contamination may be able to be remedied by synthesizing them and subsequently removing them from the measured time series.

## Chapter 7

# Conclusion

### 7.1 Thesis summary and conclusions

This thesis has been concerned with measuring the momentum transport arising from the breaking of gravity waves in the upper part of the Mesosphere Lower Thermosphere/Ionosphere (MLT/I;  $\sim 80$ -90 kilometres altitude) using a multistatic configuration of meteor radars. In the interests of improving the quality of these measurements for future analyses, a novel phase calibration technique based on the use of aircraft was also developed. This method overcame most of the deficiencies in the widely-adopted method that had been used previously.

The general motivation for measuring momentum transport in the MLT/I arises from the important role the transport plays in controlling the circulation of this part of the atmosphere, and the need for it to be correctly represented in global circulation models (GCMs). At present, progress remains to be made in incorporating observations of the momentum deposition associated with small-scale, high-frequency gravity waves in GCMs, and its dependence on location. This problem continues to motivate observational studies of gravity waves in the MLT/I, from both satellites (for the purposes of obtaining global climatologies) and ground-based instruments such as radar and lidar (to monitor the wave activity at a fixed location).

A particular problem that this thesis investigated was the coupling between tides and gravity waves that occurs as a result of the momentum deposition arising from gravity wave breaking (specifically the vertical flux of horizontal momentum, and loosely referred to here as a “momentum flux”) and the critical level filtering of gravity waves imposed by the wind variability associated with the tides. A key motivation of this was to help address the well-known gap in understanding the importance of gravity waves in



modulating the tides, and the disparity among the few observational studies of this. As was discussed in Chapter 1, ground-based instrumentation is well-suited to addressing this problem, given the need to observe such an interaction over many tidal oscillations at a fixed location.

A ground-based meteor detection radar consisting of a monostatic radar and a bistatic receiver (both located in the vicinity of Adelaide, South Australia) was used in this study to perform these observations. At the time, this radar was one of the few in the emerging class of meteor radars worldwide incorporating a bistatic receiver. Measuring winds and the vertical flux of horizontal momentum gravity wave activity using a bistatic receiver is more complex than in the conventional monostatic case, and accordingly a detailed overview of the bistatic reception geometry and wind covariance measurement approach was provided in Chapters 2 and 3. In particular, this study was the first to incorporate a bistatic meteor radar in measurements of gravity wave momentum deposition in the MLT/I.

Prior to the tidal interaction study, it was necessary to obtain a rough idea of what the uncertainties in the momentum flux estimates would be. This was done via a Monte Carlo simulation of the measurement process that emulated the radar spatial/temporal sampling characteristics as closely as possible to those associated with the observational study. The assessment of the measurement process was motivated by a number of earlier studies which showed the difficulty in measuring the fluxes with a sufficient level of accuracy and precision even with averaging times in the vicinity of one month (and some claimed that it was practically impossible to measure for the radar systems they tested). The results of the assessment were presented in Chapter 3. It was shown that for a typical momentum flux magnitude ( $20 \text{ m}^2\text{s}^{-2}$ ) and for a gravity wave spectrum based on climatological data, relative uncertainties of  $\sim 75\%$  were obtained for the monostatic system, and  $\sim 65\%$  for the multistatic. It was also found that the increase in precision associated with the inclusion of the bistatic receiver was essentially only due to the increase in meteor detections—in other words, having multiple viewing perspectives was in itself of no benefit to the flux estimation.

Another important result of Chapter 3 was the dependence noted in the momentum flux estimation uncertainty on the complexity of the gravity wave spectrum being sampled (for a 1-day integration, a relative uncertainty of  $\sim 65\%$  was obtained for a spectral model-derived wave field, and  $\sim 8\%$  for a wave field consisting of solely monochromatic waves). The same conclusion has been reached in previous studies. Essentially, this

result makes it difficult to accurately gauge the uncertainty of a momentum flux estimate derived from real data. As a compromise, we concluded that the uncertainties in the 1-day integrated results in Chapter 4 would lie somewhere between these extremes. The 10-day uncertainties would likely be close to those obtained in the simulation study, given the likelihood of a diverse spectrum of waves being observed over this period.

The tidal interaction study, presented in Chapter 4, was based around a 20-day interval in which the diurnal tide above Adelaide experienced a significant amplitude enhancement lasting several days. It was hypothesized that such a transient event may have been caused by gravity wave forcing. The study showed a complex relationship between the phase of the forcing and the tidal winds. The most significant findings were (1) an indication that the tidal amplitudes had generally been dampened by wave activity between about 88 and 92 km, but (2) that the tide had been enhanced between about 4 and 6 hours UT. The interesting aspect of the second finding is that it coincides with the time of the maximum zonal wind velocity (which was observed to obtain an unusually large maximum value of  $\sim 140 \text{ ms}^{-1}$  during the enhancement), and according to GSWM-00 model temperature predictions, the time at which the atmosphere was most unstable and gravity wave breaking was most likely to occur. The findings illustrate the need to further study the cause of transient fluctuations in tidal amplitudes.

The model developed in Chapter 3 was also used to provide an estimate of the momentum flux uncertainties in the 20-day integrated composite day case. From these results, we concluded that the signal component in the observed momentum fluxes and derived gravity wave forcing estimates would have significantly exceeded the measurement errors. We are therefore confident that the complex nature of the correlation between the gravity wave forcing and the tidal winds was not influenced by random measurement errors.

In both Chapters 3 and 4 it was verified that the most significant contributors to momentum flux estimation errors (necessitating long integration times) are 1) meteor detection rates and 2) the presence of large radial velocity errors/anomalous estimates due to transient turbulence activity. Low meteor detection rates result in larger random errors in momentum flux estimates, while radial velocity outliers can significantly bias the estimates. A rudimentary outlier rejection scheme was introduced in Chapter 3 (and applied in Chapter 4) to limit the effect of anomalous radial velocity estimates. Simulations in Chapter 3 showed that this method significantly reduces the momentum flux estimation uncertainties. However, the method was empirical, with an arbitrarily chosen

outlier rejection threshold. It was deemed preferable to try to reduce the probability of these radial velocity outliers occurring in the first place.

It is well known that receiver phase calibration errors that are not correctly compensated for may significantly impede the accuracy of angle-of-arrival (AOA) estimates from meteor radars (as discussed in Chapter 2, the AOA estimates can be aliased into the wrong quadrant of the sky). This in turn leads to the same issues affecting momentum flux estimation accuracy mentioned above: altitude estimation errors (resulting in fewer meteors available in a given altitude bin), and radial velocities being assigned to the incorrect AOA. Given the complex nature of the phase signature that can arise from mutual coupling between receivers and signal multipath, phase calibration errors may also be larger at some AOAs relative to others. Existing empirical phase calibration techniques are able to partially remedy the situation by removing the mean (across AOA) receiver channel phase errors, but cannot compensate for an AOA dependence in the errors.

Fortuitously, the Adelaide-based multistatic meteor radar operates in an environment where there is an abundance of VHF-radar-detectable commercial aircraft that transmit their GPS-derived positions via ADS-B transponders. In Chapter 5, a method that exploits the known AOA of the aircraft echoes to correct for phase calibration offsets was developed. When applied to approximately two weeks of aircraft detections from the Adelaide-based system, the method showed that there were significant phase offsets (with absolute values up to  $\sim 50^\circ$ ) at certain AOAs. When applied to meteor detections over the same period, the phase corrections resulted in a  $\sim 2\text{-}3\%$  increase in the number of meteor detections assigned to physically reasonable altitudes, and also led to smaller height distribution widths than those obtained from the empirical technique. This was clear evidence that its performance was superior to the empirical technique. A preliminary investigation of the same approach on two multistatic radars was also conducted, with results shown in Chapter 6; while there is potential for good-quality phase calibration offsets to be derived for these systems as well, the investigation highlighted the need for separating the range-coincident echoes that would typically be encountered in areas with very dense air traffic. Such processing was not performed in this work.

Provided the radar in question is in a region in which detectable aircraft traverse a large range of AOAs, the aircraft-based phase calibration technique is at the very least an excellent supplement to pre-existing phase calibration techniques. Its key strengths are the accuracy of the derived phase offsets, the low cost of the ADS-B receiver required for

its implementation, and the fact that it can be used to diagnose sources of phase errors that arise anywhere in the echo reception process—including through antenna cables and from the mutual coupling between antennas. The technique may also be implemented with radar parameters optimised for detecting meteors—i.e., it may simply be run in the background of a routine operating mode. Another particularly appealing aspect of the approach is that it is applicable to practically any spaced antenna/multifrequency radar operating in the MF-UHF band.

## 7.2 Suggestions for future work

It was noted above that there is presently a poor understanding of the role gravity waves play in modulating tidal amplitudes and phases. Meteor radars have the potential to provide observational support to this problem provided suitable integration times are used for the associated gravity wave momentum flux estimates. However, notwithstanding the measurement uncertainties and the impacts of phase calibration errors discussed at length in this thesis, two significant problems in the interpretation of momentum flux estimates from these observations remain.

The first concerns the “contamination” of the observed gravity wave spectrum by the tidal oscillations themselves. It is well-known that an attempt should be made to filter these oscillations from a wind time series prior to the momentum flux estimation. However, given the temporal variability in tidal amplitudes and phases with time, it is difficult to design a filter to completely remove them from a time series without removing some of the underlying gravity wave activity. This was evidenced in the simulated performance of the high-pass wavelet filter approach employed in this thesis: the filter was able to remove tides with amplitude and phase variability, but resulted in the underestimation of the gravity-wave-induced momentum fluxes. Fortunately, this is not a problem if only high frequency gravity waves (periods of less than  $\sim 3$  hours) are of interest. As a preliminary, future work in this area could simply be to observe if there are significant changes in the gravity wave forcing as a function of the wavelet bandpass filter frequencies. Further input from the modelling community on the specific gravity wave periods of interest would also be useful in this regard.

The second concerns the outlier rejection scheme applied in this work to the radial velocity-AOA pairs used to estimate the momentum flux. Despite being effective in reducing the momentum flux estimation uncertainty, this scheme would have precluded measurements which were associated with real wind perturbations arising from high

amplitude gravity wave activity or turbulence. The scheme should be modified to account for the expected shape of the radial velocity residual distribution for a typical distribution of gravity waves within the observed volume. As an aside, it may also be worthwhile to further investigate the nature of the wave events that are associated with significant variability in the size of wind perturbations with position/time in a given analysis window.

A related avenue for future work is the use of weights in the inverse equation associated with the momentum flux estimation. Rather than a hard exclusion of anomalous radial velocity-AOA pairs, it may be more prudent to apply a weighting factor based on their deviation from the expected radial velocity perturbation distribution. Such a weighting scheme may also prove useful in the wind estimation—as yet, the effect of using meteors close to the zenith (which are associated with larger horizontal wind uncertainties) has not been quantified.

To optimize the performance of the aircraft-based phase calibration approach—especially in the case of it being used on radars with different transmitter-receiver baselines and air traffic distributions from those in this work—a number of modifications to the method are needed. The most critical of these is to filter out aircraft echoes that are range-coincident with the one being “tracked” for phase calibration estimates. Assuming the contaminating aircraft(s) has a known AOA and Doppler velocity, a substantial improvement may be able to be achieved by synthesizing the signal associated with it and removing it from the time series.

Other potential areas for significant improvement to the method include removal of the transmitter ground pulse (applicable for bistatic receivers), weighting the phase correction estimates based on the amplitudes, and using a more robust scheme to preclude anomalous correction estimates. Minor improvements may also be obtained by implementing a scheme to detect and remove suspect/corrupted aircraft position estimates, and also by weighting the Doppler velocity discrepancies to lower zenith angles (noting that in the presence of a time offset, aircraft at low zenith angles lead to highest errors in phase correction estimates). Finally, depending on the interference environment, an interference removal scheme may also be necessary for increasing the AOA-coverage of the aircraft present and for reducing the uncertainty in the phase offset estimates.

## Appendix A

# Frequency-domain phase calibration of Buckland Park ST radar data

This Appendix shows exemplar results of a frequency-domain phase calibration technique applied by the author to multi-frequency data from the Buckland Park Stratosphere-Troposphere radar. It has been shown here to illustrate the frequency dependence of phase calibration offsets that is typical of atmospheric VHF radars, and also to provide an example of a problem that the aircraft-based phase calibration technique introduced in Chapter 5 should be able to address.

### A.1 Introduction

In much the same way as the phase difference estimates from spaced antennas may be used to measure the AOA of a target within a broad transmit beam, phase differences at spaced frequencies may be used to measure the target's range within the radar pulse width. Both of these principles may also be used simultaneously to carry out 3D imaging (see e.g., Yu [2000] for an excellent theoretical overview). The appeal of using multiple frequencies is that, for the same radar bandwidth, considerably higher precision in range can be obtained through the use of appropriate beamforming methods than by simply narrowing the radar pulse width. In the atmospheric radar community, the approach has its roots in the Frequency Domain Interferometry technique (FDI) introduced by Kudeki and Stitt [1987], which was applied to the estimation of the width of atmospheric scattering layers. The same idea was later extended to more general beamforming methods by Palmer et al. [1999] and Luce et al. [2001], who used it to provide high-resolution images of the vertical structure of scattering layers in the lower atmosphere.

As per the angular beamforming case in (5.6), the “range-beamformed” power as a

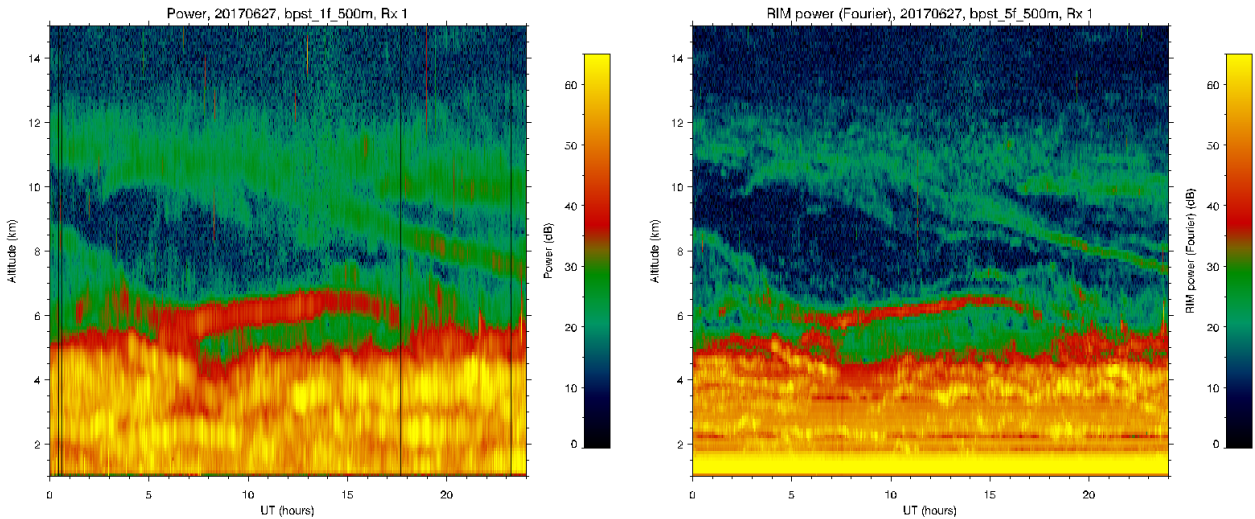


Fig. A.1: A comparison of one day of range-imaged results from the BP ST, for a pulse length of 500 m. The plot on the left contains results for a single frequency, and on the right, five equally spaced frequencies spanning a 500 kHz bandwidth.

function of range  $r$  in the standard Fourier beamforming case is given by:

$$B(r) = \mathbf{w}^\dagger \mathbf{R} \mathbf{w}, \quad (\text{A.1})$$

where the components of the covariance matrix  $\mathbf{R}$  are given by:

$$\mathbf{R}_{ij} = \text{cov}[\mathbf{x}_i, \mathbf{x}_j] = \frac{1}{N} \sum_{k=1}^N (x_{ik} - \mu_i)(x_{jk} - \mu_j)^*, \quad (\text{A.2})$$

where  $x_{ik}$  is the  $k$ th element of the time series received at the  $i$ th frequency,  $\mu_i$  is the mean of the  $i$ th time series, and  $N$  is the number of time series. The weighting vector  $\mathbf{w}$  is given by:

$$\mathbf{w}^\text{T} = \left[ e^{i2\pi f_1 r}, \dots, e^{i2\pi f_N r} \right], \quad (\text{A.3})$$

where  $f_i$  is the radar frequency associated with the  $i$ th time series, and  $r$  is the range at which the power is to be computed. An example of the results of this procedure on data from the BP ST radar are shown in Fig. A.1.

Propagation delays through the transmission lines and changes in response of the receiver electronics due to environmental effects introduce phase biases to the acquired signals that may have a frequency dependence. As per the case of spatially-dependent phase biases causing AOA estimation errors, frequency-dependent phase biases can result in errors in the sub-pulse width power estimates afforded by the range beamforming.

In the atmospheric radar community, the presence of these biases has been noted by a

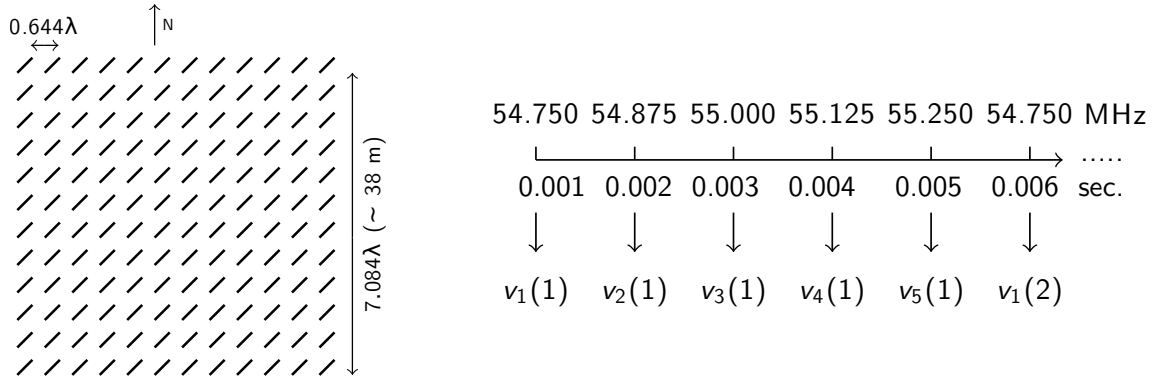


Fig. A.2: The layout of the ST array at BP (left) and the timing of the different frequencies used in the multifrequency experiment.

number of authors (e.g., Kilburn et al. [1995], Luce et al. [2001], Chen [2004], Fernandez [2004]). Chen [2004] in particular introduces an approach for empirically estimating the phase biases for each frequency. The approach exploits the fact the measured phase difference for a given frequency pair (termed the “FDI phase”) should be offset from the true value by the same amount for a target at any range. Following their formulation, the FDI phase is given by:

$$\theta = 2(k_i - k_j)r + (\phi_j - \phi_i), \tag{A.4}$$

where  $k_i$  and  $k_j$  are the wavenumbers for the  $i$ th and  $j$ th frequencies,  $r$  is the scattering layer range, and  $\phi_i$  and  $\phi_j$  are the phase offsets associated with channels  $i$  and  $j$ .

Provided that the range to the scattering layer is known accurately, this approach may be used to directly estimate the phase offset. In practice however, random error in the  $\theta$  estimates (arising from both measurement noise as well as the finite pulse and scattering layer width) make it necessary to average the  $\theta$  estimates over many samples in both time and range. We use this approach in this Appendix to phase-calibrate a sample of data from the Buckland Park Stratosphere-Troposphere (ST) radar.

## A.2 Experiment configuration

A number of multifrequency experiments were trialled on the BP ST radar during 2017. The data shown here was collected from the BP ST radar during a campaign run during April 2017, in which a 250 m transmit pulse was used, with five evenly-spaced, sequentially-transmitted frequencies spanning a bandwidth of 500 kHz between 54.75 and 55.25 MHz. A PRF of 10 kHz was used, and 10 coherent integrations were performed on each received frequency before switching to the next frequency in the sequence.



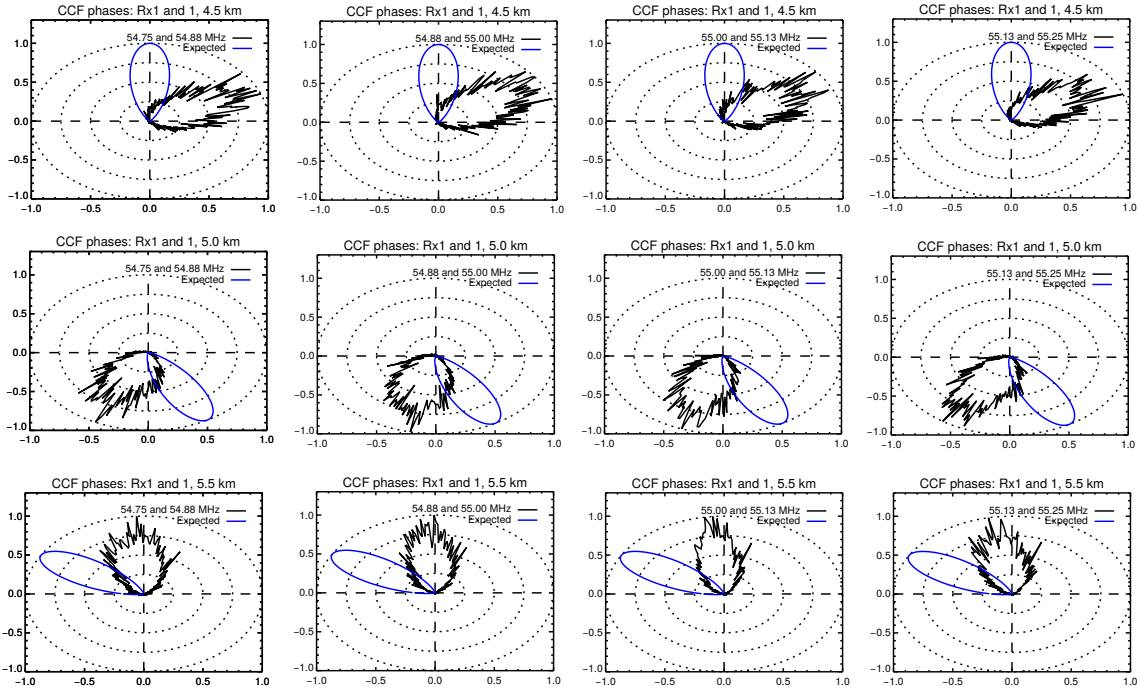


Fig. A.3: Sample phase offsets as a function of frequency difference for data collected from the multifrequency experiment on 23-Apr 2017. Results from 4.5 km range are shown in the top panel, 5.0 km in the middle, and 5.5 km in the lower. The blue lobe shows the expected distribution of phase offsets given the frequency difference pairs and echo range, and the histogram of the collected data is shown in black.

The antenna layout of the radar (technical details of radars of this type are described in Dolman et al. [2018]) along with a diagram of the sequence of transmitted/received frequencies is shown in Fig. A.2.

### A.3 Results and conclusions

Figure A.3 shows the distribution of phase differences measured between each sequential frequency pair at three selected heights, along with the predicted phase distribution based on the range and radar pulse length used. The distributions correspond to a single day of data, with a phase difference recorded for each minute-long acquisition. A fixed offset between the measured and predicted values for each frequency pair is evident. The cause of this offset has not been investigated. Phase corrections were estimated as the mean of each distribution, and were applied by simply adding the offset to the time series of the corresponding frequency.

Power profiles associated with the constituent single-frequency time series and the range-imaged results without without the corrections applied are shown in the left panel

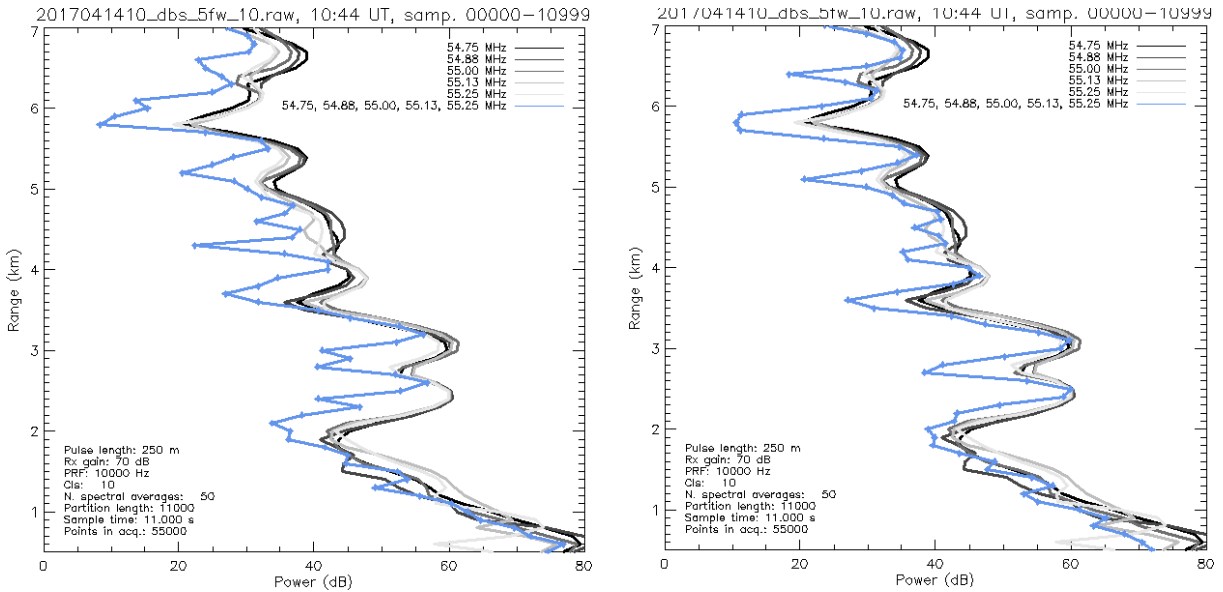


Fig. A.4: An example of the effect of the phase correction offsets on a range-power profile from the BP ST (left: no corrections, right: with corrections). Returns from each constituent frequency are shown in different shades of grey, with the range-imaged profile shown in blue.

of Fig. A.4. These profiles were integrated over a single 55 second acquisition on 23-Apr 2017. Interestingly, the range-imaged power profile is offset from the single-frequency profiles by approximately 200 m, and also shows what appears to be noise-like fluctuations at some ranges.

The range-imaged profile with the corrections applied is shown in the right panel of Fig. A.4. The range offset is essentially removed, and there are also less noise-like fluctuations in the profile.

These results verify that the statistics of echoes from atmospheric scattering layers recorded at different frequencies may be able to be used to compensate for any phase calibration errors between the corresponding multi-frequency recordings. It simply requires that an accurate radar range calibration be in place, and the assumption that returns on average come from the centre of the range gates. A downside of the approach is that it does not work effectively for large frequency separations and/or large pulse lengths. This is due to both the loss of coherence between signals with a large frequency separation, and the fact that returns can occur at large distances (and hence at large FDI phases) from the centre range of the pulse. This problem may be alleviated by using echoes from aircraft with known ranges (i.e., by using the phase calibration approach applied in Chapter 5).

## Appendix B

# WGS-84 ellipsoid coordinate transformations

The WGS-84 ellipsoid model of the Earth has been used in this thesis to represent meteor and aircraft locations. A number of coordinate transformations were required to calculate geodetic heights, latitudes and longitudes from an input range and AOA in local Cartesian coordinates, and vice versa. This appendix outlines these and the WGS-84 ellipsoid parameters.

The coordinate systems and variables used are defined as follows:

- Range-AOA: The usual local polar coordinates used for radar systems;  $R$  (range),  $\theta$  (zenith angle), and  $\phi$  (azimuth angle).
- East-North-Up (ENU): Local Cartesian coordinates  $(x, y, z)$  with origin at an arbitrary location on the Earth.  $x$  is parallel to the local  $\hat{\lambda}$ ,  $y$  to the local  $\hat{\phi}$ , and  $z$  to the local  $\hat{r}$ .
- Earth-centred, Earth-fixed (ECEF): Cartesian coordinates  $(X, Y, Z)$  with origin at the Earth's centre.
- Geodetic: distance from Earth's centre ( $r$ ), latitude ( $\varphi$ ), and longitude ( $\lambda$ ).

### B.1 WGS-84 ellipsoid parameters

The WGS-84 ellipsoid defines the semi-major axis of the Earth  $a$  as 6378137.0 m, and the semi-minor axis  $b$  as 6356752.3142 m. Quantities defined henceforth are the

“flattening” parameter  $f$ , the eccentricity squared  $e^2$ , the second eccentricity squared  $e'^2$ , and the radius of curvature of the Earth  $N$ :

$$\begin{aligned} f &= \frac{a-b}{a} \\ e^2 &= 2f(1-f) \\ e'^2 &= \frac{a^2-b^2}{b^2} \\ N &= \frac{a}{\sqrt{1-e^2\sin^2\phi}}. \end{aligned}$$

## B.2 Range-AOA $\leftrightarrow$ ENU (East-North-Up)

Range-AOA coordinates  $(r, \theta, \phi)$  may be transformed to ENU coordinates  $(x, y, z)$  via the equations:

$$\begin{aligned} x &= r \sin \theta \sin \phi \\ y &= r \sin \theta \cos \phi \\ z &= r \cos \theta, \end{aligned}$$

with the inverse transformation:

$$\begin{aligned} r &= \sqrt{x^2 + y^2 + z^2} \\ \theta &= \cos^{-1}(z/r) \\ \phi &= \text{atan2}(x, y). \end{aligned}$$

## B.3 ENU $\leftrightarrow$ ECEF

The ECEF coordinates of a location with ENU coordinates defined with respect to a geodetic position  $(r, \varphi, \lambda)$  with ECEF coordinates  $(X_0, Y_0, Z_0)$  may be evaluated via the matrix equation:

$$\begin{bmatrix} X \\ Y \\ Z \end{bmatrix} = \begin{bmatrix} -\sin \lambda & -\sin \varphi \cos \lambda & \cos \varphi \cos \lambda \\ \cos \lambda & -\sin \varphi \sin \lambda & \cos \varphi \sin \lambda \\ 0 & \cos \varphi & \sin \varphi \end{bmatrix} \begin{bmatrix} x \\ y \\ z \end{bmatrix} + \begin{bmatrix} X_0 \\ Y_0 \\ Z_0 \end{bmatrix}.$$

The inverse is to find the ENU coordinates of a location with ECEF coordinates  $(X,$

$Y, Z$ ) defined with respect to a geodetic position  $(r, \varphi, \lambda)$  with ECEF coordinates  $(X_0, Y_0, Z_0)$ . The matrix equation for this is:

$$\begin{bmatrix} x \\ y \\ z \end{bmatrix} = \begin{bmatrix} -\sin \lambda & \cos \lambda & 0 \\ -\sin \varphi \cos \lambda & -\sin \varphi \sin \lambda & \cos \varphi \\ \cos \varphi \cos \lambda & \cos \varphi \sin \lambda & \sin \varphi \end{bmatrix} \begin{bmatrix} X - X_0 \\ Y - Y_0 \\ Z - Z_0 \end{bmatrix}.$$

#### B.4 Geodetic $\leftrightarrow$ ECEF (Earth-centred, Earth-fixed)

ECEF coordinates  $(X, Y, Z)$  may be transformed to geodetic coordinates  $(r, \varphi, \lambda)$  via the equations:

$$\begin{aligned} X &= (N + z) \cos \varphi \cos \lambda \\ Y &= (N + z) \cos \varphi \sin \lambda \\ Z &= (N + z - e^2 N) \sin \varphi. \end{aligned}$$

The inverse transformation is not straightforward. As discussed by Stober et al. [2018], a number of methods are available to do this. We have used the method published by Olson [1996], noting that it involves less computational overhead but equivalent performance to the Heikkinnen [1982] method used by Stober et al. [2018].

Starting with the ECEF coordinates  $(X, Y, Z)$ , the Olson [1996] method for obtaining the geodetic coordinates  $(r, \varphi, \lambda)$  is as follows:

$$\begin{aligned} A_1 &= ae^2 \\ A_2 &= Ae^2 \\ A_3 &= 2.5A_2 \\ A_4 &= A_1 + A_2 \\ A_5 &= 1 - e^2 \\ W^2 &= X^2 + Y^2 \\ R_1^2 &= Z^2 + W^2 \\ S_2 &= Z^2/R_1^2 \\ C_2 &= W^2/R_1^2 \\ U &= A^2/R_1 \\ V &= A_2 - A_3/R_1. \end{aligned}$$

If  $C_2 > 0.3$ , the following is evaluated:

$$S_1 = \frac{|Z|}{R_1} \left( 1 + \frac{C_2(A_1 + U + VS_2)}{R_1} \right)$$

$$\varphi = \text{asin}(S_1)$$

$$C_1 = \sqrt{1 - S_1^2}.$$

If  $C_2 \leq 0.3$ , the following is evaluated:

$$C_1 = \frac{W}{R_1} \left( 1 - \frac{S_2(A_4 - U - VC_2)}{R_1} \right)$$

$$\varphi = \text{acos}(C_1)$$

$$S_1 = \sqrt{1 - C_1^2}.$$

The remaining steps are:

$$G = 1 - S_1^2 e^2$$

$$R_G = a / \sqrt{G}$$

$$R_F = A_5 R_G$$

$$U = W - R_G C_1$$

$$V = |Z| - R_F S_1$$

$$F = C_1 U + S_1 V$$

$$M = C_1 V + S_1 U$$

$$P = \frac{M}{R_F / G + F}.$$

Finally,

$$r = F + MP/2$$

$$\varphi \rightarrow \varphi + P$$

$$\lambda = \text{atan2}(Y, X).$$

If  $Z < 0$ , then the correction  $\varphi \rightarrow -\varphi$  is applied.

## B.5 Geodetic ↔ Transverse Mercator

To consistently represent horizontal distances along the Earth’s surface with respect to some reference site in this study, Transverse Mercator coordinates have been used.

The method introduced by Bowring [1989] has been used to perform the conversion between these coordinates and object positions defined as a latitude/longitude pair. For completeness, the method is outlined here.

A geodetic latitude and longitude (denoted by  $\varphi$  and  $\lambda$ , respectively) can be transformed into “Easting” ( $E$ ) and “Northing” ( $N$ ) Transverse Mercator coordinates with respect to some reference latitude/longitude pair  $(\varphi_0, \lambda_0)$  as follows:

$$\begin{aligned}
 n &= \frac{a-b}{a+b} \\
 \psi &= \operatorname{atan2}(\tan \varphi (1-n), 1+n) \\
 p &= 1 - \frac{3}{4}n \cos 2\psi \\
 q &= \frac{3}{4}n \sin 2\psi \\
 Z &= \left(1 - \frac{3}{8}n^2\right) (p + qi)^{2/3} \\
 \theta &= \psi - \Im(Z) \\
 m &= \frac{a\theta (1 + n^2/8)^2}{1+n} \\
 c &= \cos \varphi \\
 s &= \sin \varphi \\
 \omega &= \lambda - \lambda_0 \\
 \nu &= a \sqrt{\frac{1+e'^2}{1+e'^2c^2}} \\
 z &= \frac{e'^2\omega^3c^5}{6} \\
 \theta_2 &= \operatorname{atan2}(2sc \sin^2(\omega/2), s^2 + c^2 \cos \omega) \\
 E &= \nu \left[ \tanh^{-1}(c \sin \omega) + z \left(1 + \frac{\omega^2}{10} (36c^2 - 29)\right) \right] \\
 N &= m + \nu\theta_2 + \frac{z\nu\omega s}{4} (9 + 4e'^2c^2 - 11\omega^2 + 20\omega^2c^2)
 \end{aligned}$$

where  $i = \sqrt{-1}$ , and  $\Im$  is the imaginary operator. Note that the  $a$ ,  $b$  and  $e'^2$  variables are as defined in previous sections, and  $z$  is a re-definition of a previous one. The inverse transformation, which is to calculate  $\varphi$  and  $\lambda$  from  $N$  and  $E$  defined with respect to a reference latitude longitude pair  $(\varphi_0, \lambda_0)$ , is done as follows:

$$\begin{aligned}
 N &\rightarrow N + N_0 \\
 \theta &= \frac{N(1+n)}{a(1+n^2/8)^2}
 \end{aligned}$$

$$\begin{aligned}
 p &= 1 - \frac{33}{20} n \cos 2\theta \\
 q &= \frac{33}{20} n \sin 2\theta \\
 Z &= \frac{5}{4} \left( 1 - \frac{9}{16} n^2 \right) (p + qi)^{8/33} \\
 \psi &= \theta + \Im(Z) \\
 \phi &= \text{atan2}((1 + n) \tan \psi, 1 - n) \\
 c_1 &= \cos \phi \\
 s_1 &= \sin \phi \\
 \nu_1 &= a \sqrt{\frac{1 + e'^2}{1 + e'^2 c_1^2}} \\
 z &= \frac{E}{\nu_1} \\
 \theta_4 &= \text{atan2}(\sinh E, c_1) \\
 \theta_5 &= \tan \phi \cos \theta_4 \\
 \varphi &= (1 + e'^2 c_1^2) \left[ \theta_5 - \frac{e'^2}{24} E^4 \tan \phi (9 - 10c_1^2) \right] - e'^2 c_1^2 \phi \\
 \omega &= \theta_4 - \frac{e'^2}{60} E^3 c_1 \left( 10 - \frac{4E^2}{c_1^2} + E^2 c_1^2 \right) \\
 \lambda &= \omega + \lambda_0.
 \end{aligned}$$



## Appendix C

**Publication: Radio Sci., 55, e2019RS006873,  
2020**

This paper presents an investigation of the capability of a Tx-steerable VHF wind profiling radar (the Buckland Park ST radar) to detect objects in low-Earth orbit. The author of this thesis contributed to the design of radar experiments with parameters optimized for object detection, to the development of a utility to schedule particular experiments to sample the objects, and to the interpretation of the object echoes.

# Radio Science

## RESEARCH ARTICLE

10.1029/2019RS006873

## Low Earth Orbit Object Observations Using the Buckland Park VHF Radar

David A. Holdsworth<sup>1,2</sup>, Andrew J. Spargo<sup>2</sup>, Iain M. Reid<sup>2,3</sup>, and Christian Adami<sup>3</sup>

<sup>1</sup>Intelligence, Surveillance and Space Division, Defence Science & Technology Group, SA, Australia, <sup>2</sup>School of Physical Sciences, University of Adelaide, Adelaide, SA, Australia, <sup>3</sup>ATRAD Pty. Ltd, SA, Australia

### Key Points:

- A low-cost VHF wind profiling radar has been deployed for observing objects in low Earth orbit
- Over 15 days, 2,410 objects were detected, with 1,392 unique objects detected
- The radars utility for catalog maintenance is demonstrated through observations of the Tiangong-1 satellite in its last months in orbit

### Correspondence to:

D. A. Holdsworth,  
david.holdsworth@dst.defence.gov.au

### Citation:

Holdsworth, D. A., Spargo, A. J., Reid, I. M., & Adami, C. (2020). Low Earth Orbit Object Observations Using the Buckland Park VHF Radar. *Radio Science*, 55, e2019RS006873. <https://doi.org/10.1029/2019RS006873>

Received 1 MAY 2019

Accepted 20 DEC 2019

Accepted article online 2 JAN 2020

**Abstract** There is increasing interest in space situational awareness worldwide, motivating investigation of the use of nontraditional sensors for space surveillance. This paper presents preliminary results investigating the use of a VHF wind profiling radar for observing objects in low Earth orbit. This radar class is low cost relative to other radars typically applied to this task. The results reveal that 2,410 objects were detected over 15 days, with 1,392 unique objects detected. The daily detection count rates ranged from 150 to 200, and the maximum detection height observed was 2,491 km. The radar's utility for object catalog maintenance is demonstrated by its ability to determine propagation state vector errors, and through observations of the Chinese space station Tiangong-1 in the last months of its return to Earth. The results suggest the measurements may be able to provide useful ionospheric parameters such as total electron content (TEC) measurements, provided high precision ephemeris data are available for the detected objects.

**Plain Language Summary** There is increasing interest in space situational awareness due to the rapidly increasing number of objects in orbit. This has motivated investigation of the use of instruments that were not designed for space surveillance for this purpose. This paper presents preliminary results describing the use of a low-cost VHF radar designed for lower atmosphere wind measurements to observe space objects. The results reveal that 2,410 objects were detected over 15 days, with 1,392 unique objects detected. The daily detection count rates ranged from 150 to 200, and the maximum detection height observed was 2,491 km. The radar's ability to verify the prediction accuracy of object position and dynamics is demonstrated, focusing on observations of the Chinese space station Tiangong-1 in the last months of its return to Earth. The results suggest the measurements may be able to provide useful ionospheric parameters such as total electron content (TEC) measurements, provided high precision predictions of object position and dynamics are available for the detected objects.

## 1. Introduction

There is increasing interest in space situational awareness (SSA) worldwide due to the increasing number of objects in orbit (Ash et al., 2018). This number has expanded rapidly in recent years due to the advent of cube-sats, which have provided a low-cost means of entry into satellite capability (Heidt et al., 2000). The increasing number of objects in orbit has led to renewed concerns over the so-called Kessler effect (Patel, 2015), a scenario in which the density of objects in low Earth orbit (LEO) is high enough that collisions between objects could cause a cascade where each collision generates space debris that increases the likelihood of further collisions.

The increasing interest in SSA in Australia is demonstrated by the recent installation of a C-band radar at Exmouth, Western Australia, and the future installation of an optical space telescope at a neighboring site (Smith et al., 2018). Defence Science and Technology (DST) Group have been directly involved in SSA research projects (Ash et al., 2018), including operation of an optical space telescope for use during solar terminator periods (Hobson et al., 2016). The use of nontraditional space sensors has also been investigated, such as event-based sensors (Cohen et al., 2017), an experimental HF line-of-sight (LOS) radar system (Frazer et al., 2013, 2014), and the Murchison Widefield radio astronomy array (MWA) (Tingay et al., 2013) for passive radar observations of satellite reflections from FM transmitters of opportunity (Palmer et al., 2017).

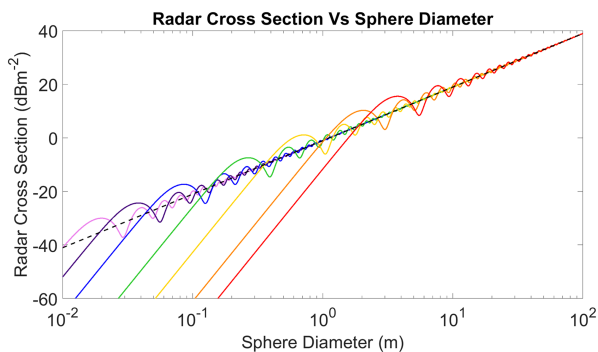


**Figure 1.** Radar cross-section V sphere diameter for various radars: DST HF LOS radar (30 MHz, red), BPST radar (55 MHz, orange), ALTAIR VHF (158 MHz, yellow) and UHF (422 MHz, green) radars, TRADEX L-band (1.32 GHz, blue) and S-band (2.95 GHz, indigo) radars, and ALCOR C-band radar (5.672 GHz, violet). The black dashed line indicates the physical optics approximation, which is equal to the projected area of a sphere.

The work presented in this paper aims to determine whether civilian atmospheric radars can also contribute to Australian SSA efforts, to further DST Group's understanding of LOS operations, and provide collaboration opportunities between and within DST Group and academia. Section 2 describes the characteristics of various space surveillance radars. Section 3 describes the Buckland Park stratosphere-troposphere (BPST) radar used in the current study, and initial observations using this radar to detect the International Space Station (ISS). Section 4 describes the analysis techniques developed for BPST satellite observations, while section 5 presents the satellite observations. An analysis of the implications of the results is presented in section 6. The paper closes with the conclusions.

## 2. Space Surveillance Radars

The Space Surveillance Network (SSN) is a network of sensors located at 20 sites worldwide. The SSN uses four primary types of sensors: mechanical (dish) radars, phased-array radars, space-based optical sensors, and the Ground-Based Electro-Optical Deep Space Surveillance (GEODSS) system.

The SSN radars mostly operate in the UHF range in order to obtain high sensitivity against small objects (<10 cm) (Hall et al., 2012). The sensitivity of various radars to different object sizes is demonstrated in Figure 1. A consequence for radars operating in the GHz range is that the radar cross section (RCS) varies significantly as the orientation of the (aspect sensitive) objects change relative to the radar, making it difficult to estimate true cross section from the observed RCS (Sato et al., 1991). At lower frequencies, the relationship between the physical cross section and the RCS simplifies, although this comes at the cost of reduced sensitivity for small targets. For instance, Figure 1 shows the RCS of a 20 cm diameter sphere is reduced by approximately 40 dB for a radar operating at 55 MHz (e.g., BPST radar: Rayleigh scatter) compared to 1.32 GHz (e.g., TRADEX L-band: Mie scatter).

There are various radars outside the SSN that have recently been commissioned or used for satellite observations. The European Space Agency (ESA) bistatic radar breadboard (Saillant & Flécheux, 2017) is a bistatic system located around Paris, northern France. It operates in the L-band for detection of space objects over a steerable field of regard defined as  $30^\circ$  in azimuth by  $25^\circ$  in elevation oriented preferably to the South. The demonstrator was designed to achieve detection of a reference target with an RCS of  $0 \text{ dBm}^2$  at a range of 500 km. The radar measures Doppler but not range: Detection is only based on Doppler measurement. DST Group operates an experimental bistatic high-frequency (HF) line-of-site (LOS) radar system (Frazer et al., 2013). Although the DST system was not designed or deployed for satellite observations, such observations provide a useful tool for verification and calibration purposes. The DST radar has been shown to detect satellites while deployed on defense trials, e.g., ISS (Frazer et al., 2013), Hubble Space Telescope (HST) (Frazer et al., 2014). The key findings from these observations are (1) the RCS of the ISS at 30 MHz is around  $50 \text{ dBm}^2$  (Frazer et al., 2013). This is significantly larger than the RCS estimates at microwave frequencies (McCant, 2017), illustrating that radars operating in the HF and lower VHF-band may provide advantages for observing large LEO objects, perhaps due to plasma-sheath effects, or resonance effects associated with the dimensions of the ISS (or its subcomponents) being comparable to the radar wavelength (Frazer & Williams, 2019); (2) HF LOS radars could be used for SSA of objects of “moderate size and ranges up to 1,000 km” (quoted from Frazer et al., 2014); (3) HF LOS radars can be used for orbit determination without using prior ephemeris information (Frazer et al., 2014); (4) due to positive range biases resulting from ionospheric group retardation effects, climatological electron densities and (ideally) ray tracing must be employed to correct the observed ranges and angles of arrival (Frazer et al., 2014).

There are also various atmospheric and ionospheric radars that have been used for satellite observations. The CAMRa radar is owned and operated by the U.K. Science and Technology Facilities Council and is located at Chilbolton in southern England (Eastment et al., 2011). CAMRa is a meteorological radar operating at S-band that has been modified for use as an experimental space surveillance sensor. It has a fully steerable 25 m dish antenna with a 0.28 degree beamwidth and a range resolution of approximately 75 m.

**Table 1**  
*Detection Sensitivity Figure of Merit and Field of View for Selected SSA Radars*

Radar	Figure of merit (dB)	Field of view	Tracking capability
ALTAIR VHF	36	Narrow	Yes
ALTAIR UHF	45	Narrow	Yes
TRADEX L-band	40	Narrow	Yes
TRADEX L-band	28	Narrow	Yes
MU Radar	18	Narrow	No
CAMRa	7	Narrow	Yes
DST HF LOS	4	Wide	No
BPST radar	-7	Narrow	No
ESA bistatic radar breadboard	-12	Wide	No

Antenna pointing is performed using two-line ephemeris (TLEs) and only the range is measured. The radar has previously been used successfully for the purposes of SSA, tracking LEO targets during two ESA tracking campaigns (Eastment et al., 2011). The Advanced Modular Incoherent Scatter Radar (AMISR) (Nicolls, 2015) is a modular, mobile UHF phased-array radar facility developed and used for scientific studies of the ionosphere. A satellite and debris tracking capability fully interleaved with scientific operations has been developed, and the AMISR systems are now used to routinely observe a large number of LEO space debris. The system detects LEO objects as small as 5–10 cm. The European Incoherent Scatter radar system (EISCAT) (Lehtinen et al., 2001) is an ionospheric research radar network operating in the ultra-high frequency band (UHF). EISCAT has detected objects down to 2 cm in size at rates of 347 per day. The Middle and Upper atmosphere (MU) radar is located at the Shigaraki Observatory of the Research Institute for Sustainable Humanosphere (RISH), Kyoto University, Japan. This radar operates at 46.5 MHz with an output power of 1 MW. The antenna array is a circular aperture of 100-m diameter, producing a beamwidth of 3.6°. The MU radar has similar sensitivity to the radars used for Air Force Space Command (AFSPC) catalog maintenance and has been deployed for space debris monitoring (Sato et al., 1991; Ikeda et al., 2017). The MAARSY mesosphere-stratosphere-troposphere (MST) is located in Andenes, Norway, and is operated by the Institute for Atmospheric Physics in Kühlungsborn, Germany. This radar has similar characteristics to the MU radar, operating at 53.5 MHz, with output power 800 kW, employing a circular aperture of 100-m diameter producing a beamwidth of 3.6°. MAARSY has performed satellite observations predominantly for radar calibration purposes (Renkwitz et al., 2013).

The key factors to consider when discussing radar SSA capabilities are the detection sensitivity, field of view, and tracking capability: i.e., beam steering to follow satellite trajectories. Table 1 summarizes these factors for some of the aforementioned radars. A common first-order detection sensitivity figure of merit (FoM) is the signal-to-noise ratio (SNR) of a target with 0 dBm<sup>2</sup> RCS at 1,000 km range from both the radar transmitter and receiver. The field of view can be regarded as wide (WFoV) or narrow (NFoV) field-of-view. WFoV radars typically employ interferometric or beamforming techniques and are capable of detecting multiple objects simultaneously. These radars are useful for new object detection and are difficult to design in a low-cost form factor. NFoV radars are typically high precision systems employing tracking capability and are cued by either a WFoV system or propagated state-vectors. The BPST radars is classified as NFoV but lacks the range resolution and tracking capability of many of the other NFoV systems described in Table 1.

In the context of discussing radar satellite observations, it is also worth mentioning that ground-based radars provide temporally persistent observations at any geographic location, while ground-based optical observations are dependent on clear atmospheric conditions.

Throughout this paper, we assume the typical radar convention that the radar location defines the coordinate system origin. The term “radial” therefore refers to components radial to the radar location rather than radial to the center of the Earth (i.e., Earth-centered coordinates).

### 3. The Buckland Park ST Radar

The Buckland Park Stratosphere-Troposphere (BPST) VHF radar ( $-34^{\circ} 37' 36.03''$ ,  $138^{\circ} 28' 3.91''$ ) is located 35 km north of Adelaide. The radar specifications are shown in Table 2. The radar is a pulsed mono-static

**Table 2**  
*BPST Radar Parameters*

Parameter	Value
Frequency, $f$ (MHz)	55
Maximum Transmit Power (kW)	40 (12 4 kW modules, i.e., 48 kW at the transmitter)
Maximum Duty Cycle (%)	10
Pulse Types	Monopulse, Barker & Complementary Codes
Receiver Filter Widths (kHz)	4, 8, 16, 32
Pulse-to-pulse Frequency Extent	$\pm 50$ kHz
Maximum Pulse Repetition Frequency (kHz)	20
Number of Transmit Antennas	144
Number of Receive Antennas	144 (Main array), 5 (Meteor array)
Combined Tx/Rx Main Array Beamwidth ( $^{\circ}$ )	4.6
Pulse Widths (m)	100-4000
Number of Receivers	6 (1-5: Meteor array, 6: Main array)
Range Sampling Resolution, $\Delta r$ (km)	0.05-2
Beam Directions (Azimuth, Zenith) (degrees)	(0, 0) "Vertical", (0, 15) "North", (90, 15) "East" (180, 15) "South", (270, 15) "West"

system operating at 55 MHz, with a peak transmit power of 40 kW. The radar was designed and manufactured by ATRAD and is operated by the University of Adelaide/ATRAD. The radar is designed primarily for measurement of tropospheric and stratospheric winds (0.5–20 km) (Dolman et al., 2018), although similar radars have been used to observe polar mesosphere summer/winter echoes (PMSE and PMWE) (Morris et al., 2004, 2011) at high latitudes. Identical systems (albeit with peak transmit power 80 kW) are deployed throughout Australia by the Bureau of Meteorology (Dolman et al., 2018).

The BPST radar transmit array consists of a  $12 \times 12$  array (hereafter referred to as the "main array") of gamma-matched linearly-polarized Yagi antennas. The inter-antenna spacing is  $0.606 \lambda$ , giving an aperture size of 24 by 24 m. The array allows 5-beam directions to be used: Vertical, and  $15^{\circ}$  off zenith in cardinal directions (North, East, South, West). Reception is performed using the main array and/or five interferometric Yagi antennas for meteor observations. The combined transmit/receive main array beam width is  $4.6^{\circ}$  degrees (half-power full-width). The maximum duty cycle is 10%. The radar employs GPS locking, allowing its transmissions to be received using an interferometric Yagi antenna array at Mylor (55 km South East of Buckland Park) for bistatic meteor observations (Spargo et al., 2019). The radar does not allow continuous operation, typically dwelling on a particular beam direction for 1–2 min, with 5 s "dead" time to allow for data transfer to the data acquisition and analysis PC.

The detection sensitivity figure of merit for the DST HF LOS radar and the BPST radar are shown in Table 2. These results suggest the DST HF LOS radar is around 7 dB more sensitive than that BPST radar. Given the DST HF LOS radar detected the ISS with an SNR in excess of 50 dB (Frazer et al., 2013), it follows that the BPST should also be able to detect the ISS when it passes through one of the five radar beams.

In order to determine the times of ISS transits through the BPST beams, SpaceTrack (<https://www.space-track.org>) TLE data were propagated using the Simplified Perturbations Model (SGP4), which computes the average path of the object through space. This analysis indicated the ISS was expected to transit the West and North beams of the BPST radar around 17:42 on 26/7/2017. A data collection was scheduled for these times using the parameters listed as "Parameter Set 1" in Table 3. The results of these observations are shown in Figure 2, illustrating the transit of the ISS through the radar beams. Note that the range

**Table 3**  
*Data Collection Parameters Sets Used for Each BPST Satellite Campaign*

Parameter	Campaign 1	Campaign 2	Campaign 3	Campaign 4
Date	2/8/2017	27/9/2018-30/9/2018	22/01/2018	07/07/2018-16/07/2018
Parameter set	2	3	4	4

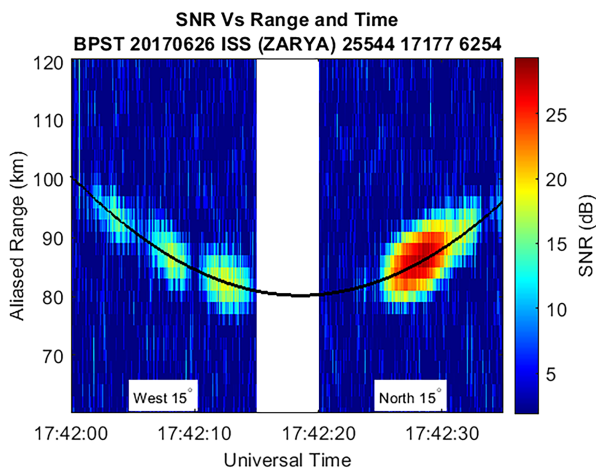


**Figure 2.** Range-time data illustrating observations of the ISS in the West (left) and North (right) beams of the BPST radar. The black line indicates the SGP4/NORAD TLE propagated range-time variation. The white gap indicates “dead” time required to allow for data transfer between the data acquisition and analysis PC.

ambiguity of 340.1 km results in the ISS being range aliased. The rapid amplitude fluctuation seen in the west beam may be attributable to either Faraday rotation effects due to the linear antenna polarization, or signal fading due to the coherent addition of signals reflected from different components of the ISS structure.

Despite the successful detection of the ISS, it was recognized that revised experiment parameters and a more sophisticated detection strategy using coherent processing techniques similar to those used by the DST HF LOS system would be required to allow detections of smaller LEO objects. The detection strategy is described in the following section.

A number of experimental campaigns have been conducted to collect satellite data to assess experiment parameters using the BPST radar, as listed in Tables 2 and 4. The experiment parameters were selected primarily for maximizing SNR rather than maximizing range resolution. Campaign 1 (Parameter Set 2) used the west beam as SGP4/NORAD TLE propagations suggested there would be more transits in this beam on the day of this campaign. Subsequent campaigns instead used the vertical beam. Further, after Campaign 1, it was realized that the range resolution could be improved by replacing

the 5-bit Barker code with 4 km resolution to a 13-bit Barker code with 2 km resolution and an increased receiver filter width without significantly compromising SNR. The range ambiguity results in most objects being range aliased, and the radial velocity ambiguity can lead to velocity aliasing. These ambiguities are not problematic for peak association with catalog objects as the object state vectors can be aliased appropriately. Campaign 4 was conducted in parallel with the Australian Defence “SpaceFest” trial. Although the BPST radar was not officially part of the SpaceFest trial, the Campaign 4 data collection was intended to provide collaboration opportunities between defense, academic, and industry partners.

To the best of our knowledge, the observations presented here represent the first explicit application of a VHF wind profiler with characteristics comparable to the BPST radar for satellite observations. Such radars typically employ spaced antenna (SA) or Doppler beam steering (DBS) techniques for estimating atmospheric winds (Dolman et al., 2018). These techniques do not require absolute power calibration, and such calibration has not been performed for the BPST radar. However, we note that similar radars have been calibrated, including the MST radar at Davis, Antarctica, which has been used to measure the RCS of PMSE (Latteck et al., 2007).

## 4. Analysis

### 4.1. Object Acceleration

The orbital velocity of a typical LEO object is around  $8 \text{ km s}^{-1}$ . A ground-based radar observing a LEO object will observe a significant increase in radial velocity (i.e., an acceleration) as the object transits the field of

**Table 4**  
Data Collection Parameters Used for BPST Satellite Observations

Parameter set	1	2	3	4
Pulse repetition frequency (Hz)	441	500	500	500
Range ambiguity (km)	340.1	300	300	300
Radial velocity ambiguity ( $\text{ms}^{-1}$ )	$\pm 80.9$	$\pm 91.7$	$\pm 91.7$	$\pm 91.7$
Pulse type	Mono-pulse	5-bit Barker	13-bit Barker	13-bit Barker
Pulse width (km)	4	4	2	2
Receiver filter width (kHz)	8	8	16	16
Minimum range (km)	10	24	30	30
Maximum range (km)	332	270	270	270
Range sampling resolution (km)	2	2	2	1
Azimuth, zenith (degrees)	(270, 15) (0, 15)	(270, 15)	(0, 0)	(0, 0)



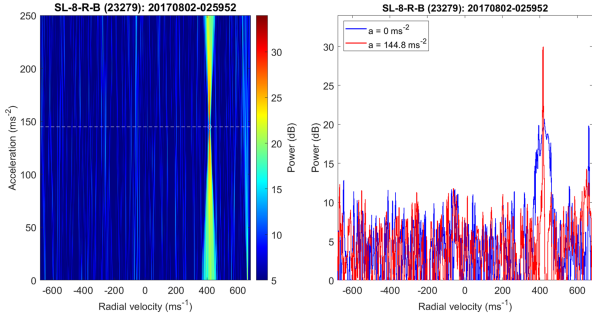


**Figure 3.** Example of acceleration processing using BPST radar data recorded during the passage of SL-R-B (NORAD ID 23279) around 2:52 Universal Time on 2nd August 2017. Left: Power Spectra as a function of input acceleration. The dotted line indicates the acceleration ( $144.8 \text{ ms}^{-2}$ ) yielding the maximum peak power. Right: Power spectra for accelerations of zero  $\text{ms}^{-2}$  (i.e., no acceleration processing) and  $144.8 \text{ ms}^{-2}$ , indicating peak power enhancement and Doppler broadening reduction obtained using acceleration processing with the appropriate input acceleration.

view. Consider a received signal dwell  $x(r,t)$  obtained for range gate  $r$  from sampling the transmission of  $N_p$  pulses with inter-pulse period  $T_p$ , where  $t = nT_p, n = 0, \dots, N_p - 1$ . An acceleration  $a(t)$  will impose a linear variation of the radial velocity as expressed by the complex phasor

$$s(t) = \exp\left(\frac{2\pi ja(t)\left(t - \left(\frac{N_p T_p}{2}\right)\right)^2}{\lambda}\right) \quad (1)$$

across the dwell, leading to broadening of the Doppler (or radial velocity) spectrum. In order to improve the detectability of the object, it is necessary to correct for the effects of acceleration. The fractional Fourier transform (Almeida, 1994) provides one means of applying this correction. However, a similar result can be achieved by multiplying the received object echo  $x(t)$  by the conjugate of  $s(t)$  (i.e., “de-ramping”)

$$y(t) = x(r,t)s^*(t), \quad (2)$$

where  $(\cdot)^*$  represents the complex conjugate operator.

The de-ramping process is applied to the BPST data using a preselected array of constant accelerations (typically  $0$ – $250 \text{ ms}^{-2}$ ) hereafter referred to as “acceleration processing.” The benefits of acceleration processing are illustrated in Figure 3, which shows the power spectra obtained using 512 samples (1.024 s duration) with different acceleration values for observations of SL-8-R-B (NORAD ID 23279) during Experiment 2. The use of an acceleration of  $144.8 \text{ ms}^{-2}$  (red) yields a larger peak power (i.e., increased detectability) and reduced spectral broadening compared to the use of zero acceleration (i.e., no acceleration processing). Figure 3 is representative of the radial velocity spectra obtained on applying acceleration processing to the BPST data in that (a) a single peak is obtained and (b) the spectral width obtained at the “optimal” acceleration is comparable to the radial velocity resolution.

The use of acceleration processing significantly increases the detectability of all objects and is a key contribution to the ability of the BPST radar to detect small objects with low SNRs. The estimation of object acceleration is a by-product of acceleration processing that can be alternatively estimated using the rate-of-change of radial velocity estimates. We note that the acceleration processing acceleration estimates are typically consistent with the estimates derived from the rate of change of radial velocity.

#### 4.2. Detection Mode Processing

The BPST produces range-time (RT) data-set  $x(r,t)$  for each dwell. Acceleration and Doppler processing (using a Hanning window) is then applied to the RT data to produce a three-dimensional data cube of range-(radial) velocity-(radial) acceleration (RVA) data  $(r,v,a)$ . The RVA data are processed using peak detection (Colegrove et al., 2006), data whitening (Turley, 1997), and peak selection. Peak detection is applied to locate the RVA cells whose log power (RVA-LP) data

$$z(\mathbf{r}, \mathbf{v}, \mathbf{a}) = 20\log_{10}|y(\mathbf{r}, \mathbf{v}, \mathbf{a})| \quad (3)$$

exceed those of adjacent cells in each dimension. For each peak  $i$ , parabolic interpolation is then applied to the RVA-LP data over the adjacent cells in each dimension  $j$  in order to produce sub-cell resolution peak location estimates. This process yields the peak power  $p_{0ij}$  (W), location  $p_{1ij}$ , peak location uncertainty (i.e., peak width  $p_{2ij}$ , and interpolation gain  $p_{3ij}$  (dB), where

$$p_{3ij} = p_{0ij} - z(\mathbf{r}, \mathbf{v}, \mathbf{a}). \quad (4)$$

The peak power is given by the sum of the power of the peak cell and the interpolation gains in each RVA dimension

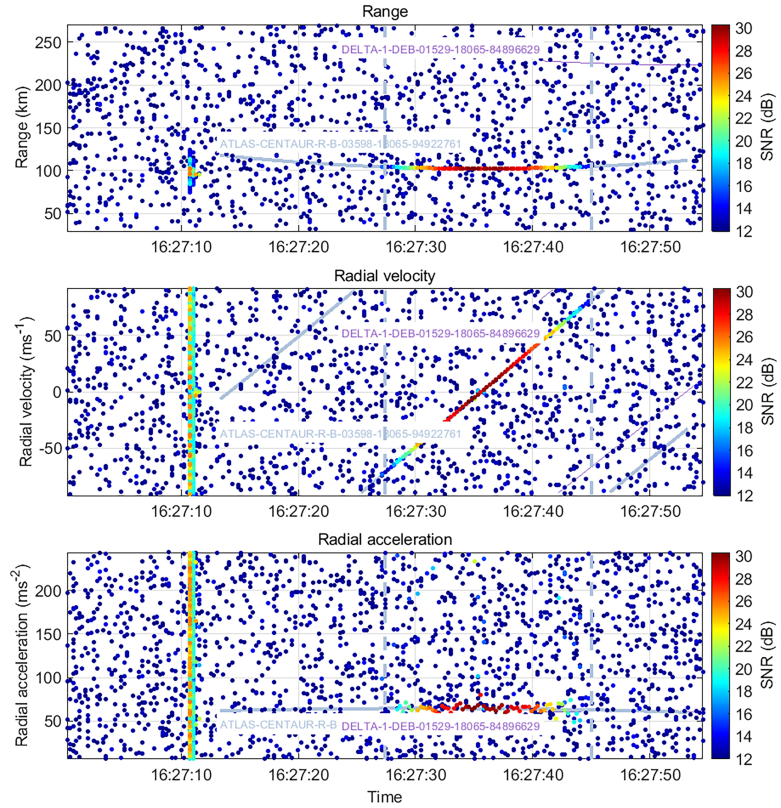


**Figure 4.** Example of range (top), radial velocity (middle), and radial acceleration peaks (bottom) obtained for the BPST radar around 16:27 universal time on 7 March 2018. The gray and purple line indicates the SGP4/SpaceTrack TLE propagated state values for Atlas-Centaur-R-B (NORAD ID 3590) and Delta-1-Deb (NORAD ID 1529). The vertical dashed lines in each plot indicate the first and last samples matching the propagated state values. The peaks distributed over all Radial velocities and accelerations at 16:27:12 result from a meteor head echo.

$$\mathbf{P}_i = \mathbf{z}(\mathbf{r}, \mathbf{v}, \mathbf{a}) + \mathbf{p}_{3i1} + \mathbf{p}_{3i2} + \mathbf{p}_{3i3}. \quad (5)$$

Data whitening is applied to the RVA data  $y(r, v, a)$  to reduce the effects of zero Hz clutter, narrowband radio-frequency interference, and under-dense meteor echoes, producing whitened RVA data  $y_w(r, v, a)$ . This is achieved using greatest-of-order statistics constant-false alarm rate (CFAR) processing, which renormalizes the “background” signal level to unity. The whitened RVA-LP data are then calculated using

$$\mathbf{z}_w(\mathbf{r}, \mathbf{v}, \mathbf{a}) = 20 \log_{10} |\mathbf{y}_w(\mathbf{r}, \mathbf{v}, \mathbf{a})|. \quad (6)$$

Peak selection is applied by selecting all peaks with SNRs exceeding a specified threshold (12 dB), where the SNR is the sum of the whitened RVA-LP power of the peak cell and the interpolation gains in each RVA dimension

$$\mathbf{S}_i = \mathbf{z}_w(\mathbf{r}, \mathbf{v}, \mathbf{a}) + \mathbf{p}_{3i1} + \mathbf{p}_{3i2} + \mathbf{p}_{3i3}. \quad (7)$$

The peak locations and uncertainties in radar units  $(r_{ij}, v_{ij}, a_{ij}), j = 1, 2$ , are obtained by multiplying the peak locations in cell units  $(\mathbf{p}_{1ij}, \mathbf{p}_{2ij}, \mathbf{p}_{3ij})$  by the cell resolutions.

An example of the peaks obtained for the vertical beam of the BPST radar during the transit of Atlas-Centaur-R-B (NORAD ID 3590) around 16:27 on 7 March 2018 is shown in Figure 4. These peaks were obtained using “overlap processing,” whereby a coherent processing interval length  $N$  is defined, with



**Table 5**  
Parameters Used for Peak Matching

Parameter	Loose step	Tight step
Object range (km), $r_w$	3	1
Object radial velocity ( $\text{ms}^{-1}$ ), $v_w$	36	1.8
Object acceleration ( $\text{ms}^{-2}$ ), $a_w$	5	3
Range offset (km), $r_b$	0	$\widetilde{\Delta r_{i1}}$
Radial velocity offset ( $\text{ms}^{-1}$ ), $v_b$	0	$\widetilde{\Delta v_{i1}}$

subsequent intervals shifted by  $M = N/O$ , where  $O$  is the overlap factor. The peaks in Figure 4 were obtained using  $N = 256$  samples (0.512 s), with  $O = 2$ , such that  $M = 128$  samples (0.256 s). The results show a clustering of high SNR peaks about the SGP4/SpaceTrack TLE propagated (aliased) range, (aliased) radial velocity, and radial accelerations between 16:27:30 and 16:27:44. Delta-1-Deb (NORAD ID 1529) also transited during this period but there are no peaks which match the propagated state vectors.

The peaks distributed over all radial velocities and accelerations around 16:27:12 of Figure 4 are the result of a meteoroid head echo. Meteoroids enter the atmosphere at speeds between 11 and 72  $\text{km s}^{-1}$ , which is up to an order of magnitude larger than LEO object speeds. The distribution of meteoroid trajectories peaks close to the zenith, and the radial velocities observed by ground based radars are therefore typically a large fraction of the absolute meteoroid velocity. In contrast, LEO object trajectories are typically tangential to the Earth, and the radial velocities observed by ground-based radars are typically a small fraction of the absolute object velocities. As a result, radial velocity of meteoroids (and hence head echoes) wraps significantly more quickly through Doppler space than LEO objects, thereby producing excessive radial velocity broadening. Meteoroid head echoes are reasonably common in the BPST satellite observations, occurring on average roughly every 5 min: i.e., of the order of 280 per day. Note that we have successfully applied the same techniques described in this paper for meteoroid head echo detection using a faster peak update rate (i.e., larger overlap) and a preselected array of accelerations.

### 4.3. Peak Matching

In order to find the peaks matching the propagated state vectors, the metric

$$M_i = \sqrt{\frac{(r_{i1} - r(t_i) - r_{ib})^2}{r_w^2} + \frac{(v_{i1} - v(t_i) - v_{ib})^2}{v_w^2} + \frac{(a_{i1} - a(t_i))^2}{a_w^2}} \quad (8)$$

is calculated for each peak  $i$ , where  $(r_{i1}, v_{i1}, a_{i1})$  are the peak locations in radar units,  $t_i$  are the peak times,  $r(t)$ ,  $v(t)$  and  $a(t)$  are the propagated object range, radial velocity, and radial acceleration at time  $t$ ,  $r_w, v_w$ , and  $a_w$  are the range, radial velocity, and radial acceleration tolerance, and  $r_{ib}$  and  $v_{ib}$  are the range and radial velocity offsets. Note that acceleration is not present in the propagated state vectors and is calculated using the temporal rate of change of the radial velocity (i.e.,  $a(t_i) = [dv/dt]_{t=t_i}$ ).

Matching is performed as a two-step process. The first step involves calculating  $M_i$  using the “loose” values in Table 5. This step accounts for non-exact matches between the peak and propagated ranges and radial velocities. This occurs due to ionospheric group retardation, which produces a positive bias in the peak range estimates (i.e.,  $r_{i1} > r(t_i)$ ), and due to errors in the propagated state vectors. An intermediate step then involves calculating the range and radial velocity offsets using the median of the difference between the peaks and propagated values (i.e.,  $\widetilde{\Delta r_{i1}}$  and  $\widetilde{\Delta v_{i1}}$ , where  $\Delta r_{i1} = r_{i1} - r(t_i)$  and  $\Delta v_{i1} = v_{i1} - v(t_i)$ , and  $(\widetilde{\phantom{x}})$  is the median operator). The final step involves recalculating  $M_i$  using the “tight” values in Table 5, which incorporates any range and radial velocity offsets, with any peaks with  $M_i \leq 1$  registered as peak matches.

Examples of matched peaks determined using this procedure are shown as vertical dashed lines in Figure 4.

### 4.4. Catalog Maintenance Mode Processing

Detection mode necessitates significant processing as it requires data covering the entire RVA search space to allow detection of objects with all possible (aliased) ranges, (aliased) radial velocities, and accelerations. In order to reduce the processing time, a “catalog maintenance mode” (CMM) was developed. This mode applies processing to a subset of ranges and accelerations about TLE propagations for each object, reducing the computational overhead considerably. This allows the coherent processing interval length  $N$  and overlap factor  $O$  to be increased, thus increasing object peak SNRs and radial velocity resolution.

The CMM implementation requires that the range subset “follows” the propagated object range  $r(t)$ . This is achieved by applying cubic-spline interpolation to the RT data  $x(r, t)$  to yield the RT data  $x'(r, t)$  for ranges  $r(t) + [-N_{r-}, \dots, N_{r+}] \Delta r$ , where  $N_{r-}$  and  $N_{r+}$  are integers and  $\Delta r$  is the range resolution. This interpolation does

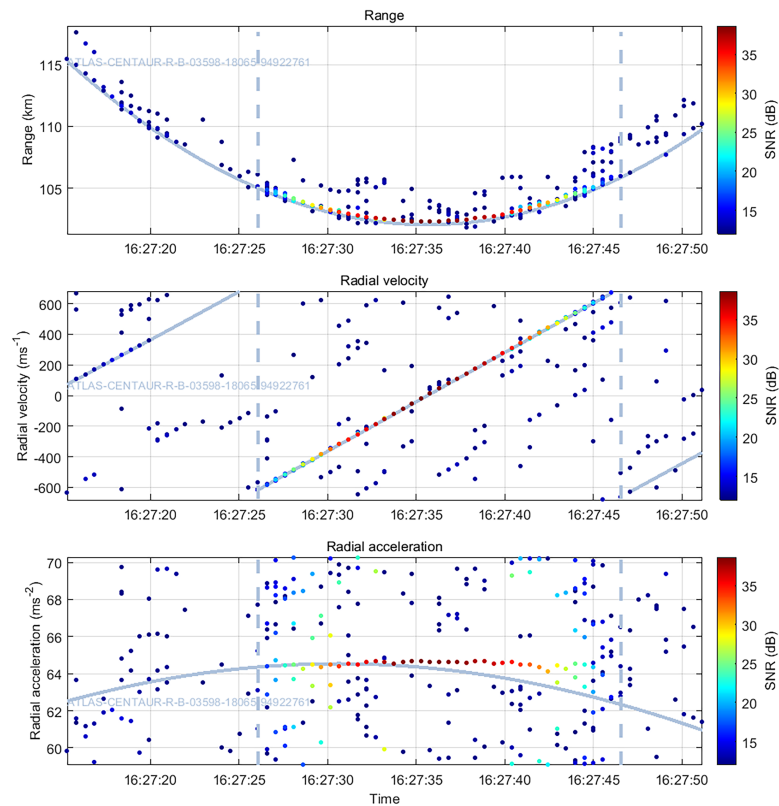


**Figure 5.** Example of range (top), radial velocity (middle), and radial acceleration peaks (bottom) obtained using catalog maintenance mode for the BPST radar around 16:27 universal time on 7 March 2018. The gray line indicates the SGP4/SpaceTrack TLE propagated state values for Atlas-Centaur-R-B (NORAD ID 3590). The vertical dashed lines in each plot indicate the first and last samples matching the propagated state values.

not incur significant SNR loss as range is oversampled by a factor of two. Once  $x'(r, t)$  has been produced, the analysis proceeds as described in section 4.2.

The analysis parameters used in catalog maintenance mode are shown in Table 5. The coherent processing interval length  $N$  and overlap factor  $O$  were chosen to yield significant object coherent gain (i.e., improved detection) while maintaining acceptable temporal resolution (0.512 s). The number of peaks required to register match  $N_m$  was selected to allow discrimination between LEO objects and long-lived meteor echoes, such as overdense or nonspecular echoes. Recognizing the finite duration of each coherent processing interval, we define the match duration  $t_d = t_{i2} - t_{i1} + T$ , where  $t_{i1}$  and  $t_{i2}$  are the times of the first and last matched peaks. A consequence of this choice of parameters is that the minimum detection duration is 8.7 s (i.e.,  $(N_m - 1)T_s + T$ ), which may limit detection of low height objects.

An example of the application of catalog maintenance mode to the same data shown in Figure 4 is shown in Figure 5. The increased coherent processing interval length (4.096 s) results in an SNR increase of 8 dB in comparison to the values used for Figure 4 (0.512 s). This SNR increase is of the magnitude expected for an eight-times increase in the coherent processing interval length (i.e.,  $10 * \log_{10}(8) = 9$  dB).

## 5. Results

The results presented in this section were obtained using catalog maintenance mode processing of the data collected during Campaigns 1 to 4. The object propagation state vectors for Campaigns 2 to 3 were determined using SpaceTrack TLEs. For Campaign 4, unless otherwise indicated, object state vectors were

**Table 6**  
Analysis Parameters Used for the Catalog Maintenance Mode Processing Results

Parameter	Value
Samples per CPI, $N$	2,048
CPI size, $T$ (s)	4.096
Overlap factor, $O$	8
Samples per step, $N_s$	256
Step size, $T_s$ (s)	0.512
Radial velocity resolution ( $\text{ms}^{-1}$ )	0.0014
Number of ranges, $N_r$ ( $= N_{r-} + N_{r+} + 1$ )	5
Number of "preceding" ranges, $N_{r-}$	1
Number of "succeeding" ranges, $N_{r+}$	3
Number of accelerations, $N_a$	9
Minimum acceleration ( $\text{ms}^{-2}$ )	$a(t) - 4$
Maximum acceleration ( $\text{ms}^{-2}$ )	$a(t) + 4$
Peaks required for match, $N_m$	10

extracted from SpaceTrack special perturbations (SP) data. SP numerically integrates the equations of motion including all necessary perturbing accelerations. The SP accelerations available include geopotential, atmospheric drag, lunar-solar gravity, direct solar radiation pressure, constant in-track duration thrust, and solid Earth and ocean tides (Bird, 2010). In contrast, SpaceTrack TLEs are computed using Simplified General Perturbations, Version 4 (SGP4) theory. SGP4 is reasonably accurate for long periods of time. However, it does not have the inherent physical and mathematical modeling to be considered accurate enough for predicting conjunction (i.e., collision) assessments. SP data are provided to Space Operation Cells, and DST obtain these data through affiliation with the Australian Space Operations Center (AUSSpOC). The SP data are available as daily files containing the propagation state vectors for all unclassified objects, and as a result, the daily file sizes are large (2 GB). DST downloads daily SP files for high-interest campaigns, such as SpaceFest.

### 5.1. Detection Statistics

The detection statistics for days where a full 24 hr of data were collected are shown in Table 6, revealing the daily detection count rates using catalog maintenance mode range from 150 to 200. The total number of object detections obtained over all campaigns was 2,410, and the total number of unique objects detected was 1,392.

The distributions of selected parameters for observation periods 2 to 4 are illustrated in Figure 6. The heights are the mean of the propagation state heights at all matching samples times. The gaps at multiples of 300 km occur because the BPST does not sample during pulse transmission and due to the 300 km range ambiguity associated with the selected PRF (500 Hz). The smallest and largest heights detected are 345.7 km (SL-4-R-B, NORAD ID 41395) and 2,491.4 km (SL-23-DEB, 37347), respectively. The second to fourth largest heights detected are associated with Globalstar satellites: 2,159.3 and 2,144.1 km (Globalstar-M035, 25851) and 2,169.0 km (Globalstar-M027, 25884). The histogram shows an exponential fall-off with increasing height,

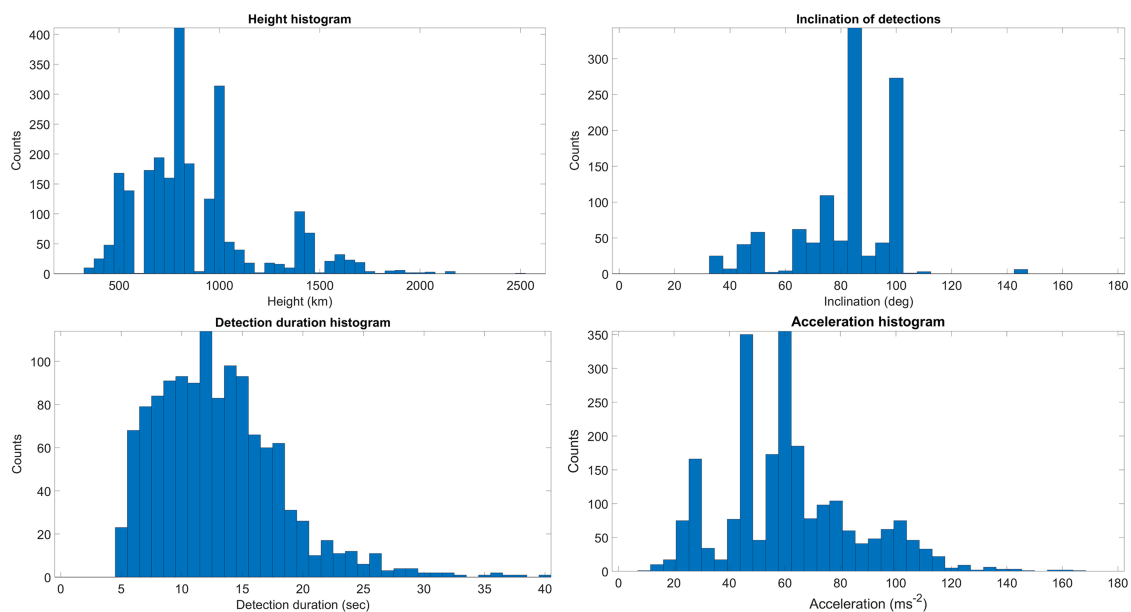


**Figure 6.** Object height (top left), inclinations (top right), detection duration (bottom right), and acceleration (bottom left) distributions obtained from observation periods 2 to 4.

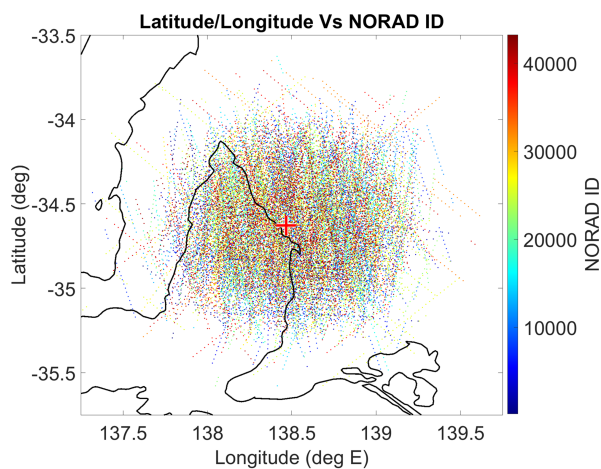


**Figure 7.** Latitude and longitude distribution obtained from observation periods 2 to 4. The red plus sign indicates the BPST radar location.

with distinct peaks observed at 800, 1,000, and 1,400 km. The 800 km peak is due to satellites with heights  $792 \pm 2$  km, comprising mainly Iridium (e.g., Iridium-117, NORAD ID 42808: detected twice) and Orbcomm-FM (e.g., Orbcomm-FM-16, 25417: detected twice) satellites. The 1,000 km peak is due to satellites with heights of  $990 \pm 40$  km, comprising mainly Cosmos satellites (e.g., COSMOS-887, 09637: detected three times) and SL-8 rocket bodies (e.g., NORAD ID 04800: detected twice). The 1,400 km peak is due to objects with heights of  $1,425 \pm 5$  km, comprising mainly Cosmos (e.g., Cosmos-1829, 17584) and Globalstar satellites (e.g., Globalstar-M097, 39072: detected five times).

The inclination values are obtained from the TLEs. The inclination histogram indicates the majority of detected objects are in prograde orbit (inclination  $< 90^\circ$ ). The peak acceleration histogram reveals values between 10 and  $167 \text{ ms}^{-2}$ . The largest (smallest) accelerations are observed for objects at smaller (larger) heights. The largest acceleration was observed for Breeze-M-DEB-(TANK) (36133) at height 462.12 km. The match detection durations range from 9 to 44 s. The former value is likely a consequence of the minimum detection dura-

tion of 8.7 s associated with the analysis parameters as described in section 4.2. The larger durations are observed for objects with larger heights. As the beam area increases with height, higher objects consequently take longer to transit the BPST beams. The largest duration observed is 44.5 s for Globalstar-M069 (31573).

The detected object latitude/longitude distribution for observation periods 2 to 4 is illustrated in Figure 7, revealing that the BPST radar is capable of detecting objects within a circle of radius approximately  $0.5^\circ$  when operating using the vertical beam. However, it is important to note that the detection latitude/longitude radius increases with object height, such that only the highest objects will occupy the full  $0.5^\circ$  circle radius.

## 5.2. Range and Radial Velocity Uncertainty

The distribution of range and radial velocity uncertainties,  $r_{i2}$  and  $v_{i2}$ , for Campaign 4 as determined from the peak interpolation procedures outlined in section 4.2 are shown in Figure 8. The range uncertainty results from the experimental parameter selection, which is dictated by the capabilities of the radar (e.g., transmit power and maximum duty cycle) and the data transfer limitations. As discussed in section 3, the radar operating parameters used for the observations presented in this paper were selected primarily for maximizing SNR rather than maximizing range resolution. The radial velocity uncertainty results from the selection of the number of samples,  $N$ , and the overlap factor  $O$ . There is an upper limit to value of  $N$  that can be used as  $N/PRF$  should not exceed the smallest object durations observed. Further, due to the matching criteria used in this paper, using a small value of  $O$  will reduce the number of peaks for short duration objects. As mentioned in section 4.3, the overlap factor is chosen to yield significantly improved detectability

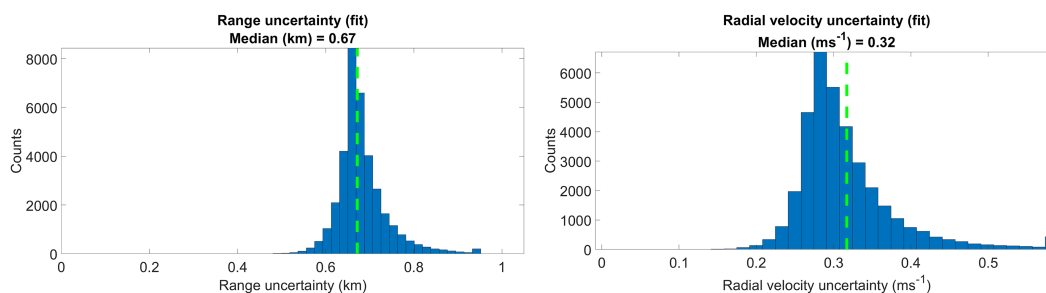


**Figure 8.** Range (left) and radial velocity uncertainty (right) distributions obtained from observation period 4. The green dashed line indicates the median of the distribution, as indicated in the plot titles.

while maintaining acceptable temporal resolution. The median radial velocity uncertainty is approximately twice the radial velocity resolution, emphasizing the observation noted in section 4 that acceleration processing yields spectral widths comparable to the radial velocity resolution.

### 5.3. Range Biases

Radars operating in the medium frequency to lower VHF bands suffer group retardation, where the measured range exceeds actual range (Davies, 1990). The group retardation  $r'$  (m) for a range  $r$  (m) can be expressed as

$$r' = \frac{c}{2} \int_0^R \frac{dr}{U(r)} - r, \quad (9)$$

where  $c$  is the speed of light ( $\text{ms}^{-2}$ ) and  $U(r)$  is the group velocity ( $\text{ms}^{-1}$ ). In the absence of a magnetic field,  $U(r)$  can be expressed in terms of the radar operation frequency  $f$  (Hz) and the plasma frequency  $f_p(r)$  (Hz)

$$U(r) = c \sqrt{1 - \frac{f_p^2(r)}{f^2}}. \quad (10)$$

The plasma frequency is given by

$$f_p r = \sqrt{\frac{N r e^2}{4\pi m \epsilon_0}}, \quad (11)$$

where  $N(r)$  is the electron density ( $\text{m}^{-3}$ ),  $e$  is the electron charge (C),  $m$  is the electron mass (g), and  $\epsilon_0$  is the permittivity of free space ( $\text{m}^{-3} \text{g}^{-1} \text{s}^4 \text{A}^2$ ).

To illustrate the object range biases, we use data from Campaign 4 where SP data are available. As this campaign used a vertical beam, we hereafter refer to the range biases as height biases. Figure 9 shows the average height bias (measured minus SP) as a function of height and hour. A minor geomagnetic storm (disturbance storm time index =  $-38$  nT) occurred on 10 March (WDC Kyoto, 2018), so this day is excluded from the campaign average and plotted separately. The geomagnetic storm has increased the group retardation, suggesting enhanced F-region electron density: i.e., a so-called “positive” storm (Prölss, 2017). Figure 9 also shows the height bias obtained from (6) using  $N(r)$  from the International Reference Ionosphere (IRI) 2016 climatological model (Bilitza et al., 2017) at the latitude and longitude of the BPST radar for March 2018. The IRI height biases show quantitative agreement with the radar estimates, although the bias is overestimated for the storm free days, indicating the IRI model electron densities are overestimated. IRI model discrepancies such as these have been noted by several studies, including those using ionospheric sounder data over the Australian region (Field, 2018). The radar estimates exhibit some discontinuities over height and time that may be attributed to the 700 m range uncertainty illustrated in Figure 8. It is also worth noting that the radial velocity biases (measured minus SP) exhibit no diurnal or geomagnetic variation, indicating they are indicative of SP and radar radial velocity uncertainties.

### 5.4. Object RCSs

As noted in section 2, the BPST radar has not been calibrated, so we are unable to present any absolute RCS estimates of the detected objects. Although SpaceTrack used to publish *microwave* radar object RCS values, this is no longer the case: RCS values are currently listed as small, medium or large. Despite these limitations, we have been able to extract some useful RCS-related information from the BPST results.

For reception on the BPST radar main array, the power returned from a target with a 55 MHz RCS  $\sigma$  is given by

$$P = \frac{P_t G^2(\theta, \varphi) \lambda^2 \sigma}{(4\pi)^3 r^4}, \quad (12)$$

where  $r$  is the target range (m),  $P_t$  is the transmit power (W),  $G(\theta, \varphi)$  is the one-way (i.e., transmit or receive) antenna pattern ( $\text{W m}^{-2}$ ), and  $\lambda$  is the radar wavelength (m). This equation indicates that the target power is

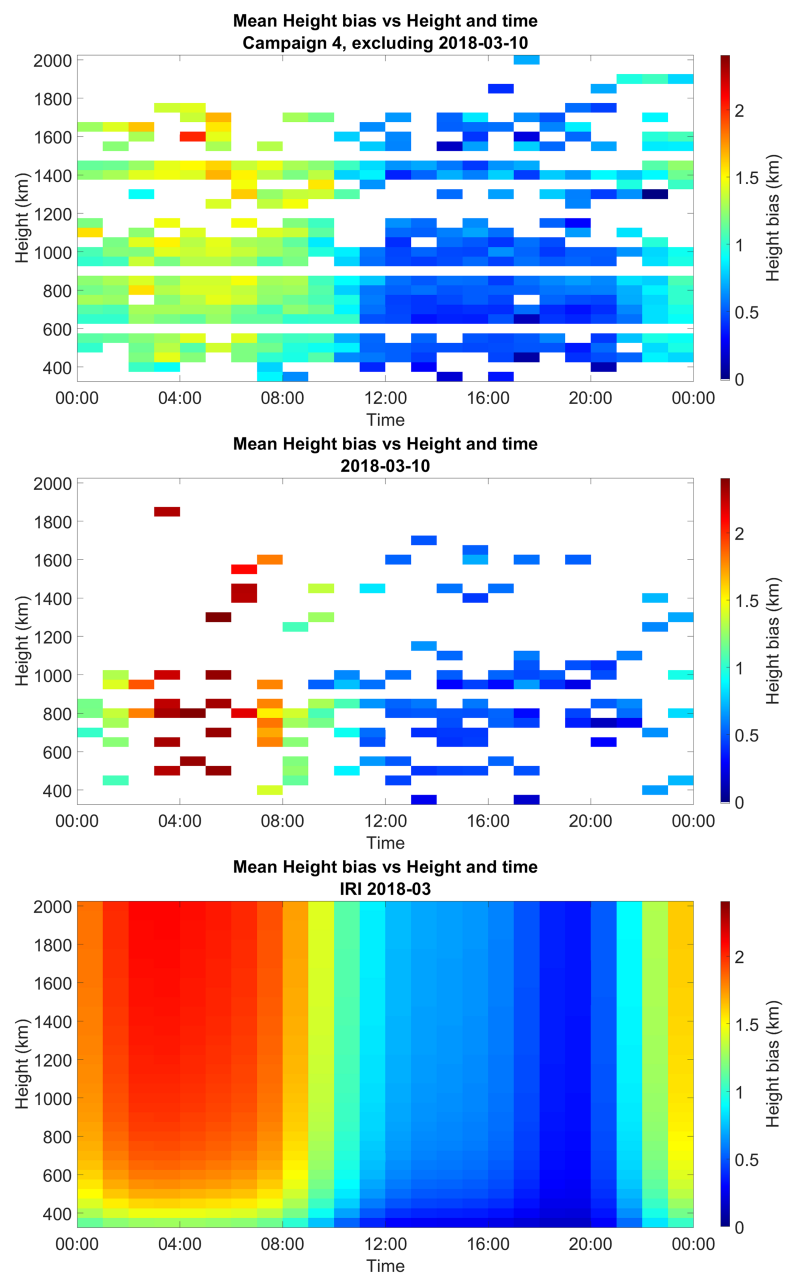


**Figure 9.** Height differences (estimated minus SP propagated) as a function of diurnal universal time for Campaign 4 excluding 10 March (top), 10 March (middle), and for the International Reference Ionosphere model for March 2018.

proportional to  $\sigma/r^4$ . Although there are no known published estimates of object RCS values in the lower-VHF band, we have used the microwave radar RCS values of McCant (2017) to approximate the corresponding values for 55 MHz. This approximation assumes (1) the detected objects can be represented by a sphere, (2) the minimum detectable sphere diameter  $d$  for the BPST radar is  $0.1 \text{ m}^2$ . Referring to Figure 1, the RCS for microwave frequencies ( $>300 \text{ MHz}$ , corresponding to the green to violet curves in Figure 1) is predominantly in the optical region for  $d > 0.1 \text{ m}^2$ , allowing use of the physical optics



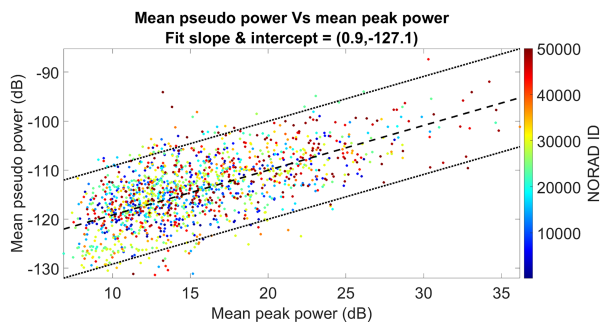


**Figure 10.** Range and RCS corrected power and a function of the mean (uncalibrated) peak power of the BPST satellite detections. The detections are coded by NORAD ID. The dashed black line indicates the results of a least squares fit, and the dotted lines indicate the fitted line  $\pm 10$  dB. The slope and intercept of the least squares fit line are indicated in the title.

uncertainty of BPST RCS estimates compared to tracking radars due to the smaller range of object aspect angles observed. Nevertheless, the least square line provides an ability to use RCS information to predict which object transits are likely to be detected by the BPST radar. The 25 smallest RCS detections made by the BPST radar are debris, with the three smallest being SL-16-Deb (22382, RCS  $-15.4$  dB), Thor-Altair-Deb (02177,  $-14.0$ ) and Delta-1-Deb-(YO) (00399,  $-13.5$ ). The smallest satellite RCS detections are the Cyclone Global Navigation Satellite System (CYGNSS) satellites (Ruf et al., 2018), with RCS values ranging from of  $-7.2$  to  $6.6$  dB. The BPST radar has detected seven of the eight CYGNSS satellites in orbit.

To further confirm the utility of the microwave radar RCS values, we define the “range and RCS corrected power,” which removes the contribution of RCS and range from the radar peak power estimates, but retains the antenna pattern contribution.

$$P_{ci} = \frac{P_i r_i^4}{\sigma_i} \tag{14}$$

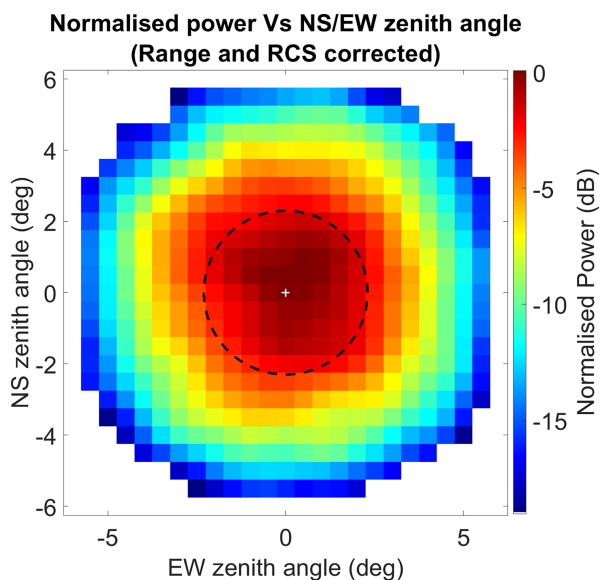


**Figure 11.** Mean normalized RCS and range corrected power as a function of East-West and North-South zenith angle. The white square indicates the zenith, while the black dashed circle of diameter  $4.6^\circ$  indicates the theoretical BPST radar half-power width.

approximation (black dashed curve in Figure 1) to convert microwave RCS values into an equivalent sphere diameter  $d_e$ , which can then be converted to the corresponding spherical RCS at 55 MHz (orange curve in Figure 1).

The 55 MHz RCSs for the object  $i$ ,  $\sigma_i$ , is used to define the “pseudo power”

$$P_{si} = \frac{G^2(\theta, \varphi)\sigma_i}{r_i^4} \tag{13}$$

Figure 10 shows the mean pseudo power  $\bar{P}_{si}$  plotted as a function of the mean peak power  $P_i$  for each detected object. The slope of the least squares fit line is close to unity, indicating that the approximation used to calculate the 55 MHz RCS values from the microwave radar RCS values is reasonable. There is an RMS uncertainty of  $\pm 5.5$  dB around the best fit line, which may be due to Faraday rotation effects, and the limited observation duration for each object. The latter effect will increase the

uncertainty of BPST RCS estimates compared to tracking radars due to the smaller range of object aspect angles observed. Nevertheless, the least square line provides an ability to use RCS information to predict which object transits are likely to be detected by the BPST radar. The 25 smallest RCS detections made by the BPST radar are debris, with the three smallest being SL-16-Deb (22382, RCS  $-15.4$  dB), Thor-Altair-Deb (02177,  $-14.0$ ) and Delta-1-Deb-(YO) (00399,  $-13.5$ ). The smallest satellite RCS detections are the Cyclone Global Navigation Satellite System (CYGNSS) satellites (Ruf et al., 2018), with RCS values ranging from of  $-7.2$  to  $6.6$  dB. The BPST radar has detected seven of the eight CYGNSS satellites in orbit.

To further confirm the utility of the microwave radar RCS values, we define the “range and RCS corrected power,” which removes the contribution of RCS and range from the radar peak power estimates, but retains the antenna pattern contribution.

$$P_{ci} = \frac{P_i r_i^4}{\sigma_i} \tag{14}$$

Figure 11 shows the normalized mean range and RCS corrected peak power as a function of zenith angle. This reveals the microwave radar RCS values are of sufficient use to confirm the correct pointing direction of the vertical beam, and confirm the theoretical antenna pattern beam width is reasonably correct.

## 6. Discussion

In order to establish the utility of the BPST radar for LEO object observations, we compare the capabilities and results obtained with other radars. In terms of smaller systems that operate outside the SSN, we compare the radar with the ESA bistatic radar breadboard (Saillant & Flécheux, 2017), the CAMRa S-band radar (Eastment et al., 2011), and the DST HF LOS radar. As of May 2017, the ESA bistatic radar breadboard had been regularly operating for more than a year and a half, and around 700 objects had been detected at ranges up to 1,000 km. The CAMRa radar is a cued sensor which makes count rate comparisons difficult. However, we note that 257 detections were made during the 12-day joint UK-Australian satellite tracking, data-fusion and cueing experiment (Eastment et al., 2014). In terms of detectability, Table 2 of Eastment et al. (2011) indicates an object with RCS  $2 \text{ m}^2$  would be detected with an SNR of  $-2$  dB at a range of 2,000 km. For comparison, the Globalstar-M035 (25851) satellite with RCS  $2.27 \text{ m}^2$  orbiting at 2,158.2 km was detected by the BPST radar with a mean (maximum) SNR of 14.8 (18.9) dB. In making these

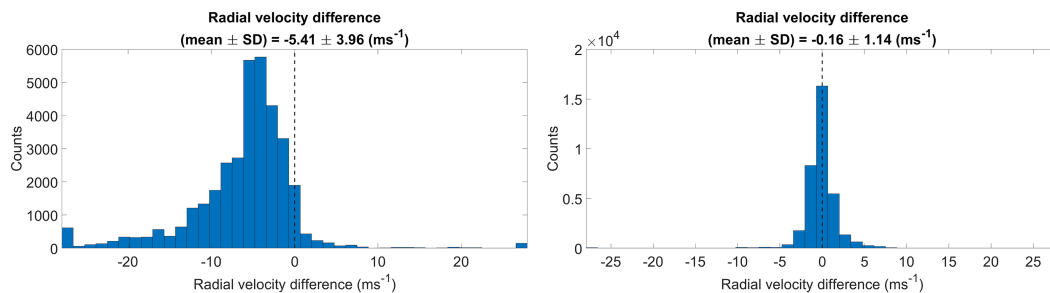


**Figure 12.** Histogram of radial velocity differences (estimated minus propagated) for Campaign 4 obtained using SpaceTrack TLEs (left) and SP data (right). The histogram values at the abscissa axis minima (maxima) include values below (above) the abscissa minima (maxima).

comparisons, we cannot vouch for the accuracy of the Globalstar-M035 (25851) RCS estimate of  $2.27 \text{ m}^2$ , and also acknowledge that the DST HF LOS radar ISS RCS estimates discussed in section 1 suggest there may be some RCS enhancement for larger LEO objects in the HF and lower-VHF bands. Nevertheless, these comparisons suggest the BPST radar is more sensitive than the ESA bistatic radar breadboard and the CAMRa S-band radar. Additionally, the BPST radar provides range, radial velocity, and acceleration measurements, whilst the ESA bistatic radar breadboard provides only radial velocity measurements and the CAMRa radar only provides range measurements—although we note Doppler and acceleration can be inferred from the rate of change of range and radial velocity respectively. The main limitation of the BPST radar with respect to the ESA bistatic radar breadboard is the inability to follow the trajectory of an object, while the main limitations with respect to CAMRa are the reduced range resolution (CAMRa) and inability to follow the trajectory of an object.

There is little information available on the count rate and detectability for the DST HF LOS radar, so comparisons between this system and the BPST radar are made on a qualitative basis. The BPST provides two technical advantages over the DST HF LOS radar: (1) It is a deployed, robust, unmanned operational system; (2) the 55 MHz operating frequency results in less ionospheric group retardation than the DST radar, which operates around 30 MHz and suffers range biases of up to 15 km. In contrast, the BPST radar has six technical disadvantages compared to the DST radar: (1) the use of the main array on reception prohibits beamforming and interferometric capabilities, thereby limiting orbit determination capability to objects that transit more than one beam; (2) the BPST system can only observe in one beam direction at a time, while the interferometric capabilities allow the DST system to detect and track multiple objects at once; (3) the narrow beam results in objects being visible for tens of seconds, compared to minutes for the DST radar; (4) the monostatic/pulsed nature of the system prohibits observation of objects with “low” (ambiguous) ranges (typically ranges  $< 3 \times$  transmit pulse length) where (range ambiguous) objects may be present; (5) the DST radar allows continuous operation, while the BPST radar requires 5 s “dead” time every 1–2 min to allow for data transfer to the data acquisition PC; (6) The DST radar allows multifrequency and multipolarization observations. Despite the limitations of the BPST radar for LEO object observations (noting that it was not designed for this application), it is a significantly less expensive option, retailing for US\$1.5 million.

An illustration of the utility of the BPST radar for catalog maintenance is shown in Figure 12. This shows histograms of the radial velocity differences (estimated minus propagated) for all peaks from Campaign 4 using SpaceTrack SGP (i.e., TLEs) and SP data. The mean (i.e., bias) and standard deviation obtained using the SP estimates are substantially smaller than the SGP estimates, confirming the statements of the increased accuracy of the SP estimates in section 5. It also apparent that there are outliers in the SP estimates, as observed at the histogram extrema. As the values at the edges of the distribution are substantially larger than the median radial velocity uncertainty ( $0.32 \text{ ms}^{-1}$ ), we attribute these values to SP state vectors errors. These errors may be associated with assumptions implicit in the SP propagations, errors in the radar measurements contributing to the SP propagations, or due to objects that have maneuvered since the radar measurements contributing to the SP propagations. These results suggest civilian radars such as the BPST can play a role in indicating which objects have erroneous SP state vectors.



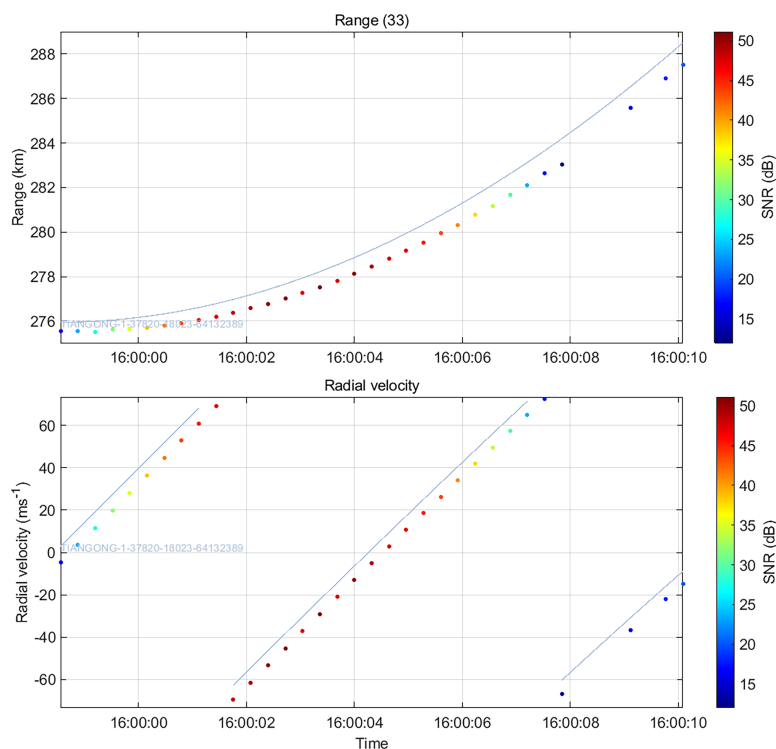


**Figure 13.** Range (top) and radial velocity (bottom) obtained for the BPST radar 10:26 Universal Time on 23 January 2018. The gray line indicates the SGP4/SpaceTrack TLE propagated state values for Tiangong-1 (37820).

A further illustration of the utility of the BPST radar for catalog maintenance are provided by observations made of the re-entering Chinese satellite Tiangong-1 (37820) in late 2017 and early 2018. Ten such transits were observed between 30 November 2017 and March 8 2018. Figure 13 illustrates the radar and TLE propagated range and radial velocity for the transit on 23 January. This reveals that the TLE propagations are approximately 0.025 s ahead of the radar measurements. Furthermore, the TLE range propagation exceeds the radar estimated range by approximately 0.5 km. This is an unusual occurrence since the radar range estimates usually *exceed* the TLE propagations by 0.5 (night) to 1.5 km (day) due to the effects of ionospheric group retardation. These results indicate that the TLE used to generate the propagations shown in Figure 13 is incorrect, most probably due to the rapid decay of the satellite orbit. The measurements were made at night (local time 02:30), where a group retardation of approximately 0.5 km may be expected, indicating the TLE range error is approximately 1 km. Interestingly, the TLE used to generate the propagations has a timestamp of 15:23, which is only 37 min before the transit. These results indicate an in-track error in the TLE, most probably associated with errors in the drag modeling utilized. It is also worth noting that the BPST radar observed one Tiangong-1 transit during Campaign 4 (8 March, 23:46 UT) where SP data were also available. We have not included plots of this transit for brevity, and since the transit was through the edge of the BPST vertical beam (the maximum zenith angle of  $9^\circ$ ) and had a lower SNR and shorter transit time than the transit shown in Figure 13. For the 8 March transit, the SP propagations led the observations by 0.75 s, and although the SP ranges appeared to be correct, the SP radial velocities exceeded the observations by  $200 \text{ ms}^{-1}$ .

We believe the BPST measurements for the two above-mentioned transits (and potentially the eight other transits) could have provided useful information for refining the Tiangong-1 SP and SGP4 orbit propagations. This emphasizes the benefits of geographic diversity made available by the BPST radar. We note that the southernmost SSN sensor is located at Exmouth ( $22^\circ\text{S}$ ) in Western Australia, leaving a large

**Table 7**  
*Number of Objects Detected in Catalog Maintenance Mode for Days in Which a Full 24 hr of Data Were Collected*

Date	Number of objects matched
28/9/2017	164
29/9/2017	171
8/3/2018	177
9/3/2018	183
10/3/2018	177
11/3/2018	204
12/3/2018	186
13/3/2018	196
14/3/2018	183
15/3/2018	153

SSN coverage gap that could be partially filled by the BPST radar (34.62°S) or similar non-traditional SSA sensors.

It is also worth noting that the BPST detects many objects that are not in the SpaceTrack catalog. This was also noted for MAARSY satellite observations (Renkwitz et al., 2013).

The campaign results presented in this paper were achieved using a single beam (15° West beam for Campaign 1, vertical beam for Campaigns 2 to 4) of the five beam directions available using the BPST radar. For catalog maintenance mode, the count rates could be increased substantially by selecting the appropriate beam direction for any objects that transit any of the five beams. The BPST radar now includes an interim capability to achieve this by allowing the specification of an appropriate beam to use at a specified time.

This capability (hereafter beam scheduling, or BS) was used to schedule dwells to observe Tiangong-1 transits (such as that shown in Figure 12) but has not been tested during a Campaign. In order to determine the number of objects that the BPST radar could potentially detect using BS, we note that the radar can only observe using one beam at a time. As a result, the radar can only detect a single object in the case where multiple objects transit different beams simultaneously. Furthermore, some objects may be detected in multiple beams (such as the ISS example shown in Figure 1). This suggests the number of objects potentially detectable using BS is not simply a multiplicative factor of five times the daily count rates shown in Table 7. Simple modeling indicates a more realistic multiplicative factor is between 3.5 and 4, suggesting potential daily count rates of between 500 and 800 objects per day. It is worth noting that the BPST radar offers limited main-array capability outside its core objective of allowing Doppler beam steering (DBS) analysis for wind profiling (Dolman et al., 2018). It should also be noted that an earlier generation ATRAD system was more suited to the observations described in this paper; the wind profiler previously installed at Mt Gambier, Australia (Reid et al., 2005), employed a similar antenna array but allowed 13 beam directions (zenith, and 7°, 14°, and 21° off-zenith at azimuths 27°, 117°, 207°, and 297°), and also provided interferometric capability using the main array. This type of system would potentially achieve daily count rates well in excess of 1,000 objects per day if BS was implemented.

The results also suggest the object measurements may be able to provide useful ionospheric measurements, as object height bias measurements can be easily converted into total electron content (TEC) measurements. This was the main motivation behind increasing the range resolution for Campaigns 3 and 4. Alas, Figures 6 and 7 suggest a further increase in range resolution is required to accurately measure TEC. A motivating factor for pursuing BPST TEC measurements is that GNSS TEC measurements are derived from slant measurements and therefore require correction to the equivalent vertical measurements. This obliquity correction assumes that the electron density profile at each position along the propagation path between the GNSS satellite and the ground-based receiver is identical to that at the receiver location. This is seldom the case due to large scale electron density gradients (Jakowski et al., 2008). Vertical beam BPST TEC measurements do not require obliquity correction and may provide increased accuracy TEC measurements. Further, the diversity of object heights may also allow electron density profiles to be measured, particularly for the top-side of the ionospheric F layer.

We conclude this section by addressing the use of climatological electron density models to correct object range biases (Frazer et al., 2014). This assumes the climatological model is fit for purpose over the geographic region to which it will be applied. Figure 7 suggests the most widely used climatological ionospheric model, IRI, overestimates the electron density during March at the location of the BPST radar. Further, Figure 7 suggests the use of climatological models will be problematic during periods of adverse solar weather effects such as solar flares, coronal mass ejections, and geomagnetic storms. This suggests data-driven real-time models such as the Jindalee Operational Radar Network (JORN) real-time ionospheric model (RTIM) (Barnes et al., 2002), or the IRI-based Ionospheric Real-Time Assimilative Model (IRTAM) (Reinisch et al., 2014), would provide the best means for correcting object range biases. Conversely, object range bias estimates could also be used as inputs to data-driven real-time models.

## 7. Conclusions

This paper has presented preliminary results investigating the use of a low-cost VHF wind profiling radar for observing objects in LEO. The results revealed that 2,410 objects were detected over 15 days, with 1,392 unique objects detected. The daily detection count rates ranged from 150 to 200, and the maximum detection height observed was 2,491 km. The radars utility for object catalog maintenance is demonstrated by its ability to determine propagation state vector errors, and through observations of the Chinese space station Tiangong-1 in the last months of its return to Earth. The results suggest the measurements may be able to provide useful ionospheric parameter measurements, such as total electron content (TEC) measurements.

### Acknowledgments

The lead author would like to thank Travis Bessell (DST) and Mark Rutten (formerly DST, now InTrack Solutions) for their interest, encouragement, and useful discussions regarding this work, and Gordon Frazer (formerly DST, now Frazer Lab) for useful discussions. There are no real or perceived financial conflicts of interests for any author. Funding for the BP ST radar was provided by the University of Adelaide, ATRAD Pty Ltd, the Australian Research Council grants DP0878144, and DP1096901, and by the Adelaide University ARC Small Grants Scheme. Andrew Spargo is supported by an Australian Government Research Training Program scholarship. The involvement of Iain Reid and Christian Adami was supported by ATRAD Pty Ltd. Data supporting the conclusions can be obtained online (<https://doi.org/10.25909/5d5fc9a986cdb>).

### References

- Almeida, L. B. (1994). The fractional Fourier transform and time-frequency representations. *IEEE Trans Signal Process.*, 42(11), 3084–3091.
- Ash, A., Skuljan, J., Scott, L., Martin, W., Wright, V., & Bessell, T. (2018). *A Summary of 5-Eyes Research Collaboration into SSA*. Paper presented at of the Advanced Maui Optical and Space Surveillance Technologies Conference (AMOS), Maui, Hawaii, 2010.
- Barnes, R. I., Gardiner-Garden, R. S., & Harris, T. J. (2002). *Real time ionospheric models for the Australian Defence Force*. Paper presented at Workshop for Applications of Radio Science (WARS), Leura, Australia 2002.
- Bilitza, D., Altadill, D., Truhlik, V., Shubin, V., Galkin, I., Reinisch, B., & Huang, X. (2017). International Reference Ionosphere 2016: From ionospheric climate to real-time weather predictions. *Space Weather*, 15(2), 418–429.
- Bird, D. (2010). *Sharing Space Situational Awareness Data*. Paper presented at of the Advanced Maui Optical and Space Surveillance Technologies Conference, Maui, Hawaii, September 14–17, 2010.
- Cohen, G., Afshar, S., van Schaik, A., Wabnitz, A., Bessell, T., Rutten, M., & Morreale, B. (2017). *Event-based sensing for space situational awareness*. Paper presented at Advanced Maui Optical and Space Surveillance Technologies Conference (AMOS), Hawaii, USA, 2017.
- Colegrove, S. B., Davey, S. J., & Cheung, B. (2006). Clutter rejection using peak curvature. *IEEE Transactions on Aerospace and Electronic Systems*, 42, 1492–1496, Oct. 2006.
- Davies, K. (1990). *Ionospheric Radio*. London, UK: IET.
- Dolman, B. K., Reid, I. M., & Tingwell, C. (2018). Stratospheric tropospheric wind profiling radars in the Australian network. *Earth Planets Space*, 70(1), 1–10. <https://doi.org/10.1186/s40623-018-0944-z>
- Eastment, J. D., Ladd, D. N., Walden, C. J., Donnelly, R. P., Ash, A., Harwood, N. M., et al. (2014). *Technical description of radar and optical sensors contributing to joint UK-Australian satellite tracking, data-fusion and cueing experiment*. Paper presented at Advanced Maui Optical and Space Surveillance Technologies Conference, Maui, Hawaii, 2016 (Vol. 1, p. 12).
- Eastment, J. D., Ladd, D. N., Walden, C. J., & Trethewey, M. L. (2011). *Satellite observations using the Chilbolton radar during the initial ESA 'CO-VT' tracking Campaign*. Paper presented at ESA European Space Surveillance Conference, INTA Headquarters, Madrid, Spain, 1–8.
- Field, D. (2018). *A new empirical climatological model of ionospheric foF2 and hmF2 and review of the International Reference Ionosphere*. M. Phil. Thesis, The University of Adelaide.
- Frazer, G. J., Meehan, D. H., & Warne, G. M. (2013). *Decametric measurements of the ISS using an experimental HF line-of-sight radar*. Paper presented at the 2013 International Conference on Radar, Adelaide, Australia, September 2013.
- Frazer, G. J., Rutten, M., Cheung, B., & Cervera, M. A. (2014). *Orbit determination using a decametric line-of-site radar*. Paper presented at Advanced Maui Optical and Space Surveillance Technologies Conference (AMOS), Maui, Hawaii, USA, September 2014.
- Frazer, G. J., & Williams, C. G. (2019). *Decametric Radar for Missile Defence*. Paper presented at IEEE Radar Conference, Boston, April 2019.
- Hall, T. D., Duff, G. F., & Maciel, L. J. (2012). The Space Mission at Kwajalein. *Lincoln Laboratory Journal*, 19(2), 48–63.
- Heidt, H., Puig-Suari, J., Moore, A. S., Nakasuka, S., & Twigg, R. J. (2000). *CubeSat: A new generation of picosatellite for education and industry low-cost space experimentation*. Paper presented at of the 12th AIAA/USU Annual Small Satellites Conference, paper SSC00-V-5, Utah State University, Logan, USA, Aug. 2000.
- Hobson, T., Clarkson, V., Bessell, T., Rutten, M., Gordon, N., Moretti, N., & Morreale, B. (2016). *Catalogue creation for space situational awareness with optical sensors*. Paper presented at Advanced Maui Optical and Space Surveillance Technologies Conference (AMOS), Hawaii, USA, September 2016.
- Ikeda, N., Nishimura, T., Iwahori, T., Yamamoto, M., Hashiguchi, H., & Yamakawa, H. (2017). Shape and Orbit Estimation Technique for Space Debris Observation Using the Middle and Upper Atmosphere Radar (MU Radar). Paper presented at Advanced Maui Optical and Space Surveillance Technologies Conference (AMOS), Hawaii, USA, September 2015.
- Jakowski, N., Mielich, J., Borries, C., Cander, L., Krankowski, A., Nava, B., & Stankov, S. M. (2008). Large-scale ionospheric gradients over Europe observed in October 2003. *Journal of Atmospheric and Solar-Terrestrial Physics*, 70(15), 1894–1903.
- Latteck, R., Singer, W., Morris, R. J., Holdsworth, D. A., & Murphy, D. J. (2007). Observation of polar mesosphere summer echoes with calibrated VHF radars at 69° in the northern and southern hemispheres. *Geophys. Res. Lett.*, 34(L14805), 2007. <https://doi.org/10.1029/2007GL030032>
- Lehtinen, M. S., Markkanen, J., Väänänen, A., & Huuskonen, A. (2001). Using EISCAT radars for space debris detection. In *Space Debris* (Vol. 473, pp. 67–71).
- McCant, M. (2017). *Median RCS values*. Retrieved from <https://www.prismnet.com/~mmccants/catalogs/index.html>
- Morris, R. J., Klekociuk, A. R., & Holdsworth, D. A. (2011). First observations of Southern Hemisphere polar mesosphere winter echoes including conjugate occurrences at 69°S latitude. *Geophys. Res. Lett.*, 38, L03811. <https://doi.org/10.1029/2010GL046298>
- Morris, R. J., Murphy, D. J., Reid, I. M., Holdsworth, D. A., & Vincent, R. A. (2004). First polar mesosphere summer echoes observed at Davis, Antarctica, (68.2°S). *Geophys. Res. Lett.*, 31, L16111. <https://doi.org/10.1029/2004GL020352>
- Nicolls, M. (2015). *Space Debris Measurements using the Advanced Modular Incoherent Scatter Radar*. Paper presented at Advanced Maui Optical and Space Surveillance Technologies Conference, Hawaii, USA, 2015.
- Palmer, J. E., Hennessy, B., Rutten, M., Merrett, D., Tingay, S., Kaplan, D., et al. (2017). *Surveillance of Space using passive radar and the Murchison Widefield Array*. Paper presented at IEEE Radar Conference, Seattle, May 2017, 1715–1720.
- Patel, N. V. (2015). *Averting space doom*, IEEE Spectrum, 52(2), pp. 16–17, February 2015. <https://ieeexplore.ieee.org/abstract/document/7024495>
- Pröls, G.W. (2017). Ionospheric F-region storms. In *Handbook of Atmospheric Electrodynamics (1995)* (pp. 205–258). CRC Press.



- Reid, I. M., Holdsworth, D. A., Kovalam, S., Vincent, R. A., & Stickland, J. (2005). The Mount Gambier VHF wind profiler. *Radio Sci.*, *40*, RS5007. <https://doi.org/10.1029/2004RS003055>
- Reinisch, B., Galkin, I., Huang, X., Vesnin, A., & Bilitza, D. (2014, May). *The Ionosphere Real-Time Assimilative Model, IRTAM-A Status Report*. Paper presented at EGU General Assembly Conference Abstracts (Vol. 16).
- Renkowitz, T., Stober, G., Latteck, R., Singer, W., & Rapp, M. (2013). New experiments to validate the radiation pattern of the Middle Atmosphere Alomar Radar System (MAARSY). *Adv. Radio Sci.*, *11*(283–289), 2013. <https://doi.org/10.5194/ars-11-283-2013>
- Ruf, C. S., Chew, C., Lang, T., Morris, M. G., Nave, K., Ridley, A., & Balasubramaniam, R. (2018). A new paradigm in Earth environmental monitoring with the CYGNSS small satellite constellation. *Scientific Reports*, *8*(1), 8782. <https://doi.org/10.1038/s41598-018-27127-4>
- Saillant, S., & Flécheux, M. (2017). *Kinematic analysis of the Exomars launcher change of orbit as detected during its passage over Europe*. Paper presented at IEEE Radar Conference, Seattle, May 2017, 1081-1086.
- Sato, T., Kimura, I., Kayama, H., & Furusawa, A. (1991). MU radar measurements of orbital debris'. *Journal of Spacecraft and Rockets*, *28*(6), 677–682. <https://doi.org/10.2514/3.26299>
- Smith C. H., Greene, B., Bold, M., & Drury, R. (2018). *Development of a new SSA facility at Learmonth Australia*, Paper presented at Advanced Maui Optical and Space Surveillance Technologies Conference, Maui, Hawaii, USA, September 2018.
- Spargo, A. J., Reid, I. M., & MacKinnon, A. D. (2019). Multistatic meteor radar observations of gravity wave-tidal interaction over Southern Australia. *Atmos. Meas. Tech. Discuss.*. <https://doi.org/10.5194/amt-2019-138>
- Tingay, S., et al. (2013). The Murchison Widefield array: The square kilometre array precursor at low radio frequencies. *Publications of the Astronomical Society of Australia*, *30*, E007. <https://doi.org/10.1017/pasa.2012.007>
- Turley, M. (1997). *Hybrid CFAR techniques for HF radar*, Paper presented at IEE Radar Conference, Oct. 1997.
- WDC Kyoto (2018). *Real-time (Quicklook) Dst Index Monthly Plot and Table*. Retrieved from [http://wdc.kugi.kyotou.ac.jp/dst\\_realtime/201803/index.html](http://wdc.kugi.kyotou.ac.jp/dst_realtime/201803/index.html)


## Appendix D

**Publication: Atmos. Meas. Tech., 12, 4791-4812, 2019**

This paper is based on the material presented in Chapters 3 and 4. The author of this thesis carried out the model development and data analysis and wrote the paper.

Atmos. Meas. Tech., 12, 4791–4812, 2019  
<https://doi.org/10.5194/amt-12-4791-2019>  
 © Author(s) 2019. This work is distributed under  
 the Creative Commons Attribution 4.0 License.



Atmospheric  
 Measurement  
 Techniques  Open Access

## Multistatic meteor radar observations of gravity-wave–tidal interaction over southern Australia

Andrew John Spargo<sup>1</sup>, Iain Murray Reid<sup>1,2</sup>, and Andrew David MacKinnon<sup>1</sup>

<sup>1</sup>Department of Physics, School of Physical Sciences, The University of Adelaide, Adelaide, 5005, Australia

<sup>2</sup>ATRAD Pty. Ltd., 20 Phillips St., Thebarton, 5031, Australia

**Correspondence:** Andrew John Spargo ([andrew.spargo@adelaide.edu.au](mailto:andrew.spargo@adelaide.edu.au))

Received: 5 April 2019 – Discussion started: 10 April 2019

Revised: 19 June 2019 – Accepted: 6 August 2019 – Published: 6 September 2019

**Abstract.** This paper assesses the ability of a recently installed 55 MHz multistatic meteor radar to measure gravity-wave-driven momentum fluxes around the mesopause and applies it in a case study of measuring gravity wave forcing on the diurnal tide during a period following the autumnal equinox of 2018. The radar considered is in the vicinity of Adelaide, South Australia (34.9° S, 138.6° E), and consists of a monostatic radar and bistatic receiver separated by approximately 55 km.

The assessment shows that the inclusion of the bistatic receiver reduces the relative uncertainty of the momentum flux estimate from about 75 % to 65 % (for a flux magnitude of  $\sim 20 \text{ m}^2 \text{ s}^{-2}$ , 1 d's worth of integration, and for a gravity wave field synthesized from a realistic spectral model). This increase in precision appears to be entirely attributable to the increased number of meteor detections associated with the combined monostatic and bistatic receivers rather than changes in the meteors' spatial distribution.

The case study reveals large modulations in the diurnal tidal amplitudes, with a maximum tidal amplitude of  $\sim 50 \text{ m s}^{-1}$  and an associated maximum zonal wind velocity of around  $140 \text{ m s}^{-1}$ . While the observed gravity wave forcing exhibits a complex relationship with the tidal winds during this period, the components of the forcing are seen to be approximately out of phase with the tidal winds above 88 km. No clear phase relationship has been observed below 88 km.

### 1 Introduction

It has been known for over three decades that the momentum deposition arising from the dissipation of atmospheric gravity waves (herein GW forcing) has a major influence on the background wind and thermal structure of the mesosphere–lower-thermosphere/ionosphere (MLT/I;  $\sim 80$ – $100$  km altitude) (Fritts, 1984). The small scales of the GWs relative to typical grid spacing in global climate models (GCMs) have led to a need to incorporate accurate parameterizations of the GW forcing within the GCMs (Kim et al., 2003; Ern et al., 2011). To support this need, there have been dozens of ground-based, satellite, and in situ studies of the associated GW momentum fluxes in the MLT/I (see e.g. Fritts et al., 2012a, and Nicolls et al., 2012, and references therein). Even so, many of the effects of GWs in the MLT/I are still acknowledged to be poorly understood, which continues to motivate major observational campaigns (e.g. Fritts et al., 2016).

In recent years, monostatic meteor radars have been the most widely deployed of those ground-based instruments (e.g. Hocking, 2005; Antonita et al., 2008; Clemesha and Batista, 2008; Beldon and Mitchell, 2009, 2010; Clemesha et al., 2009; Fritts et al., 2010a, b, 2012a, b; Vincent et al., 2010; Placke et al., 2011a, b, 2014, 2015; Andrioli et al., 2013a, b, 2015; Liu et al., 2013; de Wit et al., 2014b, a, 2016; Matsumoto et al., 2016; Riggini et al., 2016; Jia et al., 2018). This is largely due to the low cost and ease of installing and continuously running meteor radars relative to other instruments capable of making the same measurements, such as partial reflection radars (e.g. Vincent and Reid, 1983), coherent radars (e.g. Reid et al., 2018b), incoherent scatter radars (e.g. Nicolls et al., 2012), and Doppler lidars (e.g. Agner and Liu, 2015).

Like all other ground-based radar observations of momentum fluxes (see e.g. the discussions in Fritts et al., 2012a; Spargo et al., 2017; Reid et al., 2018b), there are concerns around the accuracy and precision of the estimates derived from meteor radar. As shown by Vincent et al. (2010), the measurement uncertainties are dependent on both the meteor detection rates and the complexity of the GW spectrum. Their results showed that even at the altitude of the peak of the meteor distribution, integration times of the order of a month or longer may be needed to definitively estimate the sign of the flux, for typical flux magnitudes. Fritts et al. (2012a) and Andrioli et al. (2013a), who also incorporated real-time and spatial meteor distributions and a wider variety of GW fields in their simulation, reach similar qualitative conclusions, although Fritts et al. (2012a) in particular argue that their measurement uncertainties for a composite day of data comprising measurements spanning 1 month may be much smaller than those reported in Vincent et al. (2010), due to the use of a larger total number of meteors and an assumption that the wave field in the MLT/I is often dominated by large-amplitude monochromatic waves.

Given the demonstrated sensitivities of momentum flux estimation uncertainties, it is important that all users of meteor radars appreciate the uncertainties specific to their radar configuration (the count rates and count distribution, the radar location, the time of year, and the likely GW field) prior to interpretation of their measurements. This study considers such a simulation of momentum flux measurement uncertainties from a 55 MHz meteor radar in a mid-latitude Southern Hemisphere (SH) site in Australia and bears those uncertainties in mind in the interpretation of a case study of GW forcing on the diurnal tide. The aspects of this study that are unique can be summarized as follows:

- we consider a multistatic meteor radar configuration consisting of a monostatic radar and a bistatic receiver separated by  $\sim 55$  km;
- we propagate realistic levels of receiver noise and mean phase bias to the angle-of-arrival (AOA) and radial velocity estimates that are used in the subsequent momentum flux estimation;
- a realistic GW spectral model is used to synthesize the wind field from which the momentum fluxes arise.

Section 2 briefly overviews the radar configuration, the count rates obtained, and the phase calibration offsets applied. Section 3 gives a detailed description of the simulation that estimates the momentum flux measurement uncertainties and its results. Section 4 presents a case study of momentum fluxes estimated using the radar during the austral winter and attempts to validate them by looking at the interaction between the measured fluxes and the tidal winds. Discussion and conclusions follow.

**Table 1.** Experiment parameters used for the BP meteor radar transmitter, for all data presented in this paper.

Parameter	Value
Frequency	55 MHz
Pulse width	7.2 km
Pulse code	4 bit complementary
Pulse shape	Gaussian
Pulse repetition frequency (PRF)	440 Hz
Range sampling	68.4–309.6 km
Range sampling interval	1.8 km
Peak power	40 kW
Polarization	Circular

## 2 Instrumentation

The multistatic meteor radar considered in this study consists of a stratosphere–troposphere (ST)/meteor radar located at the Buckland Park (BP) field site ( $34.6^\circ$  S,  $138.5^\circ$  E) (briefly described by Reid et al., 2018a) and a remote receiving system located near the township of Mylor, South Australia ( $35.1^\circ$  S,  $138.8^\circ$  E) (about 55 km to the south-east of BP).

In meteor mode on the BP system, a single crossed, folded dipole is used for transmission and a five-element interferometer arranged in a configuration identical to that of Jones et al. (1998) is used for reception. Three-element Yagi antennas are used for the interferometer’s receive antennas. A peak power of 40 kW is used on transmission. Other experimental parameters used are summarized in Table 1, and a detailed description of the radar hardware is given in Dolman et al. (2018).

The remote receiver system consists of a six-receive-channel digital transceiver identical to the transceiver system of the BP ST/meteor radar. In the current configuration, only five of those receive channels are used. The same five receiver antenna arrangement is used at the remote site. To permit accurate range and Doppler estimates at the remote site, the system timing, frequency, and clocks at both sites are synchronized with GPS-disciplined oscillators (GPSDOs).

The techniques used to estimate various data products from the received meteor echoes, including radial velocity, meteor position, signal-to-noise ratio (SNR), and decay time, follow those outlined in Holdsworth et al. (2004a).

The dataset considered spans 17 March to 9 September 2018, with few interruptions (the number of meteors detected per day on both receivers for this interval are shown in Fig. 1).

### 2.1 Receiver channel phase calibration

Compensating for any systematic receiver channel phase offsets plays an important role in ensuring the accuracy of the position and height estimates of the detected meteors. To calibrate the phases of the receive channels for both of the me-



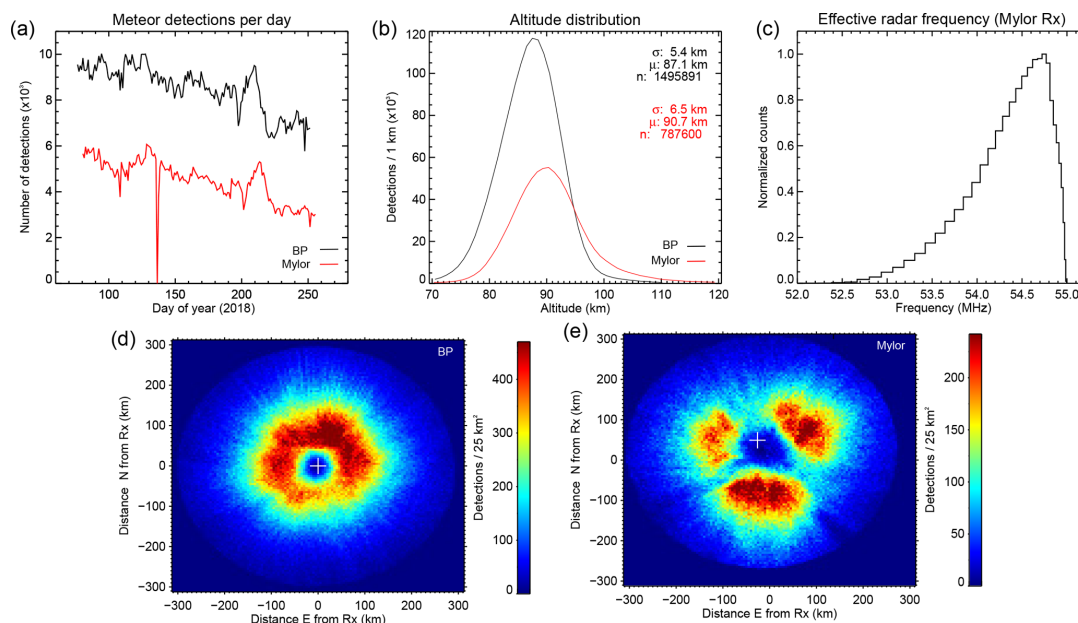


**Figure 1.** (a) The meteor detection rates for the BP and Mylor receivers over the 2018 campaign, (b) the associated distribution of meteors in altitude (right), (c) histogram of the effective radar frequency at the Mylor bistatic receiver (i.e.  $f \cos(\beta/2)$ , where  $f$  is the operating frequency and  $\beta$  is the forward scatter angle), and (d) the horizontal distribution of meteors for the BP and (e) Mylor receivers (the transmitter location in each case is denoted by a white cross).

teor receiver interferometers used in this study, we have followed the approach suggested in Holdsworth et al. (2004b).

The Holdsworth et al. (2004b) approach determines the offsets to apply to the phase differences between the centre and each of the other receive antenna channels that maximize the number of meteors within a range of heights that the meteors are expected to occur in (see Chau and Clahsen, 2019, for a generalized approach to this). For the BP system, we have used minimum and maximum permissible heights of 70 and 110 km, respectively, and 70 and 120 km for the Mylor system. A slightly larger height interval has been used for the Mylor system to allow for the effect of the distribution of Bragg wavelengths (see Fig. 1c) on the meteor height distribution width (see, e.g. Thomas et al., 1986, and Stober and Chau, 2015, Sect. 3 for a description of this effect).

The phase offsets applied to the Mylor system and the variability of the offsets for the BP system (for which a fixed calibration was used) are shown in Fig. 2. We note a stable calibration for BP but a few sudden shifts in the Mylor case; this has subsequently been determined to be due to a slight rotation of the antenna elements by local wildlife. We do not expect isolated shifts like this to have an adverse impact on the analysis performed in this paper, although to somewhat compensate for it we have performed a daily recalibration of the receiver channels (using the calibration results for each day) before subsequent processing of the data.

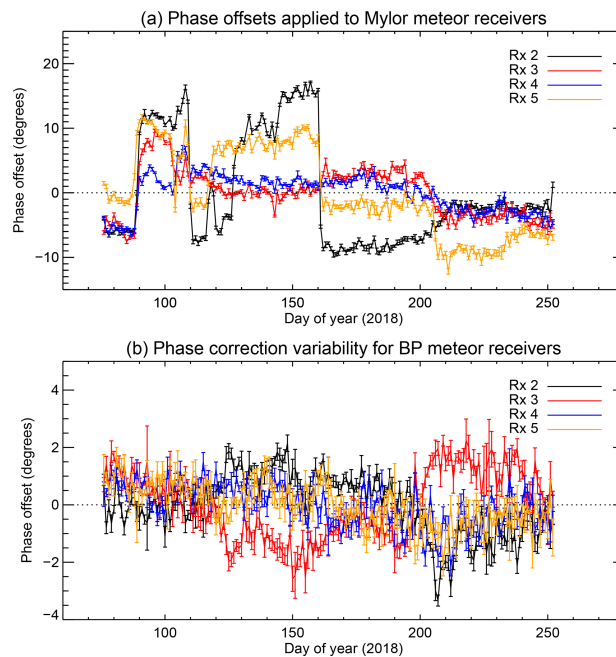


**Figure 2.** Phase offsets applied to Mylor meteor radar antennas as a function of time (a), and the phase offsets indicated by the Holdsworth et al. (2004b) calibration procedure on BP meteor radar data (b).



### 3 Simulation of wind covariance estimation

#### 3.1 Simulation overview

The aim in developing this simulation has been to quantify the uncertainties in the  $\langle u'w' \rangle$  and  $\langle v'w' \rangle$  covariance components derived from meteor echoes received in an arbitrary network of meteor radar transmitters and receivers, as well as to be able to characterize the dependence of those uncertainties on the network shape and the spectrum of the GWs constituting the input wind field. The basic workflow of the simulation (all components of which are elaborated upon in subsequent subsections) may be summarized as follows:

1. Produce a sample of meteors in space and time for each site under consideration, by sampling from realistic spatio-temporal meteor detections corresponding to each site.
2. Specify a wind field based on the superposition of monochromatic gravity waves derived from a realistic GW spectrum and compute the wind velocities at each of the simulated meteors.
3. Compute the radial wind velocity measured at the receiver associated with each meteor detection.
4. For each meteor–site combination, synthesize in-phase and quadrature (IP and Q) time series for each receiver at the site, based on the radial velocity and AOA of the meteor.
5. Add a realistically sized phase bias and noise floor to each receiver channel.
6. Estimate the radial velocity and AOA of the meteor from the simulated time series.
7. Estimate the wave field covariances using the meteors retrieved from different combinations of sites.
8. Return to step (1) and repeat for the number of realizations required to produce covariance error distributions (in the next step) of the desired statistical significance and resolution.
9. Compare the estimated covariances with those computed directly from the 3-D wind velocities at the meteors and those calculated at 2 min resolution at the origin of the coordinate system.

#### 3.2 Meteor position specification

To incorporate the dependence of the  $\langle u'w' \rangle$  and  $\langle v'w' \rangle$  uncertainties on the temporal and spatial characteristics of the meteor distribution, we have based the distributions used in the model on real measurements. For both the BP and Mylor sites, we constructed a composite day of 2-D histograms of the meteor position distributions at 5 km spatial

and hourly time resolution, using measurements from April to July 2018. These 2-D histograms were taken to represent probability distributions for the meteor positions.

The sampling from these probability distributions at the beginning of each realization was done according the following process:

1. Prescribe a number of meteor detections for the day of measurements and altitude in question (e.g.  $1340 \text{ d}^{-1}$  at 90 km for the BP radar case).
2. Use rejection sampling to distribute those meteors across the day, according to the relative number of meteors in each hour in the input probability distribution.
3. Distribute the meteors prescribed in each hour of measurements according to the spatial probability distribution for that hour, again using rejection sampling.
4. Return to step (1) and repeat for the number of days prescribed in this realization (for results presented in this paper, 1 or 10).

The horizontal position coordinates assigned to each meteor in the probability distribution (and subsequently the model) are based on the distances from the receiver site in Transverse Mercator coordinates, calculated using the method of Bowring (1989). The altitudes assigned to the meteors are derived from a uniform probability distribution, with a centre value of 90 km and a full width of 2 km (such that the simulation emulates the idea of analysing meteors from a single height bin).

#### 3.3 Meteor detection rate specification

To clarify the effect of a variable number of meteor radial-velocity–AOA pairs on the covariance error distribution, a variety of meteor detection rates have been simulated. We have endeavoured to make the detection rates used resemble the number of meteors detected across a range of heights by the combined BP–Mylor radar link (we note again though that the simulation itself is performed around a single altitude). The detection rates we have used for different heights, listed in Table 2, correspond to those averaged over April 2018 for the two receive sites, in 2 km wide bins.

#### 3.4 Wind field specification

The wind field in the simulation is comprised of tidal components and a superposition of monochromatic GWs whose amplitudes have a vertical wavenumber and frequency dependence. Diurnal and semidiurnal tidal components are assumed, with amplitudes of 25 and  $10 \text{ m s}^{-1}$  respectively. Random phases from a uniform distribution spanning the interval  $[0, 2\pi)$  are added to the phase of the zonal component of the tides at the beginning of each realization, and the meridional component is set to be in quadrature with the

**Table 2.** Meteor detection rates used for the simulations in this paper. The rates shown are per day, in 2 km wide bins centred at the altitude specified.

Altitude (km)	BP	Mylor
76	140	20
80	510	130
82	780	180
84	1080	380
86	1360	540
88	1480	640
90	1340	690
92	1010	640
96	300	350

zonal component. The 3-D wind velocity associated with the GWs at a given time  $t$  and Cartesian position vector  $\mathbf{r}$  can be written as

$$\mathbf{v} = \sum_{i=1}^{n_m} \sum_{j=1}^{n_\omega} A(m_i, \omega_j) \mathbf{v}'_{ij} \sin(\boldsymbol{\kappa}_i \cdot \mathbf{r} - \omega_j t + \phi_{ij}), \quad (1)$$

where  $m$  is the vertical wavenumber,  $\omega$  is the wave's angular frequency,  $n_m$  and  $n_\omega$  are the number of vertical wavenumbers and angular frequencies respectively in the spectral grid,  $A$  is the joint vertical-wavenumber–angular-frequency spectral amplitude,  $\mathbf{v}' = [u', v', w']$  is the vector of wind component fluctuation sizes,  $\boldsymbol{\kappa} = [k, l, m]$  is the 3-D wave vector, and  $\phi$  represents a (random for each unique  $[m_i, \omega_j]$  pair) phase offset.

As per Sect. 3.2, the coordinate system used to specify horizontal position with respect to a reference location (i.e. that embodied by the  $\mathbf{r}$  vector) is based on the Transverse Mercator distances evaluated using the Bowring (1989) method (which follow the Earth's surface and take into account its ellipsoidal shape). This is used in preference to line-of-sight distances, the use of which would result in stretching of the horizontal scales of the waves at large distances from the coordinate system origin. Furthermore, the calculated wind velocities are assumed to be in the local east–north–up (ENU) coordinates at the associated meteor positions.

To ensure that the correlations between the horizontal and vertical winds take on physically reasonable values, we have allowed the component fluctuation amplitudes to be related by the linear GW polarization relation  $w' = \frac{v_h k_h}{m}$ , where  $v_h = \sqrt{u'^2 + v'^2}$  and  $k_h = \sqrt{k^2 + l^2}$ . The horizontal components are determined by the wave propagation azimuth  $\varphi$ , through the relations  $[k, l] = k_h[\sin \varphi, \cos \varphi]$  and  $[u', v'] = v_h[\sin \varphi, \cos \varphi]$ .

In order to give the wind field a level of spatially correlated randomness akin to what is seen in mesospheric wind fields when no predominant wave scales are present, we have opted to let  $A(m, \omega)$  take on values from a gravity wave spectral model. The vertical wavenumber spectrum we have used

(Gardner et al., 1993, Eq. 7, and following their nomenclature) is given by

$$F_u(m) = 2\pi\alpha N^2 \begin{cases} m_*^{-3} \left(\frac{m}{m_*}\right)^s & m \leq m_* \\ m^{-3} & m_* \leq m \leq m_b \\ m_b^{-3} \left(\frac{m_b}{m}\right)^{5/3} & m_b \leq m \end{cases}, \quad (2)$$

where  $m$  is the vertical wavenumber of the wave, and following Gardner et al. (1993), Fig. 1, we let  $\alpha = 0.62$ ,  $N = \frac{2\pi}{3 \times 10^{-2}} \text{ s}^{-1}$ ,  $m_* = \frac{2\pi}{1.5 \times 10^4} \text{ m}^{-1}$ ,  $m_b = \frac{2\pi}{5 \times 10^{-2}} \text{ m}^{-1}$ , and  $s = 2$ . The frequency spectrum we have used (Gardner et al., 1993, Eq. 24) is given by

$$B(\omega) = \frac{p-1}{f} \left(\frac{f}{\omega}\right)^p, \quad (3)$$

where  $\omega$  is the angular frequency of the wave, and following Gardner et al. (1993), Fig. 2, we let  $f = \frac{2\pi}{7.2 \times 10^4} \text{ s}^{-1}$  and  $p = 2$ . We then simply assume that the joint vertical-wavenumber–angular-frequency spectrum is given by the product of these two spectra, i.e.

$$A(m, \omega) = F_u(m) B(\omega). \quad (4)$$

The 2-D spectrum we used for results presented in this paper consisted of 80 different vertical wavelengths and wave periods, spanning the ranges 0.5–20 km and 5–240 min (uniformly sampled in vertical wavenumber and frequency), respectively. These limits largely encompass the waves responsible for the majority of the momentum deposition in the mesosphere–lower-thermosphere (MLT) region (see e.g. Fritts and Alexander, 2003), whose momentum fluxes are of principal interest in this study.

The wave propagation azimuths were sampled from a uniform random distribution spanning  $[0, 180^\circ]$  in bearing, with the intention being to emulate a wave field whose westward-propagating waves have been removed from the spectrum through selective filtering. This led to true values for the estimates of  $\langle u'w' \rangle$  that were on average positive and values of  $\langle v'w' \rangle$  that were on average zero. Testing a wider variety of wave field configurations was considered beyond the scope of the paper.

The absolute values taken by  $A(m, \omega)$  were normalized in a way that resulted in mean values of  $\langle u'w' \rangle$  in the vicinity of  $20 \text{ m}^2 \text{ s}^{-2}$ , which is a typical value for this parameter in the MLT region (see e.g. the discussion in Fritts et al., 2012a). An example distribution of true covariances evaluated in the simulation is shown in Fig. 5b.

### 3.5 Projection of the wind velocity onto the Bragg vector

A diagram summarizing the bistatic reception geometry is shown in Fig. 3. Following the development of Protat and Zawadzki (1999), the so-called “radial velocity” measured

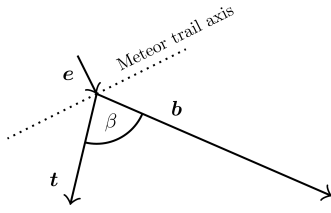


**Figure 3.** Bistatic meteor reception geometry. Using similar terminology to that in Protat and Zawadzki (1999),  $\mathbf{t}$  is a vector from the meteor to the transmitter,  $\mathbf{b}$  is a vector from the meteor to the bistatic receiver, and  $\mathbf{e}$  is a unit vector that is perpendicular to the meteor trail axis (and therefore, assuming specular reflection from the trail, is a bisector of  $\mathbf{t}$  and  $\mathbf{b}$ ).  $\beta$  is the so-called “forward scatter” angle.

by a bistatic receiver corresponds to the projection of the 3-D wind velocity onto  $\mathbf{e}$  (which is in the same direction as the Bragg vector in e.g. Stober and Chau, 2015), in turn projected onto  $\mathbf{b}$ . Mathematically, this velocity is expressed as

$$v_{\text{rm}} = \cos(\beta/2) \cdot \mathbf{v}_{\text{ecef}} \cdot \mathbf{e}, \quad (5)$$

which is the velocity that is used to produce a phase progression in the simulated receiver time series, discussed in Sect. 3.6. It should be noted that  $\mathbf{t}$ ,  $\mathbf{b}$ , and  $\mathbf{e}$  are expressed in Earth-centred, Earth-fixed (ECEF) coordinates and that the wind velocities  $\mathbf{v}$  computed in the simulation are in the local ENU coordinates of each meteor. The “ecef” subscript on  $\mathbf{v}$  is to denote  $\mathbf{v}$ ’s rotation to the ECEF coordinate system; we have followed a slightly modified version of the approach discussed in detail by Stober et al. (2018) to do this (see Appendix A). We note that we apply the same procedure for both bistatic and monostatic receivers (though of course in the monostatic case  $\mathbf{t} = \mathbf{b}$ ).

### 3.6 Receiver time series generation and parameter re-estimation

To ensure that realistic radial velocity and position estimation errors are propagated to the covariance estimation, we have opted to generate synthetic receiver time series based on the observables discussed in the previous sections and to then attempt to re-estimate the observables from the time series. The complex time series for the  $j$ th receiver is written as

$$V_j(t) = e^{i(2\pi \mathbf{A} \cdot \mathbf{d} - 4\pi v_{\text{rm}} t / \lambda + \Phi_j)} e^{-t/\tau} + n_j(t), \quad (6)$$

where  $\mathbf{A} = [\sin \theta \sin \phi, \sin \theta \cos \phi, \cos \theta]$  (where  $\theta$  and  $\phi$  are the zenith and azimuth angles of the meteor, respectively, as measured from the receiver),  $\mathbf{d}$  is a three-element vector of Cartesian displacements to the receiver antenna in question,  $\lambda$  is the radar wavelength,  $\Phi_j$  is a phase calibration offset for the  $j$ th receiver,  $\tau$  is the  $e^{-1}$  decay time of the meteor, and  $n_j(t)$  is a background noise function.

The background noise function consists of values derived from a Gaussian distribution, with a root-mean-square (rms)

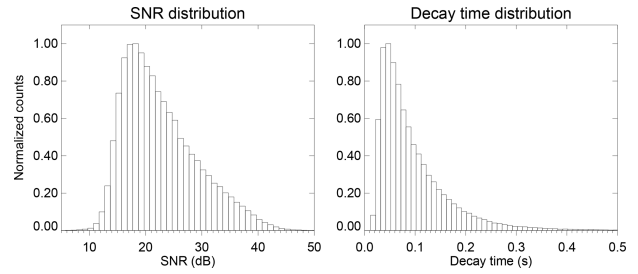


**Figure 4.** Probability distributions of SNR and decay time used in producing the receiver time series discussed in Sect. 3.6.

value derived from a probability distribution of meteor echo SNRs from the monostatic 55 MHz meteor radar at BP. The values used for  $\tau$  are also derived from a probability distribution from this radar’s data. In both cases, the data used to generate the probability distributions spanned 1–30 April 2018 and altitudes 70–110 km. Plots of these distributions are shown in Fig. 4.

The phase calibration offsets  $\Phi_j$ , which are set for each receiver at the beginning of each simulation realization, are intended to embody the consequences of incorrectly estimating the true phase calibration offsets between the receiver channels. Based on the phase calibration offset time series shown in Fig. 2, we have chosen to apply to each receiver Gaussian-distributed phase offsets with an rms value of  $2^\circ$ .

Radial velocities and meteor positions are estimated from the noise and phase-offset time series following the procedures outlined in Holdsworth et al. (2004a) (Sect. 3.11 and 3.12, respectively), with the exception that the radial velocity is corrected for the forward scatter angle in the case of bistatic reception. Using the definitions in Fig. 3 and following the approaches outlined in Stober et al. (2018) to compute the  $\mathbf{t}$  and  $\mathbf{b}$  (and  $\mathbf{e} = \frac{\mathbf{t} + \mathbf{b}}{|\mathbf{t} + \mathbf{b}|}$ ) vectors, the forward scatter angle may be estimated using

$$\beta = \cos^{-1} \left( \frac{-\mathbf{t} \cdot \mathbf{b}}{|\mathbf{t}| |\mathbf{b}|} \right), \quad (7)$$

and then Eq. (5) may be rearranged for  $\mathbf{v}_{\text{ecef}} \cdot \mathbf{e}$  to get the radial velocity.

It should be noted that in rare ( $\sim 1$  detection in every 3000) cases, we found it became impossible to estimate the AOA of the meteor unambiguously when the phase biases and noise were incorporated into the receiver time series (i.e. the error code 3 discussed in Holdsworth et al., 2004a, was encountered). In these cases, the echo in question was simply discarded from the subsequent calculation of mean winds and covariances.

### 3.7 Mean horizontal wind and tidal component estimation

The way we have estimated mean horizontal winds in this simulation is similar to that typically applied to meteor

radars in the literature (e.g. Hocking and Thayaparan, 1997; Holdsworth et al., 2004a). Our approach has been to use singular value decomposition (SVD) to solve the following inverse equation in the least-squares sense for  $\mathbf{v}$ :

$$\mathbf{v}_r = \mathbf{A}\mathbf{v}, \quad (8)$$

where  $\mathbf{v}_r$  is a  $n_{\text{met}} \times 1$  vector of radial velocities ( $n_{\text{met}}$  being the number of meteors in the time bin under consideration),  $\mathbf{v}$  is a  $2 \times 1$  vector of wind velocities, and  $\mathbf{A}$  is a  $n_{\text{met}} \times 2$  matrix whose rows take the same form as that described in Eq. (6) (without the vertical component). However, it is important to note in this case that the  $\theta$  and  $\phi$  defined in  $\mathbf{A}$  represent the orientation of the  $\mathbf{e}$  (or Bragg) vector (see Fig. 3) in the ENU coordinate system at the location of the meteor. The velocities in  $\mathbf{v}_r$  of course also represent the projection of the wind vector on the  $\mathbf{e}$  vector; i.e.  $v_{\text{rm}}/\cos(\beta/2)$ , where  $v_{\text{rm}}$  is the radial velocity measured at the receiver.

In order to remove outliers from the input radial velocity distribution, we follow the iterative scheme proposed by Hocking and Thayaparan (1997) (and subsequently used by e.g. Holdsworth et al., 2004a). This involves performing an initial fit for the wind velocities, removing the radial velocities whose value differs from the horizontally projected radial wind by more than  $25 \text{ m s}^{-1}$  and repeating the procedure until no outliers are found or until less than six meteors remain.

### 3.8 Removal of background wind and tides

To remove the previously estimated mean winds and tides from the time series, we have calculated a low-pass-filtered version of the hourly averaged horizontal wind time series using an inverse wavelet transform with a Morlet wavelet basis, linearly interpolated a wind estimate at the time of each meteor, and subtracted the radial projection of the wind from the radial velocity time series. This is in principle similar to the approach of Fritts et al. (2010a), who applied an S transform (in preference to a least-squares sinusoidal fit) in order to more completely remove transient spectral features around the tidal periods from the time series. The application of the inverse wavelet transform is described in Appendix B.

To ensure that the filtered time series pertain to tidal-like (or longer) wind oscillations (and not short-period GWs), we select a minimum scale size in the reconstruction of 6 h and a total number of scales of 250. The reconstructed time series is then interpolated to the times of each of the meteors in question, and the radial component of this wind at each of the meteor positions is subtracted from the measured radial velocity.

### 3.9 Covariance estimation

Following the removal of the mean and tidal components of the horizontal wind from the radial velocities, covariances that pertain predominantly to gravity-wave-driven wind per-

turbations are estimated. The approach we apply is based on those presented by Thorsen et al. (1997) and Hocking (2005); much like in the wind estimation, it involves using SVD to least-squares solve the following inverse equation:

$$\mathbf{v}_r'^2 = \mathbf{A}'\mathbf{v}', \quad (9)$$

where  $\mathbf{v}_r'^2$  is a  $n_{\text{met}} \times 1$  vector containing the squares of the perturbation component of the radial velocities,

$$\mathbf{v}' = \left[ \langle u'^2 \rangle, \langle v'^2 \rangle, \langle w'^2 \rangle, \langle u'v' \rangle, \langle u'w' \rangle, \langle v'w' \rangle \right]^T$$

is the vector of covariance components, and  $\mathbf{A}'$  is a  $n_{\text{met}} \times 6$  matrix whose rows read

$$\left[ \sin^2\theta \sin^2\phi, \sin^2\theta \cos^2\phi, \cos^2\theta, \sin^2\theta \sin 2\phi, \sin 2\theta \sin \phi, \sin 2\theta \cos \phi \right].$$

It is noted that, as per the wind estimation case, the  $\theta$  and  $\phi$  terms represent the orientation of the  $\mathbf{e}$  vector in ENU coordinates at the location of each meteor and that the velocities in  $\mathbf{v}_r'^2$  are based on the wind velocities' projection onto  $\mathbf{e}$ .

A two-step radial velocity outlier rejection procedure is utilized to remove meteors with dubious square radial-velocity–AOA pairs from the input distribution in an attempt to reduce the bias in the resulting covariance estimates. The first step is to discard all radial-velocity–AOA pairs that have a projected horizontal velocity of  $\geq 200 \text{ m s}^{-1}$  (by virtue of which we argue that measured horizontal velocities above this threshold are nonphysical). The second step iteratively discards the pairs that satisfy the following criterion:

$$|v_{ri}'^2 - v_{rpi}'^2| \geq \left[ \text{median} \left( \sqrt{|v_r'^2 - v_{rp}'^2|} \right) + 5 \times 1.4826 \times \text{MAD} \left( \sqrt{|v_r'^2 - v_{rp}'^2|} \right) \right]^2, \quad (10)$$

where  $v_{ri}'^2 = A_{i*}'\mathbf{v}'$  is the  $i$ th projected square radial velocity, MAD indicates the median absolute deviation operator, and 1.4826 is the factor to convert a MAD to a standard deviation, assuming the input has a Gaussian distribution. In practice, we have found that the 5-standard-deviations criterion removes outliers that are large enough to substantially bias the resulting covariance estimates, without iteratively removing an excessive number of samples that are good. The intention of using the median and MAD statistics (as opposed to mean and standard deviation) has been to reduce the bias outlying points inflict on the measured standard deviation of the distribution of  $|v_{ri}'^2 - v_{rpi}'^2|$ .

The performance of the second outlier rejection criterion on simulated data is briefly summarized in Sect. 3.11.3.

### 3.10 Truth value of the simulated covariances

To evaluate the truth value of the simulated covariances – i.e. that used to estimate the accuracy and precision of the covariances derived through inversion of Eq. (9) – we have opted to

compute the covariances at the origin of the coordinate system (in the meteor region directly above the receiver at BP) at 2 min time resolution. We found this estimate to agree extremely closely with that computed at the positions and times of the meteors incorporated in the simulation, which in turn represents the most accurate and precise estimate one could hope to obtain when inverting Eq. (9).

In the case of using wave fields generated from the previously discussed gravity wave spectral model, we found that the covariances estimated by inverting Eq. (9) are more correlated with those calculated using the above two methods than those computed by summing the covariances associated with each wave in the spectrum. Therefore, while the latter method gives the covariances that would be measured over an infinitely large sampling area/time (in a sense the expectation value of the covariances), we have refrained from using it as a truth value with a view to not overestimating the size of the simulated technique's measurement errors.

### 3.11 Simulation results

#### 3.11.1 Spectrum of gravity waves

This section considers the covariance bias distributions associated with a wind field generated using the GW spectral model discussed in Sect. 3.4. Three different time integration cases (that are later employed in this paper on real data) are tested: 1 d (which could be considered fairly high time resolution sampling of day-to-day variations), 10 d (which sacrifices time resolution for measurement precision), and a 20 d composite (which intends to gather enough meteors in each time-of-day bin for a precise covariance estimate but in doing so ignores day-to-day variations entirely).

##### 1 d integration

The biases for 15 000 realizations of 1 d integrated covariance estimations are shown in Fig. 5. It is clear that the  $\langle u'w' \rangle$  term is systematically underestimated, with larger biases present at lower count rates. The width of the bias distribution is also larger at lower count rates. For a simulated mean  $\langle u'w' \rangle$  value of  $\sim 21 \text{ m}^2 \text{ s}^{-2}$ , the distribution widths imply a  $1\sigma$  measurement uncertainty of  $\sim 65\%$  at the peak of the height distribution, and  $\sim 145\%$  at the edges of the distribution, for a multistatic configuration. The same uncertainties are  $\sim 72\%$  and  $168\%$ , respectively, for a monostatic configuration.

The width of the bias distributions for  $\langle v'w' \rangle$  are also essentially identical to those for  $\langle u'w' \rangle$ . The relative uncertainties in the measurements of this term are meaningless, as the wave propagation directions have been chosen in a way that the mean truth value of  $\langle v'w' \rangle$  is zero. What the results do illustrate, however, is that there is no bias in the case of estimating a covariance with a zero mean and that there is no change in the measurement uncertainty of the two compo-

nents arising from the temporal and spatial distribution of the meteors.

It should be noted that  $\langle u'w' \rangle$  is systematically underestimated for both configurations and for all count rate sets investigated, especially at lower count rates (the absolute error ranges from about 20% to 50%). Subsequent investigation has confirmed that this occurs when an attempt is made to remove the tidal effects incorporated in the simulated wind field (i.e. the tides are largely removed, but so is some of the variance due to the GWs). The larger biases at low count rates arise from the inability to define the tidal amplitudes and phases correctly in the presence of wind estimates with larger uncertainties and/or missing wind estimates for particular time bins. Overall, we consider the bias an unavoidable consequence of ensuring that tidal effects are not included in the measured covariances. Further discussion of this point is taken up in Sect. 5.2.

It also appears that there is no clear dependence of covariance uncertainty on the use of a monostatic or multistatic configuration, for a fixed detection rate. This is evidenced by the uncertainties at 84 km for the multistatic configuration (1460 detections) being 14.4 and  $14.5 \text{ m}^2 \text{ s}^{-2}$  for  $\langle u'w' \rangle$  and  $\langle v'w' \rangle$  respectively, as well as the corresponding uncertainties at 88 km for the monostatic configuration (1480 detections) being 15.2 and  $14.6 \text{ m}^2 \text{ s}^{-2}$ . In other words, since these uncertainties are essentially the same, we surmise that combining the detections from the monostatic and bistatic receivers only offers a lower measurement uncertainty at a given height because of the higher number of meteor detections and not because of the altered Bragg vector distribution associated with having two receiver sites.

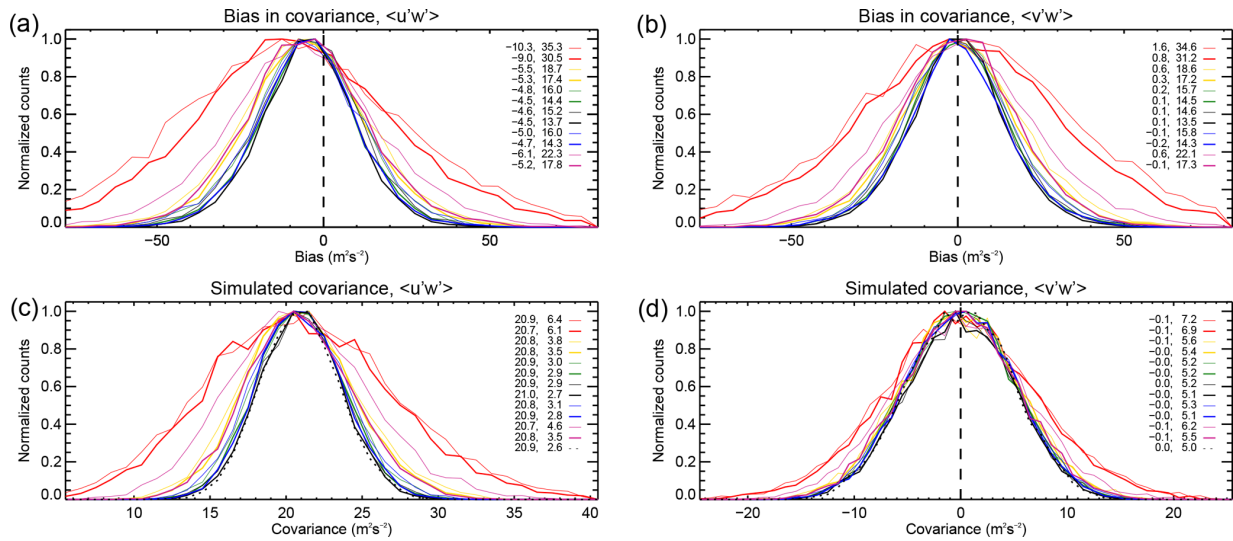
##### 10 d integration

Figure 6 shows the bias distribution for 1500 realizations of 10 d integrated covariance estimates. It is clear that the relative uncertainties in both  $\langle u'w' \rangle$  and  $\langle v'w' \rangle$  are considerably smaller than for 1 d's integration, ranging from  $\sim 50\%$  at the peak of the distribution to  $\sim 60\%$  at the edges. Interestingly, it appears as though the uncertainty is asymptoting to a minimum value, implying that the use of integration times longer than 10 d will lead to diminishing gains in measurement precision. For this reason, we have not opted to use integration times longer than this in the analysis of the BP–Mylor data in this paper.

As per the 1 d integration case,  $\langle u'w' \rangle$  has been systematically underestimated, increasingly so at low meteor detection rates. There is also no clear advantage or disadvantage associated with using the bistatic receiver, meteor detection rates aside.

##### 20 d composite

Figure 8 shows expected values of the covariance bias' mean and standard deviation for 300 realizations of a composite



**Figure 5.** Simulated wind covariance bias distributions for 1 d of integration (a, b) and the simulated covariance distributions (c, d). As discussed in Sect. 3.10, biases are calculated with respect to a reference value computed at 2 min resolution at the coordinate system origin. The lower row shows the distribution for the reference covariance in a dotted black line and the true covariances in coloured lines. The different line colours in each plot represent different simulated heights, which are a subset of those shown in Table 2 (red represents 76 km, yellow 80 km, green 84 km, black 88 km, blue 92 km, and violet 96 km). Thick lines show the distribution for the multistatic case (i.e. by combining data from BP and Mylor), and thinner lines show the monostatic case (i.e. just BP data). The mean and standard deviation evaluated from the samples’ MAD are shown in the left and right columns respectively of the arrays of numbers in each plot figure.

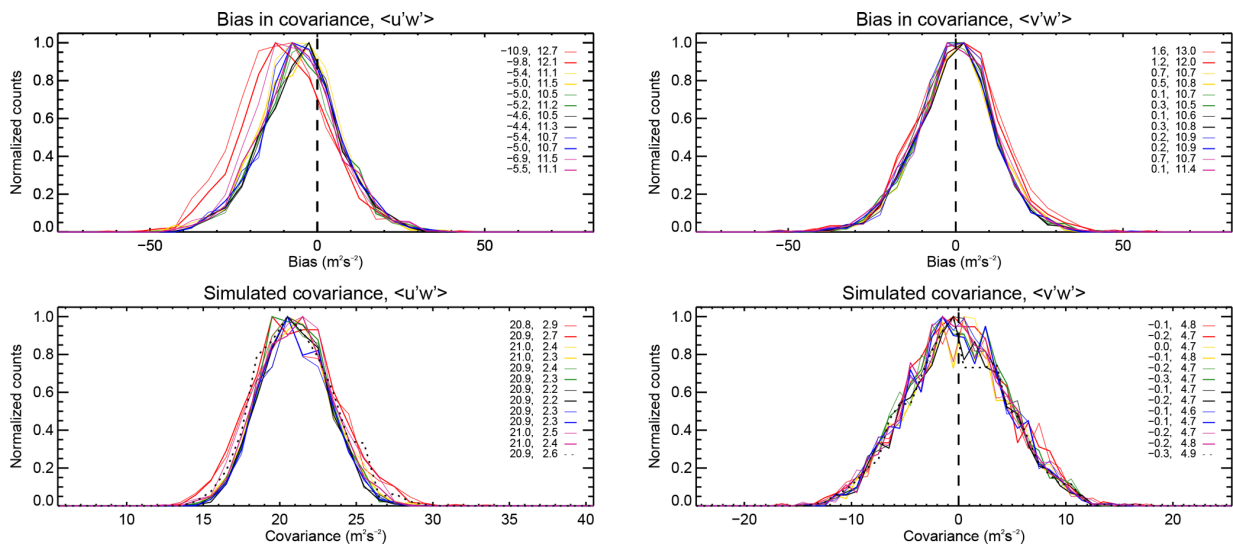


**Figure 6.** As per Fig. 5 but for 10 d of integration.

day spanning an interval of 20 d, with 3 h time bins, as a function of height from 82 to 92 km. The highest standard deviations for both  $\langle u'w' \rangle$  and  $\langle v'w' \rangle$  occur in the 06:00–9:00 and 09:00–12:00 UT bins, and the lowest occur in the 18:00–21:00 UT bin. The mean value for  $\langle u'w' \rangle$ , which is again  $\sim 21 m^2 s^{-2}$ , implies a relative uncertainty at the peak of the height distribution of about 70 % in the 18:00–21:00 UT

bin and about 85 % in the 06:00–09:00 UT bin. It should be noted that the uncertainty is as high as  $\sim 100 %$  in the 06:00–9:00 UT bin at 82 km.

Once again, a systematic underestimation of  $\langle u'w' \rangle$  is present, which as discussed in Sect. 3.11.1 is an artefact of attempting to remove tidal effects.

### 3.11.2 Monochromatic gravity wave

The previous section considered a wind field containing a multitude of waves whose spatial/temporal scales spanned a large part of the spectrum atmospheric gravity waves are expected to occupy. This section briefly addresses the other limiting case, which is that of a wind field consisting of a single monochromatic wave.

In all simulation realizations for this case, we have set the single monochromatic wave's propagation direction to  $45^\circ\text{T}$ , so as to make the true  $\langle u'w' \rangle$  and  $\langle v'w' \rangle$  covariances equal. A horizontal wavelength and phase speed has been randomly selected for each realization, from a uniform distribution with bounds [10, 60] km and [10, 40]  $\text{m s}^{-1}$ , respectively. A 1 d integration is used for the covariance estimate.

The bias distributions for 15 000 realizations are shown in Fig. 7. As per the spectral wave field case, the distribution widths are largest at the edges of the height distribution and narrowest at the peak. However, the widths are far smaller than in the spectral wave field case. Across all wavelengths and phase speeds, the simulated mean true covariance was  $\sim 38 \text{ m}^2 \text{ s}^{-2}$ , which translates to uncertainties of about 8 % and 44 % at the peak and lower edge of the height distribution respectively for the multistatic configuration. For the monostatic configuration, the same uncertainties are about 10 % and 52 %, respectively.

Similarly to the spectral wave field case, both covariance terms are systematically underestimated (ranging from about 2 % to 26 % for  $\langle u'w' \rangle$  in the multistatic configuration at the peak and lower edge of the height distribution, respectively). Interestingly,  $\langle v'w' \rangle$  is underestimated to a slightly lesser degree than  $\langle u'w' \rangle$ . Once again, there is also no clear advantage or disadvantage of using the bistatic receiver (meteor detection rates aside).

### 3.11.3 Outlier rejection criteria performance

This section shows the effect of the application of the outlier rejection criterion of Eq. (10), in the absence of tidal effects and attempted removal of them.

To emulate a radial velocity time series partially corrupted with outliers in this section, Gaussian-distributed noise with a standard deviation of  $50 \text{ m s}^{-1}$  has been added to a randomly selected 5 % of the radial velocity estimates in a given realization. We note that radial velocity errors of this size are rare in practice; they have been used to test the rejection criterion's robustness and to allow us to highlight potential downsides of not having the criterion in place.

Figure 9 shows the covariance bias distributions for the same spectral gravity field as applied in Sect. 3.11.1 and for 1 d of integration, for four cases: rejection not applied with no outliers present, rejection applied with no outliers present, rejection not applied with outliers present, and rejection applied with outliers present. The mean true values for  $\langle u'w' \rangle$

and  $\langle v'w' \rangle$  are the same as in Sect. 3.11.1, i.e.  $\sim 21$  and  $0 \text{ m}^2 \text{ s}^{-2}$ , respectively.

The application of the criterion is clearly beneficial in the presence of outliers, resulting in a reduction in relative uncertainty of the  $\langle u'w' \rangle$  estimate from about 214 % to 74 %. Interestingly, the application of the criterion in the presence of no outliers also results in a slight reduction in relative uncertainty (from about 86 % to 73 %), although it does result in  $\langle u'w' \rangle$  being underestimated (by about 20 %). This point is revisited in Sect. 5.3.

Despite the fact that it appears to introduce a small measurement bias, we still apply the criterion in the subsequent analysis of BP–Mylor data, so that we can be assured that anomalous radial velocities do not contribute to the covariance measurement errors.

## 4 Momentum flux retrievals

This section uses the methodology described in the previous section to estimate covariances from the BP–Mylor meteor radar link from 17 March 2018 through to 9 September 2018. The aim of this analysis was originally to verify that the estimated covariances and flow acceleration derived from them were physically reasonable; however, in observing an apparent tidal modulation of the covariances, we realized that the results themselves may be of more general interest.

### 4.1 Covariances during the austral winter

Plots of the mean horizontal winds and the  $\langle u'w' \rangle$  and  $\langle v'w' \rangle$  covariance terms from 17 March through to 9 September 2018 are shown in Fig. 10. Both quantities have been sampled using 2 km, non-oversampled altitude bins. We chose to evaluate the covariance terms using 10 d long windows, with a time shift of 2 d between the centres of adjacent windows, in an attempt to resolve the planetary-wave-induced modulation of the covariances. A low-pass wavelet filter with a cut-off of 2 d and a 10 d moving average has been applied to the hourly horizontal winds to evaluate the winds shown; the filtering was performed to avoid the aliasing of GW activity and tides into the wind's variability, as well as the moving average in order to more closely match the temporal sampling of the two parameters. Therefore, the winds shown should provide a good measure of the background mean winds responsible for selective filtering of the gravity wave spectrum.

As is expected for this time of year at a mid-latitude SH site (see e.g. Vincent and Ball, 1981), the eastward winds around 80 km generally increase with time from the autumnal equinox to the winter solstice ( $\sim$  days 80 and 170 respectively) and decrease toward the vernal equinox ( $\sim$  day 265). A wavelet analysis (not shown here) reveals that much of the shorter term zonal wind variability evident in the figure is transient and encompasses a spectrum of periods between about 10 and 60 d. The meridional wind, conversely,

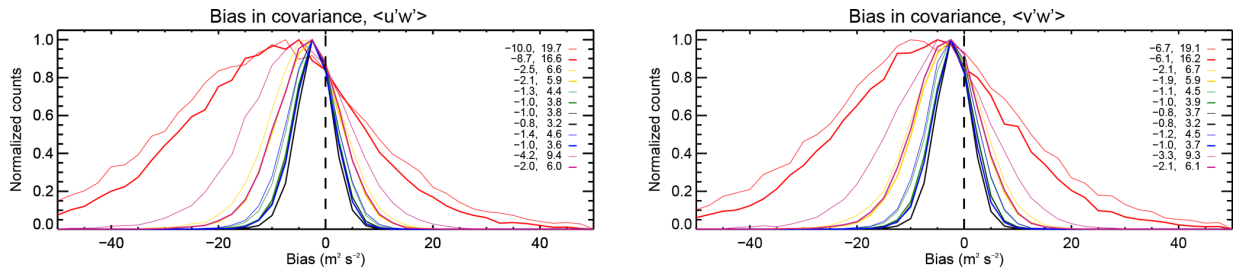


Figure 7. As per Fig. 5 but for single monochromatic GWs.

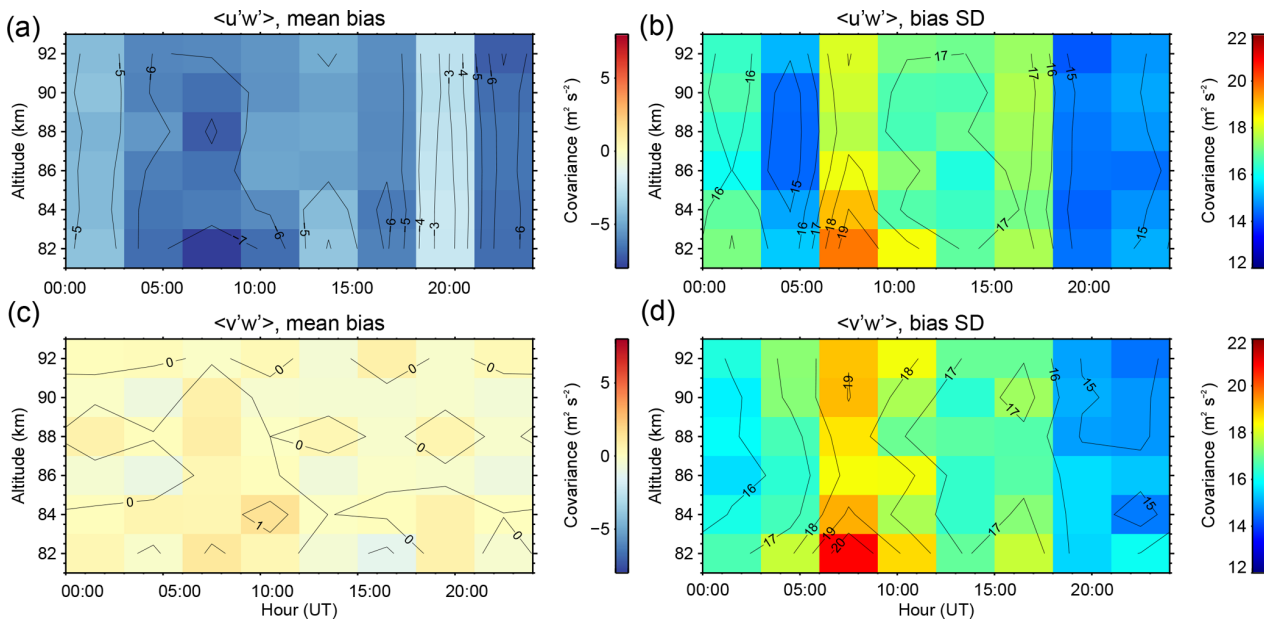


Figure 8. Means and standard deviations of the simulated  $\langle u'w' \rangle$  (a, b) and  $\langle v'w' \rangle$  (c, d) bias distributions for a 20 d composite, as a function of height, for the BP–Mylor link.

has a mean much closer to zero. Much of its variability is confined to periods around 10, 20, 25, and 40–50 d below 90 km, with variability in the 50–100 d period becoming increasingly dominant above 90 km.

The level of (anti)correlation between the covariance terms and the winds is highly variable. The  $\langle u'w' \rangle$  term appears to be anticorrelated with the zonal wind between 80 and 84 km around the winter solstice, as does  $\langle v'w' \rangle$  with the meridional wind above 88 km across a similar time interval. While pronounced levels of anticorrelation between these quantities in the mesospheric region arising from the selective filtering mechanism are typical (see e.g. the recent summary provided by Jia et al., 2018) – particularly in the zonal component – departures from these predictions are also not uncommon. As Jia et al. (2018) explains, it is difficult to conceive a mechanism for departures from this theory in the zonal component (given the dominance of eastward winds in the lower mesosphere during winter), aside from consider-

ing that the GWs may have propagated through a region with weak eastward mesospheric winds.

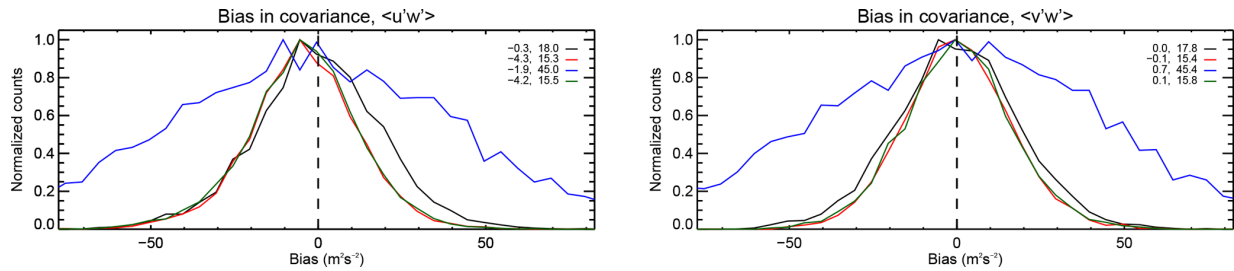
The feature we focus the remainder of this discussion on concerns the coincident enhancement in the  $\langle u'w' \rangle$  and  $\langle v'w' \rangle$  terms in the interval spanning days 100 to 120, around 90–94 km. Peak values of  $\sim 50$  and  $100 \text{ m}^2 \text{ s}^{-2}$  for  $\langle u'w' \rangle$  and  $\langle v'w' \rangle$  respectively are obtained during this interval. Interestingly, they coincide with a brief enhancement in the zonal winds at the same height and the peak of the northward phase of an oscillation in the meridional winds with periods spanning 50–100 d.

Figure 11 shows an inset of Fig. 10, spanning April 2018 (which the aforementioned covariance enhancement is centred on). In an attempt to increase the temporal resolution, the covariances in this figure have been evaluated with 1 d windows, with a time shift of 6 h between adjacent windows. Tidal components have also been removed from the winds as per Fig. 10 (i.e. in order to not alias tidal/GW activity into



4802

A. J. Spargo et al.: Momentum flux estimation using multistatic meteor radar



**Figure 9.** Covariance bias distributions for different combinations of outlier contamination and outlier rejection. Black is no rejection or outliers, red is rejection with no outliers, blue is outliers without rejection, and green is outliers with rejection.

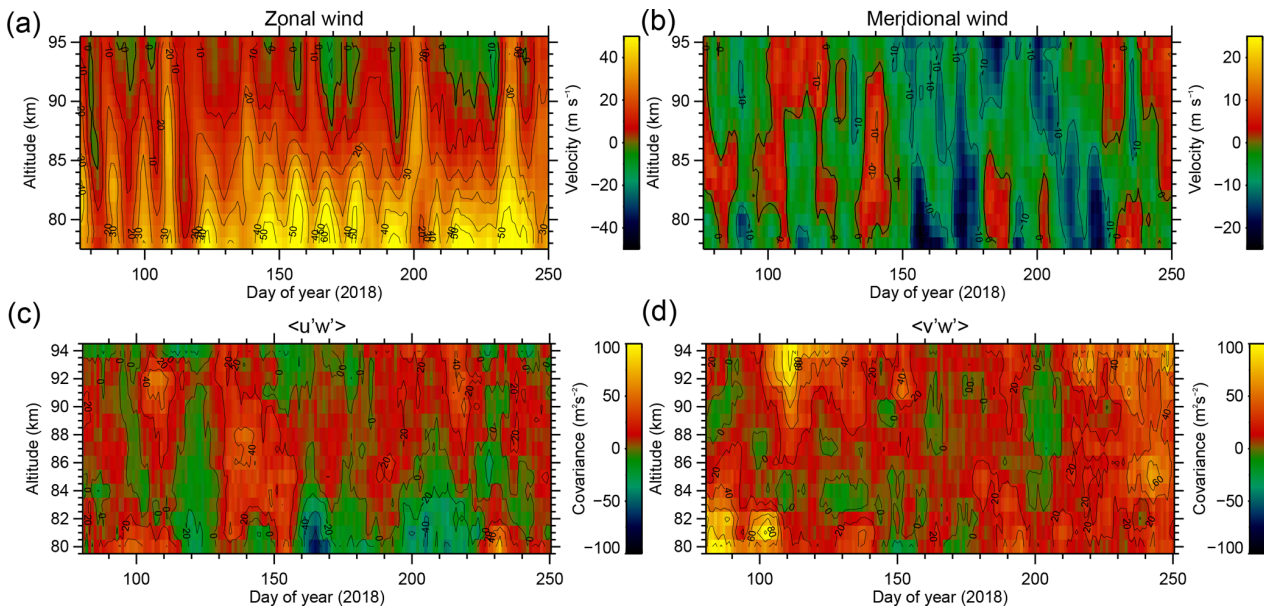


**Figure 10.** Mean horizontal winds (a, b) and the  $\langle u'w' \rangle$  and  $\langle v'w' \rangle$  covariance components (c, d) measured using the BP–Mylor link between 17 March and 9 September 2018. As discussed in Sect. 4.1, the winds shown correspond to a 10 d moving average of the hourly averaged winds with tidal components removed, and the covariances have been evaluated over 10 d windows, with a time shift of 2 d between the centres of adjacent windows.

the winds), and for a closer match to the time sampling of the covariances, no moving average has been applied.

This figure shows evidence of a pronounced periodicity around 10 d in the zonal wind, which attains its highest amplitude at approximately day 110 around 85 km. At this time and in the same altitude region, the mean meridional winds abruptly (over a period of a few days) switch from northward to southward. All of this variability is likely attributable to a superposition of planetary waves. Albeit noisy (owing to the relatively short integration time), the  $\langle u'w' \rangle$  covariance term shows an enhancement between days 105 and 110, and attains especially high positive values (exceeding  $100 \text{ m}^2 \text{ s}^{-2}$ ) at around 90 km altitude. Interestingly, the  $\langle v'w' \rangle$  enhancement lags that of  $\langle u'w' \rangle$  by several days, with a peak again in excess of  $100 \text{ m}^2 \text{ s}^{-2}$  around day 110.

We have also noted that this interval is associated with an abrupt enhancement of the amplitudes of the diurnal and semidiurnal tides. Figure 12 shows the amplitude of the horizontal wind time series reconstructed from an inverse wavelet transform (see Eq. B1), for scales between 0.4 and 0.6 d for the semidiurnal tide and between 0.8 and 1.2 d for the diurnal tide. The diurnal tide in the zonal wind is seen to reach an amplitude of  $\sim 50 \text{ m s}^{-1}$  during day 107 at a height of around 92 km and of  $35\text{--}40 \text{ m s}^{-1}$  in the meridional component around 88 km during day 109. It should be noted that the hourly averaged zonal wind velocity (not shown here) reached a maximum of about  $140 \text{ m s}^{-1}$  at 92 km during this period. The semidiurnal tide, whose amplitude is known to rarely exceed  $10 \text{ m s}^{-1}$  at Adelaide's location (e.g. Vincent et al., 1998), also reached an amplitude of  $35\text{--}40 \text{ m s}^{-1}$  during day 104 in both the zonal and meridional components, at

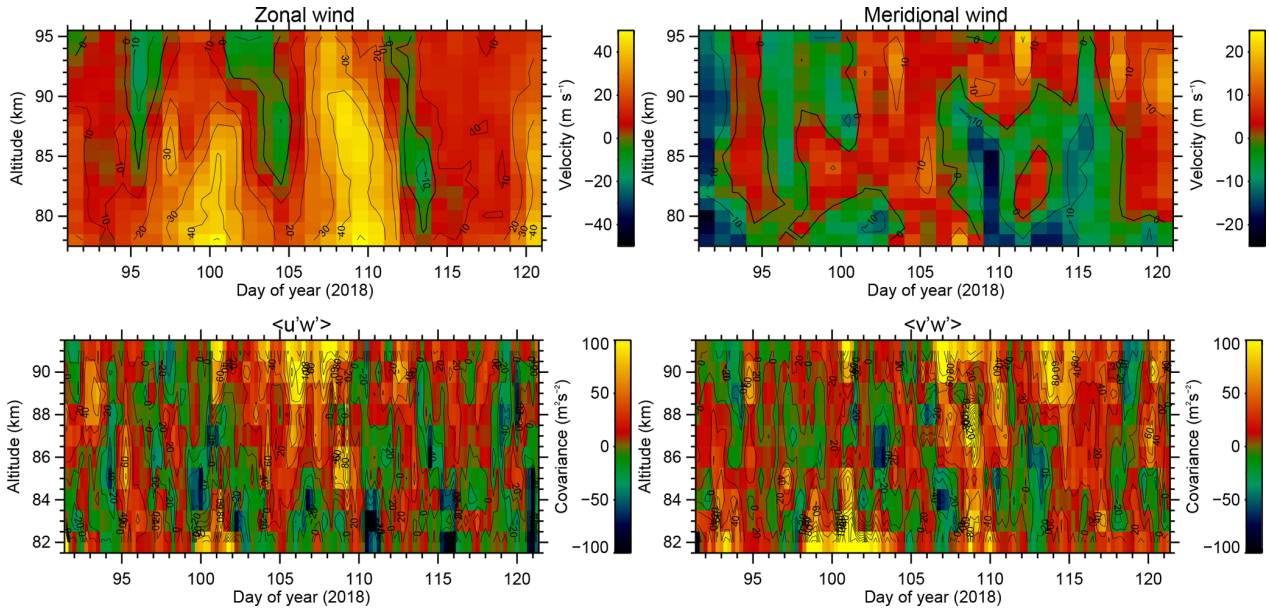


**Figure 11.** As per Fig. 10 but for April 2018. Also, in this case no moving average has been applied on the winds post-tide removal, and the covariances have been evaluated over windows of length 1 d, with a time shift of 6 h between the centres of adjacent windows.

a height of around 94 km. The figure additionally shows that the phase of the diurnal tide is modulated, with the timescale of those modulations appearing to follow the phases of the planetary wave activity in Fig. 11 – although there are no noteworthy phase changes at the times of the sudden amplitude enhancements. The semidiurnal tidal phase is persistent, and also has a well-defined vertical progression, during the few days in which its amplitude is large but clearly has little meaningful structure at other times.

The large tidal amplitudes during this period lead us to expect the propagation directions of the GWs removed from the wave spectrum by the winds to exhibit a diurnal variation. A complicating factor is that these waves may also amplify, dampen, or shift the phase of the tide, depending on the waves retained in the spectrum at the wave breaking height; the large variability in the tidal amplitudes during this period indicates that this may have indeed occurred. To provide some clarity on the extent to which the GWs have been modulated by the tide and vice versa, in the next section we examine a composite day of the tidal winds, covariances, and the implied flow accelerations over a 20 d interval spanning the interval in which the diurnal tide has a reasonably consistent phase and an enhanced amplitude.

## 4.2 Observed GW–tidal interaction

Figure 13 shows a composite day of the horizontal winds, covariances, and flow accelerations implied by the covariances, over 5–25 April 2018 (i.e. days 95–115). The composite day consists of time windows of width 3 h, with a time shift of

30 min between the centres of adjacent windows. The height binning again consists of 2 km width bins with centres separated by 1 km.

The flow accelerations (e.g. in the case of the zonal direction) have been evaluated using the expression (e.g. Fritts, 1984):

$$\langle F_x \rangle = -\frac{1}{\rho(z)} \frac{\partial}{\partial z} (\rho(z) \langle u'w' \rangle), \quad (11)$$

where  $\rho(z)$  represents the neutral density as a function of height  $z$ . The density climatology we have used has been derived from the Sounding of the Atmosphere using Broadband Emission Radiometry (SABER) satellite instrument (see Appendix C for details). Similarly to Liu et al. (2013), we also apply a low-pass filter with a cut-off wavelength of 10 km to the vertical profile of the covariance prior to evaluating its density-weighted derivative, in order to remove small-scale fluctuations from it that are clearly not associated with tidal modulation.

As expected from the amplitudes in Fig. 12, both horizontal wind components show a predominantly diurnal variation, with the meridional component lagging the zonal's by approximately 6 h across the observed height region. The time of the zonal wind maximum occurs around 00:00 UT at 92 km and 08:00–09:00 UT at 82 km.

In contrast, the  $\langle u'w' \rangle$  covariance term shows a predominantly semidiurnal variation with little vertical phase progression, maximizing at around 00:00 and 12:00 UT and minimizing around 05:00 and 20:00 UT. The  $\langle v'w' \rangle$  term is more variable with altitude, exhibiting a semidiurnal varia-

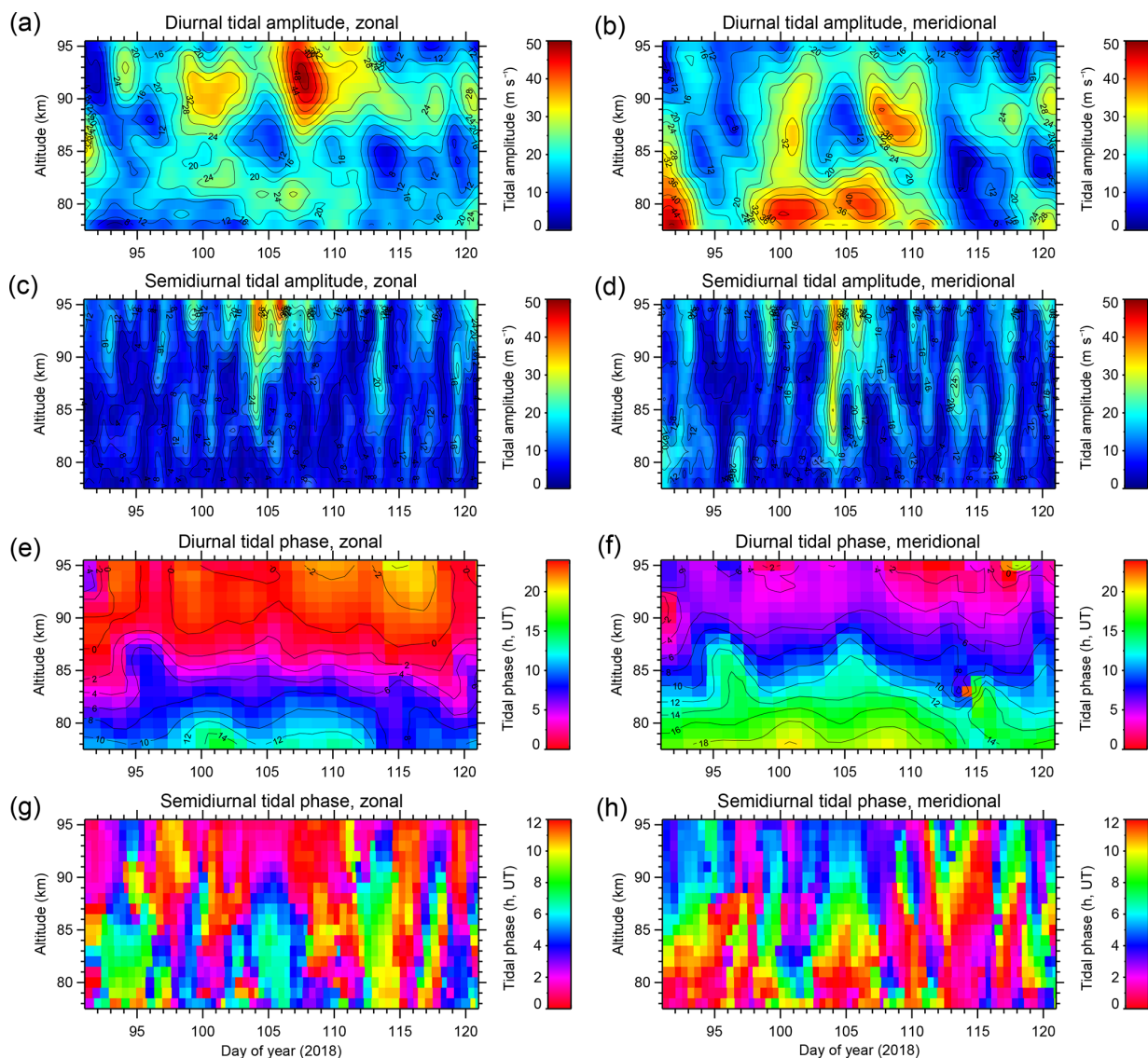


**Figure 12.** Amplitude of the diurnal (a, b) and semidiurnal (c, d) tides, and phase of the diurnal (e, f) and semidiurnal (g, h) tides as measured by the BP–Mylor meteor radar during April 2018.

tion between 82 and 84 km and a largely diurnal variation above this. The semidiurnal variation between 82 and 84 km is associated with positive covariances for the entire day except between about 18:00 and 24:00 UT, and the diurnal variation above is associated with negative covariances between about 08:00 and 15:00 UT and positive otherwise.

Between about 88 and 92 km, the zonal flow acceleration shows a pronounced minimum between 04:00 and 06:00 UT, a maximum around 13:00 UT at about 88 km, and a weaker minimum around 19:00 UT. The maximum occurs at a similar time to the corresponding zonal wind minimum, whereas the first minimum lags the zonal wind maximum by about 5 h, and the second minimum precedes it by about 5 h.

Conversely, there is little flow acceleration structure below 87 km, other than a broad maximum at about 85 km around 01:00 UT. These observations are difficult to reconcile for three reasons: (1) the wave forcing is consistent with a rapid deceleration of the zonal wind from 04:00 to 06:00 UT at around 90 km, but there appears to be no positive forcing around 20:00 UT to accelerate the wind; (2) the strong positive forcing which does occur around 13:00 UT appears to result in little wind variability; and (3) the positive forcing around 85 km between 23:00 and 04:00 UT is associated with an acceleration of the zonal wind, but this acceleration is much smaller than that around 90 km.



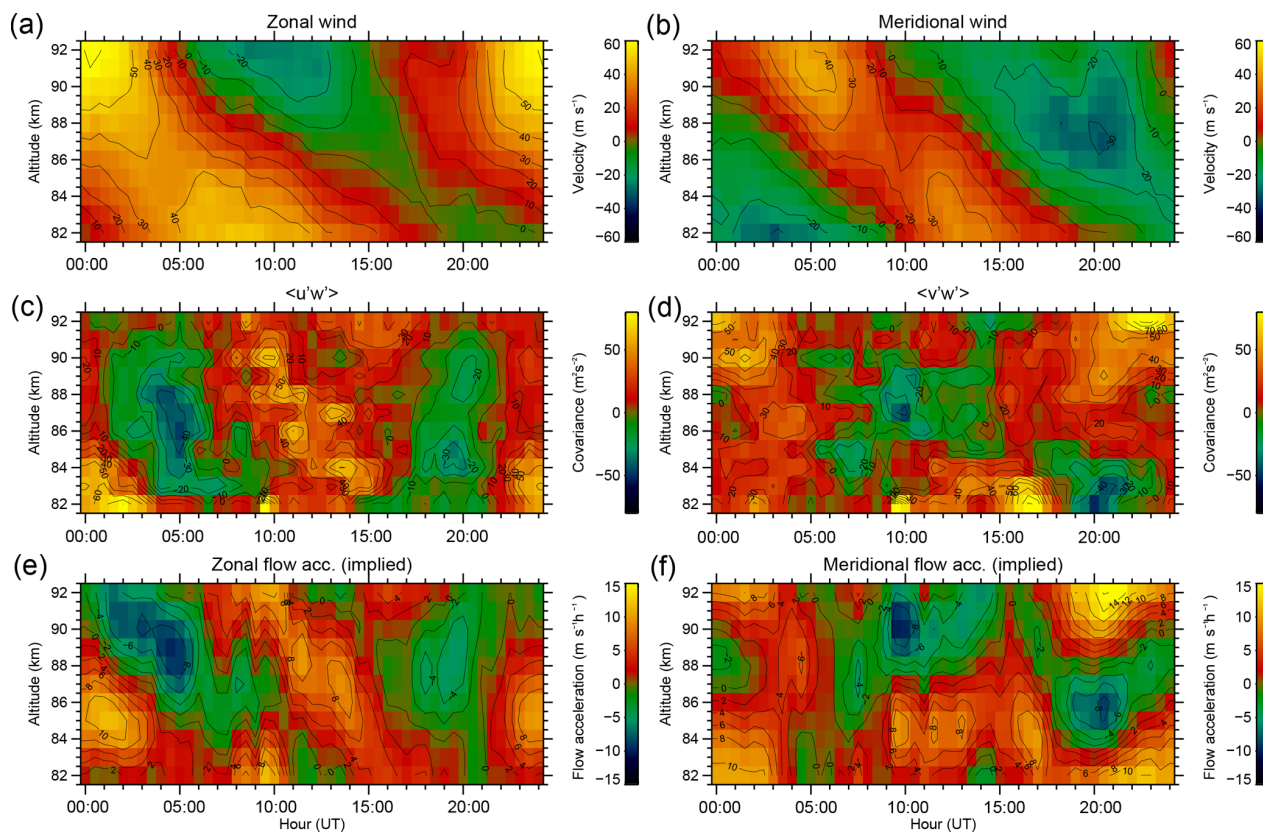


**Figure 13.** A composite day of the horizontal winds (a, b), covariances (c, d), and flow accelerations implied by the covariances (e, f), spanning 5–25 April 2018.

From 88 to 92 km, the meridional flow acceleration shows a small maximum around 04:00 UT, a minimum at about 10:00 UT, and a large maximum around 20:00 UT. As per the zonal case, this leads to a peculiar relationship with the meridional wind; the forcing's large maximum occurs at a similar time to the wind minimum, the minimum corresponds roughly with a rapid wind deceleration, and the smaller maximum corresponds with a rapid wind acceleration. As for the zonal component, there is little meridional flow acceleration structure below around 86 km.

## 5 Discussion

### 5.1 Uncertainties in $\langle u'w' \rangle$ and $\langle v'w' \rangle$ estimates

In the simulations section of this paper, we have tried to conclusively define estimates for the absolute and relative uncertainties of the  $\langle u'w' \rangle$  and  $\langle v'w' \rangle$  covariance terms as measured by the multistatic BP–Mylor meteor radar, for typical time and height sampling cases. We subsequently replicated these sampling schemes on the case study data. Even with this replication, we have noticed that there are three main

caveats in applying the uncertainties directly to the observations:

1. As shown by Kudeki and Franke (1998), the covariance estimation uncertainty is proportional to the geometric mean of the horizontal and vertical variances, in the case of sampling the wind field using a perfect anemometer. Assuming this holds for a meteor-radar-like detection distribution, this means that the absolute uncertainties of  $\langle u'w' \rangle$  and  $\langle v'w' \rangle$  reported in this paper should be similar for a given wave field, regardless of the value of  $|\langle u'w' \rangle|/|\langle v'w' \rangle|$ . Therefore, the likelihood of correctly estimating the sign of one of the components in the presence of an anisotropic wave field may not be the same as for the other component.
2. As evidenced by the differences in the distribution widths of Figs. 5 and 7 for given detection rates, the relative uncertainties of a non-zero covariance term appear to be dependent on the total frequency/scale span of all the associated waves. In our example, the relative uncertainty in the covariance for a spectral GW field is around 8 times that for a single monochromatic GW. This finding, which is qualitatively consistent with the conclu-

sion reached by Vincent et al. (2010) (for high meteor detection rates) and Fritts et al. (2012a), makes it impossible to accurately define the covariance measurement uncertainty for this radar without a priori knowledge of the GW field and its variation with time.

3. The spectral components of the wave field may vary during the integration period. This is particularly problematic for the 10 d window; for example, during a period of intense but short-lived monochromatic wave events followed by more complex wave activity, increasing the integration time may actually increase the uncertainty in the covariance estimate of the monochromatic wave activity – not only because of the likely change in the mean covariance, but also because of the noise added to the radial velocity time series by the more complex activity.

Despite these caveats, we can broadly conclude that the 10-day integrated covariances (Fig. 10), except where the absolute values are smaller than about  $10\text{--}15\text{ m}^2\text{ s}^{-2}$ , are likely to be of the correct sign. The correlation length of the features in both the time and height domains also indicates that the noise component in the signal is considerably smaller than the sum of all the modes of geophysical variability. Additionally, at this time integration there is likely to be little difference in the uncertainty at the peak and edges of the height region analysed.

The 1 d integrated covariances (Fig. 11), in contrast, are far more affected by measurement noise. There is still some degree of temporal-height correlation, especially in the region of consistently high values of  $\langle u'w' \rangle$  between days 105 and 110 above about 86 km, but very little below 84 km. The excursions below 84 km are of the same order as the simulations predict for 1 d of integration in a spectral wave field, so it may be that the noise component at these heights is considerably larger than the signal.

The 20 d composite covariances (Fig. 8), while clearly affected by measurement noise, do not show fluctuations from bin to bin of the same size as the uncertainties predicted in the corresponding simulation. This gives weight to the covariance structures observed and also suggests that the wave field being observed over the 20 d period was not as complex as the simulation's or particularly variable.

Unfortunately, it is impossible to know (using the meteor observations alone) if the discrepancies between the 1 and 10 d integration (for example, the absolute values of the covariances during the enhancement between days 105 and 110) are a result of statistical noise in the 1 d estimate or a precise estimate of a strong, transient monochromatic wave event using the 1 d integration. The observation of waves in the MLT airglow may aid in the interpretation of how monochromatic the background wave field is; in the future, we intend to complement these meteor radar case studies with images of the sodium and hydroxyl airglow taken nearby the BP site. This, in conjunction with the random re-

sampling method employed by Liu et al. (2013), may lead to more refined uncertainty estimates.

In the 10 d integrated results, the small difference in measurement error at the peak and lower edge of the height distribution (around 20 %, for an order of magnitude increase in detections) places an important question on the usefulness of further increasing the integration times/detection rates. On this point, Fritts et al. (2012a) argued that the covariance measurement error should decrease with the square root of the number of detections and, by extrapolating from the 250 % error for a 1 h integration presented in Vincent et al. (2010), concluded that their relative error for a 1-month composite should have been as low as 10 %. Our simulations suggest that an increase in precision of this magnitude cannot occur. Moreover, using a similar detection rate and a 3 h bin in our 20 d composite of a spectral model-derived wave field shown in Fig. 8, we obtain a minimum relative error of about 70 %. In saying this, we note of course that a relative error of 10 % is possible for a considerably less complex wave field.

## 5.2 Effects of tides on covariance estimates

All of our simulations have shown that a systematic underestimation of non-zero covariances arises when an attempt is made to remove tidal effects. This clearly becomes more of a problem in the presence of large-amplitude GWs with ground-based periods close to those of the tides. A number of questions about the process of tidal removal could be raised:

1. What is the importance of incorporating the momentum fluxes of gravity waves with ground-based periods close to the tides in climate models?
2. If those longer-period waves are unimportant, what is an appropriate frequency cut-off for covariance measurements?
3. If those waves are important, what is the optimal way to remove the tides?

With regard to 3, it may be that a wavelet/S transform has insufficient frequency resolution to define solely tidal features; a long-windowed harmonic fitting (as used by e.g. Andrioli et al., 2013a) may be more appropriate if there is a specific interest in GW features close to or between the tidal periods. Of course, this method assumes no variability in the tidal amplitudes, tidal periods, or in the GW spectrum. The best way forward may be to simply apply both of the methods independently and contrast their effects.

## 5.3 Radial velocity outlier removal

In Sect. 3.11.3 we showed that the radial velocity outlier rejection scheme of Eq. (10) substantially increases the covariance measurement precision in the presence of outliers. However, we note that the criterion used (especially the 5-standard-deviations aspect) has not been rigorously tested;

we merely selected it on the basis of it removing points in the distribution of  $|v_{ri}^2 - v_{rp_i}^2|$  (real and simulated) that we had noticed were spuriously affecting the covariance estimates. A more rigorous scheme would adaptively modify the thresholding based on observed characteristics of the wind field rather than simply the residual of the fit.

A complication arises from the fact that the criterion results in a more precise (albeit less accurate) covariance estimate in the absence of outliers. This also illustrates an important point about the sensitivity of the Eq. (9) inversion to the input: it is as though the data that contribute to the accuracy of the measurement actually increase the measurement's uncertainty, if they are associated with large radial velocity perturbations.

#### 5.4 Weighting of meteors in the wind/covariance estimation fits

A subject we have not addressed in this paper is the application of weights to the meteors in the inversion of Eqs. (8)/(9) to minimize the errors in the resulting winds/covariance estimates. In particular (as discussed by Hocking, 2018), at the midpoint between the transmitter and receiver sites the  $e$  vector (see Fig. 3) is vertical, meaning that the measured radial velocity corresponds to the true wind velocity projected onto the vertical. Large errors in the inverted horizontal winds/covariances may result in the presence of radial velocity errors here and at nearby locations where  $e$  is close to vertical. We decided to ignore the issue on the basis of there being a small number of meteors with sufficiently oblique entrance angles to be detected in this region; at Mylor, we found about 0.3 % of all detected meteors to have effective zenith angles (that is, the zenithal orientation of the  $e$  vector) of less than  $20^\circ$ . Nevertheless, there is still a need to quantify the usefulness a weighting scheme may have in minimizing errors arising from these meteors.

#### 5.5 Observed GW–tidal interaction

Our aim in analysing the GW-induced flow accelerations in Sect. 4.2 has been to verify that the estimated momentum fluxes were physically reasonable and devoid of tide-induced biases, as well as to contribute to the well-known gap in knowledge of GW effects on tides. Our analysis, which was centred on a 20 d interval containing an abrupt enhancement in tidal amplitudes, has yielded inconclusive results on whether the GW momentum deposition has on the whole enhanced, dampened, or changed the phase of the tidal motions. Nevertheless, the expected uncertainties in the flow accelerations based on the bias mean and standard deviations in the Fig. 8 covariances, shown in Fig. 14, indicate that the signal components between 84 and 90 km shown in Fig. 13 will have well exceeded the noise levels.

The results are complex, illustrating tidal enhancement at some times of day, dampening at others, and that there are

also times in which a forcing is present but no apparent effect on the tide is clear. A broad observation is that the forcing components have a more pronounced diurnal variability between about 86 and 92 km, with the result that the forcing dampens the tide at the tide's minimum (i.e. westward and southward phase) and shifts its phase at its maximum. Of course, our interpretation is complicated by the fact that we have no knowledge of what the tidal features may have looked like without any GW forcing.

It is widely accepted in modelling studies that GW forcing plays a role in the observed seasonal variation of the migrating diurnal tide (DW1) amplitudes (i.e. equinoctial maxima and solstitial minima) and that whether amplification or dampening of the amplitude occurs depends on the GW source spectrum (e.g. Ortland and Alexander, 2006; Yiğit and Medvedev, 2017). However, there is still ongoing debate about whether or not the forcing is responsible for all of DW1's observed amplitude and phase variability. For example, both Mayr et al. (1998) and Watanabe and Miyahara (2009) have concluded that the forcing is in phase with DW1 during the equinoxes and out of phase during the solstices, leading to DW1's amplification at the equinoxes and dampening at the solstices. Yiğit and Medvedev (2017) reached the same conclusion for the September equinox but stated that Watanabe and Miyahara (2009) may have significantly underestimated the magnitude of the forcing. In contrast, for the March equinox Lu et al. (2012) has argued that the tidal variability is caused by a superposition of GW forcing and advection terms that varies with altitude and latitude and that GW forcing exclusively dampens tidal amplitudes in the MLT/I. Moreover, Lu et al. (2012) has reported considerably larger GW forcing magnitudes than in a related modelling study by McLandress (2002).

The small number of recent observational studies that have sought to quantify the effect of GW forcing on the DW1 amplitude and phase have also yielded contradictory results. For example, using TIMED satellite data Lieberman et al. (2010) showed that while the zonal and meridional GW forcing maximizes at the equinoxes and minimizes at the solstices, the zonal forcing is in quadrature with the zonal tidal wind, and the meridional forcing is out of phase with the meridional tidal wind, leading to a zonal tide with advanced phase and a dampened meridional tide. They noted that the zonal advection due to variability in the meridional DW1 amplitude also, like the GW forcing, maximized at the equinoxes and minimized at the solstices but were not able to reconcile if this variability was a cause or an effect of the seasonal DW1 variation. Also using TIMED data, Xu et al. (2009) concluded that the GW-induced dampening of tidal amplitudes is largest during equinoxes and therefore that dampening cannot cause the observed seasonal variation in tidal amplitudes. In contrast, using measurements from a ground-based meteor radar in Hawaii ( $20.7^\circ$  N,  $156.3^\circ$  W), Liu et al. (2013) noted that GW forcing tends to slightly dampen the DW1 amplitude below 90 km but enhance it above 90 km. Using a similar

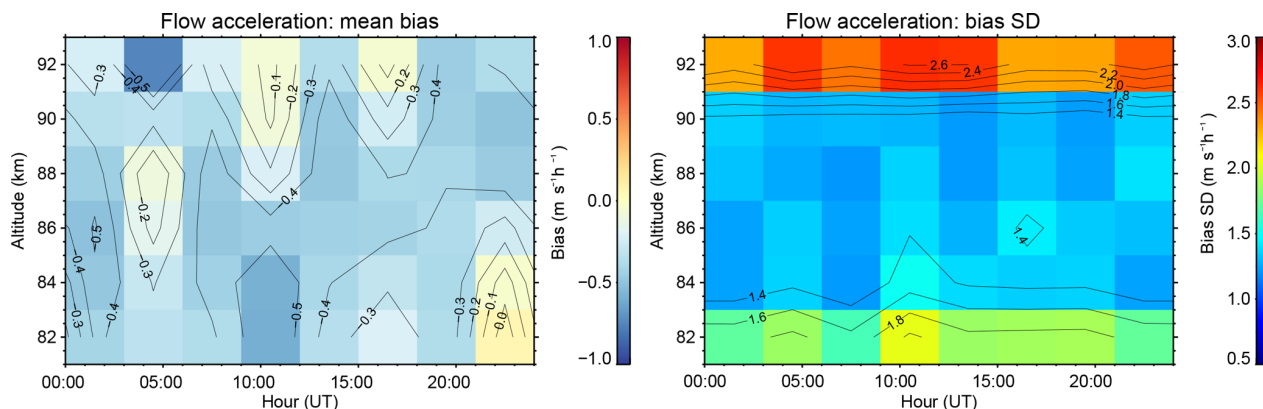


**Figure 14.** Simulated errors in flow acceleration estimates, using the bias mean and standard deviations in the Fig. 8 covariances.

approach on lidar data from Starfire Optical Range (35.0° N, 106.5° W), Agner and Liu (2015) also noted that GW forcing can amplify or dampen the DW1 amplitudes, depending on the altitude.

Tides may also interact with GWs through the diurnal variations in atmospheric stability they induce (i.e. making conditions more favourable for GW breaking and hence GW forcing at particular times of day). For example, Fritts et al. (1988) showed from observations at Scott Base, Antarctica, that the highest levels of turbulence due to convective instability occurred at the times that the vertical component of the tidal wind induced the most negative value of  $dT/dz$  (the vertical temperature gradient). Using temperature perturbations from the GSWM-98 model for the BP site, Holdsworth et al. (2001) also showed that maximum negative values of  $dT/dz$  were in phase with the maximum values of the turbulent velocity measured by the BP MF around the autumnal equinox. Using GSWM-00 output, we have noted that the maximum negative  $dT/dz$  (of  $\sim -1 \text{ K km}^{-1}$ ) should occur between 01:00 to 03:00 UT across the 85–92 km region at the BP site during the period of our composite day analysis; curiously, we observe large positive values of  $\langle F_x \rangle$  at this time just below this region and an abrupt shift in the sign of  $\langle F_x \rangle$  above it. As Holdsworth et al. (2001) notes, while a  $dT/dz$  of this size is too small to result in static instability, it still corresponds with a large level of GW forcing and the maximum eastward phase of the diurnal tide, which we have observed to be particularly large during this interval.

## 6 Conclusions

This study has defined limits on the expected uncertainties in estimates of the  $\langle u'w' \rangle$  and  $\langle v'w' \rangle$  covariance terms made using a multistatic meteor radar and has presented an example case study of using the radar to measure the GW forcing on the diurnal tide that arises from the height variation of the measured covariances. We have concluded that the extra de-

tections offered by the bistatic receiver appreciably improve the precision of the covariance measurements, although little of that improvement can be attributed to the increased Bragg vector diversity associated with having two viewing perspectives. The winds observed in the case study revealed substantial variations in the amplitude of the diurnal tide, but we were unable to conclusively show if GW forcing caused this variation. Nevertheless, our simulations have indicated that the bulk of the variability in the covariance and GW forcing we have seen far exceeds the expected measurement uncertainties and therefore that GW forcing has not been the only contributor to the tidal variability. We note that studies concerning GW forcing on tides are few and that there is a clear need for further studies at other locations. Furthermore, there is a need for a definition of the part of the GW spectrum that is most likely to contribute to forcing on the tides; this will inform what periodicities in the time series should be filtered out prior to making a covariance estimate.

Our simulations showed that 10 d integrated covariance estimates could broadly be considered reliable for our 55 MHz multistatic radar configuration; shorter integration times may of course be possible for lower-frequency radars with higher meteor detection rates. However, we did note that the uncertainty appears to asymptote towards a minimum value after about 10 d of integration; this value is clearly governed by the wave field characteristics. We also suggest that the accuracy and precision of the covariance estimates may be able to be improved slightly by using a more rigorous radial velocity outlier rejection scheme than applied here.

*Code and data availability.* The simulation code developed in this study is available on request from Andrew J. Spargo, as are the data from the BP and Mylor meteor radars.

### Appendix A: Procedure used for converting between coordinate systems

To embody the ellipticity of the Earth's surface in the estimation of meteor altitudes, Bragg vector orientations, and wind field components (for both bistatic and monostatic receiver cases), we followed the coordinate system conversion algorithms outlined by Stober et al. (2018). However, we note that we applied a correction to their reported expression of the radius of curvature of the Earth  $N(\phi)$ , viz.

$$\left[ N(\phi) = \frac{a}{\sqrt{1 - e^2 \sin^2 \phi}} \right],$$

where  $a$  is the semi-major axis of the Earth, and  $e^2$  is the first numerical eccentricity of the Earth ellipsoid.

Furthermore, in the interests of reducing computational overhead we applied the Olson (1996) method for converting ECEF coordinates to geodetic coordinates rather than the Heikkinen (1982) method used by Stober et al. (2018).

### Appendix B: Extraction of tidal features through the use of a wavelet transform

The time series reconstructed from the wavelet transform can be expressed as (Torrence and Compo, 1998, Eq. 11)

$$x_n = \frac{\delta j \delta t^{1/2}}{C_\delta \psi_0(0)} \sum_{j=0}^J \frac{\Re(W_n(s_j))}{s_j^{1/2}}, \quad (\text{B1})$$

where  $\delta j$  describes the wavelet scale separation,  $\delta t$  represents the time separation between adjacent points,  $J$  is the number of wavelet scales,  $C_\delta$  is a reconstruction factor (0.776 for the Morlet wavelet),  $\psi_0(0)$  is an energy scaling factor ( $\pi^{-1/4}$  for the Morlet wavelet),  $s_j$  represents the wavelet scales, and  $W_n(s_j)$  contains the complex wavelet transform coefficients at scale  $s_j$ . In reconstructing the hourly averaged wind time series (regardless of the time series length), we have taken  $\delta j = 0.02$ , in contrast to Torrence and Compo (1998) (Sect. 2f), who chose  $\delta j = 0.125$  in their example with the Morlet wavelet; we have done this to reduce the spacing between adjacent wavelet scales and hence improve the accuracy of the reconstruction. Also, in contrast to Torrence and Compo (1998) (Sect. 2g), we have not applied any zero padding in the application of the wavelet transform. This was done given our finding that the magnitude of artefacts at the ends of the wind time series appeared to be larger with zero padding applied.

### Appendix C: SABER-derived density climatology creation

To create a climatology of the diurnal variability in density from SABER instrument data that was representative of conditions around Adelaide during the autumnal equinox, we acquired densities from individual limb scans with tangent point latitudes spanning 28–42°S, longitudes 108–168°E, days 1 March to 31 May inclusive, and years 2008–2018 inclusive. Measurements falling into given time-of-day (hourly) and height (0.5 km) bins were averaged.

A spatial sampling region and measurement time-of-year span of this size was necessary to fill all time-of-day bins with measurements. An average over 11 years of data was performed to reduce the level of aliasing arising from GW-induced perturbations occurring in individual scans.

The climatology produced using this method had features that were qualitatively consistent with the same time averaging on NRLMSISE-00 model output from Adelaide's location. However, we did note that given density surfaces from SABER were, on average, 2 km lower than NRLMSISE-00's predictions between about 80 and 95 km. Nevertheless, the use of the SABER-derived density climatology in the production of Fig. 13 yielded almost identical flow accelerations to the use of the NRLMSISE-00 output.



4810

A. J. Spargo et al.: Momentum flux estimation using multistatic meteor radar

*Author contributions.* AJS carried out the model development and data analysis and wrote the paper. IMR contributed to the Instrumentation section and made other minor revisions to initial drafts of the paper. IMR is the principal supervisor of AJS's postgraduate candidature, and ADMK is the co-supervisor.

*Competing interests.* The meteor radars used in this study were designed and manufactured by ATRAD Pty. Ltd., and Iain Reid is the executive director of this group of companies.

*Acknowledgements.* Andrew Spargo would like to thank Jorge Chau, Chris Adami, Bob Vincent, David Holdsworth, Gunter Stober, Joel Younger, Richard Mayo, Andrew Heitmann, Yi Wen, Tom Chambers, and Baden Gilbert for useful discussions regarding this work.

*Financial support.* Andrew Spargo is supported by an Australian Government Research Training Program Scholarship. The BP ST/meteor radar is supported by ATRAD Pty. Ltd. and the University of Adelaide. The Mylor receiving site and equipment is supported solely by ATRAD Pty. Ltd.

*Review statement.* This paper was edited by William Ward and reviewed by Chris Meek and one anonymous referee.

## References

- Agner, R. and Liu, A. Z.: Local time variation of gravity wave momentum fluxes and their relationship with the tides derived from LIDAR measurements, *J. Atmos. and Sol.-Terr. Phys.*, 135, 136–142, <https://doi.org/10.1016/j.jastp.2015.10.018>, 2015.
- Andrioli, V. F., Fritts, D. C., Batista, P. P., and Clemesha, B. R.: Improved analysis of all-sky meteor radar measurements of gravity wave variances and momentum fluxes, *Ann. Geophys.*, 31, 889–908, <https://doi.org/10.5194/angeo-31-889-2013>, 2013a.
- Andrioli, V. F., Fritts, D. C., Batista, P. P., Clemesha, B. R., and Janches, D.: Diurnal variation in gravity wave activity at low and middle latitudes, *Ann. Geophys.*, 31, 2123–2135, <https://doi.org/10.5194/angeo-31-2123-2013>, 2013b.
- Andrioli, V. F., Batista, P. P., Clemesha, B. R., Schuch, N. J., and Buriti, R. A.: Multi-year observations of gravity wave momentum fluxes at low and middle latitudes inferred by all-sky meteor radar, *Ann. Geophys.*, 33, 1183–1193, <https://doi.org/10.5194/angeo-33-1183-2015>, 2015.
- Antonita, T. M., Ramkumar, G., Kumar, K. K., and Deepa, V.: Meteor wind radar observations of gravity wave momentum fluxes and their forcing toward the Mesospheric Semi-annual Oscillation, *J. Geophys. Res. Atmos.*, 113, D10115, <https://doi.org/10.1029/2007JD009089>, 2008.
- Beldon, C. L. and Mitchell, N. J.: Gravity waves in the mesopause region observed by meteor radar, 2: Climatologies of gravity waves in the Antarctic and Arctic, *J. Atmos. Sol. Terr. Phys.*, 71, 875–884, 2009.
- Beldon, C. L. and Mitchell, N. J.: Gravity wave–tidal interactions in the mesosphere and lower thermosphere over Rothera, Antarctica (68° S, 68° W), *J. Geophys. Res. Atmos.*, 115, D18101, <https://doi.org/10.1029/2009JD013617>, 2010.
- Bowring, B. R.: Transverse Mercator equations obtained from a spherical basis, *Surv. Rev.*, 30, 125–133, <https://doi.org/10.1179/sre.1989.30.233.125>, 1989.
- Chau, J. L. and Clahsen, M.: Empirical phase calibration for multistatic specular meteor radars using a beamforming approach, *Radio Sci.*, 54, 60–71, <https://doi.org/10.1029/2018RS006741>, 2019.
- Clemesha, B. R. and Batista, P. P.: Gravity waves and wind-shear in the MLT at 23° S, *Adv. Space Res.*, 41, 1472–1477, 2008.
- Clemesha, B. R., Batista, P. P., Buriti da Costa, R. A., and Schuch, N.: Seasonal variations in gravity wave activity at three locations in Brazil, *Ann. Geophys.*, 27, 1059–1065, <https://doi.org/10.5194/angeo-27-1059-2009>, 2009.
- de Wit, R. J., Hibbins, R. E., and Espy, P. J.: The seasonal cycle of gravity wave momentum flux and forcing in the high latitude northern hemisphere mesopause region, *J. Atmos. Sol.-Terr. Phys.*, 127, 21–29, 2014a.
- de Wit, R. J., Hibbins, R. E., Espy, P. J., Orsolini, Y. J., Limpasuvan, V., and Kinnison, D. E.: Observations of gravity wave forcing of the mesopause region during the January 2013 major Sudden Stratospheric Warming, *Geophys. Res. Lett.*, 41, 4745–4752, 2014b.
- de Wit, R. J., Janches, D., Fritts, D. C., and Hibbins, R. E.: QBO modulation of the mesopause gravity wave momentum flux over Tierra del Fuego, *Geophys. Res. Lett.*, 43, 4049–4055, <https://doi.org/10.1002/2016GL068599>, 2016.
- Dolman, B. K., Reid, I. M., and Tingwell, C.: Stratospheric tropospheric wind profiling radars in the Australian network, *Earth, Planets and Space*, 70, 170, <https://doi.org/10.1186/s40623-018-0944-z>, 2018.
- Ern, M., Preusse, P., Gille, J. C., Hoppelwhite, C. L., Mlynarczyk, M. G., Russell, J. M., and Riese, M.: Implications for atmospheric dynamics derived from global observations of gravity wave momentum flux in stratosphere and mesosphere, *J. Geophys. Res.*, 116, D19107, <https://doi.org/10.1029/2011JD015821>, 2011.
- Fritts, D. C.: Gravity wave saturation in the middle atmosphere: A review of theory and observations, *Rev. Geophys.*, 22, 275–308, 1984.
- Fritts, D. C. and Alexander, M. J.: Gravity wave dynamics and effects in the middle atmosphere, *Rev. Geophys.*, 41, 1003, <https://doi.org/10.1029/2001RG000106>, 2003.
- Fritts, D. C., Smith, S. A., Balsley, B. B., and Philbrick, C. R.: Example of gravity wave saturation and local turbulence production in the summer mesosphere and lower thermosphere during the STATE experiment, *J. Geophys. Res.*, 93, 7015–7025, 1988.
- Fritts, D. C., Janches, D., and Hocking, W. K.: Southern Argentina Agile Meteor Radar: Initial assessment of gravity wave momentum fluxes, *J. Geophys. Res.*, 115, D19123, <https://doi.org/10.1029/2010JD013891>, 2010a.
- Fritts, D. C., Janches, D., Imura, H., Hocking, W. K., Mitchell, N. J., Stockwell, R. G., Fuller, B., Vandeppeer, B., Hormaechea, J., Brunini, C., and Levato, H.: Southern Argentina Agile Meteor Radar: System design and initial measurements of

## A. J. Spargo et al.: Momentum flux estimation using multistatic meteor radar

4811

- large-scale winds and tides, *J. Geophys. Res.*, 115, D18112, <https://doi.org/10.1029/2010JD013850>, 2010b.
- Fritts, D. C., Janches, D., Hocking, W. K., Mitchell, N. J., and Taylor, M. J.: Assessment of gravity wave momentum flux measurement capabilities by meteor radars having different transmitter power and antenna configurations, *J. Geophys. Res.*, 117, D10108, <https://doi.org/10.1029/2011JD017174>, 2012a.
- Fritts, D. C., Janches, D., Iimura, H., Hocking, W. K., Bageston, J. V., and Leme, N. M. P.: Drake Antarctic Agile Meteor Radar first results: Configuration and comparison of mean and tidal wind and gravity wave momentum flux measurements with Southern Argentina Agile Meteor Radar, *J. Geophys. Res.*, 117, D02105, <https://doi.org/10.1029/2011JD016651>, 2012b.
- Fritts, D. C., Smith, R. B., Taylor, M., Doyle, J. D., Eckermann, S. D., Dörnbrack, A., Rapp, M., Williams, B. P., Pautet, D., Bossert, K., Criddle, N. R., Reynolds, C. A., Reinecke, P. A., Uddstrom, M., Revell, M. J., Turner, R., Kaifler, B., Wagner, J. S., Mixa, T., Kruse, C. G., Nugent, A. D., Watson, C. D., Gisinger, S., Smith, S. M., Lieberman, R. S., Laughman, B., Moore, J. J., Brown, W. O., Haggerty, J. A., Rockwell, A., Stossmeister, G. J., Williams, S. F., Hernandez, G., Murphy, D. J., Klekociuk, A. R., Reid, I. M., and Ma, J.: The Deep Propagating Gravity Wave Experiment (DEEPWAVE): An Airborne and Ground-Based Exploration of Gravity Wave Propagation and Effects from their Sources throughout the Lower and Middle Atmosphere, *B. Am. Meteorol. Soc.*, 97, 425–453, 2016.
- Gardner, C. S., Hostetler, C. A., and Franke, S. J.: Gravity wave models for the horizontal wave number spectra of atmospheric velocity and density fluctuations, *J. Geophys. Res.*, 98, 1035–1049, <https://doi.org/10.1029/92JD02051>, 1993.
- Heikkinen, M.: Geschlossene Formeln zur Berechnung räumlicher geodätischer Koordinaten aus rechtwinkligen Koordinaten, *Zeitschrift für Vermessungswesen*, 107, 207–211, 1982.
- Hocking, W. K.: A new approach to momentum flux determinations using SKiYMET meteor radars, *Ann. Geophys.*, 23, 2433–2439, <https://doi.org/10.5194/angeo-23-2433-2005>, 2005.
- Hocking, W. K.: Spatial distribution of errors associated with multistatic meteor radar, *Earth, Planets and Space*, 70, 93, <https://doi.org/10.1186/s40623-018-0860-2>, 2018.
- Hocking, W. K. and Thayaparan, T.: Simultaneous and co-located observation of winds and tides by MF and meteor radars over London, Canada (43° N, 81° W), during 1994–1996, *Radio Sci.*, 32, 833–865, <https://doi.org/10.1029/96RS03467>, 1997.
- Holdsworth, D. A., Vincent, R. A., and Reid, I. M.: Mesospheric turbulent velocity estimation using the Buckland Park MF radar, *Ann. Geophys.*, 19, 1007–1017, <https://doi.org/10.5194/angeo-19-1007-2001>, 2001.
- Holdsworth, D. A., Reid, I. M., and Cervera, M. A.: Buckland Park all-sky interferometric meteor radar, *Radio Sci.*, 39, RS5009, <https://doi.org/10.1029/2003RS003014>, 2004a.
- Holdsworth, D. A., Tsutsumi, M., Reid, I. M., Nakamura, T., and Tsuda, T.: Interferometric meteor radar phase calibration using meteor echoes, *Radio Sci.*, 39, RS5012, <https://doi.org/10.1029/2003RS003026>, 2004b.
- Jia, M., Xue, X., Gu, S., Chen, T., Ning, B., Wu, J., Zeng, X., and Dou, X.: Multiyear Observations of Gravity Wave Momentum Fluxes in the Midlatitude Mesosphere and Lower Thermosphere Region by Meteor Radar, *J. Geophys. Res.-Space*, 123, 5684–5703, <https://doi.org/10.1029/2018JA025285>, 2018.
- Jones, J., Webster, A., and Hocking, W.: An improved interferometer design for use with meteor radars, *Radio Sci.*, 33, 55–65, 1998.
- Kim, Y.-J., Eckermann, S. D., and Chun, H.-Y.: An overview of the past, present and future of gravity-wave drag parametrization for numerical climate and weather prediction models, *Atmos. Ocean*, 41, 65–98, 2003.
- Kudeki, E. and Franke, S. J.: Statistics of momentum flux estimation, *J. Atmos. Sol.-Terr. Phys.*, 60, 1549–1553, 1998.
- Lieberman, R. S., Ortland, D. A., Riggan, D. M., Wu, Q., and Jacobi, C.: Momentum budget of the migrating diurnal tide in the mesosphere and lower thermosphere, *J. Geophys. Res.-Atmos.*, 115, D20105, <https://doi.org/10.1029/2009JD013684>, 2010.
- Liu, A. Z., Lu, X., and Franke, S. J.: Diurnal variation of gravity wave momentum flux and its forcing on the diurnal tide, *J. Geophys. Res.-Atmos.*, 118, 1668–1678, 2013.
- Lu, X., Liu, H.-L., Liu, A. Z., Yue, J., McInerney, J. M., and Li, Z.: Momentum budget of the migrating diurnal tide in the Whole Atmosphere Community Climate Model at vernal equinox, *J. Geophys. Res.*, 117, D07112, <https://doi.org/10.1029/2011JD017089>, 2012.
- Matsumoto, N., Shinbori, A., Riggan, D. M., and Tsuda, T.: Measurement of momentum flux using two meteor radars in Indonesia, *Ann. Geophys.*, 34, 369–377, <https://doi.org/10.5194/angeo-34-369-2016>, 2016.
- Mayr, H. G., Mengel, J. G., Chan, K. L., and Porter, H. S.: Seasonal variations of the diurnal tide induced by gravity wave filtering, *Geophys. Res. Lett.*, 25, 943–946, 1998.
- McLandress, C. L.: The seasonal variation of the propagating diurnal tide in the mesosphere and lower thermosphere. Part I: The role of gravity waves and planetary waves, *J. Atmos. Sci.*, 59, 893–906, 2002.
- Nicolls, M. J., Fritts, D. C., Janches, D., and Heinselman, C. J.: Momentum flux determination using the multi-beam Poker Flat Incoherent Scatter Radar, *Ann. Geophys.*, 30, 945–962, <https://doi.org/10.5194/angeo-30-945-2012>, 2012.
- Olson, D. K.: Converting Earth-centered, Earth-fixed coordinates to geodetic coordinates, *IEEE T. Aero. Elec. Sys.*, 32, 473–476, <https://doi.org/10.1109/7.481290>, 1996.
- Ortland, D. A. and Alexander, M. J.: Gravity wave influence on the global structure of the diurnal tide in the mesosphere and lower thermosphere, *J. Geophys. Res.*, 111, A10S10, <https://doi.org/10.1029/2005JA011467>, 2006.
- Placke, M., Hoffmann, P., Becker, E., Jacobi, C., Singer, W., and Rapp, M.: Gravity wave momentum fluxes in the MLT—Part II: Meteor radar investigations at high and midlatitudes in comparison with modeling studies, *J. Atmos. Sol.-Terr. Phys.*, 73, 911–920, 2011a.
- Placke, M., Stober, G., and Jacobi, C.: Gravity wave momentum fluxes in the MLT—Part I: seasonal variation at Collm (51.3° N, 13.0° E), *J. Atmos. Sol.-Terr. Phys.*, 73, 904–910, 2011b.
- Placke, M., Hoffmann, P., Latteck, R., and Rapp, M.: Gravity wave momentum fluxes from MF and meteor radar measurements in the polar MLT region, *J. Geophys. Res.-Space*, 120, 736–750, <https://doi.org/10.1002/2014JA020460>, 2014.
- Placke, M., Hoffmann, P., and Rapp, M.: First experimental verification of summertime mesospheric momentum balance based on radar wind measurements at 69° N, *Ann. Geophys.*, 33, 1091–1096, <https://doi.org/10.5194/angeo-33-1091-2015>, 2015.

- Protat, A. and Zawadzki, I.: A Variational Method for Real-Time Retrieval of Three-Dimensional Wind Field from Multiple-Doppler Bistatic Radar Network Data, *J. Atmos. Ocean. Tech.*, 16, 432–449, [https://doi.org/10.1175/1520-0426\(1999\)016<0432:AVMFRT>2.0.CO;2](https://doi.org/10.1175/1520-0426(1999)016<0432:AVMFRT>2.0.CO;2), 1999.
- Reid, I. M., McIntosh, D. L., Murphy, D. J., and Vincent, R. A.: Mesospheric radar wind comparisons at high and middle southern latitudes, *Earth Planets Space*, 70, 84, <https://doi.org/10.1186/s40623-018-0861-1>, 2018a.
- Reid, I. M., Rüster, R., Czechowsky, P., and Spargo, A. J.: VHF radar measurements of momentum flux using summer polar mesopause echoes, *Earth Planets Space*, 70, 129, <https://doi.org/10.1186/s40623-018-0902-9>, 2018b.
- Riggin, D. M., Tsuda, T., and Shinbori, A.: Evaluation of momentum flux with radar, *J. Atmos. Sol.-Terr. Phys.*, 142, 98–107, 2016.
- Spargo, A. J., Reid, I. M., MacKinnon, A. D., and Holdsworth, D. A.: Mesospheric gravity wave momentum flux estimation using hybrid Doppler interferometry, *Ann. Geophys.*, 35, 733–750, <https://doi.org/10.5194/angeo-35-733-2017>, 2017.
- Stober, G. and Chau, J. L.: A multi-static and multi-frequency novel approach for specular meteor radars to improve wind measurements in the MLT region, *Radio Sci.*, 50, 431–442, <https://doi.org/10.1002/2014RS005591>, 2015.
- Stober, G., Chau, J. L., Vierinen, J., Jacobi, C., and Wilhelm, S.: Retrieving horizontally resolved wind fields using multi-static meteor radar observations, *Atmos. Meas. Tech.*, 11, 4891–4907, <https://doi.org/10.5194/amt-11-4891-2018>, 2018.
- Thomas, R. M., Whitham, P. S., and Elford, W. G.: Frequency Dependence of Radar Meteor Echo Rates, *Publ. Astron. Soc. Aust.*, 6, 303–306, 1986.
- Thorsen, D., Franke, S. J., and Kudeki, E.: A new approach to MF radar interferometry for estimating mean winds and momentum flux, *Radio Sci.*, 32, 707–726, 1997.
- Torrence, C. and Compo, G. P.: A Practical Guide to Wavelet Analysis, *B. Am. Meteorol. Soc.*, 79, 61–78, [https://doi.org/10.1175/1520-0477\(1998\)079<0061:APGTWA>2.0.CO;2](https://doi.org/10.1175/1520-0477(1998)079<0061:APGTWA>2.0.CO;2), 1998.
- Vincent, R. A. and Ball, S. M.: Mesospheric winds at low- and mid-latitudes in the southern hemisphere, *J. Geophys. Res.*, 86, 9159–9169, 1981.
- Vincent, R. A. and Reid, I. M.: HF Doppler measurements of mesospheric gravity wave momentum fluxes, *J. Atmos. Sci.*, 40, 1321–1333, 1983.
- Vincent, R. A., Kovalam, S., Fritts, D. C., and Isler, J. R.: Long-term MF radar observations of solar tides in the low-latitude mesosphere: Interannual variability and comparisons with the GSWM, *J. Geophys. Res.*, 103, 8667–8683, <https://doi.org/10.1029/98JD00482>, 1998.
- Vincent, R. A., Kovalam, S., Reid, I. M., and Younger, J. P.: Gravity wave flux retrievals using meteor radars, *Geophys. Res. Lett.*, 37, L14802, <https://doi.org/10.1029/2010GL044086>, 2010.
- Watanabe, S. and Miyahara, S.: Quantification of the gravity wave forcing of the migrating diurnal tide in a gravity wave-resolving general circulation model, *J. Geophys. Res.*, 114, D07110, <https://doi.org/10.1029/2008JD011218>, 2009.
- Xu, J., Smith, A. K., Liu, H.-L., Yuan, W., Wu, Q., Jiang, G., Mlynczak, M. G., and Russell, J. M.: Estimation of the equivalent Rayleigh friction in mesosphere/lower thermosphere region from the migrating diurnal tides observed by TIMED, *J. Geophys. Res.*, 114, D23103, <https://doi.org/10.1029/2009JD012209>, 2009.
- Yiğit, E. and Medvedev, A. S.: Influence of parameterized small-scale gravity waves on the migrating diurnal tide in Earth's thermosphere, *J. Geophys. Res.-Space*, 122, 4846–4864, <https://doi.org/10.1002/2017JA024089>, 2017.

## Appendix E

**Publication: Earth, Planets and Space, 70:129,  
2018**

This paper presents an analysis of the upward flux of horizontal momentum measurements derived using data from a narrow-beam VHF radar operating in a six-beam mode. The author of this thesis developed the simulation that characterized the performance of the momentum flux estimation technique, developed the data analysis code associated with Figs. 6, 7, 10, and 11, and contributed to writing the “Simulations” section of the paper.

## FULL PAPER

## Open Access



# VHF radar measurements of momentum flux using summer polar mesopause echoes

Iain M. Reid<sup>1,2\*</sup> , Rüdiger Rüter<sup>3</sup>, Peter Czechowsky<sup>3</sup> and Andrew J. Spargo<sup>2</sup>**Abstract**

We revisit previously unpublished analysis of observations of the dynamics of the mesopause region over the Norwegian Island of Andøya (69°N, 16°E) made during a 1-week period in summer 1987 during the Middle Atmosphere Cooperation-Summer in Northern Europe (MAC-SINE) campaign using the mobile SOUSY VHF (53.5 MHz) Doppler radar operating in a six-beam mode. We do this in the light of: (1) more recent developments in the measurement of the components of the density-normalized Reynolds stress tensor using meteor radars, and with medium-frequency partial reflection radars using the hybrid Doppler interferometric technique, and (2) satellite measurements of the absolute upward flux of horizontal momentum. We consider of the density-normalized total upward flux of horizontal momentum ( $\overline{u'w'} + \overline{v'w'}$ ) for the 83–90 km height interval. Values of the component of the density-normalized flux for the 6 min to 12.8 h period range, after the tidal components have been removed, and the effects of the aspect sensitivity on the radar beam look directions have been accounted for vary between  $5 \text{ m}^2 \text{ s}^{-2}$  below 86 km and  $13 \text{ m}^2 \text{ s}^{-2}$  above 86 km. The major contribution is from the 6 to 12.8 h period range. The results of the analysis have implications for meteor radar estimates of momentum flux and also for Doppler radar measurements of the same term in the presence of aspect-sensitive scattering.

**Keywords:** Very high-frequency radar, Momentum flux, Polar mesosphere summer echoes

**Introduction**

The challenge of the measurement of the upward flux of horizontal momentum in the mesosphere lower thermosphere (MLT) region has been explored since the work of Vincent and Reid (1983), hereinafter VR83, which presented a method for doing this using multi-beam Doppler radars, using only the assumption that the statistics of the wave field are horizontally isotropic. The measurement of this parameter is considered vital for better understanding the dynamics of the MLT (see, e.g. Fritts and Alexander 2003; Alexander et al. 2010). Progress has been made in using satellite measurements to estimate the absolute momentum flux of quasi-monochromatic gravity wave events (see, e.g. Hertzog et al. 2012; Ern et al. 2016). However, unlike these methods, the method applied by VR83 provides a measure of the net momentum flux and does not require identification of individual

gravity waves or assumptions beyond that of the statistical similarity of the wave field measured in the radar beams. This is important, as Reid et al. (1987) estimated that in a cross-spectral analysis of several radar data sets to determine gravity wave horizontal scales, only 25% of calculated cross-spectral phases had a significant coherence-squared  $[(\text{COH})^2]$  statistic. This can be interpreted as quasi-monochromatic (QM) waves being evident only about 25% of the time, a rate consistent with the frequency of occurrence of QM waves in OI and OH airglow observations (see, e.g. Reid and Woithe 2005).

Meek et al. (1985) also analysed almost a year of radar observations made near Saskatoon, Canada, for gravity wave horizontal scales and found a similar statistic. Walterscheid et al. (1999) analysed OH airglow imager data and found a higher frequency of occurrence of QM waves, varying from 41% of the observational time in winter, to 62% in summer. Reid et al. (1987), Reid and Woithe's (2005) and Walterscheid et al.'s (1999) observations are all for data from Adelaide, Australia. Based on these observational studies, we could argue that QM

\*Correspondence: ireid@atrad.com.au

<sup>1</sup> ATRAD Pty Ltd, 20 Phillips St., Thebarton 5031, Australia

Full list of author information is available at the end of the article

waves are present between 25 and 60% of the time. An additional complication in this context is whether the QM waves detected in airglow observations are freely propagating or ducted waves. The radar observations referenced above were able to identify features consistent with propagating gravity waves over a range of heights, whereas single-colour airglow observations are single height measurements, and so restricted in interpretation. This is an important topic, but its further discussion is beyond the scope of the present work.

Naturally, the effects of instrumental filtering need to be considered when discussing the representativeness of observations, and VR83, Reid et al. (1987), Reid and Woithe (2005) and Meek et al. (1985) all explicitly do this for their observations of gravity wave scales. More generally, Gardner and Taylor (1998) consider the observational limitations of gravity wave observations using lidar, radar and airglow observations. More recently, Bossert et al. (2018) have considered the measurement of momentum flux using a Na density lidar and included the chemistry of the Na response to the mountain waves. We note that the VR83 approach is not valid in the case of stationary waves. In terms of radar and Doppler lidar measurements of momentum flux, the approach of VR83 does not indicate a scale or temporal dependence in the governing equations, beyond the assumption that the statistics of the motions are horizontally homogeneous, and this was investigated by Reid (1984, 1987) using simple analytical arguments. Perhaps the best way to further investigate this is through the use of simulations, and we consider some aspects of this approach below.

VR83 used the large medium-frequency (MF) Buckland Park (BP) partial reflection (PR) radar [see Reid (2015) for a detailed discussion of this radar class], which provided good spatial and temporal coverage in the 60–95 km (day) and 80–95 km (night) height region. Powerful mesosphere–stratosphere–troposphere (MST) radars operating in the lower very high-frequency (VHF) band (typically near 50 MHz) can apply the technique but are limited by the temporal and spatial intermittency of the radar returns in the mesosphere lower thermosphere (MLT) region. Generally, in the MLT region outside of the polar mesosphere in summer, they are limited to daytime observations between 60 and 80 km. These radars are also relatively expensive and rare, and so alternate methods of measuring the momentum flux using smaller radars and optical techniques have been explored. These include an investigation of the ability of small interferometric MF PR radars to measure the flux by Thorsen et al. (1997), and an extension of Thorsen’s approach for application to ‘all-sky’ meteor radars (see, e.g. Holdsworth et al. 2004) by Hocking (2005). Except for recent work by Spargo et al. (2017), the former technique has

not been actively pursued. The approach described by Hocking has attracted much investigation, but no definitive experimental validation against an accepted measurement of momentum flux (see, e.g. Placke et al. 2015). For the various parts of the arguments for and against using the meteor technique for measuring momentum flux, see for example, the discussions in Vincent et al. (2010), Fritts et al. (2012), Riggien et al. (2016), and Spargo et al. (2017).

The strong radar returns from the summer polar mesopause region do provide a means of measuring the momentum flux in the MLT using more powerful VHF ST class radars (those with a power aperture product greater than around  $10^7$  W m<sup>2</sup>), at least in the 82–92 km height region, with relatively good spatial and temporal coverage (see, e.g. Reid et al. 1988; Rüster and Reid 1990; Love and Murphy 2016). Given the relative sparsity of such measurements, the analysis and discussion of previously unpublished momentum flux results is useful.

### Observations

Observations were obtained as part of the international Middle Atmosphere Cooperation/Summer in Northern Europe (MAC/SINE) campaign (Thrane 1990) conducted in summer 1987 using the mobile SOUSY VHF Doppler Radar located at Bleik (69°17’N, 16°01’E) on the Norwegian Island of Andøya. The radar operated for a period of 32 days with various range resolutions, pulse codes and experiments, and useful mesospheric velocities were typically obtained within the height range of about 80 to 90 km. Other results from the MAC/SINE campaign using data from the same radar and relevant to the present work have been published by Reid et al. (1988), Rüster and Reid (1990), Rüster (1992), Lübken et al. (1990), and Yi (2001). The observational period for the results analysed in this paper is 22–30 June 1987. Previously, Reid et al. (1989) looked at momentum flux measurements for the period of a few hours during 16–17 July and Rüster and Reid (1990) looked at measurements for the 23–25 June a period that covered that of the “Chaff” rocket salvo of the campaign (see, e.g. Wu et al. 2001).

### Equipment

The basic radar facility has been described by Czechowsky et al. (1984). Briefly, the radar operated at a frequency of 53.5 MHz, corresponding to a wavelength of 5.6 m. The peak pulse power used within the observational period was 100 kW, and the duty cycle 4%, resulting in an average power of 4 kW. Using an 8-bit complementary code, the pulses were phase coded, with one element being 2  $\mu$ s long, corresponding to a range resolution of 300 m. Ranges between 60.0 and 100.2 km were sampled. The antenna consisted of a phased array

of 576 four-element Yagi antennas, covering an effective area of 8880 m<sup>2</sup>, with a gain of 35.5 dB, and a one-way 3 dB beam width of 3°. After Czechowsky et al.'s (1984) description of the radar, the number of beams was increased from four to six. In the configuration applied for the work described here, all six independent beams were utilized. Using electronically controlled phase shifters, the antenna beam was directed sequentially towards the six beam directions. Beams were directed vertically (V), and at 5.6° off-zenith towards the north (N) and west (W), and at 4.0° off-zenith towards the north-east (NE), north-west (NW) and south-west (SW). The beam configuration is illustrated schematically in Fig. 1. At a height of 86 km, the distance from the zenith to the centres of the 4.0° off-zenith beams is about 6 km, and for the 5.6° off-zenith beams, 8.4 km. The beam diameters are about 4 km at this height. The mobile SOUSY radar was relocated to Svalbard to become the SOUSY Svalbard Radar (SSR) in the late 1990s and is described by Czechowsky et al. (1998), and by Hall (2009).

### Theory

#### Reynolds stress terms

The general case of the application of narrow beam Doppler radars to measure the density-normalized Reynolds stress tensor and mean winds in the MLT has been described by Reid (1987), and the theory for the beam arrangement used here has been described by Reid et al.

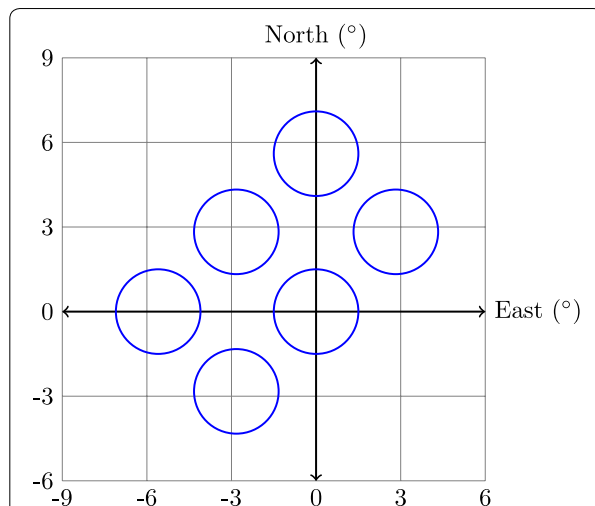


**Fig. 1** Beam arrangement of the mobile SOUSY VHF radar showing the 3-dB beam widths. Beams are directed vertically, and at 4° off-zenith towards the north-east, north-west and south-west, and at 5.6° off-zenith towards the north and west. At a height of 86 km, the distance from the zenith to the centres of the 4.0° off-zenith beams is about 6 km, and for the 5.6° off-zenith beams, 8.4 km. The beam diameters are about 4 km at this height

(1988). In the present case, apart from the mean square vertical velocity  $w'^2$ , the individual terms of the Reynolds stress tensor are not available separately and come as combinations of terms. Briefly, the mean square radial velocities measured in the NE ( $V_{NE}^2$ ) and SW ( $V_{SW}^2$ ) directed antennas can be used to determine the arithmetic sum of the upward fluxes of zonal ( $\overline{u'w'}$ ) and meridional ( $\overline{v'w'}$ ) momentum, that is, the upward flux of horizontal momentum as

$$\overline{u'w'} + \overline{v'w'} = \left( \overline{V_{NE}^2} - \overline{V_{SW}^2} \right) / \sqrt{2} \sin 2\theta_{E1} \quad (1)$$

where  $u'$ ,  $v'$  and  $w'$  are the zonal, meridional and vertical perturbation velocities, respectively, the subscripts on the variances of the radial velocities indicate the beam directions, and  $\theta_{E1}$  is the effective beam direction for the NE and SW beams. (We discuss the calculation of the effective beam direction below.) This expression may be compared with the mean absolute flux (MF) typically measured by satellite and balloon measurements (e.g. Hertzog et al. 2012) as

$$MF = \left( \overline{u'w'}^2 + \overline{v'w'}^2 \right)^{1/2} \quad (2)$$

The isotropy of the horizontal velocity field can also be calculated directly from the mean square radial velocities measured in the N ( $V_N^2$ ) and W ( $V_W^2$ ) beams as

$$\overline{v'^2} - \overline{u'^2} = \frac{\left( \overline{V_N^2} - \overline{V_W^2} \right)}{\sin^2 \theta_{E2}} - 2\left( \overline{u'w'} + \overline{v'w'} \right) \cot \theta_{E2} \quad (3)$$

where  $\theta_{E2}$  is the effective beam direction for the N and W beams. The isotropy is one of the Stokes parameters, and Eckermann (1996) provides a detailed description of the use of these parameters in the analysis of wave fields. We note that spectral rotary decomposition and the application of the Stokes parameters is usually most useful for longer (inertial) wave periods.

The mean square horizontal velocities cannot be obtained separately without further information, as they are given by (using the meridional component as an example)

$$\overline{v'^2} + 2\overline{v'w'} \cot \theta_{E2} = \frac{\left( \overline{V_N^2} - \overline{V_V^2} \right)}{\sin^2 \theta_{E2}} \quad (4)$$

and where a similar expression applies for the zonal component. Note that this is the expression that applies for the usual beam arrangement (a vertical beam and an off-vertical beam in the east–west and north–south plane) for most Doppler radars, and Eq. (4) is usually applied



to calculate the mean square horizontal velocity. Also note that the inability to separate the individual terms in our experiment comes about because the beam pointing angles all lie in one half-azimuth. A similar situation occurs with the azimuthal distribution of meteor radar detections as the Earth rotates into the meteor streams during the day. We will return to the importance of this below.

Another point to note when considering Eqs. (1), (3) and (4) is that they apply equally to the mean square spectral widths,  $\overline{\sigma'^2}$  and so can be used to investigate scales smaller than the radar pulse volume (Reid 2004), although this appears to have been little exploited.

Rather than using individual combinations of beams as we have just described, it is possible to include all of the radial velocities in a least-squares inversion to determine the mean wind components and the various covariance terms of the Reynolds stress tensor. Spargo et al. (2017) did this, following the approaches of Thorsen et al. (1997) and Hocking (2005), to determine the six components of the density-normalized Reynolds stress tensor, to the BPFM radar operating in a five-beam (E, W, N, S and V) Doppler mode. In principle, this technique can be applied to the six-beam arrangement used here to determine the various Reynolds stress terms. This is in some ways a test of the attempts to measure them from meteor radar radial velocity data, particularly given the asymmetrical distribution of meteor returns around the zenith throughout the day.

The inversion is performed on the following system of equations (constituting  $n$  radial velocity measurements):

$$\overline{V_R^2} = Av \quad (5)$$

where  $\overline{V_R^2}$  represents an  $n$ -element vector of squared radial velocity perturbations.  $A$  is an  $n \times 6$  element matrix with rows  $[\sin^2 \theta \sin^2 \phi, \sin^2 \theta \cos^2 \phi, \cos^2 \theta, \sin^2 \theta \sin 2\phi, \sin 2\theta \sin \phi, \sin 2\theta \cos \phi]$ , and  $v = [\overline{u'^2}, \overline{v'^2}, \overline{w'^2}, \overline{u'v'}, \overline{u'w'}, \overline{v'w'}]$ .

We applied the least-squares inversion to calculate the individual variances and covariances corresponding to the Reynolds stress tensor terms from our data (following the removal of tidal and longer period components as described below) and found the results to be physically unreasonable except for  $\overline{w'^2}$ , and extremely sensitive to outliers in the radial velocity vector. This is not unexpected given the governing equations described above and given that we have a direct measure of  $\overline{w'^2}$ . In addition, the sensitivity to changes in the radial velocity vector is expected to arise and occurs when solving inverse problems where the so-called coefficient matrix (here containing the direction cosines) has a high condition

number [see, e.g. Shenghui et al. (2014)]. In our case, the high condition number is predominantly brought about by the small direction cosines associated with those covariance terms which involve a horizontal component. The condition number of our problem is also further increased by the fact that the beam locations have little spatial separation, as we have allowed them to vary solely as a function of the estimated aspect sensitivity.

Our interpretation is that in solving the inverse problem for this beam geometry, large correlated errors will predominantly accumulate in those components that include horizontal terms. As a consequence, we have little confidence in the solutions the inversion algorithm produces for individual components involving a horizontal term (i.e.  $\overline{u'u'}$ ,  $\overline{v'v'}$ ,  $\overline{u'v'}$ ,  $\overline{u'w'}$  and  $\overline{v'w'}$ ). This warrants further discussion though, and the governing equations do not preclude the solutions for  $(\overline{u'w'} + \overline{v'w'})$  and  $(\overline{v'^2} - \overline{u'^2})$ , and when applied for these terms, the inversion yields similar results to the application of Eqs. (1) and (3) and confers advantages in terms of robustness and correcting for the effects of aspect sensitivity. We will return to this in the “Momentum flux” section, and in the “Simulation” section, where we show results from a simulation comparing the measurement biases inherent to the least-squares inversion and radial velocity variance differencing techniques.

#### Effective beam direction

The need to calculate an effective Doppler beam direction comes about because of the high aspect sensitivity of backscatter often returned from the atmosphere along with the relatively wide Doppler beams used with atmospheric radars (see, e.g. Reid 1990). The most commonly applied approach to account for this for fixed beam Doppler radars is described by Hocking et al. (1986), but also see similar work by Whitehead et al. (1983). Its application to the mobile SOUSY and Harz SOUSY radar data has previously been described by Reid et al. (1988), Czechowsky et al. (1988) and Reid et al. (1989). Its application to a subsection of the present data set has been described by Rüster and Reid (1990). Briefly, the ratio of powers measured in a vertical beam,  $P(0)$ , and a beam directed at an apparent off-vertical angle,  $\theta_A$ ,  $P(\theta_A)$ , can be used to determine the effective beam angle as

$$\theta_E = \arcsin \left[ \sin \theta_A \left[ 1 + \frac{\sin^2 \theta_0}{\sin^2 \theta_s} \right]^{-1} \right] \quad (6)$$

where  $\theta_0$  is the  $1/e$  radar beam half-width, and  $\theta_s$  is the  $1/e$  half-width of the angular polar diagram of the scatterers and is called the aspect sensitivity parameter. It is given by



$$\theta_s = \arcsin \sqrt{\frac{\sin^2 \theta_A}{\ln [P(0)/P(\theta_e)]} - \sin^2 \theta_0} \quad (7)$$

The spectral half-width due to beam broadening,  $f_{1/2}$ , can also be calculated using the values of  $\theta_s$  as (Hocking et al. 1986)

$$f_{1/2} = \arcsin \left[ \left( \frac{\sin^{-2} \theta_s}{\ln 2} + \sin^{-2} \theta_0 \right)^{1/2} \right] \frac{2\nu}{\lambda} \theta_s \quad (8)$$

Reid (2004) argued that beam broadening and shear broadening effects could be ignored when the beams were symmetric, for example, with beams at the same off-zenith angle in either the east–west or north–south plane, because they would be affected in the same way, and the terms due to these effects would subtract out. If this argument is correct, then Eq. (1) can be applied to spectral widths without using the correction indicated by Eq. (8).

## Analysis

### SNR, radial velocities and spectra widths

Radar returns were coherently integrated for 0.107 s, and for each beam position 64 such complex samples were obtained in each of the 135 range intervals. Data were thus obtained for 6.8-s in each of the beam directions. A new data sequence was started every 10 s, the additional time being required to switch the beam direction, and to write data to tape. The 6.8-s data sequences were Fourier transformed off-line to obtain the corresponding Doppler spectra. The first three moments of the spectra were calculated to obtain the power, mean Doppler shift and spectral width. Spectra were required to have signal-to-noise ratios exceeding 3 dB to be accepted and were checked for aliasing. The latter occurred when radial velocities exceeded  $13.1 \text{ ms}^{-1}$  and were removed by accounting for the spatial and temporal variation of the signals at each range gate and beam position. These results were averaged to produce 3-min records in each height step, and in each beam.

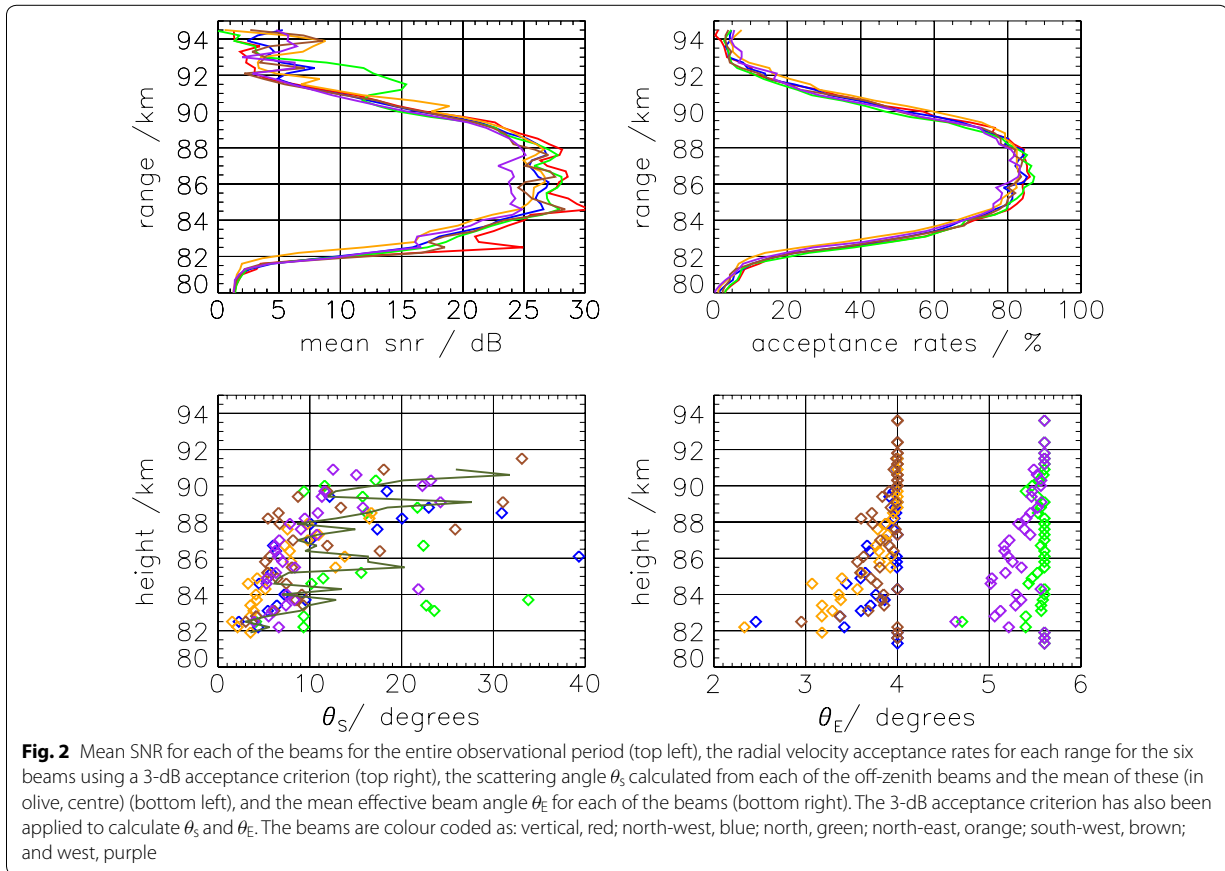
The mean power profiles for the six beams and the acceptance rates for the 3-min records are shown in Fig. 2. The acceptance rates follow the form of the power profiles and take maximum values of about 70% for the vertical and northward beams, and values of 40% near ranges of 83 and 90 km, respectively. The westward beam has the lowest powers and acceptance rates of all of the beams. When we consider the momentum flux, and its divergence with height, the strong height dependence of these rates must be kept in mind. The limited height

range over which radial velocities are available for analysis highlights the limitations of using this class of radar to measure the fluxes. Meteor radars are similarly limited, with a similar form for the acceptance rate with height, suggesting some inherent advantages in using MF partial reflections radars, although these bring their own limitations (see Reid 2015). We discuss the  $\theta_s$  and  $\theta_E$  results below.

The signal-to-noise ratios (SNRs), radial velocities and spectral widths for the 3-min averaged data are typical for this type of observation in that they are characterized by substantial temporal and spatial variability. There are periodic ‘gaps’ in the returns, and the SNRs show the influence of the semidiurnal tide in the modulation of the strength of the returned signals. This has previously been discussed by Czechowsky et al. (1989) in relation to the PMSE, who noted that strong bursts in backscattered power tended to occur in the late afternoon and early morning hours, coinciding with the time of maximum westward velocity of the semidiurnal tide. Czechowsky and Ruster (1997) noted and discussed the tendency for the spectral width to maximize above about 86 km, and this is evident in the present data set. They concluded that this was the result of the presence of cells of enhanced turbulence generated by a Kelvin–Helmholtz (KH) mechanism. This would lead to reduced aspect sensitivity in the upper parts of the PMSE, consistent with the results shown in Fig. 2. We note that clear signatures of KH instabilities were observed in wintertime using this radar by Reid et al. (1987), and more recently in PMSE over Andøya by Stober et al. (2018).

### Mean scattering angle and beam pointing angles

The mean power profiles can be used to calculate the mean scattering angle  $\theta_s$  and the mean effective angle  $\theta_E$  for each of the beams for the entire period of observation, and these results are also shown in Fig. 2. To calculate  $\theta_s$  and  $\theta_E$  the power profiles for the off-zenith beams were interpolated back to their nominal height (that is, assuming  $\theta_E = \theta_A$ ). If  $\theta_s$  could not be calculated using Eq. (6),  $\theta_E$  was set to  $\theta_A$ . These mean scattering angle results are similar to others found in the PMSE using the same technique (see, e.g. Reid 1990), but we note the considerable variability of  $\theta_s$  calculated from the different off-zenith beams, and that  $\theta_s$  is higher at the base of the layer. If we consider the ground diffraction pattern corresponding to a particular height, which is the Fourier transform of the angular polar diagram of the backscattered power for that height, we note that at least at medium frequencies, it is often anisotropic. This means that the backscatter angular polar diagram is itself anisotropic, and different off-zenith beam directions will have different values of  $\theta_E$ . Ground diffraction pattern anisotropy is



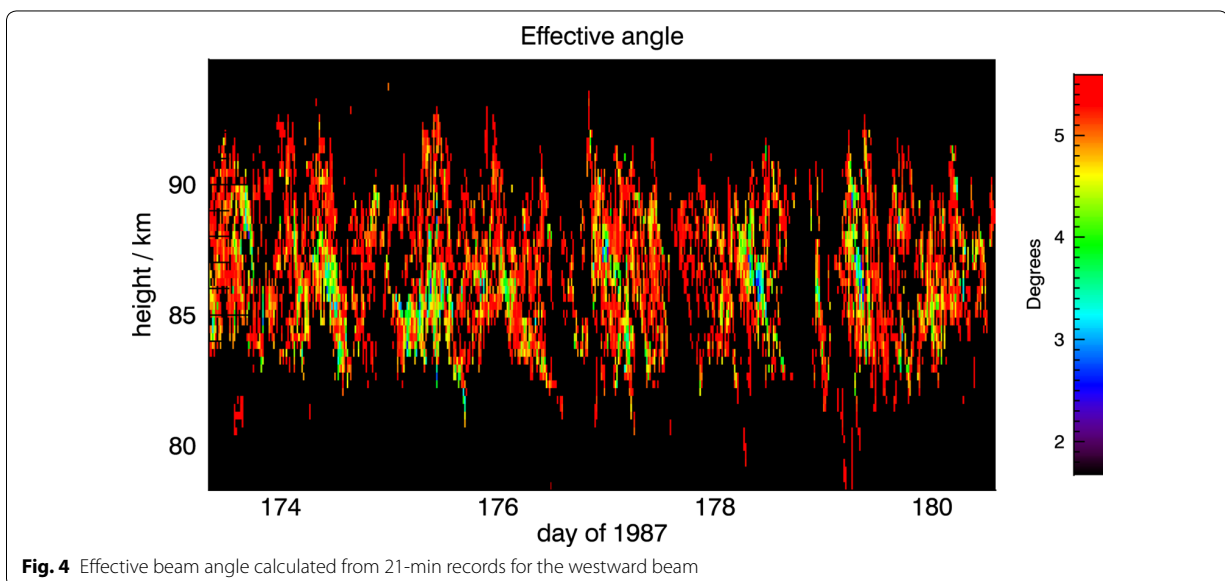
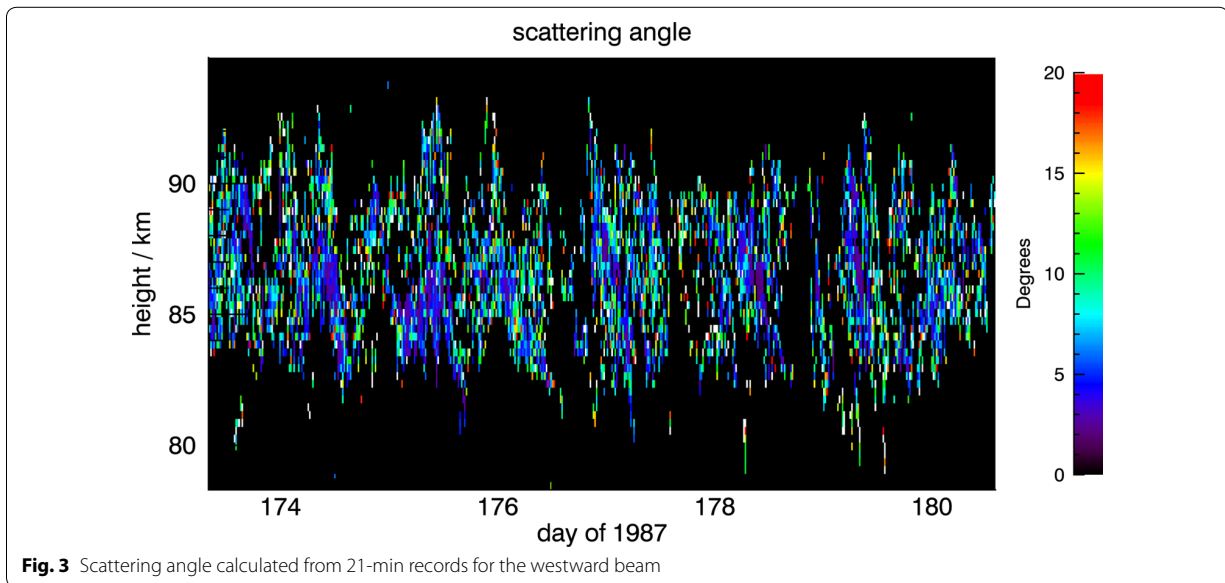
discussed in more detail in Murphy and Vincent (1993) and Reid (2015). It has significant implications in applying Eq. (1), as it assumes that a single value of  $\theta_E$  is available and can be applied.

A mean over the entire week-long data set may not produce the most representative value of beam direction on shorter time scales, and to highlight this, Fig. 3 shows the 21-min values of  $\theta_s$  for the westward beam. A clear statement on the variation with time and height is not evident, except that there is considerable variability. There is perhaps a tendency for  $\theta_s$  to be larger nearer the top of the layer. Figure 4 shows the mean effective angle corresponding to Fig. 3. While there is considerable variability, the effective beam direction is often the apparent beam angle. This is a consequence of the narrow beams and relatively small off-zenith angles used for the non-vertical beams with this radar.

To further investigate the nature of the scattering angle, Fig. 5 shows examples of its distribution for three heights: 83.1 km (yellow); 85.8 km (red); and 88.8 km (blue) for the entire observational period for 21-min averages of power. The median values are 6.8°, 7.4° and

8.7°, respectively. These results represent the mean of 21-min averages. The number of values determined for each of these heights is 197, 348, 302 from a possible 502 (39%, 69% and 60%, respectively). For the remainder of the 21-min averages during the observational period, no value of  $\theta_s$  could be determined. These results are similar in form to those reported for a 51.5-MHz radar at Resolute Bay (75°N, 95°W) for 1 month of hourly averaged observations by Swarnalingam et al. (2011).

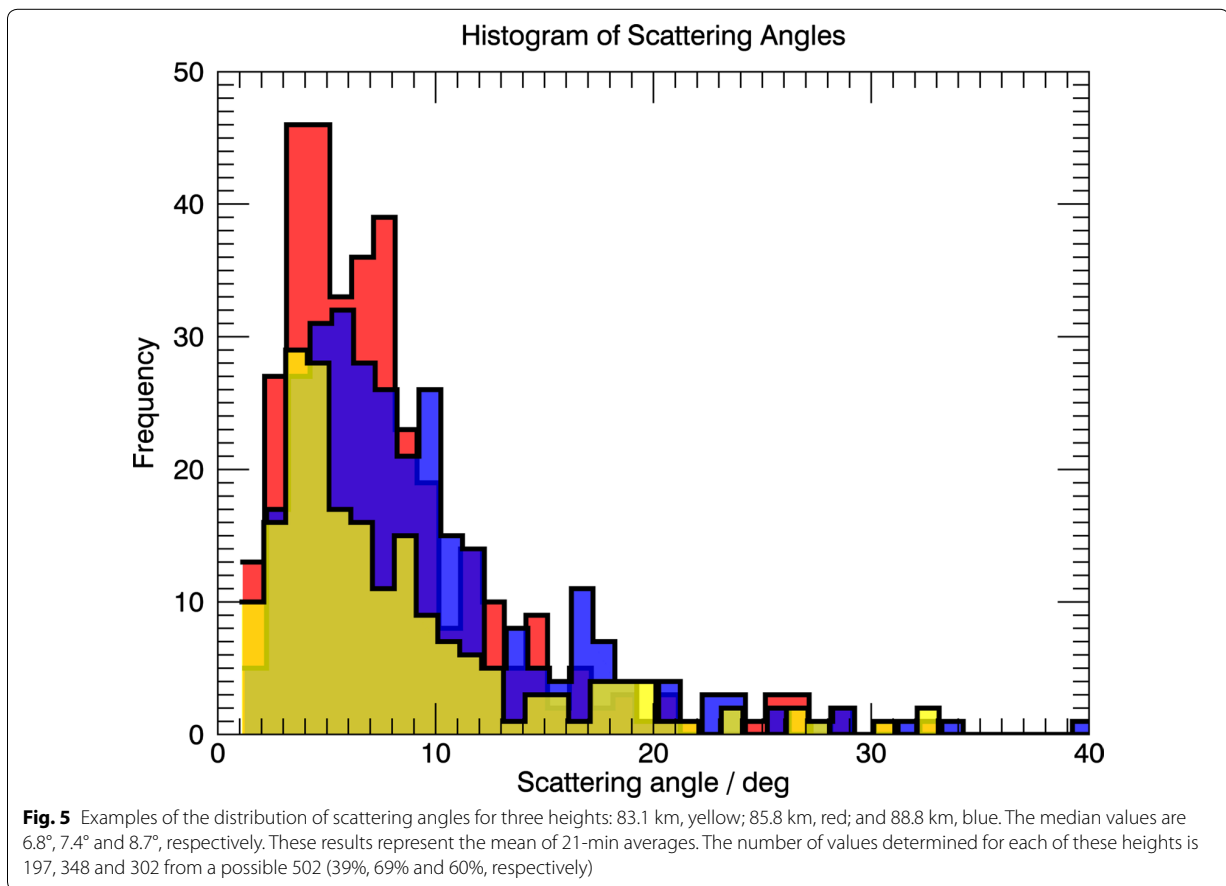
This highlights some issues around the application of Eq. (6). It is best suited to small values of  $\theta_s$  and becomes increasingly insensitive as it increases. There is also a question around the most suitable time interval over which to calculate it. Reid et al. (1988) used a mean value calculated over a period of a few hours, and Ruster and Reid (1990) used a mean calculated over a period of 2 days, matching the periods over which they calculated momentum flux. To obtain a statistically valid measure of momentum flux, long averaging intervals of the mean square radial velocities are required (see, e.g. Vincent et al. 2010). During this period  $\theta_s$  and hence  $\theta_E$  will vary, but the application of Eq. (1) requires a single value of



$\theta_E$  for the averaging interval, so we have two competing requirements. This problem is avoided by applying the least-squares inversion approach because it allows for a fit to the known radial velocities, each of which is associated with an effective beam angle. This does require some care (e.g. Andrioli et al. 2013) and is not as simple mathematically as the application of Eq. (1), but in the presence of aspect sensitivity and relative wide Doppler beams, it may be the preferred approach.

Another question arises whether the off-zenith power exceeds that in the vertical direction, and whether this

means that there is a patchy layer present, a tilted layer present, or that the scattering is quasi-isotropic? If we accept the Gaussian fall-off in power used to derive Eqs. (6) and (7), then an off-vertical power in excess of the vertical power should be treated as indicating isotropic scatter. The effective beam direction should then be set to the apparent beam direction. Whatever the underlying mechanism, the need to correct for the effective beam direction on some occasions remains. In the present work, the effect is not severe because the beamwidths are quite small, as are the off-zenith angles. With



wider beam Doppler radars, this effect could be quite large.

In this work, we have calculated  $\theta_s$  and hence  $\theta_E$  for each 3-minute record for each beam where possible and substituted the apparent beam direction when not. We then averaged the  $\theta_E$  values to obtain one value for each off-zenith angle, and used these in Eqs. (1), (3) and (4). We averaged the values of  $\theta_E$  obtained from beams with the same off-zenith angles  $\theta_A$  to obtain one  $\theta_{E1}$  and one  $\theta_{E2}$  for use in Eqs. (1) and (3). We also calculated the mean value of  $\theta_{E1}$  and  $\theta_{E2}$  for the entire observing period (Fig. 2) and used this in the same equations. We would expect the correct values of the Reynolds Stress terms to lie between these two values. We also applied the least-squares inversion approach, which fits to the radial velocities and their effective beam directions. We therefore have three estimates for the Reynolds stress terms described by Eqs. (1), (3) and (4).

Alternate approaches to measuring  $\theta_s$  using a multi-receiver radars have been described by Murphy and Vincent (1993), Holdsworth and Reid (2004) and more recently by Sommer et al. (2016). Murphy and Vincent

(1993) and Holdsworth and Reid (2004) used multi-receiver techniques to look at mid-latitude MF partial reflections and is so not entirely applicable here. Sommer et al. also used a multi-receiver approach, but looked at the PMSE at VHF over Andøya, and so is directly relevant to the present work. They used both Eq. (6) and multi-receiver approaches and found larger values of  $\theta_s$  than other studies and so argued that their results generally indicated isotropic scattering, with periods of localized anisotropic scattering process leading to higher aspect sensitivity. This interpretation is not inconsistent with our results when we note that 61, 31 and 40% of records indicate isotropic scatter (or a failure to calculate  $\theta_s$  at least) at heights of 83.1, 85.8 and 88.8 km, respectively.

#### Mean winds and tides

The tidal components during this observational period have previously been discussed by Lübken et al. (1990), Manson et al. (1992) and Ruster (1992, 1994) for the entire MAC/SINE campaign, and further details on the results of the analysis of the mean and tidal winds may be found therein. However, these components need to

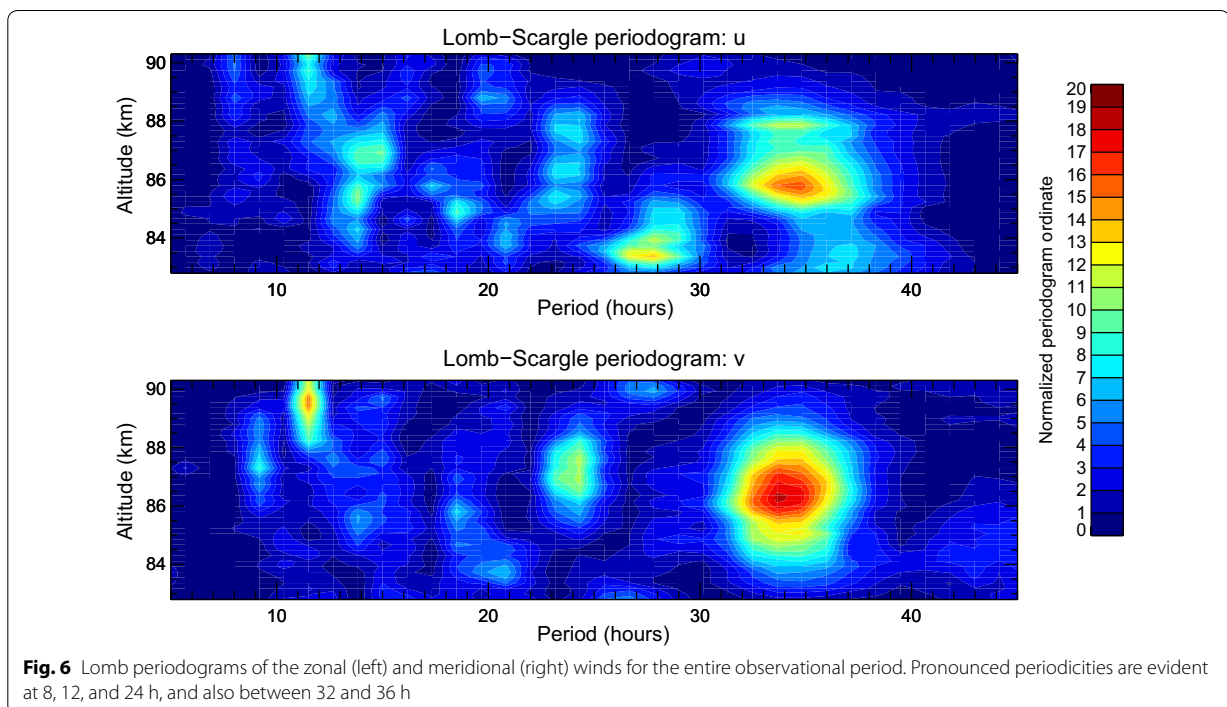
be removed from the radial velocity time series, and so we describe the approach used to calculate and remove them and note a few details. To calculate the mean and tidal winds, we follow the approach used by Spargo et al. (2017) for the BPMF Doppler radar (Reid et al. 1995; Holdsworth and Reid 2004) operating in Hybrid Doppler Interferometer (HDI) mode, and which is similar to that applied by Andrioli et al. (2013) to meteor radar radial velocities. Briefly, the radial velocities were partitioned into non-oversampled windows of width 1 h, and the three wind components ( $u, v, w$ ) were estimated using a standard least-squares formulation (e.g. Vandepuer and Reid 1995). The major periods present were determined using a Lomb periodogram, and these periods were removed from each radial velocity by subtracting from them a time-dependent radial projection of a least-squares fit  $y$  to the wind time series, of the form:

$$y = \sum_{i=0}^{n-1} \cos \frac{2\pi}{T} (t - \Phi_i) \quad (9)$$

where  $T$  is an  $n$ -element array of the significant periods, and  $\Phi$  is an  $n$ -element array of phases providing the time at which the  $i$ th component maximizes. The fits were made over windows of length 48 h. These time series were then used in any further analysis requiring the radial velocities. This is more computationally invasive approach than that of VR83.

Figure 6 shows the Lomb periodogram for the zonal and meridional wind components. Inspection of this figure indicates pronounced periodicities at 8, 12 and 24 h, and also near 28, 32 and 36 h. Ruster (1994) has discussed the nonlinear interaction of the various wind components during periods overlapping that of this data set and identified waves in the 32–38-h period range resulting from nonlinear wave–wave interactions of the third order. In addition, he found the most frequently observed periods present were those corresponding to interactions between the dominating diurnal and semidiurnal tides and planetary waves with periods of 2–3 days. In addition to second-order processes, higher-order interactions were also observed in the velocity fluctuations and in the echo power, suggesting corresponding temperature variations. We have removed the 8, 12 and 24 h tidal components, as well as the 18, 32 and 36 h periodicities evident in the Lomb periodograms using Eq. (9). The harmonic fitting limits the height coverage of the data, as it fails with limited data, and useable data are limited to heights between 82 and 91.6 km.

Figure 7 shows the mean zonal, meridional and vertical winds with the tidal components removed for the entire period of observation. The zonal wind field has a westward flow with a peak magnitude of about  $30 \text{ ms}^{-1}$ . The meridional wind is equatorward above 85 km and around zero below. The mean vertical wind is downwards below



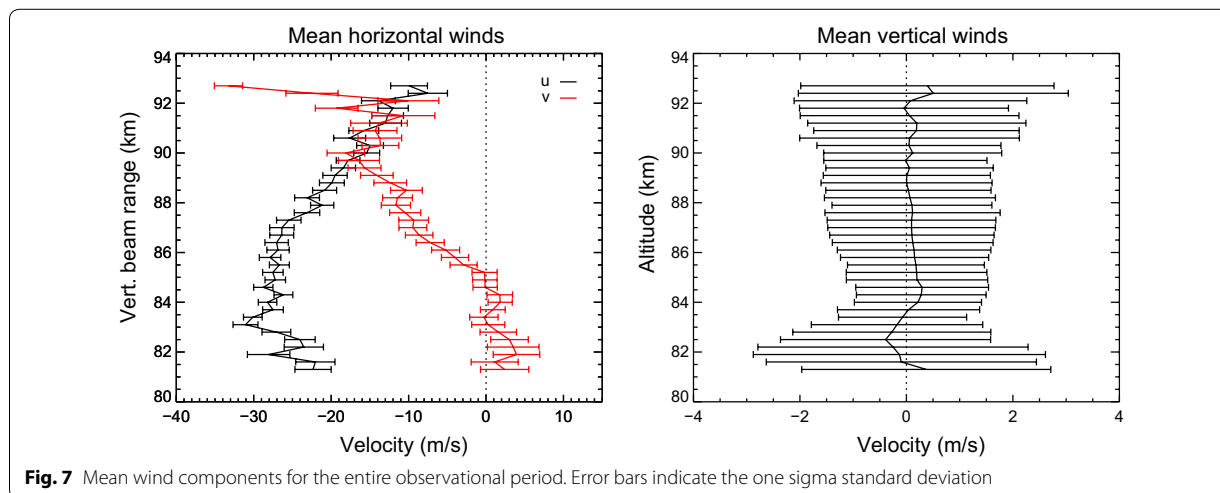


**Fig. 7** Mean wind components for the entire observational period. Error bars indicate the one sigma standard deviation

84 km and upwards above, but given the uncertainties, is effectively zero.

#### Momentum flux

For the application of the VR83 approach, after removal of the tidal and other periodicities, the 3-min time series of radial velocities and spectral widths were filtered for periods less than 1 h, for periods between 1 and 6 h, and for 6 h to the inertial period (12.8 h). We only show the results for 6 min to 12.8 h here. To filter the time series, a spline was applied, and the splined values used to fill in missing data points. A fifth-order Butterworth filter with appropriate cut-offs was then applied to this modified time series. Variances were then calculated for the filtered time series, using only values corresponding to those times when real data were obtained. All the time series were treated in the same way. Equations (1), (3) and (4) are then applied to the filtered time series. The effective beam directions were calculated using the powers measured in each of the off-zenith beams relative to that measured in the vertical beam as described above. The momentum fluxes derived for scales larger than the radar pulse volume calculated using radial velocities we call ‘superscale’, and for scales smaller than the pulse volume calculated using spectral widths, we call ‘subscale’. We calculate the superscale flux using both the VR83 and least-squares inversion approaches. We begin with the subscale results shown in Fig. 8.

#### Subscale momentum flux

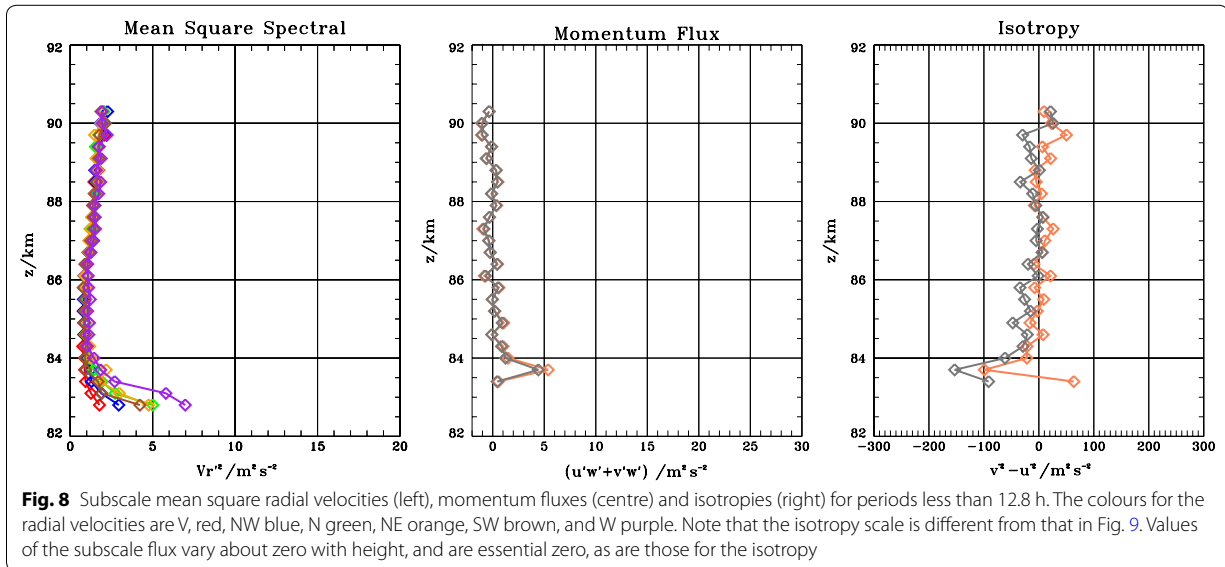
For the subscales, momentum flux values for periods less than 12.8 h are generally between  $\pm 1.0 \text{ m}^2 \text{ s}^{-2}$  except at the lowest two heights where they are  $+2 - 3 \text{ m}^2 \text{ s}^{-2}$ , and we conclude that the momentum flux for subscales

for periods less than 12.8 h is essentially zero. We have not attempted to calculate the subscale momentum flux using the inversion technique. This result is in contrast to that of Reid (2004) who did find significant fluxes. In his case, the radar pulse volume was very much larger, approximately  $4 \times 13.5 \text{ km}$  at 86 km altitude, compared to  $0.3 \times 8 \text{ km}$  here. To obtain the total arithmetic sum of the momentum flux ( $\overline{u'w'} + \overline{v'w'}$ ) for all scales for periods between 6 min and 12.8 h, the superscale and subscale momentum fluxes should be added. The small values of the subscale results mean that the total flux is essentially the same as that for the superscale flux in this case, which we now consider.

#### Superscale momentum flux

Figure 9 summarizes the mean square radial velocities, the arithmetic sum of the momentum fluxes ( $\overline{u'w'} + \overline{v'w'}$ ) and ( $\overline{v'^2} - \overline{u'^2}$ ) for scales larger than the pulse volume for periods less than 12.8 h, the inertial period. We note that the mean square radial velocities do show some noise, which propagates into the momentum flux and isotropy results. In this plot, we have shown the flux calculated using the apparent beam direction in green, and the flux calculated using the mean effective beam direction calculated for all of the 3 min observations in coral. Inspection of this plot indicates a 10–15% difference. Corrected flux values in coral are about  $5 \text{ m}^2 \text{ s}^{-2}$  below 86 km, and increase rapidly between 86.5 and 87 km to around  $13 \text{ m}^2 \text{ s}^{-2}$ , before settling back to around  $7.5 \text{ m}^2 \text{ s}^{-2}$  above about 88.5 km. The form of these plots suggests that more at the top, and less so at the bottom of the height range, values may not be representative of the average for the whole observational period. Figure 10 shows the results from the inversion approach. The form is very





similar to that of Fig. 9, and the values similar. The error bars indicate the one sigma standard deviations. The profile is perhaps less noisy than that for the VR83 approach, but clearly, the same values are being measured. For both approaches, the isotropy is negative, with values of between  $-50 \text{ m}^2 \text{ s}^{-2}$  at the lowest heights, and about  $-200 \text{ m}^2 \text{ s}^{-2}$  above.

### Simulations

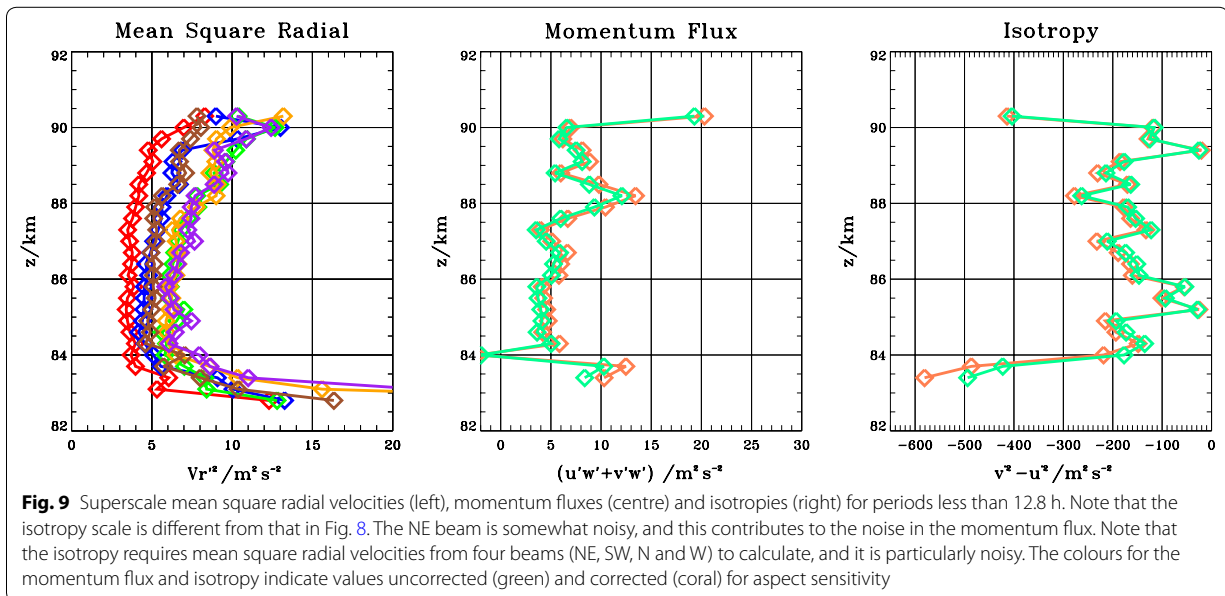
We noted in “[Reynolds stress terms](#)” section that the general inversion of the radial velocities to determine the individual terms of the Reynolds stress tensor failed to deliver physically realistic results. To provide further insight into this, we simulated the present beam arrangement in the presence of a gravity wave field following the approach of Spargo et al. (2017).

Briefly, the simulation incorporated a superposition of 37 gravity waves with periods in the range of 10–180 min, with randomly selected initial phases and propagation directions in the Eastern sector. This distribution of wave directions led to negative values of  $\overline{u'w'}$ , and near-zero values of  $\overline{v'w'}$ . Diurnal and semi-diurnal tides were also included in the wave field and were removed using the same approach as discussed in the “[Mean winds and tides](#)” section. Each covariance estimation was performed over a 48-h segment of simulated data. A total of 10000 realisations were performed, so as to be able to qualitatively illustrate the bias distribution. To simulate realistic changes in beam position, we assumed an aspect sensitivity in the model randomly varying between  $5^\circ$  and  $15^\circ$  in a temporally

correlated random manner, with a spectrum corresponding to that of the power-law temporal spectrum model in Eq. (24) of Gardner et al. (1993). Gaussian distributed errors were added to the “measured” zonal and meridional zenith angles of the beam positions, with standard deviations of  $0.25^\circ$ .

The results are shown in Fig. 11. Agreement between the VR83 approach and the least-squares inversion for both two and six beams is very good for the determination of the arithmetic sum of the fluxes. The isotropies are also in excellent agreement. We note that attempting to solve for the individual flux terms led to non-physical values. As we noted above, we interpret this as an indication that large, correlated errors had accumulated in the  $\overline{u'w'}$  and  $\overline{v'w'}$  components.

In summary, based on simple modelling, the inversion technique appears to be equivalent to the VR83 technique used for the analysis in this paper to determine the arithmetic sum horizontal momentum flux. We propose to further investigate ways to reduce the inverse problem’s condition number, and its sensitivity to outliers. We note in this context that to deal with fitting radial velocities to multisite FPI observations, Harding et al. (2015) successfully regularized the inversion problem in such a way as to produce “smooth” variations in the solved components. It is not clear how well the approach will lend itself to non-ideal observing geometries in the covariance estimation situation, but it nonetheless appears promising, in particular for application to meteor radar estimates of wind covariance.



### Summary and conclusion

For the total momentum flux for superscales and periods between 6 min and 12.8 h, values are typically between 5 and 13  $\text{m}^2 \text{s}^{-2}$ . The contribution from the 6 to 12.8 h period range dominates the other period bands. These results are consistent with those of Placke et al. (2015) who used the Saura MF radar, located close to the former position of the mobile SOUSY radar, and the VR83 approach, to measure momentum flux and who provide the mean for June 2011. Their values for  $\overline{u'w'}$  and  $\overline{v'w'}$  are both positive over the height region of our observations and take values of around 3  $\text{m}^2 \text{s}^{-2}$ , so they are generally consistent but smaller than our results when applying the same technique. They also measured the fluxes using a nearby meteor radar. The results agree somewhat over a restricted range in summer. However, these authors did not correct for aspect sensitivity, nor did they remove the tidal components from their data, so there is some uncertainty around their results.

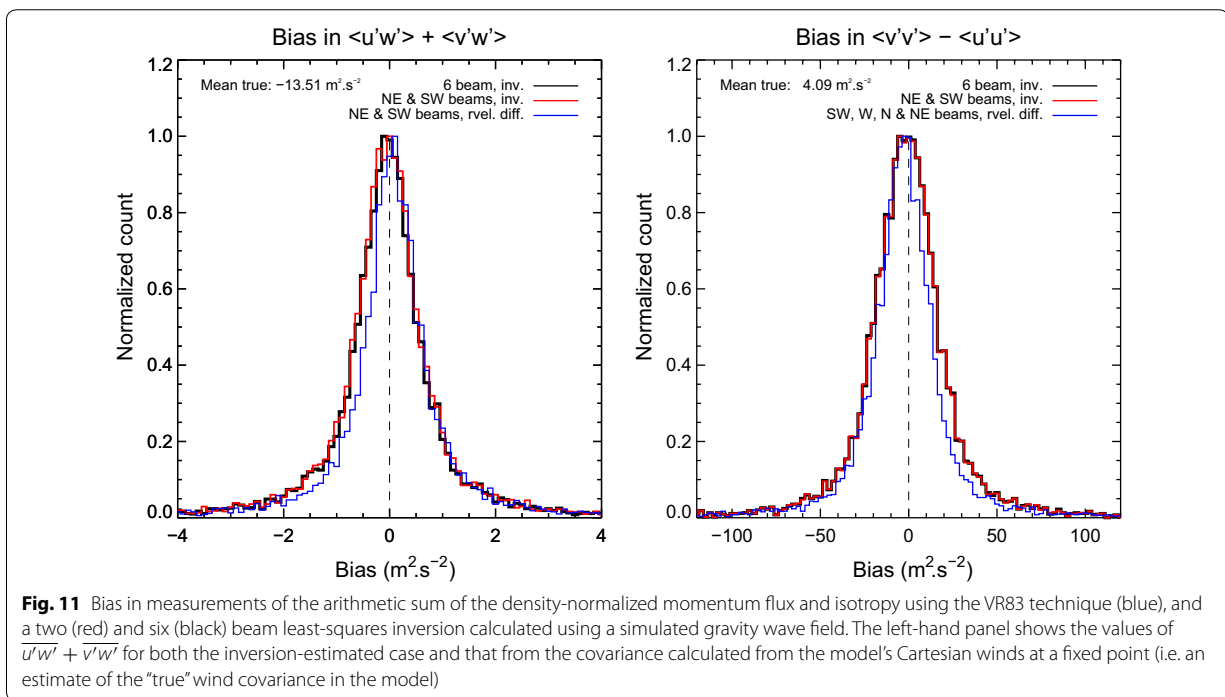
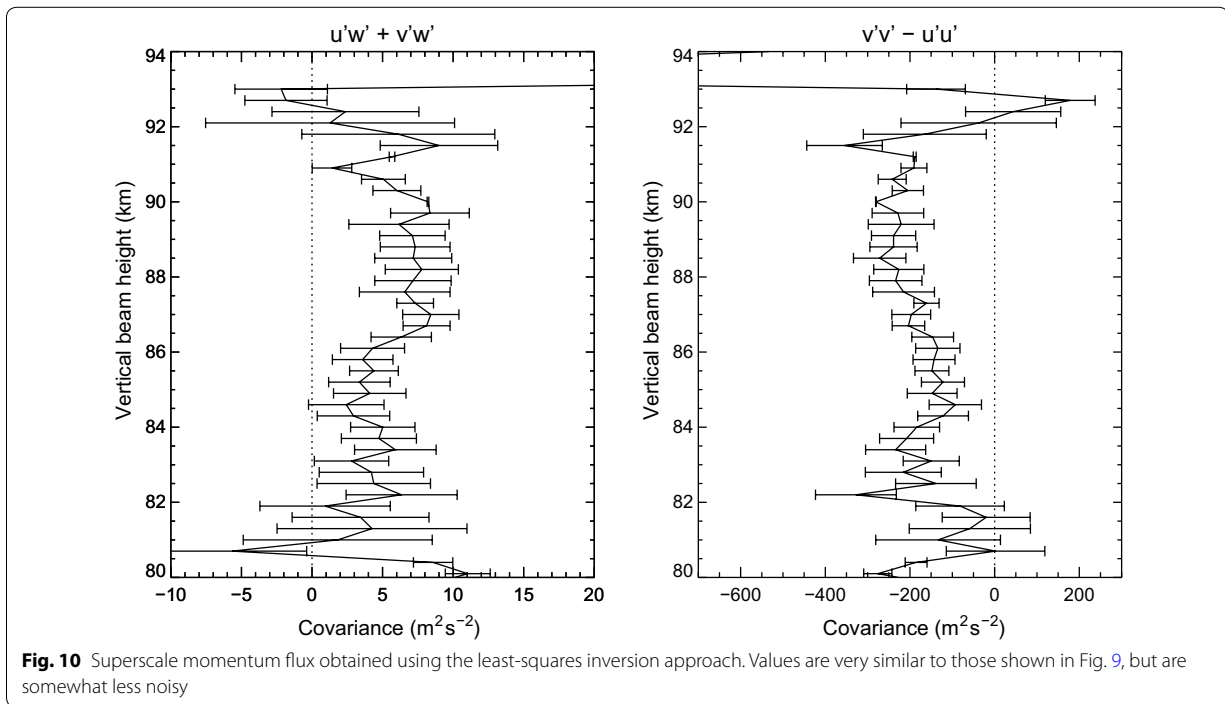
For the subscales, values are between  $\pm 1.0 \text{m}^2 \text{s}^{-2}$  and essentially zero. Simulations show that the estimates of the individual wind covariance terms from a least-squares inversion are erroneously correlated, but that the arithmetic sum of the horizontal fluxes, a term allowed by the beam geometry, is in excellent agreement with the VR83 technique (which is typically used to estimate momentum fluxes from this type of radar). We propose to further investigate ways to reduce the instability in the least-squares inversion approach.

Our results suggest that the validity of the least-squares inversion for meteor radar radial velocities to determine

momentum fluxes will depend on the azimuthal symmetry of the meteor distribution. We have seen that with our beam arrangement, which is similar to a typical meteor distribution for a particular time of day, the Reynolds stress terms cannot be individually retrieved. Furthermore, unlike the arrangement in the present work, the meteor distribution rotates throughout the day. For meteor radars with relatively low counts where the asymmetry is typically significant, it would not be clear which combinations of terms are correct at particular times of the day, and the average over the day would be suspect. Simulation results presented by Spargo et al. (2017), do show acceptable recovery of the Reynolds stress terms when using actual meteor locations derived from the Buckland Park meteor radar, but actual experimental verification of meteor radar measurements of momentum flux is still incomplete.

Inspection of the height coverage plot for the present results clearly indicates the limited height range over which representative results can be calculated (50% at 84 and 90 km, albeit at a very good range resolution of 300 m). This was a powerful radar, with an antenna area of 8880  $\text{m}^2$ , a peak power (for this work) of 100 kW, and a duty cycle of 4% ( $3.55 \times 10^7 \text{W m}^2$ ). Together with the ongoing uncertainty around the measurement of the Reynolds Stress tensor using meteor radars, this suggests that Doppler capable MF/HF partial reflection radars (e.g. Saura MF, Juliusruh MF and the Buckland Park MF), might be the reference instruments for this measurement, with height coverage from 60 to 94 km with 1–2 km height resolution. The limited height resolution





may actually be an advantage, producing a natural analogue summing of the data into 2 km bins. A reduced height resolution, perhaps 600 m, on the MST may have also been an advantage.

We recommend the use of the inversion technique for multi-beam Doppler radars in the presence of aspect-sensitive scatter because of its variable nature, and the relatively broad beams of most real-world radars. In the application of the VR83 technique, Doppler Na lidars may have a real practical advantage in good seeing conditions because of their narrow beam widths, and strong returns from the 80 to 100 km height region.

#### Abbreviations

AOA: angle of arrival; BP: Buckland Park; (COH)<sup>2</sup>: coherence squared statistic; E, W, N, S, V: east, west, north, south, vertical; HDI: hybrid Doppler interferometry; HF: high frequency; KH: Kelvin–Helmholtz; KHI: Kelvin–Helmholtz Instability; MAC-SINE: Middle Atmosphere Cooperation-Summer in Northern Europe; MF: medium frequency; MLT: mesosphere lower thermosphere; MST: mesosphere stratosphere troposphere; NE, NW, SW: north-east, north-west, south-west; PMSE: polar mesosphere summer echoes; PR: partial reflection; PRF: pulse repetition frequency; RADAR: radio detection and ranging; SOUSY: sounding system; SSR: SOUSY Svalbard radar; ST: stratosphere troposphere; VHF: very high frequency.

#### Authors' contributions

IMR wrote this paper. RR did the original data reduction and produced the radial velocity, power and spectral width time series data further analysed here. PC implemented the six-beam antenna arrangement used for this study and provided overall management of the SOUSY involvement in MAC/SINE. AJS developed the gravity wave simulations and contributed to writing this paper. All authors read and approved the final manuscript.

#### Author details

<sup>1</sup> ATRAD Pty Ltd, 20 Phillips St., Thebarton 5031, Australia. <sup>2</sup> School of Physical Sciences, University of Adelaide, Adelaide 5000, Australia. <sup>3</sup> Max Planck Institute for Solar System Research, 37077 Göttingen, Germany.

#### Acknowledgements

The authors thank the staff of the Andøya Rocket Range and the members of the SOUSY project group of the Max-Planck-Institut für Aeronomie in obtaining the measurements.

#### Competing interests

The authors declare that they have no competing interests.

#### Availability of data and materials

Data requests should be made to IMR or to the Max Planck Institute for Solar System Research.

#### Funding

The antenna system of the mobile SOUSY VHF Radar was funded by the Deutsche Forschungsgemeinschaft. The original data analysis was partly carried out using the facilities of the Gesellschaft für wissenschaftliche Datenverarbeitung in Göttingen. The involvement of IMR in the preparation of this paper was supported by ATRAD Pty Ltd. AJS is supported by an Australian Commonwealth postgraduate scholarship.

#### Publisher's Note

Springer Nature remains neutral with regard to jurisdictional claims in published maps and institutional affiliations.

Received: 27 February 2018 Accepted: 2 August 2018

Published online: 10 August 2018

#### References

- Alexander MJ, Geller M, McLandress C, Polavarapu S, Preusse P, Sassi F, Sato K, Eckermann S, Ern M, Hertzog A, Kawatani Y, Pulido M, Shaw TA, Sigmund M, Vincent R, Watanabe S (2010) Recent developments in gravity-wave effects in climate models and the global distribution of gravity-wave momentum flux from observations and models. *Q J R Meteorol Soc* 136:1103–1124. <https://doi.org/10.1002/qj.637>
- Andrioli VF, Fritts DC, Batista PP, Clemesha BR (2013) Improved analysis of all-sky meteor radar measurements of gravity wave variances and momentum fluxes. *Ann Geophys* 31:889–908. <https://doi.org/10.5194/angeo-31-889-2013>
- Bossert K, Fritts DC, Heale CJ, Eckermann SD, Snively JB, Williams BP, Reid IM, Murphy DJ, Spargo AJ, MacKinnon AD (2018) Spectral momentum flux of a mountain wave event over New Zealand. *J Geophys Res Atmos*. <https://doi.org/10.1029/2018JD028319>
- Czechowsky P, Ruster R (1997) VHF radar observations of turbulent structures in the polar mesopause region. *Ann Geophys* 15:1028–1036. <https://doi.org/10.1007/s00585-997-1028-8>
- Czechowsky P, Schmidt G, Ruster R (1984) The mobile SOUSY Doppler radar: technical design and first results. *Radio Sci* 19(1):441–450. <https://doi.org/10.1029/RS019i001p00441>
- Czechowsky P, Reid IM, Ruster R (1988) VHF radar measurements of the aspect sensitivity of the summer polar mesopause echoes over Andenes (69°N, 16°E), Norway. *Geophys Res Lett* 15:1259–1262. <https://doi.org/10.1029/GL015i011p01259>
- Czechowsky P, Reid IM, Ruster R, Schmidt G (1989) VHF radar echoes observed in the summer and winter polar mesosphere over Andøya, Norway. *J Geophys Res* 94(D4):5199–5217. <https://doi.org/10.1029/JD094iD04p05199>
- Czechowsky P, Klostermeyer J, Röttger J, Ruster R, Schmidt G (1998) The SOUSY-Svalbard-Radar for middle and lower atmosphere research in polar regions. In: Edwards B (ed) *Solar-terrestrial energy program, Proceedings of 8th Workshop on Technical and Scientific Aspects of MST Radar, Bangalore/Indien 1997*. SCOSTEP Secret., Boulder, pp 318–321. <http://hdl.handle.net/11858/00-001M-0000-0014-DAC1-6>
- Eckermann SD (1996) Hodographic analysis of gravity waves: relationships among Stokes parameters, rotary spectra and cross-spectral methods. *J Geophys Res* 101(D14):19169–19174. <https://doi.org/10.1029/96JD01578>
- Ern M, Trinh QT, Kaufmann M, Krisch I, Preusse P, Ungermann J, Zhu Y, Gille JC, Mlynarczyk MG, Russell JM III, Schwartz MJ, Riese M (2016) Satellite observations of middle atmosphere gravity wave absolute momentum flux and of its vertical gradient during recent stratospheric warmings. *Atmos Chem Phys* 16:9983–10019. <https://doi.org/10.5194/acp-16-9983-2016>
- Fritts DC, Alexander MJ (2003) Gravity wave dynamics and effects in the middle atmosphere. *Rev Geophys* 41:1003. <https://doi.org/10.1029/2001RG000106>
- Fritts DC, Janches D, Hocking WK, Mitchell NJ, Taylor MJ (2012) Assessment of gravity wave momentum flux measurement capabilities by meteor radars having different transmitter power and antenna configurations. *J Geophys Res* 117:D10108. <https://doi.org/10.1029/2011JD017174>
- Gardner CS, Taylor MJ (1998) Observational limits for lidar, radar, and airglow imager measurements of gravity wave parameters. *J Geophys Res* 103(D6):6427–6437. <https://doi.org/10.1029/97JD03378>
- Gardner CS, Hostetler CA, Franke SJ (1993) Gravity wave models for the horizontal wave number spectra of atmospheric velocity and density fluctuations. *J Geophys Res* 98(D1):1035–1049. <https://doi.org/10.1029/92JD02051>
- Hall CM, Röttger J, Kuyeng K, Sigernes F, Claes S, Chau J (2009) First results of the refurbished SOUSY radar: tropopause altitude climatology at 78°N, 16°E, 2008. *Radio Sci* 44:RS5008. <https://doi.org/10.1029/2009RS004144>
- Harding BJ, Makela JJ, Meriwether JW (2015) Estimation of mesoscale thermospheric wind structure using a network of interferometers. *J Geophys Res Space Phys* 120:3928–3940. <https://doi.org/10.1002/2015JA021025>
- Hertzog A, Alexander MJ, Plougonven R (2012) On the intermittency of gravity wave momentum flux in the stratosphere. *J Atmos Sci* 69(11):3433–3448. <https://doi.org/10.1175/JAS-D-12-09.1>
- Hocking WK (2005) A new approach to momentum flux determinations using SKIYMET meteor radars. *ANGEOS* 23(7):2433–2439. <https://doi.org/10.5194/angeo-23-2433-2005>
- Hocking WK, Ruster R, Czechowsky P (1986) Absolute reflectivities and aspect sensitivities of VHF radio wave scatterers measured with the SOUSY

- radar. *J Atmos Terr Phys* 48:131–144. [https://doi.org/10.1016/0021-9169\(86\)90077-2](https://doi.org/10.1016/0021-9169(86)90077-2)
- Holdsworth DA, Reid IM (2004) The Buckland Park MF radar: routine observation scheme and velocity comparisons. *Ann Geophys* 22:3815–3828. <https://doi.org/10.5194/angeo-22-3815-2004>
- Holdsworth DA, Reid IM, Cervera MA (2004) The Buckland Park all-sky interferometric meteor radar—description and first results. *Radio Sci* 39:RS5009. <https://doi.org/10.1029/2003RS003014>
- Love PT, Murphy DJ (2016) Gravity wave momentum flux in the mesosphere measured by VHF radar at Davis, Antarctica. *J Geophys Res Atmos* 121:12723–12736. <https://doi.org/10.1002/2016JD025627>
- Lübken F-J, von Zahn U, Manson A, Meek C, Hoppe U-P, Schmidlin FJ, Stegman J, Murtagh DP, Ruster R, Schmidt G, Widdel H-U, Espy P (1990) Mean state densities, temperatures and winds during the MAC/SINE and MAC/EPSILON campaigns. *J Atmos Terr Phys* 52:955–970. [https://doi.org/10.1016/0021-9169\(90\)90027-K](https://doi.org/10.1016/0021-9169(90)90027-K)
- Manson AH, Meek CE, Brekke A, Moen J (1992) Mesosphere and lower thermosphere (80–120 km) winds and tides from near Tromsø (70°N, 19°E): comparisons between radars (MF, EISCAT, VHF) and rockets. *J Atmos Terr Phys* 54(7–8):927–950. [https://doi.org/10.1016/0021-9169\(92\)90059-T](https://doi.org/10.1016/0021-9169(92)90059-T)
- Meek CE, Reid IM, Manson AH (1985) Observations of mesospheric wind velocities 1: gravity wave horizontal scales and phase velocities determined from spaced wind observations. *Radio Sci* 20:1363–1382. <https://doi.org/10.1029/RS020i006p01363>
- Murphy DJ, Vincent RA (1993) Estimates of momentum flux in the mesosphere and lower thermosphere over Adelaide, Australia, from March 1985 to February 1986. *J Geophys Res* 98(D10):18617–18638. <https://doi.org/10.1029/93JD01861>
- Placke M, Hoffmann P, Latteck R, Rapp M (2015) Gravity wave momentum fluxes from MF and meteor radar measurements in the polar MLT region. *J Geophys Res Space Phys* 120:736–750. <https://doi.org/10.1002/2014JA020460>
- Reid IM (1984) Radar studies of atmospheric gravity waves. Ph.D. dissertation, University of Adelaide, <http://hdl.handle.net/2440/19500>
- Reid IM (1987) Some aspects of Doppler radar measurements of the mean and fluctuating components of the wind field in the upper middle atmosphere. *J Atmos Terr Phys* 49:467–484. [https://doi.org/10.1016/0021-9169\(87\)90041-9](https://doi.org/10.1016/0021-9169(87)90041-9)
- Reid IM (1990) Radar observations of stratified layers in the mesosphere and lower thermosphere (50–100 km). *Adv Space Res* 10:7–19. [https://doi.org/10.1016/0273-1177\(90\)90002-H](https://doi.org/10.1016/0273-1177(90)90002-H)
- Reid IM (2004) MF radar measurements of sub-scale mesospheric momentum flux. *Geophys Res Lett* 31:L17103. <https://doi.org/10.1029/2003GL019200>
- Reid IM (2015) MF and HF radar techniques for investigating the dynamics and structure of the 50 to 110 km height region: a review. *Prog Earth Planet Sci* 2:33. <https://doi.org/10.1186/s40645-015-0060-7>
- Reid IM, Woithe JM (2005) Three-field photometer observations of short-period gravity wave intrinsic parameters in the 80 to 100 km height region. *J Geophys Res* 110:D21108. <https://doi.org/10.1029/2004JD005427>
- Reid IM, Ruster R, Schmidt G (1987) VHF radar observations of a cat's-eye-like structure at mesospheric heights. *Nature* 327:43–45. <https://doi.org/10.1038/327043a0>
- Reid IM, Ruster R, Czechowsky P, Schmidt G (1988) VHF radar measurements of momentum flux in the summer polar mesosphere over Andenes (69°N, 16°E), Norway. *Geophys Res Lett* 15(11):1263–1266. <https://doi.org/10.1029/GL015i011p01263>
- Reid IM, Czechowsky P, Ruster R, Schmidt G (1989) First VHF radar measurements of mesopause summer echoes at mid-latitudes. *Geophys Res Lett* 16:135–138. <https://doi.org/10.1029/GL016i002p00135>
- Reid IM, Vandeppeer BGW, Dillon SC, Fuller BM (1995) The new Adelaide medium frequency Doppler radar. *Radio Sci* 30:1177–1189
- Riggin DM, Tsuda T, Shinbori A (2016) Evaluation of momentum flux with radar. *J Atmos Solar Terr Phys* 142:98–107. <https://doi.org/10.1016/j.jastp.2016.01.013>
- Ruster R (1992) VHF radar observations in the summer polar mesosphere indicating nonlinear interaction. *Adv Space Res* 12:85–88. [https://doi.org/10.1016/0273-1177\(92\)90448-7](https://doi.org/10.1016/0273-1177(92)90448-7)
- Ruster R (1994) VHF radar observations of nonlinear interactions in the summer polar mesosphere. *J Atmos Terr Phys* 56:1289–1299. [https://doi.org/10.1016/0021-9169\(94\)90067-1](https://doi.org/10.1016/0021-9169(94)90067-1)
- Ruster R, Reid IM (1990) VHF radar observations of the dynamics of the summer polar mesopause region. *J Geophys Res* 95(D7):10005–10016. <https://doi.org/10.1029/JD095iD07p10005>
- Shenghui Z, Ming W, Lijun W, Chang Z, Mingxu Z (2014) Sensitivity analysis of the VWP wind retrieval method for single-Doppler weather radars. *J Atmos Ocean Technol* 31:1289–1300. <https://doi.org/10.1175/JTECH-D-13-00190.1>
- Sommer S, Stober G, Chau JL (2016) On the angular dependence and scattering model of polar mesospheric summer echoes at VHF. *J Geophys Res Atmos* 121:278–288. <https://doi.org/10.1002/2015JD023518>
- Spargo AJ, Reid IM, MacKinnon AD, Holdsworth DA (2017) Mesospheric gravity wave momentum flux estimation using hybrid Doppler interferometry. *Ann Geophys* 35:733–750. <https://doi.org/10.5194/angeo-35-733-2017>
- Stober G, Sommer S, Schult C, Latteck R, Chau JL (2018) Observation of Kelvin–Helmholtz instabilities and gravity waves in the summer mesopause above Andenes in Northern Norway. *Atmos Chem Phys* 18:6721–6732. <https://doi.org/10.5194/acp-18-6721-2018>
- Swarnalingam N, Hocking WK, Drummond JR (2011) Long-term aspect-sensitivity measurements of polar mesosphere summer echoes (PMSE) at Resolute Bay using a 51.5 MHz VHF radar. *J Atmos Sol Terr Phys* 73:957–964. <https://doi.org/10.1016/j.jastp.2010.09.032>
- Thorsen D, Franke SJ, Kudeki E (1997) A new approach to MF radar interferometry for estimating mean winds and momentum flux. *Radio Sci* 32(2):707–726. <https://doi.org/10.1029/96RS03422>
- Thrane EV (1990) Studies of middle atmosphere dynamics: the research projects Middle Atmosphere Co-operation/Summer in Northern Europe (MAC/SINE), and MAC/EPSILON. *J Atmos Terr Phys* 52:815–825. [https://doi.org/10.1016/0021-9169\(90\)90018-1](https://doi.org/10.1016/0021-9169(90)90018-1)
- Vandeppeer BGW, Reid IM (1995) On the spaced antenna and imaging Doppler interferometer techniques. *Radio Sci* 30:885–901. <https://doi.org/10.1029/95RS00994>
- Vincent RA, Reid IM (1983) HF Doppler measurements of mesospheric gravity wave momentum fluxes. *J Atmos Sci* 40:1321–1333. [https://doi.org/10.1175/1520-0469\(1983\)040%3c1321:HDMOMG%3e2.0.CO;2](https://doi.org/10.1175/1520-0469(1983)040%3c1321:HDMOMG%3e2.0.CO;2)
- Vincent RA, Kovalam S, Reid IM, Younger JP (2010) Gravity wave flux retrieval using meteor radars. *Geophys Res Lett* 37:L14802. <https://doi.org/10.1029/2010GL044086>
- Walterscheid RL, Hecht JH, Vincent RA, Reid IM, Woithe J, Hickey MP (1999) Analysis and interpretation of airglow and radar observations of quasi-monochromatic gravity waves in the upper mesosphere and lower thermosphere. *J Atmos Terr Phys* 61:461–478. [https://doi.org/10.1016/S1364-6826\(99\)00002-4](https://doi.org/10.1016/S1364-6826(99)00002-4)
- Whitehead JD, From WR, Jones KL, Monro PE (1983) Measurement of movements in the ionosphere using radio reflections. *J Atmos Terr Phys* 45(5):345–351. [https://doi.org/10.1016/S0021-9169\(83\)80039-7](https://doi.org/10.1016/S0021-9169(83)80039-7)
- Wu Y-F, Xu J, Widdel H-U, Lübken F-J (2001) Mean characteristics of the spectrum of horizontal velocity in the polar summer mesosphere and lower thermosphere observed by foil chaff. *J Atmos Terr Phys* 63:1831–1839. [https://doi.org/10.1016/S1364-6826\(01\)00062-1](https://doi.org/10.1016/S1364-6826(01)00062-1)
- Yi F (2001) Short-term variability and temporary structures of tides and mean wind in the polar summer mesosphere. *J Atmos Sol Terr Phys* 63:749–757

## Appendix F

**Publication: Ann. Geophys., 35, 733-750,  
2017**

This paper presents an analysis of the momentum fluxes derived using multi-beam data from the Buckland Park MF radar. In addition, it characterizes the performance of the momentum flux estimation technique for a variety of different radar configurations that were associated with the data collection. This work is based on the thesis of Spargo [2016], although a number of revisions were made to that work during the author's PhD candidature (the literature review, discussion and the content of Sect. 4.3) prior to publishing it in this paper.

Ann. Geophys., 35, 733–750, 2017  
https://doi.org/10.5194/angeo-35-733-2017  
© Author(s) 2017. This work is distributed under  
the Creative Commons Attribution 3.0 License.



## Mesospheric gravity wave momentum flux estimation using hybrid Doppler interferometry

Andrew J. Spargo<sup>1</sup>, Iain M. Reid<sup>1,2</sup>, Andrew D. MacKinnon<sup>1</sup>, and David A. Holdsworth<sup>1,3</sup>

<sup>1</sup>Department of Physics, School of Physical Sciences, The University of Adelaide, Adelaide, 5005, Australia

<sup>2</sup>ATRAD Pty. Ltd., 20 Phillips St., Thebarton, 5031, Australia

<sup>3</sup>National Security & ISR Division, Defence Science and Technology Group, Edinburgh, 5111, Australia

Correspondence to: Andrew J. Spargo (andrew.spargo@adelaide.edu.au)

Received: 19 December 2016 – Revised: 10 May 2017 – Accepted: 10 May 2017 – Published: 12 June 2017

**Abstract.** Mesospheric gravity wave (GW) momentum flux estimates using data from multibeam Buckland Park MF radar (34.6° S, 138.5° E) experiments (conducted from July 1997 to June 1998) are presented. On transmission, five Doppler beams were symmetrically steered about the zenith (one zenith beam and four off-zenith beams in the cardinal directions). The received beams were analysed with hybrid Doppler interferometry (HDI) (Holdsworth and Reid, 1998), principally to determine the radial velocities of the effective scattering centres illuminated by the radar. The methodology of Thorsen et al. (1997), later re-introduced by Hocking (2005) and since extensively applied to meteor radar returns, was used to estimate components of Reynolds stress due to propagating GWs and/or turbulence in the radar resolution volume. Physically reasonable momentum flux estimates are derived from the Reynolds stress components, which are also verified using a simple radar model incorporating GW-induced wind perturbations. On the basis of these results, we recommend the intercomparison of momentum flux estimates between co-located meteor radars and vertical-beam interferometric MF radars. It is envisaged that such intercomparisons will assist with the clarification of recent concerns (e.g. Vincent et al., 2010) of the accuracy of the meteor radar technique.

**Keywords.** Meteorology and atmospheric dynamics (waves and tides; instruments and techniques) – radio science (remote sensing)

### 1 Introduction

There has recently been particular interest in the use of specular returns from all-sky interferometric meteor radar to measure the gravity wave (GW)-driven vertical fluxes of horizontal momentum (herein momentum fluxes) in the mesosphere–lower thermosphere/ionosphere (MLT/I; ~80–100 km altitude) (e.g. Antonita et al., 2008; Clemesha and Batista, 2008; Beldon and Mitchell, 2009, 2010; Clemesha et al., 2009; Fritts et al., 2010a, b, 2012a, b; Vincent et al., 2010; Placke et al., 2011a, b, 2014, 2015; Andrioli et al., 2013a, b, 2015; Liu et al., 2013; de Wit et al., 2014b, a, 2016; Matsumoto et al., 2016; Riggan et al., 2016). This has largely arisen from a need to obtain improved spatial coverage in the parameterization of GWs and their associated momentum transport in climate models of the whole atmosphere (e.g. Kim et al., 2003; Ern et al., 2011), and the suggestion (Hocking, 2005) that such measurements can be made accurately in the MLT/I (with integration times of the order of 2 months) using relatively low-cost commercial meteor radar systems. Nevertheless, there are concerns over the accuracy and precision of the momentum flux estimates from this technique (e.g. Vincent et al., 2010). In this paper, a previously established technique which makes use of partial reflections from the mesosphere at medium frequency (MF) is re-visited and contrasted with the meteor technique. Our aim in doing this has been to determine if interferometric MF radars, in particular those which have a small antenna aperture and only transmit a vertical beam, are viable candidates for verifying momentum flux estimates from meteor radars.

Direct measurements of momentum fluxes in the MLT/I were pioneered by Vincent and Reid (1983), in a study that

utilized partial reflection returns from the Buckland Park MF radar (34.6° S, 138.5° E). Their experiment consisted of transmitting a broad, vertically directed beam, and applying Doppler beam steering (DBS) (Woodman and Guillen, 1974) to narrower, fixed receive beams, offset from the zenith in the cardinal (initially east and west) directions (herein referred to as a “complementary” beam arrangement). The momentum fluxes were then estimated from the difference in the beams’ mean square radial velocities. Similar approaches have since been applied to the same system (e.g. Fritts and Vincent, 1987; Reid and Vincent, 1987; Murphy and Vincent, 1993, 1998) and to other high-frequency (HF) and very high-frequency (VHF) radars at various sites (e.g. Fukao et al., 1988; Reid et al., 1988; Fritts and Yuan, 1989; Fritts et al., 1990, 1992; Sato, 1990, 1993, 1994; Tsuda et al., 1990; Wang and Fritts, 1990, 1991; Hitchman et al., 1992; Nakamura et al., 1993; Murayama et al., 1994; Placke et al., 2014, 2015; Riggin et al., 2016). It was obvious in some of these studies, especially those involving radars with relatively broad ( $\gtrsim 3^\circ$ ) transmit and receive beams, that the aspect sensitivity (or Bragg anisotropy; Muschinski et al., 2005) of the partially reflecting scatterers illuminated by the transmit beam needed to be measured and/or accounted for, or else the apparent receive beam zenith angles would overestimate the true values (see, e.g., Reid and Vincent (1987); Murphy and Vincent (1993) for two such approaches).

Thorsen et al. (1997) introduced an extension of the Vincent and Reid (1983) approach for radars with an interferometric capability, which accounted for the “brightness distribution” (the normalized angular and Doppler-frequency power spectral density; see, e.g., Woodman, 1997) in the radar receive beam(s). The authors applied this approach to a broad, vertically transmitted MF radar beam and relied on geophysical variability in the brightness distribution to obtain a sufficient number of radial velocity–pointing direction pairs to solve for the mean winds and wind covariances. An important assumption they made was that the “true” measured fluctuations in the weighted angle of arrival exceeded those due to statistical estimation errors. Despite the apparent validity of this assumption for the radar utilized, and the retrieval of momentum fluxes that appeared to be physically reasonable, no such studies incorporating interferometric radar techniques at MF have since been published.

Hocking (2005) later demonstrated the application of the Thorsen et al. (1997) technique to returns from specular meteor echoes, for estimation of momentum fluxes. There have been a number of concerns raised over the accuracy and precision of the estimates that have since been reported. Those concerns of relevance to this paper, which are related only to the wind field and scatterer location characteristics (and are valid for both the meteor and partial reflection approaches), may be summarized as follows:

1. The assumption of statistical stationarity of the wind and wave field over the volume spanned by the scatter-

ers. As discussed by Reid (1987), this assumption is independent of the beam configuration (or brightness distribution) used to sample the wind field. Additionally, if the beam configuration is anything other than complementary, the momentum flux estimates will only converge to the true value for horizontal wave scales much larger than the beam separation.

This is clearly more problematic for meteor observations, where angle-of-arrival (i.e. the “effective receive beams” of the radar) distributions peak at large off-zenith angles (typically 40–50°) and are often asymmetric in azimuth for integration times less than a few hours. An example of an approach to alleviate the former effect can be found in the design of the SAAMER and DrAAMER systems (Fritts et al., 2010b, 2012b), in which a larger transmitting aperture was used to increase the signal-to-noise (SNR) of returns (and hence number of detections) at small zenith angles. While reducing the total number of detections, such an approach also has the advantage of increasing the relative contribution of the perturbation component of the vertical wind to the radial velocity, as well as reducing errors in meteor height estimates.

2. The required integration time for statistical significance of the estimates. Kudeki and Franke (1998) showed that, for a perfect dual-beam “anemometer”, at least 16 days of integration is required to reliably estimate a momentum flux in the stratosphere, if one assumes that the flux represents a fraction of around 1 % of the mean horizontal and vertical variance. Accounting for the effects of measurement noise and finite spatial correlation of the wind fluctuations (as would be relevant in the case of using a radar sampling multiple, separated volumes), Thorsen et al. (2000) came to a similar conclusion. Also, in their modelling assessment of the meteor technique, Vincent et al. (2010) argued that integration times of over 1 month are necessary for accurate momentum flux estimation, in approximate agreement with the findings of Kudeki and Franke (1998) and Thorsen et al. (2000) for the dual-beam technique.

A contrary argument was put forward by Fritts et al. (2012a). They independently assessed the meteor technique, and argued that the large-amplitude monochromatic gravity waves often observed in the MLT/I region would result in stronger correlations between component velocity fluctuations (i.e. larger ratios of momentum flux to mean variance) than Kudeki and Franke (1998) assumed, and that the required integration time would be reduced from 16 days by around a factor of 20.

Additionally, Riggin et al. (2016) suggested that the use of longer integration times may reduce the measured correlation between vertical and horizontal mo-

**A. J. Spargo et al.: Mesospheric gravity wave momentum flux estimation**

735

tions, and hence lead to systematic underestimation of momentum fluxes.

3. The contamination of momentum flux estimates by temporal wind shear (leading to overestimation of the true fluxes). Some authors (e.g. Fritts et al., 2010b, 2012a, b) have opted to remove the temporal shear imposed by tides and planetary waves by fitting these components to the Cartesian winds, and then subtracting their radial projection from the radial velocities prior to momentum flux estimation. Andrioli et al. (2013a, b, 2015) also attempted to remove the same shears by fitting them, directly evaluating the contribution of the fitted components to the momentum fluxes, and then subtracting these from those estimated previously.

This paper presents the application of hybrid Doppler interferometry (HDI) (Holdsworth and Reid, 1998) and the Thorsen et al. (1997) estimator to momentum flux determination from the large-aperture Buckland Park MF radar. In HDI, Doppler beams are created and steered in hardware, and multiple-receiver interferometry is used on reception to form the actual receive beams. Therefore, the paper represents the first application of the Thorsen et al. (1997) estimator to an MF radar with beam steering applied on transmission, as well as on reception. The use of off-zenith transmission in HDI allows for greater beam directivity and hence SNR in the received off-zenith beams (for a given receiver array geometry). Additionally, the HDI analysis yields a radial velocity estimate at an effective beam position (EBP) corresponding to the peak of a fitted Gaussian brightness distribution. This means that the aspect sensitivity in the partially reflecting scattering surfaces is directly accounted for in the velocity estimation.

Section 2 describes the experiment configuration utilized on the Buckland Park MF in this study, and the array characteristics at the time (transmit/receive polar diagrams and data acceptance rate). Section 3 evaluates the ability of the radar to determine momentum fluxes by simulating the radar's sampling of a model GW-perturbed wind field with a pre-determined spatiotemporal distribution of EBPs based on real data. Section 4 presents momentum flux estimates from experiments conducted between July 1997 and June 1998 using the Buckland Park MF radar. Discussion and conclusions follow.

## 2 HDI implementation on the Buckland Park MF radar

The Buckland Park MF radar, located about 36 km NNW of Adelaide, South Australia, operates at a frequency of 1.98 MHz. It consists of 89 crossed half-wave dipole antennas, each aligned  $\sim 4^\circ$  west of north, arranged on a rectangular grid with a circular outline of diameter  $\sim 1$  km. The basic

antenna spacing is  $\frac{3\lambda}{5}$  ( $\sim 91.4$  m) (where  $\lambda$  is the radar wavelength). A detailed description of the hardware, configurable experiments and analyses can be found in Reid et al. (1995) and Holdsworth and Reid (2004).

The HDI experiments presented here were conducted across four multi-day campaigns during July, September, and October 1997 and June 1998 (see Fig. 4 for an indication of data availability during these periods). The radar utilized 20 channels for transmission and 16 channels for reception. For both transmit and receive modes, each channel was connected to three antennas on the array. The channels were phased to sequentially form transmit and receive beams in five directions: one vertical, and four at small off-zenith angles in the cardinal directions. As shown in Fig. 1 (the antenna configuration for June 1998), 60 antennas on the north-south-oriented array were used for transmission, and a total of 48 antennas on either orientation for reception. The antenna configuration was varied slightly during and between experiments, as necessitated by antenna outages.

Modelled far-field transmit and receive polar diagrams for the Fig. 1 configuration are shown in Fig. 2. In both cases, the signal phase has been progressed by about  $48^\circ$  per column of the array (increasing to the right), so as to steer the beam approximately  $13^\circ$  west of the zenith. As in the real experiment, the three antennas constituting each group have been driven with an equivalent phase, which has been evaluated for the centroid of each group. The main lobe of the transmit beam is approximately circular with a half-power half-width (HPHW) of about  $5.7^\circ$ . There appears to be some influence of side/grating lobes in the opposite sector of the sky, though given their power relative to the main lobe and their large zenith angles, it is not expected that they will result in ambiguous radial velocities. The receive polar diagram (which is used for beam synthesis in HDI) is slightly wider, with a half-width of around  $10^\circ$ . There are side/grating lobe influences in the opposite sector of the sky, though again these are not expected to be of major concern.

The sampled range gates encompassed the height range 50–102 km (daytime) and 74–102 km (overnight), in 2 km bins. The transmit pulse's half-power half-width (HPHW) was 2 km. The pulse repetition frequency was fixed at 100 Hz for daytime observations, and 20 Hz for night time, with 20 and 4 software coherent integrations applied, respectively. The time series recorded for each beam contained 560 points (i.e. a record length of 112 s), and the beam direction was changed every 2 min. The beam sequence was [vertical, north, east, south, west], with an off-zenith angle of  $12^\circ$  used for 1997 experiments, and  $13^\circ$  for 1998.

HDI was applied to analyse each 112 s raw data record. Briefly, this involved the synthesis of beams in software (using the post-statistics steering method; Kudrinskiy and Woodman, 1990) across an  $11 \times 11$  grid of positions centred on the nominal transmitted beam position, bounded by the  $e^{-1}$  width of the receive beam in the cardinal directions. The EBP was set to the position of the peak of a 2-D Gaussian fit-

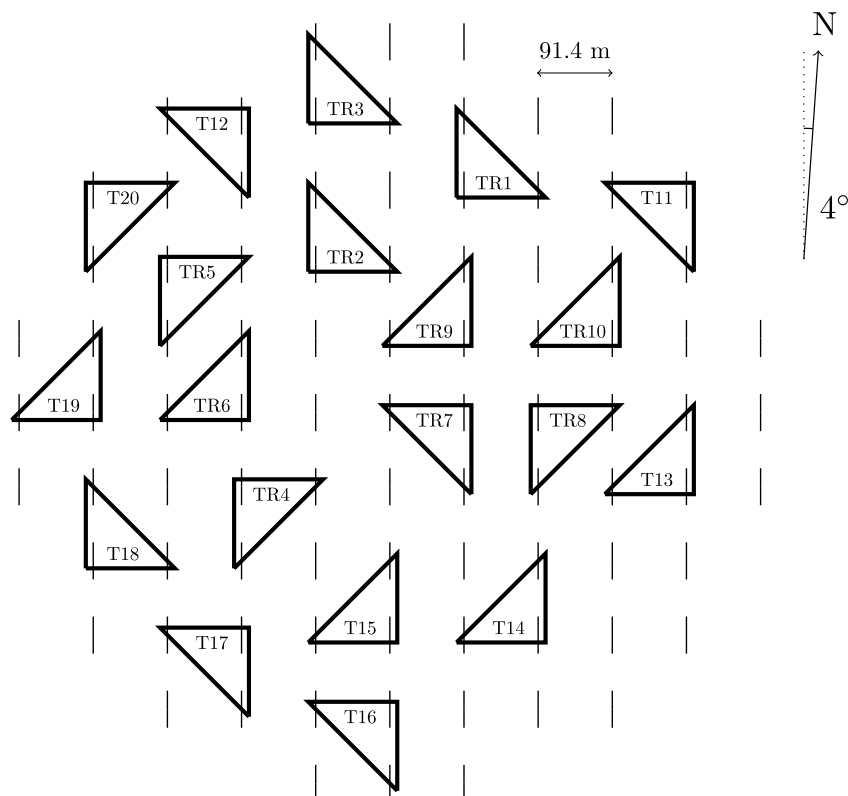


**Figure 1.** Antenna configuration used in the June 1998 HDI experiments. Each thin vertical line denotes an approximately north–south-oriented antenna. For ease of viewing, antenna elements have not been drawn to scale. Each bold triangle indicates a group of antennas that were connected to a given transmit or receive channel: “TR” denotes both transmit and receive, and “T” transmit only.

**Table 1.** Error codes for the HDI analysis.

Code	Error
1	Low dynamic range, or interference rejection
2	SNR < -6 dB
3	Off-zenith beams: projected horizontal velocity > 200 ms <sup>-1</sup>
4	Power maximum too close to edge of synthesized beam directions to estimate EBP
5	Azimuth angle of EBP not within 45° of transmitted beam azimuth
6	Zenith angle of EBP < 0°
7	Zenith angle of EBP > transmitted beam zenith
8	Insufficient good power estimates with synthesized beam angle to estimate EBP

ted to the distribution of signal power across this grid. The beam was then restered to the EBP, and power, SNR, radial velocity, and spectral width estimates were subsequently estimated using standard Doppler analysis (Woodman and Guillen, 1974).

An example of the EBPs determined with HDI is shown in Fig. 3. Substantial fluctuations in the EBP relative to the transmitted beam directions are clear, as is an effect of atmospheric aspect sensitivity in the lower range gates. Further discussion of these points is taken up in Sect. 5.

The scenarios under which the analysis failed on any given data record are summarized in Table 1. Acceptance rates (and hence data availability) based on these error codes for the four conducted experiments are shown in Fig. 4. It is clear that acceptance rates of greater than 75 % were obtained during the day across all range gates between 76 and about 90 km. At night more than 75 % of data were rejected below about 80 km; the accepted data in this region have still been included in the analysis presented here, and so it is acknowledged that the reported momentum flux estimates may



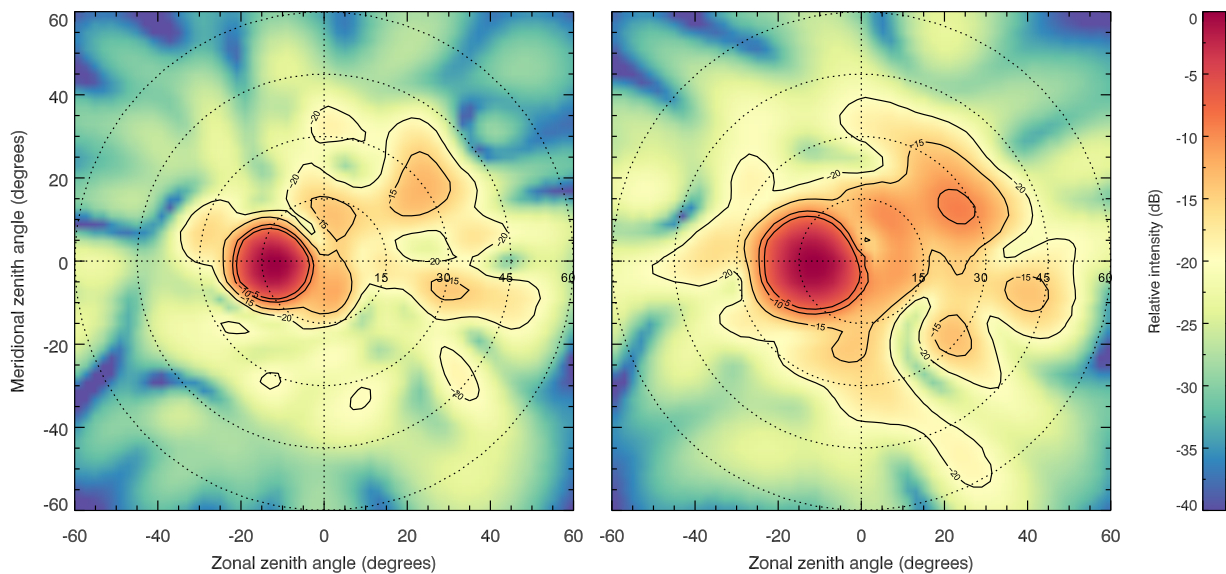


**Figure 2.** Modelled transmit (left) and receive (right) polar diagrams for the antenna configurations in Fig. 1, and used for the HDI experiments. Phasing has been applied to steer the beam away from the zenith; see text for details. The models were produced in EZNEC v. 5.0.63.

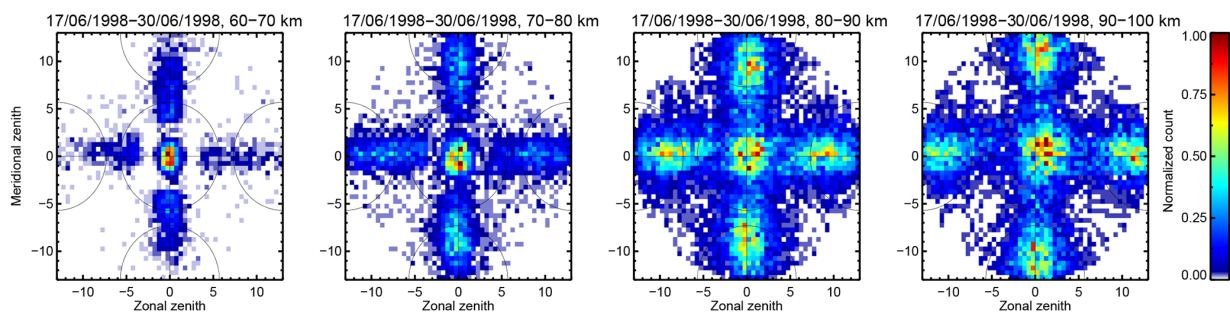


**Figure 3.** Normalized 2-D histograms of the EBPs estimated by HDI at selected range gates for the June 1998 experiment. The thin black circles approximately denote the half-power half-width contours of the transmitted beams ( $5.7^\circ$  in all cases shown).

be biased towards the daytime values (as an aside, note that this is a result of diurnal changes in ionospheric reflectivity (and hence received signal SNR), rather than an artefact of the HDI analysis). The October 1997 and June 1998 results are also still analysed as a single experiment, despite the clear radar outages.

### 3 Simulation of momentum flux estimation

A simple computer model has been created to obtain a qualitative assessment of the accuracy and precision of the momentum flux estimates from the five-beam Doppler, vertical beam HDI, and meteor radar techniques. The model propagates monochromatic gravity and tidal waves over the field of view of a “radar”, which samples radial wind velocities at positions and times corresponding to real records of the re-

spective radar techniques. The approach used has parallels to those used in the following previous works:

1. Fritts et al. (2010a), who evaluated the abilities of a new meteor radar on Tierra del Fuego ( $53.8^\circ$  S,  $67.8^\circ$  W) to measure gravity wave momentum fluxes. The wind fields simulated included mean winds, diurnal and semidiurnal tides, and propagating gravity waves with variable phase angles and time-varying amplitudes, and the scattering locations used were based on observed meteor distributions.
2. Fritts et al. (2012a), who employed the same tests as Fritts et al. (2010a) on a new meteor radar on King George Island ( $62.1^\circ$  S,  $58.7^\circ$  W), and three more conventional meteor radars.

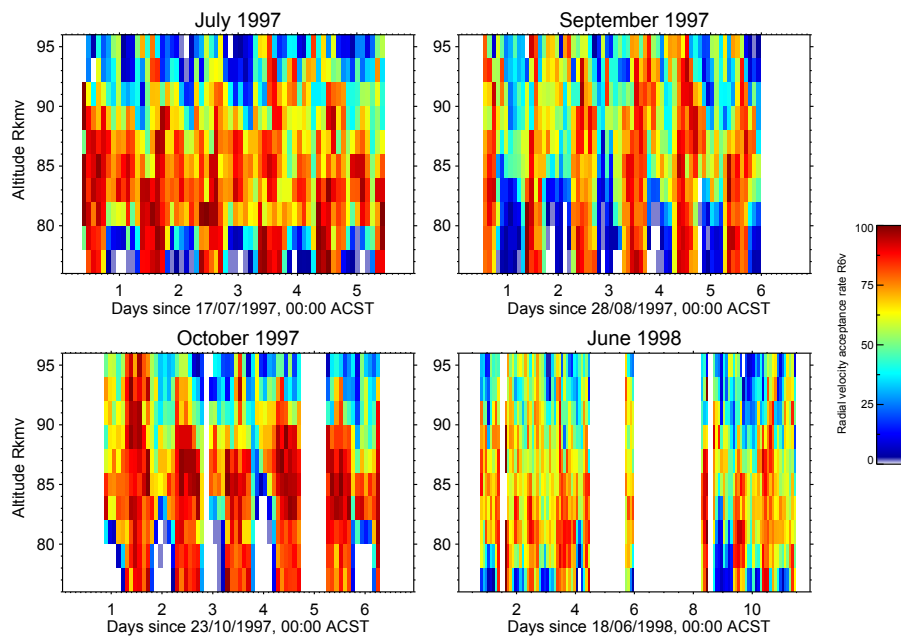


**Figure 4.** Acceptance rate profiles for the four HDI experiments.

3. Andrioli et al. (2013a), who employed tests similar to those in Fritts et al. (2010a) (tides with finite vertical wavelengths and 2-day Rossby waves were also included) on a meteor radar in Cachoeira Paulista (23° S, 14° W).
4. Nicolls et al. (2012), who applied an approach similar to that used in Fritts et al. (2010a) to narrow-beam fixed-look phased array radars.
5. Vincent et al. (2010), who used a Monte Carlo-based simulation of monochromatic gravity waves with random phases, propagation directions and amplitudes to assess the ability of a meteor radar to measure mean winds and momentum fluxes.
6. Murphy (1992), who used a time-varying wind field to simulate the effects of pointing angle variations on momentum flux extraction with an MF Doppler radar.

### 3.1 Simulation description

The model is based around the following workflow (where necessary, the individual steps are described in more detail in subsequent subsections):

1. Specify a wind field analytically.
2. Acquire an ensemble of scattering positions and times (and add Gaussian-distributed uncertainties to a copy of the positions).

3. Evaluate radial projections of the wind velocity at the “correct” positions/times (measurement noise is effectively added to the radial velocities due to uncertainty in the scattering position).
4. Evaluate the momentum flux components by inverting the fluctuating radial velocity components at the noise-influenced positions/times.
5. Evaluate the momentum flux components by computing the covariances of the wind field at a fixed position directly above the simulated radar.
6. Loop back to 1, and repeat for a different realization of the wind field/different uncertainties in the scattering positions.
7. Investigate the mean and standard deviation of the differences between the results of 4 and 5 (herein referred to in the text and in Figs. 6–9 as “biases”).

#### 3.1.1 Wind field specification

The wind field in the model is comprised of a fixed “mean flow” background velocity (with speed  $v_0$ , bearing  $\varphi_0$ , and no height variation or vertical component), and a superposition of linear waves (which can resemble gravity, Rossby, or tidal waves). It is parameterized in space and time as the velocity vector:

$$v = v_0 + \sum_{i=0}^{n-1} v'_i \sin(\kappa_i \cdot r - \omega_i t), \quad (1)$$

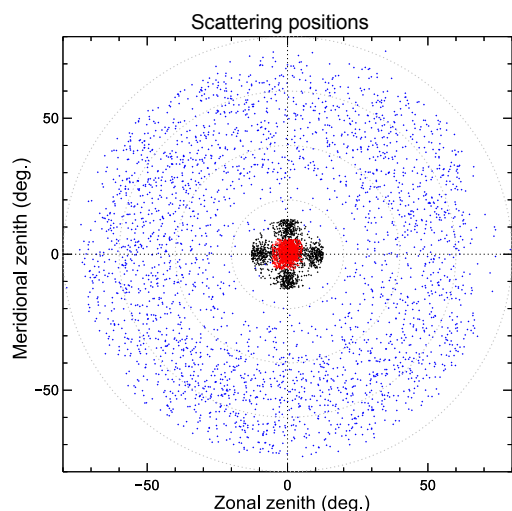


**Figure 5.** A 48 h sample of scattering position data used in the model (black: 5BD; red: VBD; blue: meteor.) See text for details.

where  $v_0 = [v_0 \sin \varphi_0, v_0 \cos \varphi_0, 0]$  is the fixed background velocity,  $n$  is the number of included waves,  $v'_i = [U_i, V_i, W_i]$ ,  $\kappa_i = [k_i, l_i, m_i]$  and  $\omega_i$  are the vectors of component wave amplitudes, wave vectors, and angular frequencies respectively for the  $i$ th wave,  $r = [x, y, z]$  is the Cartesian position vector, and  $t$  is the time since some arbitrary zero.

Prior to a simulation, the background wind vector, the number of waves to include, and the horizontal perturbation amplitude  $v_h$ , propagation direction  $\varphi$ , ground-based phase speed  $c_p$ , and ground-based period  $T$  for each wave are specified. The remaining parameters in (Eq. 1) are computed using known dispersion and polarization relations (see, e.g., Fritts and Alexander, 2003). The radial component of the wind field is then evaluated at a set of EBPs and times corresponding to those recorded in real samples of Buckland Park MF Doppler/VHF meteor radar measurements (see Fig. 5). For simplicity, the wave parameters are evaluated at a fixed height. A “flat-Earth” coordinate system is also assumed, so that  $r_j = [z \tan \theta_j \sin \phi_j, z \tan \theta_j \cos \phi_j, z]$ , where  $j$  represents the position index, and  $\theta$  and  $\phi$  correspond to the zenith and azimuth angles of the scattering locations, respectively.

### 3.1.2 Spatiotemporal sampling configurations

The basis of all the scattering positions used in the model is shown in Fig. 5. The scattering positions for the five-beam Doppler (herein 5BD) technique were obtained from the June 1998 experiment discussed in Sect. 2, from the range gate centred on 88 km. The temporal order of the points was preserved, in hope to best account for the effects on the beam position of structures in electron density propagating over the radar’s field of view.

Only data with zero error code (see Table 1) were selected, and so some of the points in the resulting time series were missing. To avoid further complicating the results of this simulation with the effects of missing data, an attempt has been made to fill in these gaps and hence make the off-vertical beam dataset “continuous” (i.e. to have the four beams present in each 10 min steering cycle). To do this, the nominal azimuth for each of the off-vertical beams was firstly subtracted from the azimuth of the EBP recorded for each beam. These “wrapped positions” were then assigned to the four off-vertical beams in temporal order, and were “unwrapped” by re-adding the nominal azimuth of the beam the position had been assigned to. The vertical beam positions were simply assigned to subsequent 2 min records in temporal order, again removing the effect of temporal gaps.

A configuration utilizing solely vertical beam data from the 5BD experiment (herein V5BD) was also considered in the model. This resembles an analysis that could be applied on systems with no (practical or otherwise) capability for beam steering on transmission. Vertical transmission in that experimental case was only applied for 2 min per 10 min steering cycle, and so a 10 min analysis interval has been used to represent it here.

A slight variation on the V5BD was also included, which was based on data from experiments consisting of a solely vertical transmitted beam (herein VBD). The HDI-derived EBPs in this case were obtained from experiments run between 20 June 1997 and 15 July 1997, again from the range gate centred on 88 km and from a beam with a half-power half-width of  $5.7^\circ$ . It should be noted that this technique only differs from the V5BD in that it uses a sampling interval of 2 (rather than 10) min, and also obviously employs a different sample of EBPs from a vertical beam.

A fourth simulated technique based on MF radar Doppler returns was intended to emulate that used in older (and the only yet reported in the literature) MF Doppler experiments for momentum flux estimation, which did not incorporate direct estimates of the EBP (instead they were calculated based on aspect sensitivity estimates; see Sect. 1). In the model, this technique uses radial velocities evaluated at the same positions and times as those in the 5BD technique, but the velocities are assumed to be from scatterers located at fixed zenith angles in the appropriate Cardinal directions. The fixed zenith angle used here was  $9^\circ$  (recall that the transmitted beam was steered to a zenith of  $12^\circ$ ). Herein, this technique is referred to as “conventional five-beam Doppler” (C5BD).

Finally, a technique based on 55 MHz all-sky meteor radar data was included. For this case, data from the Buckland Park meteor radar recorded during May 2014 at heights between 88 and 90 km were used. The radar obtained a peak count rate of around  $60 \text{ h}^{-1}$  over this height interval and period.

**Table 2.** A summary of the gravity wave parameters used in the different test wind field cases. (The subscript  $i$  on a given parameter denotes the value of the parameter for the  $i$ th wave in a specific case.  $R_1$  refers to a random number derived from a uniform probability distribution with bounds  $[1, 2]$ . The remaining quantities are defined in Sect. 3.1.1.)

Case	$v_0$ (ms <sup>-1</sup> )	$\varphi_0$ (°)	$n_{\text{waves}}$	$v_h$ (ms <sup>-1</sup> )	$\varphi$ (°)	$c_p$ (ms <sup>-1</sup> )
1	30	45	1	20	55	50
2	0	–	37	$[3_1, \dots, 3_{37}]$	$[0_1, 5_2, \dots, 180_{37}]$	$R_1 \times [50_1, \dots, 50_{37}]$

**Table 3.** Summary of different Doppler techniques referred to in this paper. See Sect. 3.1.2 for more details on each technique.

Name	Abbrev.	Description
Five-beam Doppler	5BD	Four beams in cardinal directions + a vertical beam
Vertical five-beam Doppler	V5BD	Vertical subset of beams from 5BD
Vertical beam Doppler	VBD	Vertical beams at 5BD's sampling interval
Conventional five-beam Doppler	C5BD	Off-zenith beams from 5BD, but without EBP information (inferred from aspect sensitivity)

### 3.1.3 EBP error

Errors of the form

$$[\epsilon_{xj}, \epsilon_{yj}] = \sigma \theta_j [\epsilon_1 \sin \phi_j, \epsilon_2 \cos \phi_j] \quad (2)$$

– where  $\epsilon_{xj}$  and  $\epsilon_{yj}$  are the errors along the  $x$ - and  $y$ -direction cosines respectively,  $\epsilon_1$  and  $\epsilon_2$  are two numbers drawn from a Gaussian distribution with unit variance, and  $\sigma$  is the desired standard deviation of the distribution – were added to the direction cosines of each scattering position (where  $\theta_j$  and  $\phi_j$  are the zenith and azimuth angles of the scattering positions, respectively). A  $\sigma$  value of  $1^\circ$  was used to represent the meteor technique, and  $1.5^\circ$  for techniques based on the Buckland Park MF radar (justification of these values is provided in Spargo (2016), p. 62–63 – though it is highly likely that the latter is an overestimate of the true value). The wind field was evaluated at the points without the error, and in the inversions described in the next subsection, they were interpreted to be at locations corresponding to the positions with the added error.

### 3.1.4 Estimation of the Reynolds stress components

The spatial distribution of radial velocities at this point will contain contributions from the gravity and tidal waves specified in Eq. (1). Contributions from the latter are not desired in the Reynolds stress component estimates here. To remove them, a method similar to that devised in Andrioli et al. (2013a) is applied; it firstly involves estimating the “background mean” wind field by partitioning the radial velocity (and corresponding EBP) data into non-oversampled windows of width one hour. Wind velocities are estimated using a standard least-squares formulation (e.g. Vandeppeer and Reid, 1995). The tidal wave contributions are removed from each radial velocity by subtracting from them a time-dependent radial projection of a least-squares fit  $y$  to wind

time series, of the form

$$y = \sum_{i=0}^{n-1} \cos \frac{2\pi}{T_i} (t - \Phi_i), \quad (3)$$

where  $T$  is an  $n$ -element array of periods (in this work,  $[1/3, 1/2, 1, 2]$  days) and  $\Phi$  is an  $n$ -element array of phases (in this case giving the time at which the  $i$ th component maximizes). It should be acknowledged that Fritts et al. (2010a, b, 2012a, b) used an “ $S$ -transform” Gaussian wavelet fit to estimate diurnal and semidiurnal tidal components from meteor radar time series. While this approach does allow for amplitude and phase modulation of the tidal components in the time series, the Andrioli et al. (2013a) approach is applied here on the basis of the ease of its implementation.

For the 5BD, V5BD, VBD, and meteor techniques, the wind field variance and covariance components are then calculated from the residuals by the inversion technique described in Thorsen et al. (1997) (their Eq. 15). Note that the selection of the length of data over which this inversion is to be applied is clearly a compromise of increasing time resolution (shorter windows) and correctly sampling longer-period and/or larger-scale fluctuations (favouring longer windows). The effect of the data length on the bias in the returned momentum flux component estimates is discussed in the next sections.

To emulate the C5BD technique, momentum flux components are calculated using the Vincent and Reid (1983) estimator.

### 3.2 Test cases

Two different wind field “configurations” have been used in the model; they are summarized in Table 2. The first case considers a single gravity wave of horizontal amplitude  $20 \text{ ms}^{-1}$  propagating to the north-east. In this case, the horizontal and vertical perturbation components are out of phase

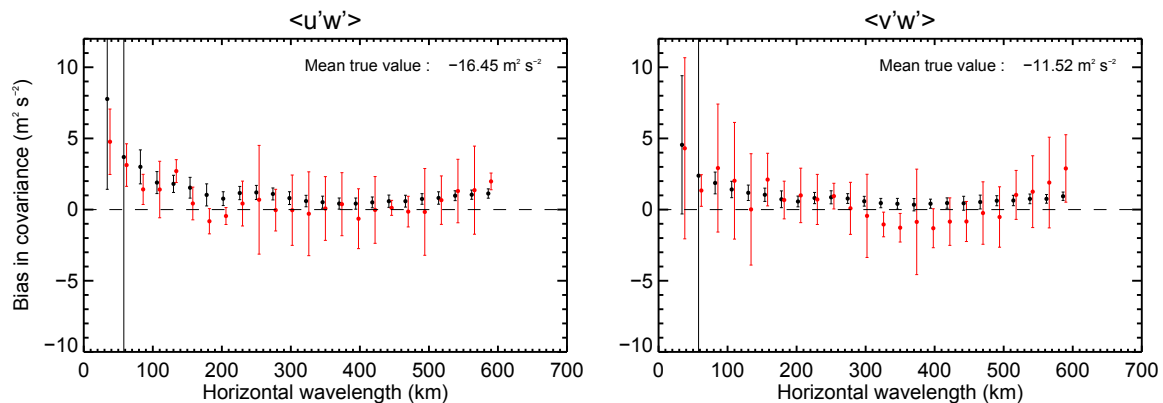


**Figure 6.** A comparison of the biases in the model covariance terms extracted from the 5BD (black) and VHF meteor radar (red) techniques, averaged over a 48 h period, with individual bin widths (or integration times) of length 2 h, for the single wave case. The error bars show the standard deviation in the bias determined over 200 realizations of the initial gravity wave phase/scattering position errors.

(as  $m \propto -\sqrt{k^2 + l^2}$ , and  $k, l > 0$ ) – i.e.  $\langle u'w' \rangle, \langle v'w' \rangle < 0$ . The second case considers an ensemble of 37 smaller-amplitude waves propagating in uniformly distributed directions in the eastern sector; here only  $\langle u'^2 \rangle, \langle v'^2 \rangle, \langle w'^2 \rangle$ , and  $\langle u'w' \rangle$  will take on non-zero values, with  $\frac{\langle u'^2 \rangle}{\langle w'^2 \rangle} \approx 1$  and  $\frac{\langle u'^2 \rangle}{\langle w'^2 \rangle} \approx 15$ . The waves will have a net propagation direction due east, so  $\langle u'w' \rangle < 0$ . The two configurations are intended to emulate the limiting cases observed in real mesospheric wind fields: the first obviously a case in which a single well-defined monochromatic wave dominates the spectrum, and the second in which a spectrum of equal-amplitude waves from an isotropic source propagate with component directions opposite to that of the background wind.

With exception to the final case discussed (Fig. 9), the simulations were performed over a sequence of gravity wave periods so as to test the sensitivity of the techniques to waves of differing scales. A total of 200 realizations were performed at each period in order to obtain a distribution of the measured momentum flux component biases. At the start of each realization, the initial phases of all waves considered were assigned a random value in the interval  $[0, 2\pi)$ . In the case of the second configuration, the periods of each of the 37 waves in a given realization were varied by obtaining periods from the equation  $T_i = R_2 \times T_i$ , with  $R_2$  being selected from a uniform distribution with bounds  $(\frac{3}{4}, \frac{5}{4})$ . This was essentially done to reduce the correlation distance of the wave field. The phase speeds of the waves in the second configuration were determined as indicated in Table 2.

In each realization, diurnal and semidiurnal tides with fixed amplitudes of 15 and 20  $\text{ms}^{-1}$  respectively were also superposed onto the wind field. Their horizontal wavelengths and phase speeds were adjusted to resemble those of real atmospheric tides (i.e. with horizontal wavelengths equal to the ratio of the Earth's circumference and the tidal mode num-

ber, and phase speeds such that a full cycle of a given tidal component would be completed in the ratio of 24 h and the tidal mode number). The spatial variability of the tides was included so that the tide-induced bias of the momentum flux estimates (particularly those derived from the meteor technique) could be inferred (it is assumed that the subtraction of the fit in Eq. 3) will remove most of the temporal variability).

### 3.2.1 Single gravity wave

The biases for the 5BD and meteor technique momentum fluxes for a wind field with a single gravity wave (Case 1), plotted against the horizontal wavelength of the wave (for a fixed phase speed of 50  $\text{ms}^{-1}$ ), are shown in Fig. 6. Each panel shows a mean value of the “true” components across all the periods examined. Each result is the average of all 2 h blocks in a 48 h time series, over 200 wave field realizations and scattering position errors. The error bars shown depict the standard deviation in the bias of the estimates across all samples (herein, the “accuracy” of the results will be taken to refer to the size of the mean bias, and the “precision” to the size of the standard deviation of the bias).

On the whole, it is clear for such a wave field that both techniques will statistically measure the sign of momentum flux components correctly, and to a similar level of accuracy. The 5BD generally obtains better precision, although it has a tendency to underestimate these components, especially at low and high horizontal wavelengths. This occurs as a result of a failure of the technique to sample full wave cycles. It indicates the requirement for continuous sampling windows (or “integration times”) much longer than the maximum gravity wave period under investigation, if unbiased estimates of the covariances at those periods are sought. The obvious downside to this approach is the required assumption for stationarity of the wave field for the duration of the sampling window (this is more likely to be satisfied for a shorter window).



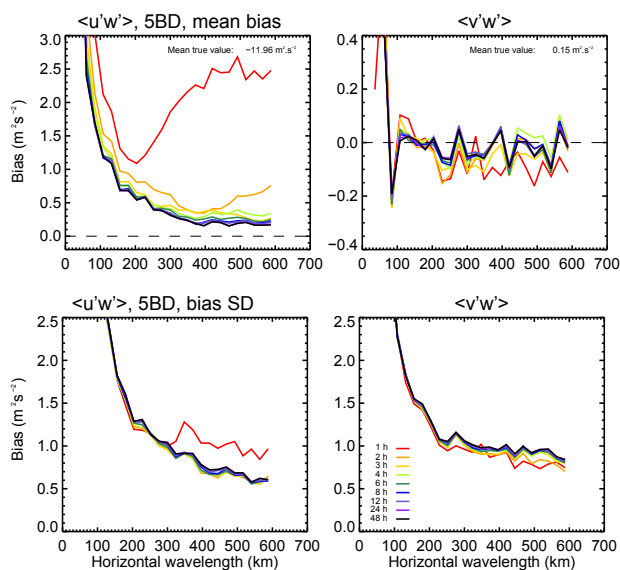


**Figure 7.** A comparison of the biases in the model momentum flux terms extracted from the 5BD technique for different integration times (1, 2, 3, 4, 6, 8, 12, 24, and 48 h, with colours as shown in the key), for a spectrum of waves propagating in the eastern sector (Case 2). Average biases are shown in the upper panels, and the standard deviations of the biases in the lower panels.

The 5BD technique also appears to obtain very low accuracy and precision when the horizontal wavelength considered is such that wave period does not sufficiently exceed the time taken (10 min) for a full five-beam cycle (note that  $T = \lambda/c_p$  (where  $\lambda$  is the horizontal wavelength) and so the wave period matches the experiment sampling time for horizontal wavelengths of around 30 km). The fact that the true flux is substantially underestimated at horizontal wavelengths shorter than this indicates an aliased sampling of the wave field at these wavelengths.

### 3.2.2 Effects of different integration times

Figures 7 and 8 explore the effect of varying the integration time, for Case 2 (which corresponds to an ensemble of waves propagating in the eastern sector). In both of these figures, the upper panels show the mean biases in  $\langle u'w' \rangle$  and  $\langle v'w' \rangle$  as a function of average horizontal wavelength of the waves in the ensemble (200 realizations of horizontal wavelength and initial wave phases per average horizontal wavelength), and the lower panels show the standard deviation of the bias in the samples used to compute those means.

Results for the 5BD technique are shown in Fig. 7. It is clear that an underestimation of the true value of the non-zero  $\langle u'w' \rangle$  occurs at large horizontal wavelengths for shorter integration times. Increasing the integration time generally reduces the bias, though the level of improvement diminishes rapidly once windows much longer than the maximum grav-

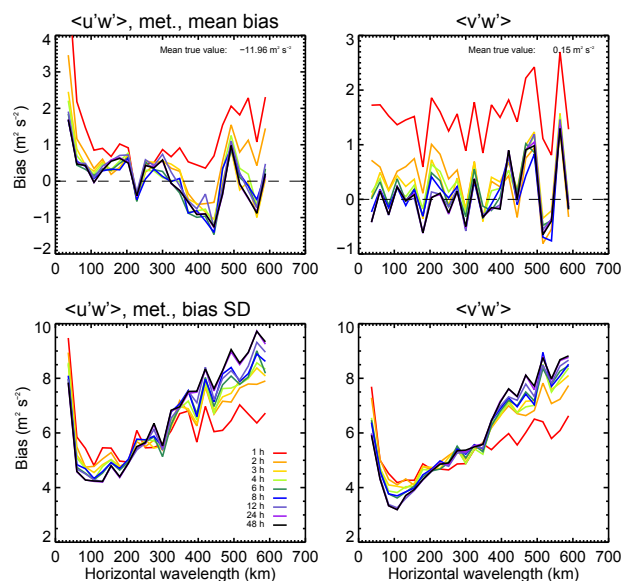


**Figure 8.** As per Fig. 7, but for the all-sky meteor technique.

ity wave period considered are used (note that the average phase speed used in this case is  $50 \text{ ms}^{-1}$ , and so the maximum average wave period shown in Fig. 7 is about 200 min). It is also clear that there is little effect of integration time on the precision of the results for the 5BD technique.

In contrast, results for the meteor technique in Fig. 8 have accuracies exhibiting less dependence on integration time (with biases only readily apparent for the 1 h window), but whose standard deviations are highly dependent on the integration time. In fact, the best precision is obtained for the shortest window used. It is also worth noting that the meteor technique's precision is worse than the 5BD's, and also worsens with average horizontal wavelength of the waves (whereas the 5BD's improves). At present, we do not have an explanation for either of these features.

Clearly, the selected integration time in the analysis is a compromise between the desired accuracy and precision of the techniques. On the basis of our desire to obtain the most accurate possible results for the 5BD and other similar techniques, 48 h windows are adopted for the analysis presented herein.

### 3.2.3 Spectrum of gravity waves

Figure 9 compares the momentum flux estimate biases of the meteor technique and the four Doppler techniques discussed in Sect. 3.1.2. In contrast to the previous section, a “wide” spectrum of gravity waves is used in this case, with the periods of the waves selected from a uniform distribution with bounds (6180) min (and with the propagation direction of the waves spanning the entire eastern sector as in Case 2). The results from a total of 10 000 realizations (each with differ-

ent scattering position errors, wave periods, and initial wave phases) are shown. The first two entries in the upper-right corner of each panel indicate the mean and standard deviation of the corresponding distribution. A third statistic, given by  $1.4826 \times \text{MAD}$ , where MAD is the median absolute deviation of the distribution, is also given; it corresponds approximately to the standard deviation of the distribution subject to the outlier robustness of the MAD, and if the distribution itself were Gaussian (Rousseeuw and Croux, 1993). This has been shown along with the “true” standard deviation, since a few large outliers were present in some of the bias samples – especially those of the Doppler techniques. Standard deviations greatly exceed MAD values for these cases.

The results imply that it is possible to measure momentum flux terms of the correct sign with the V5BD and VBD techniques (for a wave field with a realistic non-zero momentum flux), albeit with less accuracy than both the 5BD and meteor techniques and less precision than the 5BD technique. Like the 5BD technique, both of these techniques have also shown a tendency to underestimate the non-zero  $\langle u'w' \rangle$  term in the model.

The C5BD results show poorer precision than the VBD (but greater than the V5BD) and are also substantially biased. The technique overestimates the non-zero  $\langle u'w' \rangle$  term and also clearly estimates a non-zero  $\langle v'w' \rangle$  term, for which the corresponding true value in the model is very close to zero.

These modelling results have shown, at least qualitatively, the pleasing result that the momentum flux estimation and tide removal procedures employed work to a satisfactory level on all variations of the Doppler technique tested. We particularly stress the finding that EBPs from the V5BD experiment exhibit a spatial variability sufficient to estimate these terms reliably. We also note again that this result incorporates a modelled EBP uncertainty that is likely much larger than that in reality but that is ultimately extremely difficult to quantify (Klövekorn, 1992).

## 4 HDI experiment campaigns

### 4.1 Analysis procedure

The analysis performed here on HDI radial velocities follows the methodology applied to Doppler data in the previous section, making use of the 5BD, V5BD and C5BD techniques to estimate momentum fluxes.

The C5BD technique required that pattern scale data (derived from the full correlation analysis (FCA) Briggs, 1985) exist in the routine analysis run concurrently with the Doppler experiments. Each of the analyses also required the pre-determination of tidal components in the measured velocities, which were projected onto the radial velocities (if they were Cartesian components, as in the first and third techniques) and subtracted from them prior to evaluating any stress terms. An outline of the procedure used to determine

the mean winds and momentum flux components is given below.

1. Partition the 2 min resolution data from a given campaign, as well as the concurrent FCA, into non-oversampled 2 h blocks (steps 2 to 7 pertain to each separate 2 h block).
2. Using the pattern scale and axial ratio information derived from the FCA, calculate circularly averaged values of the aspect sensitivity parameter,  $\theta_s$  (see, e.g., Lesicar and Hocking, 1992).
3. Calculate the altitude of each Doppler measurement (from the recorded line-of-sight ranges) using two different techniques:
  - a. Simply assume that the zenith angle of the return is equal to the HDI-derived EBP ( $\theta_e$ ).
  - b.
    - i. Interpolate a  $\theta_s$  value from the averaged SA-FCA data at an altitude corresponding to the range of the Doppler measurement (assuming  $\theta_a = \theta_e$ , where  $\theta_a$  is the transmitted beam direction). The interpolant should be determined from a block of data centred on the time of interest, with a block width of the order of a few days. In this study, a block length of 14 days has been used, given the high variance observed in  $\theta_s$  on short timescales.
    - ii. Use the interpolant to calculate an FCA-derived  $\theta_e$ .
    - iii. Use the acquired  $\theta_e$  to calculate the “true” altitude of the Doppler measurement from its original range.
4. Using the two sets of altitudes calculated in Step 3, partition each block into 2 km width bins, with the lowest bin starting at 70 km and the highest at 96 km. For brevity, call the set of bins pertaining to those measurements with altitudes derived from the HDI-based  $\theta_e$  “A”, and those from the second method “B”.
5. By applying the inversion of Vandeppeer and Reid (1995) on A, estimate the mean horizontal and vertical winds. Scale the system of equations with the radial velocity variances evaluated using the equation (Doviak and Zrnić, 1993):

$$\text{var}(V_r) = \frac{\lambda^2}{4n\delta^2} \left[ \frac{\sigma_{vn}}{4\sqrt{\pi}} + 2\sigma_{vn}^2 \frac{N}{S} + \frac{1}{12} \left( \frac{N}{S} \right)^2 \right], \quad (4)$$

where  $\delta$  is the time gap between subsequent samples,  $n$  is the number of pulses per coherent integration,  $\sigma_v$  is the spectral (or velocity distribution) width,  $\frac{N}{S}$  is the inverse of the calculated SNR, and  $\sigma_{vn} = \frac{2\sigma_v\delta}{\lambda}$ . If fewer

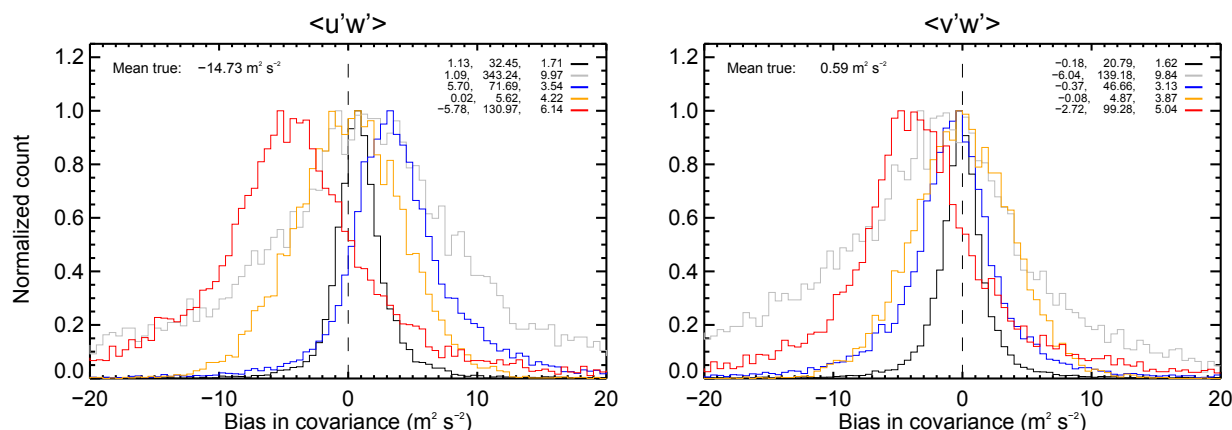


**Figure 9.** Normalized histograms showing the biases in the wind field covariance components, evaluated using the 5BD (black), V5BD (grey), VBD (blue), meteor (orange), and C5BD (red) techniques. The biases' mean, standard deviation, and standard deviation evaluated from the samples' median absolute deviation (see text for details) are also indicated in sequential order in three-element arrays for each technique in the upper-right corner of the plots.

than 10 measurements exist across all available beams, consider the wind estimate for this block as “missing”. If calculating winds based on a single beam (e.g. the vertical beam), only compute this if at least three measurements exist. Refer to these velocity estimates as  $\langle v_A \rangle$ .

- Evaluate mean radial velocities for each nominal beam direction in  $B$ . Remove points more than 3 standard deviations from the means, and recalculate the means. Refer to them as  $\langle V_{radBi} \rangle$  (for the  $i$ th beam direction). If there are fewer than two points in a given beam, consider this measurement as “missing” and do not perform any further analysis on it.
- Estimate mean horizontal and vertical winds from  $B$ , using data from pairs of off-zenith beams of opposite azimuths. Adjust  $\theta_a$  only for the local value of  $\theta_s$  (i.e. do not apply any correction to the apparent azimuthal angle). Refer to the wind estimates as  $\langle v_B \rangle$ .
- Re-partition the 2 min resolution Doppler and FCA data into 48 h blocks, with the centre of each block displaced by 6 h from the adjacent one (the remaining steps pertain to each separate 48 h block).
- Perform a least-squares fit for (Cartesian) tidal/planetary wave components in  $\bar{v}_A$ . The fit should be performed over a window encompassing data in the vicinity of the block currently being analysed. In this study, a window width of 4 days (centred on the current block) was used.
- Subtract a radial projection of the fitted components from the individual radial velocity records in  $A$ .

- Estimate the variance and covariance components from the residuals using the Thorsen et al. (1997) inversion. Again, scale the system of equations with the radial velocity variances.
- Repeat steps 9 and 10 for the mean radial velocity time series  $\langle V_{radBi} \rangle$ .
- Simultaneously solve for  $\langle u'w' \rangle$  and  $\langle v'w' \rangle$  using the Vincent and Reid (1983) estimator.

#### 4.2 Momentum fluxes

Unweighted average profiles of the momentum flux components for the four campaigns and the three Doppler techniques are shown in Figs. 10 and 11. The results shown have been evaluated at 2 km resolution, from 76 to 94 km. The uncertainties shown correspond to the standard error in the mean at each height evaluated over each campaign.

In general, the 5BD and C5BD results show the best level of agreement, with especially good agreement at heights where acceptance rates are high. A noteworthy result is the very similar vertical structure from the three techniques' measurements of  $\langle u'w' \rangle$  during the June 1998 campaign around 80–90 km. While the V5BD results do show large departures from the those of the other two techniques, it is encouraging to see some level of qualitative agreement. We again stress the point that no transmission beam steering has been used to acquire the V5BD results.

As an aside, the better agreement between the 5BD and C5BD techniques (relative to those from the V5BD) also lends support to the simulation results presented in Fig. 9. However, there does not appear to be substantial qualitative evidence that the C5BD technique systematically overestimates the covariance components, as the results in Fig. 9 predict.



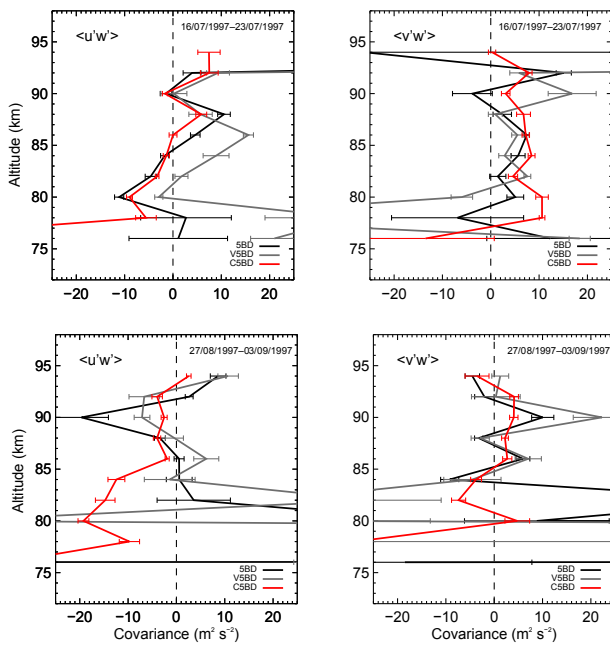


**Figure 10.** Vertical profiles of the momentum flux components obtained from the July 1997 (upper panels) and September 1997 (lower panels) campaigns. The error bars shown correspond to the standard error in the mean of the samples at each height.

### 4.3 Body forces and Coriolis torques

In an attempt to verify the validity of these experimental results, we (following the approaches of, e.g., Placke et al., 2015 and Reid and Vincent, 1987) have computed the body forces arising from the vertical divergence of the density-weighted wind field covariance, and have compared them to the Coriolis torque due to the perpendicular mean wind. These quantities should be equal when zonally averaged. Mathematically, the relation is expressed as

$$\langle F_x \rangle = -\frac{1}{\rho} \frac{\partial (\rho \langle u'w' \rangle)}{\partial z} = f \langle v \rangle, \quad (5)$$

where  $\rho$  is the atmospheric density and  $f$  is the Coriolis parameter. Preliminary calculations of these quantities for the four campaigns are shown in Figs. 12 and 13. The densities used were derived from the NRLMSISE-00 model for Buckland Park's location, evaluated at a time resolution of 1 day for an entire year and height resolution of 2 km (with a corresponding density extracted for each height and time spanned by the radar data). Following Reid and Vincent (1987), a function has been fitted to the density-weighted covariance profiles so as to reduce the effects of measurement noise on their derivatives. A quartic polynomial was used here, and was found to adequately replicate most of the major features in the profiles. It also led to smaller least-squares residuals than lower-order polynomials, and lacked the spurious “edge

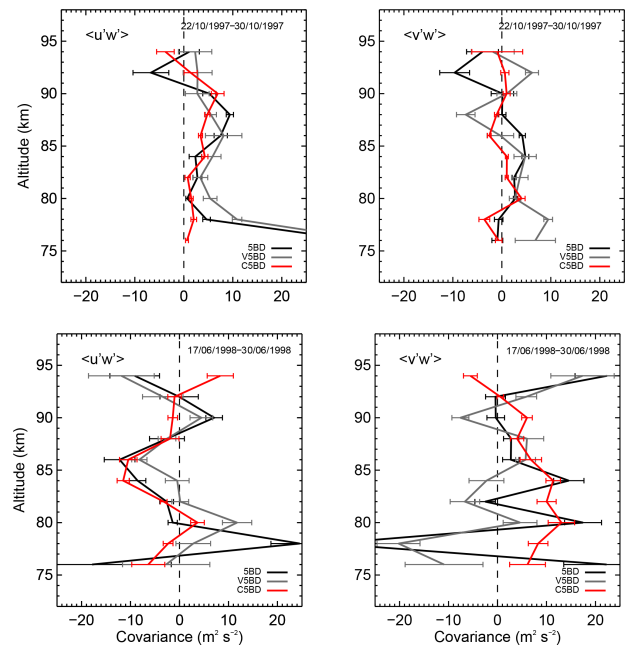


**Figure 11.** As per Fig. 10, for the October 1997 (upper panels) and June 1998 (lower panels) campaigns.

effects” associated with higher orders. The fit was weighted by the inverse square standard error of the individual covariance estimates.

The body force uncertainty  $\sigma_{bf}$  (expressed in the error bars on the profiles of Figs. 12 and 13) was evaluated via the equation

$$\sigma_{bf} = \sqrt{g^T R g}, \quad (6)$$

where  $R$  is the covariance matrix of the least-squares fit parameters (e.g. Tellinghuisen, 2001; Markwardt, 2009),  $g_i = \frac{\partial}{\partial \alpha_i} \left( \frac{dF}{dz} \right)$ , where  $F$  is the analytical form of the fitted function and  $\alpha_i$  are the fit parameters, and  $T$  is the transpose operator. It was assumed that the NRLMSISE-00-derived densities had zero uncertainty.

The vertical structures of the mean inferred body forces and Coriolis torques show few similarities, in both the zonal and meridional planes. Some of these discrepancies may be explained by noting that the relation between the two quantities is only valid for a zonal average. Additionally, the results presented here are centred on the winter months; during this time, planetary waves can propagate into the MLT/I, and may both contribute to the body force and change the “local” mean wind in such a way as to filter gravity waves from the wave spectrum (Andrews et al., 1987). Only the body force contributions from gravity waves have been considered here.

Nevertheless, the inferred body forces are generally large enough to balance the Coriolis torque due to the orthogonal wind. Their senses are also consistent with what is expected:

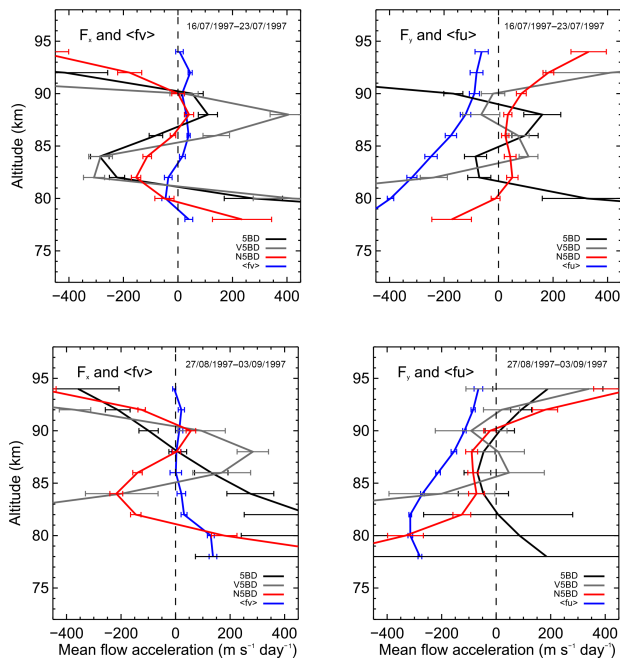


**Figure 12.** Vertical profiles of the zonal and meridional body forces (determined by three independent techniques) and corresponding accelerations due to Coriolis torques, obtained from the July 1997 (upper panels) and September 1997 (lower panels) campaigns.

for example, in the July 1997 and June 1998 cases, the body forces are predominantly westward in the heights of the highest acceptance rates. This is consistent with a deceleration of eastward MLT/I winds during winter.

Other studies of the same intercomparisons have had mixed conclusions, which is not surprising given that good local agreement between the quantities is not necessarily expected. Reid and Vincent (1987) compare Coriolis torques and inferred body forces using measurements derived from the Buckland Park MF radar, essentially encompassing all seasons and, as in this study, having measurements taken as part of dedicated campaigns lasting several days. They noted that the zonal body force was usually of the correct sense to balance the Coriolis torque due to the meridional wind, though the agreement varied from excellent (e.g. May 1982, their Fig. 12h) to poor (e.g. July 1982, their Fig. 12j). Hall et al. (1992) used 17 days of measurements from the Saskatoon MF radar (summer, 1989) to perform a similar comparison, and found good agreement between the zonal body force and meridional torque, but poor agreement in the orthogonal plane. Frame et al. (2000) also considered this intercomparison, using 1 month of data from the Buckland Park and Christchurch (New Zealand) MF radars (May 1992). They obtained good agreement between the gravity-wave-driven body forces and Coriolis torques in the zonal and meridional directions at Christchurch but inconsistent results at Buckland Park. In a more recent study employing DBS on the

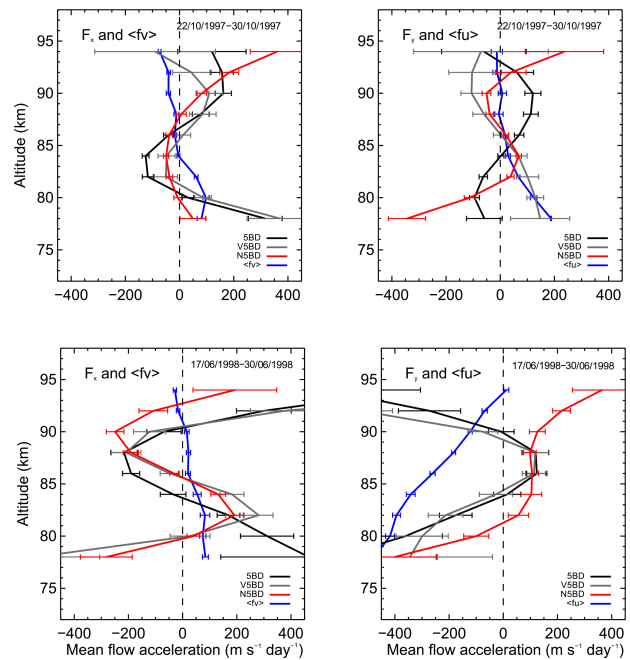


**Figure 13.** As per Fig. 12, for the October 1997 (upper panels) and June 1998 (lower panels) campaigns.

Saura MF radar, Placke et al. (2015) note good agreement between body forces and Coriolis torques during summer in the MLT/I, but not during winter (as done here, attributing the winter result to planetary wave contributions to the momentum flux).

## 5 Discussion and conclusions

This study has suggested, through the use of both synthesized and real observations, that vertical beam MF radars can measure momentum fluxes in the MLT/I to an acceptable degree of accuracy and precision. This implies that the EBP distribution brought about by refractive index irregularities propagating through a fixed vertical beam volume should contain a sufficient spread of radial velocity–pointing direction pairs to solve for the wind field covariances. In particular, we believe this sheds new light on the Thorsen et al. (1997) study, which attempted to make the same assessment through the use of the small-aperture interferometric Urbana MF radar (which transmitted a solely vertical beam). We speculate that the main reason this study has not been followed up is because of the lack of confidence in the community around making momentum flux estimations without steering narrow beams about the zenith, as done in the original studies beginning with Vincent and Reid (1983) (the C5BD in the present paper). We have compared these two approaches in this paper, and have largely found their results to be consistent. It is also clear that a substantial EBP spread occurs in the 5BD

**A. J. Spargo et al.: Mesospheric gravity wave momentum flux estimation**

747

results for the same reason as in the VBD; however, as the 5BD-C5BD intercomparison suggests, this is of little consequence, even if the received beam positions are not measured interferometrically.

We thus conclude that vertical beam interferometric MF radars are viable candidates to use for testing momentum flux estimates from interferometric meteor radars, over which there are well-known concerns regarding accuracy and precision, as discussed in Sect. 1. However, we stress that there is more work to be done concerning the prediction of the wave field conditions under which 5BD and V5BD-like techniques will show large discrepancies.

This study did consider basic testing of the meteor technique as well in a simulated setting, using a synthetic GW field consisting of a superposition of monochromatic waves, in much the same way as in previous studies such as Vincent et al. (2010), Fritts et al. (2012a), and Andrioli et al. (2013a). The drawback of the present and these older studies is the lack of realism of the simulated wave field (i.e. its finite spatial correlation, and transient features) and subsequent simulation of the response to this of the typically large EBP distributions of the meteor technique. Placke et al. (2011a) went a step further in this context by using a wind field output from a mechanistic model, but ultimately did not consider a realistic spatiotemporal distribution of meteors in sampling that wind field. In performing the simulations shown in Fig. 8 in the present study, we noticed that the bias standard deviation in the meteor technique's covariance estimates was highly sensitive to the spectral width of the wave field used (i.e. the frequency spanned by the superposed waves, for a given average horizontal wavelength). In the case of using a wave field in which all the superposed waves had equal wavelengths, the bias standard deviation in both the covariance estimates increased by a factor of around 2, relative to that shown in Fig. 8. Clearly, the technique's precision is highly dependent on the correlation length of the wind field (as the assumption in item 1 of Sect. 1 implies), and so a simulation which incorporates this to a realistic extent, along with the spatiotemporal sampling characteristics of a meteor radar, is needed to more fully understand this technique's limitations.

A potential problem with all Doppler beam-steering measurements of momentum fluxes in the presence of non-uniform volume scatter (and hence EBP distributions that may deviate away from an idealized complementary beam arrangement) concerns the extent to which accurate estimates of the vertical wind velocity perturbation can be obtained. A good contemporary review of the well-known biases inherent in volume-scatter-derived wind measurements in the presence of correlations between refractive index fluctuations and the underlying dynamics is provided by Fritts et al. (2012c). This study used a numerical algorithm to compute off-zenith backscatter from simulated Kelvin–Helmholtz instabilities in the mesospheric region (Franke et al., 2011), and revealed the biases in the obtained Doppler spectra as a function of the stage of turbulence development. Simulation-based ap-

proaches like this clearly underpin future investigations of the validity of the partial reflection Doppler techniques employed in the present paper.

*Code and data availability.* The IDL source code used to produce all analyses and plots in this paper is available from the authors upon request, as are the raw and HDI-analysed Buckland Park MF radar data.

*Competing interests.* The authors declare that they have no conflict of interest.

*Acknowledgements.* Funding for this research was provided by the Australian Research Council grants A69943065, DP0450787, DP0878144, and DP1096901 and by the Adelaide University ARC Small Grants Scheme. Andrew J. Spargo would like to thank Bob Vincent for numerous useful discussions regarding this work, and Chris Adami and Jonathan Woithe for technical support. The C source code used in this work for the NRLMSISE-00 model is maintained by Dominik Brodowski, and is available at <https://www.brodo.de/space/nrlmsise/>.

The topical editor, Christoph Jacobi, thanks Ramkumar Thokulwa and two anonymous referees for help in evaluating this paper.

**References**

- Andrews, D. G., Holton, J. R., and Leovy, C. B.: Middle atmosphere dynamics, 40, Academic press, 1987.
- Andrioli, V. F., Fritts, D. C., Batista, P. P., and Clemesha, B. R.: Improved analysis of all-sky meteor radar measurements of gravity wave variances and momentum fluxes, *Ann. Geophys.*, 31, 889–908, 2013a.
- Andrioli, V. F., Fritts, D. C., Batista, P. P., Clemesha, B. R., and Janches, D.: Diurnal variation in gravity wave activity at low and middle latitudes, *Ann. Geophys.*, 31, 2123–2135, <https://doi.org/10.5194/angeo-31-2123-2013>, 2013b.
- Andrioli, V. F., Batista, P. P., Clemesha, B. R., Schuch, N. J., and Buriti, R. A.: Multi-year observations of gravity wave momentum fluxes at low and middle latitudes inferred by all-sky meteor radar, *Ann. Geophys.*, 33, 1183–1193, <https://doi.org/10.5194/angeo-33-1183-2015>, 2015.
- Antonita, T. M., Ramkumar, G., Kumar, K. K., and Deepa, V.: Meteor wind radar observations of gravity wave momentum fluxes and their forcing toward the Mesospheric Semi-annual Oscillation, *J. Geophys. Res.-Atmos.*, 113, D10115, <https://doi.org/10.1029/2007JD009089>, 2008.
- Beldon, C. L. and Mitchell, N. J.: Gravity waves in the mesopause region observed by meteor radar, 2: Climatologies of gravity waves in the Antarctic and Arctic, *J. Atmos. Sol. Terr. Phys.*, 71, 875–884, 2009.
- Beldon, C. L. and Mitchell, N. J.: Gravity wave–tidal interactions in the mesosphere and lower thermosphere over Rothera, Antarctica (68° S, 68° W), *J. Geophys. Res. Atmos.*, 115, D18101, <https://doi.org/10.1029/2009JD013617>, 2010.

- Briggs, B. H.: The analysis of spaced sensor records by correlation techniques, in: Handbook for MAP, Extended abstracts, Presented at MAP Symposium, Kyoto, Japan, 26–30 November 1984, edited by: Kato, S., 18, 166 pp., 1985.
- Clemesha, B. R. and Batista, P. P.: Gravity waves and wind-shear in the MLT at 23° S, *Adv. Space Res.*, 41, 1472–1477, 2008.
- Clemesha, B. R., Batista, P. P., da Costa, R. A. B., and Schuch, N.: Seasonal variations in gravity wave activity at three locations in Brazil, *Ann. Geophys.*, 27, 1059–1065, 2009.
- de Wit, R. J., Hibbins, R. E., and Espy, P. J.: The seasonal cycle of gravity wave momentum flux and forcing in the high latitude northern hemisphere mesopause region, *J. Atmos. Sol. Terr. Phys.*, 127, 21–29, <https://doi.org/10.1016/j.jastp.2014.10.002>, 2014a.
- de Wit, R. J., Hibbins, R. E., Espy, P. J., Orsolini, Y. J., Limpasuvan, V., and Kinnison, D. E.: Observations of gravity wave forcing of the mesopause region during the January 2013 major Sudden Stratospheric Warming, *Geophys. Res. Lett.*, 41, 4745–4752, 2014b.
- de Wit, R. J., Janches, D., Fritts, D. C., and Hibbins, R. E.: QBO modulation of the mesopause gravity wave momentum flux over Tierra del Fuego, *Geophys. Res. Lett.*, 43, 4049–4055, <https://doi.org/10.1002/2016GL068599>, 2016.
- Doviak, R. J. and Zrnić, D. S.: *Doppler Radar and Weather Observations*, Academic Press, Inc., 1993.
- Ern, M., Preusse, P., Gille, J. C., Hepplewhite, C. L., Mlynczak, M. G., Russell, J. M., and Riese, M.: Implications for atmospheric dynamics derived from global observations of gravity wave momentum flux in stratosphere and mesosphere, *J. Geophys. Res.-Atmos.*, 116, D19107, <https://doi.org/10.1029/2011JD015821>, 2011.
- Frame, D. J., Lawrence, B. N., Fraser, G. J., Vincent, R. A., and Dudhia, A.: A new technique for evaluating mesospheric momentum balance utilizing radars and satellite data, *Ann. Geophys.*, 18, 478–484, <https://doi.org/10.1007/s00585-000-0478-z>, 2000.
- Franke, P. M., Mahmoud, S., Raizada, K., Wan, K., Fritts, D. C., Lund, T., and Werne, J.: Computation of clear-air radar backscatter from numerical simulations of turbulence: 1. Numerical methods and evaluation of biases, *J. Geophys. Res.-Atmos.*, 116, D21101, <https://doi.org/10.1029/2011JD015895>, 2011.
- Fritts, D. C. and Alexander, M. J.: Gravity wave dynamics and effects in the middle atmosphere, *Rev. Geophys.*, 41, 1003, <https://doi.org/10.1029/2001RG000106>, 2003.
- Fritts, D. C. and Vincent, R. A.: Mesospheric momentum flux studies at Adelaide, Australia: Observations and a gravity wave-tidal interaction model, *J. Atmos. Sci.*, 44, 605–619, 1987.
- Fritts, D. C. and Yuan, L.: Measurement of Momentum Fluxes near the Summer Mesopause at Poker Flat, Alaska, *J. Atmos. Sci.*, 46, 2569–2579, [https://doi.org/10.1175/1520-0469\(1989\)046<2569:MOMFNT>2.0.CO;2](https://doi.org/10.1175/1520-0469(1989)046<2569:MOMFNT>2.0.CO;2), 1989.
- Fritts, D. C., Tsuda, T., VanZandt, T. E., Smith, S. A., Sato, T., Fukao, S., and Kato, S.: Studies of Velocity Fluctuations in the Lower Atmosphere Using the MU Radar. Part II: Momentum Fluxes and Energy Densities, *J. Atmos. Sci.*, 47, 51–66, [https://doi.org/10.1175/1520-0469\(1990\)047<0051:SOVFIT>2.0.CO;2](https://doi.org/10.1175/1520-0469(1990)047<0051:SOVFIT>2.0.CO;2), 1990.
- Fritts, D. C., Yuan, L., Hitchman, M. H., Coy, L., Kudeki, E., and Woodman, R. F.: Dynamics of the equatorial mesosphere observed using the Jicamarca MST radar during June and August 1987, *J. Atmos. Sci.*, 49, 2353–2371, 1992.
- Fritts, D. C., Janches, D., and Hocking, W. K.: Southern Argentina Agile Meteor Radar: Initial assessment of gravity wave momentum fluxes, *J. Geophys. Res. Atmos.*, 115, D19123, <https://doi.org/10.1029/2010JD013891>, 2010a.
- Fritts, D. C., Janches, D., Iimura, H., Hocking, W. K., Mitchell, N. J., Stockwell, R. G., Fuller, B., Vandeppeer, B., Hormaechea, J., Brunini, C., and Levato, H.: Southern Argentina Agile Meteor Radar: System design and initial measurements of large-scale winds and tides, *J. Geophys. Res.-Atmos.*, 115, D18112, <https://doi.org/10.1029/2010JD013850>, 2010b.
- Fritts, D. C., Janches, D., Hocking, W. K., Mitchell, N. J., and Taylor, M. J.: Assessment of gravity wave momentum flux measurement capabilities by meteor radars having different transmitter power and antenna configurations, *J. Geophys. Res.-Atmos.*, 117, D10108, <https://doi.org/10.1029/2011JD017174>, 2012a.
- Fritts, D. C., Janches, D., Iimura, H., Hocking, W. K., Bageston, J. V., and Leme, N. M. P.: Drake Antarctic Agile Meteor Radar first results: Configuration and comparison of mean and tidal wind and gravity wave momentum flux measurements with Southern Argentina Agile Meteor Radar, *J. Geophys. Res.-Atmos.*, 117, D02105, <https://doi.org/10.1029/2011JD016651>, 2012b.
- Fritts, D. C., Wan, K., Franke, P. M., and Lund, T.: Computation of clear-air radar backscatter from numerical simulations of turbulence: 3. Off-zenith measurements and biases throughout the lifecycle of a Kelvin-Helmholtz instability, *J. Geophys. Res.-Atmos.*, 117, D17101, <https://doi.org/10.1029/2011JD017179>, 2012c.
- Fukao, S., Sato, T., May, P. T., Tsuda, T., Kato, S., Inaba, M., and Kimura, I.: A systematic error in MST/ST radar wind measurement induced by a finite range volume effect: 1. Observational results, *Radio Sci.*, 23, 59–73, 1988.
- Hall, G. E., Meek, C. E., and Manson, A. H.: MF radar interferometry measurements of fluxes and Coriolis accelerations over Saskatoon (52° N, 107° W), *Geophys. Res. Lett.*, 19, 2293–2296, 1992.
- Hitchman, M. H., Bywaters, K. W., Fritts, D. C., Coy, L., Kudeki, E., and Surucu, F.: Mean Winds and Momentum Fluxes over Jicamarca, Peru, during June and August 1987, *J. Atmos. Sci.*, 49, 2372–2383, [https://doi.org/10.1175/1520-0469\(1992\)049<2372:MWAMFO>2.0.CO;2](https://doi.org/10.1175/1520-0469(1992)049<2372:MWAMFO>2.0.CO;2), 1992.
- Hocking, W. K.: A new approach to momentum flux determinations using SKiYMET meteor radars, *Ann. Geophys.*, 23, 2433–2439, <https://doi.org/10.5194/angeo-23-2433-2005>, 2005.
- Holdsworth, D. A. and Reid, I. M.: Comparison of Spaced Antenna and Doppler Interferometer techniques using the Mt Gambier ST profiler, Proceedings of the Fourth International Symposium on Tropospheric Profiling: Needs and Technologies, Snowmass, Colorado, 20–25 September, 1998.
- Holdsworth, D. A. and Reid, I. M.: The Buckland Park MF radar: routine observation scheme and velocity comparisons, *Ann. Geophys.*, 22, 3815–3828, <https://doi.org/10.5194/angeo-22-3815-2004>, 2004.
- Kim, Y.-J., Eckermann, S. D., and Chun, H.-Y.: An overview of the past, present and future of gravity-wave drag parametrization for numerical climate and weather prediction models, *Atmos. Ocean*, 41, 65–98, 2003.

## A. J. Spargo et al.: Mesospheric gravity wave momentum flux estimation

749

- Klövekom, P.: Radar Array Interferometry and Vertical Velocities in the Upper Atmosphere, Honours thesis, University of Adelaide, Department of Physics and Mathematical Physics, 1992.
- Kudeki, E. and Franke, S. J.: Statistics of momentum flux estimation, *J. Atmos. Sol. Terr. Phys.*, 60, 1549–1553, 1998.
- Kudeki, E. and Woodman, R. F.: A poststatistics steering technique for MST radar applications, *Radio Sci.*, 25, 591–594, 1990.
- Lesicar, D. and Hocking, W. K.: Studies of seasonal behaviour of the shape of mesospheric scatterers using a 1.98 MHz radar, *J. Atmos. Terr. Phys.*, 54, 295–309, 1992.
- Liu, A. Z., Lu, X., and Franke, S. J.: Diurnal variation of gravity wave momentum flux and its forcing on the diurnal tide, *J. Geophys. Res. Atmos.*, 118, 1668–1678, 2013.
- Markwardt, C. B.: Non-linear Least-squares Fitting in IDL with MPFIT, in: *Astronomical Data Analysis Software and Systems XVIII*, edited by: Bohlender, D. A., Durand, D., and Dowler, P., Astronomical Society of the Pacific Conference Series, 411, p. 251, 2009.
- Matsumoto, M., Shinbori, A., Riggan, D. M., and Tsuda, T.: Measurement of momentum flux using two meteor radars in Indonesia, *Ann. Geophys.*, 34, 369–377, <https://doi.org/10.5194/angeo-34-369-2016>, 2016.
- Murayama, Y., Tsuda, T., and Fukao, S.: Seasonal variation of gravity wave activity in the lower atmosphere observed with the MU radar, *J. Geophys. Res.-Atmos.*, 99, 23057–23069, <https://doi.org/10.1029/94JD01717>, 1994.
- Murphy, D. J.: Measurements of Energy and Momentum in the Mesosphere, Ph.D. thesis, 1992.
- Murphy, D. J. and Vincent, R. A.: Estimates of momentum flux in the mesosphere and lower thermosphere over Adelaide, Australia, from March 1985 to February 1986, *J. Geophys. Res.-Atmos.*, 98, 18617–18638, 1993.
- Murphy, D. J. and Vincent, R. A.: Mesospheric momentum fluxes over Adelaide during the 2-day wave: Results and interpretation, *J. Geophys. Res.-Atmos.*, 103, 28627–28636, 1998.
- Muschinski, A., Lehmann, V., Justen, L., and Teschke, G.: Advanced radar wind profiling, *Meteorol. Z.*, 14, 609–625, <https://doi.org/10.1127/0941-2948/2005/0067>, 2005.
- Nakamura, T., Tsuda, T., Yamamoto, M., Fukao, S., and Kato, S.: Characteristics of gravity waves in the mesosphere observed with the middle and upper atmosphere radar, 1, Momentum flux, *J. Geophys. Res.*, 98, 8899–8899, 1993.
- Nicolls, M. J., Fritts, D. C., Janches, D., and Heinselman, C. J.: Momentum flux determination using the multi-beam Poker Flat Incoherent Scatter Radar, *Ann. Geophys.*, 30, 945–962, <https://doi.org/10.5194/angeo-30-945-2012>, 2012.
- Placke, M., Hoffmann, P., Becker, E., Jacobi, C., Singer, W., and Rapp, M.: Gravity wave momentum fluxes in the MLT – Part II: Meteor radar investigations at high and midlatitudes in comparison with modeling studies, *J. Atmos. Sol. Terr. Phys.*, 73, 911–920, 2011a.
- Placke, M., Stober, G., and Jacobi, C.: Gravity wave momentum fluxes in the MLT – Part I: seasonal variation at Collm (51.3° N, 13.0° E), *J. Atmos. Sol. Terr. Phys.*, 73, 904–910, 2011b.
- Placke, M., Hoffmann, P., Latteck, R., and Rapp, M.: Gravity wave momentum fluxes from MF and meteor radar measurements in the polar MLT region, *J. Geophys. Res. Sp. Phys.*, 120, 736–750, 2014.
- Placke, M., Hoffmann, P., and Rapp, M.: First experimental verification of summertime mesospheric momentum balance based on radar wind measurements at 69° N, *Ann. Geophys.*, 33, 1091–1096, <https://doi.org/10.5194/angeo-33-1091-2015>, 2015.
- Reid, I. M.: Some aspects of Doppler radar measurements of the mean and fluctuating components of the wind field in the upper middle atmosphere, *J. Atmos. Terr. Phys.*, 49, 467–484, 1987.
- Reid, I. M. and Vincent, R. A.: Measurements of mesospheric gravity wave momentum fluxes and mean flow accelerations at Adelaide, Australia, *J. Atmos. Terr. Phys.*, 49, 443–460, 1987.
- Reid, I. M., Rüster, R., Czechowsky, P., and Schmidt, G.: VHF radar measurements of momentum flux in the summer polar mesosphere over Andenes (69° N, 16° E), Norway, *Geophys. Res. Lett.*, 15, 1263–1266, 1988.
- Reid, I. M., Vandeppeer, B. G. W., Dillon, S. C., and Fuller, B. M.: The new Adelaide medium frequency Doppler radar, *Radio Sci.*, 30, 1177–1189, 1995.
- Riggan, D. M., Tsuda, T., and Shinbori, A.: Evaluation of momentum flux with radar, *J. Atmos. Sol. Terr. Phys.*, 142, 98–107, 2016.
- Rousseeuw, P. J. and Croux, C.: Alternatives to the median absolute deviation, *J. Am. Stat. Assoc.*, 88, 1273–1283, 1993.
- Sato, K.: Vertical Wind Disturbances in the Troposphere and Lower Stratosphere Observed by the MU Radar, *J. Atmos. Sci.*, 47, 2803–2817, [https://doi.org/10.1175/1520-0469\(1990\)047<2803:VWDITT>2.0.CO;2](https://doi.org/10.1175/1520-0469(1990)047<2803:VWDITT>2.0.CO;2), 1990.
- Sato, K.: Small-Scale Wind Disturbances Observed by the MU Radar during the Passage of Typhoon Kelly, *J. Atmos. Sci.*, 50, 518–537, [https://doi.org/10.1175/1520-0469\(1993\)050<0518:SSWDOB>2.0.CO;2](https://doi.org/10.1175/1520-0469(1993)050<0518:SSWDOB>2.0.CO;2), 1993.
- Sato, K.: A statistical study of the structure, saturation and sources of inertio-gravity waves in the lower stratosphere observed with the MU radar, *J. Atmos. Terr. Phys.*, 56, 755–774, [https://doi.org/10.1016/0021-9169\(94\)90131-7](https://doi.org/10.1016/0021-9169(94)90131-7), 1994.
- Spargo, A. J.: Radar Measurements of Gravity Wave Characteristics in the MLT, Master's thesis, University of Adelaide, School of Physical Sciences, 2016.
- Tellinghuisen, J.: Statistical error propagation, *J. Phys. Chem. A*, 105, 3917–3921, 2001.
- Thorsen, D., Franke, S. J., and Kudeki, E.: A new approach to MF radar interferometry for estimating mean winds and momentum flux, *Radio Sci.*, 32, 707–726, 1997.
- Thorsen, D., Franke, S. J., and Kudeki, E.: Statistics of momentum flux estimation using the dual coplanar beam technique, *Geophys. Res. Lett.*, 27, 3193–3196, 2000.
- Tsuda, T., Kato, S., Yokoi, T., Inoue, T., Yamamoto, M., VanZandt, T., Fukao, S., and Sato, T.: Gravity waves in the mesosphere observed with the middle and upper atmosphere radar, *Radio Sci.*, 25, 1005–1018, 1990.
- Vandeppeer, B. G. W. and Reid, I. M.: On the spaced antenna and imaging Doppler interferometer techniques, *Radio Sci.*, 30, 885–901, 1995.
- Vincent, R. A. and Reid, I. M.: HF Doppler measurements of mesospheric gravity wave momentum fluxes, *J. Atmos. Sci.*, 40, 1321–1333, 1983.
- Vincent, R. A., Kovalam, S., Reid, I. M., and Younger, J. P.: Gravity wave flux retrievals using meteor radars, *Geophys. Res. Lett.*, 37, L14802, <https://doi.org/10.1029/2010GL044086>, 2010.

750

**A. J. Spargo et al.: Mesospheric gravity wave momentum flux estimation**

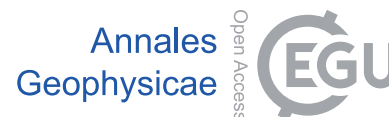
- Wang, D.-Y. and Fritts, D. C.: Mesospheric Momentum Fluxes Observed by the MST Radar at Poker Flat, Alaska, *J. Atmos. Sci.*, 47, 1512–1521, [https://doi.org/10.1175/1520-0469\(1990\)047<1512:MMFOBT>2.0.CO;2](https://doi.org/10.1175/1520-0469(1990)047<1512:MMFOBT>2.0.CO;2), 1990.
- Wang, D.-Y. and Fritts, D. C.: Evidence of Gravity Wave-Tidal Interaction Observed near the Summer Mesopause at Poker Flat, Alaska, *J. Atmos. Sci.*, 48, 572–583, [https://doi.org/10.1175/1520-0469\(1991\)048<0572:EOGWIO>2.0.CO;2](https://doi.org/10.1175/1520-0469(1991)048<0572:EOGWIO>2.0.CO;2), 1991.
- Woodman, R. F.: Coherent radar imaging: Signal processing and statistical properties, *Radio Sci.*, 32, 2373–2391, <https://doi.org/10.1029/97RS02017>, 1997.
- Woodman, R. F. and Guillen, A.: Radar observations of winds and turbulence in the stratosphere and mesosphere, *J. Atmos. Sci.*, 31, 493–505, 1974.

## Appendix G

**Publication: Ann. Geophys., 35, 567-582,  
2017**

This paper presents a comparison of airglow-derived temperatures and airglow intensities from two ground-based optical instruments at the Buckland Park field site and satellite-based measurements of the same quantities. It also uses a measurement of the height of constant density surfaces derived from meteor radar data in conjunction with the height-resolved satellite temperatures to infer the variability in the airglow emission height. The author of this thesis performed all the analysis and prepared all figures presented in the paper, and also contributed to writing the paper.

Ann. Geophys., 35, 567–582, 2017  
www.ann-geophys.net/35/567/2017/  
doi:10.5194/angeo-35-567-2017  
© Author(s) 2017. CC Attribution 3.0 License.



## Seasonal MLT-region nightglow intensities, temperatures, and emission heights at a Southern Hemisphere midlatitude site

Iain M. Reid<sup>1,2</sup>, Andrew J. Spargo<sup>2</sup>, Jonathan M. Woithe<sup>1</sup>, Andrew R. Klekociuk<sup>2,3</sup>, Joel P. Younger<sup>1,2</sup>, and Gulamabas G. Sivjee<sup>4</sup>

<sup>1</sup>ATRAD Pty Ltd, 20 Phillips St., Thebarton, 5031, Australia

<sup>2</sup>School of Physical Sciences, University of Adelaide, Adelaide 5000, Australia

<sup>3</sup>Antarctica and the Global System, Australian Antarctic Division, Department of the Environment and Energy, Kingston, Tasmania, Australia

<sup>4</sup>Embry Riddle Aeronautical University, Department Physical Sciences, Daytona Beach, FL 32114, USA

Correspondence to: Iain M. Reid (ireid@atrad.com.au)

Received: 25 January 2017 – Revised: 23 March 2017 – Accepted: 23 March 2017 – Published: 18 April 2017

**Abstract.** We consider 5 years of spectrometer measurements of OH(6–2) and O<sub>2</sub>(0–1) airglow emission intensities and temperatures made near Adelaide, Australia (35° S, 138° E), between September 2001 and August 2006 and compare them with measurements of the same parameters from at the same site using an airglow imager, with the intensities of the OH(8–3) and O(<sup>1</sup>S) emissions made with a filter photometer, and with 2 years of Aura MLS (Microwave Limb Sounder) v3.3 temperatures and 4.5 years of TIMED SABER (Thermosphere Ionosphere Mesosphere Energetics and Dynamics Sounding of the Atmosphere using Broadband Emission Radiometry) v2.0 temperatures for the same site. We also consider whether we can recover the actual emission heights from the intercomparison of the ground-based and satellite observations. We find a significant improvement in the correlation between the spectrometer OH and SABER temperatures by interpolating the latter to constant density surfaces determined using a meteor radar.

**Keywords.** Atmospheric composition and structure (airglow and aurora)

### 1 Introduction

Observations of OH and O<sub>2</sub> rotational temperatures provide a relatively simple method of routinely measuring temperatures in the atmosphere at altitudes near 87 and 94 km, respectively, at night. The OH emission in particular has been extensively studied using ground-based instruments (e.g. Se-

menov et al., 2013) and using satellite-based instruments (e.g. Xu et al., 2010, 2012) and has been modelled in some detail (e.g. Grygalashvyly et al., 2014; Sonnemann et al., 2015). There are rather more ground-based observational sites in the Northern Hemisphere (NH) than the Southern Hemisphere (SH). For example, Semenov et al. (2013) summarise 27 NH and 9 SH sites, which includes some historical locations. Reisin et al. (2014) summarise contemporary sites in the Network for the Detection of Mesospheric Change (NDMC) and include 13 NH and 6 SH sites. The addition of a new ground-based 5-year OH(6–2) and O<sub>2</sub>(0–1) rotational temperature data set from another SH site is therefore useful.

Routine observations of OH(6–2) and O<sub>2</sub>(0–1) rotational temperatures began in 2001 at the Buckland Park (BP) field site located near Adelaide (35° S, 138° E), Australia, using a Czerny–Turner spectrometer, although some limited measurements of the OH(6–2) emission were made earlier using a similar instrument, prior to it being relocated to Antarctica (Hobbs et al., 1996). Detailed descriptions of the system used in the present study, its automated mode of operations, and its data acquisition facilities have been reported by Sivjee and Shen (1997).

In this paper, we describe the results from the spectrometer for the 5-year period from September 2001 until August 2006, when it ceased operation. We compare the spectrometer OH(6–2) and O<sub>2</sub>(0–1) temperatures and emission intensity results with OH(8–3) and O(<sup>1</sup>S) emission intensities from a three-field photometer (3FP) (see, e.g., Reid et



al., 2014) that has operated at the site since 1995 and with OH(6–2) and O<sub>2</sub>(0–1) temperatures and emission intensities from an imager with a temperature capability that has been operated at the site since 2001 (see, e.g., Hecht et al., 1997) by Aerospace Corporation. We also compare the spectrometer results with v3.3 temperatures from the Microwave Limb Sounder (MLS) instrument on the Aura satellite for the period between 8 August 2004 and 1 August 2006 and with v2.0 temperatures from the Sounding of the Atmosphere using Broadband Emission Radiometry (SABER) instrument on board the Thermosphere Ionosphere Mesosphere Energetics and Dynamics (TIMED) satellite for the period between 26 January 2002 and 1 August 2006. The MLS data were quality-screened according to criteria recommended by Livesey et al. (2011). In this study, we assume that the OH(6–2) and O<sub>2</sub>(0–1) rotational level populations are in local thermodynamic equilibrium, which seems a fair assumption based on the agreement with other techniques, but we do note the work of Noll et al. (2016), which indicates that some care may be required in the interpretation of high-altitude OH rotational temperature results for high and even  $v'$ .

A detailed interpretation of ground-based passive airglow observations is often limited by the lack of information about the actual emission height, which may change with time of day and time of year. Younger et al. (2015) have described a new technique for determining the height of a constant density surface at altitudes of 78–85 km using meteor radar data. In this work, we compare 1 year of spectrometer OH(6–2) and SABER temperatures using the assumption that the OH(6–2) emission height follows a constant density surface using meteor-radar-derived neutral density measurements. This allows us to gain a better understanding of this aspect of our observations and significantly improves the correlation between the two observations.

## 2 Equipment

The BP field site is home to several instruments for investigating the atmosphere. In addition to the Czerny–Turner spectrometer and meteor radar, which we describe below, the instruments of most interest to this work are the 3FP and the Aerospace Imager. The 3FP has been described by Woithe (2000), Ding et al. (2004), Reid and Woithe (2005, 2007), and Reid et al. (2014). It measures the intensity of the O(<sup>1</sup>S) 558 nm and OH(8–3) 730 nm airglow emission every minute at night, during moon-free cloudless periods. The Aerospace imager is described by Hecht et al. (1994) and is of particular interest here because of the work of Gelinás et al. (2008), hereinafter G08, who describe observations made using the imager of O<sub>2</sub>(0,1) and OH(6,2) intensity and temperatures made at BP and Alice Springs (23°48' S, 133°53' E) during the period from 2002 to 2005.

### 2.1 Czerny–Turner spectrometer

The spectrometer is a high-throughput, modified Czerny–Turner spectrometer fitted with long, Fastie-type, curved entrance slits. The detector is a 1024 × 1024 Peltier and water-cooled charge-coupled device (CCD) coupled to large aperture  $f/1.2$  lenses. More detail is given in Sivjee and Shen (1997). The instrument's wavelength and intensity response were calibrated using a krypton reference spectrum and a reference black body emitter. The first calibration occurred in December 2000 at the commissioning, and the grating was reset on 14 December 2001 when a new calibration was performed. This calibration was then used until the instrument was decommissioned due to an acquisition system hardware failure in 2007. Before any data analysis was carried out, a dark image was subtracted from a data image to remove intensity contributions from instrument noise. Generally, the dark image was recorded once an hour during data acquisition.

#### 2.1.1 OH temperatures

OH temperature estimates were calculated using the standard “ratio of lines” method from the (6–2) OH band. The J constants for each OH line were obtained from Mies (1974), the Einstein A coefficients for each OH line from Langhoff et al. (1986), the rotational terms for each OH transition from Coxon and Foster (1982), and the nominal centre wavelengths (in nm) of each transition OH line emission were obtained from Greet et al. (1998).

Due to very low intensity, the P1(6) and P1(7) lines proved too difficult to definitively characterise in general, so they (and temperature estimates based on them) were omitted from the process. During the analysis, it was also observed that jitter on the P1(5) line due to sampling resolution and low intensity was unacceptably high compared to P1(2), P1(3), and P1(4) and that consequently temperatures calculated using P1(5) often differed wildly from the others. As a result, the “average” OH temperature uses the temperatures derived from the P1(2) : P1(3) and P1(2) : P1(4) ratios.

Two different methods were used to estimate the intensity of the OH lines. The simplest, referred to as the “height” method, used the peak's maximum recorded value. The alternative, dubbed the “intensity” method, used an integrated intensity under the peak. Both methods yield similar results although the height method may be slightly better if the spectrum is a little noisy. The main problem with the intensity method is that it is hard to positively identify the integration bounds at times due to the limited pixel resolution relative to the peak widths, and this can lead to integration inaccuracies.

#### 2.1.2 O<sub>2</sub> temperatures

Unlike the OH temperatures there is no analytical method for calculating temperatures from the O<sub>2</sub> band. Consequently,

one must take the recorded spectrum and compare it against a temperature-dependent model spectrum. The temperature which gives a model which is a best fit for the recorded spectrum is deemed to be the O<sub>2</sub> temperature. In the case of the spectrometer data, there is considerable difficulty in carrying out this process because the shape of the O<sub>2</sub> band emission often differs from that of the model. This can cause the software to converge on a local best fit which may not be accurate. The practical result of this is a temperature time series which is much noisier than that produced from the OH analysis. The model spectrum used here is based on Krassovsky et al. (1962). Both the “integrated intensity” and “peak height” properties were used separately to compare the model and recorded spectrum. The peak height results tended to be the better of the two due to difficulties in identifying equivalent integration bounds in the spectra, particularly in the presence of noise in the recorded spectrum.

## 2.2 Meteor radar

The meteor radar used in this work is described by Holdsworth et al. (2004a). It is an ATRAD meteor detection radar (MDR) and operated at Buckland Park between 16 July 2002 and 25 January 2004 before being relocated to Darwin in northern Australia. This radar operates at a frequency of 33.2 MHz, with a peak power of 7.5 kW, has one “all-sky” transmit antenna, and uses a five-antenna interferometer on reception to detect meteor echoes in the 70 to 110 km height range. For the observations we discuss here, typical daily height-resolvable underdense meteor counts at BP varied between 9000 and 14 000 per day over the year, and usable winds were determined between heights of 75 and 100 km. A 55 MHz meteor radar similar to that described by Reid et al. (2006) commenced operation at BP at the beginning of 2006, but the spectrometer ceased operation soon after, and there are limited coincident measurements from the two instruments.

Note that we do not attempt to derive temperatures from the meteor radar measured diffusion coefficients here, as for example, described in Holdsworth et al. (2006), as there are significant limitations in this approach (see Lee et al., 2013; Younger et al., 2014). However, Lee et al. (2016) have described a new method of estimating temperatures near the mesopause region using meteor radar observations by calibrating their meteor radar against Aura MLS temperatures. This approach looks promising and has some similarities to the approach we describe below in Sect. 4.3.1.

## 2.3 Aura MLS and TIMED SABER temperatures

To further investigate our temperature results, we considered Aura MLS and TIMED SABER observations. Two important aspects of the satellite measurements to be considered in our comparisons are the vertical resolution and the known bias. The vertical resolution (the averaging kernel width) of the

MLS at 0.46 Pa is about 14–15 km, and the bias is cold by up to 2 K (Schwartz et al., 2008). The vertical resolution of SABER in the mesopause region is superior at about 2 km (Remsberg et al., 2003), and this motivates our use of these measurements in preference to the Aura MLS measurements in Sect. 4.3.2 below.

We accepted satellite measurements within a 500 km radius of Buckland Park and a time difference for the satellite and ground-based measurements of 30 min (that is, satellite measurements were only used if they are preceded or followed by a ground-based measurement within 30 min). The latter was based on the findings of French and Mulligan (2010). However, we do note that in their study, no substantial change in bias between satellite and ground-based measurements was detected when the time difference between ground and satellite observations was varied between 15 min and 8 h.

Initially, we applied a Gaussian weighting kernel to the satellite-derived temperatures as per empirically determined weighting functions for the OH(6–2) (Baker and Stair, 1988) and the O<sub>2</sub>(0–1) (McDade et al., 1998) emissions. We later refined this approach to better determine the actual emission heights, and this is discussed in Sect. 4 below.

## 3 Results

### 3.1 Spectrometer

Figures 1 and 2 show the temperatures and intensities through the night and through the year for the OH and O<sub>2</sub> emissions, respectively. Here we have used a superposed year to reduce the noise in these images. Inspection of these figures indicates that the OH temperatures are clearly less noisy than the O<sub>2</sub> temperatures, and a dominant annual oscillation (AO) is evident. The variation of the O<sub>2</sub> is harder to determine, but upon further inspection, a semi-annual oscillation (SAO) is discernible.

In the OH temperatures, minimum temperatures are observed in summer, with a general increase in temperature between the autumnal and vernal equinoxes. During this period, the temperatures are greatest at dawn and dusk. There is a tendency for the temperature to be greatest at equinox, resulting in a semi-annual variation in temperature, which is strongest late in the night, although there is a mid-winter maximum present as well. The OH intensity tends to be a minimum in the middle of the night throughout the year, with a tendency to a maximum around dusk. There is a general brightening between day 120 and day 250, but with a 30 to 40-day periodicity also evident during this interval.

In the O<sub>2</sub> temperatures, there is a general increase in temperature at the time of the autumnal (March) equinox, with the highest temperatures towards the end of the night at this time. There is a similar but less dramatic increase beginning around the time of the spring equinox. The O<sub>2</sub> intensity

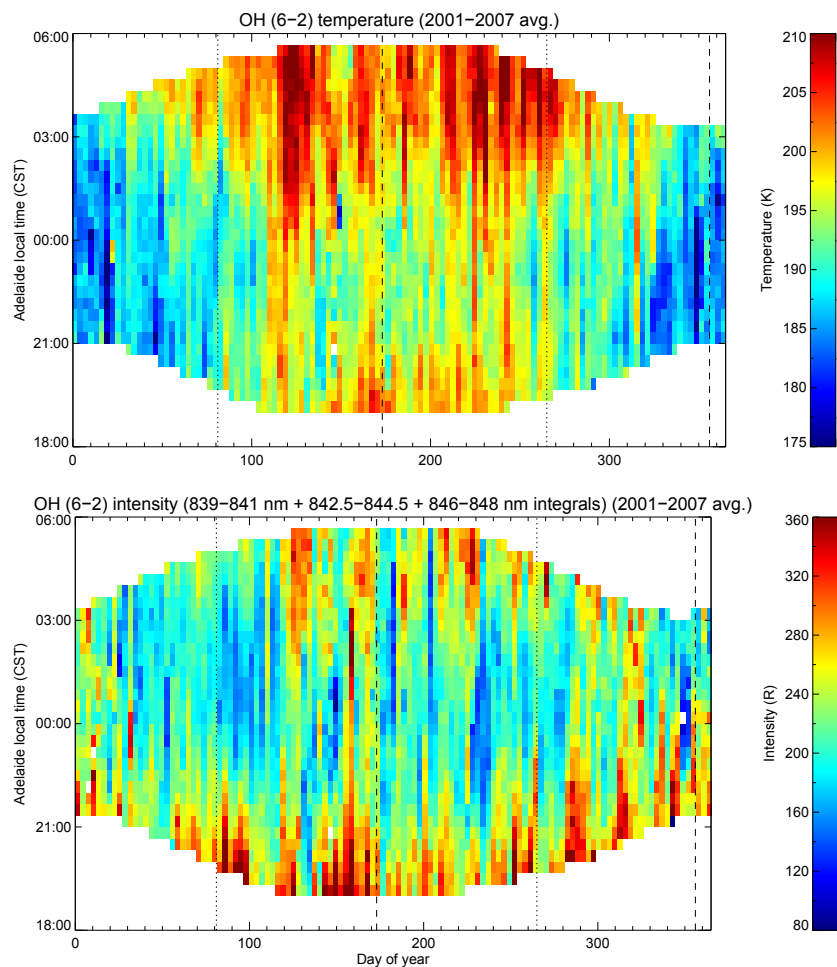


**Figure 1.** Top: the OH(6–2) temperature plotted as a function of time of day and time of year for a superposed year. The equinoxes are indicated by dotted lines, the solstices by dashed lines. Minimum temperatures are observed in summer, with a general increase in temperature between the equinoxes. During this period, the temperatures are greatest at dawn and dusk. There is a tendency for the temperature to be greatest between the autumnal equinox and the vernal equinox, with a semi-annual variation in temperature, which is strongest late in the night, although there is a mid-winter maximum present as well. Bottom: as for top panel but for the OH(6–2) emission intensity.

shows a brightening at the equinoxes, particularly later in the night, with the vernal equinox being the brightest part of the year throughout the night.

To quantify the variation of the temperature and intensity data through the night, we follow Reid et al. (2014) and divide the period between 18:00 and 06:00 LT into four 3 h blocks of data. We then analyse each 3 h data block using a Lomb–Scargle periodogram to determine the dominant periods present. The significant periods identified in the Lomb periodograms are then used in a harmonic analysis to determine the mean amplitudes and phases of these periods through the period of observation and to estimate the geophysical variation through the night. We also calculate the Lomb–Scargle periodogram for the entire night.

This analysis indicates that OH temperatures are dominated by an annual oscillation (AO), while in the O<sub>2</sub> tem-

peratures, the semi-annual oscillation (SAO) dominates. In the OH temperature Lomb spectra, there are also significant peaks near the SAO and AO periods in the nightly mean, with the SAO peak only appearing at a significant level in the second half of the night. There is a significant peak at the terannual oscillation (TAO) period in the first 3 h block of the night. In the O<sub>2</sub> temperature Lomb spectra, the nightly mean includes significant peaks near the SAO and AO periods. There is power at the TAO and quasi-biennial oscillation (QBO) periods, but not at a 99 % significance level. While the QBO is not significant at the 99 % level, we note that QBO-related variations have been repeatedly found in the mesosphere–lower thermosphere (MLT) region in a number of different parameters including tidal wind amplitudes (Xu et al., 2009) and constituent abundances (Zhu et al., 2015). We have also discussed the QBO and quasi-terannual oscilla-

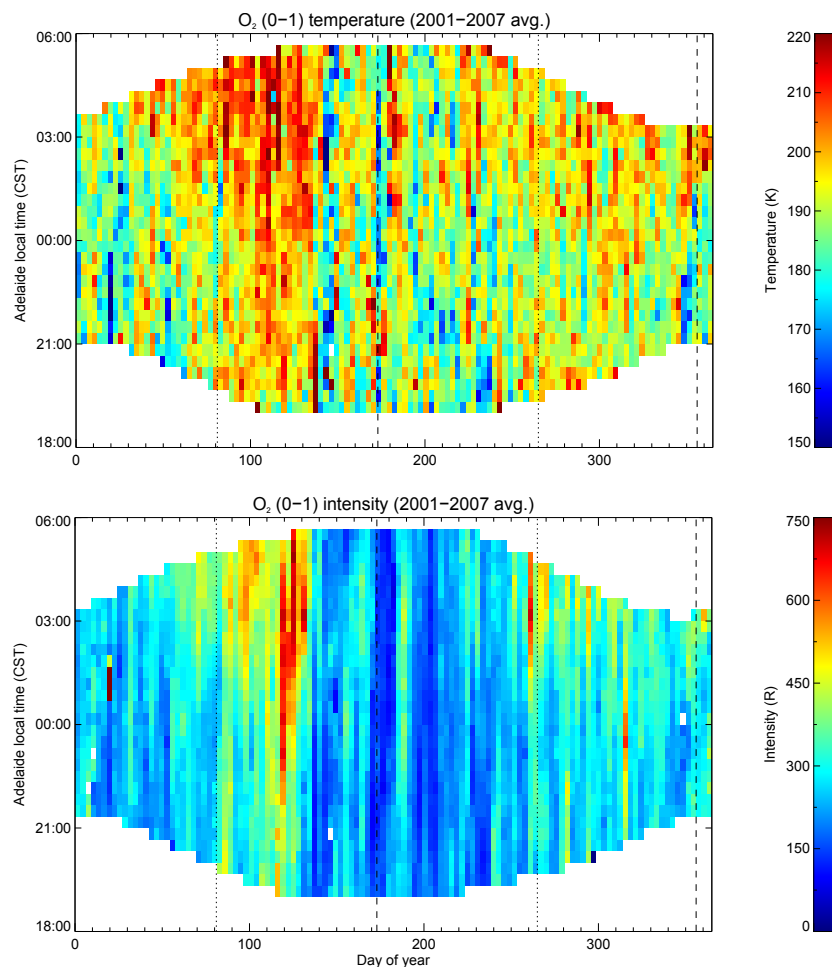


**Figure 2.** Top: the O<sub>2</sub>(0–1) temperature plotted as a function of time of day and time of year for a superposed year. The equinoxes are indicated by dotted lines, the solstices by dashed lines. There is a general increase in temperature at the time of the autumnal equinox, with the highest temperatures towards the end of the night at this time. There is a similar but less dramatic increase beginning around the time of the spring equinox. Bottom: as for top panel but for the O<sub>2</sub>(0–1) emission intensity.

tion (QTO) previously in our analysis of long-term measurements of the intensity of the O(<sup>1</sup>S) and OH(8–3) nightglow intensity at Adelaide (Reid et al., 2014).

When the composite years for the four 3 h blocks are examined for the nightly OH variation, we see a change from a predominately annual variation at the beginning of the night to an annual variation with a semi-annual variation superposed on it. In the case of O<sub>2</sub>, the temperature variation is generally noisy, but a semi-annual periodicity dominates and strengthens through the night. These variations likely suggest an interaction between tides and the SAO and AO. For example, recent work by Jones Jr. et al. (2017), who used the thermosphere–ionosphere–mesosphere electrodynamics general circulation model (TIME-GCM) to investigate the Thermospheric SAO in density, found that the SAO in the concentration of atomic oxygen in the MLT is forced by non-

linear, resolved-scale variations in the advective, net tidal, and diffusive transport of O. This is also consistent with our analysis of the variation of the intensity of the O(<sup>1</sup>S) and OH(8–3) nightglow through the night at Adelaide and the local time dependence of amplitude of the SAO and AO in those emissions (Reid et al., 2014).

Only the AO and SAO are significant at the 99 % level through the entire night, and our results for harmonic fits to the entire observational period for these periods are summarised quantitatively in Table 1. In the OH, the SAO maximises in the autumn and the AO in the winter. The SAO takes a value of 2.1 K and the AO a value of 6.6 K. In the case of the O<sub>2</sub> temperatures, both the SAO and AO maximise in the autumn, with the SAO dominant at 5.1 K, about twice the magnitude of the AO at 2.6 K. We do note here that the mean and uncertainty in each component in the fit to the nightly

**Table 1.** Results of the harmonic fits to the spectrometer OH(6–2) and O<sub>2</sub>(0–1) rotational temperature time series for the entire observational period (September 2001 until August 2006). Phase indicates the first maximum after 1 January. Amplitudes of the AO and SAO are given both relative to the mean temperature and in Kelvin.

OH(6–2) and O <sub>2</sub> (0–1) temperatures (Sep 2001–Aug 2006)					
Emission	Mean (K)	AO		SAO	
		Amplitude (K)	Phase (days)	Amplitude (K)	Phase (days)
OH (~ 87 km)	192 K	3.44 ± 0.32 %	184 ± 4	1.10 ± 0.69 %	88 ± 7
		6.60 ± 0.61 K	3 Jul (winter)	2.11 ± 1.32 K	29 Mar (autumn)
O <sub>2</sub> (~ 94 km)	201 K	1.27 ± 0.44 %	130 ± 22	2.51 ± 0.63 %	107 ± 5
		2.56 ± 0.89 K	10 May (autumn)	5.05 ± 1.27 K	17 Apr (autumn)

mean agree with the average mean and uncertainty of the amplitudes and phases of those components calculated from the vector means of their amplitudes and phases for the three 4 h blocks. This indicates that the nightly means are representative in that the uncertainties capture the variation through the night.

To further examine the variation of the harmonic components through time, we applied a wavelet spectral analysis to the time series of the 30-day average temperatures (Torrence and Compo, 1998). The results are shown in Fig. 3 (bottom panel; as for Fig. 3 (top panel), but for the O<sub>2</sub>(0–1) temperatures). The SAO is the dominant periodicity in this time series, with more power in the AO later in the observational period. There is power in the wavelet spectrum at the period of the QBO, particularly after 2003, but not at a significant level when averaged over the entire observational period. The top panel shows the wavelet power spectrum for the OH temperature, along with the time series of 30-day averaged values and their standard deviations and the corresponding Lomb periodogram. The time series is dominated by the AO, which is consistent across the observational period in amplitude and phase. The SAO is present in the second half of the observational period, and the QBO is at its centre. In the lower panel, the O<sub>2</sub> temperatures show a dominant SAO, with more power in the AO later in the observational period. There is power in the wavelet spectrum across the period of observation for the QBO, but not at a significant level.

Figure 4 shows the results of a fit of the AO and SAO only for the OH(6–2) and O<sub>2</sub>(0–1) temperatures and intensities. In the case of the OH, there is general agreement in form, with a dominant AO with maxima mid-year, that is, in winter. In the case of the O<sub>2</sub>, there is stronger agreement in form, in this case, a dominant SAO, maximising at the equinoxes. Reid et al. (2014) considered a long series of observations of the OH(8–3) and O(<sup>1</sup>S) intensities made at Buckland Park, and shown on these plots are the 3FP OH(8–3) and O(<sup>1</sup>S) intensities from their work corresponding to the same observational period. The agreement in form is good in the case of the OH results and strong in the case of the O<sub>2</sub>(0–1) and O(<sup>1</sup>S) results.

### 3.2 Satellite temperatures

Table 2 gives a summary of the spectrometer OH(6–2) and O<sub>2</sub>(0–1) mean temperatures compared to the Aura MLS mean temperatures using the coincidence criteria described above. We have weighted the measurements with simple Gaussian functions based on Baker and Stair (1988) for the OH(6–2) emission and McDade (1998) for the O<sub>2</sub>(0–1) emission. We have also weighted the spectrometer OH results with the SABER 1.6 and 2.0 μm OH volume emission rates (VERs). The uncertainty in the mean in this table corresponds to the standard deviations of the samples.

#### 3.2.1 Aura MLS v3.3 temperatures

The MLS data have been selected according to the v3.3 status, quality, threshold, and convergence values recommended by the MLS Science Team (Livesey et al., 2011). The Aura MLS mean temperatures weighted according to the estimated OH(6–2) profile shown in Table 2 are lower than the spectrometer mean, with a difference of 7.5 K, but the results agree to within the experimental error. There is generally good agreement between the amplitudes and phases of the AO as measured by the two instruments, but not to within the experimental error for the SAO. We have included the temperatures of the Aura MLS corresponding to the 0.46 Pa level in this table, and these agree with the spectrometer observations to within the experimental error for the mean, the AO, and the SAO. We will further discuss the significance of this below.

The O<sub>2</sub>(0–1) mean temperature from the spectrometer is significantly higher than those in the Aura MLS measurements weighted in altitude by the estimated O<sub>2</sub>(0–1) profile specified in McDade (1998), and it is clearly biased high. The AO amplitudes agree to within the experimental error, but the phases do not. The SAO amplitudes and phases agree to within the experimental error. We do note that Aura MLS retrievals at pressures of less than 0.1 Pa are not suitable for scientific use. This should be noted in the comparisons of the MLS with O<sub>2</sub> temperatures shown in Table 2.

**Table 2.** Comparison between coincident Aura MLS and TIMED SABER and spectrometer temperatures. The Aura MLS results are for 8 August 2004 to 1 August 2006 and the TIMED SABER results for 26 January 2002 to 1 August 2006.  $N$  is the number of points in each sample. Note that the Aura MLS  $O_2$  weighting is marginal with respect to the lowest recommended pressure (0.001 hPa). See text for further details.

Aura MLS and spectrometer temperatures 8 Aug 2004 to 1 Aug 2006							
Emission	Measurement	Mean (K)	$N$	AO		SAO	
				Amplitude (K)	Phase (days)	Amplitude (K)	Phase (days)
OH (~ 87 km)	Spectrometer, OH(6–2)	$191.0 \pm 10.0$	7260	$5.3 \pm 0.2$	$168 \pm 2$	$3.2 \pm 0.2$	$83 \pm 1$
	Aura MLS, OH weighting	$183.5 \pm 8.2$	159	$4.6 \pm 0.4$	$164 \pm 5$	$3.9 \pm 0.4$	$97 \pm 3$
	Aura MLS, 0.46 Pa	$190.4 \pm 7.3$	159	$5.1 \pm 0.4$	$167 \pm 4$	$3.7 \pm 0.4$	$87 \pm 3$
$O_2$ (~ 94 km)	Spectrometer, $O_2(0-1)$	$205.3 \pm 34.0$	5477	$4.7 \pm 0.7$	$105 \pm 8$	$3.7 \pm 0.7$	$109 \pm 5$
	Aura MLS, $O_2(0-1)$	$183.7 \pm 8.3$	159	$4.1 \pm 0.9$	$148 \pm 13$	$4.5 \pm 0.8$	$105 \pm 6$
TIMED SABER and spectrometer temperatures, 26 Jan 2002 to 1 Aug 2006							
Emission	Measurement	Mean (K)	$N$	AO		SAO	
				Amplitude (K)	Phase (days)	Amplitude (K)	Phase (days)
OH (~ 87 km)	Spectrometer, OH(6–2)	$191.2 \pm 10.2$	27 702	$6.3 \pm 0.1$	$182 \pm 1$	$1.6 \pm 0.1$	$84 \pm 1$
	TIMED SABER, 1.6 $\mu\text{m}$ OH VER	$192.9 \pm 10.8$	1407	$8.4 \pm 0.4$	$177 \pm 3$	$2.3 \pm 0.4$	$95 \pm 5$
	TIMED SABER, 2.0 $\mu\text{m}$ OH VER	$193.3 \pm 10.4$	1407	$7.2 \pm 0.3$	$175 \pm 3$	$2.3 \pm 0.4$	$98 \pm 5$
$O_2$ (~ 94 km)	Spectrometer, $O_2(0-1)$	$204.4 \pm 31.7$	21 154	$1.7 \pm 0.4$	$150 \pm 11$	$5.4 \pm 0.4$	$102 \pm 2$
	TIMED SABER, $O_2(0-1)$	$190.5 \pm 11.0$	1373	$1.2 \pm 0.5$	$118 \pm 20$	$2.4 \pm 0.5$	$98 \pm 5$

### 3.2.2 TIMED SABER v2.0 temperatures

Table 2 also gives a summary of the same spectrometer temperatures compared to the coincident measurements from TIMED SABER. In contrast to the Aura MLS result, this comparison indicates that the mean spectrometer OH(6–2) temperatures are lower than the TIMED SABER temperatures, being 1.7 and 2.1 K lower than the OH 1.6  $\mu\text{m}$  and OH 2.0  $\mu\text{m}$  weighted temperatures, respectively. All mean OH temperatures agree to within the experimental uncertainty. The SABER 1.6 and 2.0  $\mu\text{m}$  AO amplitudes do not agree, but the corresponding phases and those of the SAO amplitudes and phases do agree. The TIMED SABER AO and SAO results do not agree with those from the spectrometer, but inspection of the results suggests that both instruments are measuring the same thing and that we have underestimated the spectrometer errors.

Like the Aura MLS temperatures, the  $O_2(0-1)$  spectrometer temperatures are greater than the TIMED SABER measurement when weighted to similar height ranges, in this

case by 13.9 K. The spectrometer  $O_2(0-1)$  mean temperatures are clearly biased high, although as we see below the AO and SAO amplitudes are very like those from the other instruments considered here. Given the larger number of coincident measurements with the spectrometer and the greater level of confidence in the TIMED SABER measurements at upper mesospheric heights, the TIMED SABER measurements have been used in preference to the Aura MLS measurements to recalibrate the spectrometer  $O_2(0-1)$  mean temperature throughout the remainder of this paper.

## 4 Discussion

### 4.1 Temperatures

As we have noted above, there have been many ground-based observational studies of midlatitude airglow temperatures in the Northern Hemisphere (e.g. She and Lowe, 1998; Bittner et al., 2002; López-González et al., 2007). Similar studies in the Southern Hemisphere are rarer (e.g. Buriti et al., 2004).

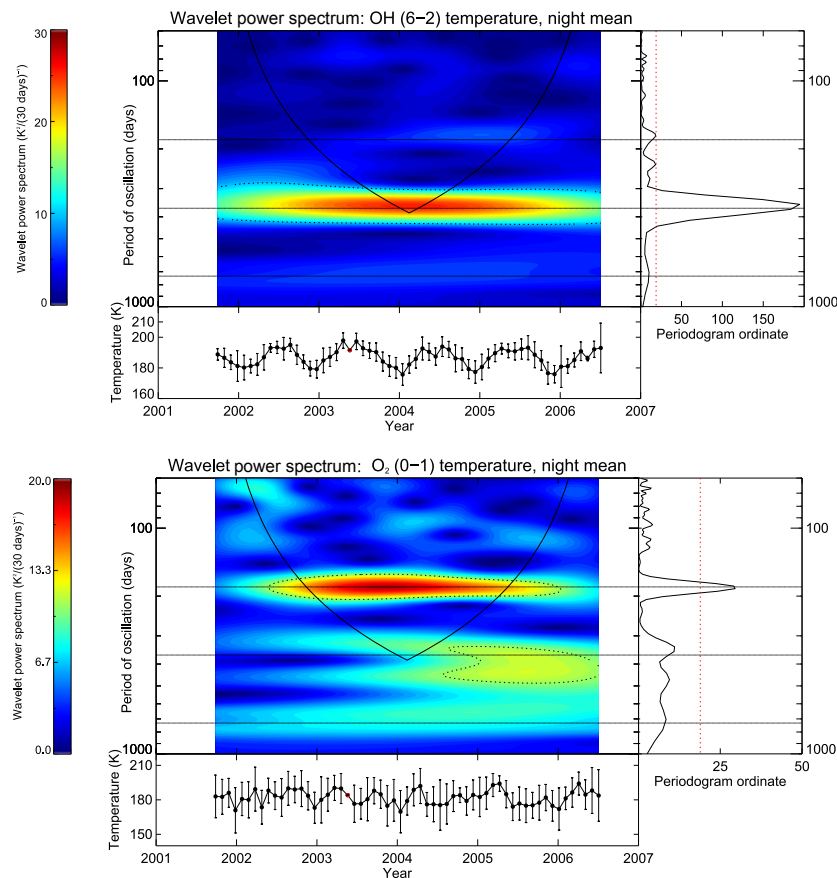


**Figure 3.** Top: the wavelet power spectrum for the OH(6–2) temperature (top) with the time series of 30-day averaged values and their standard deviations (bottom) and the corresponding Lomb periodogram (right). The periods of the SAO, AO, and QBO are indicated by the horizontal grey lines. The time series is dominated by the AO, which is consistent across the observational period in amplitude and phase. The SAO is present in the second half of the observational period and the QBO at its centre. Bottom: as for top panel, but for the O<sub>2</sub>(0–1) temperatures. The SAO is the dominant periodicity in this times series, with more power in the AO later in the observational period. There is power in the wavelet spectrum at the period of the QBO, particularly after 2003, but not at a significant level when averaged over the entire observational period.

The most important of these for the present work is that of G08, which used coincident data from the Aerospace Buckland Park airglow imager. Table 3 summarises the OH(6–2) temperature results from the present study, along with those from G08, who also include corresponding results from the TIME-GCM (Roble and Ridley, 1994). For this table, the periods of BP spectrometer observation times have been matched to those of G08. There is generally good agreement between these measurements, but not always to within the experimental uncertainties. However, we can summarise the results by saying that the mean temperature is in the range of 188 to 192 K with a mean of 190 K, the AO is consistently about 3 times larger than the SAO and maximises in winter, and the SAO takes its first maximum in autumn.

Table 3 also summarises the O<sub>2</sub>(0–1) temperature results and again compares these with G08 and the TIME-CGM. Again, we note that the mean from the present study is biased

high, with a value 14.6 K greater than that of G08. However, the amplitudes of the AO and SAO agree to within their experimental uncertainties. The SAO is about twice the magnitude of the AO in the case of the experimental results, whereas the TIME-GCM has an AO a little larger than the SAO. The SAO phases are generally consistent, taking the first maxima in autumn, while the AO results for this study differ from the G08 and TIME-GCM results in taking their first maximum in autumn rather than in winter. We have already noted the noisy nature of our O<sub>2</sub>(0–1) temperature results, and it may be that we have underestimated the uncertainties in our measurements in this case. Table 3 also includes MLT temperature results from the Wind Imaging Interferometer (WINDII) instrument on the Upper Atmosphere Research Satellite (UARS) (Shepherd et al., 2004), to which G08 also refer, and these are in general agreement with the ground-based observations.

**Table 3.** OH and O<sub>2</sub> results from the current study compared with other observations and the TIME-GCM. The time interval for the current results was selected to match that for G08. See text for details.

Annual and semi-annual oscillation for OH emission temperatures					
OH temperature	Mean (K)	AO		SAO	
		Amplitude (K)	Phase (days)	Amplitude (K)	Phase (days)
OH(6–2)	192	6.7 ± 0.5	183 ± 4 2 Jul (winter)	2.0 ± 1.4	89 ± 10 30 Mar (autumn)
G08 OH(6, 2)	189.2 ± 0.3	10.2 ± 0.4	213 ± 2	3.0 ± 0.5	113 ± 4
G08 TIME-GCM OH(6, 2)	188.1 ± 0.1	9.1 ± 0.2	184 ± 1	2.6 ± .2	94 ± 2
WINDII, 87 km (35° S) (Shepherd et al., 2004)	192.0 ± 8.5	5.8 ± 0.3	151.1 ± 15.7	1.8 ± 1.2	118.7 ± 8.0
Huang et al. (2006) (SABER, 2002 to 2004)				2.4	99
Xu et al. (2007) (SABER 2002 to 2006)	195	12.5		3.0	Mid-year
Annual and semi-annual oscillation for O <sub>2</sub> emission temperatures					
O <sub>2</sub> temperature	Mean (K)	AO		SAO	
		Amplitude (K)	Phase (days)	Amplitude (K)	Phase (days)
O <sub>2</sub> (0–1)	201	1.8 ± 0.5	113 ± 34 23 Apr (autumn)	5.1 ± 1.1	103 ± 3 13 Apr (autumn)
G08 O <sub>2</sub> (0, 1)	186.4 ± 0.3	2.6 ± 0.5	221 ± 10	4.7 ± 0.4	92 ± 3
G08 TIME-GCM O <sub>2</sub> (0, 1)	188.9 ± 0.2	3.6 ± 0.2	206 ± 4	2.2 ± .2	84 ± 3
Huang et al. (2006) (SABER, 2002 to 2004)				2.5	108

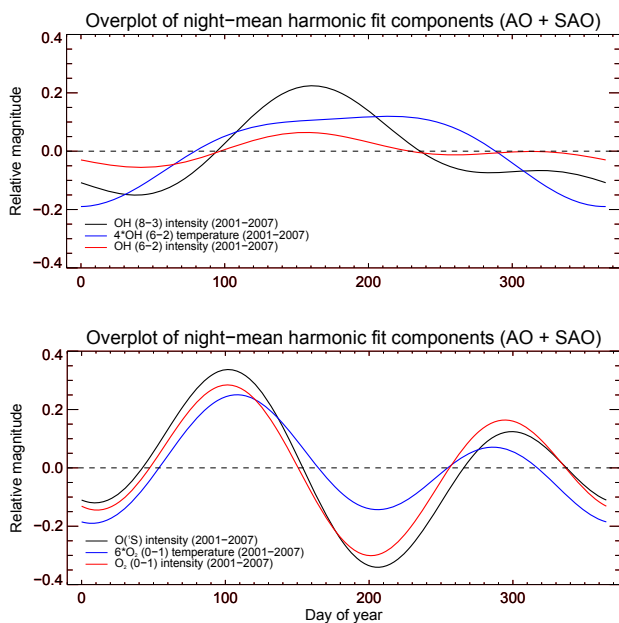
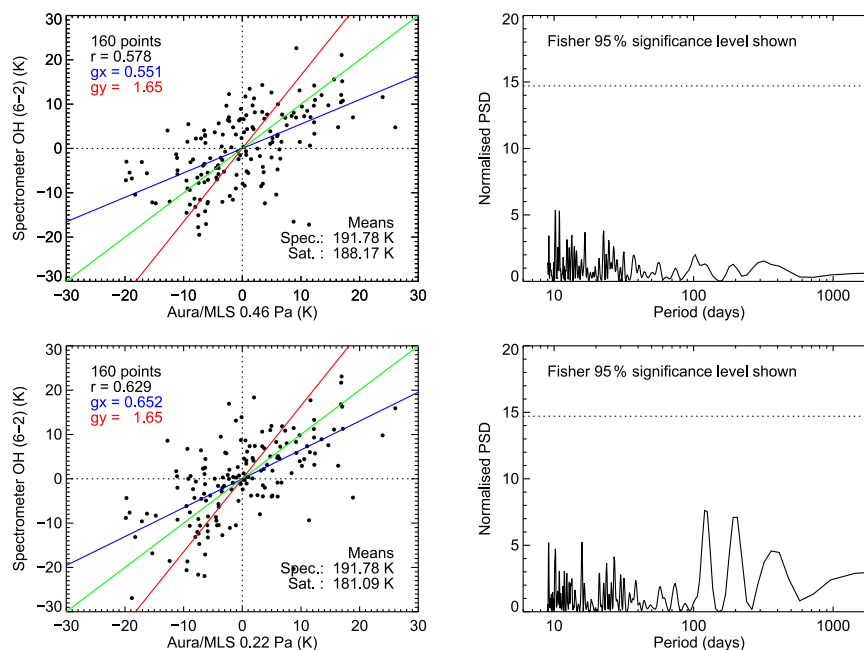
**Figure 4.** Top: a comparison of AO and SAO harmonic fits to the OH(6–2) rotational temperature and intensity from the spectrometer and the corresponding OH(8–3) intensity from the 3FP for the period 2001 to 2007. Bottom: as for top panel, but for the O<sub>2</sub>(0–1) rotational temperature and intensity and the corresponding O(<sup>1</sup>S) intensity from the 3FP.

Table 3 also summarises TIMED SABER results from Xu et al. (2007) and Huang et al. (2006). Xu et al. (2007) used TIMED SABER observations to examine long-term variations in zonal mean temperatures in the years 2002 to 2006. Their results indicate that the mean was 195 K for 86 km at 40° S and that the AO maximises mid-year with a value of 12.5 K. They found the SAO was weaker in amplitude with a value of 3 K, both results being consistent with ours. They also found a QBO with an amplitude of 0.4 K. We do not find a significant QBO in our OH(6–2) nightly mean temperatures, which would correspond to the height of Xu et al.'s (2007) observations near 86 km. It is significant in the 00:00 to 03:00 LT data block, however. Huang et al. (2006) also looked at SABER observed temperatures but concentrated on the QBO and SAO. They found the SAO at 35° S to be 2.4 K with a phase of 99 days at 87 km and 2.5 K with a phase of 108 days at 94 km, in agreement with the results of the present study and with the others summarised in Table 3. More recently, Zhang et al. (2017) analysed TIMED SABER results from January 2002 to February 2015 and provided results for the SAO at 85 km in good general agreement with our spectrometer OH(6–2) results.

#### 4.2 Temperature and intensity intercomparison

In the case of the OH emission shown in Fig. 4, a strong correlation between the temperature and intensity is typical of other studies. For example, Shepherd et al. (2007) looked at winter results from Resolute Bay (74.7° N) and Espy et al. (2007) looked at two sites in Sweden (59.5 and 57.4° N). Both studies showed a strong correlation throughout the year,





**Figure 5.** Examples of the comparison between the spectrometer OH temperatures and the Aura MLS temperatures. The panels on the left show the correlation values between the spectrometer and Aura MLS temperatures for the 0.46 Pa (top) and the 0.22 Pa (bottom) retrieval levels. The blue and red lines indicate lines of best fit made assuming all experimental errors are in the Aura MLS and the spectrometer, respectively. The green line indicates the  $y = x$  line. The right-hand panels indicate Lomb–Scargle periodograms for the residuals between the spectrometer and Aura MLS temperatures corresponding to the left-hand panels.

with the latter study also finding a seasonal dependence in the level of correlation. Espy et al. (2007) suggested that this was due to a variation in the mixing ratio of atomic oxygen due to vertical motion. Smith (2012) considered temperature and intensity observations of OH(6–2) made at Millstone Hill (42.6° N, 71.5° W), a site with a co-latitude somewhat closer to ours. He found a strong correlation, with a marked seasonal dependence and concluded that dynamical effects dominated photochemical effects. The correlation between the two parameters was highest during the autumn and lowest during the summer by a factor of over 3.6. He suggested that the summer minimum resulted from an increase in mesospheric gravity wave activity during the summer, a feature not predicted by the Mass-Spectrometer-Incoherent-Scatter (MSIS) model (Hedin, 1991) data but clearly observed by Ern et al. (2011) in High Resolution Dynamics Limb Sounder (HIRDLS) and SABER measurements of gravity wave momentum flux in the stratosphere and mesosphere. The OH(6–2) results from the present study are consistent with Smith’s (2012) results. We also note that the OH(8–3) results show a very similar form to the OH(6–2) results.

In the case of the O<sub>2</sub>(0–1) emission, we see a strong correlation between the temperature and the intensity and with the OI 558 nm emission intensity. Reid et al. (2014) have also noted that at Adelaide there is a striking correspondence be-

tween the O<sub>2</sub>(0–1) temperature maximum, the time of greatest O(<sup>1</sup>S) brightness (Reid and Woithe, 2007), and the time of the maximum meridional wind, which would correspond to the downward phase of the diurnal tide at equinox later in the night. This is consistent with the transport of atomic oxygen down into the MLT region and the brightening of the O(<sup>1</sup>S) and OH(8–3) airglow late in the night as observed at the autumnal equinox.

### 4.3 Determination of the OH emission height

Thus far we have assumed that the OH emission occurred at a fixed and known geometrical height. In the next two sections, we consider whether we can improve on this assumption, firstly by looking for the height of the minimum residual between the spectrometer and the satellite temperatures for different satellite pressure heights and then by interpolating the SABER temperatures to a fixed density surface derived from meteor radar observations.

#### 4.3.1 Comparison of spectrometer OH and Aura MLS temperatures at different Aura MLS constant pressure levels

The simplest Gaussian averaging kernel we have applied to the satellite data assumes that the OH layer is at a fixed altitude. However, when we use the assumption of a fixed

height for the OH emission and plot the residual temperature (ground-based – satellite), we find that the residuals for the Gaussian-weighted satellite data show a seasonal behaviour, suggesting that the mean emission height is changing throughout the year. When we examine the Lomb–Scargle periodograms of the residuals for temperatures at a series of constant pressure surfaces derived from the Aura MLS observations using the same conditions for coincidence as described earlier, we find that the residual minimises for MLS temperature estimates at the native retrieval level of 0.46 Pa ( $\sim 83.3$  km), with a correlation value of  $r = 0.58$ . This is shown in Fig. 5. This figure also shows the results for the 0.22 Pa ( $\sim 87.6$  km) retrieval level. The long period components (TAO, SAO, AO) of the residual are larger at this level, but the correlation is better at  $r = 0.63$ . All the peaks in both residuals are below the 99 % significance level, but given the width of the emission layer, this approach is not likely to be a good predictor of the retrieval level of best agreement. We should note here that in the height range of 70–90 km there are only four or five retrieval levels, and in the present study, it is not clear that we can distinguish between results at the 0.22 and 0.46 Pa retrieval levels.

We have included the 0.46 Pa result in Table 2 for the period between 8 August 2004 and 1 August 2006 as an example. The 0.46 Pa Aura MLS and spectrometer OH(6–2) results agree quite closely, with the mean of the former being 1.4 K lower than the latter. This difference is consistent with the bias reported for MLS (see Livesey et al., 2011). We note that there is arguably better agreement between the OH spectrometer result and the Aura MLS temperature at the 0.46 Pa retrieval level, with the AO and SAO amplitudes and phases at the 0.46 Pa retrieval level in closer agreement with the spectrometer results than those from the fixed weighting function.

Irrespective of the actual level of best agreement, the behaviour of these residuals suggests that the OH temperatures measured by the spectrometer are more closely associated with the layer being tied to a constant pressure surface rather than a fixed geometric height. This would be consistent with the density of atomic oxygen being tied to the background density (see, e.g., Marsh et al., 2006) and with the model results for the hydroxyl layer of Grygalashvyly et al. (2014).

#### 4.3.2 Comparison of spectrometer OH temperatures with SABER temperatures at meteor-radar-derived density levels

Additional information about the OH emission heights may be obtained by calibrating meteor radar results using Aura MLS (or SABER) densities, as Younger et al. (2015) have shown. They showed that a constant density surface may be determined in the 78 to 85 km height region from vertical profiles of meteor trail radar echo decay times. Additional work by P. J. Younger (personal communication, 2016) indicates that a second upper constant density surface between

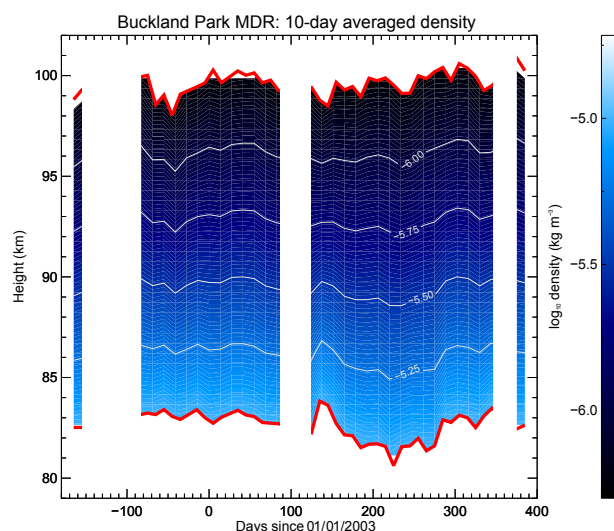


**Figure 6.** The geometric heights for 10-day average fixed density surfaces for 14 May 2002 to 28 January 2004 determined from the meteor radar. This diagram has been prepared using the difference in the estimate of the geometric height of two constant density surfaces to calculate the density scale height,  $H^*$ . The density profile is then interpolated between the two surfaces. Once the density or temperature dependence of the airglow layer is known, the density profile can be used to infer the height to which airglow temperatures correspond.

95 and 100 km may be determined. With some assumptions, this allows the constant density surfaces to be determined independently of satellite measurements after “calibration” for a particular meteor radar wavelength. While we do not have meteor radar observations for the entire period of the spectrometer observations, we do have coincident 33.2 MHz meteor radar,  $T_{\text{OH}}$ ,  $T_{\text{O}_2}$ , and SABER observations between 14 May 2002 and 28 January 2004. We now consider this period for further intercomparison as an example of this approach.

First, we weight the SABER temperatures with a Gaussian emulating the OH VER (which is centred on interpolated heights of “fixed” density and has a full width at half minimum (FWHM) of 8 km). Then we use two methods to evaluate the density scale height,  $H^*$ , from which a grid of fixed density surfaces is created. In the first approach, we evaluate  $H^*$  (assuming  $H^* = H$ , the pressure scale height) using an interpolated SABER temperature at the height in question, and in the second, we estimate  $H^*$  directly from the slope of the two densities at the two heights predicted by the meteor technique. These were found to be effectively equivalent.

The meteor data used in this work were acquired before the development of the phase calibration technique described by Holdsworth et al. (2004b) which uses the meteor echoes themselves to calibrate the radar. A post-statistics approach was used to improve the phase characteristics of the meteor

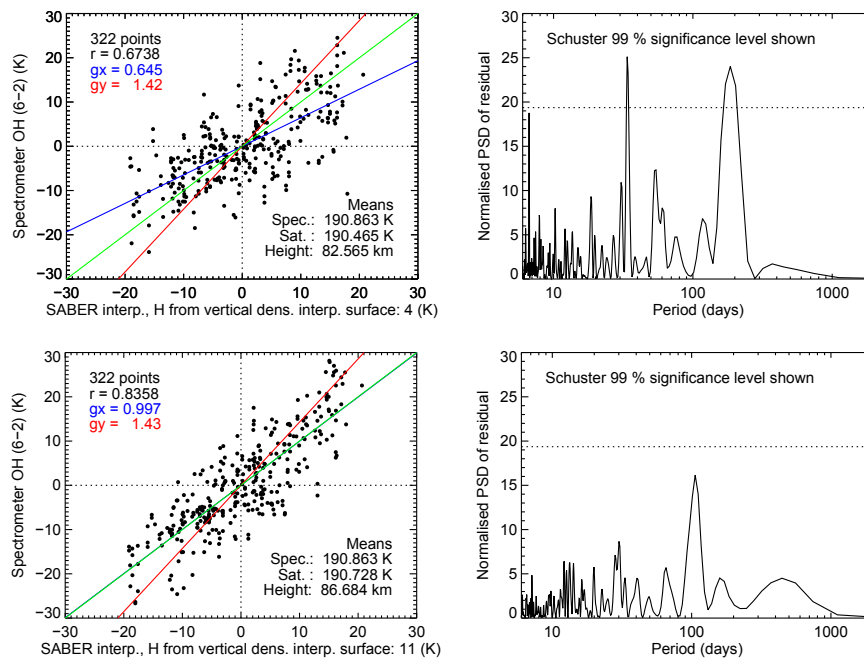


**Figure 7.** Two examples of the comparison between the spectrometer OH temperatures and the SABER temperatures interpolated to constant density surfaces. The panels on the left show the correlation values between the spectrometer and SABER temperatures for two density surfaces. The blue and red lines indicate lines of best fit made assuming that all experimental errors are in the SABER and spectrometer, respectively. The green line indicates the  $y = x$  line. The right-hand panels indicate Lomb–Scargle periodograms for the residuals between the spectrometer and SABER temperatures corresponding to the left-hand panels.

**Table 4.** Comparison between coincident TIMED SABER and spectrometer temperatures for the period 16 July 2002 to 25 January 2004 when the meteor radar data were available to calculate the neutral density.  $N$  is the number of points in each sample. See text for further details.

TIMED SABER and spectrometer temperatures, 16 Jul 2002 to 25 Jan 2004							
Emission	Measurement	Mean (K)	$N$	AO		SAO	
				Amplitude (K)	Phase (days)	Amplitude (K)	Phase (days)
OH (~ 87 km)	Spectrometer, OH(6–2)	$190.4 \pm 9.9$	5,699	$7.7 \pm 0.2$	$186 \pm 1$	$3.3 \pm 0.2$	$76 \pm 1$
	SABER, MDR density	$190.7 \pm 10.9$	322	$9.0 \pm 0.8$	$186 \pm 5$	$3.5 \pm 0.9$	$72 \pm 5$
	SABER, 1.6 $\mu\text{m}$ OH VER	$191.3 \pm 10.6$	279	$8.5 \pm 0.8$	$186 \pm 5$	$2.9 \pm 0.9$	$81 \pm 7$
	SABER, 2.0 $\mu\text{m}$ OH VER	$192.4 \pm 10.4$	279	$7.8 \pm 0.8$	$182 \pm 6$	$3.2 \pm 0.9$	$86 \pm 7$

returns, but because the radar was being used in a variety of different experimental modes during this period, it likely that the data are not of the quality of more recent meteor radar observations, and 10-day averages were used to determine the fixed density contours. These are shown in Fig. 6. Inspection of this figure indicates that variations in geometrical height of the constant density surfaces are generally less than 2 km on this timescale.

Figure 7 shows two examples of the comparison between the spectrometer and SABER temperatures on constant density surfaces. The density surface in the upper panels corresponds exactly to the lower curve height estimates, and the one in the lower panels corresponds to a surface interpo-

lated between the lower and upper curves. Using the  $\log_{10}\rho$  values for the lower- and upper-curve heights predicted by P. J. Younger (personal communication, 2016) for Tromsø (which are  $-4.99 \pm 0.07$  and  $-6.19 \pm 0.18 \text{ kg m}^{-3}$ , respectively), we estimate that the  $\log_{10}\rho$  value for the surface in the lower panels of Fig. 6 is  $-5.29 \pm 0.25 \text{ kg m}^{-3}$ . The summary of the correlation and temperature differences for the entire height range is shown in Fig. 8. The maximum correlation obtained in the 79 to 95 km height range is about 0.84, at a mean height of just under 87 km (86.7 km). The lowest mean discrepancy between the two data sets is also at the same height, which is negligible (0.14 K). This represents our best level of mean agreement and correlation obtained

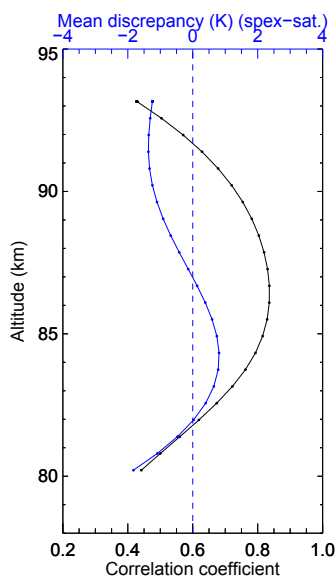


**Figure 8.** The correlation coefficient and the mean discrepancy between the spectrometer OH temperatures and the SABER temperatures when the latter are interpolated to a series of constant density levels. See text for further details.

between the spectrometer and SABER (and Aura, for that matter) temperatures (including weighting with OH VER and using measurements on fixed pressure surfaces). This means that the airglow layer appears to track the constant density surfaces estimated by the meteor technique more closely than the VER and pressure surface estimates provided by SABER.

To extend the intercomparison beyond a simple correlation, we harmonically analysed the OH data as we have done above. The results are shown in Table 4. This table shows a comparison between the spectrometer OH results for the period of the meteor radar observations, along with the coincident SABER results, both for the meteor radar determined constant density surfaces (“SABER MDR”) and for the 1.6 and 2.0  $\mu\text{m}$  OH VERs. Inspection of this table suggests good general agreement overall between the different weightings, with better agreement between the spectrometer OH and SABER MDR results for the mean temperature and the phase of the SAO but not for the other parameters, where either the 1.6 and 2.0  $\mu\text{m}$  OH VER weightings do better. So, while the overall correlations are improved by using a density surface weighting, the individual results from the harmonic fits are not necessarily improved. Clearly, further intercomparisons using more recent meteor radar results is suggested.

It is pleasing that the mean geometric height for the OH emission determined here ( $\sim 86.7$  km) is consistent with the empirically determined value of Baker and Stair (1988), and so the conclusions we reached earlier on the long-term variation of the airglow intensity and temperature variations remain valid. We also note that a 16-night comparison by Zhao et al. (2005) between the University of Illinois Na

wind and temperature lidar and the Utah State University CEDAR Mesospheric Temperature Mapper at the summit of Haleakalā Crater in Hawaii (20.8° N, 156.2° W) found a mean nocturnal altitude of 88.6 km with a nocturnal variability of  $\pm 3.0$  km for the OH(6,2) band emission layer. Trials with more recent meteor radar observations indicate that quality density estimates are possible with a 4 h sampling (P. J. Younger, personal communication, 2016). This strongly suggests that a meteor radar could be used to better determine the airglow emission height over relatively short timescales.

## 5 Summary and conclusions

OH(6–2) and O<sub>2</sub>(0–1) airglow emission observations show significant annual and semi-annual oscillations in both temperature and intensity. In the OH(6–2), the SAO maximises in the autumn and the AO in the winter. The AO takes a peak value of  $6.6 \pm 0.6$  K and the SAO a peak value of  $2.1 \pm 1.3$  K. In the case of the O<sub>2</sub>(0–1) temperatures, both the SAO and AO maximise in the autumn, with the SAO dominant at  $5.1 \pm 1.3$  K, about twice the magnitude of the AO at  $2.6 \pm 0.9$  K. The intensities show a similar variation through the year, with that between the O<sub>2</sub>(0–1) temperatures and intensities being striking. The O(<sup>1</sup>S) intensity shows a similarly strong agreement with the O<sub>2</sub>(0–1) temperature and intensity.

OH(6–2) temperatures measured in the present work agree well with coincident measurements, with TIME-GCM results, and with WINDII observations reported previously by Gelinat et al. (2008). Our O<sub>2</sub>(0–1) temperatures overestimate their mean but otherwise generally agree well with their results. Our results also agree with SABER and Aura MLS results presented previously for our location.

We used Aura MLS and TIMED SABER results to compare with our spectrometer results. We find good agreement between our OH(6–2) temperature measurements and OH weighted Aura MLS results for the mean, AO, and SAO, all agreeing to within the experimental uncertainty, with the suggestion of a downward bias in the Aura MLS mean temperature. We find better agreement between the techniques when we use the Aura MLS results from the 0.46 and 0.22 Pa retrieval levels where the residuals between the techniques minimise and the correlation coefficients maximise.

Our spectrometer O<sub>2</sub>(0–1) mean temperature results are biased high but agree with those from O<sub>2</sub>(0–1) weighted Aura MLS results to within the experimental uncertainty. The amplitude of the AO and the amplitude and phase of the SAO agree for the two techniques, but the phases of the AO do not. We note that we are at the limit of the validity for the Aura MLS measurements and that our O<sub>2</sub>(0–1) observations are quite noisy.

In the case of the SABER results, we find SABER 1.6 and 2.0  $\mu\text{m}$  VER weighted temperatures and the spectrometer OH(6–2) mean temperatures agree well over the 4.5 years of coincident measurements, but not to within the experimental

580

I. M. Reid et al.: Seasonal MLT-region nightglow intensities, temperatures, and emission heights

uncertainties. The spectrometer O<sub>2</sub>(0–1) temperatures agree to within the experimental uncertainties with the SABER temperatures using an O<sub>2</sub>(0–1) weighting, but the spectrometer uncertainties are large and the mean temperature is clearly an overestimate.

We used the SABER temperature results to show that the OH airglow emission heights appear to follow meteor-radar-derived constant density surfaces, and even at the relatively coarse sampling resolution of 10 days, using this to calculate the emission height significantly improves the correlation between the spectrometer OH and the SABER temperatures. Based on more recent meteor observations, this suggests that its application to more recent meteor radars would offer a way of better determining the actual emission height over time periods of 6 h or less.

*Data availability.* Aura MLS data are available from <http://disc.sci.gsfc.nasa.gov/Aura/data-holdings/MLS>. TIMED SABER data are available from <http://saber.gats-inc.com/data.php>. Buckland Park radar and optical data are available from the University of Adelaide upon request.

*Competing interests.* ATRAD Pty Ltd partially funded this work through the involvement of Iain M. Reid, Jonathan M. Woithe, and Joel P. Younger. An ATRAD meteor detection radar was used for the meteor observations used here.

*Acknowledgements.* Funding for this research was provided by the Australian Research Council grants A69943065, DP0450787, DP0878144, and DP1096901, by the Adelaide University ARC Small Grants Scheme, and by ATRAD Pty Ltd. The IDL wavelet analysis software was provided by C. Torrence and G. Compo, and is available at <http://atoc.colorado.edu/research/wavelets/>.

The topical editor, A. J. Kavanagh, thanks A. Liu and one anonymous referee for help in evaluating this paper.

## References

- Baker, D. J. and Stair, A. T.: Rocket measurements of the altitude distributions of the hydroxyl airglow, *Phys. Scripta*, 37, 611, doi:10.1088/0031-8949/37/4/021, 1988.
- Bittner, M., Offermann, D., Graef, H.-H., Donner, M., and Hamilton, K.: An 18-year time series of OH rotational temperatures and middle atmosphere decadal variations, *J. Atmos. Sol.-Terr. Phys.*, 64, 1147–1166, doi:10.1016/S1364-6826(02)00065-2, 2002.
- Buriti, R. A., Takahashi, H., Gobbi, D., de Medeiros, A. F., Nepomuceno, A. A., and Lima, L. M.: Semiannual oscillation of the mesospheric airglow at 7.4° S during the PSMOS observation period of 1998–2001, *J. Atmos. Sol.-Terr. Phys.*, 66, 567–572, doi:10.1016/j.jastp.2004.01.009, 2004.
- Coxon, J. A. and Foster, S. C.: Rotational analysis of hydroxyl vibration–rotation emission bands: Molecular constants for OH X2Π, 6 ≤ ν ≤ 10, *Can. J. Phys.*, 60, 41–48, doi:10.1139/p82-006, 1982.
- Ding, F., Yuan, H., Wan, W., Reid, I. M., and Woithe, J. M.: Occurrence characteristics of medium-scale gravity waves observed in OH and OI nightglow over Adelaide (34.5° S, 138.5° E), *J. Geophys. Res.*, 109, D14104, doi:10.1029/2003JD004096, 2004.
- Ern, M., Preusse, P., Gille, J. C., Hepplewhite, C. L., Mlynarczyk, M. G., Russell III, J. M., and Riese, M.: Implications for atmospheric dynamics derived from global observations of gravity wave momentum flux in stratosphere and mesosphere, *J. Geophys. Res.*, 116, D19107, doi:10.1029/2011JD015821, 2011.
- Espy, P. J., Stegman, J., Forkman, P., and Murtagh, D.: Seasonal variation in the correlation of airglow temperature and emission rate, *Geophys. Res. Lett.*, 34, L17802, doi:10.1029/2007GL031034, 2007.
- French, W. J. R. and Mulligan, F. J.: Stability of temperatures from TIMED/SABER v1.07 (2002–2009) and Aura/MLS v2.2 (2004–2009) compared with OH(6-2) temperatures observed at Davis Station, Antarctica, *Atmos. Chem. Phys.*, 10, 11439–11446, doi:10.5194/acp-10-11439-2010, 2010.
- Gelinas, L. J., Hecht, J. H., Walterscheid, R. L., Roble, R. G., and Woithe, J. M.: A seasonal study of mesospheric temperatures and emission intensities at Adelaide and Alice Springs, *J. Geophys. Res.*, 113, A01304, doi:10.1029/2007JA012587, 2008.
- Greet, P. A., French, W. J. R., Burns, G. B., Williams, P. F. B., Lowe, R. P., and Finlayson, K.: OH(6-2) spectra and rotational temperature measurements at Davis, Antarctica, *Ann. Geophys.*, 16, 77–89, doi:10.1007/s00585-997-0077-3, 1998.
- Grygalashvyly, M., Sonnemann, G. R., Lübken, F.-J., Hartogh, P., and Berger U.: Hydroxyl layer: Mean state and trends at midlatitudes, *J. Geophys. Res.-Atmos.*, 119, 12391–12419, doi:10.1002/2014JD022094, 2014.
- Hecht, J. H., Walterscheid, R. L., and Ross, M. N.: First measurements of the two-dimensional horizontal wave number spectrum from CCD images of the nightglow, *J. Geophys. Res.*, 99, 11449–11460, doi:10.1029/94JA00584, 1994.
- Hecht, J. H., Walterscheid, R. L., Woithe, J., Campbell, L., Vincent, R. A., and Reid, I. M.: Trends in airglow imager observations near Adelaide, Australia, *Geophys. Res. Lett.*, 24, 587–590, 1997.
- Hedin, A. E.: Extension of the MSIS thermospheric model into the middle and lower atmosphere, *J. Geophys. Res.*, 96, 1159–1172, doi:10.1029/90JA02125, 1991.
- Hobbs, B. G., Reid I. M., and Greet, P. A.: Mesospheric rotational temperatures obtained from the OH(6-2) transition at Adelaide, Australia, *J. Atmos. Terr. Phys.*, 58, 1337–1344, doi:10.1016/0021-9169(95)00168-9, 1996.
- Holdsworth, D. A., Reid, I. M., and Cervera, M. A.: Buckland Park all-sky interferometric meteor radar, *Radio Sci.*, 39, RS5009, doi:10.1029/2003RS003014, 2004a.
- Holdsworth, D. A., Tsutsumi, M., Reid, I. M., Nakamura, T., and Tsuda, T.: Interferometric meteor radar phase calibration using meteor echoes, *Radio Sci.*, 39, RS5012, doi:10.1029/2003RS003026, 2004b.
- Holdsworth, D. A., Morris, R. J., Murphy, D. J., Reid, I. M., Burns, G. B., and French, W. J. R.: Antarctic mesospheric temperature estimation using the Davis mesosphere-stratosphere-troposphere radar, *J. Geophys. Res.*, 111, D05108, doi:10.1029/2005JD006589, 2006.



## I. M. Reid et al.: Seasonal MLT-region nightglow intensities, temperatures, and emission heights

581

- Huang, F. T., Mayr, H. G., Reber, C. A., Russell, J. M., Mlynczak, and Mengel, J. G.: Stratospheric and mesospheric temperature variations for the quasi-biennial and semiannual (QBO and SAO) oscillations based on measurements from SABER (TIMED) and MLS (UARS), *Ann. Geophys.*, 24, 2131–2149, doi:10.5194/angeo-24-2131-2006, 2006.
- Jones Jr., M., Emmert, J. T., Drob, D. P., and Siskind, D. E.: Middle atmosphere dynamical sources of the semiannual oscillation in the thermosphere and ionosphere, *Geophys. Res. Lett.*, 44, 12–21, doi:10.1002/2016GL071741, 2017.
- Krassovsky, V. I., Shefov, N. N., and Yarin, V. I.: Atlas of the airglow spectrum 3000–12400 Å, *Planet. Space Sci.*, 9, 883–915, doi:10.1016/0032-0633(62)90008-9, 1962.
- Langhoff, S. R., Werner, H. J., and Rosmus, P.: Theoretical transition probabilities for the OH Meinel system, *J. Mol. Spectrosc.*, 118, 507–529, doi:10.1016/0022-2852(86)90186-4, 1986.
- Lee, C., Kim, J.-H., Jee, G., Lee, W., Song, I.-S., and Kim, Y. H.: New method of estimating temperatures near the mesopause region using meteor radar observations, *Geophys. Res. Lett.*, 43, 10580–10585, doi:10.1002/2016GL071082, 2016.
- Lee, C. S., Younger, J. P., Reid, I. M., Kim, Y. H., and Kim, J.-H.: The effect of recombination and attachment on meteor radar diffusion coefficient profiles, *J. Geophys. Res.-Atmos.*, 118, 3037–3043, doi:10.1002/jgrd.50315, 2013.
- Livesey, N. J., Read, W. G., Froidevaux, L., Lambert, A., Manney, G. L., Pumphrey, H. C., Santee, M. L., Schwartz, M. J., Wang, S., Cofield, R. E., Cuddy, D. T., Fuller, R. A., Jarnot, R. F., Jiang, J. H., Knosp, B. W., Stek, P. C., Wagner, P. A., and Wu, D. L.: EOS MLS Version 3.3 Level 2 data quality and description document, version 3.3x-1.0, JPL D-33509, Jet Propul. Lab., Pasadena, California, 2011.
- López-González, M. J., García-Comas, M., Rodríguez, E., López-Puertas, M., Shepherd, M. G., Shepherd, G. G., Sargoytchev, S., Aushv, V. M., Smith, S. M., Mlynczak, M. G., Russell, J. M., Brown, S., Cho, Y.-M., and Wiens, R. H.: Ground-based mesospheric temperatures at mid-latitude derived from O<sub>2</sub> and OH airglow SATI data: Comparison with SABER measurements, *J. Atmos. Sol.-Terr. Phys.*, 69, 2379–2390, doi:10.1016/j.jastp.2007.07.004, 2007.
- Marsh, D. R., Smith, A. K., Mlynczak, M. G., and Russell III, J. M.: SABER observations of the OH Meinel airglow variability near the mesopause, *J. Geophys. Res.*, 111, A10S05, doi:10.1029/2005JA011451, 2006.
- McDade, I. C.: The photochemistry of the MLT oxygen airglow emissions and the expected influences of tidal perturbations, *Adv. Space Res.*, 21, 787–794, doi:10.1016/S0273-1177(97)00674-1, 1998.
- Mies, F.: Calculated vibrational transition probabilities of OH(X<sup>2</sup>Π), *J. Mol. Spectrosc.*, 53, 150–188, doi:10.1016/0022-2852(74)90125-8, 1974.
- Noll, S., Kausch, W., Kimeswenger, S., Unterguggenberger, S., and Jones, A. M.: Comparison of VLT/X-shooter OH and O<sub>2</sub> rotational temperatures with consideration of TIMED/SABER emission and temperature profiles, *Atmos. Chem. Phys.*, 16, 5021–5042, doi:10.5194/acp-16-5021-2016, 2016.
- Reid, I. M. and Woithe, J. M.: Three Field Photometer Observations of short period gravity wave intrinsic parameters in the 80 to 100 km height region, *J. Geophys. Res.*, 110, D21108, doi:10.1029/2004JD005427, 2005.
- Reid, I. M. and Woithe, J. M.: The variability of the 558 nm OI airglow intensity measured over Adelaide, Australia, *Adv. Space Res.*, 39, 1237–1247, doi:10.1016/j.asr.2007.01.061, 2007.
- Reid, I. M., Holdsworth, D. A., Morris, R. J., Murphy, D. J., and Vincent, R. A.: Meteor observations using the Davis mesosphere-stratosphere-troposphere radar, *J. Geophys. Res.*, 111, A05305, doi:10.1029/2005JA011443, 2006.
- Reid, I. M., Spargo, A. J., and Woithe, J. M.: Seasonal variations of the nighttime O(<sup>1</sup>S) and OH(8-3) airglow intensity at Adelaide, Australia, *J. Geophys. Res.-Atmos.*, 119, 6991–7013, doi:10.1002/2013JD020906, 2014.
- Reisin, E. R., Scheer, J., Dyrland, M. E., Sigernes, F., Deehr, C. S., Schmidt, C., Höppner, K., Bittner, M., Ammosov, P. P., Gavril'yeva, G. A., Stegman, J., Perminov, V. I., Semenov, A. I., Knieling, P., Koppmann, R., Shiokawa, K., Lowe, R. P., López-González, M. J., Rodríguez, E., Zhao, Y., Taylor, M. J., Burti, R. A., Espy, P. J., French, W. J. R., Eichmann, K.-U., Burrows, J. P., and von Savigny, C.: Traveling planetary wave activity from mesopause region airglow temperatures determined by the Network for the Detection of Mesospheric Change (NDMC), *J. Atmos. Sol.-Terr. Phys.*, 119, 71–82, doi:10.1016/j.jastp.2014.07.002, 2014.
- Remsberg, E., Lingenfelter, G., Harvey, V. L., Grose, W., Russell III, J., Mlynczak, M., Gordley, L., and Marshall, B. T.: On the verification of the quality of SABER temperature, geopotential height, and wind fields by comparison with Met Office assimilated analyses, *J. Geophys. Res.*, 108, 4628, doi:10.1029/2003JD003720, 2003.
- Roble, R. G. and Ridley E. C.: A thermosphere-ionosphere-mesosphere electrodynamics general circulation model (TIME-GCM): Equinox solar cycle minimum simulations (30–500 km), *Geophys. Res. Lett.*, 21, 417–420, doi:10.1029/93GL03391, 1994.
- Schwartz, M. J., Lambert, A., Manney, G. L., Read, W. G., Livesey, N. J., Froidevaux, L., Ao, C. O., Bernath, P. F., Boone, C. D., Cofield, R. E., Daffer, W. H., Drouin, B. J., Fetzer, E. J., Fuller, R. A., Jarnot, R. F., Jiang, J. H., Jiang, Y. B., Knosp, B. W., Krueger, K., Li, J.-L. F., Mlynczak, M. G., Pawson, S., Russell III, J. M., Santee, M. L., Snyder, W. V., Stek, P. C., Thurstans, R. P., Tompkins, A. M., Wagner, P. A., Walker, K. A., Waters, J. W., and Wu, D. L.: Validation of the Aura Microwave Limb Sounder temperature and geopotential height measurements, *J. Geophys. Res.*, 113, D15S11, doi:10.1029/2007JD008783, 2008.
- Semenov, A. I., Shefov, N. N., and Medvedeva, I. V.: Longitudinal variations in the hydroxyl emission: 1. Temperature, *J. Geomagn. Aero.*, 53, 492–501, doi:10.1134/S0016793213040129, 2013.
- She, C. Y. and Lowe, R. P.: Seasonal temperature variations in the mesopause region at mid-latitude: comparison of lidar and hydroxyl rotational temperatures using WINDII/UARS OH Height profiles, *J. Atmos. Sol.-Terr. Phys.*, 60, 1573–1583, doi:10.1016/S1364-6826(98)00082-0, 1998.
- Shepherd, M. G., Evans, W. F. J., Hernandez, G., Offermann, D., and Takahashi, H.: Global variability of mesospheric temperature: Mean temperature field, *J. Geophys. Res.*, 109, D24117, doi:10.1029/2004JD005054, 2004.
- Shepherd, G. G., Cho, Y.-M., and Liu, G.: Correlations of mesospheric variability and their relation to the large-scale circulation during polar winter, *J. Atmos. Sol.-Terr. Phys.*, 69, 2279–2291, doi:10.1016/j.jastp.2007.06.007, 2007.

- Sivjee, G. G. and Shen, D.: Auroral optical emissions during the solar magnetic cloud event of October 1995, *J. Geophys. Res.*, 102, 7431–7437, doi:10.1029/97JA00195, 1997.
- Smith, S. M.: Seasonal variations in the correlation of mesospheric OH temperature and radiance at midlatitudes, *J. Geophys. Res.*, 117, A10308, doi:10.1029/2012JA017884, 2012.
- Sonnemann, G. R., Hartogh, P., Berger, U., and Grygalashvyly, M.: Hydroxyl layer: trend of number density and intra-annual variability, *Ann. Geophys.*, 33, 749–767, doi:10.5194/angeo-33-749-2015, 2015.
- Torrence, C. and Compo, G. P.: A practical guide to wavelet analysis, *B. Am. Meteorol. Soc.*, 79, 61–78, doi:10.1175/1520-0477(1998)079<0061:APGTWA>2.0.CO;2, 1998.
- Woithe, J. M.: Optical studies of the mesospheric region, PhD Thesis, University of Adelaide, available at: <http://hdl.handle.net/2440/37859> (last access: January 2016), 2000.
- Xu, J., Smith, A. K., Yuan, W., Liu, H.-L., Wu, Q., Mlynczak, M. G., and Russell III, J. M.: Global structure and long-term variations of zonal mean temperature observed by TIMED/SABER, *J. Geophys. Res.*, 112, D24106, doi:10.1029/2007JD008546, 2007.
- Xu, J., Smith, A. K., Liu, H.-L., Yuan, W., Wu, Q., Jiang, G., Mlynczak, M. G., Russell III, J. M., and Franke, S. J.: Seasonal and quasi-biennial variations in the migrating diurnal tide observed by Thermosphere, Ionosphere, Mesosphere, Energetics and Dynamics (TIMED), *J. Geophys. Res.*, 114, D13107, doi:10.1029/2008JD011298, 2009.
- Xu, J., Smith, A. K., Jiang, G., Gao, H., Wei, Y., Mlynczak, M. G., and Russell III, J. M.: Strong longitudinal variations in the OH nightglow, *Geophys. Res. Lett.*, 37, L21801, doi:10.1029/2010GL043972, 2010.
- Xu, J., Gao, H., Smith, A. K., and Zhu, Y.: Using TIMED/SABER nightglow observations to investigate hydroxyl emission mechanisms in the mesopause region, *J. Geophys. Res.*, 117, D02301, doi:10.1029/2011JD016342, 2012.
- Younger, J. P., Lee, C. S., Reid, I. M., Vincent, R. A., Kim, Y. H., and Murphy, D. J.: The effects of deionization processes on meteor radar diffusion coefficients below 90 km, *J. Geophys. Res.-Atmos.*, 119, 10027–10043, doi:10.1002/2014JD021787, 2014.
- Younger, J. P., Reid, I. M., Vincent, R. A., and Murphy, D. J.: A method for estimating the height of a mesospheric density level using meteor radar, *Geophys. Res. Lett.*, 42, 6106–6111, doi:10.1002/2015GL065066, 2015.
- Zhao, Y., Taylor, M. J., and Chu, X.: Comparison of simultaneous Na lidar and mesospheric nightglow temperature measurements and the effects of tides on the emission layer heights, *J. Geophys. Res.*, 110, D09S07, doi:10.1029/2004JD005115, 2005.
- Zhang, Y., Sheng, Z., Shi, H., Zhou, S., Shi, W., Du, H., and Fan, Z.: Properties of the Long-Term Oscillations in the Middle Atmosphere Based on Observations from TIMED/SABER Instrument and FPI over Kelan, *Atmosphere*, 8, 7, doi:10.3390/atmos8010007, 2017.
- Zhu, Y., Kaufmann, M., Ern, M., and Riese, M.: Nighttime atomic oxygen in the mesopause region retrieved from SCIAMACHY O(<sup>1</sup>S) green line measurements and its response to solar cycle variation, *J. Geophys. Res.-Space*, 120, 9057–9073, doi:10.1002/2015JA021405, 2015.

## References

- Agner, R. and A. Z. Liu (2015). Local time variation of gravity wave momentum fluxes and their relationship with the tides derived from LIDAR measurements. *J. Atmos. and Sol.-Terr. Phys.* 135, pp. 136–142. ISSN: 1364-6826. DOI: <https://doi.org/10.1016/j.jastp.2015.10.018>.
- Alexander, M. J., M. Geller, C. McLandress, S. Polavarapu, P. Preusse, F. Sassi, K. Sato, S. Eckermann, M. Ern, A. Hertzog, et al. (2010). Recent developments in gravity-wave effects in climate models and the global distribution of gravity-wave momentum flux from observations and models. *Quart. J. Roy. Meteor. Soc.* 136.650, pp. 1103–1124.
- AMS Glossary (2012). *Glossary of Meteorology, American Meteorological Society*.
- Andrews, D. G. and M. E. McIntyre (1976). Planetary Waves in Horizontal and Vertical Shear: The Generalized Eliassen-Palm Relation and the Mean Zonal Acceleration. *J. Atmos. Sci.* 33.11, pp. 2031–2048. DOI: [https://doi.org/10.1175/1520-0469\(1976\)033<2031:PWIHAV>2.0.CO;2](https://doi.org/10.1175/1520-0469(1976)033<2031:PWIHAV>2.0.CO;2).
- Andrioli, V. F., P. P. Batista, B. R. Clemesha, N. J. Schuch, and R. A. Buriti (2015). Multi-year observations of gravity wave momentum fluxes at low and middle latitudes inferred by all-sky meteor radar. *Ann. Geophys.* 33.9, pp. 1183–1193. DOI: [doi:10.5194/angeo-33-1183-2015](https://doi.org/10.5194/angeo-33-1183-2015).
- Andrioli, V. F., D. C. Fritts, P. P. Batista, and B. R. Clemesha (2013a). Improved analysis of all-sky meteor radar measurements of gravity wave variances and momentum fluxes. *Ann. Geophys.* 31.5, pp. 889–908. DOI: [doi:10.5194/angeo-31-889-2013](https://doi.org/10.5194/angeo-31-889-2013).
- Andrioli, V. F., D. C. Fritts, P. P. Batista, B. R. Clemesha, and D. Janches (2013b). Diurnal variation in gravity wave activity at low and middle latitudes. *Ann. Geophys.* 31, pp. 2123–2135. DOI: [doi:10.5194/angeo-31-2123-2013](https://doi.org/10.5194/angeo-31-2123-2013).
- Antonita, T. M., G. Ramkumar, K. K. Kumar, and V. Deepa (2008). Meteor wind radar observations of gravity wave momentum fluxes and their forcing toward the Mesospheric Semiannual Oscillation. *J. Geophys. Res. Atmos.* 113.D10.



- Baggaley, W. J. (2009). Meteoric Ionization: The Interpretation of Radar Trail Echoes. *The Radio Science Bulletin* 239.
- Beldon, C. L. and N. J. Mitchell (2009). Gravity waves in the mesopause region observed by meteor radar, 2: Climatologies of gravity waves in the Antarctic and Arctic. *J. Atmos. Sol. Terr. Phys.* 71.8, pp. 875–884.
- Beldon, C. L. and N. J. Mitchell (2010). Gravity wave–tidal interactions in the mesosphere and lower thermosphere over Rothera, Antarctica (68°S, 68°W). *J. Geophys. Res. Atmos.* 115.D18.
- Booker, J. R. and F. P. Bretherton (1967). The critical layer for internal gravity waves in a shear flow. *J. Fluid Mech.* 27.03, pp. 513–539.
- Bossert, K., D. C. Fritts, P.-D. Pautet, B. P. Williams, M. J. Taylor, B. Kaifler, A. Dörnbrack, I. M. Reid, D. J. Murphy, A. J. Spargo, and A. D. MacKinnon (2015). Momentum flux estimates accompanying multiscale gravity waves over Mount Cook, New Zealand, on 13 July 2014 during the DEEPWAVE campaign. *J. Geophys. Res.*
- Bowring, B. R. (1989). Transverse Mercator equations obtained from a spherical basis. *Survey Review* 30.233, pp. 125–133. DOI: 10.1179/sre.1989.30.233.125.
- Bretherton, F. P. (1969). Momentum transport by gravity waves. *Quart. J. R. Met. Soc.* 95, pp. 213–243.
- Bretherton, F. P. (1966). The propagation of groups of internal gravity waves in a shear flow. *Quarterly Journal of the Royal Meteorological Society* 92.394, pp. 466–480.
- Cepelcha, Z., J. Borovička, W. G. Elford, D. O. ReVelle, R. L. Hawkes, V. Porubčan, and M. Šimek (1998). Meteor phenomena and bodies. *Space Science Reviews* 84.3-4, pp. 327–471.
- Chau, J. L., D. L. Hysell, K. M. Kuyeng, and F. R. Galindo (2008). Phase calibration approaches for radar interferometry and imaging configurations: equatorial spread F results. *Ann. Geophys.* 26.8, pp. 2333–2343. DOI: 10.5194/angeo-26-2333-2008.
- Chau, J. L., J. M. Urco, J. P. Vierinen, R. A. Volz, M. Clahsen, N. Pfeffer, and J. Trautner (2019). Novel specular meteor radar systems using coherent MIMO techniques to study the mesosphere and lower thermosphere. *Atmos. Meas. Tech.* 12.4, pp. 2113–2127. DOI: 10.5194/amt-12-2113-2019.
- Chau, J. L., T. Renkwitz, G. Stober, and R. Latteck (2014). MAARSY multiple receiver phase calibration using radio sources. *J. Atmos. Sol. Terr. Phys.* 118, pp. 55–63. ISSN: 1364-6826. DOI: <https://doi.org/10.1016/j.jastp.2013.04.004>.

- Chau, J. L. and R. F. Woodman (2001). Three-dimensional coherent radar imaging at Jicamarca: comparison of different inversion techniques. *J. Atmos. Sol. Terr. Phys.* 63.2-3, pp. 253–261. ISSN: 1364-6826. DOI: [http://dx.doi.org/10.1016/S1364-6826\(00\)00142-5](http://dx.doi.org/10.1016/S1364-6826(00)00142-5).
- Chen, J.-S. (2004). On the phase biases of multiple-frequency radar returns of mesosphere-stratosphere-troposphere radar. *Radio Sci.* 39.5. ISSN: 1944-799X. DOI: 10.1029/2003RS002885.
- Chen, J.-S., J. Röttger, and Y.-H. Chu (2002). System phase calibration of VHF spaced antennas using the echoes of aircraft and incorporating the frequency domain interferometry technique. *Radio Sci.* 37.5, pp. 13-1-13-13. DOI: 10.1029/2002RS002604.
- Clahsen, M. (2018). Error analysis of wind estimates in specular meteor radar systems. MA thesis. Universitat Rostock.
- Clemesha, B. R., P. P. Batista, R. A. B. da Costa, and N. Schuch (2009). Seasonal variations in gravity wave activity at three locations in Brazil. *Ann. Geophys.* 27, pp. 1059–1065.
- Clemesha, B. R. and P. P. Batista (2008). Gravity waves and wind-shear in the MLT at 23°S. *Adv. Space Res.* 41.9, pp. 1472–1477.
- Crary, A. (1950). Stratosphere winds and temperatures from acoustical propagation studies. *J. Meteor.* 7.3, pp. 233–242.
- Dolman, B. K., I. M. Reid, and C. Tingwell (2018). Stratospheric tropospheric wind profiling radars in the Australian network. *Earth, Planets and Space* 70.1, p. 170.
- Dunkerton, T. J. (1982). Stochastic parameterization of gravity wave stresses. *J. Atmos. Sci.* 39.8, pp. 1711–1725.
- Egito, F., V. Andrioli, and P. Batista (2016). Vertical winds and momentum fluxes due to equatorial planetary scale waves using all-sky meteor radar over Brazilian region. *J. Atmos. Sol. Terr. Phys.* 149, pp. 108–119. ISSN: 1364-6826. DOI: <https://doi.org/10.1016/j.jastp.2016.10.005>.
- England, S., A. Dobbin, M. Harris, N. Arnold, and A. Aylward (2006). A study into the effects of gravity wave activity on the diurnal tide and airglow emissions in the equatorial mesosphere and lower thermosphere using the Coupled Middle Atmosphere and Thermosphere (CMAT) general circulation model. *J. Atmos. Sol. Terr. Phys.* 68.3, pp. 293–308. ISSN: 1364-6826. DOI: <https://doi.org/10.1016/j.jastp.2005.05.006>.

- Ern, M., P. Preusse, J. C. Gille, C. L. Hepplewhite, M. G. Mlynczak, J. M. Russell, and M. Riese (2011). Implications for atmospheric dynamics derived from global observations of gravity wave momentum flux in stratosphere and mesosphere. *J. Geophys. Res. Atmos.* 116.D19. ISSN: 2156-2202. DOI: 10.1029/2011JD015821.
- Fernandez, J. R. (2004). Interferometric studies of Polar Mesosphere Summer Echoes over Northern Scandinavia. PhD thesis. Univeristy of Nebraska.
- Forbes, J. M., G. Jun, and M. Saburo (1991). On the interactions between gravity waves and the diurnal propagating tide. *Planetary and Space Science* 39.9, pp. 1249–1257. ISSN: 0032-0633. DOI: [https://doi.org/10.1016/0032-0633\(91\)90038-C](https://doi.org/10.1016/0032-0633(91)90038-C).
- Fritts, D. C., D. Janches, and W. K. Hocking (2010a). Southern Argentina Agile Meteor Radar: Initial assessment of gravity wave momentum fluxes. *J. Geophys. Res. Atmos.* 115.D19.
- Fritts, D. C., D. Janches, W. K. Hocking, N. J. Mitchell, and M. J. Taylor (2012a). Assessment of gravity wave momentum flux measurement capabilities by meteor radars having different transmitter power and antenna configurations. *J. Geophys. Res. Atmos.* 117.D10.
- Fritts, D. C., D. Janches, H. Iimura, W. K. Hocking, J. V. Bageston, and N. M. P. Leme (2012b). Drake Antarctic Agile Meteor Radar first results: Configuration and comparison of mean and tidal wind and gravity wave momentum flux measurements with Southern Argentina Agile Meteor Radar. *J. Geophys. Res. Atmos.* 117.D2.
- Fritts, D. C., S. A. Smith, B. B. Balsley, and C. R. Philbrick (1988). Example of gravity wave saturation and local turbulence production in the summer mesosphere and lower thermosphere during the STATE experiment. *J. Geophys. Res.* 93, pp. 7015–7025.
- Fritts, D. C., D. Janches, H. Iimura, W. K. Hocking, N. J. Mitchell, R. G. Stockwell, B. Fuller, B. Vandeppeer, J. Hormaechea, C. Brunini, et al. (2010b). Southern Argentina Agile Meteor Radar: System design and initial measurements of large-scale winds and tides. *J. Geophys. Res. Atmos.* 115.D18.
- Fritts, D. C. (1984). Gravity wave saturation in the middle atmosphere: A review of theory and observations. *Rev. Geophys.* 22.3, pp. 275–308.
- Fritts, D. C. and M. J. Alexander (2003). Gravity wave dynamics and effects in the middle atmosphere. *Rev. Geophys.* 41.1.
- Fritts, D. C., T. Tsuda, T. E. VanZandt, S. A. Smith, T. Sato, S. Fukao, and S. Kato (1990). Studies of Velocity Fluctuations in the Lower Atmosphere Using the MU

- Radar. Part II: Momentum Fluxes and Energy Densities. *J. Atmos. Sci.* 47.1, pp. 51–66. DOI: 10.1175/1520-0469(1990)047<0051:SOVFIT>2.0.CO;2.
- Fritts, D. C. and R. A. Vincent (1987). Mesospheric momentum flux studies at Adelaide, Australia: Observations and a gravity wave-tidal interaction model. *J. Atmos. Sci.* 44.3, pp. 605–619.
- Fritts, D. C. and L. Yuan (1989). Measurement of Momentum Fluxes near the Summer Mesopause at Poker Flat, Alaska. *J. Atmos. Sci.* 46.16, pp. 2569–2579. DOI: 10.1175/1520-0469(1989)046<2569:MOMFNT>2.0.CO;2.
- Fritts, D. C., L. Yuan, M. H. Hitchman, L. Coy, E. Kudeki, and R. F. Woodman (1992). Dynamics of the equatorial mesosphere observed using the Jicamarca MST radar during June and August 1987. *J. Atmos. Sci.* 49.24, pp. 2353–2371.
- Fritts, D. C., R. B. Smith, M. Taylor, J. D. Doyle, S. D. Eckermann, A. Dörnbrack, M. Rapp, B. P. Williams, D. Pautet, K. Bossert, et al. (2016). The Deep Propagating Gravity Wave Experiment (DEEPWAVE): An Airborne and Ground-Based Exploration of Gravity Wave Propagation and Effects from their Sources throughout the Lower and Middle Atmosphere. *Bull. Amer. Meteor. Soc.* 97.3, pp. 425–453.
- Fukao, S. and K. Hamazu (2014). *Radar for Meteorological and Atmospheric Observations*. Springer Japan. DOI: 10.1007/978-4-431-54334-3.
- Fukao, S., T. Sato, P. T. May, T. Tsuda, S. Kato, M. Inaba, and I. Kimura (1988). A systematic error in MST/ST radar wind measurement induced by a finite range volume effect: 1. Observational results. *Radio Sci.* 23.1, pp. 59–73.
- Gardner, C. S., C. A. Hostetler, and S. J. Franke (1993). Gravity wave models for the horizontal wave number spectra of atmospheric velocity and density fluctuations. *J. Geophys. Res. Atmos.* 98.D1, pp. 1035–1049. ISSN: 2156-2202. DOI: 10.1029/92JD02051.
- Green, J. S. A. (1972). Large-scale motion in the upper stratosphere and mesosphere: an evaluation of data and theories. *Phil. Trans. R. Soc. Lond.* A334, pp. 577–583.
- Greenhow, J. S. and J. E. Hall (1960). The Importance of Initial Trail Radius on the Apparent Height and Number Distributions of Meteor Echoes. *Mon. Not. R. Astron. Soc.* 121.2, pp. 183–196. ISSN: 0035-8711. DOI: 10.1093/mnras/121.2.183.
- Hamilton, K. (1996). Comprehensive meteorological modelling of the middle atmosphere: a tutorial review. *J. Atmos. Terr. Phys.* 58.14, pp. 1591–1627.
- Haurwitz, B. (1961). Frictional effects and the meridional circulation in the mesosphere. *J. Geophys. Res.* 66.8, pp. 2381–2391.

- Heikkinnen, M. (1982). Geschlossene Formeln zur Berechnung räumlicher geodätischer Koordinaten aus rechtwinkligen Koordinaten. *Z. Ermess.* 107, pp. 207–211.
- Heising, R. A. (1928). Experiments and Observations Concerning the Ionized Regions of the Atmosphere. *Proc. Inst. Radio Engrn.* 16, pp. 75–99.
- Hines, C. (1960). Internal atmospheric gravity waves at ionospheric heights. *Can. J. Phys.* 38.11, pp. 1441–1481.
- Hitchman, M. H., K. W. Bywaters, D. C. Fritts, L. Coy, E. Kudeki, and F. Surucu (1992). Mean Winds and Momentum Fluxes over Jicamarca, Peru, during June and August 1987. *J. Atmos. Sci.* 49.24, pp. 2372–2383. DOI: 10.1175/1520-0469(1992)049<2372:MWAMF0>2.0.CO;2.
- Hocking, W. K. (2005). A new approach to momentum flux determinations using SKiYMET meteor radars. *Ann. Geophys.* 23.7, pp. 2433–2439.
- Hocking, W. K. (2018). Spatial distribution of errors associated with multistatic meteor radar. *Earth, Planets and Space* 70.1, p. 93. ISSN: 1880-5981. DOI: 10.1186/s40623-018-0860-2.
- Hocking, W. K. and T. Thayaparan (1997). Simultaneous and co-located observation of winds and tides by MF and meteor radars over London, Canada (43°N, 81°W), during 1994-1996. *Radio Sci.* 32, pp. 833–865. DOI: <https://doi.org/10.1029/96RS03467>, .
- Holdsworth, D. A., R. A. Vincent, and I. M. Reid (2001). Mesospheric turbulent velocity estimation using the Buckland Park MF radar. *Ann. Geophys.* 19.8, pp. 1007–1017.
- Holdsworth, D. A. (2005). Angle of arrival estimation for all-sky interferometric meteor radar systems. *Radio Sci.* 40.6. DOI: doi:10.1029/2005RS003245.
- Holdsworth, D. A., D. J. Murphy, I. M. Reid, and R. J. Morris (2008). Antarctic meteor observations using the Davis MST and meteor radars. *Adv. Space Res.* 42.1, pp. 143–154. ISSN: 0273-1177. DOI: <https://doi.org/10.1016/j.asr.2007.02.037>.
- Holdsworth, D. A., I. M. Reid, and M. A. Cervera (2004a). Buckland Park all-sky interferometric meteor radar. *Radio Sci.* 39.5. DOI: doi:10.1029/2003RS003014.
- Holdsworth, D. A., A. J. Spargo, I. M. Reid, and C. Adami (2020). Low Earth Orbit Object Observations Using the Buckland Park VHF Radar. *Radio Sci.* 55.2, e2019RS006873. DOI: 10.1029/2019RS006873.
- Holdsworth, D. A., M. Tsutsumi, I. M. Reid, T. Nakamura, and T. Tsuda (2004b). Interferometric meteor radar phase calibration using meteor echoes. *Radio Sci.* 39.5. DOI: doi:10.1029/2003RS003026.

- Houghton, J. (1978). The stratosphere and mesosphere. *Quart. J. Roy. Meteor. Soc.* 104.439, pp. 1–29.
- Janches, D., W. Hocking, S. Pifko, J. L. Hormaechea, D. C. Fritts, C. Brunini, R. Michell, and M. Samara (2014). Interferometric meteor head echo observations using the Southern Argentina Agile Meteor Radar. *J. Geophys. Res.: Space Phys.* 119.3, pp. 2269–2287. DOI: 10.1002/2013JA019241.
- Jia, M., X. Xue, S. Gu, T. Chen, B. Ning, J. Wu, X. Zeng, and X. Dou (2018). Multiyear Observations of Gravity Wave Momentum Fluxes in the Midlatitude Mesosphere and Lower Thermosphere Region by Meteor Radar. *J. Geophys. Res. Space Phys.* 123.7, pp. 5684–5703. DOI: 10.1029/2018JA025285.
- Jones, J., A. Webster, and W. Hocking (1998). An improved interferometer design for use with meteor radars. *Radio Sci.* 33.1, pp. 55–65.
- Kellogg, W. W. and G. F. Schilling (1951). A proposed model of the circulation in the upper stratosphere. *J. Meteor.* 8.4, pp. 222–230.
- Kilburn, C., S. Fukao, and M. Yamamoto (1995). Extended period frequency domain interferometry observations at stratospheric and tropospheric heights. *Radio Sci.* 30.4, pp. 1099–1109. DOI: <https://doi.org/10.1029/95RS00639>.
- Kim, Y.-J., S. D. Eckermann, and H.-Y. Chun (2003). An overview of the past, present and future of gravity-wave drag parametrization for numerical climate and weather prediction models. *Atmos. Ocean* 41.1, pp. 65–98.
- Kudeki, E. and S. J. Franke (1998). Statistics of momentum flux estimation. *J. Atmos. Sol. Terr. Phys.* 60.16, pp. 1549–1553.
- Kudeki, E. and G. R. Stitt (1987). Frequency domain interferometry: A high resolution radar technique for studies of atmospheric turbulence. *Geophys. Res. Lett.* 14.3, pp. 198–201. ISSN: 1944-8007. DOI: 10.1029/GL014i003p00198.
- Kuong, R.-M., Y.-H. Chu, S.-Y. Su, and C.-L. Su (2003). The Chung-Li VHF Radar as a Meteor Radar: System Phase Bias Estimation and Experimental Results. *Terr., Atmos. and Oc. Sci. COSPAR Colloquia Series* 14.2. Ed. by L.-H. Lyu, pp. 113–132. DOI: [https://doi.org/10.1016/S0964-2749\(02\)80227-X](https://doi.org/10.1016/S0964-2749(02)80227-X).
- Lee, C. S., J. P. Younger, I. M. Reid, Y. H. Kim, and J.-H. Kim (2013). The effect of recombination and attachment on meteor radar diffusion coefficient profiles. *J. Geophys. Res.: Atmos.* 118.7, pp. 3037–3043. DOI: 10.1002/jgrd.50315.
- Leovy, C. (1964). Simple models of thermally driven mesospheric circulation. *J. Atmos. Sci.* 21.4, pp. 327–341.

- Lieberman, R. S., D. A. Ortland, D. M. Riggan, Q. Wu, and C. Jacobi (2010). Momentum budget of the migrating diurnal tide in the mesosphere and lower thermosphere. *J. Geophys. Res. Atmos.* 115.D20. DOI: 10.1029/2009JD013684.
- Lilly, D. K. (1972). Wave momentum flux - a GARP problem. *Bull. Amer. Met. Soc.* 53, pp. 17–13.
- Lin, T.-H., Y.-H. Chu, C.-L. Su, and K.-F. Yang (2019). Radar phase offset estimate using ionospheric field-aligned irregularities and aircraft. *Terr., Atmos. and Oc. Sci.* 30, pp. 803–820. DOI: 10.3319/TA0.2019.05.09.01.
- Lindzen, R. S. (1981). Turbulence and stress owing to gravity wave and tidal breakdown. *J. Geophys. Res.* 86.C10, pp. 9707–9714.
- Lindzen, R. S. and S. Chapman (1969). Atmospheric tides. *Space Science Reviews* 10.1, pp. 3–188.
- Liu, A. Z., X. Lu, and S. J. Franke (2013). Diurnal variation of gravity wave momentum flux and its forcing on the diurnal tide. *J. Geophys. Res. Atmos.* 118.4, pp. 1668–1678.
- Liu, X., J. Xu, H.-L. Liu, and R. Ma (2008). Nonlinear interactions between gravity waves with different wavelengths and diurnal tide. *J. Geophys. Res.: Atmos.* 113.D8. DOI: 10.1029/2007JD009136.
- Lu, X., H.-L. Liu, A. Z. Liu, J. Yue, J. M. McInerney, and Z. Li (2012). Momentum budget of the migrating diurnal tide in the Whole Atmosphere Community Climate Model at vernal equinox. *J. Geophys. Res. Atmos.* 117.D7. DOI: 10.1029/2011JD017089.
- Luce, H., M. Yamamoto, S. Fukao, D. Helal, and M. Crochet (2001). A frequency domain radar interferometric imaging (FII) technique based on high-resolution methods. *J. Atmos. Sol. Terr. Phys.* 63.2-3, pp. 221–234. ISSN: 1364-6826. DOI: [http://dx.doi.org/10.1016/S1364-6826\(00\)00147-4](http://dx.doi.org/10.1016/S1364-6826(00)00147-4).
- Matsumoto, M., A. Shinbori, D. M. Riggan, and T. Tsuda (2016). Measurement of momentum flux using two meteor radars in Indonesia. *Ann. Geophys.* 34, pp. 369–377. DOI: doi:10.5194/angeo-34-369-2016.
- Mayr, H. G., J. G. Mengel, K. L. Chan, and H. S. Porter (1998). Seasonal variations of the diurnal tide induced by gravity wave filtering. *Geophys. Res. Lett.* 25.7, pp. 943–946.
- McIntyre, M. E. (1981). On the “wave momentum” myth. *J. Fluid Mech.* 106, pp. 331–347.
- McKinley, D. W. R. (1961). *Meteor Science and Engineering*. McGraw-Hill.

- McLandress, C. L. (2002). The seasonal variation of the propagating diurnal tide in the mesosphere and lower thermosphere. Part I: The role of gravity waves and planetary waves. *J. Atmos. Sci.* 59.5, pp. 893–906.
- McLandress, C. (1998). On the importance of gravity waves in the middle atmosphere and their parameterization in general circulation models. *J. Atmos. Sol. Terr. Phys.* 60.14, pp. 1357–1383. ISSN: 1364-6826. DOI: [https://doi.org/10.1016/S1364-6826\(98\)00061-3](https://doi.org/10.1016/S1364-6826(98)00061-3).
- Meyer, C. K. (1999). Gravity wave interactions with the diurnal propagating tide. *J. Geophys. Res.: Atmos.* 104.D4, pp. 4223–4239. DOI: 10.1029/1998JD200089.
- Miyahara, S. and J. M. Forbes (1991). Interactions between gravity waves and the diurnal tide in the mesosphere and lower thermosphere. *Met. Soc. of Japan* 69, pp. 523–531.
- Moss, A. C., C. J. Wright, R. N. Davis, and N. J. Mitchell (2016). Gravity-wave momentum fluxes in the mesosphere over Ascension Island (8°S, 14°W) and the anomalous zonal winds of the semi-annual oscillation in 2002. *Ann. Geophys.* 34.2, pp. 323–330. DOI: 10.5194/angeo-34-323-2016.
- Murayama, Y., T. Tsuda, and S. Fukao (1994). Seasonal variation of gravity wave activity in the lower atmosphere observed with the MU radar. *J. Geophys. Res. Atmos.* 99.D11, pp. 23057–23069. ISSN: 2156-2202. DOI: 10.1029/94JD01717.
- Murphy, D. J. and R. A. Vincent (1993). Estimates of momentum flux in the mesosphere and lower thermosphere over Adelaide, Australia, from March 1985 to February 1986. *J. Geophys. Res. Atmos.* 98.D10, pp. 18617–18638.
- Murphy, D. J. and R. A. Vincent (1998). Mesospheric momentum fluxes over Adelaide during the 2-day wave: Results and interpretation. *J. Geophys. Res. Atmos.* 103.D22, pp. 28627–28636.
- Muschinski, A., V. Lehmann, L. Justen, and G. Teschke (2005). Advanced radar wind profiling. *Meteorol. Z.* 14. DOI: 10.1127/0941-2948/2005/0067.
- Nakamura, T., T. Tsuda, M. Yamamoto, S. Fukao, and S. Kato (1993). Characteristics of gravity waves in the mesosphere observed with the middle and upper atmosphere radar, 1, Momentum flux. *J. Geophys. Res.* 98, pp. 8899–8899.
- Olson, D. K. (1996). Converting Earth-centered, Earth-fixed coordinates to geodetic coordinates. *IEEE Trans. Aerosp. Electron. Syst.* 32.1, pp. 473–476. ISSN: 0018-9251. DOI: 10.1109/7.481290.



- Ortland, D. A. and M. J. Alexander (2006). Gravity wave influence on the global structure of the diurnal tide in the mesosphere and lower thermosphere. *J. Geophys. Res.* 11. DOI: 10.1029/2005JA011,467.
- Palmer, R. D., S. Vangal, M. F. Larsen, S. Fukao, T. Nakamura, and M. Yamamoto (1996). Phase calibration of VHF spatial interferometry radars using stellar sources. *Radio Sci.* 31.1, pp. 147–156. DOI: 10.1029/95RS02319.
- Palmer, R. D., T.-Y. Yu, and P. B. Chilson (1999). Range imaging using frequency diversity. *Radio Science* 34.6, pp. 1485–1496. ISSN: 1944-799X. DOI: 10.1029/1999RS900089.
- Placke, M., P. Hoffmann, and M. Rapp (2015). First experimental verification of summertime mesospheric momentum balance based on radar wind measurements at 69°N. *Ann. Geophys.* 33.9, pp. 1091–1096.
- Placke, M., P. Hoffmann, E. Becker, C. Jacobi, W. Singer, and M. Rapp (2011a). Gravity wave momentum fluxes in the MLT—Part II: Meteor radar investigations at high and midlatitudes in comparison with modeling studies. *J. Atmos. Sol. Terr. Phys.* 73.9, pp. 911–920.
- Placke, M., P. Hoffmann, R. Latteck, and M. Rapp (2014). Gravity wave momentum fluxes from MF and meteor radar measurements in the polar MLT region. *J. Geophys. Res. Sp. Phys.* 120.1, pp. 736–750. DOI: 10.1002/2014JA020460.
- Placke, M., G. Stober, and C. Jacobi (2011b). Gravity wave momentum fluxes in the MLT—Part I: seasonal variation at Collm (51.3°N, 13.0°E). *J. Atmos. Sol. Terr. Phys.* 73.9, pp. 904–910.
- Press, W. H., S. A. Teukolsky, W. T. Vetterling, and B. P. Flannery (1992). *Numerical Recipes in C: The Art of Scientific Computing*. Cambridge University Press.
- Protat, A. and I. Zawadzki (1999). A Variational Method for Real-Time Retrieval of Three-Dimensional Wind Field from Multiple-Doppler Bistatic Radar Network Data. *J. Atmos. Oc. Tech.* 16.4, pp. 432–449. DOI: 10.1175/1520-0426(1999)016<0432:AVMFRT>2.0.CO;2.
- Reid, I. M. (2015). MF and HF radar techniques for investigating the dynamics and structure of the 50 to 110 km height region: A review. *Prog. Earth Planet. Sci.*
- Reid, I. M., A. J. Spargo, J. M. Woithe, A. R. Klekociuk, J. P. Younger, and G. G. Sivjee (2017). Seasonal MLT-region nightglow intensities, temperatures, and emission heights at a Southern Hemisphere midlatitude site. *Ann. Geophys.* 35.3, pp. 567–582. DOI: 10.5194/angeo-35-567-2017.

- Reid, I. M., B. G. W. Vandeppeer, S. C. Dillon, and B. M. Fuller (1995). The new Adelaide medium frequency Doppler radar. *Radio Sci.* 30.4, pp. 1177–1189.
- Reid, I. M. and J. M. Woithe (2005). Three-field photometer observations of short-period gravity wave intrinsic parameters in the 80 to 100 km height region. *J. Geophys. Res.: Atmos.* 110.D21. DOI: 10.1029/2004JD005427.
- Reid, I. M. and J. P. Younger (2012). 60 years of meteor radar at Adelaide. *13th International Workshop on Technical and Scientific Aspects of MST Radar*.
- Reid, I. M. and J. P. Younger (2016). 65 years of meteor radar research at Adelaide. Vol. Proceedings of the IMC, Egmond.
- Reid, I. M. (1987). Some aspects of Doppler radar measurements of the mean and fluctuating components of the wind field in the upper middle atmosphere. *J. Atmos. Terr. Phys.* 49.5, pp. 467–484.
- Reid, I. M., R. Rüster, P. Czechowsky, and G. Schmidt (1988). VHF radar measurements of momentum flux in the summer polar mesosphere over Andenes (69°N, 16°E), Norway. *Geophys. Res. Lett.* 15.11, pp. 1263–1266.
- Reid, I. M., R. Rüster, P. Czechowsky, and A. J. Spargo (2018). VHF radar measurements of momentum flux using summer polar mesopause echoes. *Earth, Planets and Space* 70.1, p. 129.
- Reid, I. M. and R. A. Vincent (1987). Measurements of mesospheric gravity wave momentum fluxes and mean flow accelerations at Adelaide, Australia. *J. Atmos. Terr. Phys.* 49.5, pp. 443–460.
- Renkowitz, T., C. Schult, R. Latteck, and G. Stober (2015). Validation of the radiation pattern of the VHF MST radar MAARSY by scattering off a sounding rocket’s payload. *Adv. Radio Sci.* 13.B. Pp. 41–48.
- Ribstein, B. and U. Achatz (2016). The interaction between gravity waves and solar tides in a linear tidal model with a 4-D ray-tracing gravity-wave parameterization. *J. Geophys. Res.: Space Phys.* 121.9, pp. 8936–8950. DOI: 10.1002/2016JA022478.
- Richter, J. H., F. Sassi, R. R. Garcia, K. Matthes, and C. A. Fischer (2008). Dynamics of the middle atmosphere as simulated by the Whole Atmosphere Community Climate Model, version 3 (WACCM3). *J. Geophys. Res.* 113.D8.
- Riggin, D. M., T. Tsuda, and A. Shinbori (2016). Evaluation of momentum flux with radar. *J. Atmos. Sol. Terr. Phys.*

- Robertson, D. S., D. T. Liddy, and W. G. Elford (1953). Measurements of winds in the upper atmosphere by means of drifting meteor trails I. *J. Atmos. and Terr. Phys.* 4, pp. 255–270.
- Sato, K. (1994). A statistical study of the structure, saturation and sources of inertio-gravity waves in the lower stratosphere observed with the MU radar. *J. Atmos. Terr. Phys.* 56.6, pp. 755–774. ISSN: 0021-9169. DOI: [http://dx.doi.org/10.1016/0021-9169\(94\)90131-7](http://dx.doi.org/10.1016/0021-9169(94)90131-7).
- Sato, K. (1990). Vertical Wind Disturbances in the Troposphere and Lower Stratosphere Observed by the MU Radar. *J. Atmos. Sci.* 47.23, pp. 2803–2817. DOI: 10.1175/1520-0469(1990)047<2803:VWDITT>2.0.CO;2.
- Sato, K. (1993). Small-Scale Wind Disturbances Observed by the MU Radar during the Passage of Typhoon Kelly. *J. Atmos. Sci.* 50.4, pp. 518–537. DOI: 10.1175/1520-0469(1993)050<0518:SSWDOB>2.0.CO;2.
- Schlatter, N., T. Grydeland, N. Ivchenko, V. Belyey, J. Sullivan, C. L. Hoz, and M. Blixt (2013). Radar interferometer calibration of the EISCAT Svalbard Radar and a additional receiver station. *J. Atmos. Sol. Terr. Phys.* 105-106, pp. 287–292. ISSN: 1364-6826. DOI: <https://doi.org/10.1016/j.jastp.2012.11.017>.
- Sica, R. J. and A. T. Russell (1999). How many waves are in the gravity wave spectrum? *Geophys. Res. Lett.* 26.24, pp. 3617–3620. DOI: <https://doi.org/10.1029/1999GL003683>.
- Smith, A. K. (2012). Global Dynamics of the MLT. *Surveys in Geophysics* 33.6, pp. 1177–1230. ISSN: 1573-0956. DOI: 10.1007/s10712-012-9196-9.
- Spargo, A. J. (2016). Radar Measurements of Gravity Wave Characteristics in the MLT. MA thesis. University of Adelaide, School of Physical Sciences.
- Spargo, A. J., I. M. Reid, A. D. MacKinnon, and D. A. Holdsworth (2017). Mesospheric gravity wave momentum flux estimation using hybrid Doppler interferometry. *Ann. Geophys.* 35, pp. 733–750. DOI: <https://doi.org/10.5194/angeo-35-733-2017>.
- Steel, D. I. and W. G. Elford (1991). The height distribution of radio meteors: comparison of observations at different frequencies on the basis of standard echo theory. *J. Atmos. Terr. Phys.* 53.5, pp. 409–417. ISSN: 0021-9169. DOI: [https://doi.org/10.1016/0021-9169\(91\)90035-6](https://doi.org/10.1016/0021-9169(91)90035-6).
- Stober, G. and J. L. Chau (2015). A multi-static and multi-frequency novel approach for specular meteor radars to improve wind measurements in the MLT region. *Radio Sci.* 50.5.

- Stober, G., J. L. Chau, J. Vierinen, C. Jacobi, and S. Wilhelm (2018). Retrieving horizontally resolved wind fields using multi-static meteor radar observations. *Atmos. Meas. Tech.* 11.8, pp. 4891–4907. DOI: 10.5194/amt-11-4891-2018.
- Sugar, G. R. (1964). Radio propagation by reflection from meteor trails. *Proceedings of the IEE*. DOI: DOI:10.1109/PROC.1964.2801.
- Sullivan, J. M., N. Ivchenko, M. Lockwood, T. Grydeland, E. M. Blixt, and B. S. Lanchester (2006). Phase calibration of the EISCAT Svalbard Radar interferometer using optical satellite signatures. *Ann. Geophys.* 24.9, pp. 2419–2427. DOI: 10.5194/angeo-24-2419-2006.
- Thomas, R. M., P. S. Whitham, and W. G. Elford (1986). Frequency Dependence of Radar Meteor Echo Rates. *Proc. ASA* 6.3, pp. 303–306.
- Thorsen, D., S. J. Franke, and E. Kudeki (1997). A new approach to MF radar interferometry for estimating mean winds and momentum flux. *Radio Sci.* 32.2, pp. 707–726.
- Torrence, C. and G. P. Compo (1998). A Practical Guide to Wavelet Analysis. *Bull. Amer. Meteor. Soc.*
- Tsuda, T., S. Kato, T. Yokoi, T. Inoue, M. Yamamoto, T. VanZandt, S. Fukao, and T. Sato (1990). Gravity waves in the mesosphere observed with the middle and upper atmosphere radar. *Radio Sci.* 25.5, pp. 1005–1018.
- Valentic, T. A., J. P. Avery, S. K. Avery, and R. C. Livingston (1997). Self-survey calibration of meteor radar antenna arrays. *IEEE Trans. Geosci. Remote Sens.* 35.3, pp. 524–531. ISSN: 1558-0644. DOI: 10.1109/36.581960.
- Vaudrin, C. V., S. E. Palo, and J. L. Chau (2018). Complex Plane Specular Meteor Radar Interferometry. *Radio Sci.* ISSN: 1944-799X. DOI: 10.1002/2017RS006317.
- Vierinen, J., J. L. Chau, H. Charuvil, J. M. Urco, M. Clahsen, V. Avsarkisov, R. Marino, and R. Volz (2019). Observing mesospheric turbulence with specular meteor radars: A novel method for estimating second order statistics of wind velocity. *Earth and Space Science.*
- Vincent, R. A. and S. M. Ball (1981). Mesospheric winds at low- and mid-latitudes in the southern hemisphere. *J. Geophys. Res. Space Phys.* 86.A11, pp. 9159–9169.
- Vincent, R. A., S. Kovalam, D. C. Fritts, and J. R. Isler (1998). Long-term MF radar observations of solar tides in the low-latitude mesosphere: Interannual variability and comparisons with the GSWM. *J. Geophys. Res. Atmos.* 103.D8, pp. 8667–8683. DOI: 10.1029/98JD00482.

- Vincent, R. A., S. Kovalam, I. M. Reid, and J. P. Younger (2010). Gravity wave flux retrievals using meteor radars. *Geophys. Res. Lett.* 37.14.
- Vincent, R. A. and I. M. Reid (1983). HF Doppler measurements of mesospheric gravity wave momentum fluxes. *J. Atmos. Sci.* 40.5, pp. 1321–1333.
- Vincent, R. A. (2015). The dynamics of the mesosphere and lower thermosphere: a brief review. *Prog. Earth Planet. Sci.* 2.1, pp. 1–13.
- Wang, C. Y. and Y. H. Chu (2001). Interferometry investigations of blob-like sporadic E plasma irregularity using the Chung-Li VHF radar. *J. Atmos. Terr. Phys.* 63, pp. 123–133.
- Wang, D.-Y. and D. C. Fritts (1990). Mesospheric Momentum Fluxes Observed by the MST Radar at Poker Flat, Alaska. *J. Atmos. Sci.* 47.12, pp. 1512–1521. DOI: 10.1175/1520-0469(1990)047<1512:MMFOBT>2.0.CO;2.
- Wang, D.-Y. and D. C. Fritts (1991). Evidence of Gravity Wave–Tidal Interaction Observed near the Summer Mesopause at Poker Flat, Alaska. *J. Atmos. Sci.* 48.4, pp. 572–583. DOI: 10.1175/1520-0469(1991)048<0572:E0GWIO>2.0.CO;2.
- Watanabe, S. and S. Miyahara (2009). Quantification of the gravity wave forcing of the migrating diurnal tide in a gravity wave-resolving general circulation model. *J. Geophys. Res.* 114.D7. DOI: 10.1029/2008JD011218.
- de Wit, R. J., R. E. Hibbins, and P. J. Espy (2014a). The seasonal cycle of gravity wave momentum flux and forcing in the high latitude northern hemisphere mesopause region. *J. Atmos. Sol. Terr. Phys.* 127, pp. 21–29.
- de Wit, R. J., R. E. Hibbins, P. J. Espy, Y. J. Orsolini, V. Limpasuvan, and D. E. Kinnison (2014b). Observations of gravity wave forcing of the mesopause region during the January 2013 major Sudden Stratospheric Warming. *Geophys. Res. Lett.* 41.13, pp. 4745–4752.
- de Wit, R. J., D. Janches, D. C. Fritts, and R. E. Hibbins (2016). QBO modulation of the mesopause gravity wave momentum flux over Tierra del Fuego. *Geophys. Res. Lett.* 43.8, pp. 4049–4055. ISSN: 1944-8007. DOI: 10.1002/2016GL068599.
- Woodman, R. F. (1997). Coherent radar imaging: Signal processing and statistical properties. *Radio Sci.* 32.6, pp. 2373–2391. ISSN: 1944-799X. DOI: 10.1029/97RS02017.
- Xu, J., A. K. Smith, H.-L. Liu, W. Yuan, Q. Wu, G. Jiang, M. G. Mlynczak, and J. M. Russell (2009). Estimation of the equivalent Rayleigh friction in mesosphere/lower thermosphere region from the migrating diurnal tides observed by TIMED. *J. Geophys. Res.* 114.D23103. DOI: 10.1029/2009JD012209.

- Yigit, E. and A. S. Medvedev (2017). Influence of parameterized small-scale gravity waves on the migrating diurnal tide in Earth's thermosphere. *J. Geophys. Res. Space Phys.* 122.4, pp. 4846–4864. DOI: 10.1002/2017JA024089.
- Younger, J. P. and I. M. Reid (2017). Interferometer angle-of-arrival determination using precalculated phases. *Radio Sci.* ISSN: 1944-799X. DOI: 10.1002/2017RS006284.
- Younger, J. P., I. M. Reid, and R. A. Vincent (2013). Mutual coupling of antennas in a meteor radar interferometer. *Radio Sci.* 48.2, pp. 118–121. ISSN: 1944-799X. DOI: 10.1002/rds.20026.
- Younger, J. P., I. M. Reid, R. A. Vincent, and D. J. Murphy (2015). A method for estimating the height of a mesospheric density level using meteor radar. *Geophys. Res. Lett.* 42.14, pp. 6106–6111. DOI: 10.1002/2015GL065066.
- Younger, J. P. (2011). Theory and Applications of VHF Meteor Radar Observations. PhD thesis. The University of Adelaide.
- Yu, T.-Y. (2000). Radar Studies of the Atmosphere using Spatial and Frequency Diversity. PhD thesis. University of Nebraska.